National Academy of Sciences of Ukraine

Institute for Information Recording of the NAS of Ukraine

Institute for Information Recording Uzhgorod laboratory of optoelectronics and photonics materials of the Institute for Information Recording of the NAS of Ukraine

Technical Center of the NAS of Ukraine

Uzhgorod National University

INTERNATIONAL MEETING

CLUSTERS AND NANOSTRUCTURED MATERIALS
(CNM-6)

Uzhgorod *Vodograj* Ukraine,
5-9 October 2020

PROGRAM & MATERIALS
OF THE MEETING

Uzhgorod
2020

УДК 536:669
ББК 34

Published by the decision of the Organizing Committee of CNM-6 and the Academic Council of the Institute for Information Recording NAS of Ukraine

Materials of the International Meeting "Clusters and nanostructured materials (CNM-6)" – Uzhgorod, Ukraine, 2020 – 374 p.

The materials represent the contents of meeting's reports based on the results of fundamental and applied works on topical questions in the field of nanostructured systems, nanomaterials and nanotechnologies. Main attention is given to the consideration of problems of nanophysics and nanoelectronics, to atomic and electronic structure of cluster and nanostructured materials, amorphous alloys, nanostructured films and coatings, colloidal and biofunctioal materials, to study of their properties. The results of investigations in the field of supramolecular chemistry, synthesis of nanoparticles, nanostructores and multifunctional nanomaterials, physico-chemistry of superficial phenomena and diagnostics of nanosystems are presented.

The edition is designed for scientists, engineers, higher school lecturers, post-graduates and students of corresponding specialities.

ISBN 978-966-02-9366-3

ORGANIZING COMMITTEE:

Chairmen:

Naumovets' A.G. (Kiev, Ukraine)

Co-Chairmen:

Kryuchin A.A. (Kiev, Ukraine)
Uvarov V.M. (Kiev, Ukraine)

Members:

Beljaev O.E., Bespalov S.A., Brodin M.S. Chekhun V.F., Kartel M.T., Komisarenko S.V., Koshechko V.G., Kuchuk-Yatsenko S.I., Malchevskii I.A., Pekhnyo V.I., Petrov V.V., Pokhodenko V.D., Ragulya A.V., Semynozhenko V.P., Vlaykov G.G., Voevodin V.M., Vysochanskii Yu.M.

Secretary:

Rubish V.M. (Uzhgorod, Ukraine)

International program committee:

Agabekov V.(Belarus), Bilous A.G. (Ukraine), Bih L.(Morocco), Bulavin L. (Ukraine), Elouadi B. (France), Firstov S.A. (Ukraine), Flakhbart K. (Slovakia), Gomonnai A. (Ukraine), Horbyk P.(Ukraine), Kikineshi O.(Hungary), Kladko V. (Ukraine), Kranjčec M.(Croatia), Kopcansky P.(Slovakia), Kryuchyn A.(Ukraine), Kuchmiy S.(Ukraine), Lukyanchuk I.(France), Marchenko O. (Ukraine), Matolin V. (Czech Republic), Mezzane D.(Morocco), Poklonskiy (Belarus), Poroshin V. (Ukraine), Prokopenko V. (Ukraine), Rizak V.(Ukraine), Studenjak I. (Ukraine), Veres M. (Hungary), Vityaz' P. (Belarus), Vysochanskii Yu. (Ukraine), Wojciechowski W. (Poland), Yatsenko L. (Ukraine)

Local Organizing Committee:

Rubish V., Kabatcii V.,Mykaylo O., Makar L., Pop M., Yasinko T.

PROGRAM

MONDAY, 5^{TH} OF OCTOBER, 2020

8^{00} – 13^{00} – registration of CNM’6 participants

13^{00} – 14^{00} – lunch

15^{00}– 15^{15} – Opening MEETING (official speakers)

PLENARY
Chairman: **Karbivskyy V.**

15^{15} – 15^{55} – THERMAL TRANSPORT IN VAN DER WAALS CRYSTALS MM'P2(S,Se)6 (M - Cu, Ag; M' - In, Bi) WITH DIFFERENT DIPOLE ORDERING
Liubachko V., Oleaga A., Salazar A., Glukhov K., Kohutych A., Pogodin A., **Vysochanskii Yu.**

15^{55} –16^{30} – coffee-break

16^{30} –17^{10} – PHOTORREFRACTIVE AND DIELECTRIC PARAMETERS OF DOUBLE-DOPED $Sn_2P_2S_6$ CRYSTALS
M. Tsyhyka, S. Hasynets, A. Molnar, R. Pavlyshyn, К. Glukhov, A. Кohutych, **A. Grabar**

17^{10} –17^{50} – COMPUTER-INTEGRATED MODEL OF As-S ATOMIC CLUSTERS CONDENSATION
Ivanitsky V.P., Kovtunenko V.S., Ryaboschuk M.M.

17^{50} –18^{20} – LASER RECORDING OF NANOSIZED ELEMENTS ON THIN FILMS OF CHALCOGENIDE GLASSY SEMICONDUCTORS
KryuchynA.A., Petrov V.V., Rubish V.M., Kostyukevych S.O.

18^{20} –18^{50} – INNOVATIVE NANOMATERIALS AND DEVELOPMENTS AT THE NATIONAL ACADEMY OF SCIENCES-USE AND OPPORTUNITIES FOR COMMERCIALIZATION
Bespalov S.A., Malchevsky I. A., **Uvarov V. N.**

19^{00}– 20^{00} – dinner

TUESDAY, 6TH OF OCTOBER, 2020

8^{00} – 9^{00} – breakfast

PLENARY
Chairman: **Rubish V.**

9^{00}– 9^{40} – **MODEL CALCULATIONS OF THE COMPLEX CRYSTALS PHONON SPECTRUM DISPERSION**
Nebola I.I.

SECTION

9^{40}– 10^{00} – OPTICALLY ACTIVE COATING BASED ON CHALCOHENID GLASSES FOR MIDDLE IR RANGE PHOTODETECTORS
Kabatsii V.M.

10^{00} – 10^{20} – GOLD NANOPARTICLES FOR BIOMEDICAL APPLICATION
Mukha Iu., Vityuk N., Khodko A., Severynovska O., Eremenko A.

10^{20} – 10^{50} – coffee-break

SECTION
Chairman: **Nebola I.**

10^{00} – 12^{20} – ON THE GROWTH AND PROPERTIES OF PURE AND Ag-DOPED ZnO NANOCOMPOSITES
Ievtushenko A., Karpyna V., Shtepliuk I., Ericksson J., Yakimova R., Khranovskyy V.

12^{20} – 12^{40} – THE MORPHOLOGY, ELECTRONIC STRUCTURE, OPTICAL PROPERTIES AND CYTOTOXICITY OF Ag-DOPED ZnO NANOSTRUCTURES
Ievtushenko A., Khyzhun O., Karpyna V., Bykov O., Zahornyi M., Dzhagan V., Yukhymchuk V., Valakh M., Zagorodnya S., Naumenko K.3, Zaremba P., Khranovskyy V.

12^{40} – 13^{00} – GLUCURONIC ACID-BASED HYDROGELS
Dil K.V., Okovityy S.I., Kondratyuk N.V.

13^{00} – 14^{00} – lunch

SECTION
Chairman: **Barabash M.**

14^{00} – 14^{20} – EPR STUDY OF MAGNETIC NANOPARTICLES ENSEMBLES PROMISING FOR BIOMEDICAL APPLICATIONS
Konchits A.A., Shanina B.D., Krasnovyd S.V., Shevchenko Yu.B., Petranovs’ka A.L., Rieznichenko L.S.

14^{20} – 14^{40} – BINDING OF CALIX[4]ARENE TO THE A-KNOB OF FIBRIN: IN SILICO PROVES IN VITRO
Didkivkyi V.A., Hrabovskyi O.O., Humenyuk A.S., Selikhova A.I., Banya M.O., Cherenok S.O., Chernyshenko V.O.

14^{40} – 15^{00} – OBTAINING TECHNOLOGY OF HYBRID NANOMATERIALS CARBON NANOTUBES - GRAPHENE NANOPARTICLES
Sementsov Yu.I., Ivanenko K.O., Grebelna Yu.V., Kartel M.T., Karachevtseva L.A., Makhno S.M., Zhuravskyi S.V., Wang Bo, Yang Weiyou

15^{00} – 15^{30} – coffee-break

SECTION
Chairman: **Ivanitsky V.**

15^{30}– 15^{50} – MANIFESTATION OF FERROELECTRIC PROPERTIES OF ALUMINUM-SUBSTITUTED NANOSIZED LITHIUM-IRON SPINELS
Kaykan L.S., Sijo A.K., Mazurenko J.S., Ostapovych N.V.

15^{50}– 16^{10} – INVESTIGATION OF THE MORPHOLOGY AND LUMINESCENCE PROPERTIES OF MG-DOPED ZnO NANOSTRUCTURES GROWN AT DIFFERENT SUBSTRATE TEMPERATURES
Myroniuk D. V., Karpyna V. A., Myroniuk L. A., Khranovskyy V. D., Ievtushenko A. I.

16^{10}– 16^{30} – ULTRASONIC AND MAGNETIC-FIELD-ASSISTED ARRANGEMENT OF NANOSIZED CRYSTALLITES OF COBALT-CONTAINING LAYERED DOUBLE HYDROXIDES
Pashkevich Yu. G., Salak A. N., Vieira D. E. L., Lukienko I. M., Shapovalov Yu. O., Fedorchenko A. V., Fertman E. L., Babkin R. Yu., Shilin A. D., Rubanik V.V., Rubanik V. V. Jr., Ferreira M. G. S., Vieira J. M.

16^{30}– 18^{00} – POSTER SECTION (DISCUSSION)

19^{00}– 20^{00} – dinner

WEDNESDAY, 7TH OF OCTOBER, 2020

8^{00} – 9^{00} – breakfast

PLENARY
Chairman: **Rubish V.**

9^{00}– 9^{40} – THE SPECIAL TECHNOLOGIES OF SYNTHESIZING MATERIALS WITH SPECIFIC PROPERTIES
Zhiguts Yu.Yu.

SECTION
Chairman: **Zhiguts Yu.**

9^{40} – 10^{00} – NEW TECHNOLOGIES OF DIFFUSION SATURATION TITANIUM OF STEEL SURFACE
Zhiguts Yu.Yu., Krajnjaj I.I., **Karpovych V.A.**

10^{00} – 10^{20} – RESEARCH OF TECHNOLOGIES FOR PRODUCING FUNCTIONAL COATINGS BY COMBINED METHODS OF SHS-ALLOYING SURFACES OF STEEL BY METALS
Zhiguts Yu.Yu., Segeda Yu.V., **Kasynetsj S.O.**

10^{20} –10^{40} – EQUIPMENT FOR PLASMA SPRAYING
Zhiguts Yu.Yu., Legeta Ya.P., **Strukov B.M.**

10^{40} –11^{10} – coffee-break

SECTION
Chairman: **Zhiguts Yu.**

11^{10} – 11^{30} – INTEGRATED DIFFUSION SATURATION OF THERMITE STEEL SURFACE BY POLYMERS
Zhiguts Yu.Yu., **Zub I.M.**

11^{30} – 11^{50} – PONDEROMOTIVE FORCES AS A REASON FOR DESTRUCTION OF VIRUS INTERACTING WITH NANOPARTICLES
V. Lozovski, **N. Rusinchuk** and V. Lysenko

11^{50} – 12^{10} – JOINT ADSORPTION OF METHANE AND WATER ON HYDROPHOBIC AND HYDROPHILIC SILICA ADSORBENTS
Turov V.V., Gun'ko V.M., **Krupska T.V.**

12^{10} – 12^{30} – PHOTOCHEMICAL SYNTHESIS OF METAL-SEMICONDUCTOR COMPOSITES BASED ON CRYSTALLINE GRAPHITIC CARBON NITRIDE FOR PHOTOCATALYTIC HYDROGEN PRODUCTION
Shvalagin V.V., Korzhak A.V., Kutsenko O.S., Kuchmiy S.Ya.

12^{30} – 12^{50} – SERS SUBSTRATES BASED ON LATERALLY ORDERED GOLD NANOSTRUCTURES FOR DETECTING ORGANIC MOLECULES
Hreshchuk O.M., Yukhymchuk V.O., Dzhagan V.M., Indutnyi I.Z., Min’ko V.I., Lytvyn P.M., Danko V.A.

13^{00} – 14^{00} – lunch

14^{00} – 14^{20} – METALLIC REPLICA OF THE NANOSTRUCTURED TEMPLATE SURFACE AS A TOOL FOR SMART TEXTILES
Barabash M.Yu., Suprun N.P., Pozhilov-Nesmiyan G.M., Martynchuk V.E., Kolesnichenko A.A., Rybov L.V., Litvin R.V.

14^{20} – 14^{40} – FESEM STUDY OF SURFACE MORPHOLOGY OF ARRAYS OF NOBLE METALS NANOPARTICLES
Makar L.I., Mudry S., Rubish V.M., Shtablavyi I., Yasinko T.I.

14^{40} –15^{10} – coffee-break

15^{10} – 18^{00} – POSTER SECTION (DISCUSSION)

19^{00}– 20^{00} – dinner

THURSDAY, 8TH OF OCTOBER, 2020

8^{00} – 9^{00} – breakfast

PLENARY

Chairman: **Karbivskyy V.**

9^{00} – 9^{40} – FORMATION OF Ag AND Au NANOPARTICLES ARRAYS AND SOME ASPECTS OF THEIR PRACTICAL USE
Rubish V.M.

9^{40} – 10^{20} – ON THE LONGITUDINAL ELECTRO-SCALAR WAVE IN THE NANOSTRUCTURES, WAVE GUIDES AND MAXWELL ELECTRODYNAMICS
Simulik V.M., Zajac T.M.

10^{20} –10^{50} – coffee-break

SECTION

Chairman: **Simulik V.**

10^{50} – 11^{10} – MULTIPLE MECHANISMS OF HOLOGRAPHIC GARTING RECORDING IN POLYMER NANOCOMPOSITES WITH GOLD NANOPARTICLES
S. Kokenyesi, I.Csarnovich, S.Molnar, A. Bonyar, D. Alkhalil, A.Burunkova

11^{10} – 11^{30} – THE POLARIZABILITY OF METAL NANOISLANDS ON A DIELECTRIC SUBSTRATE
Korotun A.V., Titov I.M., Rubish V.M.

11^{30} – 11^{50} – INNOVATIVE NANOLAYER VACUUM ARC COATINGS FOR SURFACE HARDENING OF PRODUCTS THAT OPERATE IN DIFFICULT CONDITIONS
Stolbovoy V.A., Andreev A.A., Voevodin V.N., Serdiuk I.V., Dolomanov A.V.

11^{50} – 12^{10} – THERMOMAGNETIC EFFECT IN NANOFILMS AND CAPILLARIES
Shevchenko S.I., Konstantinov A.M.

12^{10} – 12^{30} – FORMATION OF THIN DRY DRAWN GRAPHITE FILMS AND PROPERTIES OF PHOTOSENSITIVE GRAPHITE/n-InSe JUNCTIONS
Savitskii P.I., Kovalyuk M.Z., Tovarnitskii M.V., **Kovalyuk Z.D.**

12^{30} – 12^{50} – SAPATIALLY MODULATED PHASES IN ANTIFERRODISTORTIVE MULTIFERROICS
Anna N. Morozovska, Eugene A. Eliseev, Deyang Chen, **Vladislav Shvetz,** Christopher T. Nelson, and Sergei V. Kalinin

13^{00} – 14^{00} – lunch

SECTION
Chairman: **Zajac T.**

14^{00} – 14^{20} – OPTICAL CUBIC NONLINEARITY OF THIN FILMS OF PALLADIUM OXIDE: VALUE, DYNAMICS AND NATURE
V. Liakhovetskyi, A. Brodin, V. Rudenko, M. Brodyn, V. Styopkin

14^{20} – 14^{40} – MANIFESTATION OF FERROELECTRIC PROPERTIES OF ALUMINUM-SUBSTITUTED NANOSIZED LITHIUM-IRON SPINELS
Kaykan L.S., Sijo A.K., Mazurenko J.S., Ostapovych N.V.

14^{40} – 15^{00} – SYNTHESIS AND CHARACTERIZATIONS OF COLLOIDAL Ag_2ZnSnS_4 AND Cu_2ZnSnS_4 NANOCRYSTAL THIN FILMS DEPOSITED BY SPIN-COATING
Mazur N.V., Dzhagan V.M., Havrylyuk Ye.O., Valakh M.Ya., Kapush O.A., Hreshchuk O.M., Yukhymchuk V.O.

15^{00} – 15^{20} – THE MECHANISMS AND DYNAMICS OF ANTIOXIDANT ACTION OF NANOCERIA AND CERIA-BASED NANOPARTICLES
Vladyslav Seminko, Pavel Maksimchuk, Ganna Grygorova, Elena Okrushko, Yuri Malyukin

15^{20} –15^{50} – coffee-break

SECTION
Chairman: **Ivanitsky V.**

15^{50} – 16^{10}– ELECTRICAL PROPERTIES OF MERCURY MODIFIED AMORPHOUS SELENIUM
Kyrylenko V.K., **Rubish V.M.**, Nykyruy L., Pisak R.P., Durkot M.O., Zapukhlyak Z.R., Fedelesh V., Uvarov V.N.

16^{10} – 16^{30}– AMORPHOUS CHALCOGENIDES WITH PHASE-CHANGE EFFECT
Durkot M.O., **Kyrylenko V.K.**, Kryuchyn A.A., PetrovV.V., Pop M.M., Rubish V.M., Yurkin I.M.

16^{30} – 18^{00}– POSTER SECTION (DISCUSSION)

19^{00}– 20^{00} – dinner

FRIDAY, 9TH OF OCTOBER, 2020

8^{00} – 9^{00} – breakfast

Satellite conference ACCELERATE

Invited lectures:

Chairman V. Rizak

9^{00} **Grand opening of the ACCELERATE Satellite Session**

9^{30} Vladimir Matolin, Salma Baghdadi, Natalia Popovych, Vitalii Bilanych, Oleksandr Chobal, Vasyl Rizak
The outpost CERIC-ERIC in Ukraine: Current State and Prospects

10^{00} Matúš Orendáč, Slavomír Gabáni, Pavol Farkašovský, Emil Gažo, Jozef Kačmarčík, Gabriel Pristáš, Konrad Siemensemeyer, Natalya Shitsevalova, and Karol Flachbart
Magnetic phases in two-dimensional geometrically frustrated Shastry-Sutherland system TmB4

10^{30} Vladimir Matolin, Natalia Tsudi, Natalia Popovych, Vasyl Rizak
Investigating the short range order of chalcogenide amorphous materials by photoelectron spectroskopy

11^{00} Leonid Dubrovinsky, Iryna Chobal, Anna Pakhomova, Oleksandr Chobal, Aleksandr Kurnosov, Volodymyr Adamiv, Vasyl Rizak
Structural, mechanical and thermodynamic properties of lithium potassium tetraborate crystals under high pressure: DFT calculations and synchrotron radiation X-ray diffraction

11^{30} M. Vorokhta, L. Piliai, I. Khalakhan, D. Tomeček, P. Fitl, M. Vrňata, J. Lančok, I. Matolínová,
V. Matolín
Near ambient pressure XPS for in operando study of gas sensors

12^{00} Bih.L., Guranich P.P., Mykaylo O.A., Pisak R.P., Rizak I.M., Rubish V.M., Solomon A.M., Tsiple M.
Structure and properties of chalcohalodenide glasses and composities on their basis

12^{30} Elouadi B., Barj M., Gasinets S.M., Guranich P.P., Makar L.I., Mykaylo O.A., Pop M.M., Rizak I.M., Rubish V.M., Solomon A.M.
Nanocomposities with ferroelectric properties in As(Ge)-Sb-S(Se)-I system

13^{00}-14^{30} Dinner

Chairman V. Rubish

14^{30} Latyshev V., Kozejova M., Vorobiov S., Shylenko O., You. H., Komanicky V.
Non-precious metal catalyst systems prepared by magnetron sputtering for hydrogen evolution reaction

15^{00} Kostyuk O.B., Głowa Ł., Naidych B.P., Tsymbalyuk T.P., Mezhylovska L.Y., Nykyruy L.I.
Analysis of the Growth and Crystal Structure for Pb0.9Cd0.1Te:Pb Thin Films

15^{30} Lofaj F., Shilenko O., Bilanych V.S., Bilanych B.V., Komanicky V., Feher A., Rizak V.M.
Investigation of laser induced effects in As-Se glasses and films based on them by nano- and microindentation methods

16^{00} Korposh S. O., Trikur I. I., Sichka M.Y., Tsoma I. Y., Rizak V. M.
Bacteriorhodopsin as a biological material for optical recording, processing and security information.

16^{30} Zapukhlyak Z.R., Rubish V.M., Wisz G., Yavorskyi R.S., Nykyruy L.I.
SCAPS simulation of ZnO/CdS/CdTe/CuO heterostructure for photovoltaic application

17^{00} Csach K., Bilanych V.S., Jurikova A., Miskuf J., Bilanych V.V., Rizak V.M.
Studies of As-Se glasses and films based on them by differential scanning calorimetry

17^{30} Popovych N., Gažova Z., Rizak V.M.
Application of the photoelectron spectroscopy to study the organic materials properties: adenine molecules and amyloid fibers

18^{00} **Discussion of invited lectures and closing ceremony of the ACCELERATE Satellite Session**

18^{20} **Closing MEETING**

POSTERS

EFFECT OF Se-CONTENT DOPING ON ELECTRONIC, DYNAMICAL AND MECHANICAL PROPERTIES OF $TlInS_2$ LAYERED CRYSTAL

T. Babuka, O.O. Gomonnai, K.E. Glukhov, L.Yu. Kharkhalis, A.V. Gomonnai, D.R.T. Zahn, M. Makowska-Janusik

DEVELOPMENT OF HIGH-EFFICIENT SOLAR CELLS WITH PYRAZOLINE LUMINOPHOR COATING LAYER

Ie.V. Beliak, D.Yu. Manko

MIXING AND SELF-ORGANIZATION OF THE STRUCTURE OF MATERIALS UNDER SEVERE PLASTIC DEFORMATION

Beygelzimer Y., Kulagin R., Davydenko O., Dmitrenko V.

ELECTROCHEMICAL SYNTHESIS OF NANOCRYSTALLINE Mo-RICH SUPERALLOYS

Bersirova O.L., Kublanovsky V. S.

INDENTATION SIZE EFFECTS AND MECHANICAL PROPERTIES OF SUPERIONIC MIXED CRYSTALS WITH ISOVALENT CATION SUBSTITUTION

Bilanych V.S., Skubenych K.V., Babilya M.I., Pogodin A.I., Studenyak I.P.

ELECTRONIC STRUCTURE OF Na_2GeSe_3 CRYSTALS

Bletskan D.I., Vakulchak V.V., Studenyak I.P.

THIN FILMS OF SAMARIUM VANADATE NANOPARTICLES FOR ENHANCED LIGHT HARVESTING OF NEAR UV AND VISIBLE LIGHT

Chukova O.V., Dorofeeva A.I., Nedilko S.A., Nedilko S.G., Voitenko T.A., Paszkowicz W., Rahimi Mosafer H.S., Manousaki M., Savva K., Stratakis E.I.

PROXIMITY-INDUCED TRIPLET SUPERCONDUCTIVITY IN $Bi_2Sr_2Ca_2Cu_3O_{6+X}:La_{2/3}Sr_{1/3}MnO_3$ NANOCOMPOSITES

Dmitrenko V.Yu., Krivoruchko V.N., Tarenkov V.Yu.

SURFACE MORPHOLOGY AND OPTICAL CHARACTERISTICS OF ARRAYS OF RANDOMLY DISTRIBUTED GOLD NANOPARTICLES

Durkot M.O., Kyrylenko V.K., Tarnaj A.A., Vlaykov G.G., Kremenitsky V.V., Novichenko V.M.

DIELECTRIC PROPERTIES OF $Cs_2Ag_2P_2Se_6$ CRYSTALS

Molnar A., **Gal D.**, Ban H., Haysak A.

THERMOKINETICS OF FORMATION AND OXIDATION OF CARBON NANOFORMS

Garbuz V.V., Silinska T.A., Kuzmenko L.M., Petrova V.A.

FIRST PRINCIPLES STUDY OF FERROELECTRIC AND ANTIFERROMAGNETIC STATES IN MIXED $M1M2P_2S(Se)_6$ CRYSTALS

Glukhov K.E., Babuka T.Ya., Kharkhalis L.Yu., Vysochanskii Yu.M.

DETERMINATION OF TOXICITY OF HYBRID NANOCOMPLEXES COMPRISING NANOPARTICLES OF GADOLINIUM ORTHOVANADATE AND CHOLESTEROL

Goltsev A.M., Malyukin Yu.V., Bondarovych M.O., Babenko N.M., Gayevska Yu.O., Dubrava T.G., Volkova N.O., Klochkov V.K., Ostankova L.V.

INVESTIGATION OF RADIOPROTECTIVE ACTIVITY OF CERIUM OXIDE CEO$_{2\text{-}X}$ AND ORTHOVANADATE Gd$_{0.9}$Eu$_{0.1}$VO$_4$ NANOPARTICLES *IN VIVO*

Grygorova G.V., Klochkov V.K., Yefimova S.L.

EFFECT OF INCREASING THE THERMAL CONDUCTIVITY OF SOME MOLECULAR CRYSTALS

Yu.V. Horbatenko, O.O. Romantsova, A.I. Krivchikov, O.A. Korolyuk

DIELECTRIC PROPERTIES CHANGES IN AGED GLASSY SELENIUM

Horvat A.A., Mikla V.V., Minkovich V.V., Molnar A.A., Solomon A.M., Rubish V.M.

SYNTHESIS AND CRYSTAL STRUCTURE OF NEW MIXED ORTHOVANADATES Pr$_{0.5}R_{0.5}$VO$_4$ (R = Sm, Gd, Dy, Er, Yb)

Hreb V.M., Tupys A.M., Vasylechko L.O.

ORTHOVANADATE GdYVO$_4$:Eu^{3+} NANOPARTICLES WITH SWITCHABLE REDOX-ACTIVITY

Hubenko K. O., Yefimova S. L., Maksimchuk P. O., Kavok N. S., Klochkov V. K., Malyukin Yu. V.

TEMPERATURE DEPENDENCE OF SURFACE-DOPED TiO$_2$ EMISSION

O. F. Isaieva, V.I. Dzhagan, V. Shymanovska, D.R.T. Zahn, G.Yu. Rudko

THE DIELECTRIC FUNCTION OF THE COMPOSITE WITH THE METAL-GRAPHENE NANORODS

Karandas Ya.V., Korotun A.V., Titov I.M.

MECHANISMS OF FORMATION AND PHYSICAL PROPERTIES OF 2D-STRUCTURES Al AND In

Karbivska L.I., Smolyak S.S., **Karbivskyy V.L.**, Romansky A.A.

TECHNOLOGICAL APPROACH TO ZnO NANOSTRUCTURES GROWTH FROM METALORGANIC COMPOUNDS FOR PHOTOCATALYTIC APPLICATIONS

KARPYNA V.A., MYRONIUK L.A., MYRONIUK D.V., BYKOV O.I., ZAHORNYI M.M., Ievtushenko A.I.

TOPOLOGY OF BAND STRUCTURE AND SPATIAL DISTRIBUTION OF ELECTRON DENSITY IN SEMICONDUCTORS OF In-Se SYSTEM

Kharkhalis L.Yu., Liakh M.V., Glukhov K.E. , Babuka T.Ya.

AB INITIO INVESTIGATION OF STRUCTURAL AND ELECTRONIC PROPERTIES OF THE INSE DILUTED MAGNETIC MATERIALS

Kharkhalis L.Yu., Glukhov K.E., Babuka T. Ya., Korolevych O.O.

CNTS FORMATION BY PRODUCTS OF METHANE AIR CONVERSION AT MODERATE TEMRERATURES

Khovavko A., Nebesniy A., Svyatenko A., Filonenko D., Kotov V., Bondarenko B., Nie G.

STRUCTURE AND MECHANICAL PROPERTIES OF VACUUM ARC V-O-N COATINGS

Klimenko I.O., Belous V.A., Kolodiy I.V., Vasilenko R.L., Kuprin A.S., Ovcharenko V.D., Tolmachova G.N. , Gilewicz A., Warcholinski B.

IMPACT OF ABERRATIONS AND DEFOCUSING ON SPECKLE SUPPRESSION EFFICIENCY IN LASER PICO PROJECTORS WHEN USING NANO-STRUCTURAL DOE BASED ON THIN FILM

Kliuieva T.Yu.

MAGNETICALLY SENSITIVE NANOCOMPOSITES WITH CARBON-CONTAINING SURFACE

Gorbyk P.P., Petranovska A.L., Dzyubenko L.S., Oranska O.I., Abramov M.V., Palyanytsya B.B., Kulyk T.V., **Korniichuk N.M.**, Kusyak A.P., Kusyak N.V.

THE MAPS OF THE ELECTROMAGNETIC WAVES IN THE NANOCOMPOSITE WITH METALLIC 1D-INCLUSIONS

Korotun A.V., Pavlishche N.I.

THE MECHANISM OF FORMATION OF POROUS STRUCTURE OF THE DERMIS COLLAGEN MODIFIED ECOSAFETY DIFFERENT CRYSTALS OF NATURAL MINERALS

Kozar Oksana

X-RAY LUMINESCENCE OF CADMIUM-MODIFIED THIN FILMS OF ARSENIC DISULFIDE

Krasilinets V.M., Loya V.Yu., Chychura I.I., Birov M.M., Popovich K.P., Edinak O.V.

ELECTROCHEMICAL PARAMETERS OF THIN TIN FILMS IN CYCLING IN LITHIUM-ION BATTERIES

Kublanovsky V., Globa N., Nikitenko V., Babenkov E., Shmatok Yu., Bersirova O.

ACID TREATED CRYSTALLINE GRAPHITIC CARBON NITRIDE, A NEW MATERIAL FOR VISIBLE LIGHT SELECTIVE ORGANIC COMPOUNDS PHOTO-OXIDATION

Kuchmiy S.Ya., Shvalagin V.V., Kompanets M.O.

EFFECT OF SILVER BY COPPER SUBSTITUTION ON FERRIELECTRIC PROPERTIES IN $CuInP_2X_6$ LAYERED COMPOUNDS

Liubachko V., Oleaga A., Salazar A., Vysochanskii Yu., Kohutych A., Pogodin A.

FORMATION OF HGSE NANOCYSTALLINE INCLUSIONS IN THE MATRIX OF AMORPHOUS SELENIUM FILMS

MakarL.I., Mudry S., Nykyruy L., Pisak R.P., Rubish V.M., Shtablavyi I., Bespalov S.A., Solomon A.M., Yavorskyi R.S.

IMPROVING HYDROXYL RADICAL SCAVENGING PROPERTIES OF CeO_{2-X} NANOCRYSTALS BY DOPING AND UV PRE-IRRADIATION

Maksimchuk P.O., Seminko V.V., Sedyh O.O., Aslanov A.V., Malyukin Yu.V.

ATOMIC FORCE SPECTROSCOPY FOR SORPTION PROPERTIES ESTIMATIONS OF FILMS IN SENSOR APPLICATIONS

Malyuta S.V., Rusavsky A.V., Nazarov O.M., Lytvyn P.M.

ELECTRICAL AND MAGNETIC PROPERTIES OF POLYMER NANOCOMPOSITES BASED ON NICKEL FERRITE MODIFIED WITH COPPER SULFIDE

Mazurenko R.V., Prokopenko S.L., Abramov M.V., Gunja G.M., Makhno S.M., Gorbyk P.P.

GOLD NANOPARTICLES-COATED OPTICAL FIBRE-TIP PROBES FOR COMMON AND ULTRAFAST SERS

Morozov Ye.M.

AB INITIO CALCULATIONS OF CRYSTAL AND ELECTRONIC STRUCTURE OF SOLID SOLUTIONS BASED ON LEAD CHALCOGENIDES

Nykyruy L.I., **Naidych B.P.**, Kostyuk O.

PHONON SPECTRA OF THE Cu_7SiS_5I AND Ag_7SiS_5I CRYSTALS

Nebola I.I., Katanytsia A.F., Shteyfan A.Ya., Sidey V.I., Ochkay I.I., Studenyak I.P.

PECULIARITIES OF DOUBLE ELECTRON-PHONON RESONANCE IN RAMAN SPECTRA OF GRAPHENE AND SINGLE-WALLED CARBON NANOTUBES

Nikolenko A.S., Strelchuk V.V., Stubrov Yu.Yu. and Gubanov V.O.

PHOTOLUMINESCENT AND STRUCTURAL PROPERTIES OF THIN ZnO FILMS DOPED WITH RARE EARTH METALS

Oberemok O.S., Dubikovskyi O.V, Sabov T.V, Kosulya O.V, Melnik V.P, Kladko V.P, Romanyuk B.M, Popov V.G, Gudymenko O.Yo.

MASS SPECTROMETRY STUDY OF CLUSTERS FORMATION BETWEEN DIMETHYL SULFOXID AND ANTIBIOTICS

Pashynska V.A., Kosevich M.V., Gomory A.

OPTICAL PROPERTIES OF X-RAY IRRADIATED $(Ga_{0.4}In_{0.6})_2Se_3$ FILMS

Studenyak I.P., **Pop M.M.**, Kranjčec M., Solomon A.M., Suslikov L.M.

X-RAY AND FESEM STUDY OF MERCURY MODIFIED CRYSTALLIZED SELENIUM FILMS

Rubish V.M., Makar L.I., Mudry S., **Pisak R.P.**, Shtablavyi I., Solomon A.M., Katanova L.

ELECTRICAL CONDUCTIVITY OF SUPERIONIC CERAMIC BASED ON Ag_7SiS_5I NANOPOWDER

Pogodin A.I., **Shender I.O.**, Filep M.J., Kokhan O.P., Studenyak I.P.

USING MECHANICAL ALLOYING FOR MAX PHASES FORMATION AS PRECURSORS OF GRAPHENE-LIKE CARBIDES OF MXENES TYPE

Solonin Yu.M., **Savyak M.P.**, Korablov D.S.

MODEL CALCULATIONS OF THE LAWS OF DISPERSION OF THE PHONON SPECTRUM OF $BaTiO_3$ CRYSTALS WITH PARTIAL INHABITANCE OF DIFFERENT CRYSTALLOGRAPHIC POSITIONS

I.M. Shkyrta, I.I. Nebola

INFLUENCE OF MONOMER STRUCTURES ON THE MORPHOLOGIES AND OPTICAL PROPERTIES OF J-AGGREGATES

Alexander Sorokin, Roman Grynyov, Irina Ropakova, Igor Borovoy, Svetlana Yefimova, Yuri Malyukin

COOLING OF SUPERHEATED SURFACES BY NANOFLUIDS AND IT SIMULATION BY CFD.

Eugene Strativnov

MODIFICATION OF TEXTILE MATERIALS FOR MEDICAL PURPOSE BY NATURAL NANOTUBES

Suprun N.P., Ivanov I.O., Brichka A.V., Redko Ya.V.

CRIOCHEMICAL SYNTHESIS OF $Ni_XZn_{1-X}Fe_2O_4$ NANOPARTICLES AND STUDY OF THEIR PROPERTIES

Timashkov I.P., Shlapa Yu.Yu., Solopan S.O.

FORMATION OF SURFACE RELIEF GRATINGS IN AMORPHOUS As-Se FILMS BY POLARIZATION HOLOGRAPHY

M.L.Trunov and V.K. Kyrylenko

DYNAMICS OF PHOTOREFRACTIVE EFFECT IN $Sn_2P_2S_6$ CRYSTALS STUDIED BY MODULATION TECHNIQUE

M. Tsyhyka, S. Hasynets, A. Kohutych, A. Grabar

POLARIZATION STATES IN CORE-SHELL FERROELECTRIC NANOPARTICLES FOR ADVANCED APPLICATIONS

Morozovska A.N., **Tulaidan V.V.**, Eliseev E. A., Hertel R., Reshetnyak V. Yu., Evans D.R.

AUTOMATATION OF FIBER OPTIC THERMOMETERS WITH GaAs NANO-POWDERS AS TEMPERATURE SENSITIVE ELEMENTS

Turianytsia I.I., Chychura I.I. Kutchak S.V.

PROBIOTIC LACTOBACTERIA FOR CREATION OF SELENIUM CONTAINING DIETARY SUPPLEMENT

Tymoshok N.O., Bitutyky V.S., Kharchuk M.S., Kharchyshyn V.M., Lazarenko L.M., Kalinichenko S.V., Spivak M.Ya.

CALIX[4]ARENE C-956 INHIBITORY ACTION KINETIC ON PLASMA MEMBRANE Ca^{2+},Mg^{2+}-ATPASE ACTIVITY OF SMOOTH MUSCLE CELL

Veklich T.O., Shkrabak O.A., Golden O.V., Kardash O.O., Kosterin S.O.

THE EFFECT OF GOLD NANOPARTICLES ON SEMINIFEROUS TUBULES OF THE TESTES AFTER VITRIFICATION

Volkova N.O., Yukhta M.S., Goltsev A.M.

OPTICAL PROPERTIES OF As_2S_3-Bi_2S_3 NANOCRYSTALLINE COMPOSITE

Voynarovych I.M.

RAMAN SPECTROSCOPIC STUDY OF NANO-SIZED AMORPHOUS LAYERS OF SELENIUM AND PLASMON STRUCTURES “Au NPS/ Se FILM”

YASINKO T.I., YUKHYMCHUK V.O., RUBISH V.M., MINKOVICH V.V., MIKLA V.I., MAKAR L.I., HRESHCHUK O.M., HORVAT A.A.

SURFACE NANOSCALE STRUCTURE OF SUPERCONDUCTING FILMS PROBED BY JUNCTION SPECTROSCOPY

ZHITLUKHINA E.S.

SOME APPLICATIONS OF NANOSTRUCTURED MATERIALS AS INTERMEDIATE LAYER FOR RESISTANCE BUTT WELDING OF HIGH TEMPERATURE ALLOYS

ZIAKHOR I.V., KUCHUCK-YATSENKO S.I., ZAVERTANNYI M.S., NAKONECHNYI A.O., RADCHENKO L.M.

VACUUM DIFFUSION WELDING OF HIGH NB CONTAINING TIAL ALLOY WITH NI-BASED ALLOY

PETRUSHYNETS L.V., FALCHENKO IU.V., **ZIAKHOR I.V.**, FEDORCHUK V.E., NAKONECHNYI A.O.

PLENARY

THERMAL TRANSPORT IN VAN DER WAALS CRYSTALS MM'$P_2(S,Se)_6$ (M - Cu, Ag; M' - In, Bi) WITH DIFFERENT DIPOLE ORDERING

Liubachko V.[1], Oleaga A.[2], Salazar A.[2], Glukhov K.[1], Kohutych A.[1],
Pogodin A.[1], **Vysochanskii Yu.[1]**

[1]*Institute for Solid State Physics and Chemistry, Uzhhorod University, Pidgirna Str. 46, 88000 Uzhhorod, Ukraine*
[2]*Departamento de Física Aplicada I, Escuela de Ingeniería de Bilbao, UPV/EHU, Plaza Ing. Torres Quevedo 1, 48013 Bilbao, Spain*

The big family of metal thio- and selenophosphates compounds is attracting huge interest from the scientific community as multifunctional van der Waals layered materials, searching for the development of 2D - materials with correlated magnetic, structural and ferroelectric properties. In particular, layered crystals of hexachalcogenohypodiphostates with the general formula MM'P_2X_6 (M, M' - metal cations, X - S, Se) are promising candidates as they are semiconductors with an intermediate bandgap suitable for new electronic applications, while they also exhibit (anti)ferroelectric, (anti)ferromagnetic and piezoelectric properties. The knowledge of their thermal properties, alongside with the ferroelectric ones, is necessary for their applications in technological devices, including the possibility of finding compositions with exceptionally low thermal conductivity.

We present a complete study of the compounds with M - Cu, Ag; M' - In, Bi and X - S, Se in the form of $AgBiP_2(S,Se)_6$ and $CuBiP_2Se_6$ monocrystals. Due to their layered character, the anisotropic thermal properties (thermal diffusivity and thermal conductivity) were evaluated in two directions: one contained in the layers and another one perpendicular to them. Thermal diffusivity was measured with a high-resolution technique, paying special attention to the presence or absence of any kind of dipole ordering which should be appreciated as some kind of singularity on the thermal diffusivity curves as a function of temperature; heat capacity was calculated from first principles theories and, combining both physical properties, thermal conductivity have been extracted [1, 2].

A complete explanation of the thermal properties as ions are substituted has been developed, showing the role played by disorder, electronic levels hybridization, ion coordination, or size on the second order Jahn-Teller effect. The evolution of the thermal diffusivity and the thermal conductivity with temperature has shown, on the one hand, strong thermal anisotropies and, on the other hand, that heat is effectively transferred by phonons, with some of the compounds (especially those with Bi) presenting very low values due to the enhancement of phonon scattering events, expressing a strong anharmonic behavior, which is justified in detail on the basis of interactions among optical and acoustic phonon branches as well as the presence of electron lone pairs. This study opens the possibility of designing new materials for applications where a low thermal conductivity is essential.

1. V. Liubachko, A. Oleaga, A. Salazar, A. Kohutych, K. Glukhov, A. Pogodin, Yu. Vysochanskii. Thermal diffusivity and thermal conductivity in layered ferrielectric materials $M^{1+}M^{3+}P_2(S,Se)_6$ (M^{1+} = Cu, Ag; M^{3+} = In, Bi) // Phase Transitions 2019, – V. 92, – P. 494 - 499.
2. V. Liubachko, A. Oleaga, A. Salazar, A. Kohutych, K. Glukhov, A. Pogodin, Yu. Vysochanskii. Cation role in the thermal properties of layered materials $M^{1+}M^{3+}P_2(S,Se)_6$ (M^{1+} = Cu, Ag; M^{3+} = In, Bi) // Phys. Rev. Materials 2019, – V. 3, – P. 104415-1 – 104415-9.

PHOTORREFRACTIVE AND DIELECTRIC PARAMETERS OF DOUBLE-DOPED $Sn_2P_2S_6$ CRYSTALS

M. Tsyhyka, S. Hasynets, A. Molnar, R. Pavlyshyn,
K. Glukhov, A. Kohutych, **A. Grabar**

Uzhhorod National University, Institute for Solid State Physics and Chemistry,
Pidhirna 46, Uzhhorod 88000, Ukraine
al_grabar@hotmail.com

The report presents the results of studies of optical, dielectric and photorefractive characteristics of $Sn_2P_2S_6$ crystals doped with various metals, as well as doped simultaneously with pairs of elements (Sb + Cu, Sb + Ag, Te + Cu, Te + Ag), in the amount of 1 mol.% of each element. The purpose of this modification is to find the optimal combinations to improve the photorefractive (PR) characteristics, i.e. increase the coefficient of two-wave mixing and accelerate the rate of the PR lattice formation. The spectral dependences of the optical absorption coefficient in the region of transparency, dielectric spectra, as well as the dependence of the two-wave interaction coefficient Γ at different periods of the photorefractive lattice and the intensities of He-Ne laser radiation (633 nm) were measured in all grown samples. It was found that a significant improvement of these parameters is observed only in samples doped with 1% copper and 1% antimony.

By approximating the dependences of the coefficient Γ on the period of the PR grating, the model parameters were obtained, namely, the electro-optical coefficient and the concentration of photoactive centers. From a comparison of the PR parameters of the samples with double doping of Cu and Sb, and the crystals doped only with Sb, it follows that copper atoms partially compensate the vacancy defects that are present in single-doped crystals. This assumption correlates with the results of the *ab initio* calculations of electron spectra of $Sn_2P_2S_6$ with embedded Sb and Cu atoms, which indicate that defect energy states of these two impurity atoms are forming a common impurity level. It is also shown that a significant advantage of such double-doped samples is the higher temporal stability of the gain Γ, in comparison with the $Sn_2P_2S_6$: Sb and $Sn_2P_2S_6$: Te crystals.

COMPUTER-INTEGRATED MODEL OF AS-S ATOMIC CLUSTERS CONDENSATION

Ivanitsky V.P.[1], Kovtunenko V.S.[2], Ryaboschuk M.M.[1]

[1]*National University of Uzhhorod, Engineering department, Universytetska Street 14, 88000, Uzhhorod, Ukraine*
[2]*Cherkasy State University of Technology, Shevchenko Blvd 460, 18006, Cherkasy, Ukraine*

For modeling with the use of first-principle quantum mechanical methods of condensation processes of four- and five-atomic As_nS_m clusters, it is sufficient to take a flat monolayer of the graphite structure with 12 carbon atoms the free valences of which are saturated with hydrogen as the smallest fragment of the carbon substrate. Theoretically, there have been investigated the condensation processes of 12 different clusters which are more stable in vapor phase and have different dimensional structure: chain, polygon, branched structure of a " star" shape, spatial shape of a "roof" type and closed polyhedron. For all such shapes of isomorphic forms of clusters the energies of their adsorption on the carbon substrate have been determined. For this, there has been used the value of full energy of the atomic system, consisting of a monolayer, substrate and the appropriate As_nS_m cluster optimally placed above its centre.

The analysis of modeling results shows that the adsorption on the carbon substrate of most As_nS_m clusters occurs due to the break of one or two of their chemical bonds followed by their transformation into the chain shape, which is covalently bonded with the substrate by its end atoms. Thus, the saturating hydrogen atoms of the substrate didn't form strong chemical bonds with atoms of clusters and had a little effect on energy and geometric parameters of their adsorption. Separate clusters with pentagon and polygon shapes are highly probable to be also adsorbed on the substrate without changes in their spatial shape due to Van der Waals forces (for As_4 molecules this is the main adsorption mechanism). In all cases the area of As_nS_m clusters during adsorption is positioned in parallel to the substrate surface.

The system achieves a deeper energy minimum if during adsorption not only the structure transformation of As_nS_m clusters occurs, but also the atomic structure of the carbon substrate changes, to a certain extent, especially on the edges and in the vicinity of those carbon atoms which are covalently bonded with the cluster. The most important of them are the change in their hybridization type from sp^2 to sp^3 by such atoms and their elevation above the surface of the graphite monolayer. Also, such changes have been substantially more significant if the covalent bonding of the cluster had occurred with the participation of more independent edge carbon atoms.

In most cases the value of adsorption energy of As_nS_m clusters on the carbon substrate can be approximately calculated based on the difference in energy levels of chemical bonds of the system before and after adsorption. However, such values are approximately~20 % higher than the values calculated with the use of the quantum-mechanical method DFT. Such differences are namely due to the forces of the mechanical tensions inside the system.

LASER RECORDING OF NANOSIZED ELEMENTS ON THIN FILMS OF CHALCOGENIDE GLASSY SEMICONDUCTORS

KryuchynA.A.[1], Petrov V.V.[1], Rubish V.M.[1], Kostyukevych S.O.[2]

[1]Institute for Information Recording, NAS of Ukraine 2, Shpak str., 03113 Kyiv, Ukraine
[2]V. Lashkaryov Institute of Semiconductor Physics, NAS of Ukraine 41, prospect Nauky, 03028 Kyiv, Ukraine

At all stages of the creation of optical recording systems, thin films of chalcogenide vitreous semiconductors (ChVS) were widely used and continue to be used, which allowed the registration of elements with dimensions that were determined mainly by the resolution of the focusing systems of the exposing radiation. Inorganic resists based on chalcogenide glassy semiconductors have a high resolution due to the small size of the main structural units and strong covalent bonds, which can be used in optical lithography [1, 2]. Laser recording was performed on ChVS films of different compositions, which were determined mainly by their field of application. It was possible to record elements of the order of λ / 2 on thin ChVS films. Thin films of chalcogenide glass systems have been successfully used for recording master discs CDs in formats CD and DVD [1]. The nonlinearity of the exposure characteristic associated with local heating of the material in the recording area and the generation of a large number of electron-hole pairs contributes to the creation of micro- and nano-relief structures by focused laser radiation on the films of chalcogenide glassy semiconductors [1]. The maximum reduction in the diameter of the recorded the marks was obtained by the authors of the study, who reported experimental results in the formation of the marks with a diameter of about 100 ~ 150 nm on thin films of chalcogenide alloy with a semiconductor laser with a wavelength of λ = 650 nm and a focusing lens with a numerical aperture of 0.65 (NA). Obtaining the sizes of the marks smaller than the diffraction limit (the diameters of the labels are approximately 1/10 of the focused light spot) is explained by the nonlinear absorption of a thin film of radiation with a Gaussian intensity distribution [3]. The thermolithographic recording method was used to record the marks. Due to the fact that the thermolithographic recording mode is unstable, the formation of nanoscale relief structures on thin films of chalcogenide glassy semiconductors by diffraction-limited optical systems is problematic the formation of nanoscale relief structures on thin films of chalcogenide glassy semiconductors by diffraction-limited optical systems is problematic. For the formation of nanosized elements and structures, it was proposed to use near-field systems for focusing optical radiation or to change the structure of the thin-film recording medium [4].

To record nanoscale structures, it is proposed to use the technology of excitation of metal nanoparticles and to expose photosensitive layers based on chalcogenide glassy semiconductors with optical near-field radiation. Nobel metal nanoparticles with sizes of about tens of nanometers can have a significant impact on information recording processes in various types of optical and magnetic media. The technology of using nanoparticles is one of the ways to overcome the diffraction limit in the process of recording information and the formation of nanoscale structures by diffraction-limited optical systems. Nobel metal nanoparticles placed in a certain way in the recording medium can act as plasmonic antennas, concentrating the recording radiation in a region much smaller in size determined by the resolution ability of diffraction-limited optical systems [6]. The influence of nanoantennas in chalcogenide semiconductors on the formation of submicron structures in them is being actively studied. Optical nanoantennas are the metallic nanostructures which confine electromagnetic waves into sub-wavelength volumes at resonant conditions. Combining extremely large electromagnetic field enhancement in plasmonic resonant nanoantenna with high optical nonlinearity of chalcogenide glass leads to a low-threshold broadband light generation scheme in sub-wavelength chip-scale structures [7]. The problem is in choosing the placement of noble metal nanoparticles in the structure of the photosensitive layer to implement the recording of nanoscale structures.

Increasing the resolution of recording media based on glassy chalcogenide semiconductors can be achieved by selecting recording modes and compositions of glasses, in which the most pronounced nonlinearity of the exposure characteristics of the photosensitive material,and the introduction into the structure of the recording media of nanoparticles of nobel metals for excitation of local plasmon resonance

1. Petrov V., Kryuchin A., Kostyukevich S., Rubish V. Inorganic Photolithography. Kyiv: Institute for Physics of Metals, NAS of Ukraine, 2007. – 196 p.
2. Vlcek M., Jain Himani. Nanostructuring of chalcogenide glasses using electron beam lithography //Journal of Optoelectronics and Advanced Materials, 2006. – V.8, No.6. – p. 2108-2111.
3. Wei J., Jiao X. Super-resolution nanopatterns and optical recording in chalcogenide phase change thin films by direct laser writing //Proc. SPIE 7125, Eighth International Symposium on Optical Storage and 2008 International Workshop on Information Data Storage, 712505 (19 March 2009); https://doi.org/10.1117/12.825533
4. Kryuchyn A.A., Petrov V.V., Rubish V.M., Trunov M.L., Lytvyn P.M., Kostyukevich S.A. Formation of Nanoscale Structures on Chalcogenide Films // Phys. Stat. Solidi B, 2017. – P. 1700405. https://doi:10.1002/pssb.201700405.
5. Trunov M.L., Lytvyn P.M., Nagy P.M., Csik A., Rubish V.M., Kökényesi S. Light-induced mass transport in amorphous chalcogenides: Toward surface plasmon-assisted nanolithography and near-field nanoimaging // Phys. Stat. Solidi (B) Basic Research, 2014. – V.251, No.7. – P. 1354-1362. https://doi.org/10.1002/pssb.201350296
6. O’Connor D., Zayats A.V. The third plasmonic revolution //Nature Nanotechnology, 2010. – V.5, No.7. – p. 482–483. doi:10.1038/nnano.2010.137.
7. Duman H. Design and fabrication of resonant nanoantennas on chalcogenide glasses for nonlinear photonic applications- 2013 https://tezarsivi.com/design-and-fabrication-of-resonant-nanoantennas-on-chalcogenide-glasses-for-nonlinear-photonic-applications.

INNOVATIVE NANOMATERIALS AND DEVELOPMENTS AT THE NATIONAL ACADEMY OF SCIENCES-USE AND OPPORTUNITIES FOR COMMERCIALIZATION

S.A.Bespalov[1], I. A. Malchevsky[1], **V. N. Uvarov[2]**

[1]*Presidium of NAS of Ukraine, 54, Volodymyrska st., 01030, Kyiv, Ukraine*
[2]*G.V. Kurdumov Institute of Metal Physics, NASU, 36, Academican Vernadsky Blvd., 036680, Kyiv, Ukraine*

The results of the works carried out at the National Academy of Sciences of Ukraine about creation and investigation of the structure and properties, about the usage of solid surface and multilayer nanostructures, carbon nanomaterials, nanoparticles, nanopowders and consolidated on their basis materials, nanomaterials for medical and biological purposes, alloys in the nanostructured state, nanocomposites materials are discussed.

MODEL CALCULATIONS OF THE COMPLEX CRYSTALS PHONON SPECTRUM DISPERSION

Nebola I.I.

Uzhhorod National University, Voloshin str., 54, 88000, Uzhhorod, Ukraine
e-mail: ivan.nebola@uzhnu.edu.ua

Numerical simulation of the dispersion dependences of single-particle excitations in complex crystalline compounds opens up the possibility of predicting the physical properties of new materials, which is especially important in studying the lattice dynamics of partially disordered objects with various disturbances in both structure and chemical composition.

Symmetric description taking into account additional "physical" parameters (colour, phase, charge sign, spin, etc.) in the description of the crystal structure allowed to create a theory of colour symmetry [1] and the concept of superspace symmetry [2]. Based on the generalized symmetry, it is convenient and clear to describe the structure using $(3+d)-$dimensional models to describe complex crystalline formations, united by a single metric and the scale of the function of the protocrystal carrier [3]. The formation of $(3+d)-$dimensional metrics is based on its higher symmetry and is associated with additional internal "phase" $d-$dimensional space, which makes it possible to describe complex crystals and systems as natural $(sa\times sa\times sa)-$superlattices.

The compositional features of the realization of complex crystals and solid solution systems by the mechanism of filling various atoms and vacancies of translationally equivalent positions given by the protocrystal basis, are covered by the concept of supraspace symmetry**.** In this case, various combinations of the protocrystal bases and real crystalline formation can be taken into account together with all possible variants of the compositional filling of crystallographic positions; the latter allows taking into account their partial filling. Using a complete set of modulation vectors allows to determine the amplitudes of mass modulation functions and on their basis to generate a generalized dynamic matrix of a real physical object and a matrix of mass perturbation. The first is given in the form of a superposition of protocrystal dynamic matrices defined at different points of the Brillouin zone (ZB) connected by modulation vectors. The second is described by the amplitudes of mass modulation functions, which are modified by various filling of the positions of crystallographic orbits [4, 5].

В запропонованому підході дисперсійні криві фононного спектру кристалічної сполуки визначаються, як розв’язки матричного рівняння при умові рівності нулеві визначника виду: In the proposed approach, the dispersion curves of the crystalline compound phonon spectrum are defined as solutions of the matrix equation under the condition that the determinant of the form:

$$\left|D_{\alpha\beta}(k+q_i)-\omega^2\delta_{\alpha\beta}\delta_{ij}-\omega^2\rho_{(i-j)}\delta_{\alpha\beta}\right|=0, \qquad (1)$$

is equal to zero,

where $D_{\alpha\beta}(k+q_i)-$ dynamic matrices of a monoatomic protocrystal defined at ZB points, $(k+q_i)$, $\rho_{(i-j)}=\rho_i(q_i,\Delta^* b^*_{i\,j})$ - the amplitudes of the mass modulation function given for the modulation vector (q_i-q_j), $k-$ wave vector, q_i- modulation vectors, α,β – coordinates x,y,z. The solution of the matrix equation relatively to $\omega^2(k)$ allows to determine the phonon spectrum dispersion dependences, and taking into account various variants of the compositional filling - to track their genesis [5].

Dynamic matrices of the protocrystal $D_{\alpha\beta}(k+q_i)$ are determined from the ratio:

$$D_{\alpha\beta}(k+q_i)=\sum_{(n\neq 0)}\alpha_n\frac{n_\alpha n_\beta}{n^2}\left(1-e^{i(k+q_i)n}\right), \qquad (2)$$

where $\alpha_n -$ the force constant of atom interaction in $0-$position and $n-$neighbouring atom, $n_\alpha, n_\beta -$ vector projections n on the axis α, β.

In the equidistant approximation, the force characteristic depends only on the distance between the atoms and, then, the interaction of different atoms, which are in equidistant positions, is the same. This allows to form a dynamic matrix in quasi-diagonal form. In the non-equidistant approximation $\alpha_n -$is determined both as the distance between the positions and as the difference in physical characteristics of the objects that occupy them.

The values of the amplitudes of the mass characteristics $\rho(q_j)$ are obtained by solving a system of equations relative to the amplitudes of the mass modulation functions $\rho(q_j) = \rho_j$:

$$m(r_k) = \sum_{j=1}^{s} \rho(q) e^{iq_j r_k}, \tag{3}$$

where $s-$ the number of possible positions of atoms in the superlattice, $m(r_k)$ - mass characteristics in these positions, q_j –an array of modulation vectors, the number of which coincides with the number of positions in the superlattice.

The developed mathematical software allows calculations of dispersion curves within the Brillouin zone.

1. Копцик В.А. Теоретико-групповые методы в физике реальных кристаллов и теории фазовых переходов /В.А. Копцик// Теоретико-групповые методы в физике.: Труды междунар. семинара. – М.: Наука. – 1980. – С. 368-381.
2. Janssen T. On the lattice dynamics of incommensurate crystal phases /T. Janssen// J.Phys.C: Solid State Phys. – 1979. – V.12, No.24. – P. 5381-5392.
3. Небола И.И. Генезис структуры и колебательных спектров кристаллов с $(sa\times sa\times sa)-$сверхрешеткой /И.И. Небола, А.Ф. Иваняс, В.Я. Киндрат// Физ. тверд. тела. – 1993. – Т.35, № 7. – С. 1852-1866.
4. 3+D Dimensional bases for the complex crystals lattice dynamics modeling / [I.I. Nebola, I.M. Shkirta, A.F. Katanytsia, A.K.V. Dolynai] // The 19th Small triangle meeting on theoretical physics. – Medzilaborce, 2017.– p. 141-148.
5. Model research of phonon spectra of argyrodites family / [I.I. Nebola, A.Ja. Shteyfan, V.I. Sidey, A.F. Katanytsia, I.P. Studenyak, I.M. Shkyrta] // Semiconductor Physics, Quantum Electronics & Optoelectronics. – 2018. – v. 21, № 2. – p. 134-138.

THE SPECIAL TECHNOLOGIES OF SYNTHESIZING MATERIALS WITH SPECIFIC PROPERTIES

Zhiguts Yu.Yu.

Uzhhorod National University, 46, Pidgirna Str., Uzhhorod, Ukraine, 88000

The lack of materials with required complex of physical, chemical, mechanical, technological and auxiliary properties for the relevant functional purposes has raised an urgent problem of synthesizing corresponding alloys and developing technologies of their production. Synthesis of materials with specific properties will allow not only the new areas of their application to be opened, but also the new trends in further scientific research to be formulated. Combined methods of material synthesis are based on the use of the two types of reactions, namely, the metallothermic ones and the self-propagating high-temperature synthesis (SHS). Combined processes versatility is related to the possibility of synthesizing almost any cast material, i.e. ferrous alloys, non-ferrous metals and alloys, instrumental, high-speed and special steels, as well as materials being produced earlier by the metal powder industry techniques only, i.e. hard alloys, carbide steel etc.

1. Subject relevance. The urgent industrial problem of nowadays is not only creation of new materials but also improvement of traditional material properties and advance development of technologies of their production. Detailed studies of the problem allow us to state that this task could be successfully solved by using specially synthesized alloys produced by combined processes based on the combustion of exothermic powder mixtures.

The above technologies are based on the combined processes and allow the predetermined structure to be synthesized with specified alloy properties at cast formation with the use of synthesized materials for the emergency repairs of products, part surface layer recovery and for the use of the synthesized alloy for the cast saving in the exothermic cast additive technologies.

The synthesis technologies developed in this work differ from traditional ones by a series of obvious advantages: the lack of need in the powerful electric energy power supplies, the possibility to use simple and cheap casting equipment, the high process productivity (alloy synthesis time may vary from 30 seconds to a couple of minutes), the possibility of using secondary production waste – graphite electrode grinding, aluminium or magnesium chips, iron cinder, blue powder, i.e. the dust from the filters of the casting shops producing manganese alloys. All the aforementioned have caused an urgent need in carrying out research described in this paper. The above technologies could be successfully applied to save metal at the high-volume and mass production factories producing casts and instruments. Creating materials on the basis of the self-propagating high-temperature synthesis (SHS) and combined (metallothermy + SHS) processes as well as studying the influence of new technological methods of metal production on the cast microstructure, chemical composition and mechanical properties have gained large practical importance. Their use in the existing casting technologies, e.g. in producing steel casts with thermite cast additives increases considerable process efficiency.

2. Research goal. The main goal of the present research was to predict the structure and the phase composition of the synthesized alloys, to elucidate the influence of combined technologies on the material properties and to determine the most optimal areas of the above alloys application. In addition, this work is intended to study the synthesized materials, namely the thermite cast iron, alloy steel, construction steel, stainless steel, rapid tool steel, hard alloys, carbide steel, non-ferrous alloys etc.

3. Theoretical part. Taking into account the necessity to predict the alloy structure, phase composition and properties, the authors have developed the principles of the synthesized alloy formation. The techniques based on the above principles allowed the exothermic burden adiabatic combustion temperatures to be determined. The methods of geometric thermodynamics for the structure optimization and prediction were modified as well.

Method of recovering the exothermic mixture adiabatic combustion temperature and selecting reactions suitable for the alloy synthesis. To find the boundary conditions of the alloy synthesis the authors have developed a method on the basis of adiabatic temperature dependence on the molar composition of synthesized compounds. This allowed the synthesis reactions to be divided into two principal groups. The first of them includes those reactions, the adiabatic temperature of which is higher than the temperature of separation of the synthesized alloy and slag. These reactions are applicable for the alloy formation. The second group of reactions occurring at the ingredient interaction results in the formation of an alloy in a form of separate "grains" in the slag or leads to the slag part non-separation from the alloy itself. These reactions are not acceptable for further experimental use.

After determining the burden composition according to the stoichiometric coefficients and after correcting them by the burden component fixation coefficients, it is recommended to calculate the metallothermic reaction adiabatic combustion temperature T_a [1–3]. In these calculations of the burden adiabatic combustion temperature according to the methods developed, the aluminum sublimation was not taken into account giving the error of finding T_a and the reaction heat Q_r. However, in spite notwithstanding, the mixture reaction temperatures must (heat sink being taken into account) be sufficient to smelt the reaction components and products ($T_{mel(FeO)} = 1640K$; $T_{mel(Fe_3O_4)} = 1810K$; $T_{mel(Fe)} = 1800K$; $T_{mel(Al)} = 830K$; $T_{mel(Al_2O_3)} = 2320K$). That is, the principal criterion of the cast production is that T_a for all reactions must exceed the reaction product temperature T_{mel}. The T_a value calculation, obviously, does not take into account the heat losses during combustion and the completeness of reactants transformation into reaction products.

Taking into account the condition that all the heat is spent to heat the burden up, i.e. the enthalpies of the initial and final products are equal, we find:

$$\sum_{i=1}^{k}\left(H(T_a)-H(T_o)\right)_i = Q, \qquad (1)$$

where T_a is the adiabatic combustion temperature; T_0 is the initial temperature; Q is the reaction heat and k is the number of reaction products.

In more complex equations, when more than three reaction products were produced, T_a was found in accordance with the following formula:

$$T_a = \frac{Q - \Sigma H_i(T_{meli}) - \Sigma L_i + \Sigma C_{ip}\cdot T_{meli}}{\Sigma Cilic}, \qquad (2)$$

where C_i and L_i are the reaction product heat capacity and smelting heat, respectively; γ is the liquid phase part in the combustion product;

$$\begin{cases} \gamma = 0 \text{ at } \mathrm{T_a} < \mathrm{T_{mel}}; \\ \gamma = 0 \text{ at } \mathrm{T_a} > \mathrm{T_{mel}}. \end{cases} \qquad (3)$$

Obviously, due to the lack of the full data table on the C dependence on T at high temperatures [1–3], we extrapolated the values in accordance with the suggested conclusions:

$$C_{sol}(T_{mel})=7n\cdot b \text{ (J/mole·deg)}, \qquad (4)$$

where $C_{sol}(T_{mel})$ is the product heat capacity at the smelting temperature; n is a number of atoms in the product molecule and b is the coefficient of transition from kkal to J.

For the linear dependence of the specific heat on the temperature at $T_{lik}<T<T_{mel}$:

$$C(T) = C^* + \frac{C_{mel} - C^*}{T_{mel} - T^*}\left(T - T^*\right), \qquad (5)$$

where C^* is the experimental specific heat value at $T=T^*$; T^* is the maximal experimental temperature at the $C(T)$ determination.

4. Experimental part. The experimental studies carried out by the authors were stimulated by the necessity to confirm the development of a complex of theoretical notions. This work was carried out to synthesize the different-class thermite steels and cast irons, alloyed steels, tool materials (high-carbon, high-speed and highly alloyed steels), hard cast alloys and carbide steels, ferrous (i.e. copper, aluminium etc.) alloys.

Taking into account the data of the studies we have developed and realized the production of the different carbon steels as a result of the aluminothermic reduction of the iron cinder with introduction of carbon and ferrous alloys into the thermite. Based on the special alloys of exothermic burdens, the thermal steels 20GL–35GL, 30GSL, 32XO6L–40XL, 20X5ML (with the perlite-ferrite structure) and 20X5TL, 40X9C2L (with the martensitic structure) were obtained [3]. It has been found that introduction of more than 20% dopants to the thermite mixture results in the termite alloy and slag separation termination in the conditions of the laboratory thermite microsmeltings at the burden mass below 300 g. In case of the exothermic burden mass from 0.3 to 5 kg, the dopant content in it could reach 25%, while for the 5–50 kg masses it is 30%.

High percentage content of impurities and ferrous alloys excessively "cools" the exothermic reaction, and then the calculated burden composition for the high alloy steel does not ensure the optimal combustion temperature of the exothermic mixture. In this case it is necessary to use the other, different from the above one, direction of the alloy steel synthesis. It is related to the synthesis of a preset alloy chemical composition not by adding a certain quantity of ferrous alloys but by composing a special exothermic burden comprising the alloying oxides (e.g., Cr_2O_3, CrO_3, NiO, CuO, V_2O_5 and others) and the iron cinder reduced by aluminium in the course of the aluminothermic process. The technique of the relevant calculations and the synthesis technology have been developed to obtain the thermite high alloys. For instance, this allowed the 12X18H10T steel on the basis of the Fe, Ni, Cr oxide to be synthesized [3]. Titanium was introduced into the exothermic burden not in the form of TiO_2 but as the 30% ferrous titanium due to the low titanium reducibility from its oxides using aluminium. The burden composition was as follows: Cr_2O_3 – 17,2%; Fe_3O_4 – 50%; NiO – 6,6%; Al – 26,2% [3]. Both carbon and titanium at their introduction into the metallothermic burden move the synthesis reaction from the metallothermic class to the combined one, i.e. to that involving the metallothermic reaction and the SHS reaction. The chemical analysis of the synthesized metal samples has demonstrated poor chromium reducibility from its oxides.

Continuing this work, we have carried out the experiments in the research-production conditions with the use of the above burden compositions for the cast additions of the alloy steels [3]. The use of the graphite pot leads to a slight nihard strength increase. In general, the microsmelting conditions establish such intense melt cooling regime that the influence of the reactor lining stops dominating. All the casts made of the nihards had no external signs of shrink holes and cast cutting and macroanalysing confirmed these conclusions. No chemical composition liquation over the cast volume was found.

Synthesized thermite wear-proof cast irons, i.e. nihards, relate to the chromium-nickel martensitic cast irons, graphitizing probability of which at the alloy synthesis using the aluminothermic method decreases significantly due to the large temperature gradient and high rates of heat removal. The microstructural analysis has shown that in the thermite cast irons the cementite content is not less than 50% that results in the 1000 – 1050 HV hardness.

Continuing this work, we succeeded to combine the metallothermic and the SHS processes to obtain the tungsten-cobalt hard alloys according to the following reaction scheme:

$$AO \rightarrow A + BO \quad \text{and} \quad A + C \rightarrow AC,$$

where A, B, C are the synthesis elements; O is the oxidizer (say, oxygen etc.); AC are the reaction products (i.e. carbides, silicide’s and so on); BO is a slag.

The studies of the microstructure and the properties of the alloys produced allow the following results to be presented, e.g., for the high-speed steel “P18” (analogue 3355): grain size – 10, hardness HRC – 65–67, σ_b=2600 MPa, heat resistant 913–928 K.

Solution of the industrial problem related to the synthesis of the superheated copper bronze alloys (“БрАЖ 10-4” – analogue C95400 and “БрОЦС 5-5-5” – analogue LG2) in the industrial conditions has become a proof of the "combined" technology flexibility.

Thus, we succeeded to prevent the excessive roasting of expensive components of the bronze alloy exothermic burden and to reduce (by 60%) the bronze alloy mass for the casting addition.

Another promising direction of the use of developed exothermic burden compositions is the development of the thermite smelting technology on the basis of simultaneous reduction of certain compounds. This technology provides a possibility to produce the copper alloy cast in the inaccessible areas, not specialized agricultural shops and even in the field conditions with no classical casting equipment and electric energy power supplies.

As known, the simplicity of the transition from the laboratory experiments to the industrial production is a specific feature of technologies based on the metallothermic reactions. In this case the combustion process is considerably simplified and its indices are improved for the large volumes of the metallothermic burden [3].

One more direction of the use of the combined (SHS + metallothermy) synthesis processes is the hard alloy material smelting onto the steel or cast iron surfaces. Especially promising from this viewpoint are the technologies that combine the laser surface hardening (LSH) with the SHS-based smelting. An example of such use of the complex technologies is given below.

The mixture of the Ti powder (68 mass %), C powder in a form of a smoke black (18 mass %) and the Fe powder (14 mass %) was used instead of the light-absorbing paint. The above mixture was deposited onto the Steel 10 and Steel 20 surfaces with the subsequent drying in the air producing the 80, 200 or 500 μm layer.

Thermochemical calculations have shown that in such mixture almost all Ti reacts at the expense of the oxygen-free combustion with carbon producing the TiC carbide. Carbon excess and very small amount of titanium jointly alloy iron producing a liquid steel of eutectoid composition that at rapid cooling is transformed into troostite in the 80 μm thick layers. These layers were ignited by the ray of the continuous CO_2 laser with longitudinal pumping at the 150 W power and 25–35 $W \cdot m^{-2}$ (at the 0.3–2.0 mm "spot" diameter). Scanning speed was varied within the 10–20 $mm \cdot s^{-1}$ range. In series of studies to provide additional protection of the melted surface we have used a focusing attachment with a possibility of additional surface blowing with inert and less active gases (Ar, CO_2, N_2 etc.). After the experiment, we measured the macro- and microhardness in the alloyed layer, thermal influence zone and in the main alloy. The typical microstructure of such ~500 μm thick layer strengthened by combined processes due to the SHS and LSH combination.

Thus, in these studies we succeeded to organize the SHS process in the relatively thin layer at the expense of using the LSH to solve two tasks simultaneously: heating, smelting and carbonization of iron, as well as the Ti particles smelting and "burning" in carbon with the TiC carbide production.

5. Conclusions. The results of the theoretical and experimental studies presented above are related to the synthesis of materials by combined technologies based on the metallothermy and SHS. On the basis of developed methods of calculations the compositions of burdens have been found and a wide spectrum of different-type alloys have been synthesized.

The specific features of smelting using combined methods have been found, the mechanical properties and the structure of alloys produced have been studied, the recovery coefficients for the alloy elements in the metallothermic and combined processes have been found. In addition, the technologies of the thermite welding and smelting onto the super-hard surfaces have been developed, while combining the LSH and SHS processes in one operation allowed one to solve a complex of technical problems of production of the carbide steel-like materials and hard alloys on the metal surface.

1. Zhiguts, Yu.Yu. (2004). The method for calculating the metallothermic charge for the supply of cast irons. *Engineering Science,* 9, 43-46.
2. Zhiguts, Yu.Yu., & Pokhmurski, V.I. (2005). The materials, synthesized metallothermy and SHS-processes. *Report of the National Academy of Sciences of Ukraine*, 8, 93-99.
3. Zhiguts, Yu.Yu., & Lazar, V.F. (2014). *The technologies and features of alloys synthesized by combined processes*. Uzhgorod, Invazor.

FORMATION OF Ag AND Au NANOPARTICLES ARRAYS AND SOME ASPECTS OF THEIR PRACTICAL USE

Rubish V.M.

Institute for Information Recording Uzhgorod laboratory of optoelectronics and photonics materials of the Institute for Information Recording of the NAS of Ukraine,
4, Zamkovi skhody St., 88000 Uzhgorod, Ukraine

The results of the some investigations (devoted to the design of eguipment and technological conditions for the formation of silver and gold nanoparticles (NPs) arrays of various morphology; study of optical charactericties and surface morphology of NPs arrays; study of photoinduced mass-transport in chalcogenide amorphous films under band-gap light irradiation and processes of surfase relief gratings (SRGs) formation; investigation of influence of near-field illumination on the formation of surface reliefs in chalcogenide amorphous films in the composite structures "Ag(Au)NPs / chalcogenide film" under the appropriate excitation of surphace plasmon resonance by means of laser radiation; investigation of the structure of nanosized chalcogenide films by the SERS (surface-enhanced Raman spectroscopy) method which carried out at the Uzhgorod laboratory of optoelectronics and photonics materials of the Institute for Information Recording NAS of Ukraine, are discussed.

ON THE LONGITUDINAL ELECTRO-SCALAR WAVE IN THE NANOSTRUCTURES, WAVE GUIDES AND MAXWELL ELECTRODYNAMICS

Simulik V.M.[1], Zajac T.M.[2]

[1]*Institute of Electron Physics, NAS of Ukraine, 88017, Uzhgorod, 21 Universitetska Str.*
[2]*Uzhgorod National University, Engineering-technical Faculty, Department of Electronic Systems, 88000, Uzhgorod, 13 Kapitulna Str.*

The theoretical and experimental description of the longitudinal electromagnetic waves is a subject of the different level discussions. There are many indications of the existence of such waves in different media. Note, for example, the longitudinal waves in plasmons and in plasma. Nevertheless, these oscillations only sometimes are considered as the electromagnetic ones. The longitudinal electromagnetic waves are well known to waveguide engineers. Let us mark especially the recent observations of the longitudinal electric wave in an interacting laser beams. On the other hand, it is well known fact that the Maxwell equations for the free electromagnetic field contain only the transverse solutions.

The purpose of this study is to draw attention to the existence of longitudinal electro-scalar waves in nanostructures. In this short article, we consider the role of such waves and an explanation of their existence within the framework of Maxwell's standard electrodynamics. The brief review of the contemporary general experimental and theoretical situation with the longitudinal-scalar electromagnetic waves investigations is given.

In [1] the theory of electromagnetic waves in a crystal, where excitons are produced, has been considered. The strictly-longitudinal electric waves are shown to exist in such crystal. In [2] the interaction of an electromagnetic wave with nanostructure of a cylindrical form with nonlinear dependence of dielectric permeability on a field is considered. The mathematical model and algorithm of finding of a longitudinal electromagnetic wave considering influence of a transverse wave and contribution of potential of interaction near a singular point of system is offered. On the basis of the developed algorithm numerical results for a metal nanocluster were received. Recently in [3] the properties of longitudinal electromagnetic oscillations in metals and their excitation at planar and spherical surfaces have been studied.

It is well known that the electromagnetic field in the waveguide is not purely transverse, but has longitudinal components. Moreover, on the basis of waveguides "Longitudinal-scalar electromagnetic wave radiating device RU 2287212 C1" has been suggested [4].

Recently in [5] a simple experimental method for generating an intense longitudinal electric field from transverse electromagnetic waves (laser pulses) with radially symmetric polarization has been presented. A method of receiving longitudinal electric waves from interacting transverse electromagnetic waves was developed in different contemporary experiments with laser pulses [6-9], see also the theoretical comments in [10].

The authors of theoretical article [11] have studied the problem of plasmons in a QED vacuum. It has been shown that the bosonized version of (1+1)-dimensional QED admits the existence of classical stable time-periodic solutions, i.e., standing waves of the longitudinal electric field and the vacuums polarization density. Note that assertions about longitudinal electromagnetic waves in plasma are known from [12, 13]. Recent information on longitudinal electric and scalar waves in antennas can be found in [14].

The goal of this paper is to contribute in the problem by means of standard classical electrodynamics, e.g., by the exact solutions of well-defined physical and mathematical systems of the Maxwell equations. Below we presented the result that the longitudinal wave component of the electric field strength vector (together with longitudinal scalar wave) is the exact solution of the standard Maxwell equations with specific gradient-type case of electric current and charge densities.

Note that in literature one can find some confusion in using the notions "longitudinal electric wave" and "longitudinal wave component of the electric field strength vector". It leads to the confusion in understanding.

The question about longitudinal electromagnetic waves is the old problem of classical electrodynamics. There is a large probability that N. Tesla was the first in such investigations. Nevertheless, today it is difficult to distinguish the legends about N. Tesla from his real investigations, see, e.g., [15]. The first known theoretical model has been considered in [16]. Longitudinal electromagnetic waves between parallel plates were investigated.

The hypothesis about the longitudinal electromagnetic waves, which presence in the mathematical formalism follows from the massless Dirac equation, (on the basis of a link between the massless Dirac and slightly generalized Maxwell equations) was suggested in [17]. The start in [17] was related to the results [18]. Following [17, 18], in [19, 20] we have been presented our preliminary point of view on this problem. Longitudinal electric wave appears in [19, 20] in the pair with scalar wave. Here the problem on the longitudinal electromagnetic waves is considered independently (without any relation to the massless Dirac equation and the Maxwell equations in the Dirac-like form), see the article [21] as well. The further review can be found in [14].

In the period after our publications [19, 20] an interest to the problem of longitudinal electromagnetic waves in electrodynamics has been arose. The problem on longitudinal electromagnetic waves is today the subject of different investigations. Many authors used essentially our results [19, 20], but, unfortunately, without any reference to [19, 20] (see, e.g., K.J. van Vlaenderen, A. Waser, Hadr. J. 24 (2001)). The necessary comments on some publications of that kind are already given in [14].

As ordinarily in the foundations of the electromagnetic field theory the system of units $\varepsilon=\mu=\hbar=c=1$ is chosen. In the Minkowski space-time $\mathrm{M}(1,3)=\{x\equiv(x^{\mu})=(x^{0}=t,\vec{x}\equiv(x^{j}))\}$; $\mu=\overline{0,3}$, $\mathrm{j}=1,2,3$, the metric is given by $g=(g^{\mu\nu})=(+---)$, $a^{\mu}=g^{\mu\nu}a_{\nu}$, and summation over the twice repeated indices is implied. In our main calculations we use the rigged Hilbert space $\mathrm{S}^{3,4}\subset\mathrm{H}^{3,4}\subset\mathrm{S}^{3,4*}$, where the Schwartz test function space $\mathrm{S}^{3,4}$ is dense in the Schwartz generalized function space $\mathrm{S}^{3,4*}$ and $\mathrm{H}^{3,4}$ is the quantum-mechanical Hilbert space of 4-component functions over $\mathrm{R}^{3,}\subset\mathrm{M}(1,3)$.

Consider the Maxwell equations in the form

$$\begin{aligned}&\partial_{0}\vec{E}-\mathrm{curl}\vec{H}=-\mathrm{grad}E^{0},\ \ \partial_{0}\vec{H}+\mathrm{curl}\vec{E}=0,\\&\mathrm{div}\vec{E}=-\partial_{0}E^{0},\ \ \mathrm{div}\vec{H}=0.\end{aligned}\qquad(1)$$

The first description and application of the form (1) was given in [19, 20]. Compare (1) with the standard Maxwell equations for the free field

$$\begin{aligned}&\partial_{0}\vec{E}-\mathrm{curl}\vec{H}=0,\ \ \partial_{0}\vec{H}-\mathrm{curl}\vec{E}=0,\\&\mathrm{div}\vec{E}=0,\quad \mathrm{div}\vec{H}=0,\end{aligned}\qquad(2)$$

and with the standard Maxwell system with electric sources.

From the physical point of view, equations (1) are the partial case of the standard Maxwell equations (the partial case of a standard classical electrodynamics). In this case, the current $\vec{j}(x)$ and charge $\rho(x)$ densities have the form

$$\vec{j}(x)=-\mathrm{grad}E^{0}(x),\ \ \rho(x)=-\partial_{0}E^{0}(x).\qquad(3)$$

The mathematical point of view shows that objects (1) and (2) are the different systems of partial differential equations. Indeed, the general solution of the system (2) is well known and is given by the transverse electromagnetic waves only. The presence of the longitudinal solutions [19, 20] of the system (1) follows from the existence of additional partial derivatives $\partial_{0}E^{0}$ and $\mathrm{grad}E^{0}$ in (1). Therefore, any contradiction with mathematical physics is absent. On the other hand the restriction on the form (3) of sources is absent in classical electrodynamics. Thus, the contradiction with classical electrodynamics is absent as well. It is the reason why the result of [19, 20] on the presence of longitudinal electric and scalar waves is quite possible in the framework of ordinary classical electrodynamics.

Consider at first the general solutions of the system (2):

$$\vec{E}(x)=\frac{1}{(2\pi)^{3/2}}\int d^{3}k\sqrt{\frac{\omega}{2}}\left[\left(c^{1}_{\vec{k}}\vec{\mathrm{e}}_1+c^{2}_{\vec{k}}\vec{\mathrm{e}}_3\right)e^{-ikx}+\left(c^{*1}_{\vec{k}}\vec{\mathrm{e}}^{*}_1+c^{*2}_{\vec{k}}\vec{\mathrm{e}}^{*}_3\right)e^{ikx}\right],$$

$$\vec{H}(x)=\frac{i}{(2\pi)^{3/2/}}\int d^{3}k\sqrt{\frac{\omega}{2}}\left[\left(c^{1}_{\vec{k}}\vec{\mathrm{e}}_1-c^{2}_{\vec{k}}\vec{\mathrm{e}}_2\right)e^{-ikx}-\left(c^{*1}_{\vec{k}}\vec{\mathrm{e}}^{*}_1-c^{*2}_{\vec{k}}\vec{\mathrm{e}}^{*}_2\right)e^{ikx}\right]. \tag{4}$$

Here $(\vec{E}(x),\vec{H}(x))$ are the real electric and magnetic field strengths, $c^{1}_{\vec{k}},c^{2}_{\vec{k}}$ are the complex quantum-mechanical momentum-helicity amplitudes of a photon (the amplitudes of the transverse electromagnetic waves),

$$kx=\omega t-\vec{k}\vec{x},\quad \omega=\sqrt{\vec{k}^{2}}, \tag{5}$$

and the 3-component basis vectors $(\vec{e}_1,\vec{e}_2,\vec{e}_3)$, which, without any loss of generality, can be taken as

$$\vec{\mathrm{e}}_1=\frac{1}{\omega\sqrt{2(k^1k^1+k^2k^2)}}\begin{vmatrix}\omega k^2-ik^1k^3\\ -\omega k^1-ik^2k^3\\ i(k^1k^1+k^2k^2)\end{vmatrix},\quad \vec{\mathrm{e}}_2=\vec{\mathrm{e}}^{*}_1,\quad \vec{\mathrm{e}}_3=\frac{\vec{k}}{\omega}, \tag{6}$$

are the eigen vectors of the quantum-mechanical helicity operator for the spin s = 1.

The general solution (4) is ordinarily found by the Fourier method, and the normalization factor $C\equiv\sqrt{\frac{\omega}{2(2\pi)^{3}}}$ in (4) is taken from the condition

$$P^{0}=\frac{1}{2}\int d^{3}x\left(\vec{E}^{2}+\vec{H}^{2}\right)=\int d^{3}k\omega\left(\left|c^{1}_{\vec{k}}\right|^{2}+\left|c^{2}_{\vec{k}}\right|^{2}\right), \tag{7}$$

i.e., from the demand to have the dimension of energy. The conservation law of momentum is given by the Pointing vector.

It is interesting to find the general solution of the system (1), which is expected to have another (maybe not only transverse) form. The Fourier method in the corresponding rigged Hilbert space leads to the general solution (some details on the useful functional spaces are given in [22]):

$$\begin{gathered}\vec{E}(x)=\frac{1}{(2\pi)^{3/2}}\int d^{3}k\sqrt{\frac{\omega}{2}}\left[\left(c^{1}_{\vec{k}}\vec{\mathrm{e}}_1+c^{2}_{\vec{k}}\vec{\mathrm{e}}_2+\alpha_{\vec{k}}\vec{\mathrm{e}}_3\right)e^{-ikx}+\left(c^{*1}_{\vec{k}}\vec{\mathrm{e}}^{*}_1+c^{*2}_{\vec{k}}\vec{\mathrm{e}}^{*}_2+\alpha^{*}_{\vec{k}}\vec{\mathrm{e}}^{*}_3\right)e^{ikx}\right],\\ \vec{H}(x)=\frac{i}{(2\pi)^{3/2}}\int d^{3}k\sqrt{\frac{\omega}{2}}\left[\left(c^{1}_{\vec{k}}\vec{\mathrm{e}}_1-c^{2}_{\vec{k}}\vec{\mathrm{e}}_2\right)e^{-ikx}-\left(c^{*1}_{\vec{k}}\vec{\mathrm{e}}^{*}_1-c^{*2}_{\vec{k}}\vec{\mathrm{e}}^{*}_2\right)e^{ikx}\right],\\ E^{0}(x)=\frac{1}{(2\pi)^{3/2}}\int d^{3}k\sqrt{\frac{\omega}{2}}\left(\alpha_{\vec{k}}e^{-ikx}+\alpha^{*}_{\vec{k}}e^{ikx}\right).\end{gathered} \tag{8}$$

It is easy to see that here the electric field strength $\vec{E}(x)$ contains (together with the ordinary transverse waves) the longitudinal wave as well. This longitudinal electric wave is determined by the amplitude $\alpha_{\vec{k}}$. The scalar function $E^{0}(x)$ specifies the electric current and charge densities in the Maxwell system (1). The scalar wave $E^{0}(x)$ is longitudinal as well and is determined by the amplitude $\alpha_{\vec{k}}$.

The validity of the solution (8) can be verified by the direct substitution of (8) into equations (1). The analysis of found solutions (8) demonstrates that longitudinal components are located near the corresponded current and charge densities, which are the sources of such fields. It follows from the fact that current and charge densities and the corresponded longitudinal components in the solutions are determined by the same amplitudes $\alpha_{\vec{k}},\alpha^{*}_{\vec{k}}$. The best examples of corresponding physical reality are such big charges as the whole water area of closed sea, the planet Earth in general, and their oscillations, and corresponding longitudinal electric and scalar waves.

1. S.I. Pekar, The theory of electromagnetic waves in a crystal in which excitons are produced, Sov. Phys. JETP. **6** (1958) 785-796.
2. L. Uvarova, Ya. Burenok, Modeling of propagation of transverse and longitudinal electromagnetic waves in nanostructures with nonlinear properties, Int. J. Pure Appl. Math. **109** (2016) 691-707.
3. V.V. Datsyuk, O.R. Pavlyniuk, Properties of longitudinal electromagnetic oscillations in metals and their excitation at planar and spherical surfaces, Nano. Res. Lett. **12** (2017) 473.
4. J.N. Kuznetsov, Longitudinal-scalar electromagnetic wave radiating device, Patent of Russian Federation, RU 2287212 C1, Bull. is.31 (10.11.2006).
5. G. Miyaji, N. Miyanaga, K. Tsubakimoto, K. Sueda, K. Ohbayashi, Intense longitudinal electric fields generated from transverse electromagnetic waves, Appl. Phys. Lett. **84** (2004) 3855-3857.
6. S.C. Tidwell, D.H. Ford, W.D. Kimura, Generating radially polarized beams interferometrically, Appl. Opt. **29** (1990) 2234-2239.
7. R. Dorn, S. Quabis, G. Leuchs, Sharper focus for a radially polarized light beam, Phys. Rev. Lett. **91** (2003) 233901.
8. V.G. Niziev, V.P. Yakunin, N.G. Turkin, Generation of polarisation-nonuniform modes in a high-power CO_2 laser, Quantum Electronics **39** (2009) 505-514.
9. T.M. Jeong, S. Bulanov, S. Weber, G. Korn, Analysis on the longitudinal field strength formed bytightly-focused radially-polarized femtosecond petawatt laser pulse, Optics Express **26** (2018) 33091-33107.
10. Y.I. Salamin, Fields and propagation characteristics in vacuum of an ultrashort tightly focused radially polarized laser pulse, Phys. Rev. A **92** (2015) 053836.
11. E.Yu. Petrov, A.V. Kudrin, Plasmons in QED vacuum, Phys. Rev. A **94** (2016) 032107.
12. L.M. Kovrizhnykh, V.N. Tsytovich, Interaction of longitudinal and transverse waves in plasma, Sov. Phys. JETP. **19** (1964) 1494-1499.
13. L.S. Bogdankevich, A.A. Rukhadze, Excitation of longitudinal electromagnetic waves in a restricted plasma by injection of relativistic electron beams, Sov. Phys. JETP. **35** (1972) 126-132.
14. V.M. Simulik, Longitudinal electromagnetic waves in the framework of standard classical electrodynamics, arXiv: 1606.01738v2, [physics. class-ph], (2020) 23 p.
15. S. Nedic, Longitudinal waves in electromagnetism - toward a consistent theory, Galilean Electrodynamics **28** (2017) 91-96.
16. V.C.A. Ferraro, H.T. Flint, Longitudinal electromagnetic waves between parallel plates, Proc. Phys. Soc. **53** (1941) 170-181.
17. N.P. Khvorostenko, Longitudinal electromagnetic waves, Rus. Phys. J. **35** (1992) 223-227.
18. V.M. Simulik, Connection between the symmetry properties of the Dirac and Maxwell equations. Conservation laws, Theor. Math. Phys. **87** (1991) 386-393.
19. I.Yu. Krivsky, V.M. Simulik, General solution of the Maxwell equations with gradient-like sources and longitudinal electromagnetic waves, in Proceedings of the First International conference "Non-Euclidean geometry in modern physics. BGL-1. "Uzhgorod, Ukraine, 13-16 August 1997, P.193-199.
20. I.Yu. Krivsky, V.M. Simulik, On the longitudinal electromagnetic waves, Uzhgorod University Sci. Herald, Ser. Phys. **2** (1998) 121-125.
21. V. Simulik, I. Gordievich, T. Zajac, Slightly generalized Maxwell system and longitudinal components of solution, J. Phys. Conf. Ser. **1416** (2019) 012033.
22. V. Simulik, Relativistic quantum mechanics and field theory of arbitrary spin, Nova Science, New York, 2020, 341 p.

ORAL

METALLIC REPLICA OF THE NANOSTRUCTURED TEMPLATE SURFACE AS A TOOL FOR SMART TEXTILES

Barabash M.Yu[1]., Suprun N.P[2]., Pozhilov-Nesmiyan G.M[2]., Martynchuk V.E[1].,
Kolesnichenko A.A[1]., Rybov L.V[1]., Litvin R.V[1].

[1]Technical Center, N.A.S. of Ukraine, 13, Pokrovs'ka St., 04070 Kyiv, Ukraine
[2]Kyiv National University of Technologies and Design (KNUTD)
Nemyrovycha-Danchenka Street, 2 Kyiv 01011 Ukraine

The purpose of the work is to establish the possibility of using the technique of replicating the nanostructured templates surface as a tool for smart textiles. The replication of the simplest nanoobjects – 2D nanostructures of gold-amorphous molecular semiconductor (AMS) by injection molding of plastic from a template sample was tested. The task of developing a textiles structural dyeing method using nanotechnology in the processes of nanoimprint or crazing is relevant. The developed lattice samples with an area of about 5 cm^2 and a period of about 700 nm were made using an electrostatic template created by holographic lithography in counter beams. The surface of the template was metallized with gold by thermal evaporation in vacuum. Replicas of the lattice were obtained by electroforming [1]. The mold-forming surfaces of the casting replicas were deposited from Ni-Co alloy as a solid surface layer with thickness of 150 μm. Subsequently, the upgrading of replica's surface by nickel was continued in another bath to a thickness of 2 mm.

1. *Барабаш М.Ю., Супрун Н.П., Колесніченко А.А., Гринько Д.О., Леонов Д.С., Сперкач С.О.* Металева репліка поверхні наноструктурного темплату як інструмент «розумного» текстилю // Наносистеми, наноматеріали, нанотехнології. – 2020. – Т.18, № 2. – С. 345-356.

SERS-SUBSTRATES BASED ON LATERALLY ORDERED ARRAYS OF NANOCAVITY OF NOBLE METALS

Dan`ko V.A.[1], Bandarenka H.V.[2], Dolgyi A.L.[2], Indutnyi I.Z[1],
Lytvyn P. M.[1], Lukaniuk M.V.[1], Mynko V.I.[1], Redko S.V.[2]

[1]*V. Lashkaryov Institute of Semiconductor Physics Natl. Acad. of Sci. of Ukraine.*
45 Prospect Nauky, 03028, Kyiv, Ukraine.
[2]*Belarusian State University of Informatics and Radioelectronics,*
6,P. Brovki Street, Minsk 220013 Belarus

The high sensitivity of surface-enhanced Raman scattering (SERS) spectroscopy is increasingly being used for the diagnosis of substances in chemistry, physical and biological sciences, environmental monitoring and medical diagnostics. The giant enhancement of Raman scattering is explained by the interaction of incident light with metallic nanostructures (nanoparticles, nanotips, rough surfaces, laterally ordered relief nanostructures, etc.). Such interaction leads to a significant increase in the electric field of exciting electromagnetic radiation and scattered light as a result of the excitation of surface plasmons in such nanostructures (SERS substrates) [1].

A disadvantage of traditional SERS-substrates is the impossibility of registering the full spectrum of high-molecular compounds due to the fact that not all bonds of such a molecule fall into the places of localization of the plasmon excitation field [2]. This problem can be overcome by using so-called plasmonic nanocavities or antinanoparticles [3]. This opens up the possibility of obtaining the SERS spectrum, in which all the bands characteristic of the target molecule are present, since it can be located inside the nanocavity and will be uniformly exposed to the electromagnetic field.

The simulation of the distribution of the electric field strength at the surface of nanostructures (nanocavities) was carried out using the COMSOL Multiphysics 5.3a platform (AC/DC module). A normally directed plane wave with wavelengths of 473, 532, 633, 785, and 980 nm was used to simulate the exciting light. Nanocavities in a silver film, as well as that in silicon, conformally coated with silver, were considered. Calculations have shown that the maximum of the field strength, which is formed due to internal re-reflection in silver nanocavities, shifts from the bottom to the inlet of the nanocavity with an increase in the excitation wavelength from 473 to 980 nm. Localization of the electric field strength maximum in the center of the nanocavity is characteristic for 633 nm and 785 nm. Similar results were obtained for nanocavities in silicon, conformally coated with a 20 nm thick silver film. The only difference is that, for samples with a more thin silver film, the region of increased electric field strength is more blurred in the bulk of the nanocavity. Thus, the simulation results showed that cavities can be formed in a semiconductor or dielectric layer and then covered with a layer of a plasmon-supporting metal (silver or gold) 20 - 100 nm thick. In our work, chalcogenide glass (CG) is used as a relief-forming layer.

This paper presents the results of the development and optimization of the processes of formation of SERS substrates in the form of two-dimensional arrays of noble metal nanocavities using interference photolithography [4] based on a two-layer chalcogenide photoresist. For the formation of nanocavities with a deep relief (up to 500 nm), it was proposed to use a two-layer chalcogenide photoresist consisting of successively deposited layers of $As_{10}Ge_{30}S_{60}$ and $As_{40}S_{30}Se_{30}$. The top layer of $As_{40}S_{30}Se_{30}$ is a high-resolution light-sensitive photoresist and can be used to obtain an interference lithographic mask. The $As_{10}Ge_{30}S_{60}$ layer is practically insensitive to light, but is mechanically and thermally more stable in comparison with $As_{40}S_{30}Se_{30}$. This layer is used to form a matrix of nanocavities of a given shape and size. The recording of interference structures on chalcogenide films was performed using an interference pattern from helium-cadmium

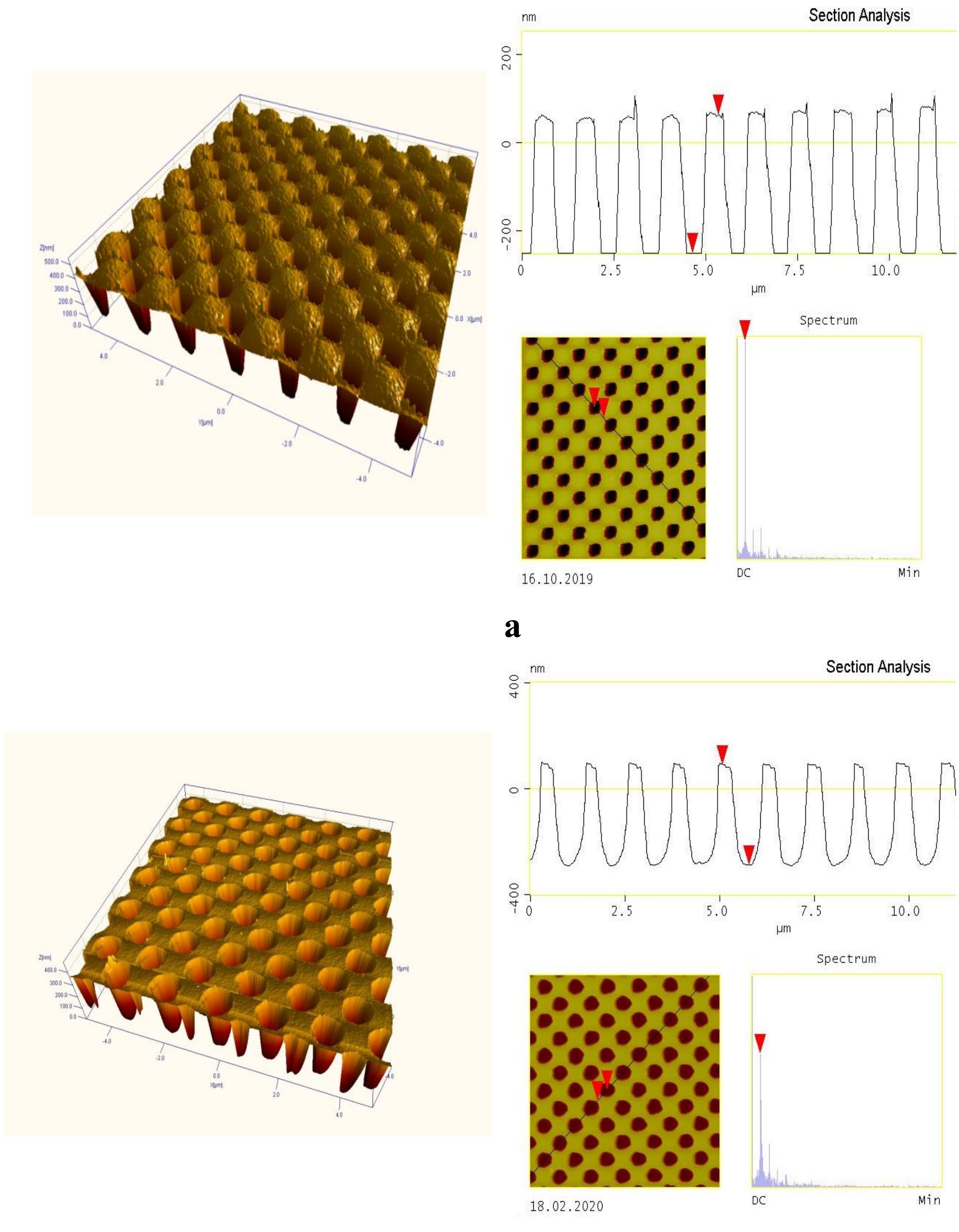

a

B

Fig. 1. AFM images and cross-section of SERS-substrate for detecting high-molecular compounds with a period of 1207 ± 0.5 nm and different filling factor.

laser radiation (wavelength $\lambda = 441.6$ nm) with a given spatial frequency. The etching of the photoresist and metal after exposure was monitored in situ by recording non-photoactive longwave light was diffracted from the relief structure. After removal of the photoresist residues, washing and drying, the formed periodic structure of the nanocavities array in the $As_{10}Ge_{30}S_{60}$ film was obtained. After optimization of the parameters of the processes of vacuum deposition of layers, interference exposure of a two-layer photoresist, post-exposure processing of the photoresist and relief-forming layers, and taking into account the simulation results, prototypes of SERS substrates were made -

substrates with different spatial frequencies (from 1200 to 800 mm^{-1}) and depths of nanocavities (from 250 up to 500 nm). As a result of scanning the surface of substrates based on nanocavities in CGs with a diameter of 370–700 nm and a depth of 125–400 nm, quasi-conformally coated with films of silver 40–90 nm thick and gold films 20–50 nm thick, it was shown that the intensity of the SERS signal from lysozyme molecules, adsorbed on silver nanocavities is three times higher than on gold nanocavities.

Thus, as a result of numerical simulation of the electric field strength distribution in nanocavities based on noble metals when a light wave falls and surface plasmons are excited, it is established that a region of high electric field strength is formed inside the cavity. This effect is almost identical both for cavities in silver layers and in layers of other substances conformally coated with a silver layer. The use of such nanocavities with sizes larger than 500 nm allows efficient analysis of the structure of macromolecules by surface-enhanced Raman light scattering spectroscopy, since macromolecules completely overlap with regions of increased electric field strength inside the nanocavities. It is shown that the technology of interference lithography based on two-layer chalcogenide photoresists makes it possible to form effective SERS substrates in the form of laterally ordered matrices of nanocavities with specified morphological characteristics (spatial frequency, nanocavity sizes, composition and thickness of a conformal metal coating) for detecting high-molecular compounds.

1. Moskovits, M. Surface-enhanced spectroscopy. *Rev. Mod. Phys.* **57**, 783–826 (1985).
2. G. Arzumanyan, N. Doroshkevich, K. Mamatkulov, S. Shashkov, K. Girel, H. Bandarenka, V.Borisenko, Phospholipid detection by surface-enhanced Raman scattering using silvered porous silicon substrates, Physica Status Solidi (a) 2017, 214 (8), 1600915; https://doi.org/10.1002/pssa.201600915.
3. T.A. Kelf, Y. Sugawara, R.M. Cole, J.J. Baumberg, Localized and delocalized plasmons in metallic nanovoids, Phys. Rev. B. 74, 245415-1 (2006).
4. Dan’ko V., Indutnyi I., Min’ko V., Shepelyavyi P.: Interference photolithography with the use of resists on the basis of chalcogenide glassy semiconductors. Optoelectronics Instrum. DataProcess. 2010, 46:483–490.

CARBIDE PHASES NUCLEATION DURING MELTS ELECTROLYSIS

Malyshev V.V., Gab A.I., Shakhnin D.B., **Demochko M.V.**

Open International University of Human Development “Ukraine”, 26, Lvivska St., 03115 Kyiv, Ukraine

We studied mechanisms of Mo and W carbides high-temperature electrochemical synthesis and initial stages of crystal nucleation by the electrochemical methods used in the study of phase formation with simultaneous investigation of the microstructure of the substrate surface and electrolysis products. The experimental apparatus consisted of resistance furnace with stainless steel reactor, of analytical Radiometer Voltalab PST 050 for measuring voltammograms and galvanostatic switch (potential-time) curves, which are, in fact, the dependences of the electrode potential on time after the action of the initial current pulse, and of equipment for the microstructural studies based on MBS-9 microscope. Measurements were performed in the three-electrode cell. The anode, platinum crucible, simultaneously served as melt container; the working electrode was the edge electrode (made from different metals) of 0.5-1.0 mm diameter fused in quartz glass. The reference electrode was diaphragmed platinum-oxygen electrode O_2, Pt|Na_2WO_4-20 mol%WO_3 or was consisted of pressed Mo_2C and W_2C strips on platinum current lead. After being washed with distilled water, the deposits were studied on the DRON-4 X-ray diffractometer and in the Stereoscan S-4 scanning electron microscope. The grain size was averaged over 50-100 grains. The surface morphology of the layers was determined in the Camebax scanning electron microscope.

Mechanism of high-temperature electrochemical synthesis of molybdenum and tungsten carbides. The reduction wave of lithium molybdate was observed at voltammogram of Na_2WO_4-Li_2MoO_4 (1-5 mol%)-Li_2CO_3 molten system at potential –1.6-1.7V versus Pt (O_2)/Na_2WO_4-WO_3 (20 mol%) reference electrode. Adding of lithium carbonate up to 2.5 mol% does not allow to observe the CO_3^{2-} reduction wave. Instead, however, the high increase of MoO_4^{2-} reduction wave and its shift to electropositive region are observed. During further rise of lithium carbonate concentration at voltammetric curves one can observe CO_2 reduction wave at more positive potentials. At the same time the MoO_4^{2-} and CO_2 joint reduction wave arises. At carbonate concentration 8 mol% all three processes combines into the one wave stretched along the potential axis. Galvanostatic and potentiostatic electrolysis at these conditions give only one product – Mo_2C.

The electroreduction of the carbonate and tungstate ions in a sodium tungstate melt was discussed in literature. It is difficult to detect the reduction wave of lithium tungstate on the background of Na_2WO_4. Adding lithium tungstate up to 20 mol% gave rise to no waves but caused a positive shift of the voltammetric curve relative to that of pure tungstate. A wave is detectable only at lithium tungstate concentrations above 20 mol%. The reduction wave of Li_2WO_4 is observed at its concentration 40 mol % and a potential of –1.8 to –1.9 V relative to a Pt (O_2)/Na_2WO_4-WO_3 (20 mol%) electrode. Adding lithium carbonate to the Na_2WO_4-Li_2WO_4 melt initially causes an increase in the height of the lithium tungstate reduction wave. The reduction wave of the carbonate ion, followed by lithium tungstate electroreduction, appears at lithium carbonate concentration of 10 mol%. At the lithium carbonate concentration of 15 mol %, the tungstate and carbonate reduction waves merge in a single broad electroreduction wave. Potentiostatic electrolysis data, in relation to the Li_2CO_3 concentration are follows: 0-10 mol% - W; 0.1-2.5 – W and W_2C traces; 2.5-5.0 mol % – W, W_2C and WC traces; 5.0-7.5 – W_2C, WC; 7.5-10.0 – WC, W_2C; 10.0-15.0 – WC.

Molybdenum and tungsten carbides coatings electrodeposition. Coatings electrodeposition was realized from Na_2WO_4-Li_2MoO_4-Li_2CO_3 and Na_2WO_4-Li_2WO_4-Li_2CO_3. Molybdenum carbide coatings form if Li_2MoO_4 concentration in the melt is 2.5-7.5 mol%, Li_2CO_3 concentration – 2.5-10.0 mol %. At higher concentrations of Li_2MoO_4, in parallel with tungsten carbide, molybdenum oxides and free carbon are observed, at less concentration – metallic molybdenum.

More available industrial reactant is MoO_3. Using it as molybdenum source, lithium carbonate concentration must be 2 times higher than using Li_2MoO_4. Continuous deposits of Mo_2C

were obtained at 1073-1223 K (the higher is temperature, the largher deposit grains are). However, at 1073 K carbide layer is 10 μm thick and has low adhesion to substrate. At temperature lower than 1073 K deposits in the form of powder are obtained. Continuous, uniform, absolutely pore-freecoatings with good adhesion were obtained at cathode current density 0.01-0.1 A/cm^2. Molybdenum carbide deposition rate is 5-20 μm/h (at cathode current density 0.02-0.1 A/cm^2), thickness of these coatings up to 200 μm, current yield of Mo_2C in form of coating is 90%. With electrolysis duration increases current yield of Mo_2C decreases. Tungsten carbide coatings were deposited from Na_2WO_4-Li_2WO_4(40 mol%)-Li_2CO_3 (10-15mol%) melt, with electrodeposition regularities (including carbonate usage) being the same. Thickness of W_2C is up to 100 μm, current yield of W_2C in the form of coating is up to 75%. The microhardness of Mo_2C is 17.6-18.6 GPa, while that of W_2C is 28.4-30.4 GPa. As the result of coating deposition, the durability of steel specimens increases 5-9 times, and the abrasive resistance – 4-6 times.

Initial stages of nucleation of carbide phases. It is known that carbide electrodes in tungstate-molybdate-carbonate melts of certain compositions have equilibrium electrode potentials. These results were also confirmed by the study of the reaction kinetics in electrodeposition of carbide coatings onto solid electrodes. The deposition of carbide onto the solid foreign substrate at the switched-on current is characterized by three important features: the shift of the potential to the electronegative region, the shift of the potential to the electropositive region untill reaching the certain value (stationary state), and the equilibrium value of the potential of the deposited compound after switching-off of the current.

It is established that the first crystals start growing immediately after the appearance of the peak on the potentiodynamic curves. The repeated switching-on of the current within a short period of time (5-10 s) does not give rise to peak formation. These facts indicate that the crystallization overvoltage is associated with three-dimensional nucleation. Based on the experimental results, we evaluated the crystallization overvoltage due to considerable energy consumption for component nucleation at the first moments of synthesis. These overvoltages at the Ag electrodes in the temperature range 973-1023 K reach the values of 8-20 mV. The carbide deposition onto the substrates prepared from the same solid materials was not accompanied by crystallization overvoltage. Maximum value of initial overvoltage η_{max} consisting of steady overvoltage during long-term current passing and of crystallization overvoltage is directly proportional to electrode surface area. Under these conditions, the stage of surface diffusion does limit the rate of the process at the electrode. With an increase of the rate of carbide deposition, the number of crystallization centers increases, which reduces deceleration related to surface diffusion. As a result, higher overvoltages seem to change the limiting stage so that the process rate is determined either by the rate of electron transfer or by the rate of diffusion from the melt volume.

An increase in the melt temperature may complicate the crystallization process because of the interaction between the deposited components and the material matrix. For metals forming alloys with the deposited components, crystallization overvoltage is observed for a surface oxide film. After mechanical treatment of the surfaces of the working electrodes, they were electrochemically polished with simultaneous control of the substrate state in a microscope. The time of electrical polishing was determined with allowance made for the dissolution time of mechanically damaged layers of metal surface.

A typical potentiodynamic curve corresponding to carbide electrodeposition onto the native substrate over wide temperature (973-1173 K) and current density (i = 0.02-0.40 A/cm^2) ranges indicates the absence of any hindrances to crystallization and any passivating films on the surface. To determine the degree of the substrate inertness, we studied the overvoltage maximum and the time of its formation during electrocrystallization of Mo_2C under galvanostatic conditions on the Mo, Ti, Ni, Ag, Cu, Pt, and Mo_2C substrates. The choice of the material of the working electrode was made with due regard for its metallochemical properties and phase diagrams of binary metal systems with the Mo and C components.

It is characteristic that the height of the overvoltage maximum for the above metals is proportional to the reciprocal time of their formation. This seems to be associated with the partial penetration of the deposited components into the substrate bulk due to solid-phase diffusion, which allowed us to qualitatively characterize the degree of inertness of the substrate material. Thus, crystallization overvoltage η_{max} on the Ni substrate is observed only at certain current-density values. On a Pt substrate, one observes noticeable depolarization with two distinct waves that seem to correspond to the formation of alloys with different compositions.

An increase in the melt temperature usually activates the cathode surface, increases the rate of mutual diffusion of the deposited components of the synthesized material and the substrate, and also intensifies their chemical interaction. We showed experimentally that Mo_2C electrodeposition at temperatures above 1173 K, even in the case of an inert Ag substrate, is accompanied by depolarization due to alloy formation. Measurements performed over the wide temperature range (973-1123 K) indicate a regular change of the initial stages of Mo_2C electrocrystallization on the substrate with an increase in temperature. An increase in the temperature up to 1173 K removes the crystallization hindrances at the moment of formation of stable aggregates of new phase. A further increase in the temperature results in the fixation of obvious depolarization processes. The crystallization overvoltage increases with an increase in the current density.

According to literature data, if the decelerated stage is the stage of primary formation of three-dimensional nuclei, then the following relationship should be fulfilled: $\lg\tau = A + (K/\eta^2)$, where τ is the time of formation of three-dimensional nuclei, A and K are the constants dependent on the the electrode material, and η is the crystallization overvoltage. In actual fact, the experimental points in the $\lg\tau$-$1/\eta^2$ coordinates fit the straight lines at different melt temperatures. The further deposit growth proceeds by the layer-by-layer mechanism.

Epitaxial ratio of carbides galvanic coatings. The epitaxial growth of Mo_2C on molybdenum or tungsten substrate by melt electrolysis has not been studied. Heteroepitaxial layers were obtained by electrocrystallizing of molybdenum carbide from melt on monocrystalline substrates of molybdenum and tungsten of different orientations at 1173 K and with cathode current density being 10^3 Am^{-2}. The deposits were investigated by X-ray diffraction method with the use of DRON-3 diffractometer and Camebax scanning electron microscope. For example, at Mo_2C deposition on monocrystalline seeds made of Mo and W not only dimensional, but also structural mismatch is observed.

The structure in which molybdenum carbide crystallization is hexagonal close-packed structure with the lattice parameters: a=3.002 A, c=4.722 A. The structure of molybdenum and tungsten is a body-centered cubic structure with the lattice parameters: a_{Mo}=3.147 A, a_w=3.165 A. Thus, when molybdenum carbide is deposited on molybdenum and tungsten single crystals, there is not only a dimensional but also a structural discrepancy. Therefore, obtaining of monocrystalline molybdenum carbide layers can be hardly expected.

However, under these crystallization conditions, molybdenum carbide layers with one or two orientations were obtained on monocrystalline molybdenum with the {110}, {100}, {112} and {111} orientations and on tungsten with the {110} and {112} orientations.

The microstructure of the surface of Mo_2C deposited on a {110} Mo face consists of layers extended in the [1210] direction. In the other faces of both molybdenum and tungsten however, molybdenum carbide crystallizes as hexahedral platelets differently oriented relative to the substrate. The main plane present in the deposit is the basal {001} plane.

The following heteroepitaxial relations were determined using X-ray structure analysis:
(1010) {0001} Mo2C || (110) [110] Mo
(2023) Mo2C || (100) Mo
(1011) Mo2C || (100) Mo
(1120) [0001] || Mo2C || (111) [112] Mo
(1122) Mo2C || (112) Mo

When Mo_2C is deposited on monocrystalline tungsten with the orientations {110} and {112}, other heteroepitaxial relations occurred:
(1011) Mo2C || (100) W
(0001) Mo2C || (110) W

(1013) Mo2C || (112) W

From the analysis of the relations obtained and the surface morphology it can be concluded that molybdenum single crystals with the {110} orientation are the most suitable substrates for obtaining monocrystalline molybdenum carbide layers under the given conditions.

Conclusions. Mechanisms of high-temperature electrochemical synthesis of molybdenum and tungsten carbides from tungstate-molybdate-carbonate melts were studied. The conditions of qualitive galvanic coatings on different materials were determined experimentally.

This experimental study of the initial stages of Mo_2C electrocrystallization from tungstate-molybdate-carbonate melts with electrodes prepared from various materials over a wide temperature range allows us to put forward the following concepts of nucleation. Using inert substrates at T<1073-1173 K, we observed considerable crystallization hindrances associated with the formation of three-dimensional nuclei. An increase in the electrolysis temperature facilitates diffusion of atoms of the components into the substrate, which results in a decrease of the crystallization overvoltage. Simultaneously, a transition from the three- to two-dimensional nucleation is evidenced and, in some instances, associated to depolarization phenomena due to solid-phase saturation of the electrode boundary layers with the components (molybdenum and carbon) and alloy formation.

BINDING OF CALIX[4]ARENE TO THE A-KNOB OF FIBRIN: *IN SILICO* PROVES *IN VITRO*

Didkivkyi V.A.[1], Hrabovskyi O.O. [1], Humenyuk A.S.[1], Selikhova A.I.[2], Banya M.O.[1],
Cherenok S.O.[2], Chernyshenko V.O.[1]

[1] *Palladin Institute of biochemistry, NAS of Ukraine, 9, Leontovych Str., 01054, Kyiv, Ukraine*
[2] *Institute of organic chemistry, NAS of Ukraine, 5, Murmanska Str., 02660,*
Kyiv, Ukraine

C-145 (octasodium salt of calix[4]arene-tetra-methylene-bis-phosphonic acid) was previously considered as a specific antithrombotic agent that affects fibrin polymerization [1]. Hydrophobic hole of calix[4]arene molecule was expected as the active site that specifically blocks polymerization sites of fibrin 'A'-knobs [2]. To prove this hypothesis we compared the action on fibrin polymerization of calix[4]arenes C-145 and C-937 (disodium salt calix[4]arene-methylene-bis-phosphonic acid) that differ by the number of methylene-bis-phosphonic moieties – four and one respectively.

The change of turbidity during fibrin clot formation induced by APTT-reagent in the presence of calix[4]arenes was measured using a Multiscan reader (ThermoFisher Scientific, USA).

To investigate the interactions between the fibrin molecule and calix[4]arenes the molecular docking method was performed using Autodock vina software. The structure of the fibrinogen molecule, defined by X-ray crystallography (PDB Entry: 3GHG), was taken as a basic model, in which, however, there were no N-terminal regions of Aα-chains, which play a major role in interactions. Missing parts were modelled using Modeller 9.19.

Turbidity studies showed that at the concentration of 25 μm C-145 completely inhibits fibrin formation, while C-937 prolonged the lag period by 60 seconds compared to the control value. The effect of C-937 on the exponential growth phase and the final turbidity of the media were not observed. At a concentration of 5 μM C-145 prolongs the polymerization lag-period more than twice and 2.5 times inhibits the rate of fibrin clot formation. C-937 at the same concentration extended the lag-period by 25 s compared to the control.

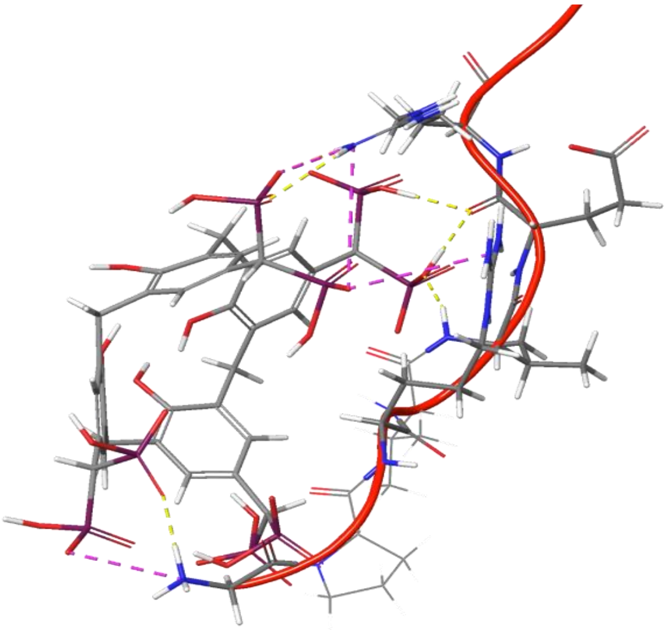

Fig.1. Binding mode between calix[4]arene C-145 and N-terminus of Aα-chain of the fibrin molecule

According to the molecular docking data three bisphosphonate moieties are involved in the interaction of C-145 with the Aα-chain of fibrin, forming hydrogen bonds with Gly17, Arg19, Val21, Glu22, Arg23 (Fig. 1). At the same time, the complex between C-937 and fibrin is less stable because it is only stabilized by hydrogen bonds between one bisphosphonate moiety and Arg19, Glu22, Arg23, His24 (Fig. 2).

Thus our results directly showed the much higher anti-polymerization efficacy of C-145 in comparison to C-937. The conclusion about the importance of bisphosphonate moieties in the fibrin interaction with calix[4]arene was proven by molecular docking.

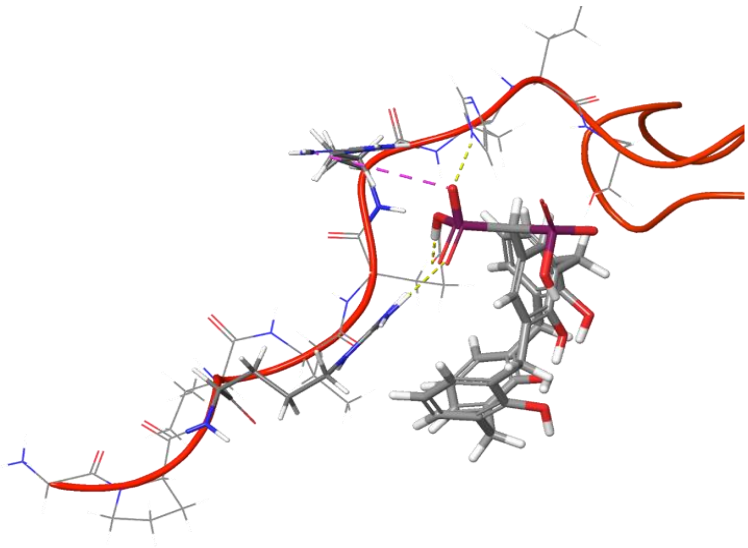

Fig.2. Binding mode between calix[4]arene C-937 and N-terminus of Aα-chain of the fibrin molecule

The research was a part of Project according to the targeted complex program of NAS of Ukraine for fundamental research “Prospective fundamental studies and innovations of nanomaterials and nanotechnologies for the industry, healthcare and agriculture 2020-2024”.

1. Chernyshenko V.O., Korolova D.S., Dosenko V.E., [et al.]. Calix[4]arene C-145 Effects on Plasma Haemostasis // Pharm Anal Acta. 2015, – V. 6. – P. 406.
2. Lugovskoi E.V., Gritsenko P.G., Koshel T.A., [et al.]. Calix[4]arene methylenebisphosphonic acids as inhibitors of fibrin polymerization // FEBS J., 2011. – V. 278. – P. 1244-1251.

GLUCURONIC ACID-BASED HYDROGELS

Dil K.V., Okovityy S.I., Kondratyuk N.V.

Oles Honchar Dnipro National University
Gagarin Avenue, 72, Dnipro, 49000 Ukraine
katerina.vlodimirovna@ukr.net

Today, nutrition is an important factor in the impact of metabolic metabolism. The question of ways to remove xenobiotics, which is impossible to avoid getting into the body, is acute. Despite the very wide range of functional products and studies of the action of biologically active substances (BAS), to determine the role of nutrition in the development of metabolism remains problematic.

Research in the field of modeling structures and studying the characteristics of food products containing functional ingredients with a high concentration of BAS are relevant and important for the implementation of the idea of shaping human health. Uronic acids have a sufficient range of technological properties and physiological features aimed at the detoxifying effect of heavy metals and radionuclides. Today, glucuronic acid from its raw materials (xanthan and licorice extract) is important for study. Glucuronic acid is actively involved in the inactivation of xenobiotics.

The aim was: modeling of food process media based on xanthan and licorice root extract.

Tasks:

- substantiate the development of food processing environments based on components that contain glucuronic acid;
- model models of glucuronic acid, xanthan and licorice root.

The object of the study are gels containing glucuronic acid.

Subjects of research:

- quantum chemical models of glucuronic acid, xanthan and licorice root;
- solutions based on a mixture of xanthan and licorice root extract.

Research methods were to study quantum chemical models of glucuronic acid dimers using the PM3 method. Quantum chemical models of the functional units of xanthan and glycyrrhizin were built using HyperChem 8.0.8, the models were visualized using GaussView 5.0.8

Physico-chemical parameters of the finished product were studied by conventional methods.

The influence of technological factors on the structural-mechanical and physico-chemical properties of glucuronic acid-based hydrogels has been studied. The influence of additionally introduced substances on organoleptic and structural-mechanical characteristics of GGK is studied.

The result of the study. On the basis of quantum chemical models, new types of thermo- and acid-stable food films have been created, which are based on combinations of uronate polysaccharides of xanthan and glycyrrhizin, capable of self-formation and biodegradation.

Using quantum chemical models of xanthan *(Fig.1)* and glycyrrhizin *(Fig.2)*, glucuronic acid *(Fig.3)* formulations of hydrogels have been developed that can become a medium for the formation of useful foods for humans.

Developed products can provide rapid gastric emptying, enteral absorption of nutrients from the raw materials of these and other products, increase physical performance and prevent fatigue and stress. All products are sweet in taste, but do not contain sugar, which allows them to be classified as dietary and diabetic products.

It should be noted that the useful properties of glucuronic acid are realized in the composition of the predicted food products during consumption, as the content of the components allows to ensure its activity in the structure of glycyrrhizin and the release of xanthan from the macromolecule. The processes of activation and release are controlled by gastrointestinal acidity and gastric motility.

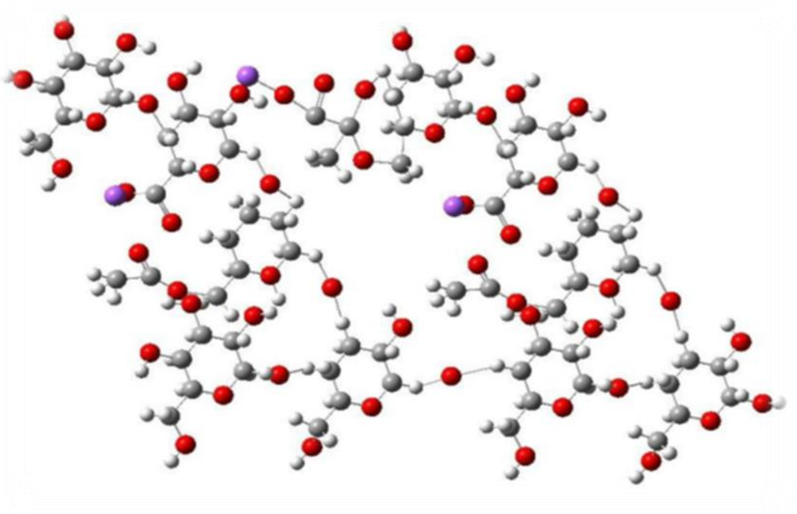

Fig. 1. Quantum chemical model of xanthan dimer

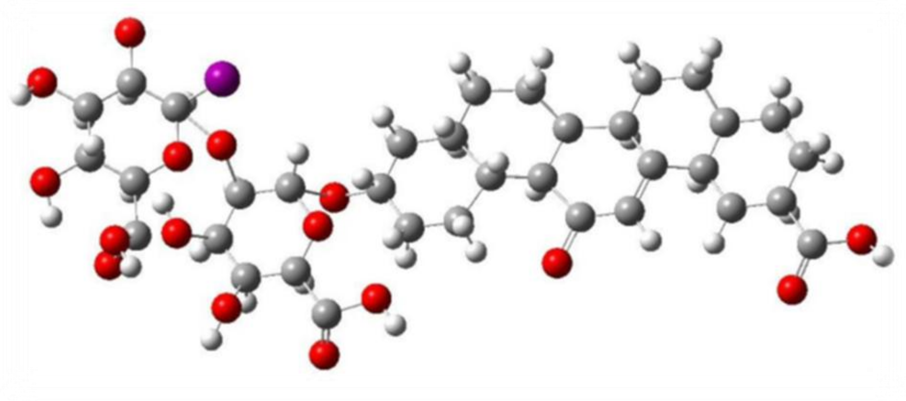

Fig.2. Quantum chemical model of glyrizinin

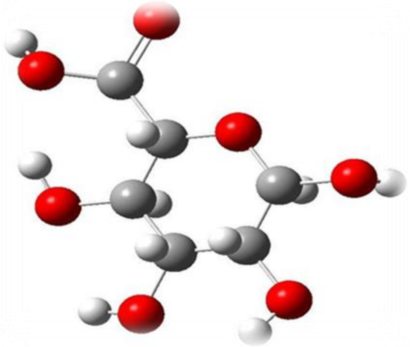

Fig.3. Quantum chemical model of glucuronic acid

Conclusions. The processes of formation of hydrogels on the basis of glucuronic acid are theoretically substantiated in the work. It is predicted that these systems act as a matrix that immobilizes biologically active substances of high reactivity in the environment and in the stomach. Keeping such compounds intact allows the motility of the stomach to deliver them to the target organs and release from the matrix, which is destroyed by the change of pH (from 1.2-1.8 to 6.8.-7.2) when entering the department small intestine.

Quantum chemical was proposed as the best method for modeling, which fully reflects the chemistry of the composition. Models of basic polysaccharides involved in the gelation process are given.

According to the results of quantum chemical modeling, and taking into account the rheological properties of xanthan hydrogels and solutions containing glycyrrhizin associates, the ratios of glucuronide-containing raw materials between themselves and water were derived.

ECO-FRIENDLY SYNTHESIS OF METAL NANOPARTICLES AND THEIR BIOLOGICAL BENEFITS FOR PROBIOTICS DEVELOPMENT

Dybkova K.[1], Rieznichenko L.[2], Dybkova S.[2], Gruzina T.[2]

[1]*Biology and Medicine Institute Science Educational Center of Taras Shevchenko National University of Kyiv, Glushkova Av., 2, Kyiv, 02000, Ukraine*
[2]*F.D. Ovcharenko Institute of Biocolloidal Chemistry NAS of Ukraine, Vernadskogo Av., 42, Kyiv, 03142, Ukraine*

Modern developments of probiotic preparations for the treatment of dysbacteriosis in human's and animal's organisms are aimed at finding substances that can stimulate the metabolic activity of cells of probiont strains and thus accelerate the release of probiotic cultures from a lyophilized state. Such activators of the physiological activity of the microorganisms can be metal nanoparticles. Now there is an increased interest in nanomaterials that obtained by the methods of "green synthesis" and with using of eco-friendly reagents, which increase their biocompatibility. At the same time, using of various nanoparticles preparations require a detailed assessment of their potential danger to the genetic apparatus of prokaryotes and eukaryotes.

The purpose of the work was to synthesize nanoparticles of metals (gold and silver) using eco-friendly reagents that ensure their biocompatibility in the composition of probiotic preparations and to study their biosafety in terms of genotoxicity.

For the synthesis of gold and silver nanoparticles, a 5% solution of tannin was used as a reducing agent. Tannin is an extremely biocompatible substance and also exhibits astringent, anti-inflammatory and antimicrobial effects. $H[AuCl_4]\cdot 3H_2O$ was used as initial substance to synthesize gold nanoparticles in aqueous solution. Silver nanoparticles were synthesized using silver nitrate, tannin, and potassium carbonate.

The synthesized gold and silver nanoparticles were visualized by transmission electron microscopy. Three preparations of gold sol with a concentration of 38.6 μg/ml by metal and two preparations of silver sol with a concentration of 0.8 mg/ml by metal were synthesized. Gold nanopreparations were represented by spherical nanoparticles with an average particles size 10 nm (1st preparation), 20 nm (2 preparations) and 30 nm (3 preparations). Silver nanopreparations consisted of spherical nanoparticles with an average size of 25 nm (first preparation) and 30 nm (second preparation).

The genotoxicity of the synthesized metal nanoparticles were assessed by the Comet assay in alkaline conditions according to the Guidelines of the Ministry of Health of Ukraine "Assessment of the safety of nanopreparations". The essence of the Comet assay consists on registration of differences in electrophoretic mobility of DNA that when migrates to the anode forms electrophoretic track, which alike "tail", whose parameters depend on the level of damage to the experimental DNA. Visualization of "DNA-comets" has been provided by fluorescence microscopy (fluorescence microscope "LUMAM R8" (exciting filter 490 nm, dichroic mirror 510 nm, reflective filter 530 nm, magnification X200-400)). For each micropreparation 200 "DNA-comets" without "tails" overlays have been analyzed. Analysis of "DNA-comets" was carried out visually by dividing on 5 relative types with appropriate number from 0 to 4 for each "DNA-comet". The level of DNA damage in this case has been defined like "DNA-comet" index (IDNA), which calculated by the formula:

$$\mathrm{IDNA} = (0n_0+1n_1+2n_2+3n_3+4n_4)/\Sigma,$$

where n_0-n_4 – number of each type "DNA-comets", Σ – sum of "DNA-comets".

Evaluation of the genotoxicity of nanopreparations *in vitro* by the Comet assay was carried out using the following cell culture lines: Chinese hamster (CHO-K1); hepatocarcinoma (HEp-2 line); transplanted culture fibroblasts of mice (line L929).

In vitro tests of the genotoxicity of the synthesized metal nanoparticles have shown that the gold nanoparticles with the average sizes of 10 and 20 nm have been characterized like genotoxic. Such nanoparticles are potentially dangerous for the genetic apparatus of a eukaryotic cell.

All other tested synthesized nanopreparations (30 nm gold nanoparticles, 25 and 30 nm silver nanoparticles) didn’t reveal genotoxic properties. So, the gold nanoparticles 30 nm in size, silver nanoparticles 25 nm and 30 nm, in the synthesis of which biocompatible tannin was used, can be recommended for biotechnological using as protectors and stimulators of physiological and biochemical parameters of microbial cells in conditions of lyophilization stress and their long-term storage.

DEVELOPMENT OF OPTICAL SENSORS USING METAL NANOPARTICLES FOR MONITORING OF PATHOGENS AND TOXINS

Dybkova S.M.[1], Gruzina T.G.[1], Rieznichenko L.S.[1,2]

[1]*F.D. Ovcharenko Institute of Biocolloidal Chemistry NAS of Ukraine, Vernadskogo Av., 42, Kyiv, 03142, Ukraine*
[2]*Institute of Veterinary Medicine NAAS of Ukraine, Donetska Str., 30, Kyiv, 13151, Ukraine*

Strict control of food products' contamination by various pathogens and toxins and the necessity for continuous monitoring of the sterility of different biotechnological industries make the relevance of the development of modern highly sensitive, rapid and quite cheap control methods. Modern bio- and nanosensors are among the devices which parameters correspond to the above-mentioned requirements for such control [1, 2]. The use of metal nanoparticles in the construction of sensors allows to highly increase their selectivity and sensitivity owing to unique physical and chemical properties of such nanomaterials [3].

The goal of the work was to study the approaches for the development of optical sensors based on the synthesized metal nanoparticles to provide the rapid monitoring of pathogens and food toxins.

Nanoparticles of gold (AuNP), silver (AgNP), copper (CuNP) and iron (FeNP) with different size and shape have been synthesized to study their potential as the component for optical nanosensors construction.

It is known that the range of nanoparticles' properties strongly depends on their size, composition, shape, surface characteristics, and so on. All these parameters can significantly affect the nature of the nanoparticles interaction with biomolecules and cells, including bacteria ones. Therefore, to develop optical nanosensors with high sensitivity and response rate it is necessary to understand the effects of used metal nanoparticles on biomolecules as well as physiological and biochemical parameters of pathogenic and opportunistic bacterial cells – potential targets for detection.

The interaction of CuNP (20 nm), FeNP (40 nm), AuNP (30 nm), AuNP (20 nm), AgNP (20 nm), AgNP (30 nm) with pathogenic bacteria strains of *Escherichia*, *Salmonella*, *Staphylococcus*, *Streptococcus* and *Clostridium* have been studied. It was shown that the synthesized metal nanoparticles with certain size and shape were actively accumulated both on the surface and inside the studied bacteria cells changing the main physiological and biochemical characteristics of the microorganisms like growth rate and enzyme activity.

Based on the revealed peculiarities of the metal nanoparticles interaction with bacteria cells approaches to optimize the methods for monitoring and control the content of coliform bacteria and *Escherichia coli* have been developed. It was shown that the use of the synthesized iron, silver and gold nanoparticles can accelerate the time of the officially recommended chromogenic reaction by 9 times. The sensitivity of the proposed method using the chromogenic environment with gold, silver or iron nanoparticles is also increased (1×10^3 CFU/ml) in contrast to the sensitivity limit of the chromogenic reaction for the presence of *E. coli* beta-galactosidase using Colilert (R) -18 (sensitivity 2×10^4 CFU/ml).

The features of contact interaction of the synthesized metal nanoparticles with biomolecules have been studied using different types of amino acids and proteins.

It was shown, for the synthesized spherical gold nanoparticles with the average particles size 20 nm and 30 nm the revealed peculiarities of interaction with amino acids can serve as a basis for the construction of an optical nanosensor to determine the quality of food by the content of biogenic amines.

The viability of the proposed approach was tested on samples of seafood (mussels): fresh products and those stored in inappropriate conditions. According to the test results, a visual change of color from red to blue was observed in the sample with mussels' homogenate after their improper storage conditions (Fig. 1), while the test sample of fresh products did not cause the color change of nanoparticles. It should be noted that the organoleptic characteristics (color, odor, elasticity, etc.) of mussels' sample after improper storage conditions did not differ from the fresh product.

Fig. 1. Testing the quality of fresh mussels (left, red color) and improper storage conditions (right, blue color) using synthesized gold nanoparticles.

Thus, the obtained data show the perceptiveness of the synthesized metal nanoparticles use in development and construction of simple, sensitive optical nanosensors to rapid determination of pathogens and food toxins.

1. Bu T., Jia P., Liu J. et al. 2019 Diversely positive-charged gold nanoparticles based biosensor: A label-free and sensitive tool for foodborne pathogen detection. *Food Chemistry: X*. 3 100052
2. Peng H., Chen I. A. 2019 Rapid Colorimetric Detection of Bacterial Species through the Capture of Gold Nanoparticles by Chimeric Phages. *ACS Nano*. 13 1244−1252
3. Abdel-Karim R. et al 2020 Review — Nanostructured Materials-Based Nanosensors. *J. Electrochem. Soc.* 167 037554

PHOTOLUMINESCENT PROPERTIES PARTIALLY UNZIPPED CARBON NANOTUBES.

Danilov M.O., Rusetskiy I.A., **Fomanyuk S.S.**, Kolbasov G.Ya.

[1]*V.I.Vernadskiy Institute of General and Inorganic Chemistry of the National Academy of Science of Ukraine, 32/34 Academic Palladin Avenue, Kyiv, 03142, Ukraine.*
e-mail: Foma7@ukr.net

The development methods for the synthesis of carbon nanoparticles is a promising area of research since it allows one to obtain environmentally friendly and safe for medical purposes photoluminescent materials [1]. Of particular interest are monolayer or bilayer carbon nanoparticles and nanotubes, since they have interesting optical properties by the plasmon effect and blue photoluminescence. In combination with their harmlessness to living organisms, these properties are useful for creating sensitive optical materials for the determination of cadmium in biological fluids [2] and bioviazulization of the action of antitumor drugs in medicine [3]. Carbon nanoparticles luminesce due to defects and edge carbon atoms. For research, we used partially unzipped multi-walled carbon nanotubes obtained by us by the electrochemical method [4]. To enhance of the photoluminescence, partially unzipped multi-walled carbon nanotubes (PUMCNTs) were subjected to ultrasonic crushing at a frequency of 22 kHz 150 W/cm^2 on a UD-11 ultrasonic device. Micrographs of such PUMCNTs are shown in Fig. 1 where the cuts are seen on a partially unzipped nanotube along its entire length Fig. 1a, and fully unzipped nanotube is shown as an unfolded sheet in Fig. 1b.

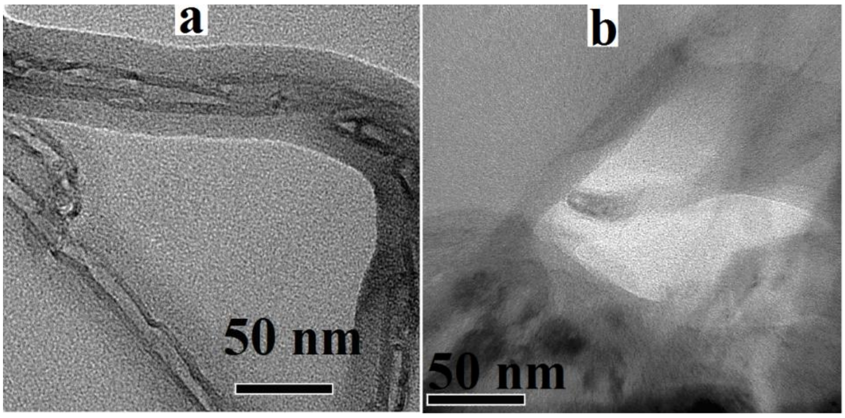

Fig.1 SEM of electrochemically obtained PUMWNT a) partially unzipped b) fully unzipped

Samples of multi-walled carbon nanotubes have different in degrees of unzips depending on the time of electrochemical oxidation. Thus, samples of multi-walled nanotubes, partially and fully unzipped multi-walled nanotubes, were studied by the method of luminescence spectroscopy. Sample 1 is initial MWCNTs, sample 2 after electrochemical oxidation for 2 hours is partially unzipped and sample 3 after electrochemical oxidation for 4 hours is fully unzipped carbon nanotubes. In fig. 2 shows the results of photoluminescence investigations of samples of PUMWNT after 1 hour ultrasonic treatment at 22 kHz (150 W/cm^2).

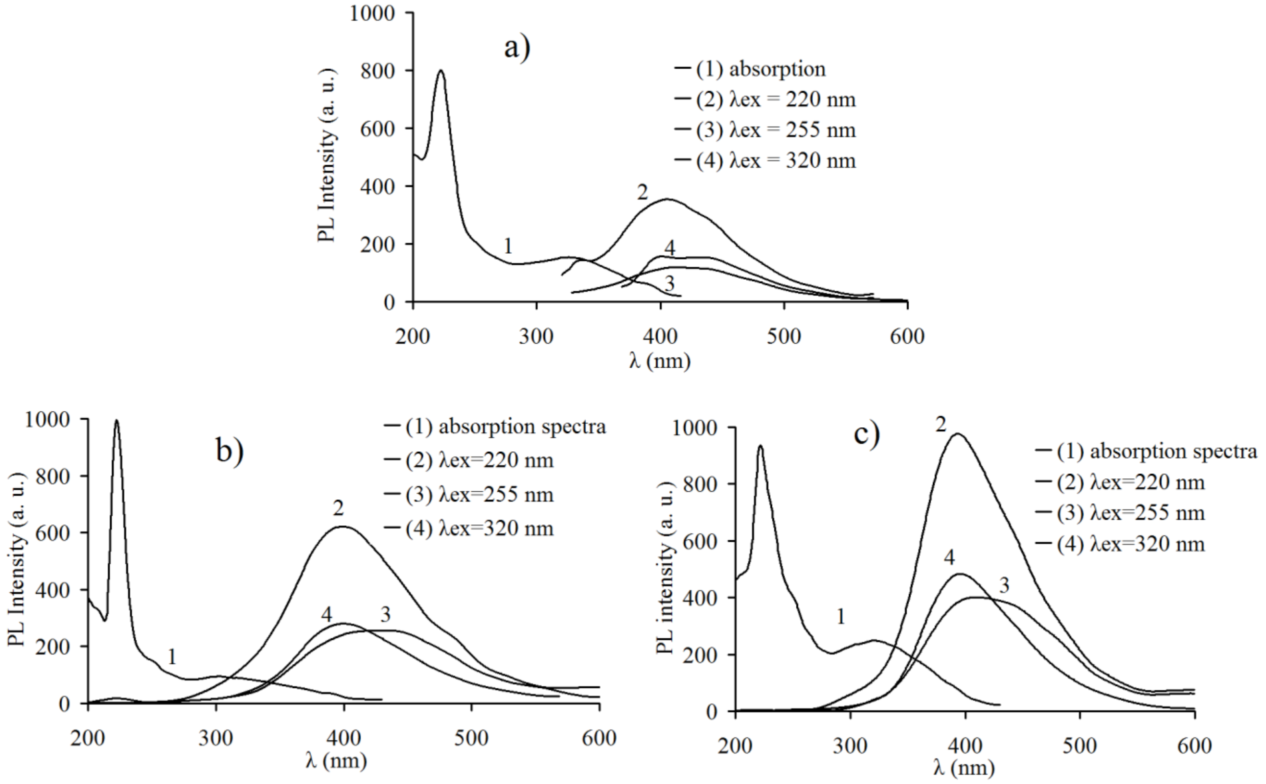

Fig. 2 PL excitation spectrum and photoluminescence spectra at different excitation wavelengths after 1 hour of ultrasonic treatment on a UD-11 ultrasonic device with a frequency of 22 kHz (150 W/cm^2) 0.1 g of powder of PUMWNT in 50 ml distilled water a) sample 1.
a) sample. 2. b) sample No. 3.

After ultrasonic treatment, a colloidal solution is formed, which, as can be seen from Fig. 2, upon excitation by UV light with wavelengths of 220, 255, and 320 nm at the maxima of the PL excitation spectrum, leads to a blue glow of the sample at a maximum of 400-430 nm. Luminescence investigations shown that the degree unzipping carbon nanotubes after 1 hour of ultrasonic treatment with a frequency of 22 kHz (150 W/cm^2) on the UD-11 (ultrasonic device) affects on increase of luminescence intensity (Fig. 2b, sample 3) comparatively (sample 2, Fig. 2 a), but the shape and position of the PL spectra in Fig. 2 at that a remain unchanged. Carbon materials can luminescent due to edge and internal structural defects of carbon nanoparticles. In our case, the maximum of the PL spectrum in Fig. 2 at 400 nm at light absorption at 220-240 nm with a shoulder of 257 nm and a peak at 320 nm, respectively. A broad peak at 220–240 nm with a shoulder of 257 is attributed to the $\pi - \pi$ * transition of aromatic bonds –C = C– and sp2 hybridized –C – C– carbon bonds [5]. For bilayer and single-walled carbon nanotubes with a decrease in diameter from 3 to 1 nm, the peak at 240 nm shifts to the UV region to 206 nm [6]. Based on these data [6], the scatter of the carbon nanoparticles obtained by us is 1.5–3 nm. The peak of light absorption at 320 nm is caused by the terminal groups C = O / COOH, OH, and C-O-C of carbon nanoparticles [7]. Usually this peak for carbon nanoparticles is observed at 350-360 nm [3] but in the case of one or two-layer carbon nanoparticles with a lateral layer of 0.5-1.3 nm, it shifts to the UV region at 320 nm [8-10]. Accordingly, we can conclude that during ultrasonic treatment in a colloidal solution, one or two-layer small carbon nanoparticles of small size 1.5-3 nm dominate. Thus, electrochemical oxidation and ultrasonic crushing promote the formation of nanosized carbon fragments of nanotubes with a more number of defects and groupings that contribute to photoluminescence.

1. Zhang G., Sun X. Size Control Methods and Size-Dependent Properties of Graphene chapter from: Graphene Science Handbook, Size-Dependent Properties CRC Press 2020

2. Li L.L., Ji J., Fei R., [et al.]. A facile microwave avenue to electrochemiluminescent two-color graphene quantum dots, Adv. Funct. Mater., 2012. – V.22. – N.14. – P.2971-2979.
3. Wu B., Zhu R., Wang, M. [et al.]. Fluorescent carbon dots from antineoplastic drug-Etoposide for bioimaging in vitro and in vivo. J. Mater. Chem. B., 2017. – V.5. –N.38 –P.7796-7800.
4. Danilov M.O., Rusetskii I.A., Dovbeshko G.I., [et al.]. Electrochemical Synthesis Partially Unzipped Multi-Walled Carbon Nanotubes as Electrode Materials for Fuel Cells. ECS Trans., 2019. – V.95. –N.1. – P.273-282.
5. Emam A.N., Loutfy S.A., Amany A.M., [et al.]. Cyto-toxicity, biocompatibility and cellular response of carbon dots–plasmonic based nano-hybrids for bioimaging RSC Adv., 2017. – V.**7**. – P.23502-23514.
6. Rance G.A., Marsh D.H., Nicholas R.J., [et al.]. UV–vis absorption spectroscopy of carbon nanotubes: Relationship between the π-electron plasmon and nanotube diameter. Chemical Physics Letters, 2010. – V.493. N.1-3. – P.19-23.
7. Pan D. Zhang J., Li Z., [et al.]. Hydrothermal route for cutting graphene sheets into blue-luminescent graphene quantum dots Adv Mater., 2009. – V.22. – N.6. – P.734-738.
8. Dong Y., Shao J., Chen C., [et al.]. Blue luminescent graphene quantum dots and graphene oxide prepared by tuning the carbonization degree of citric acid. Carbon., 2012. – V.50. N.12. – P.4738-4743.
9. Hong G.L., Zhao H.L., Deng H.H., [et al.]. Fabrication of ultra-small monolayer graphene quantum dots by pyrolysis of trisodium citrate for fluorescent cell imaging. Int J Nanomedicine., 2018. – V.13. – P.4807-4815
10. Wang S., Chen Z.-G., Cole I., [et al.]. Structural evolution of graphene quantum dots during thermal decomposition of citric acid and the corresponding photoluminescence. Carbon., 2015. – V.82 – P.304-313

PHOTOSENSITIVE NANOCOMPOSITES BASED ON TiO_2 NANOTUBES AND PARTIALLY UNZIPPED CARBON NANOTUBES

Rusetskiy I.A., Danilov M.O**.,** **Fomanyuk S.S.**, Smilyk V.O., Kolbasov G.Ya

[1]*V.I.Vernadskiy Institute of General and Inorganic Chemistry of the National Academy of Science of Ukraine, 32/34 Academic Palladin Avenue, Kyiv, 03142, Ukraine. e-mail: Foma7@ukr.net*

For increasing the efficiency of photoconversion on semiconductor electrodes, various methods are used to influence on their surface. These methods include: surface treatment with solutions of metal salts, the adsorption of which reduces the rate of recombination at their interface; sensitization of electrodes with organic compounds (chlorophyll, dyes); use of electrodes based on semiconductor heterostructures; deposition on their surface the layers or island films or nanoscale particles of metals, deposition on their surface conductive polymers or carbon structures. TiO_2 and TiO_2 nanotubes are widely used as a photosensitive electrode. Due to its large bandgap, titanium oxide absorbs light in the ultraviolet region. To expand the absorption region, the surfaces of TiO_2 nanotubes are subjected for various methods of exposure.

Promising material for photoanodes for electrochemical solar energy converters are the nanostructured semiconductor materials with a high light absorption coefficient in the visible region of the spectrum. These are, in particular, the composites based on metal chalcogenides and partially unzipped multi-walled carbon nanotubes.

Partially unzipped multi-walled carbon nanotubes (PUMWCNTs) were obtained by electrochemical anodic oxidation of multi-walled carbon nanotubes in 80% sulfuric acid. The presence of PUMWCNTs was proved by the methods of X-ray diffraction analysis, electron microscopy and Raman spectra. It is shown that the degree of unzipping of multi-walled carbon nanotubes depends on the time of electrochemical oxidation of these materials. It is assumed that controlled synthesis of partially unzipped multi-walled carbon nanotubes is possible [1].

On the previously prepared surface with TiO_2 (NT-TiO_2) nanotubes by painting method were deposited carbon nanotubes and PUMWCNTs. CdS particles were applied on the surface using the SILAR method. An analysis of the IR spectra of the modified films revealed O — H and C = O groups, which corresponds to the structure of partially unzipped multi-walled carbon nanotubes. Highly active edge groups with carboxyl, epoxy, and hydroxyl groups allow better bonding with TiO_2 than pristine carbon nanotubes. The presence of these groups allows faster transfer of electrons in photoelectrochemical processes.

It was found from the current-voltage characteristics under illumination of the synthesized photoelectrodes, that on the composite structure modified with partially unzipped carbon nanotubes (NT-TiO_2 / PUMWCNTs / CdS), occurs shift of the potential of the point of maximum power output to the negative region. Analysis of the photocurrent quantum yield of the NT-TiO_2 / PUMWCNTs / CdS composite showed that this structure is sensitive in the 350-450 nm spectral range. This indicates an increase of the efficiency of photoelectrodes after its modification. Modification of electrodes with partially unzipped multi-walled carbon nanotubes led to an improvement in the relaxation characteristics of photosensitive electrodes.

1. Danilov M.O., Rusetskii I.A., Dovbeshko G.I., Fomanyuk S.S., Kolbasov G.Ya. Electrochemical Synthesis Partially Unzipped Multi-Walled Carbon Nanotubes as Electrode Materials for Fuel Cells. // ECS Trans. – 2019. – V.95, № 1 – P. 273-282.

INFLUENCE OF VACUUM ANNEALING ON THE DISPERSION OF RHODIUM AND IRIDIUM NANOFILMS DEPOSITED ONTO OXIDE MATERIALS

Gab I.I.[1], Stetsyuk T.V.[1], Shakhnin D.B.[2]

[1]Frantsevich Institute for Materials Science Problems, NAS of Ukraine,
3, Krzhyzhanovskogo St., 03142 Kyiv, Ukraine
[2]University "Ukraine", 23, L'vivska St., 03115 Kyiv, Ukraine

In-depth studies of the thin metal films physical properties are stimulated by the wide practical application of metal condensates in many fields of technology. In particular, during joining of such non-metallic materials as oxide and non-oxide ceramics, single crystals, carbon-based materials, etc., by brazing or pressure welding, metal coatings of different thicknesses applied onto these materials are often used. The surface metallization of such materials provides their sufficient wetting with molten metals which determines the very possibility of a soldered joint formation, as well as the strength and other properties of the joints.

Such active adhesive materials as titanium, niobium, and hafnium are the most often used for brazing of non-metallic materials [1–5]. Platinum and palladium coatings at non-metals surface are also widely used in engineering [6–9]. These metals are of interest because joints obtained using them can work in an oxidizing environment at high temperatures. Of some interest for the similar purpose are such more refractory metals as rhodium and iridium which were also studied in this work.

Since metallized non-metallic parts must be heated up to sufficiently high temperatures (1300–1600 °C) during brazing or pressure welding, study of dispersion processes occurring during annealing in these metal nanofilms is not only of scientific interest but also of practical importance for the development of production processes for joining of non-metallic materials.

Rhodium and iridium films 100 nm thickness have been deposited by electron-beam sputtering onto well polished and annealing surfaces of alumina and zirconia substrate. All starting films were continuous without noticeable defects. After annealing them in vacuum, the behavior of rhodium and iridium films on alumina and zirconium ceramics was identical; and after heating them up to a temperature 1300 °C, no significant changes were detected in them. Increasing the annealing temperature up to 1400 °C intensified significantly the dispersion process of films which are disintegrated into large conglomerates being interconnected partially, although the film residues still cover more than 80% of the oxide substrates surface (Fig. 1, a). Further increase in the annealing temperature is accompanied by a rapid process of the films dispersion: at a temperature 1600 °C, films were decomposed completely into individual round droplets covering only about 5% of the substrate surface (Fig. 1, b). Thus, oxide surfaces have lost almost completely the metallization layer and therefore become completely unsuitable for subsequent brazing or pressure welding because metal solders do not wet the oxides, and such materials joining is possible only through the metallization layer.

Slightly less refractory platinum films at the oxides surface behave in approximately the same way under the same conditions (Fig. 2).

Of interest was the result of the control experiment on the influence of the medium on the dispersion of the rhodium film, when the annealing was performed in air at a temperature 1600 °C (Fig. 3). The photomicrograph shows that the film is partially dispersed but still covers more than 80% of the oxide substrate surface. Therefore, the presence of oxygen during the annealing of precious metal films significantly affects the process of their coagulation, reducing the surface tension of the film metal and increasing its adhesion to the nonmetallic substrate (thereby playing a positive role in terms of brazing in air) compared with the area occupied by it during annealing in vacuum.

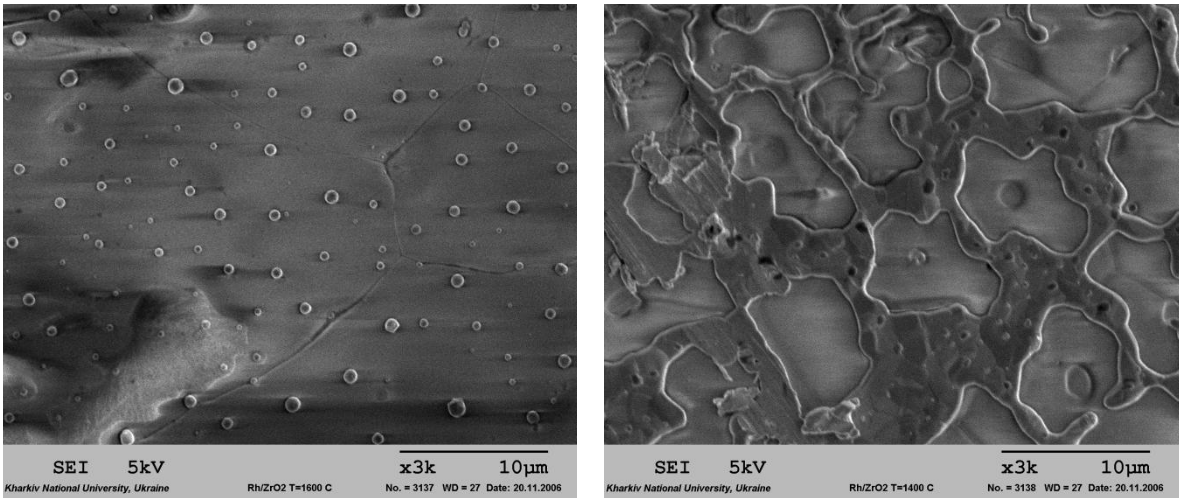

a b

Fig. 1. SEM image of rhodium nanofilm 100nm thickness deposited onto zirconia ceramics and further annealed in vacuum at different temperatures, x3000: a – 1400 ^{o}C; b – 1600 ^{o}C

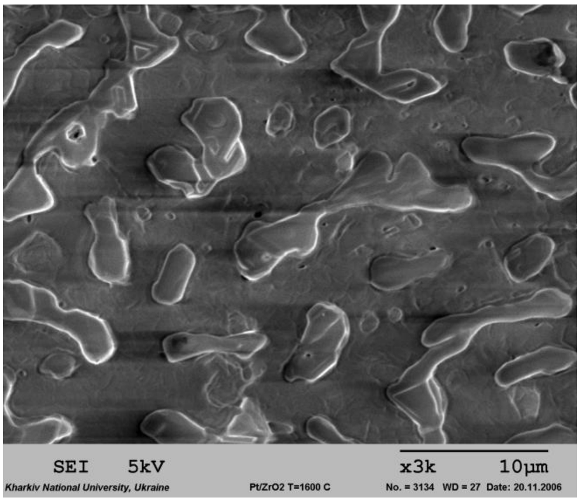

Fig. 2. SEM image of platinum nanofilm 100nm thickness deposited onto zirconia ceramics and further annealed in vacuum at 1600 ^{o}C, x3000

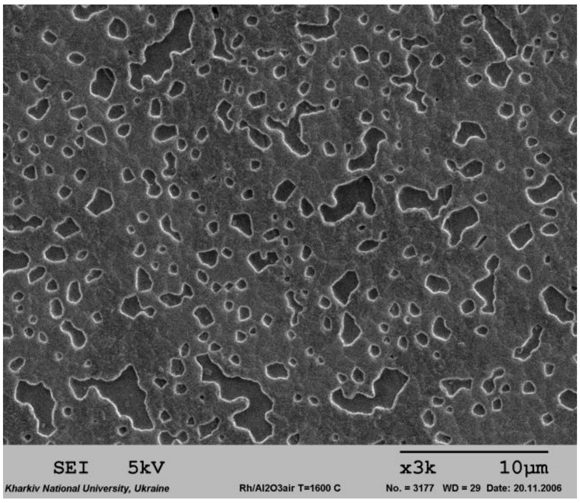

Fig. 3. SEM image of rhodium nanofilm 100nm thickness deposited onto alumina ceramics and further annealed in air at 1600 ^{o}C, x3000

Thus, it is recommendable to carry out the joining process by brazing or pressure welding of oxide non-metallic materials with metal solders in vacuum at temperatures not exceeding 1400 °C. The same procedures can be performed in air even at 1600 °C, and the resulting joints can be operated even in the air at temperatures up to 1600–1700 °C.

1. R. A. Marks, J. D. Sugar, and A. M. Glaeser, J. Mater. Sci., **36**, No. 23: 5609 (2001).
2. R. A. Marks, D. R. Chapmen, D. T. Danielson, and A. M. Glaeser, Acta Mater., **48**, No. 18 – 19: 4425 (2000).
3. Ю. В. Найдич, И. И. Габ, В. С. Журавлев, В. Ф. Дуброва, А. Н. Гордыня, Сварочное производство, 2: 12 (1989).
4. В. В. Мельников, С. В. Еремеев, С. Е. Кулькова, Журнал технической физики, **81**, No. 10: 114 (2011).
5. И. И. Габ, В. С. Журавлев, Д. И. Куркова, Т. В. Стецюк, Ю. В. Найдич, Порошковая металлургия, № 7/8: 69 (1997).
6. E. Ciftyurek, K. Sabolsky, and E. M. Sabolsky, Sensors and Actuators B: Chemical, **181**: 702 (2013).
7. J. D. Wrbanek and K. L. H. Laster, Preparation and Analysis of Platinum Thin Films for High Temperature Sensor Applications (NASA/TM 2005-213433) (January, 2005).
8. И. И. Амиров, В. В. Наумов, М. О. Изюмов, Р. С. Селюков, Письма в ЖТФ, **39**, No. 2: 68 (2013).
9. J. Y. Shim, J. D. Lee, J. M. Jin, H. Cheong, and S. Lee, Solar Energy Materials and Solar Cells, **93**, No. 12: 2133 (2009).

PECULIARITIES OF METAL NANOPARTICLES INTERACTION WITH ENZYMES IN DEVELOPMENT OF EXPERIMENTAL ELECTROCHEMICAL BIOSENSORS

Gruzina T.G.[1], Dybkova S.M.[1], Rieznichenko L.S.[1,2]

[1]*F.D. Ovcharenko Institute of Biocolloidal Chemistry NAS of Ukraine, Vernadskogo Av., 42, Kyiv, 03142, Ukraine*
[2]*Institute of Veterinary Medicine NAAS of Ukraine, Donetska Str., 30, Kyiv, 13151, Ukraine*

Direct electron transfer between enzymes and the electrode surface is important for creating efficient biosensor systems [1-3]. Recent studies suggest that gold nanoparticles (AuNP) of various sizes can be effectively used to enhance direct electron transfer between enzymes (glucose oxidase, dehydrogenase, horseradish peroxidase, etc.) and electrodes of various types [1].

Due this, the obtaining of effective complexes of enzymes with metal nanoparticles, especially gold nanoparticles, can be relevant to improve the efficiency of electrochemical sensors and requires careful study.

Using different reducing agents gold and silver nanoparticles with different size, shape and pH have been synthesized to study the features of their interaction with enzymes. Glucose oxidase and lysozyme were used as model enzymes.

Peculiarities of contact interaction of enzymes with synthesized gold and silver nanoparticles of different nature and size were investigated by the methods of optical spectroscopy, transmission electron microscopy (TEM) and gel electrophoresis in agarose.

It was shown that lysozyme is actively bonded with spherical gold nanoparticles of average size 20 nm at concentration range 1-10 mcg/ml of the protein. The rise of the protein content up to 30 mcg/ml promoted stabilization of the protein-nanoparticles system. In the case of 30 nm spherical gold nanoparticles interaction with lysozyme the active binding has been revealed at the 1-50 mcg/ml and 70-100 mcg/ml concentration range of protein, while the system stabilization has been defined at the concentration range 50-70 mcg/ml. The contact interaction of lysozyme and silver nanoparticles with average particles size 20 nm and 30 nm was characterized by active binding at the whole investigated concentration range (1-100 mcg/ml) of protein.

For the system glucose oxidase – gold nanoparticles it was revealed the ability to form electroactive complexes, but the nature of the interaction and the possibility of complex formation by the binding of nanoparticles to the enzyme depends on the nature and size of the particles. Figures 1 and 2 show the absence of interaction (Fig. 1) and active binding (Fig. 2) of glucose oxidase with different types of gold nanoparticles of the same average size 20 nm (AuNP 2 and AuNP 4) (TEM data confirmed by the results of optical spectroscopy).

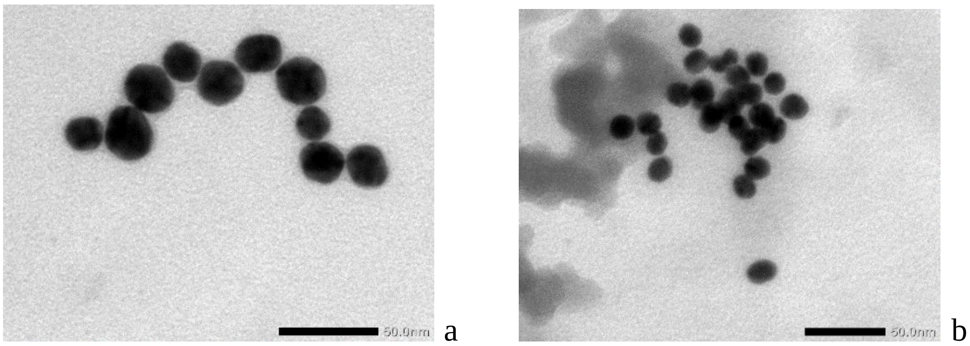

Fig. 1. TEM data of 20 nm gold nanoparticles (AuNP 2) in 20 mM phosphate buffer (AuNP 2 + PB) (a) and after contact interaction with glucose oxidase (AuNP 2 + GO) (b) - the absence of gold nanoparticles interaction with glucose oxidase (Centre of collective usage NAS of Ukraine at D.K. Zabolotny Institute of Microbiology and Virology of the NASU, JEM-1400 (Jeol, Japan)).

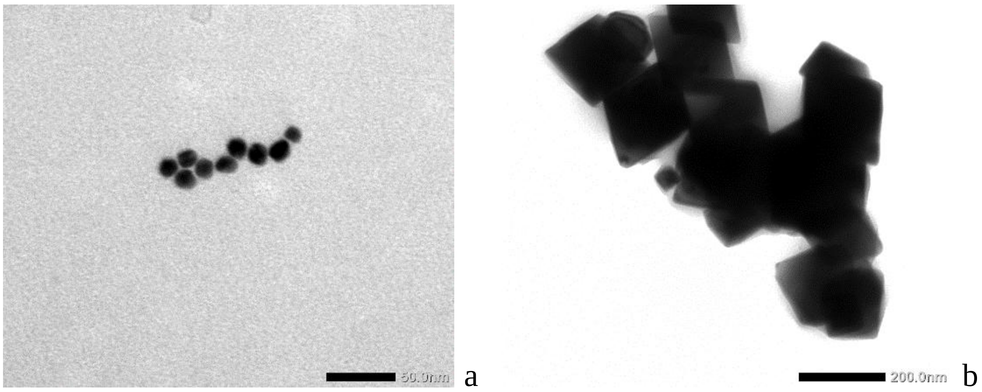

Fig. 2. TEM data of 20 nm gold nanoparticles (AuNP 4) in 20 mM phosphate buffer (AuNP 4 + PB) (a) and after contact interaction with glucose oxidase (AuNP 4 + GO) (b) - the active binding of gold nanoparticles and glucose oxidase (Centre of collective usage NAS of Ukraine at D.K. Zabolotny Institute of Microbiology and Virology of the NASU, JEM-1400 (Jeol, Japan)).

To control the received complex of glucose oxidase and gold nanoparticles the gel electrophoresis in agarose was used. According to the received electrophoregram data the formation of electroactive complexes of glucose oxidase with gold nanoparticles can be indicated.

Revealed peculiarities can be used to optimize the construction of a sensitive element of the electrochemical bio- and nanosensors based on the enzymes and metal nanoparticles.

Acknowledgement. The authors are thankful to the stuff of Centre of collective usage NAS of Ukraine at D.K. Zabolotny Institute of Microbiology and Virology of the NASU for help in TEM studies.

1. Malel E., Mandler D. 2019 Direct electron transfer between glucose oxidase and gold nanoparticles; when size matters. *ChemElectroChem*. **6** 147–154
2. Hu Z. et al. 2017 Direct Electron Transfer of Glucose Oxidase in Carbon Paper for Biofuel Cells and Biosensors. *Int. J. Electrochem. Sci.* **12** 7103 – 7120 doi: 10.20964/2017.08.24
3. Luong J.H., Glennon J.D., Gedanken A. et al. 2017 Achievement and assessment of direct electron transfer of glucose oxidase in electrochemical biosensing using carbon nanotubes, graphene, and their nanocomposites. *Microchim Acta*. **184** 369–388

DEVELOPMENT OF THIN-FILM TECHNOLOGIES FOR PRODUCTION OF METAL MICROSTRIP IONIZING RADIATION DETECTOR FOR APPLICATION IN MEDICINE

Hladkovskyi V.V., Fedorovich O.A., Kostin E.G., Petriakov V.O., Hladkovska O.V.,
Polozov B.P., Rokytskyi O.A.

Institute for Nuclear Research, NAS of Ukraine, 47, pr. Nauky, 03028, Kyiv, Ukraine
vovahlad@gmail.com

In cooperation with the International Associated Laboratory (LIA IDEATE, STCU project №P9903), a technology was developed and a series of new types of metal microstrip detectors (MMD) on silicon substrates were manufactured. MMD are position-sensitive ionizing radiation detectors with extremely high radiation resistance (over 100 MGy). Features of MMD are their transparency (sensor thickness ~ 2 μm) for radiation flows, high spatial resolution (1-25 μm), low operating voltage (20 V), and unique manufacturing technology [1].

MMD manufacturing technology consists of several technological processes: coating of silicon wafers with an insulating layer ($SiO_2 + Si_3N_4$); ion-plasma deposition of nickel films on the insulating layer; photolithography and chemical etching of nickel films; plasma chemical etching of silicon substrates. As a result, we get 128-nickel strips (free of silicon substrate) with a size of 3500×110 μm on an area of 35×35 mm^2. The distance between the strips is 20 μm, and the thickness is ~ 2 μm.

The metal films depositing of titanium (Ti) and nickel (Ni) on the surface of silicon wafers with a layer of silicon dioxide and silicon nitride ($SiO_2 + Si_3N_4$) is one of the important steps in the production of these detectors. The nickel films it have poor adhesion to Si_3N_4, because Ni is chemically weakly active in relation nitrogen. Therefore, Ti was chosen as a thin adhesion sublayer, because he has a higher adhesion to substrates, which containing nitrogen. The deposition of metal films was performed using the thermoionic method developed by us [2]. As shown in [3], the films deposited by this method have a number of useful properties: high adhesion and corrosion resistance, low porosity and high density, which is close to the density of solid metal. In this case, high corrosion resistance of Ni films is manifested as the resistance to etching processes in photolithography and plasma chemical etching in halogen-containing gases.

The essence of the thermoionic method of deposition of metal films is that the metal vapor obtained in the evaporator is additionally ionized. Then, the ionic component of the metal vapor is accelerated by the negative potential on the substrate. The ionic component of the steam flow affects the crystal structure of the obtained film, and leads to an increase in its physical and technological properties.

It should be borne in mind that metal films deposited at low substrate temperatures (T_{sb}) are characterized by a high degree of dispersion, low density (not dense connection of crystallites among themselves), high concentration of defects of condensation origin. This fact is of a general nature for films of all substances according to the Movchan-Demchyshyn structural-band model [4], which was developed by Thornton for ionic deposition methods [5]. These structural defects can significantly reduce the mechanical strength of the substrate-free film. The high dispersion and reduced density at $T_{sb} < 0.3 \times T_{melt}$ K is manifested in an increase in the fragility of metal films. Here T_{melt} K is the melting point in degrees Kelvin.

In view of the above, the deposition of such films should be carried out at a sufficiently high substrate temperature to obtain high adhesion and dense structure of the strips. We chose the deposition temperature of nickel films 440 °C, which is slightly more than $0.4 \times T_{melt}$ K for the specified metal and is 417 °C. According to the structural-zone model of Movchan, Demchyshyn and Thornton, dense films with a dense grain boundary grow at this temperature.

Mechanical stresses arising from the difference between the coefficients of linear expansion of silicon and nickel are a significant problem in the deposition of metal films at high substrate temperatures. In our case, the nickel films when cooled from the deposition temperature to room temperature are in a stretched state. This stress state can cause delaminating of the films with poor adhesion. Since, ion bombardment during deposition increases the adhesion of the film to the substrate, the number of punctures decreases (i.e. local places of peeling of the film from the substrate) and increases the mechanical strength.

Therefore, when cooled to room temperature and released from the substrate, the nickel films deposited at the selected temperature could be plastically deformed rather than torn. The films have increased fragility and low tensile strength at low deposition temperatures. The cooling was performed slowly from 440 °C to a temperature of 150 °C to reduce the stress state of nickel strips, which occurs when cooling to room temperature. The final cooling temperature of 150 ° C was chosen because in the deformed Ni most of the excess defects that occur during tensile deformation and disappear during exposure to temperatures above 100 °C - 150 °C. Here we mean the deformation of the tensile strength of the nickel film upon cooling. Observations in the MII-4 microscope of the profile of scratches applied to the film by a diamond pyramid indicate that the film at the edges of the scratches was deformed as a weakly stressed plastic material.

However, after cooling to room temperature, the tension in the films remains. This leads to the peeling of the strips from the substrate during various technological operations. The separation of the film takes place on a silicon substrate, which indicates the high adhesion of Ni to the intermediate layers. These residual stresses are greater the thicker the nickel film. In some cases, the strips should be stronger when it is necessary to obtain narrow strips (less than 30-50 microns wide), with a working area (hanging in the air) greater than 10 mm. The working area of the strips at a thickness of 1-2 µm is limited to a length of 10 mm [6].

To solve this problem, a method was developed to increase the thickness of the strips by galvanic extension. This method allows increasing the thickness of the strips to the desired value, using a thin layer of precipitated Ni with high adhesion. In this case, it is enough to deposit a thin layer of Ni (0.2-0.3 µm) and then increase it galvanically to the required thickness.

We made a simplified stand for measuring the breaking force of strips deposited and grown by galvanic method. The measurements showed that the strips made by both methods have almost the same strength, close to solid polycrystalline nickel. It was experimentally shown that galvanic nickel is not stressed, and levels the tension in the deposited nickel film.

The plasma-chemical etching of protective films of silicon nitride and silicon dioxide was performed on the front side in the working area of the detector to a depth of 20 - 40 µm, in a plasma-chemical reactor (PCR) with a controlled magnetic field [7]. Highly selective plasma-chemical etching of the silicon substrate to a depth of 360 - 500 µm to the surface of nickel strips on the gate side was also performed.

Fig. 1. Image of the working area of the manufactured MMD.

The use of controlled magnetic fields in PCR allows to increase the plasma density, as well as to reduce its heterogeneity along the PCR axis. The ability to control the energy of chemically active ions with all other constant parameters of the discharge is another feature of this PCR. The energy of chemically active ions can be regulated in the range of 20 - 700 eV. The use of PCR with low ion energies allows to minimize scattering and radiation damage to the treated surface due to ion bombardment at low ion energies. The optimal etching rate in this case was about 2.5 µm / min at an ion energy of 80 eV and a discharge current of 6 A. Thus, a series of 128 strip detectors with fully etched Si in the working range of 16 × 16 mm^2 was made (Fig. 1).

1. Fedorovich O., Kovalchuk O., Pugatch V. et al. Metal micro-detectors: Development of “transparent” position sensitive detector for beam diagnostics. // Problems of Atomic Science and Technology, Series “Plasma Physics” – 2012. - V. 6 (82). - P. 196-198
2. Kostin E.G. Application of discharges in vapor of evaporated metals for the film deposition from the ionized stream. // Problems of atomic science and technology. Series: Plasma electronics and new methods of acceleration (5), – 2006, – № 5. – P.131-135.
3. Belevsky V.P., Belous M.V., Kostin E.G. et al. The effect of ion bombardment during the deposition of films on the formation of their structure, electrophysical and physicotechnological properties. // Electronic equipment. Ser. 3. Microelectronics. M.: Central Research Institute "Electronics". – 1977. – Issue 5 (84). – P. 104-111.
4. Movchan BA, Demchishin AV. Study of the structure and properties of thick vacuum condensates of nickel, titanium, tungsten, aluminum oxide and zirconium dioxide. // Fiz. Metal. Metalloved. – 1969, –Vol. 28, – №4, P. 654-660.
5. Thornton J.A. The microstructure of sputter deposited coatings. // J. Vac. Sci. Technol. – 1986.– Vol. A4, Iss. 6,– P. 3059-3065.
6. Патент на винахід UA 111418 від 25.04.16 р. Дата подання: 30.09.2014. Винахідники: Пугач В.М., Федорович О.А., Петряков В.А., Ковальчук О.С., Костін Є.Г. Детектор заряджених частинок та іонізуючих випромінювань і спосіб його виготовлення.
7. Hladkovskiy V. V., Fedorovich O. A., Polozov B. P. et al. The bias voltage and its influence on the etching rate of silicon. // Problems of atomic science and technology. – 2015. – V. 6. – P. 146–150.

SERS SUBSTRATES BASED ON LATERALLY ORDERED GOLD NANOSTRUCTURES FOR DETECTING ORGANIC MOLECULES

Hreshchuk O.M.[1], Yukhymchuk V.O.[1], Dzhagan V.M.[1], Indutnyi I.Z.[1], Min’ko V.I.[1], Lytvyn P.M.[1], Danko V.A.[1]

[1]*V. Lashkaryov Institute of Semiconductor Physics, National Academy of Sciences of Ukraine, 45 Prospect Nauky, Kyiv-03028, Ukraine*

Nowadays high attention is devoted to the optical investigation of biomolecules. One of the promising optical methods for their detection and identification is surface-enhanced Raman spectroscopy (SERS). It includes all benefits of Raman spectroscopy, such as easy in preparation of samples for investigation, express testing, non-destructive analysis, chemical analysis of compounds etc. Simultaneously SERS eliminates the disadvantage of a weak Raman signal due to the small scattering cross section.

Such benefits facilitate the broad application of SERS in such fields as biology, chemistry, ecology, criminalistics, environment protection, medicine, archeology, art, material science, pharmacology etc. [1].

In the SERS process, there are two enhancement mechanisms: electromagnetic (EM) and chemical. EM mechanism is based on the effect of strong enhancement of local field caused by resonant excitation of surface plasmons in metallic nanostructures. Optical properties of surface plasmon depend on the morphology of SERS substrates, such as size and form of nanostructures, their arrangement over the surface, and used metal (typically gold, silver). Besides EM, there can be a chemical enhancement that arises in case of chemical bound between the molecule and metallic nanoparticle that induce resonance energy transfer between them. Additional strong contribution into Raman intensity could be obtained by the special design of nanostructures to form sharp edges or to allocate nanoparticles close to each other to facilitate the formation of so-called "hot spots", where the intensity of EM field is much higher than average on the SERS substrate.

There are many techniques for producing of SERS substrates, some of them produce good substrates, such as electron beam nanolithography, but are quite complex, expensive and time-consuming. Opposite to this method, there is a relatively simple method, such as thermal vacuum deposition, but in this case, obtained nanostructures are randomly positioned on the surface and there is some size distribution. An alternative method could be an interference photolithography. It allows the realization of laterally ordered nanostructures with the possibility of size controlling that will facilitate to the identical enhancement of Raman scattering on the surface. This method is relatively cheap and easy to realize.

We have developed SERS substrates by using the interference photolithography method. Combined investigation of the morphology and optical characteristics of realized substrates was made by scanning electron microscopy, atomic force microscopy, optical absorbance and surface-enhanced Raman scattering.

The important stage is to verify the morphology of produced SERS substrates with arrays of nanostructures by AFM and SEM methods. Fig. 1 shows the AFM image of as-prepared SERS substrate with a chess-like ordered array of gold nanoislands with an average height of 55 nm and lateral dimensions at the base of 200 nm and 150-200 nanometer distance between the islands. The period of this array is 297±0.5 nm. Noteworthy, islands have not a single apex but a "crone" with 4-7 separate peaks.

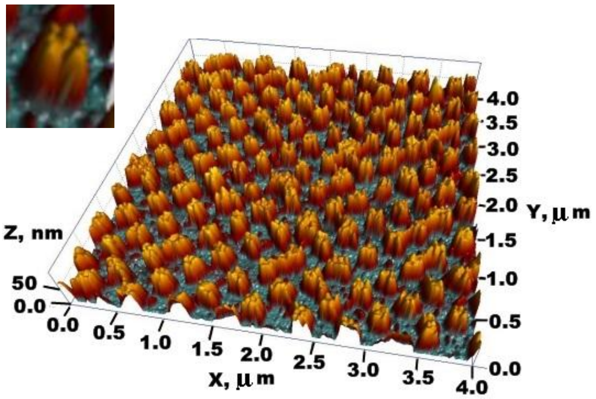

Fig. 1. AFM image of the initial SERS substrate obtained by the interference photolithography method. Inset: the enlarged image of a single island.

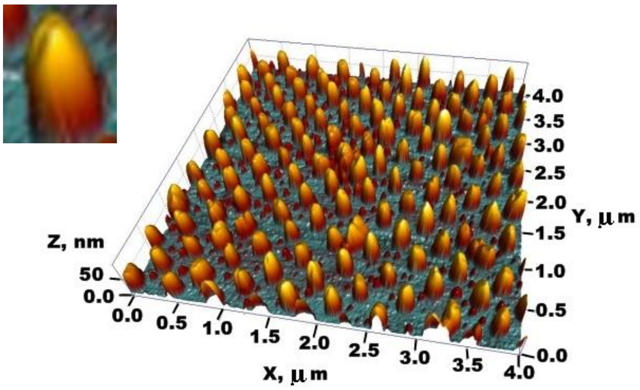

Fig. 2. AFM image of the same SERS substrate as in Fig. 1 but after annealing at 420° C. Inset: the enlarged image of a single island.

In order to improve the crystallinity of the as-formed nanoislands, they were subjected to thermal annealing. Fig. 2 shows the same SERS substrate as in Fig. 1, but after annealing at 420° C in a vacuum. As seen from the AFM images, both the shape and size of islands have significantly changed after annealing. Their apex became rounded with a single peak, their average height increased from 55 to 67 nm, the lateral dimensions at the base decreased from 200 to 180 nm, and the distance between them increased by 20%. Moreover, numerous connections between the adjacent islands, caused by incomplete photoresist removal, disappeared after annealing.

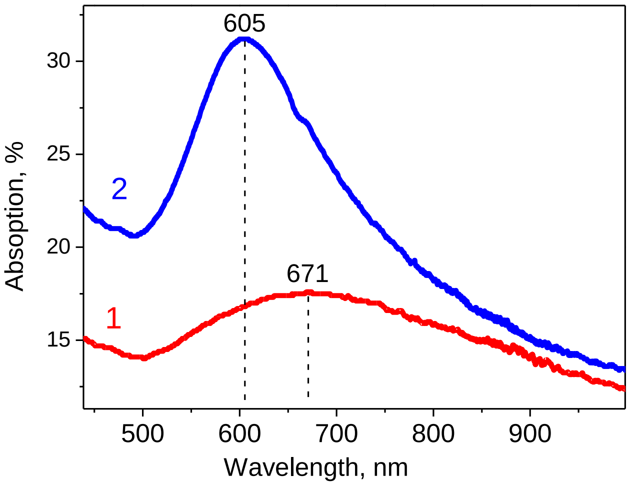

Fig. 3. Optical absorption spectra of laterally ordered gold nanostructures: 1 - as-prepared, 2 -annealed.

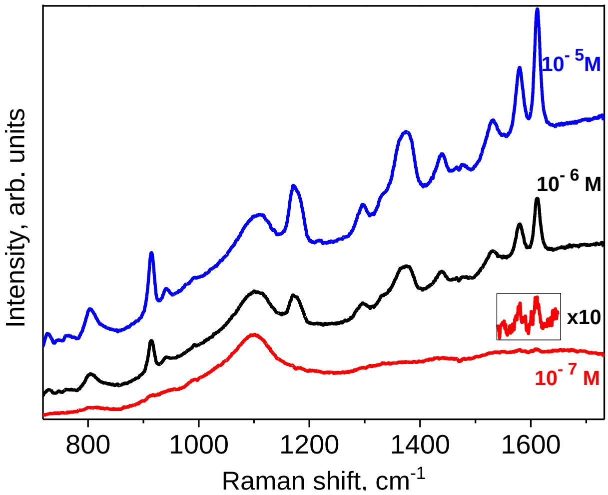

Fig. 4. Raman spectra of CV molecules deposited on the previously used SERS substrate, which was annealed at 300 °C, at various concentrations of molecules on their surface.

Thermal annealing also helped to improve the optical absorbance characteristics of developed substrates. In Fig. 3 optical absorption spectra of fabricated nanostructured SERS substrates before (curve 1) and after annealing (curve 2) are presented. As can be seen from figure after annealing, the plasmon absorption band shifts significantly to the blue side, from 671 to 605 nm, and its width gets notably smaller, from 264 to 128 nm. The larger width of the band in the initial sample is obviously due to the large distribution of the size of islands and, as well as by interconnections between some islands. The latter causes an increase in propagation length of plasmon oscillations in metallic nanostructures, while reducing their oscillation frequency. Finally, a less dense crystalline structure of as-deposited gold is supposed to contribute to increase of the plasmon bandwidth too. Thermal annealing caused the sharpening of the plasmon-absorbed band that possibly could improve the resonant conditions of SERS enhancement of studied molecules.

For the investigation of enhancement properties of SERS substrates, low concentration of molecules of crystal violet (CV) was deposited on them by the drop-casting method. It was shown that it is possible to register SERS signal from the CV molecules to concentration of 10^{-7} M (Fig. 4). Also, it was shown that after annealing of the substrates with CV at the temperature of 300 °C, the molecules on the sample surface "burn out" completely and the SERS substrate can be used again. To test this, the CV molecules were repeatedly deposited by drop-casting onto previously used not annealed SERS substrates. After the additional annealing (at 300 °C for 15 min) Raman results were similar.

Therefore, in this work efficient SERS substrates made by the interference photolithography were developed. It was shown that laterally ordered arrays of nanostructures were obtained. Their morphology and optical characteristics were improved by the thermal annealing. It was shown that they efficiently enhance Raman scattering of organic molecules and substrates could be repeatedly used after annealing.

1. Schlücker, S., Bell, S., Charron, G., Cortés, E. [et at] (2019). Towards Reliable and Quantitative SERS: from Key Parameters to Good Analytical Practice // Angewandte Chemie International Edition, 2019. – V. 59. – Iss. 14. – P. 5454-5462.

ON THE GROWTH AND PROPERTIES OF PURE AND Ag-DOPED ZnO NANOCOMPOSITES

Ievtushenko A.[1], Karpyna V.[1], Shtepliuk I.[1,2], Ericksson J.[2], Yakimova R.[2], Khranovskyy V.[2]

[1]I. Frantsevich Institute for Problems in Material Science, NAS of Ukraine,
3 Krzhizhanovsky Str., 03142, Kyiv, Ukraine
[2]Department of Physics, Chemistry and Biology, Linköping University, S-581 83,
Linköping, Sweden

Zinc oxide (ZnO) is a wide-gap semiconductor material which attracts much attention of scientific community due to its unique properties that are perspective for device developments in such scientific areas as physics, material science, chemistry, biochemistry, etc. The investigation of ZnO in form of nanostructures (NS) are the most promising and interesting because of the potential applications for nano-scale optoelectronic devices, such as light-emitting diodes, field-effect transistors, ultraviolet lasers, solar cells and especially for the development of effective photocatalyst materials. Last year, pure and doped ZnO NS is being studied as a fast, cost-effective, and eco-friendly photocatalytic material for the clean-up of the environment from persistent organic pollutants as well for air disinfections from bacteria and viruses [1-3].

In our report, we present the results of investigations of the influence of substrate temperature and the value of Ag concentration on the microstructure, optical, and electrical properties of ZnO NS. Hence, ZnO NS were deposited on Si substrates by Atmospheric pressure metal-organic chemical vapor deposition (APMOCVD) using single source solid-state zinc acetylacetonate (Zn(AA)) precursor. Doping by silver was realized in-situ via adding 1 and 10 wt. % of Ag acetylacetonate (Ag(AA)) to zinc precursor. The substrate temperature was changed in the range of 220 – 550 °C. The scanning, transmission electron, and Kelvin probe force microscopy, energy dispersive X-ray analysis (EDXA), photoluminescence (PL), and four-point probe electrical measurements were used for samples characterization.

Scanning electron microscopy (SEM) shows that the application of Zn(AA) precursor leads to the formation of film-like ZnO NS. It was found that silver additives play the role of crystallization centers for ZnO nano- and microcrystal growth. Ag doping affects the ZnO microstructure via changing the nucleation mode into heterogeneous and thus transforming the polycrystalline films into a matrix of highly c-axis textured hexagonally faceted nanorods. It was demonstrated that the medium substrate temperature range most favorable for growing well-defined ZnO:Ag nanocrystals enlarged in length with pencil-like geometry (Fig.1,a). The higher substrate temperatures of deposition promote the formation of ZnO nanowires (Fig.2, b).

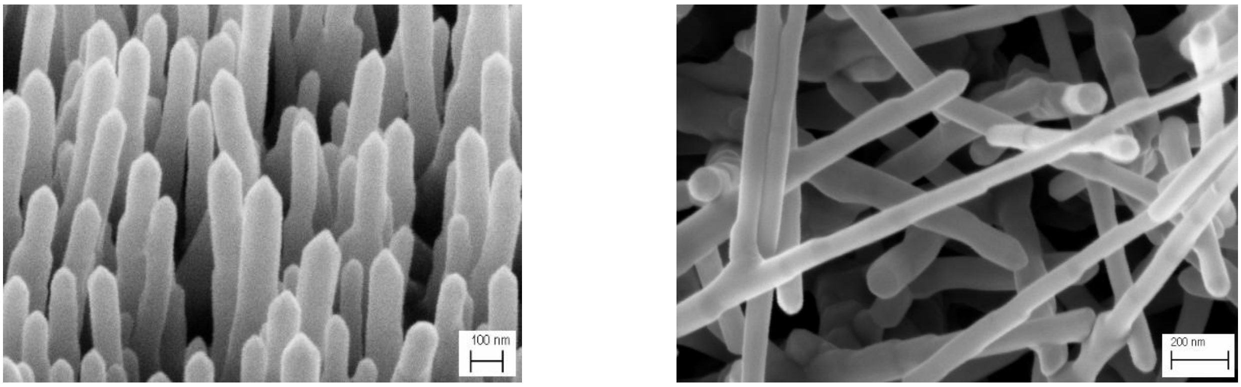

a) b)

Fig.1. SEM images of ZnO:Ag NS deposited at different substrates temperature and Ag content.

Kelvin probe force microscopy accompanied by electrical measurement was used for the determination of behavior for Ag species in ZnO lattice. By Kelvin probe force microscopy was shown that the work function value increases from 4.45 to 4.75 eV with Ag content enhancement in ZnO. Therefore, it is reasonable to assume that Ag species incorporated into ZnO as donor type defect occupying interstitial sites in ZnO lattice. The electrical resistance of ZnO NS was found to be less temperature dependent upon Ag doping, while work function of both pure and Ag-doped materials was varying, due to both electronic properties and crystal structure quality variation. Based on the obtained results, it is suggested that NS deposition at lower temperatures (220 – 300 °C) is more favorable for *p*-type doping of ZnO.

It was observed, that near-band edge emission of ZnO NS was enhanced with Ag doping as a result of quenching deep-level emission. It was also revealed that Ag tends to promote the formation of basal plane stacking faults defect, as it was observed by HR TEM. In PL spectra of heavily Ag-doped ZnO NS (10 wt.% of Ag) PL peak at 3.31 eV is appeared due to the presence of stacking faults defects in basal planes. Increasing dopant content and growth temperature leads to a significant increasing in PL intensity of Ag-doped ZnO NS. In the case of heavily Ag-doped ZnO NS the observed increase of visible and ultraviolet emissions can be understood like plasmon amplification which can be used for the development of effective ZnO photocatalyst based on Ag-doped NS.

In summary, Ag doping leads to n-type conductivity of Ag-doped ZnO NS and increases significantly the intensity of photoluminescence of Ag-doped NS in comparison with undoped ZnO NS. It was observed, that ZnO doped with high Ag content displays splitting of NBE emission peak due to basal plane stacking faults defects the presence of which was also confirmed by TEM investigations.

We believe that Ag-doped ZnO NS, easily grown by APMOCVD, can be used for the designing of effective light-emitting diodes and lasers, as well as for the development of the photocatalytic devices for the disposal of the environment from bacteria and organic pollutants, etc.

Acknowledgements. This work was partially supported by the research project of NAS of Ukraine "The development of photocatalytic nanocomposites for viruses inactivation in the air" (№40/20-H) and was partially supported by the research projects of NAS of Ukraine "Development of innovative photocatalytic nanostructured materials based on ZnO and TiO_2" (528/IPM-11/20).

1. Khan S.H., Pathak B., ZnO based Photocatalytic Degradation of Persistent Pesticides: A Comprehensive Review// Environmental Nanotechnology, Monitoring and Management, 2020. – V. 13. – 100290.
2. Ong C. B., Ng L. Y., Mohammad A. W., A review of ZnO nanoparticles as solar photocatalysts: Synthesis, mechanisms and applications//Renewable and Sustainable Energy Reviews, 2018– V. 81– P. 536-551.
3. Kezhen Q., Cheng B., Yu J., Ho W., Review on the improvement of the photocatalytic and antibacterial activities of ZnO// Journal of Alloys and Compounds, 2017. – V. 727– P. 792 – 820.

THE MORPHOLOGY, ELECTRONIC STRUCTURE, OPTICAL PROPERTIES AND CYTOTOXICITY OF Ag-DOPED ZnO NANOSTRUCTURES

Ievtushenko A.[1], Khyzhun O.[1], Karpyna V.[1], Bykov O.[1], Zahornyi M.[1], Dzhagan V.[2],
Yukhymchuk V.[2], Valakh M.[2], Zagorodnya S.[3], Naumenko K.[3], Zaremba P.[3], Khranovskyy V.[4]

[1]I. Frantsevich Institute for Problems in Material Science, NAS of Ukraine, 3 Krzhizhanovsky Str., 03142, Kyiv, Ukraine
[2]V. Lashkaryov Institute of Semiconductor Physics, NAS of Ukraine, 45 Nauky pr., 03028, Kyiv, Ukraine
[3]D.Zabolotny Institute of Microbiology and Virology, NAS of Ukraine,
154 Acad. Zabolotny Str., 03143, Kyiv, Ukraine
[4]Department of Physics, Chemistry and Biology, Linköping University, S-581 83, Linköping, Sweden

Last decades, ZnO as a semiconductor material attracts the attention of many research groups all over the world due to direct wide band gap (3.37 eV at room temperature) and a large exciton binding energy (60 meV) which makes it perspective for designing various kind of optoelectronic devices for ultraviolet or visible wavelength range. ZnO nanostructures (NS) are also interesting because of the potential applications for nano-scale optoelectronic devices, such as light emitting diodes (LED), field effect transistors (FETs), solar cells, and ultraviolet (UV) lasers [1]. The last few years, ZnO NS have been more actively studied as a cost-effective and eco-friendly photocatalytic material for the cleaning of the environment from persistent organic pollutants, bacteria as well as viruses [2, 3].

Ag-doped ZnO NS were grown at different substrate temperatures on polished Si substrates coated by silver (Ag) films by Atmospheric pressure metal organic chemical vapor deposition (APMOCVD) using mixtures of zinc acetylacetonate (Zn(AA)) and (Ag(AA)) precursors. X-ray diffraction (XRD), scanning electron microscopy (SEM), energy dispersive X-ray analysis (EDXA), X-ray photoelectron spectroscopy (XPS), Raman and photoluminescence spectroscopy as well as cytotoxicity measurements MTT assay were used for the samples characterization.

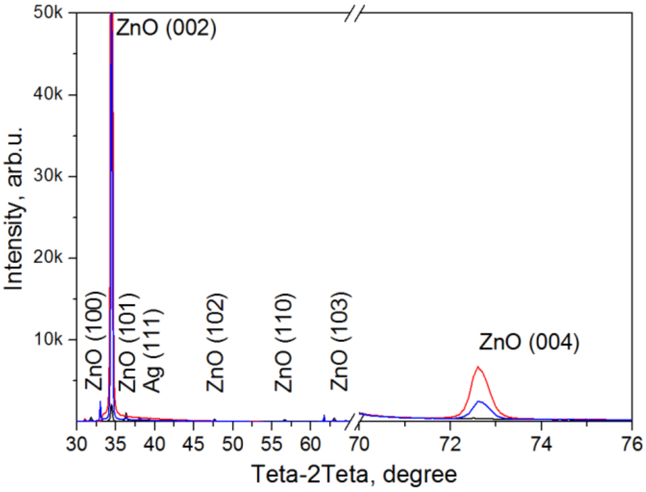

Fig.1 XRD patterns of ZnO:Ag NS deposited on Si substrates coated by Ag thin film.

The XRD, EDXA and XPS measurements confirm the growth of ZnO doped by different Ag content. The XRD patterns of ZnO:Ag NS are shown in Fig. 1. All ZnO NS have wurtzite structure and were textured along c-axis what is confirmed by the presence of intense (002) and (004) diffraction peaks (Fig.1). SEM images, presented on Fig.2, confirm the growth of ZnO:Ag NS with different morphology that depends on the Ag concentration and substrates temperatures.

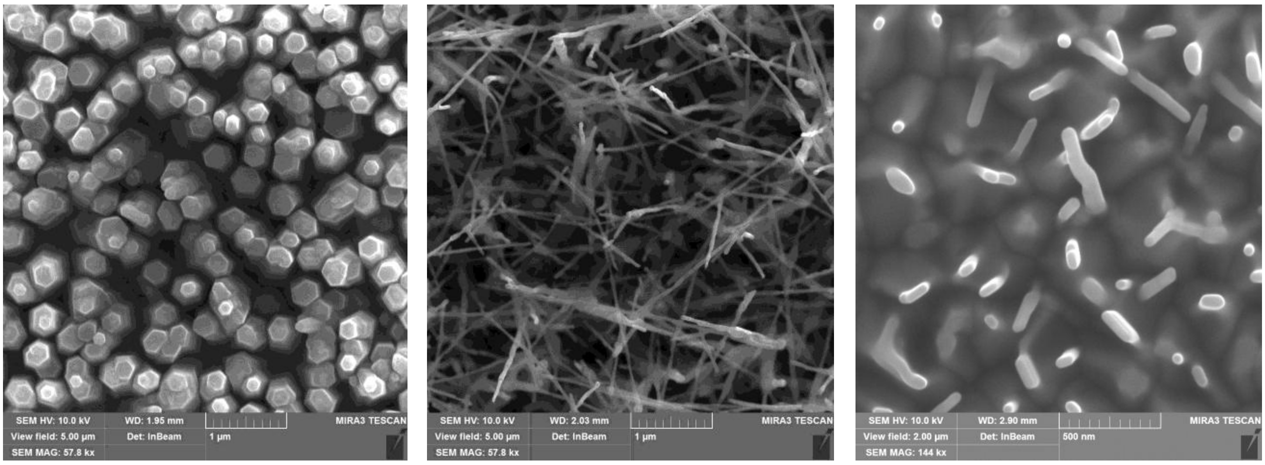

Fig 2. SEM images of ZnO:Ag NS deposited on Si substrates coated by Ag thin film.

It was shown that an apparent difference in the optical properties of the ZnO NS under the study is the various absolute intensity of the photoluminescence (PL) as well as the different ratios of the excitonic (near band emission) and trap- (surface-) related bands. Raman spectra (Fig. 3) acquired at resonant excitation (325 nm) revealed noticeable changes in the fundamental optical (LO) phonon range, indicating the effect dopant on the local lattice structure and, possibly, the influence of a different crystallite sizes in different samples. Moreover, the effect of Ag dopant on the relative intensity and spectral lineshape of the phonon overtones (2LO) evidences changes in resonance conditions as well as in the magnitude of electron-phonon coupling. The studied ZnO:Ag NS reveal also different dependence of the resonant Raman and PL spectra with the variation of the exciting laser power, which can be related to the difference in the heat conductivity and photocharging, respectively.

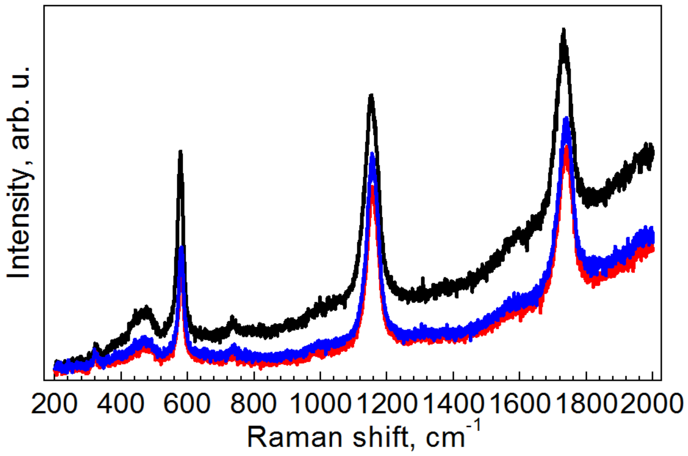

Fig.3 Raman spectra of ZnO:Ag NS deposited on Si substrates coated by Ag thin film.

The cytotoxicity of ZnO NS doped by different concentration of Ag and undoped ZnO film for comparison was performed by using the MTT test, which is based on determining the functioning of the dehydrogenase activity of mitochondria. Monolayer cell cultures of epithelioid origin MDBK (Madin-Darby bovine kidney cells) sensitive to human adenovirus and MDCK (Madin-Darby canine kidney cells) sensitive to influenza virus were used. The study procedure included 24 hours of exposure of the plates in growth medium for cell cultures at 37ºC. The medium was then added to the monolayer of cell cultures without dilution and at dilutions of 1:10 and 1:100. Analysis of cells was performed at 24, 48, and 72 hours by adding 10 µl of MTT solution (5 mg/ml). Subsequent to four hours of incubation at dark, the formazan crystal of MTT reduction was dissolved in DMSO and absorbance was measured using a microtitre plate ELISA reader Multiskan FC (Thermo Scientific, USA). The effect of cytotoxicity of the samples was quantified as the percentage of control absorption of the reduced dye MTT at 540 nm. All experiments were repeated three times to test for sensitivity. Cell viability was assessed by the ability of living cells to reduce the yellow MTT dye to a blue formazan crystal. The results of toxicity investigation are presented in Table 1.

Table 1. Cytotoxic effect of ZnO samples in MDBK and MDCK cells culture

	The percentage of suppression of cell viability in the time range (in hours) of sampling					
	24		48		72	
	MDBK	MDCK	MDBK	MDCK	MDBK	MDCK
Pure ZnO film	0	7.97	19.8	11.34	39.33	22.28
ZnO:Ag_1 NS (0.5 at.% of Ag)	0	15.49	5.17	11.24	10.16	20.89
ZnO:Ag_2 NS (7.0 at.% of Ag)	82.8	6.27	88.26	36.1	77.68	38.1
ZnO:Ag_3 NS (7.0 at.% of Ag)	76.29	14.33	82.04	18.85	68.83	20.79
Si substrate	1.0	11.9	0	9.77	0	9.9

As a result of the provided studies, it was found that the Si substrate, which was used for ZnO film and ZnO NS growth, did not contain toxic elements for cell cultures. It should be noted the different sensitivity of MDBK and MDCK cultures to test of pure and Ag-doped ZnO samples. The toxic effect of pure ZnO film, deposited on Si substrate, was about 40% after 72 hours in MDBK cells. A pronounced cytotoxic effect was determined for the sample ZnO:Ag_2 NS in both cell cultures. It should be noted that this sample was the largest in area comparison with ZnO:Ag_1 and ZnO:Ag_3 samples. As you can see from Table 1, the enhancement of Ag content in ZnO NS leads to the increasing their toxic effect. At a dilution of 1:10, the percentage inhibition of cell viability did not exceed 15%. The presented results allow us to conclude that the morphology of ZnO NS and the values of Ag content sufficiently influence on sample toxicity. Also, this investigation sheds light on the stability of ZnO NS in different test solvents.

The influence of Ag content and substrate temperatures on the structure, morphology, electronic and optic properties, and toxicity of ZnO:Ag NS, deposited by APMOCVD on coated by Ag Si substrates, will be presented and discussed in detailed.

1. Lashkarev G. V., Shtepliuk I. I., Ievtushenko A. I., et.al. Properties of solid solutions, doped film, and nanocomposite structures based on zinc oxide // Low temperature physics, 2015. –V. 41, 2. –P.129-140.
2. Khan S.H., Pathak B., ZnO based Photocatalytic Degradation of Persistent Pesticides: A Comprehensive Review// Environmental Nanotechnology, Monitoring and Management, 2020. – V. 13. – 100290.
3. Kezhen Q., Cheng B., Yu J., Ho W., Review on the improvement of the photocatalytic and antibacterial activities of ZnO// Journal of Alloys and Compounds, 2017. – V. 727– P. 792 – 820.

Acknowledgements. This work was partially supported by the research project of NAS of Ukraine “The development of photocatalytic nanocomposites for viruses inactivation in the air” (№40/20-H) and was partially supported by the research projects of NAS of Ukraine “Development of innovative photocatalytic nanostructured materials based on ZnO and TiO_2” (528/IPM-11/20).

OPTICALLY ACTIVE COATING BASED ON CHALCOHENID GLASSES FOR MIDDLE IR RANGE PHOTODETECTORS

Kabatsii V.M.

Mukachevo State University, 26, Uzhhorodska street, 89608 Mukachevo, Ukraine

The main elements of a modern optoelectronic sensor are known to be semiconductor sources and photodetectors. One of the important components of such a sensor is a photodetector, which must not only have a high efficiency to convert the incident radiation into electric current, but also have the appropriate spectral distribution of photosensitivity and speed. Therefore, the improvement of photodetectors (PhD), especially in the infrared (IR) range of the spectrum is of great importance [1].

The purpose of our research is to increase the sensitivity of PhD operating in optoelectronic sensors at room temperature in the spectral range of 2-5 μm by applying to the active elements (AE) PhD optically active coating of a given shape based on multicomponent glassy alloys from chalcogenide systems Ge– (Ga, As, Sb) - Se.

PhD placed on the substrate of the TO-18 case were investigated. The active elements of the AF are made on the basis of heterostructures with p-n junctions based on solid solutions InAs / InAsSb / InAsSbP / and GaSb / GaInAsSb / AlGaAsSb.

A radical solution to simplify the technology of obtaining AE structures and increase the critical angles is achieved by applying an optically active coating of a given shape on AE PhD flat design with a high refractive index and low absorption coefficient for incident radiation.

Promising and technological materials for applying an optically active coating are transparent in the IR region of the spectrum chalcogenide glassy semiconductors. Chalcogenide glasses (ChG), which were used in studies, are transparent in a wide range of the optical range with a given refractive index, provide good adhesion to the material of the AE and the body, are consistent with their coefficients of thermal expansion, do not change the spectral characteristics of AE and technology good in manufacturing.

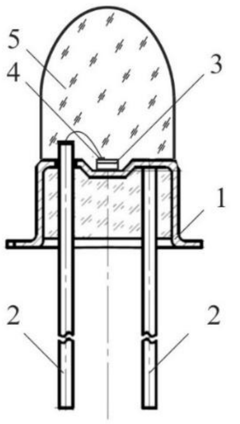

Fig.1 Optical coating of AE photodetector on TO-18 body:
1 – body; 2– current leads;
3– AE of the photodetector;
4– electrical contact;
5– chalcogenide glass

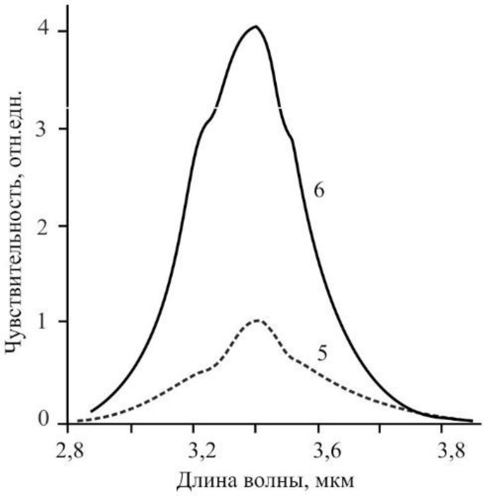

Fig 2. Spectra of AE photosensitivity before (5) and after applying the optical coating (6).

To obtain the maximum external output of the AE radiation, the optimal geometric shape of the optical coating was calculated (Fig. 1). The lower part of the optical coating shape takes into account the height of the coating surface, which does not emit radiation, due to total internal reflection, and the upper part of the coating shape was obtained taking into account the necessary (given theoretically) directional pattern. This form of optical coating conveniently combines the possibility of a more complete use of the light flux emitted by the AE with the possibility of its simultaneous focusing in the desired direction [2].

Our proposed method for applying an optical coating of a given shape based on multicomponent chalcogenide glasses [3] and a device for its implementation [4] have shown high reproducibility of specified forms of an optical coating. The photosensitivity spectra of the PhD obtained by us before and after the application of the optical coating are shown in Fig. 2.

The use of glassy alloys from multicomponent chalcogenide systems Ge - (Ga, As, Sb,) - Se as materials for optical coating made it possible to increase the efficiency of the used emitting AEs by 3.0–5.0 times, and the AE of photodetectors is at least 2.0-2.5 times in relation to similar photodetectors in which a hermetically sealed coating is used based on a polymer compound and 3.0-4.0 times in relation to photodetectors in which the sealing is carried out using a metal cover and transparent window for radiation.

1. В.Г.Вербицький, І.М.Вікулін, П.П.Воробієнко, В.М.Годованюк, В.Б.Каток, Ш.Д.Курмашев, В.І.Осінський, І.П.Панфілов, В.В.Рюхтін, Г.О.Сукач. Розробка високоефективних мікро-, нанотехнологій оптоелектроніки і комунікаційних систем на їх основі. Київ: ЛОГОС. (2009). 302 с.
2. Пат. № 112695 Україна. Фотоприймач. Кабацій В. М., Блецкан Д. І. (2016). Бюл. № 19.
3. Патент № 88565 Україна. Захисне, просвітлююче та фокусуюче покриття на основі халькогенідного скла і спосіб його нанесення. Блецкан Д. І., Кабацій В. М.(2009). Бюл. № 20.
4. Патент № 95127 Україна. Об’ємне оптичне покриття та пристрій для його нанесення. Блецкан Д. І., Кабацій В. М. (2011). Бюл. № 13.

NEW TECHNOLOGIES OF DIFFUSION SATURATION TITANIUM OF STEEL SURFACE

Zhiguts Yu.Yu., Krajnjaj I.I., **Karpovych V.A.**

Uzhhorod National University, 46, Pidgirna Str., Uzhhorod, Ukraine, 88000

The article is devoted to the study of the influence of combined surface material processing, which combines self-propagating high-temperature synthesis and laser surface hardening. The authors carried out theoretical calculations of the adiabatic temperature of the synthesis reaction. In addition, the authors discovered the microstructure of steel after a combined treatment, which consists of classical carbon steel (base) and carbides of various types. A separate study revealed the properties of phases and the microhardness of the surfaced material and the possible applications of synthesized alloys.

Introduction. The laser surface hardening (LSH) of metals was discovered in 1965. It has won strong positions in technology of metals [1]. Nowadays in the whole world hundreds of patents have been awarded to branch inventions including those dealing with combination of LSH with SHS (self-propagating high-temperature synthesis). One of them is dedicated to combining of LSH (Laser Surface Hardening) with SHS (self-propagating high-temperature synthesis) [2-7]. Formerly SHS was combined with other technologies of surface hardening of components [5-7].

In addition, one of the materials combining strength, reliability and durability is steel. Therefore, it is used for the manufacture of critical products subject to heavy loads. High temperature, static and dynamic loads, aging of steel lead to irreversible changes in its structure. The surface layers of parts and tools are most affected, therefore, the structure and properties of surface layers have a major impact on the performance of products.

The establishment and search for new integrated technologies to improve of physical and mechanical properties of alloys is an urgent task of modern materials science. The solution to this problem requires the improvement of existing and the creation of new methods of metal processing to increase their operational stability.

Integrated plasma saturation of the surface of steel with alloying elements is able to create a functionally gradient surface layer with unique mechanical, technological and special properties and make research aimed at creating such surfaces relevant. That is why recently more and more attention has been paid to methods of surface treatment of steels [1, 2, 3].

One of the main, most promising methods of coating is plasma coating in combination with laser initiation of combustion in exothermic mixtures (SHS). In this case, the surface can be saturated with boron, chromium, silicon, and also saturate immediately with two components: titanium, boron chromium and simultaneously several elements chromium and silicon, boron and titanium [2, 3, 6, 7].

Combined processing causes changes in the structure and stress state of steels. The basis of the processes is the study of the kinetics of the transformations occurring in the metal and the factors affecting this kinetics. Knowledge of the laws of diffusion processes of chemical-thermal treatment will significantly increase the efficiency of the search for new materials and optimal methods for their processing.

The main efforts of researchers studying the processes of combined processing are focused on establishing the mechanisms and laws of diffusion penetration of various elements into the metal base or on studying the nature of growth and properties of the formed diffusion zones.

The aim of the present work is to study the effect of titanium diffusion on increasing the operational stability of machine parts and tools by changing the phase composition, physical and mechanical properties of diffusion layers when alloying a steel surface as a result of using a complex technological process combining LHS and SHS.

Qualitative and quantitative characteristics of the process of surface saturation with titanium are the thickness of the diffusion layer, the distribution of the concentration of the diffusing element over the thickness of the layer, the phase composition and properties of the layer (hardness, wear resistance, corrosion resistance). The structure of layers saturated with titanium substantially depends on the composition of the mixture, on the method of saturation, on the temperature and duration of the process, on the composition of steel.

All these factors affect the final result and determine the physical and mechanical properties of the surface layer after saturation.

Theoretical and experimental research. The impotent problem within the LSH is the decreasing of the losses of beam energy because of its reflection by the surface of metal under machining. In the given investigation, as well as in the invention [1, 2], the mixture of powders Ti (65%), carbon in black state (18%) and Fe (14% by mass) were used in the role of light-absorbing paint. The mixture was damped by solution of 2 % latex in gasoline, and then it was put on the surface of stalls of mark 10 and 20 and was dried in an open air, forming the layer 80, 200 or 500 mkm thick. Thermochemical calculations showed that in such a mixture practically all Ti interacts, thanks to non-oxygen combustion, with carbon, forming the carbide TiC. The seer plus of carbon and very small account of Ti alloy the iron forming liquid steel of condition, which under fast cooling turns into troostite in layers of 80 mkm thick.

This reaction is strongly exothermic and is accompanied by great decreasing of Hibbs free energy:

$$\Delta G^{o}=-183{,}0246+0{,}01008T\ \mathrm{kJ\cdot mol^{-1}},\ T=298-1155\ \mathrm{K};$$

$$\Delta G^{o}=-186{,}9709+0{,}01325T\ \mathrm{kJ\cdot mol^{-1}},\ T=1155-2000\ \mathrm{K}.$$

The adiabatic temperature of non-oxygen combustion of equiatomic mixture Ti-C equals to 3200 K. The real temperature of combustion of selected mixture 68% (% in mass particles) is more than 1850 K that provides the formation of hard-liquid dross (TiC-melding) with the large interval liquids solid us. The formation of dross instead of one-phase alloy influences positively on the quality of surface of hardened layer after its full growing hard and cooling as well as on supporting of this layer even on inclined planes.

It is important to note that in the mentioned non oxygen combustion none of nonmetallic phase and its including is formed. Welding of hardened layer with basic metal is obtained automatically „metallurgic ally", excluding the necessity of soldering or other methods of connecting one alloy (e.g. instrumental) with other (e.g. with the basis of cutting tool).

In typical microstructure of metal in cross-cut of harded layer got under density og power 17 $\mathrm{W\cdot m^{-2}}$, diameter of „spot" − 0,4 mm, the speed of scanning 12 min/s and expense of argon (for the defense of Ti from air oxidation) − 0,5 l/s is shown. The thickness of alloy is ~500 mkm. This layer consists of ~50% particles TiC and ~50%(by volume) of metal link-instrumental carbon steel of type "У8" (fig. 1).

The investigations made have proved that the microhardness of carbides TiC is higher than the hardness of steel almost 10 times. Thus, in the given work we managed to organize the SHS process in comparatively thin layer thanks to using of LSH technology simultaneously for solving of two tasks: for heating, flashing and carbonating of an iron; for flashing Ti particles and its „combustion" in carbon with forming of carbides TiC.

In the figure, the two TiC carbides during their synthesis "burnt" steel with high local heat release and deeply rooted in the bond, shown with two vertical arrows (fig. 2). Wi shown also evident that in the zone of intense thermal influence the microstructure of steel acquired a very shallow columnar structure with a slight inclination of thin dendrites.

The figure 2 demonstrated full cross section of the microstructure, and the range changed of microhardness by depth of structural components of the surface layer (Fe-C-Ti system) within 1220-1570 HV.

The substitution of a part of iron powder by the powder of carbon ferrochrome (e.g. 12%Fe+2%FeCr instead of 14%Fe in the formulae of SHS mixture) allows to get layers of carbidosteel with the link not in the shape of steel "У8" but from alloyed steel "X12" which after fast cooling of these layers thanks to accelerated drain of heat to cold metal of the basis gets austenite-martensite-carbide structure.In the process of work of the instrument such metal link additionally grows hard thanks to pre-transforming of austenite into martensite and getting older of the later one. The hard of such a carbidosteel reaches HV1400 (14000MPa).

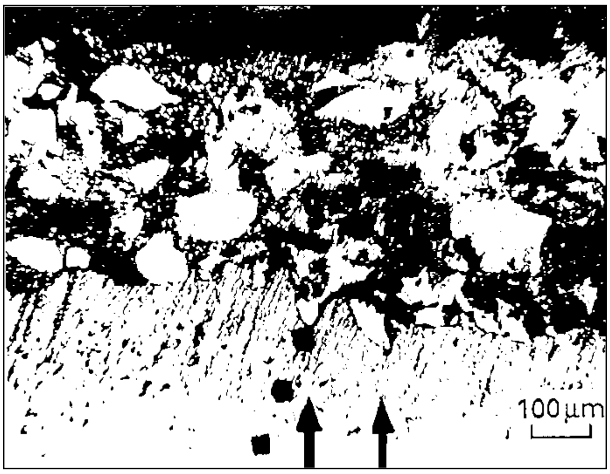

Fig. 1. Microstructure of the strengthened layer with semi-fused TiC particles

Fig. 2. Microstructure of cross-section of steel microsection after combined strengthening of LSH and SHS. A light arrow shows the direction along which the wells from the meter of the microhardness are located. The etching was carried out by nital

The substitution of a part of iron in the SHS-mixture by ferrochrome increases greatly corrosion resistance of carbidosteel and decreases its oxidizing wear in the process of its exploitation. The substitution of carbon in SHS-mixtures by the powder is also long-range. The same effect is obtained also with the substitution in another field of hot machining of metals namely the using of SHS-reactions for inmoulding process (modification within of the form) in casting manufacturing.

The substitution of carbon in SHS-mixtures by the powder of boron is also perspective. In such a case it is possible to reach the liquidus-solidus interval to 1500 K, that in other technologies it is practically impossible to meet. Thus, while the above mentioned method on the one hand high refractory diborides TiB_2 and CrB_2 (with high hardness) are formed and, on the other hand, very easily melted complex eutectics are formed.

Conclusions. 1. Combination of LSH and SHS in one operation allows to solve the whole complex of technical problems connected with producing of materials with high hardness like carbidosteels and hard alloys on metal surface.

2. Evolution of inner chemical heat in SHS-mixtures allows to decrease the power of laser radiation. 3. New complex technological process allows to build up wearied surfaces of parts of machines and devices to the high of 0,5 mm.

1. Жигуц Ю. Ю., Лазар В. Ф. Технології отримання та особливості сплавів синтезованих комбінованими процесами // Ужгород: Видавництво «Інвазор», 2014. – 388 с.
2. Жигуц Ю. Ю., Опачко І. І. Вплив лазерного поверхневого зміцнення і СВС на структуру обробленого матеріалу // Міжвузівський збірник Луцького національного технічного університету «Наукові нотатки». – 2015. – № 49. – С. 58 - 61.
3. Жигуц Ю. Ю., Лазар В. Ф., Хом’як Б. Я. Перспективні технології засновані на комбінованих процесах // Науковий вісник Мукачівського державного університету. Журнал наукових праць. – № 22 (17). Мукачево. 2017. – С. 29 - 40.
4. Zhiguts Yu. Yu., Vivtharskuj O. V. Using SHS for synthesis of nanostructures in hard alloys and karbidostal’s // Clusters and nanostructured materials (CNM-4’2015) Комплексне забезпечення якості технологічних процесів та систем: 4 international meeting, 12-16 October 2015.: materials conf. – Uzhorod: Ukraine, 2015. – С. 141.
5. Жигуц Ю. Ю., Лазар В. Ф., Хом’як В. Я. Перспективи використання твердих сплавів та карбідосталей для металообробного інструменту // Прогресивні технології в машинобудуванні: 5-а Всеукраїнська науково-техн. конф., 08-12 лютого 2016 р.: Збірник наукових праць. – Львів: Національний університет «Львівська політехніка», – 2015. – С. 45 - 48.
6. Zhiguts Yu. Development of SHS technology / Yu.Zhiguts, Ya.Legeta, Yu.Golovka // Prospects of world science –2019: XV intern. scientific and practical conf., 30 July 2019 - 7 August 2019: Materials of the conf. – Sheffield: Science and education LTD, 2019. – № 8. – P. 61 - 63.
7. Жигуц Ю.Ю. Комбінована технологія: лазерне поверхневе зміцнення і СВС / Ю.Ю.Жигуц, А.С.Колесниченко // Матеріали школи-конф. молодих вчених «Сучасне матеріалознавство: фізика, хімія, технології (СМФХТ – 2019)», 27-31 травня 2019 р.: – Ужгород: Водограй Україна, ФЩП Сабов А.М. – С. 80 - 81.

RESEARCH OF TECHNOLOGIES FOR PRODUCING FUNCTIONAL COATINGS BY COMBINED METHODS OF SHS-ALLOYING SURFACES OF STEEL BY METALS

Zhiguts Yu.Yu., Segeda Yu.V., **Kasynetsj S.O.**

Uzhhorod National University, 46, Pidgirna Str., Uzhhorod, Ukraine, 88000

The widespread use of modern machines and designs of parts made of cast materials operating at high temperatures, in conditions of intensive wear and cyclic loads, often imposes a set of requirements which surround methods of doping, the creation of new alloys it is impossible or impractical from an economic point of view. In this case, the decision of the question is linked to the creation of on the surface products functional coatings that meet the requirements of operation.

Promising in this respect is the use of diffusion saturation of the surface alloying elements in the implementation SHS-doping, the essence of which consists in applying a layer of metal on the surface of the part using SHS process. Currently, methods of SHS-alloying elements Ti, W, Mo, Cr applicable to cast steels are poorly understood. Therefore, the research and development of technology of hardening of cast steel elements of the system Ti, W, Mo, Cr diffusion methods SHS-saturation, which allows to increase operational properties of such steels is an important task [1].

The purpose of the study. The purpose of work is research and development of technologies for producing functional coatings on alloy steels by the methods of diffusion of SHS-saturation system elements Ti, W, Mo, Cr, allowing to improve the performance properties of such steels and the study of the influence of technological parameters of diffusion SHS-saturation on the kinetics of formation of functional coatings, as well as the influence of technological parameters of the modes of diffusion of SHS of saturation on physical and mechanical properties of products made of cast steels (abrasion resistance, crack resistance, heat resistance).

Surface saturation Cr, W and Ti is carried out to improve heat resistance, oxidation resistance and other properties. Tungsten increases the static, dynamic and fatigue strength of steel, eliminating the tendency to internal oxidation, prevents the grain growth, increases the hardness and cutting properties of the steel due to the formation of carbides, increases heat resistance of steel. With the introduction of chromium steels chromium significantly increases the ductility, toughness, strength and hardenability, lowers the threshold of cold brittleness. Titanium increases the strength and elasticity of steel, promotes the formation of fine-grained structure [1-6].

From literature and patent sources it is known that all methods can be divided into three groups: chemical (including electrochemical), physical and mechanical. Each of the methods has advantages and disadvantages. The choice of the optimal treatment method depends on the cost, size, and number of parts, and operating conditions. Promising in this respect are the methods of diffusion of SHS-saturation, which have energy autonomy, high performance, simplicity of equipment and very little time for implementation in production.

Diffusion saturation of metal surface alloying elements is an effective method to improve the durability of various components, which change the chemical composition, structure and properties of surface layers of metal. The method of SHS-doping, the essence of which is applied to the exothermic layer on the surface of the product, the initiation of the reaction and diffusion alloying elements in steel, has several advantages: does not require special surface preparation; provides high adhesion of the coating to the base material; does not affect the basic structure of the metal; gives the product the required performance properties; allows you to save expensive steel. Using this method opens up the possibility of its use not only for hardening, but also for the restoration of parts for various purposes.

For the manufacture of an exothermic SHS mixture, powder materials were used, namely iron powders: “ПЖВ” 2.160.26 (“GOST” 9849-86); “ПЖВ” 4.450.28 (“GOST” 9849-86); “ПЖР” 2.200.28 (“GOST” 98-86). The particle size of the powders was in the range of 20...200 microns. Carbon was introduced into the mixture in the composition of powders of carbon-containing components of the “ГИСМ” (special artificial low-graphite graphite) “TU” 48-20-54-84. Powders were weighed on a “ВЛКТ-500-М” balance, and mixing in a cone mixer. For research, prismatic samples from cast steels 45, 75, size 55x10x10 mm were used. The low-carbon ferrochrome “ФХ 001 А” and “ФХ 001 Б”, ferrovanadium “ФВд50У0,5” and “ФВд40У1” with particle sizes of 60...100 μm, nickel powder “ПНЕ-01” with a particle size of 20...100 μm were used as components for diffusion SHS saturation; “ПМ-003” molybdenum powder with particle sizes of 60...120 microns. Ammonium chloride, sodium fluoride and sodium chloride were used as activators. For the manufacture of the coating, mixed components of the charge were used in a cone mixer, then static cold pressing was performed on “2ПГ-125” and “Р-250” hydraulic presses with the addition of a binder in the form of 10% dissolved latex in alcohol and sintering in a muffle furnace in a protective-reducing environment. After that, hot prepressing of the blanks was carried out. Compression tests of the samples were carried out using universal plants that meet the requirements of “GOST” 7855-68. Bending tests were carried out on a universal testing machine “УМЭ-10ТМ”. Impact strength was determined according to “GOST” 26528-85 on a KM-30A pendulum head with a maximum impact energy of 294 J. Heat resistance tests were carried out in an electric furnace in an air atmosphere at T=773-973 K. Heat resistance was determined by the weight loss of the samples on an analytical balance through every 4 hours with an accuracy of 0,1 mg. Crack resistance tests were carried out using a “ПМТ-3” microhardness tester. The wear test of the coatings was carried out on a friction machine. To study the microstructure, a light microscope was used. Wear resistance was evaluated by the wear rate of the samples, determined by the change in linear wear at constant load. The microstructure of the samples was studied using UNIVAR metallographic microscopes, and electronic micro-X-ray spectral analysis was used for substructures using a "CAMEBAX-MBX 70" scanning electron microscope equipped with a computer and software. X-ray phase analysis was performed on a “ДРОН-2,0” diffractometer.

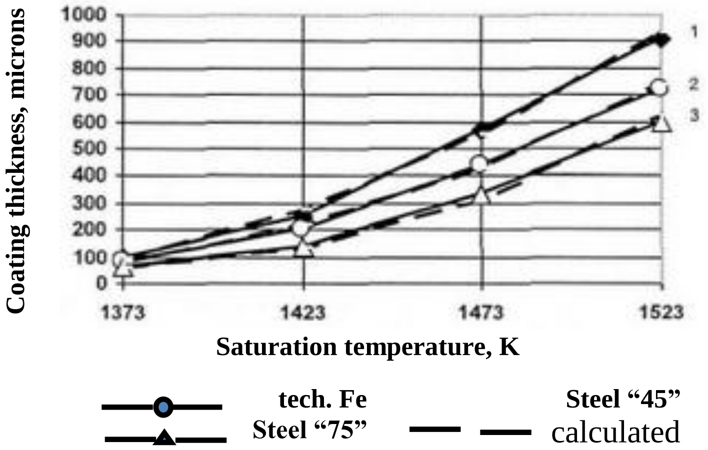

Fig. 1. Dependence of coating thickness on saturation temperature
(δ_1=0,019t^2-49,524t+32271,5; δ_2=0,0161t^2-42,016t+27601,9; δ_3=0,019t^2-5l, 404t+34818,7)

When conducting research, the nature of the change in the thickness of the diffusion layer on the composition of the mixture, its combustion temperature and aging, carbon content and type of activator was established. The effect of temperature on the coating thickness at diffusion saturation is shown in fig. 1. It can be seen that the coating thickness in the considered temperature range increases according to a law close to a quadratic parabola. This character of the dependence can be explained by the fact that with an increase in the saturation temperature, the number of structural defects, the density of vacancies, and dislocations decreases. Fig. 2 shows the dependence of the coating thickness on the saturation time at T=1373 K. It can be seen that with increasing exposure time, the coating thickness in the materials considered increases and reaches a maximum value at a time of 12 minutes. A further increase in time leads to an increase in the coating thickness at T=1373 K. In diffusion saturation with powder mixtures, the saturation process occurs due to the formation of active atoms Ti, W, Mo, Cr. Free atoms are deposited on the surface of the sample, and then diffuse deep. The introduction of an activator promotes the promotion of atoms of Cr, Ti, W, Mo. The increase in the number of these elements in the surface layer is gradual, which leads to the formation of a practically non-porous coating.

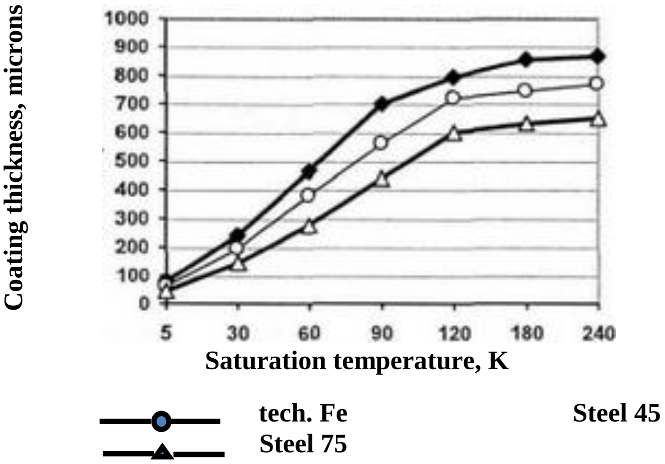

Fig. 2. Dependence of coating thickness on saturation time (at T=1373 K)

In the study of the influence of the activator, it was determined that the greatest activity at a temperature T_{ad}=1423 K and a saturation time of 12 minutes possesses sodium fluoride.

An increase in the porosity of powder steel leads to an increase in the coating thickness, fig. 3. This is due to the fact that the saturating elements first penetrate into the pores, fill them, and only then diffuse into the iron matrix. An increase in the carbon content in the powder mixture leads to a decrease in the thickness of the coating as a result of the peculiarities of its redistribution in steel during diffusion saturation.

During X-ray phase analysis, iron carbides, complex carbides of iron, chromium and carbide of titanium, tungsten and molybdenum were found in the coating. The authors found that in samples saturated at T=1473 K for 12 min, molybdenum and chromium are distributed evenly over the surface of the sample. Tungsten diffuses in small amounts, so its distribution is uneven.

The study of the conditions for the formation of SHS functional coatings by the method for the Ti-W-Mo-Cr system was carried out on steels 45 and 75.

The results of X-ray phase analysis of the coating obtained by SHS alloying of steel 75 are shown in fig. 3. In the hardening coating, there are phases of iron carbides (Fe_3C) and chromium (Cr_2C_3), complex iron carbide and chromium $(Cr, Fe)_7C_3$, as well as molybdenum carbide (MoC).

It was found that the thickness of the coating obtained on 45 steel with optimal CHC alloying parameters is 15-30 µm with a 100% continuity of fig. 3.

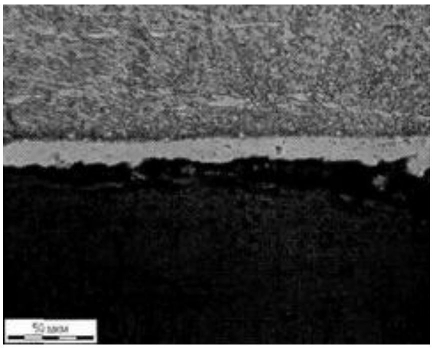

Fig. 3. The continuity and thickness of coating, the obtained SHS-alloying steel 45

Studies have also shown that after SHS-doping microhardness of steel 45 exothermic mixture of Ti-W-Mo-Cr increased 3 times in comparison with the microhardness of this same steel untreated.

In subsequent studies conducted mechanical and service properties of cast steels with coatings of the composition Ti-W-Mo-Cr, obtained by diffusion of SHS-saturation. The authors found that the powder of the steel after diffusion SHS-saturation have a compressive strength higher than similar unsaturated. The Flexural strength of the samples with carbon content of 0,45 and 0,75 by weight % after saturation and is 138 and 172 MPa, respectively, which is 22...25 % higher in bending strength similar to the unsaturated samples.

It is established that diffusion saturation of Ti-W-Mo-Cr increases the heat resistance of cast steels at T=573-973 K in 2-3 times in comparison with unsaturated. Noted that the heat resistance of the investigated experimental steel due to the virtually non-porous structure and, as a consequence, a dense reinforcing coating.

It is shown that the fracture toughness of steel 45 subjected to diffusion SHS-saturation after hot forging, higher fracture toughness steel 45п obtained diffusion SHS-saturation, followed by hot stamping.

It was also found that a cast steel with such coatings can be used as heat resistant materials at temperatures up to 973 K. however, their heat resistance is at the level of heat-resistant steel “12X18H9T”, and heat resistance superior to other steels, not subjected to processing in 5...7 times.

Conclusions. A diffusion SHS alloying technology has been developed for a complex alloy based on titanium powder, tungsten, and other elements, which is much more efficient than saturation during furnace heating. It was established that the introduction of NaF or NH_4Cl activator into the saturating exothermic mixture allows a 2,0...4,5 times increase in the thickness of the diffusion layer and the content of alloying elements in it.

The authors determined the kinetic dependences of the change in the thickness of the diffusion layer and it is shown that in the process of diffusion saturation, the thickness of the diffusion layer is 60-900 μm.

Using X-ray spectral analysis and X-ray diffraction analysis, it was found that the diffusion layer obtained by the combined method consists of iron carbides (Fe_3C) and chromium (Cr_7C_3), complex iron and chromium carbides $(Cr, Fe)_7C_3$, molybdenum carbides (Mo_2C), and solid solution chromium in iron.

The authors also found that the wear resistance of steel surfaces hardened by combined diffusion SHS saturation with Cr, Mo, Ni, and V elements increases by 2–4 times, and heat resistance at T=573–973 K by 2–3 times, which allows to increase the service life of parts 2-3 times, and the roughness of the surfaces obtained by combined treatment at optimal parameters does not exceed 5 microns.

1. Жигуц Ю. Ю., Лазар В. Ф. Технології отримання та особливості сплавів синтезованих комбінованими процесами // Ужгород: Видавництво «Інвазор», 2014. – 388 с.
2. Жигуц Ю. Ю., Опачко І. І. Вплив лазерного поверхневого зміцнення і СВС на структуру обробленого матеріалу // Міжвузівський збірник Луцького національного технічного університету «Наукові нотатки». – 2015. – № 49. – С. 58 - 61.
3. Жигуц Ю. Ю., Лазар В. Ф., Хом’як Б. Я. Перспективні технології засновані на комбінованих процесах // Науковий вісник Мукачівського державного університету. Журнал наукових праць. – № 22 (17). Мукачево. 2017. – С. 29 - 40.
4. Zhiguts Yu. Yu., Vivtharskuj O. V. Using SHS for synthesis of nanostructures in hard alloys and karbidostal’s // Clusters and nanostructured materials (CNM-4’2015) Комплексне забезпечення якості технологічних процесів та систем: 4 international meeting, 12-16 October 2015.: materials conf. – Uzhorod: Ukraine, 2015. – С. 141.
5. Zhiguts Yu. Development of SHS technology / Yu.Zhiguts, Ya.Legeta, Yu.Golovka // Prospects of world science – 2019: XV intern. scientific and practical conf., 30 July 2019 - 7 August 2019: Materials of the conf. – Sheffield: Science and education LTD, 2019. – № 8. – P. 61 - 63.
6. Жигуц Ю.Ю. Комбінована технологія: лазерне поверхневе зміцнення і СВС / Ю.Ю.Жигуц, А.С.Колесниченко // Матеріали школи-конф. молодих вчених «Сучасне матеріалознавство: фізика, хімія, технології (СМФХТ – 2019)», 27-31 травня 2019 р.: – Ужгород: Водограй Україна, ФЩП Сабов А.М. – С. 80 - 81.

MANIFESTATION OF FERROELECTRIC PROPERTIES OF ALUMINUM-SUBSTITUTED NANOSIZED LITHIUM-IRON SPINELS

Kaykan L.S.[1], Sijo A.K.[2], Mazurenko J.S.[2], Ostapovych N.V.[2]

[1]Vasyl Stefanyk Precarpathian National University, 57 Shevchenko St., 76018 Ivano-Frankivsk, Ukraine
[2]Department of Physics, Mary Matha Arts and Science College, Manathavady, Kerala, India-670645
[3]Ivano-Frankivsk National Medical University, 2, Halytska St., 76000 Ivano-Frankivsk, Ukraine

Ferrites are a very good class of electrical materials due to their high resistance and low losses and can have significant technological applications in a wide range of frequencies [1]. In addition, in a certain temperature range, some ferrites may also exhibit ferroelectric properties [2]. Aluminum-substituted nanosized ferrites obtained by the sol-gel auto-combustion method near temperatures of 350-400 K show the characteristic behavior of both Arrhenius curves and temperature dependences of the real part of the dielectric constant.

Thus, for samples with x=0.6, 0.8 and 1.0 there is a section of the approximating curve with a positive slope to the temperature axis (Fig. 1), similar to the metal, which indicates the existence in the temperature range (350 - 400K) ferroelectric properties.

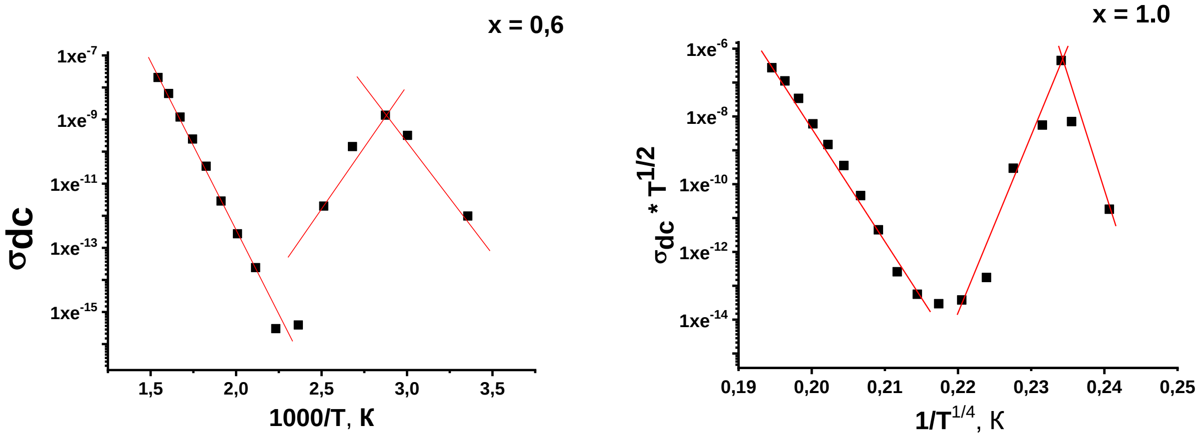

Fig.1. Measured value of the real part of the inverse temperature dependent conductivity for nanosized aluminum-substituted lithium spinel obtained by the method of sol-gel auto-combustion with aluminum content x = 0.6 and x = 1.0

Polycrystalline ferrites at room and near room temperatures are mainly characterized by a hopping type of conductivity in which the electron jumps between ions of the same element that is in different valence states. In the considered systems, such ions are divalent and trivalent iron localized in octahedral cavities of a spinel lattice.

The activation energies of the hopping conductivity of aluminum-substituted nanosized lithium-iron ferrite, calculated based on the temperature dependences of the conductivity are given in the table 1.

To analyze the anomalous behavior of the temperature dependences of the conductivity, we conducted studies of the temperature behavior of the real part of the dielectric constant.

Fig. 2 shows the dependence of the real part of the dielectric constant on temperature for samples with replacement by aluminum ions x = 0.6.

Table 1. Aluminum content dependence of the average values of activation energy of jumping mechanism of conductivity ΔE(eV) for aluminum-substituted lithium-iron ferrites

x	**0.2**	**0.4**	**0.6**	**0.8**	**1.0**
ΔE_1, eV	0,14	0,33	0,30	0,33	0,43
ΔE_2, eV	0,09	0,14	0,09	0,13	0,12

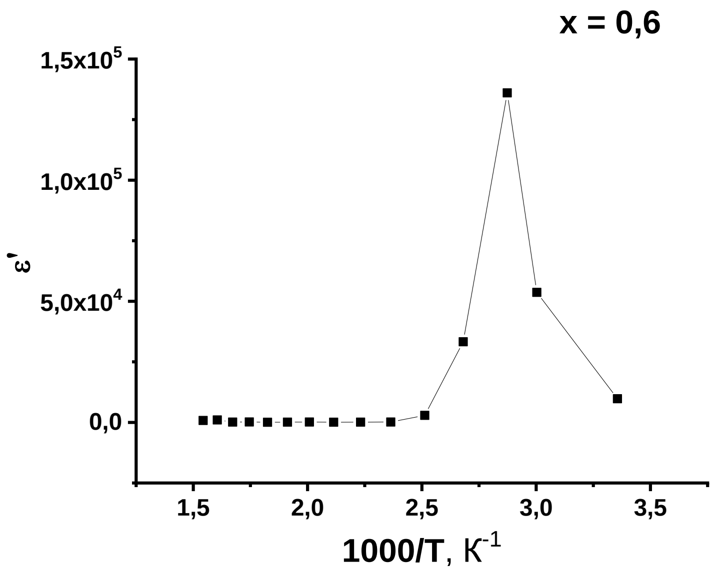

Fig.2. Dependence of the real part of the dielectric constant on temperature.

The observed characteristic maximum in these dependencies indicates the existence of ferroelectric domains in the temperature range 350 - 400K. It should be noted that a similar nature of the temperature behavior of the dielectric constant is also observed in unsubstituted lithium ferrite. Obviously, the positive slope of the Arrhenius curves of the samples when replaced by aluminum ions with x = 0.6, 0.8 and 1.0 in the considered temperature range is explained by the residual polarization of the grain boundaries of micro-regions formed during the synthesis of nanoscale ferrites by external field.

The study of complex impedance showed that the influence of grain boundaries increases with decreasing particle size. The hodographs show that the area of the semicircle responsible for the complex impedance of the grains is practically absent and only a distorted arch is observed, which degenerates into a straight line inclined almost at an angle of 450 to the positive direction of the Z' axis (Fig. 3).

This behavior of holographs indicates the predominant role of the grain boundary of the formed crystallites compared to the response of bulk regions. This is another confirmation of the fact that when the size of the crystallites decreases to the nanometer range, the influence of the grain boundaries plays a dominant role, which contributes to the electro-physical properties of the studied systems.

Studies have shown that the observed values of resistance and capacitance of grain boundaries are greater than the corresponding observed values of grains. The resistance of grains and grain boundaries decreases to x = 0.1, and then increases with a subsequent increase in the aluminum content, which is in good agreement with electrical measurements.

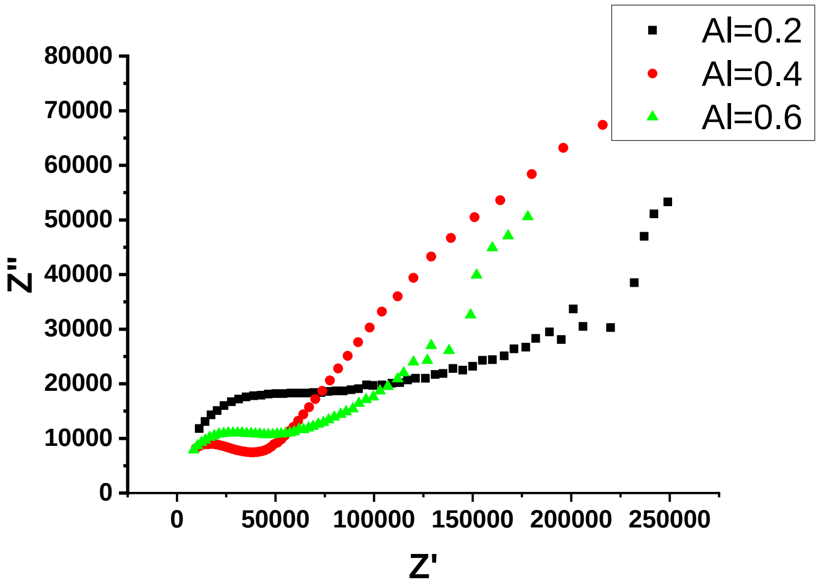

Fig.3. Cole-Cole diagrams of $Li_{0.5}Fe_{2.5-x}Al_xO_4$ systems synthesized by the sol-gel auto combustion method.

Nanosized ferrite $Li_{0.5}Fe_{2.5-x}Al_xO_4$ was synthesized by the method of citrate gel auto combustion at pH equal to six. The average size of the crystallites ranged from 38 to 41 nm. The lattice parameter, the size of the crystallites and the density decrease with the Al content, which is explained based on the ionic radius and the density of the Al^{3+} backgrounds. Dielectric properties showed a normal dependence on frequency, which is explained based on Coops' theory and Maxwell-Wagner model. AC conductivity first increases to $x = 0.1$, then decreases with increasing Al content. The saturation magnetization decreases with the content of Al^{3+} in lithium ferrite. It was found that near temperatures of 350 - 400 K, the temperature dependence of the real part of the conductivity and dielectric constant exhibit anomalous behavior, which probably indicates the ferroelectric properties of this material. Complex impedance measurements showed the presence of a weakly high-frequency semicircle and a low-frequency fragment for all samples, indicating that the capacitance and resistance of the samples are related to the properties of the grains and grain boundaries. From the measurements and the data obtained, it can be concluded that the substitution of Al^{3+} plays an important role in modifying the magnetic and electrical properties of lithium ferrites, suitable for microwave applications and devices for energy generation.

1. Fazio E.De, Bercoff P.G., Jacobo S.E. Electromagnetic properties of manganese–zinc ferrite with lithium substitution // Journal of Magnetism and Magnetic Materials, 2011. – V. 323. – P. 2813–2817.
2. Малышев А.В., Пешев В.В. Аномалии диэлектрических свойств сегнетоподобного типа в поликристаллическом литий-титановом феррите // Известия вузов. Физика, 2007. – Т. 50. – N. 2. – С. 59-61.

EPR STUDY OF MAGNETIC NANOPARTICLES ENSEMBLES PROMISING FOR BIOMEDICAL APPLICATIONS

Konchits A.A.[1], Shanina B.D.[1], Krasnovyd S.V.[1], Shevchenko Yu.B.[2], Petranovs’ka A.L.[3], Rieznichenko L.S.[4]

[1]*V. Lashkaryov Institute of Semiconductor Physics NASU, Prospect Nauky, 41, Kyiv 03028, Ukraine*
[2]*Institute for Nuclear Research NASU, Prospect Nauky, 47, Kyiv 03028, Ukraine*
[3]*Chuiko Institute of Surface Chemistry NASU, General Naumov str. 17, Kyiv, 03164, Ukraine*
[4]*F.D. Ovcharenko Institute of Biocolloidal Chemistry NASU, Acad. Vernadsky Boulevard, 42, Kyiv, 03142, Ukraine*

Abstract. The paper presents the results of studying the properties of silver and copper nanoclusters, as well as Fe_3O_4:Gd:B complexes which are promising for usage in biomedical problems. Magnetic resonance is applied as the main method. It is established the dependence of the nanoparticles magnetic resonance properties on the medium in which they are (in solution or dry samples). For lyophilized ensembles of Ag and Cu nanoparticles, the dependence of their magnetic resonance properties on the interaction with molecular oxygen, which induces nanoparticles oxidation, is described. It is shown that the properties of the complex magnetic system Fe_3O_4:Gd:B as a key structural element in a promising method of neutron capture oncotherapy, can be described in detail due to the difference in g-factors of individual components and, as a consequence, the dependence of the resulting g-factor on the ratio of the components.

Introduction

Ensembles of nanoparticles (NPs) are widely used in biology and medicine for the preparation of antibacterial drugs, targeted drug delivery, use as contrast agents in MRI, in oncological thermotherapy, etc. [1-3]. The search of the most suitable methods and substances for the effective solution of a wide range of problems in nanomedicine continues actively.

This paper presents the results of studying the magnetic resonance properties of silver and copper NP, which are promising for usage in biomedicine. The magnetic resonance characteristics of the Fe_3O_4:Gd:B complex, which today is one of the main candidates for usage in neutron capture oncotherapy [4], have been studied for the first time.

1. *Paramagnetic properties of ensembles of Ag and Cu nanoparticles*

The magnetic properties of Au, Ag, Cu, etc. NP have been actively studied over the past decade. Significant progress has been achieved in recent years, when the key role of nonstoichiometric composition of NP was established, which is associated with their partial oxidation under specific synthesis conditions [5-7]. EPR studies of silver and copper nanoparticles synthesized at the Institute of Biocolloidal Chemistry are presented below.

Figure 1 shows the EPR spectrum of silver NP, which were lyophilized (dehydrated) especially for EPR measurements.

It is seen from Figure 1 that the spectrum consists of four narrow lines against a background of a wider spectrum. Center of the spectrum has a g-factor g=2.034. The value of the g factor and the number of lines in the spectrum give reason to believe that it belongs to small Ag clusters with the number of atoms from about 2 to 5 [3]. This result confirms the well-known tendency of silver NP to oxidize, with small Ag clusters being the most stable.

A similar situation with oxidation, but more interesting from the point of view of the dynamics of EPR spectra, was observed in a lyophilized system of Cu NP. Figs. 2a and 2b show the spectra of Cu NPs after 8 hours and 10 days after sample preparation, respectively.

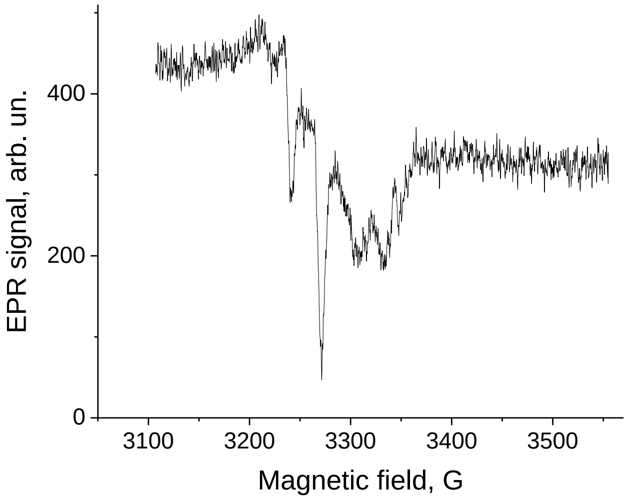

Fig. 1. The EPR spectrum of lyophilized silver NP after 3 days of exposure to air.

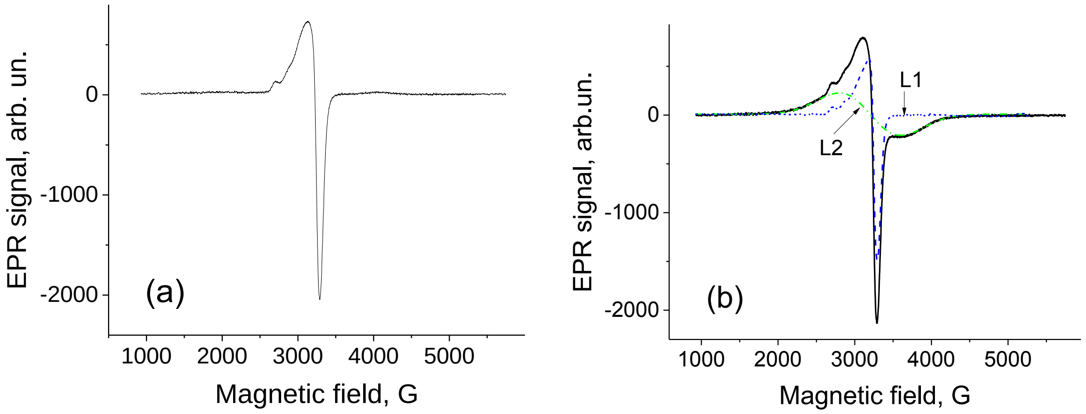

Fig. 2. EPR spectra of Cu NP after 8 hours (a) and 10 days (b) of keeping the sample in air.

The spectrum in Fig. 2a is typical for Cu^{2+} ions diluted in a nonmagnetic matrix. The hyperfine structure inherent in the EPR spectra of copper is not very clearly manifested due to the large width of the individual hyperfine components of the spectrum. As it was found, when the sample is kept in air, another signal gradually increases in it, the intensity of which reaches saturation in 10-15 days (Fig. 2b). In Fig. 2b shows the experimental spectrum and its decomposition into two lines L1 and L2. Line L1 completely coincides with the spectrum in Fig. 2a, and the L2 line differs significantly from it. It has a Gaussian shape, g-factor g=2.095, and line width ΔH_{pp}=0.8 kG, which do not change during the entire time of the formation of this line. Most likely, the L2 line belongs to partially oxidized copper NP, as it observed in [6] under specific conditions for the synthesis of NPs.

2. *Magnetic resonance properties of complex* Fe_3O_4*: Gd: B*

Magnetite Fe_3O_4 is a widely known ferromagnetic material. At room temperatures, nanostructured magnetite shows ferromagnetic or superparamagnetic behavior depending on the size of the particles. We found that for NP with a size of d ~ 20 nm and less it is a superparamagnetic, the width of the magnetic resonance line which depends on d. Thus, diluted in paraffin Fe_3O_4 NP with sizes 20 and 10 nm, show the EPR spectra with line widths □ΔH_{pp}=1.8 and 0.8 kG, respectively. Therefore, in order to achieve high resolution in experiments with complex Fe_3O_4:Gd:B we used Fe_3O_4 NP with size d =10 nm.

Fundamentally important is the magnetic behaviour of Gd. The ground state of the Gd (III) ion ($4f^7$) is $^8S_{7/2}$, and since S>1, the EPR spectrum with 2S+1=8 lines is observed [8]. In solutions, the spectrum changes due to motion fluctuations so that the total width and shape of the spectrum is determined by the parameters of the splitting tensor in zero field (ZFS) and time τ_c, where τ_c is the correlation time of rotational diffusion or other motion fluctuation [9].

Two types of samples have been studied: samples of NPs Fe_3O_4:Gd:B in aqueous solution (no coagulation of NPs) with a varied composition of components, and dry samples. FMR/EPR spectra were observed in both types of samples, but the samples in solution were more stable in terms of their magnetic resonance properties, so they were the focus. To reduce the effect of water on the quality factor of the resonator of the EPR spectrometer, thin glass tubes with an inner diameter of approximately 1 mm were used. Fig. 3 shows the magnetic resonance spectra of the following samples: 1- Fe_3O_4; 2- Fe_3O_4:B=1:10; 3- Fe_3O_4:Gd=1:1; 4- Fe_3O_4:Gd:B=1:1:10; 5- Fe_3O_4:Gd=1:10; 6- Gd only.

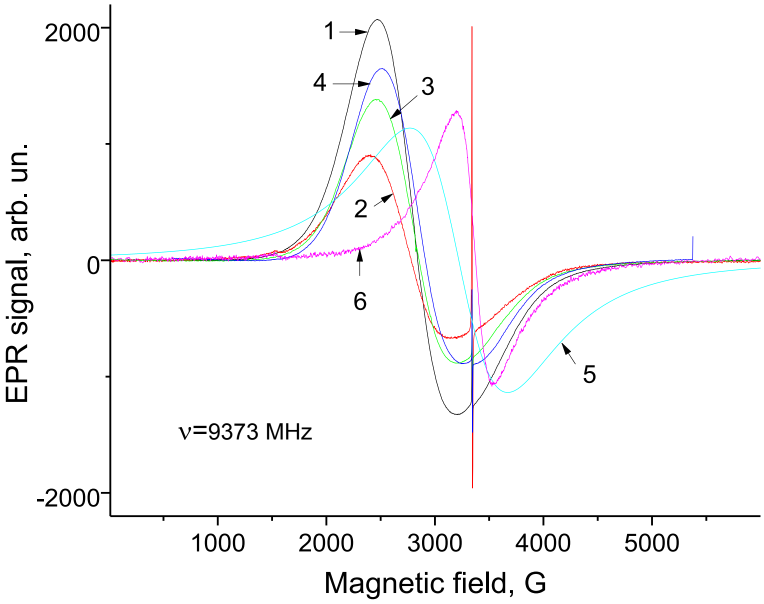

Fig. 3. EPR spectra of samples 1-6 (colored online). The narrow line at H=3.34 kG – Reference sample αC/Si (carbon dangling bonds, g=2.0026, $N_s=1.6\cdot10^{16}$ spins). The gain was chosen to be optimal for recording the spectrum of each sample.

Fig. 3 shows that spectra of various samples differ in both the magnitude of the resonance field H_{res} (i.e. the g-factor) and the width ΔH_{pp} and the shape of the lines. Samples containing Fe have a significantly wider line width than the sample with only Gd. It should be noted that Gd signal is about 10-20 times weaker than in the sample with Fe_3O_4 with the same concentration. Therefore, for a better understanding of the mixture properties we prepared a special sample # 5 with the Fe:Gd ratio =1:10 so that the signals from Fe_3O_4 and the Gd were comparable in intensity and the contributions from Fe_3O_4 and Gd could be distinguished. No signals from boron were detected directly, but its possible contribution to the values of H_{res} and the shape of the observed signals is not excluded. Processing of the obtained spectra made it possible to determine H_{res}, □ΔH_{pp} and g-factor for each sample. In Fig. 4 shows, as an example, the results of measurements of the g-factor of samples of various compositions.

Analysis of the entire set of the data obtained (H_{res}, ΔH_{pp}, g-factor) made it possible to describe by an understandable way the behaviour of the spectra in various samples.

From Fig. 3 it is easy to see that in samples 1-4 with a predominance of the contribution to magnetization due to Fe_3O_4, the ΔH_{pp} value gradually increases, in sample 5 ΔH_{pp} it sharply increases, and in sample 6 with pure Gd ΔH_{pp} drops sharply. The values of H_{res}, that is, the value of g-factors, also change correspondingly (Fig. 4). It is seen from Fig. 4 that the value of the g-factor clearly tracks the change in the relative contributions of Fe_3O_4 and Gd, not excluding the possibility of a slight influence of boron.

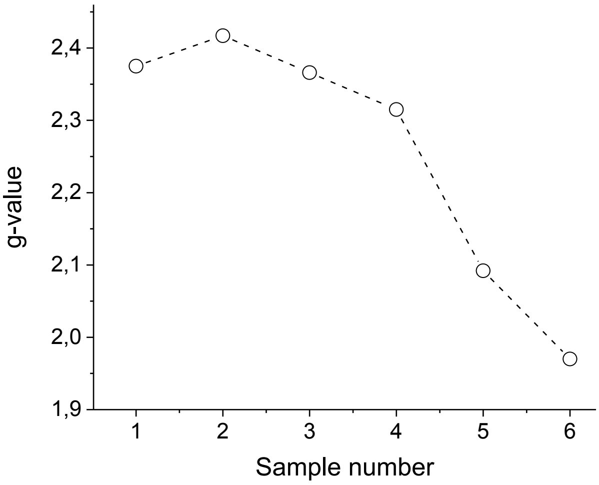

Fig. 4. The measured value of the effective g-factor for samples 1-6.

Conclusions. EPR signals in the ensembles of Ag and Cu nanoparticles, change during storage in air due to oxidation processes. In the case of Ag NP, the most stable are small clusters of several Ag atoms. In the ensemble of Cu NP during their storage in air, in addition to the EPR spectrum from Cu^{2+}, a new intense spectrum is gradually formed, which can be associated with the processes of nonstoichiometric oxidation of NP [5, 6].

Magnetic resonance studies of the complex Fe_3O_4: Gd: B show that it is possible to measure not only its general magnetic characteristics, but also to separate the contributions of individual components of this magnetic complex, in particular, the contribution of Gd. In total, this is an integral part of the formation and development of the method of neutron capture therapy of oncological diseases.

1. EMR/ESR/EPR Spectroscopy for Characterization of Nanomaterials. Ed. Ashutosh Kumar Shukla. Springer, 2017.
2. K.G. Lopat’ko, E.G. Aftadilianz, Ya.V. Zaulichnyj, M.V. Karpez. Trudy Instituta problem materialovedenija im. I.N. Franzevicha, 2010, №1, P. 232.
3. Spartak S. Khutsishvili, Nikolay I. Tikhonov, Marina V. Lesnichaya, at al. Functional Materials Lett. V. 10, No. 2 (2017) 1650077.
4. G.J. Lavrenchuk, Yu.B. Shevchenko, V.V. Trishin, at al. Jaderna fizika ta enerhetyka, 2016, V. 17 № 3, P. 276-286.
5. A.J. Marenco, D.B. Pedersen, S. Trudel. Journal of Materials Chemistry C. 2017. DOI: 10.1039/c7tc00879a
6. A.J. Marenco, D.B. Pedersen, S. Trudel. J. Phys. Chem. C, 21 Mar 2016. DOI: 10.1021/acs.jpcc.6b00699
7. A. Kharchenko, V. Zholobenko, A. Vicente, C. Fernandez, H. Vezin, V. De Waele, S. Mintova. Phys. Chem. Chem. Phys., 1ss. 4 (2018) 2880-2889. DOI: 10.1039/C7CP07650A
8. Abragam A, Bleaney B, 1970, Electron Paramagnetic Resonance of Transition Ions (Oxford University Press) p. 335.
9. R.B. Clarkson, A.I. Smirnov, T.I. Smirnova, H. Kang, R.L. Belford, K. Earle, and J.H. Freed. Molecular Physics, 95:6, (1998) 1325-1332. DOI: 10.1080/00268979809483262

THERMOMAGNETIC EFFECT IN NANOFILMS AND CAPILLARIES

Shevchenko S.I., **Konstantinov A.M.**

B.Verkin Institute for Low Temperature Physics and Engineering of NAS of Ukraine,
47 Nauky Ave., Kharkiv, 61103, Ukraine

In this paper, attention is drawn to a new polarization mechanism that should take place in superfluid dielectric systems in the presence of a temperature gradient and magnetic field. Superfluid ^{4}He is known to be characterized by two unique properties, one of which is superfluidity, and the other is often referred to as superthermal conductivity, or thermal counterflow. The enormous value of the effective thermal conductivity coefficient in the superfluid state is explained by the fact that the heat transfer in He II is related to the motion of the normal component. The mass flow transported by the normal component is compensated by the mass flow transported by the superfluid component, i.e. a counterflow, where the heat is transferred due to internal convection, occurs. It is extremely important that the condition of the absence of mass flow should be satisfied only on average, i.e. only the mass flow averaged over the area of the system should vanish. In general, the local mass flow should not vanish. Since the motion of any dielectric in a magnetic field leads to its polarization, a local dipole moment in the presence of a magnetic field will be connected to the local mass flow in superfluid helium, and an average electric field can emerge outside the system. As a result, a thermomagnetic effect similar to the Nernst–Ettingshausen effect in conducting systems can occur in superfluid systems. It turned out, however, that the magnitude of the electric potential emerging in superfluid systems is very sensitive to the geometry of the system and the orientation of the magnetic field. Thus, the effect is absent in a circular capillary, whereas in the case of an elliptical capillary with axes a and b, the electric field can vary by several orders of magnitude depending on the direction of the magnetic field relative to the ellipsoid axes.

In this work the features of the effect for a number of samples with various geometries are considered: the distribution of the electric field in the surrounding space for helium filling the capillary of circular, elliptical and triangular cross-sections is obtained. It is shown that the effect also takes place for the helium film covering the capillary of elliptical cross-section. The laminar mode of fluid flow is considered. It is determined that the potential and the electric field outside the sample are proportional to the cube of the characteristic transverse size of the vessel d. However, by changing the size of the vessel, the magnitude of the effect can be significantly increased only within certain limits. The reason is that if d increases at a fixed fluid velocity, the laminar motion of the liquid becomes turbulent, and we go beyond the limits of applicability for our calculation.

It is known that when the thermal counterflow reaches some critical value, the laminar motion is destroyed due to the emergence of quantized vortices and vortex rings in a superfluid liquid, which then form a vortex tangle (state T1). Further studies have shown that there is a second critical thermal counterflow, above which the vortex density significantly increases (state T2). The transition from state T1 to state T2 is associated with the transition to the turbulent state of the normal component. The results significantly depend on the shape of the channel. Two transitions occur in elliptical channels with dimensions $a \approx b$. At $a \square b$ only one transition to the T2 state occurs. Two transitions, apparently, should be observed in case of a triangular channel.

In the work the maximum possible values of the electric field (for the laminar mode) are found. It is shown that in order to obtain the maximum electric potential it is necessary to use a slit in the magnetic field directed across it. It is determined the transverse dimension of the slit b_c corresponding to the maximum potential. For the capillary with the length $L = 1\,cm$ and the temperature difference $\Delta T = 10^{-3} K$ between its ends $b_c = 10^{-3} cm$.

It is shown that the predicted thermomagnetic effect also takes place in case of a nonstationary temperature gradient, in particular, in the propagation of the second sound (capillaries) and third sound (nanofilms). The electric fields that arise above the nanofilm during the propagation of the third sound in the presence and in the absence of a magnetic field are compared. The appearance of electric fields above the film in the absence of a magnetic field was presented earlier by the authors in the works [1-2].

In conclusion, it is predicted that the thermal counterflow in superfluid helium placed in a magnetic field which is orthogonal to the thermal counterflow leads to the emergence of an electric field in the surrounding space. This effect is caused by the counterflow nature of thermal conductivity in superfluid systems. A summary of the results obtained is published in [3-4].

1. Shevchenko S.I. Non-stationary Thermal Electromotive Force Generated by Third Sound / S.I. Shevchenko, A.M. Konstantinov // JETP Letters. – 2016. – V. 104, No. 7. – P. 489-493.
2. Shevchenko S.I. Non-stationary Thermal Electromotive Force Generated by Third Sound / S.I. Shevchenko, A.M. Konstantinov // J. Low Temp. Phys. – 2019. – V. 194, No. 1/2. – P. 1-13.
3. Shevchenko S.I. Heat Superconductivity and Electrical Activity of Superfluid Systems / S.I. Shevchenko, A.M. Konstantinov // JETP Letters. – 2019. – V. 109, No. 12. – P. 790-794.
4. Shevchenko S.I. Thermal counterflow and electrical activity of superfluid systems in a magnetic field / S.I. Shevchenko, A.M. Konstantinov // Low Temp. Phys. – 2020. – V. 46, No. 1. – P. 57-69.

MULTIPLE MECHANISMS OF HOLOGRAPHIC GARTING RECORDING IN POLYMER NANOCOMPOSITES WITH GOLD NANOPARTICLES

J.Burunkova[1], D. Alkhalil[1], **S. Kokenyesi**[2], I.Csarnovich[2], S.Molnar[2], A. Bonyar[3]

[1]ITMO University, St. Petersburg, Russia, [2] University of Debrecen, Debrecen, Hungary
[3] Technical University of Budapest, Hungary,

Following the modern scientific and practically very useful direction of research and development of polymer nanocomposites with combined effects of photopolymerization superimposed by plasmon-induced processes we investigated acrylate-based nanocomposites with Irgaqure784 initiator and silicon oxide nanoparticles as well as gold nanoparticles in different regimes of illumination. Essential was the fact, that the initiator was sensitive in UV –VIS spectral range, so it was possible initiate polymerization in standard way as well as at the plasmon resonance wavelength of gold nanoparticles near 532 nm. So green and blue light emitting laser illuminations were combined in different regimes of interference picture recording. Peculiarities of polymerization processes were also investigated under simple UV illumination. The details of initiator photodecomposition and polymer chain formation mechanisms at the presence of gold nanoparticles plasmon fields and different combination of irradiation wavelengths or intensities were investigated. The results relate the mechanism and efficiency of holographic volume and surface grating recording based on photopolymerization and mass-transport, diffusion processes of organic matrix and nanoparticles.

The authors acknowledge the financial support of the GINOP-2.3.2-15-2016-00041 project.

SYNTHESIS AND PROPERTIES OF MULTIFUNCTIONAL MAGNETOSENSITIVE NANOCOMPOSITES AND MAGNETIC FLUID WITH TARGET-ORIENTED NATURAL COMPONENTS

Petranovska A.L.[1], Abramov M.V.[1], Korniichuk N.M.[1], **Gorbyk P.P.[1]**, Kusyak N.V.[2],
Kusyak A.P.[2], Lukyanova N.Yu.[3], Chekhun V.F.[3]

[1]*Chuiko Institute of Surface Chemistry, NAS of Ukraine, 17 General Naumov str., Kyiv 03164, Ukraine*
[2]*Ivan Franko Zhytomyr State University, 40 V. Berdychevska str., Zhytomyr 10008, Ukraine*
[3]*R. E. Kavetsky Institute of Experimental Pathology, Oncology and Radiobiology, NAS of Ukraine, 45 Vasylkivska str., Kyiv 03022, Ukraine*

The research is aimed at development the concept of chemical design of magnetosensitive nanocomposites (MNCs) with multilevel hierarchical nanoarchitecture, characterized by the functions of "nanoclinics" and medical-biological nanorobots.

Such MNCs perform the functions of recognizing microbiological objects in biological environments; deposit and targeted delivery of drugs to target cells and organs; complex local chemo-, immuno-, neutron-capture-, hyperthermic-, photodynamic therapy and magnetic resonance imaging diagnostics in real time; detoxification of the body by adsorption of cell decomposition residues, viral particles, heavy metal ions, etc. and their removal by magnetic field.

To create these MNCs researchers use nanostructuresof the core-shell type based on single-domain magnetite, which contain oncological drugs of different functional purpose and with different mechanisms of action, such as antimetabolite from the group of pyrimidine antagonists cytotoxic drug gemcitabine (HC).

Such NCs are characterized by a unique set of physical, chemical and biological properties, the ability to function effectively in the composition of magnetic fluids (MF) based on saline solution (NSS) and can be prototypes of new magnetically sensitive drugs and forms.

To provide MNCs and MF function of targeted drug delivery, they are modified for recognition of specific microbiological objects. Recently, the study of the use of natural mechanisms of endocytosis and various types of nanostructures for the delivery of drugs to tumors with the involvement of ligands is a priority.

As ligands directed against tumor-associated receptors, there may be hormones, vitamins, growth factors and lectins that are excessively present on the surface of tumor cells and have a limited distribution in normal tissues.

At present, the methods of modern nanotechnology are actively developing magnetosensitive and nonmagnetic conjugates for targeted delivery of HC to malignant cells, which will reduce systemic toxicity. The use of conjugation of the drug on the surface of nanoparticles with slow release of the drug potentially provides a longer presence of the drug in the bloodstream at the desired level.

In this work as an antibody (AB) HER2 (Neu, ErbB-2, CD340) was chosen. It is a membrane protein, a tyrosine proteinkinase of the EGFR / ErbB epidermal growth factor receptor family encoded by the human gene ErbB-2. Amplification of the HER2 gene plays an important role in the pathogenesis and progression of certain aggressive types of cancer. HER2 is an important biomarker and therapeutic target of the disease, associated with aggressiveness of the tumor and unfavorable prognosis. It is known that HER2 AB is considered to be one of the optimal for treatment of such diseases as human breast cancer, in particular in the presence of liver metastasis.

Lectins are a group of proteins of non-immune origin that recognize carbohydrates with extremely high specificity. Due to this property, lectins are ideal for reading the "sugar code" on the surface of all cells and recorded in the structure of specific epitopes of sugar. Lectins provide cellular communication at the molecular level and are involved in many physiological and pathophysiological processes. Pathogenic bacteria and viruses use lectins to attach to the host tissue, which is one of the prerequisites for the development of infection.

Blocking the adhesion of a specific pathogen with lectin inhibitors is the basis of anti-adhesive therapy, an alternative method of treating infections caused by multidrug-resistant bacterial strains.

There fore, in this work for the synthesis of MNCs and MF with the function of targeted drug delivery, promising for use in oncology, we selected AB HER2 and lectin Bacillus subtilis IIB B-7724.

Thanks to lectin, the arsenal of biologically active substances with cytotoxic and antitumor activity expands. The aim of the work is the synthesis and study of properties promising for use in targeted antitumor therapy, new multifunctional MNCs and MF based on magnetite, a drug with the function of targeted delivery of natural components - HER2 and lectin *Bacillus subtilis IMV B-7724.*

Research methods:

Specific surface area and pore size were determined by the method of nitrogen thermal desorption using KELVIN 1042 Sorptometer. The size (MNPs) was estimated by the formula $D_{\mathrm{BET}} = 6/(\rho S_{\mathrm{BET}})$, where ρ – is the density, S_{BET} – the value of the specific surface area calculated by the theory of polymolecular adsorption of Brunauer, Emmett and Teller (BET). Investigation of the surface condition of nanodispersed samples was performed by IR spectroscopy (Fourier spectrometer "Perkin Elmer", model 1720X). To calculate the concentration of hydroxyl groups on the surface of nanostructures used the method of differential thermal analysis in combination with differential thermogravimetric analysis. The method of differential thermal analysis (DTA) in combination with differential thermogravimetric analysis (DTGA) was used. Registration of thermograms was carried out using a derivatograph Q-1500D (Hungary) in the temperature range of 20-1000 ° C at a heating rate of 10 ° $\mathrm{C \cdot min^{-1}}$. The cristal structure of nanoparticles was determinated by X-ray diffraction (XRD). XRD measurements were perfomed using DRON-4-07 diffractometer with Cu/Kα radiation (λ = 0.1542 nm) and Ni filter. Investigation of morphology and size distribution of NPs were performed in water solutions. The size and shape of the NPs were determined by electron microscopy methods using Transmission Electron Microscope JEOL 1200 EX (Tokyo, Japan) with a tungsten filament operating at a 120 kV acceleration voltage. The TEM samples were diluted in deionizer water, dropping it onto a carbon coated copper grid (EM Resolutions Ltd) and were dried at room temperature for 12 hours. The magnetization of the samples was measured using a vibrating magnetometer at a frequency of 228 Hz at room temperature. Measurement of optical density, absorption spectra and GC concentration in solutions was performed by spectrophotometric analysis (Spectrometer Lambda 35 UV / Vis Perkin Elmer Instruments). The thickness of the adsorbed layer of GC in the composition of NCs Fe_3O_4/GC was determined by magnetic granulometry. Magnetic fluids based on Fe_3O_4 and physiological solution, stabilized with sodium oleate and polyethylene glycol, containing GC and HER2 antibody (Fe_3O_4/ol. Na/GC/PEG/HER2 + NNS) were synthesized. The cytotoxic/cytostatic activity of MF against MDA-MB-231 aggressive tumor cells with high proliferative and metastatic activity of triple-negative human breast cancer was studied.

It was found that the use of MF composition (Fe_3O_4/ol. Na/GC/PEG/HER2 + NNS) with C(Fe_3O_4) = 0.05 $\mathrm{mg \cdot ml^{-1}}$, C(GC) = 0.004 $\mathrm{mg \cdot ml^{-1}}$ and C (AB HER2) = 0,013 $\mu\mathrm{g \cdot ml^{-1}}$ showed a synergistic effect and reduced the number of viable breast cancer cells to 51%.

It is proved that the use of MR based on the Fe_3O_4/GC/HER2 complex is characterized by increased antitumor efficacy compared to the traditional use of the GC drug, with a significant reduction (four times) in its dose.

The prospects of further studies of MF Fe_3O_4/ol. Na/GC/PEG/HER2 + NNS in order to create a magnetically controlled drug for use in targeted antitumor therapy are shown.

Spectrophotometric studies of *Bacillus subtilis IMB B-7724* were performed and a calibration graph was constructed in the range of concentrations of 0.06 - 0.4 $\mathrm{mg \cdot ml^{-1}}$ (λ = 280 nm). (Figs. 1, 2).

The processes of lectin immobilization on the surface of magnetite and carbon-containing NC $Fe_3O_4/Al_2O_3/C$ from NNS at room temperature were studied.

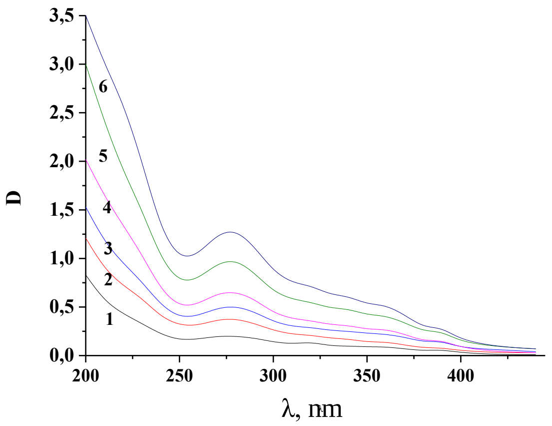

Fig. 1. UV spectrum of *Bacillus subtilis IMB B-772* at concentrations of 1-0.06; 2-0.1; 3-0.15; 4-0.2; 5-0.3; 6-0.4 mg·ml^{-1}

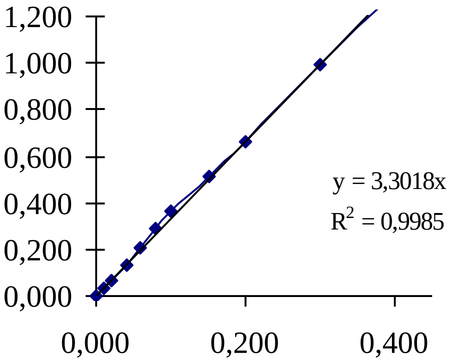

Fig. 2. Calibration graph of lectin *Bacillus subtilis IMB B-7724* in the range of concentrations of 0.06-0.4 mg·ml^{-1} (λ = 280 nm

Kinetic studies of lectin adsorption on the surface were performed and isotherms were constructed.

It was found that the adsorption capacity on magnetite is 21.9 mg·g^{-1}, and on NCs $Fe_3O_4/Al_2O_3/C$ - 39.7 mg·g^{-1} within the initial concentrations of lectin 0.06–0.4 mg·ml^{-1} (Fig. 3)

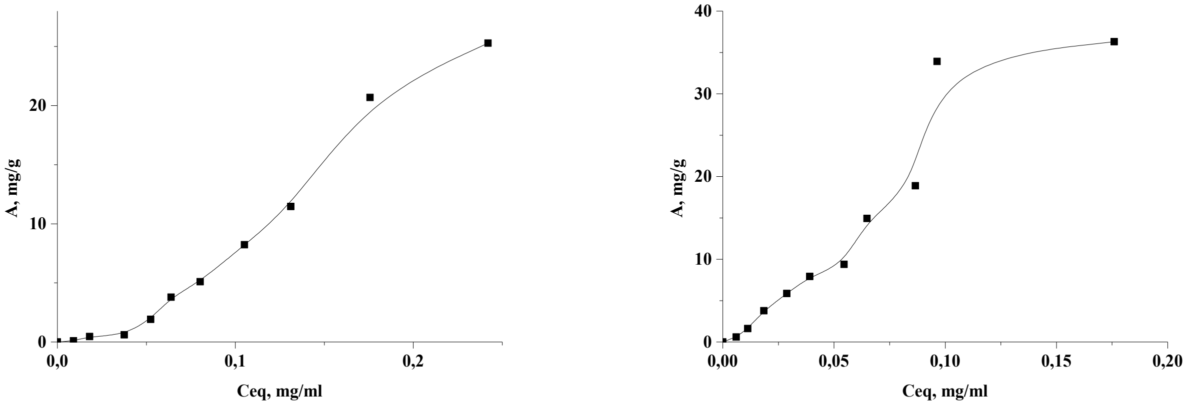

Fig. 3. Isotherms of sorption of lectin on the surface of magnetite (a) and $Fe_3O_4/Al_2O_3/C$ (b).

A technique for lectin immobilization and co-immobilization of lectin with cisplatin (CP) on the surface of magnetic fluid nanoparticles has been developed.

The following nanocomposite colloidal systems were synthesized: Fe_3O_4/ol.Na; Fe_3O_4/ol. Na/ lectin; Fe_3O_4/ol.Na/CP/ lectin with concentrations: C Fe_3O_4 = 0.003 g·ml^{-1}, C lectin = 0.2 mg·ml^{-1}, C CP = 0.4 mg·ml^{-1}.

A series of samples of nanocomposites and magnetic fluids with immobilized lectin were transferred for further research on bioactivity in vitro, in vivo in R.E. Kavetsky Institute of Experimental Pathology, Oncology and Radiobiology

THE POLARIZABILITY OF METAL NANOISLANDS ON A DIELECTRIC SUBSTRATE

Korotun A.V.[1], Titov I.M.[2], Rubish V.M.[3]

[1]National University "Zaporizhzhia Politechnic", 64, Zhukovskogo St., 69063 Zaporizhzhya, Ukraine
[2]UAD Systems, 84 Alexandrovska St., 69002, Zaporizhzhya, Ukraine
[3]Institute for Information Recording, NAS of Ukraine, 4, Zamkovi skhody St., 88000 Uzhgorod, Ukraine

In the quasi-static quadrupole approximation for the case of normal incidence of light, a relation is obtained for the polarizability of a metal nanoisland on a dielectric substrate. The calculations were performed for an island gold film. The existence of two plasmon resonances, caused by the presence of interfaces with the external medium and the dielectric substrate, is established.

Introduction. An increase in the density of information recording on optical media is associated with the use of nanostructured recording materials with characteristic sizes of structures of tens of nanometers [1]. Due to the strong confinement of electrons and photons at the nanoscale level such materials make it possible to use individual nanoparticles or their groups to represent information units. This, in turn, allows the development of breakthrough optical data storage methods with ultra-high recording density, extremely long data storage life and ultra-low power consumption [2].

In the recent time, several nanostructured photosensitive materials based on metal nanoparticles have been proposed and implemented. The characteristics of such materials mainly depend on localized surface plasmon resonance associated with the excitation of collective oscillations of free electrons in a nanoparticle when it is irradiated with light with a certain wavelength. Surface plasmons are extremely sensitive to the geometry and size of nanoparticles.

One of the most effective plasmon-active structures are island films, in which the islands can be in the form of hemispherical nanoparticles. Surface plasmon resonance in nanoparticles opens up new possibilities for the creation of spectrally selective absorbing coatings on the basis of such films [3], and also leads to an increase in the fluorescence signal, infrared spectroscopy and Raman scattering. In addition, island films of metals can be effectively used in photovoltaics and solar cells [4], as well as in catalysis. Therefore, the problem of calculating the polarizability of metal hemispheres on a substrate, forming an island film, and the characteristics of surface plasmons in such systems is urgent.

Problem statement and basic relationships. Consider a metallic nanoisland in the form of a hemisphere with a radius and dielectric constant T(ω) (medium 1). The hemisphere is located on a dielectric substrate (Fig. 1) with a dielectric constant T_d (medium 2), and the dielectric constant of the environment T_m (medium 3). The auxiliary region 4 in the substrate has a dielectric constant T_d for generality (medium 4).

Due to the anisotropy of the system, there are two independent solutions - for the cases of an external field $\mathscr{E}$ perpendicular and parallel to the plane of the substrate - environment section (Fig. 1). Hence, there are two independent components of the polarizability tensor of a hemispherical metal nanoparticle: axial $\alpha_{\parallel}$, corresponding to the direction of the external field perpendicular to the substrate and parallel to the axis z ($\mathscr{E} \,||\, Oz$), and transverse $\alpha_{\perp}$, when the external field is parallel to the substrate and perpendicular to the axis z ($\mathscr{E} \perp Oz$). The latter case corresponds to normal incidence of light.

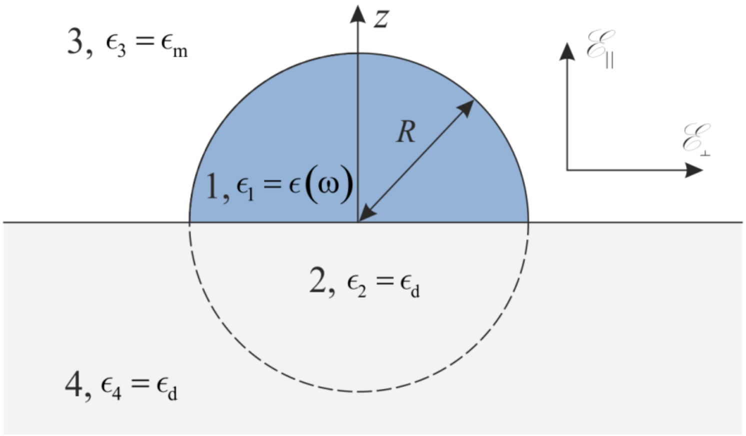

Fig.1. Schematic representation of a hemisphere on a substrate

If the nanoparticle size is much smaller than the wavelength, the quasi-static approximation can be used to solve the problem. In this case, the potential created by the hemisphere in the entire space is determined by solving the Laplace equation

$$\Delta\varphi = 0\,. \tag{1}$$

Let us consider the case of normal incidence of a light wave, when the external field is perpendicular to the z axis. It should be noted that, in the dipole approximation, the case under consideration does not differ from the classical problem of the polarizability of a metal sphere in an electric field. Therefore, we will work in the quadrupole approximation. In this approximation, the potentials inside and outside the hemisphere have the form:

$$\begin{gathered}
\varphi_1(r,\ \theta,\ \phi) = \left[A_1 r P_1^1(\cos\theta) + A_2 r^2 P_2^1(\cos\theta)\right]\cos\phi;\\
\varphi_2(r,\ \theta,\ \phi) = \left[\frac{B_1}{r^2}P_1^1(\cos\theta) + \frac{B_2}{r^3}P_2^1(\cos\theta) - \mathscr{E}_0 r P_1^1(\cos\theta)\right]\cos\phi;\\
\varphi_3(r,\ \theta,\ \phi) = \left[\frac{C_1}{r^2}P_1^1(\cos\theta) + \frac{C_2}{r^3}P_2^1(\cos\theta) - \mathscr{E}_0 r P_1^1(\cos\theta)\right]\cos\phi;\\
\varphi_4(r,\ \theta,\ \phi) = \left[D_1 r P_1^1(\cos\theta) + D_2 r^2 P_2^1(\cos\theta)\right]\cos\phi,
\end{gathered} \tag{2}$$

where $P_1^1(\cos\theta)$ and $P_2^1(\cos\theta)$ are the associated Legendre polynomials of the first and second order; ϕ is the polar angle, θ is the azimuth angle, r is the radius.

The unknown coefficients A_i, B_i, C_i, D_i $(i = 1,\ 2)$, which are included in (2), can be found from the boundary conditions – the conditions for the continuity of the potential and the normal component of the electric induction vector on the flat boundary between two hemispheres and half-spaces and on the hemispherical boundary between the sphere and half-space

$$\begin{gathered}
\varphi_1\big|_{r=R} = \varphi_3\big|_{r=R}\,, \qquad \varphi_2\big|_{r=R} = \varphi_4\big|_{r=R}\,,\\
\mathrm{T}(\omega)\frac{\partial\varphi_1}{\partial r}\bigg|_{r=R} = \mathrm{T}_\mathrm{m}\frac{\partial\varphi_3}{\partial r}\bigg|_{r=R}\,, \qquad \frac{\partial\varphi_2}{\partial r}\bigg|_{r=R} = \frac{\partial\varphi_4}{\partial r}\bigg|_{r=R}\,,
\end{gathered} \tag{3}$$

$$\begin{gathered}
\varphi_1\big|_{\theta=\frac{\pi}{2}} = \varphi_4\big|_{\theta=\frac{\pi}{2}}\,, \qquad \varphi_2\big|_{\theta=\frac{\pi}{2}} = \varphi_3\big|_{\theta=\frac{\pi}{2}}\,,\\
\mathrm{T}(\omega)\frac{\partial\varphi_1}{\partial\theta}\bigg|_{\theta=\frac{\pi}{2}} = \mathrm{T}_\mathrm{d}\frac{\partial\varphi_3}{\partial\theta}\bigg|_{\theta=\frac{\pi}{2}}\,, \qquad \mathrm{T}_\mathrm{d}\frac{\partial\varphi_2}{\partial\theta}\bigg|_{\theta=\frac{\pi}{2}} = \mathrm{T}_\mathrm{m}\frac{\partial\varphi_4}{\partial\theta}\bigg|_{\theta=\frac{\pi}{2}}\,.
\end{gathered} \tag{4}$$

At large distances from the hemisphere, the potential is determined by the dipole term of solution (2), and the dipole polarizability, respectively, is proportional to the coefficient C_1. Solving the system of algebraic equations following from boundary conditions (3) and (4), we obtain the following expression for the dimensionless transverse component of the polarizability tensor in the quadrupole approximation

$$\tilde{\alpha}_{\perp}=\frac{C_1}{2R^3\mathscr{E}_0}=\frac{\left(\varepsilon_{\mathrm{d}}+5\varepsilon_{\mathrm{m}}\right)\varepsilon^2\left(\omega\right)+\left(3\varepsilon_{\mathrm{d}}+5\varepsilon_{\mathrm{m}}\right)\varepsilon_{\mathrm{m}}\varepsilon\left(\omega\right)-4\varepsilon_{\mathrm{d}}\varepsilon_{\mathrm{m}}^2}{\left(4\varepsilon_{\mathrm{d}}+5\varepsilon_{\mathrm{m}}\right)\varepsilon^2\left(\omega\right)+2\left(3\varepsilon_{\mathrm{d}}^2+5\varepsilon_{\mathrm{m}}^2+9\varepsilon_{\mathrm{d}}\varepsilon_{\mathrm{m}}\right)\varepsilon\left(\omega\right)+2\varepsilon_{\mathrm{d}}\varepsilon_{\mathrm{m}}\left(3\varepsilon_{\mathrm{d}}+4\varepsilon_{\mathrm{m}}\right)}. \quad (5)$$

Here the dielectric Drude function is used for metal

$$\varepsilon\left(\omega\right)=\varepsilon^{\infty}-\frac{\omega_p^2}{\omega^2+\gamma_{\mathrm{eff}}^2}+\mathrm{i}\frac{\omega_p^2\gamma_{\mathrm{eff}}}{\omega\left(\omega^2+\gamma_{\mathrm{eff}}^2\right)}, \quad (6)$$

where ω_p is the plasmon frequency; γ_{eff} is the effective relaxation rate, which is defined as

$$\gamma_{\mathrm{eff}}=\gamma_{\mathrm{bulk}}+\gamma_{\mathrm{s}}=\gamma_{\mathrm{bulk}}+\mathscr{A}\frac{v_F}{\ell_{\mathrm{eff}}}=\gamma_{\mathrm{bulk}}+\frac{1}{2}\left(\frac{\omega_p}{\omega}\right)^2\frac{v_{\mathrm{F}}}{R}. \quad (7)$$

Calculations of the frequency dependences of the real and imaginary parts of the transverse polarizability component (Fig. 2) were carried out for the case of Au nanoislands ($\varepsilon^{\infty}=9.84$, $\gamma_{\mathrm{bulk}}=3.45\cdot10^{13}\ \mathrm{s}^{-1}$) located on a glass substrate. It should be noted that $\mathrm{Re}\,\tilde{\alpha}_{\perp}\left(\hbar\omega\right)$ it is an alternating function of frequency, in contrast to $\mathrm{Im}\,\tilde{\alpha}_{\perp}\left(\hbar\omega\right)$, which is always positive. The number of minima and maxima, as well as their value for $\mathrm{Re}\,\tilde{\alpha}_{\perp}$ and $\mathrm{Im}\,\tilde{\alpha}_{\perp}$, substantially depends on the radius of the island. So, as the radius increases, the number of extrema and their absolute values also increase. At an island radius $R=10$ nm, there are one maximum and one minimum $\mathrm{Re}\,\tilde{\alpha}_{\perp}$, and one maximum $\mathrm{Im}\,\tilde{\alpha}_{\perp}$. With increasing radius (curves *2* and *3*), additional extrema appear on the curves $\mathrm{Re}\,\tilde{\alpha}_{\perp}\left(\hbar\omega\right)$ and $\mathrm{Im}\,\tilde{\alpha}_{\perp}\left(\hbar\omega\right)$, and the first minimum $\mathrm{Re}\,\tilde{\alpha}_{\perp}$ corresponds to the first maximum $\mathrm{Im}\,\tilde{\alpha}_{\perp}$. The maxima of the imaginary part of the polarizability correspond to surface plasmon resonance, and the presence of two peaks is due to the presence of two interfaces between the metal nanoisland: with the external medium and the dielectric substrate.

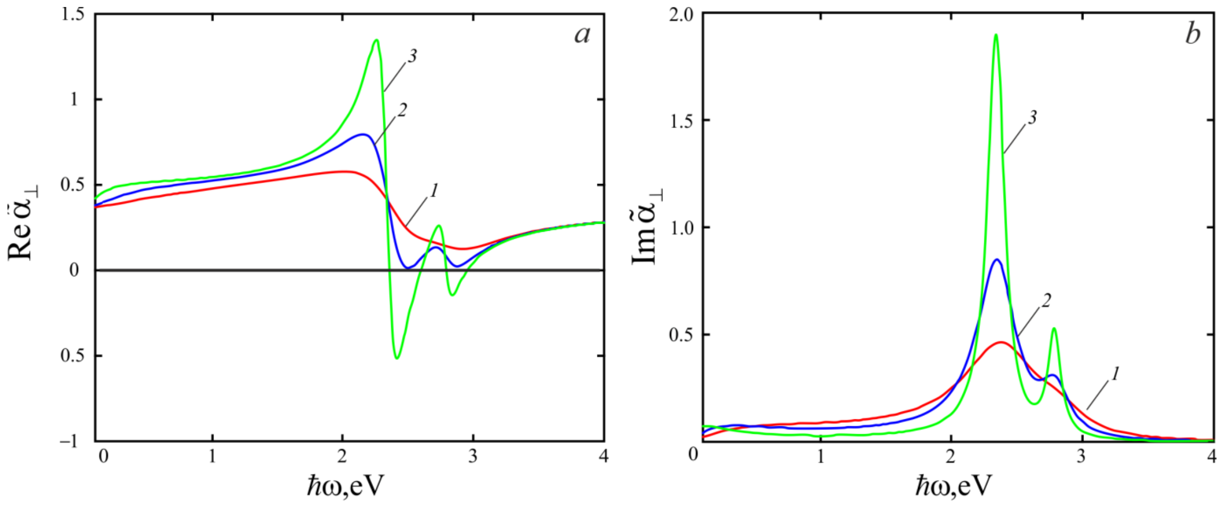

Fig. 2. Frequency dependences of the real (*a*) and imaginary (*b*) parts of the transverse polarizability component of Au nanoislands on glass ($\varepsilon_{\mathrm{d}}=2.25$), environment - air ($\varepsilon_{\mathrm{m}}=1$) at different radii: *1* – $R=10$ nm; 2 – $R=20$ nm; 3 – $R=50$ nm

Conclusions. The electrostatic problem of determining the potential in the "hemispherical metal nanoparticle - dielectric substrate" system is solved in the quasi-static quadrupole approximation. The frequency dependences of the transverse component of the polarizability tensor are obtained.

It was found that with an increase in the radius of the nanoparticle, plasmon resonances become more pronounced, and the second resonance appears at $R \approx 20$ nm. The presence of two resonances is explained by the existence of two interfaces - with the environment and the substrate.

1. Петров В.В., Крючин А.А., Беляк Є.В. [et al.]. Multi-Photon Microscopy and Optical Recording. – Київ: Академперіодика, 2016. – 156 с.
2. Min G., Qiming Z., Simone L. Nanomaterials for optical data storage // Nat. Rev. Mater., 2016. – V.1 – N. 16070.
3. Held M., Stenzel O., Wilbrandt S. [et al.]. Manufacture and characterization of optical coatings with incorporated copper island films // Appl. Opt., 2012. – V.51. – P. 4436-4447.
4. Santbergen R., Temple T.L., Liang R. [et al.]. Application of plasmonic silver island films in thin-film silicon solar cells // J. Opt., 2012. – V.14. – id. 024010.

FORMATION OF THIN DRY DRAWN GRAPHITE FILMS AND PROPERTIES OF PHOTOSENSITIVE GRAPHITE/n-InSe JUNCTIONS

Savitskii P.I., Kovalyuk M.Z., Tovarnitskii M.V., **Kovalyuk Z.D.**

I.M. Frantsevich Institute for Problems of Materials Science, the National Academy of Sciences of Ukraine, Chernivtsi Branch, 5, Iryna Vilde Str., 58001, Chernivtsi,e-mail: chimsp@ukrpost.ua

Future advances in graphene-like 2D materials are associated with new van der Waals heterostructures. The possibility of combining graphene with other layered 2D crystals in nanoscale structures offers new opportunities for nanodevice fabrication. The future success of the ‘van der Waals heterostructures’ conception depends on understanding of the processes at graphene/ layered semiconductor interface. Drawing with a graphite rod/pencil is the cheapest and simplest way of the solvent-free deposition of nanocomposite graphene-based films. Indium monoselenide offers unique opportunities for applications in optoelectronics and nanoelectronics. The recent spark of interest in this material is associated with the observation of strong quantization effects in mechanically exfoliated InSe nanosheets and the reported possibility of tuning the band gap by reducing the flakes’ thickness down to several nanometers [1]. Despite there are many techniques for deposition of thin graphite films, our attention was attracted by a new technologically simple method for fabrication of high quality graphite/semiconductor junctions using dry drawn graphite films. In this report, we demonstrate that this technique can be applied for fabrication of photosensitive graphite/*n*-InSe junctions with reproducible parameters. A detailed analysis of the electrical and photoelectric properties of the graphite/*n*-InSe junctions prepared by transferring a dry drawn graphite film onto the van der Waals surface (0001) of *n*-InSe substrate is done.

For our studies InSe single crystals were grown using the Bridgman method from a non-stoichiometric melt of $In_{1.03}Se_{0.97}$. The results of X-ray diffraction (XRD) measurements revealed that the obtained crystals were rhombohedral γ-InSe (R3m space group) with the lattice parameters a = 4.002 and c = 24.961 Å. The room temperature Hall effect measurements showed that the InSe crystals exhibited *n*-type conductivity with a carrier density in the range 10^{14} to 10^{15} cm^{-3}. In addition, the electron mobility was found to be between 800 and 1000 $cm^2/V\cdot s$.

A schematic illustration of the procedure used to fabricate the graphite/*n*-InSe Shottky-type junctions is shown in Fig. 1.

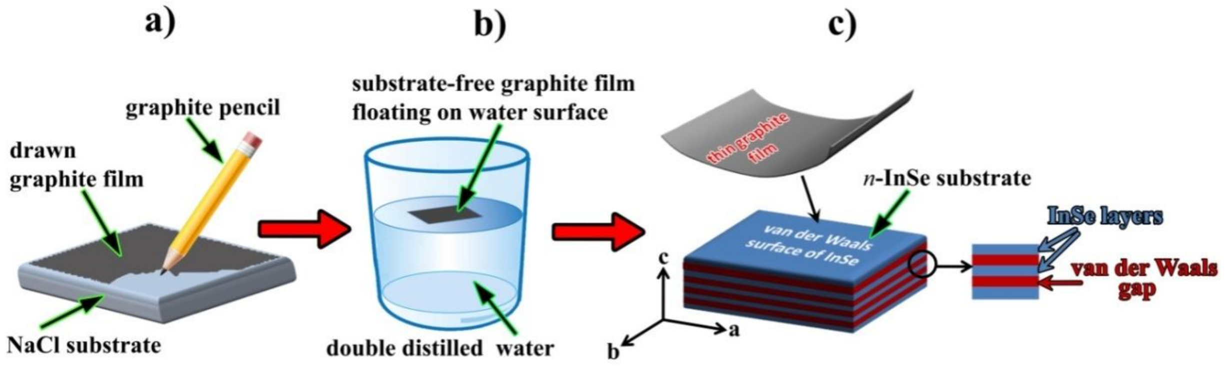

Fig. 1. A scheme of the fabrication procedure of graphite/*n*-InSe Schottky-type junctions:

(a) drawing a thin graphite film onto a NaCl substrate with a graphite pencil;

(b) transfer of the “graphite/NaCl substrate” structure onto the water surface and subsequent dissolving of the salt substrate;

(c) transfer of the released semitransparent thin graphite film from water surface onto the van der Waals surface (0001) of *n*-InSe single crystal substrate.

For the graphite film fabrication and subsequent transfer, we used a recently proposed technique described in [2] in more details. According to this technique, a homogeneous graphite layer is firstly drawn on a mechanically polished salt (NaCl) substrate (in our case with typical dimensions of 4×4×1 mm^3) using a pure graphite rod (pencil). Then the NaCl substrate (with the graphite film drawn on top of it) is gently placed onto the surface of double distilled water. The graphite/NaCl structure is floating on the water surface during several minutes until the underlying NaCl substrate is dissolved in the water. As a result, we obtain a substrate-free dry drawn thin graphite film floating on water surface. The interconnection forces between a large number of graphitic nanodomains and overlapped ultrathin graphite sheets are strong enough to keep the film together and resist water surface tension. This graphite film can be easily transferred onto an arbitrary substrate for further characterization and/or device fabrication. Here, the semitransparent thin graphite films were transferred from water surface onto the van der Waals surface (0001) of *n*-InSe single crystal substrates. An abrupt graphite/*n*-InSe junction is formed due to the adhesive van der Waals force between the thin graphite film and atomically smooth (0001) surfaces of *n*-InSe.

In addition, in order to measure electrical and optical properties of the obtained thin graphite films, we transferred them also onto glass substrates. Using the four-probe method, we established that at room temperature the graphite films possessed the sheet resistance of around 385 Ω/sq. The optical transmittance was found to be ~21.2% at 550 nm. The micro-interferometry measurements revealed the thickness of the graphite films to be in the range 180-200 nm.

The AFM patterns of the surface (0001) of *n*-InSe substrate demonstrate that it is almost atomically smooth with a root mean square (RMS) roughness of ≈ 0.08 nm, whereas the surface morphology of the dry drawn graphite films in the graphite/*n*-InSe structure is rougher with the RMS roughness ≈ 0.39 nm. So, the surface of the graphite/*n*-InSe structure under investigation is smooth enough, which is very important for good mechanical adhesion between the graphite film and *n*-InSe substrate. The room temperature *J-V* characteristics of the graphite/*n*-InSe junctions, forward biased when a positive voltage is applied to the graphite film, show a rectification with low leakage current densities at reverse bias. Well pronounced rectifying behaviour confirms the formation of a high-quality electrical junction between the thin graphite film and *n*-InSe substrate. The junctions show a rectification ratio (*RR*), the ratio of forward current density (J_{for}) to reverse current density (J_{rev}), to be of about 200 at the applied voltage of 0.9 V. The obtained *RR* value is higher or comparable with that reported for other InSe-based junctions [3]. The value of Schottky barrier height φ_b=0.49 V was determined by extrapolating the linear part of the forward *J-V* characteristic towards the intersection with the voltage axis. From the measured impedance spectra and their modelling it is found that the series resistance R_s of the junction is 3.5 kΩ. This value is affected by the resistance of the quasi-neutral regions of the *n*-InSe substrate. For our junctions, its high value is caused by the low conductivity of *n*-InSe single crystals across the layers.

In order to take into account, the value of the series resistance R_s=3.5 kΩ, the experimental *J-V* curve was replotted using the equation

$$J = J_s\left[\exp\left(\frac{q(V-JR_s)}{nkT}\right)-1\right], \tag{1}$$

where *J* is the current density, $J_s=A^*T^2\exp(-q\varphi_b/k_BT)$ is the saturation reverse biased current density, $q\varphi_b$ is the zero bias Schottky barrier height, A^* is the Richardson constant, *V* is the applied voltage, *q* is the elementary charge, *k* is the Boltzmann's constant, *T* is temperature and *n* is the ideality factor. It is found that the linear segment of the *J-V* dependence corresponding to Eq. (1) becomes longer. The slope of the linear segment of the *J-V* dependence at a low forward bias $3kT < V < 0.4$ was used to calculate the ideality factor *n* from the following equation [4]:

$$n = \frac{q}{kT}\frac{\Delta V}{\Delta \ln J}. \tag{2}$$

The value of *n* was established to be 3.3. This high value indicates on a deviation of our junction from an ideal Schottky barrier diode for which *n* = 1. The deviation from the ideality points out the domination of recombination on defect-related interface states. Their presence invariably leads to an increase of the ideality factor. At higher bias voltage $V > 0.4$ V the forward *J-V* branch can be described by the linear dependence $J = V - V_0 R_S$, where $V_o \approx 0.49$ V is the cut-off voltage determined from the forward *J–V* characteristic. At high current density the *J-V* characteristic reflects mainly the contribution of the voltage drop across the series resistance R_s, but not the real charge transport mechanisms through the potential barrier The reverse *J-V* dependence in the lg(J_{rev}) vs. lg(V_{rev}) coordinates represents a straight line with a slope ≈1 within the bias $0<|V|<2$. It indicates that this dependence obeys a linear ohmic law $J_{rev} \sim V_{rev}$. The observed voltage dependence of the reverse biased current density reflects the current transport through an insulator layer [5].

Fig. 2 shows the frequency dependences of the *C-V* characteristics of the graphite/*n*-InSe junctions measured at a low a.c. signal under the reverse bias from 0 to -3 V. The observed linear $C^{-2}(V)$ dependences indicate on uniformly distributed uncompensated donors in the *n*-InSe substrate [4]. Thus, the investigated graphite/*n*-InSe structure can be considered as an abrupt electric junction. The value of the built-in potential V_{bi} was established by extrapolating the linear dependence $C^{-2}(V)$ to the interception with the voltage axis. The $C^{-2}(V)$ curves depend on a.c. frequency and are shifted to higher values of C^{-2} with increasing in frequency. The observed frequency dependence is due to the influence of their series resistance R_s. To determine the real value of the built-in potential V_{bi}, the received cut-off voltage was approximated to the zero frequency (the inset in Fig. 1) according to the equation $V_{cut\text{-}off} = f(\omega^2)$ [4], where $\omega = 2\pi f$ and f is the linear frequency of the a.c. testing signal. As one can see, the approximated value ($V'_{bi} = 1.01$ V) is overestimated in comparison to the InSe energy gap (E_g=1.26 eV). The difference between the V_{bi} values determined from *J-V* and *C-V* characteristics may be affected by interfacial states. The only reliable parameter we can obtain from the *C-V* characteristics is the density of uncompensated donors N_D in *n*-InSe substrate. Its determined value equals to $N_D = 4.77\times10^{14}$ cm^{-3} and is in good agreement with the results of our Hall effect measurements.

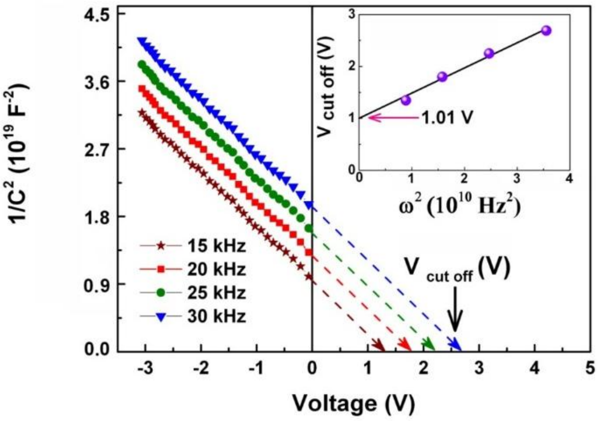

Fig. 2. Room temperature *C-V* characteristics of the graphite/*n*-InSe junction measured at different frequencies of the a.c. signal. The inset shows the $V_{cut\ off} = f(\omega^2)$ plot.

Fig. 3 shows the plot of the room temperature photocurrent quantum efficiency η versus photon energy indicating a broad-band spectral photosensitivity of the obtained graphite/*n*-InSe junctions. The spectrum is characterized by the band width $\delta_{1/2} = 0.96$ eV at its half-height. The abrupt long-wavelength edge of the η spectrum is observed at the photon energies close to the InSe bandgap energy. This long-wavelength exponential increase of the $\eta = f(h\nu)$ dependence is associated with light absorption in InSe and is characterized by a high value of the slope $S \approx 50$ eV^{-1} derived from the following equation [4]:

$$S = \Delta(\ln \eta)/\Delta h\nu, \tag{7}$$

where $h\nu$ is the photon energy. The junctions are photosensitive in the spectral region from about 1.2 eV to 2.95 eV, which demonstrates their potential as photodetectors for a wide range. Note that a well pronounced exciton peak was found in the photocurrent quantum efficiency spectrum at the photon energy of $E_{ex} = E_g - E_b = 1.249$ eV (Fig.3), where $E_g = 1.264$ eV and $E_b = 0.015$ eV are the direct-band gap energy and exciton binding energy in bulk InSe at T = 300 K, respectively [1, 6]. The presence of the exciton peak at room temperature indicates a high quality of the InSe substrate, as it is known that excitonic absorption is not observed in imperfect crystals.

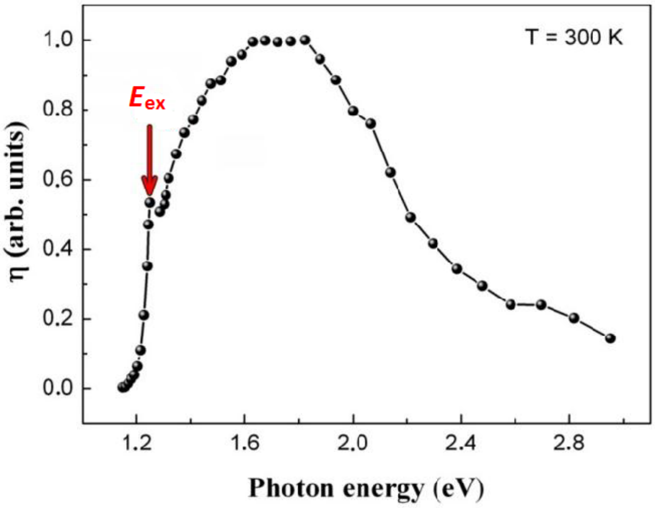

Fig. 3. Room temperature photocurrent quantum efficiency spectrum
for the graphite/*n*-InSe junction.

The obtained results demonstrate that these devices can operate efficiently at room temperature in both photoconductive and photovoltaic modes and therefore they are promising candidates for the near-infrared and visible spectrum photodetectors. It should be noted that photodetectors based on InSe and GaSe crystals have been reported to exhibit very good radiation resistance to high-energy irradiations [3, 7]. In addition, graphite is well known to be highly resistant to all types of radioactivity. Therefore, it is expected that the graphite/*n*-InSe junctions will provide high radiation resistance as well.

In summary, we demonstrated the formation of photosensitive Schottky-type graphite/*n*-InSe junctions as a result of direct mechanical adhesion when a substrate-free thin dry drawn graphite film is transferred from water surface onto atomically smooth van der Waals (0001) surfaces of *n*-InSe crystals. The applied fabrication technique showed surprisingly good reproducibility despite its technological simplicity. The obtained graphite/*n*-InSe junctions show relatively high broad-band photosensitivity in the spectral region from about 1.2 eV to 2.95 eV thus demonstrating technological potential of this pair for photodetector applications. They are promising due to graphite's mechanical stability and resistance to radioactive radiation, high temperature, and most chemicals.

1. G.W. Mudd, S.A. Svatek, T. Ren, A. Patanè, et al., *Adv. Mater*., 2013. **25**, 5714 ,
2. Brus V.V., Maryanchuk P.D., *Appl. Phys. Lett*., 2014, **104**, No 17,173501 (3 pages).
3. Z.D. Kovalyuk, O.A. Politanska, V.G. Tkachenko, et al., *J. Nucl. Mater*., 2009, **385**, 489.
4. Sze S.M., Ng K.K, Physics of Semiconductor Devices. - New Jersey, John Wiley & Sons, 2007.
5. M.A. Lampert, P. Mark, Current injection in solids, Academic Press, New York, 1970.
6. N.Balakrishnan, Z.R.Kudrynskyi, M.W. Fay, G.W.Mudd, et al., *Adv. Optical Mater*., 2014, **2**, 1064.
7. Z.D. Kovalyuk, V.M. Katerynchuk, I.V. Mintyanskii, et al., *Mater. Sci. Eng. B,* 2005, **118**, 147.

AMORPHOUS CHALCOGENIDES WITH PHASE-CHANGE EFFECT

Durkot M.O.[1], **Kyrylenko V.K.[1]**, Kryuchyn A.A.[1], PetrovV.V. [1], Pop M.M.[1,2], Rubish V.M[1],
Yurkin I.M.[2]

[1] *Institute for Information Recording, NAS of Ukraine,4 , Zamkovi schody St., 88000, Uzhgorod Ukraine*
[2] *Uzhgorod National University, 3, Narodna sq., 88000, Uzhgorod, Ukraine*

Thin films of antimony chalcogenides are suitable for creation of phase-change memory (PCM) devices that works on the basis of reversible “amorphous phase ↔ crystalline phase” transition.

In this work the results of the investigations temperature dependences electric resistance *R* and optical transmission θ of Sb_xSe_{100-x} ($40 \leq x \leq 70$) and Sb_yTe_{100-y} ($50 \leq y \leq 75$) amorphous films are reported.

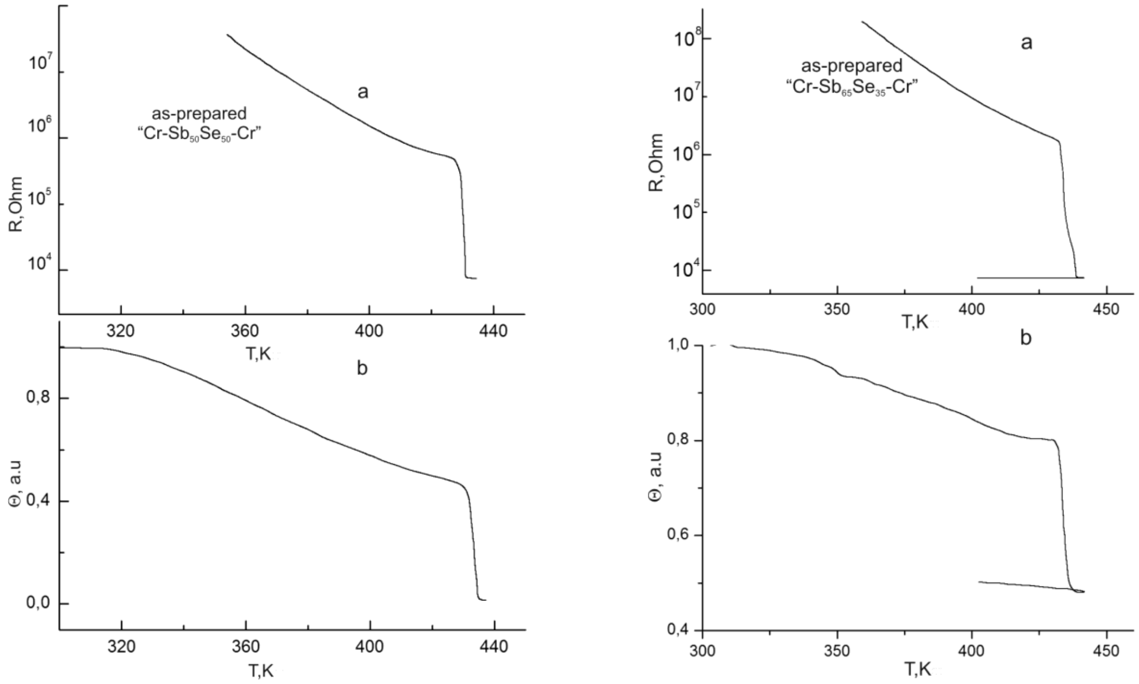

Fig. 1. Temperature dependencies *R* (*a*) and *θ* (*b*) of “Cr layer-Sb_xSe_{100-x} film- Cr layer” samples at q=2.2 K/min

Nonisotermal crystallization of Sb_xSe_{100-x} and Sb_yTe_{100-y} films was investigated by the method, which allows simultaneously measurements of optical transmission and electric resistance on the one sample. Investigations of $R(T)$ and $\theta(T)$ dependences were carried out on planar structures “metal layer-calcogenide film-metal layer” in the temperature range of 290-550 K at heating rates (q) with interval 0.75-8.8 K/min. The accuracy of temperature measurement was ±0.5 K. Registration of the change of optical transmission was carried out at λ=880 nm. The thickness of metal layers (Ni, Cr, Ag) and chalcogenide films – ~ 100-300 nm. Chalcogenide amorphous films were obtained by the method of vacuum evaporation of the corresponding composition of crystalline alloys from quasiclosed effusion cells.

The results of investigations are presented in Fig. 1-3. It was established that crystallization of films is accompanied by a sharp decrease of *R* and *θ*. The change of resistance rich of 2-3 (Sb-Se system) and 3-4 (Sb-Te system) orders higher of magnitude. Parameters of phase transition (the transition starting temperature T_{ph} from amorphous to crystalline state and temperature range of transition ΔT_{ph}) depends on the chemical composition of the films and the heating rate. It is shown that the increase of the heating rate leads to a shift of the T_{ph} and ΔT_{ph} in the higt temperature region. For Sb_xSe_{100-x} films the values ΔT_{ph} equal 3-12 K (q=2.2 K/min) and for Sb_yTe_{100-y} – 5-15 K (q=1.8 K/min).

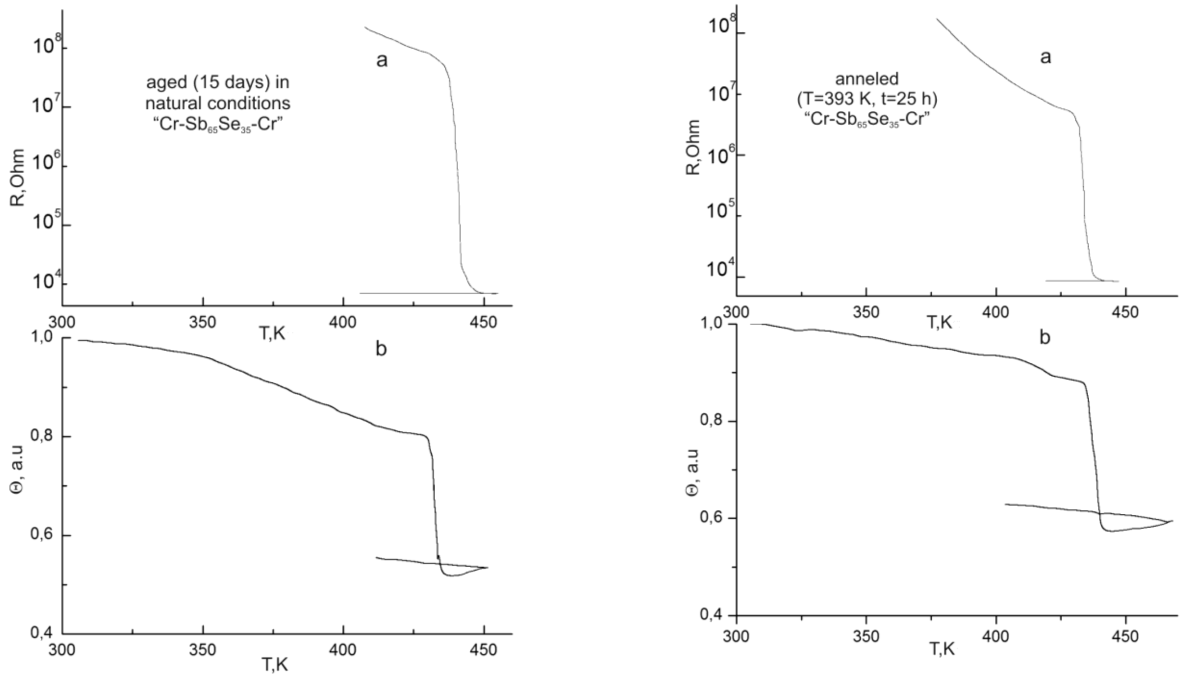

Fig. 2. Temperature dependencies *R* (*a*) and θ (*b*) of "Cr layer-$Sb_{65}Se_{35}$ film-Cr layer" samples at *q*=2.2 K/min

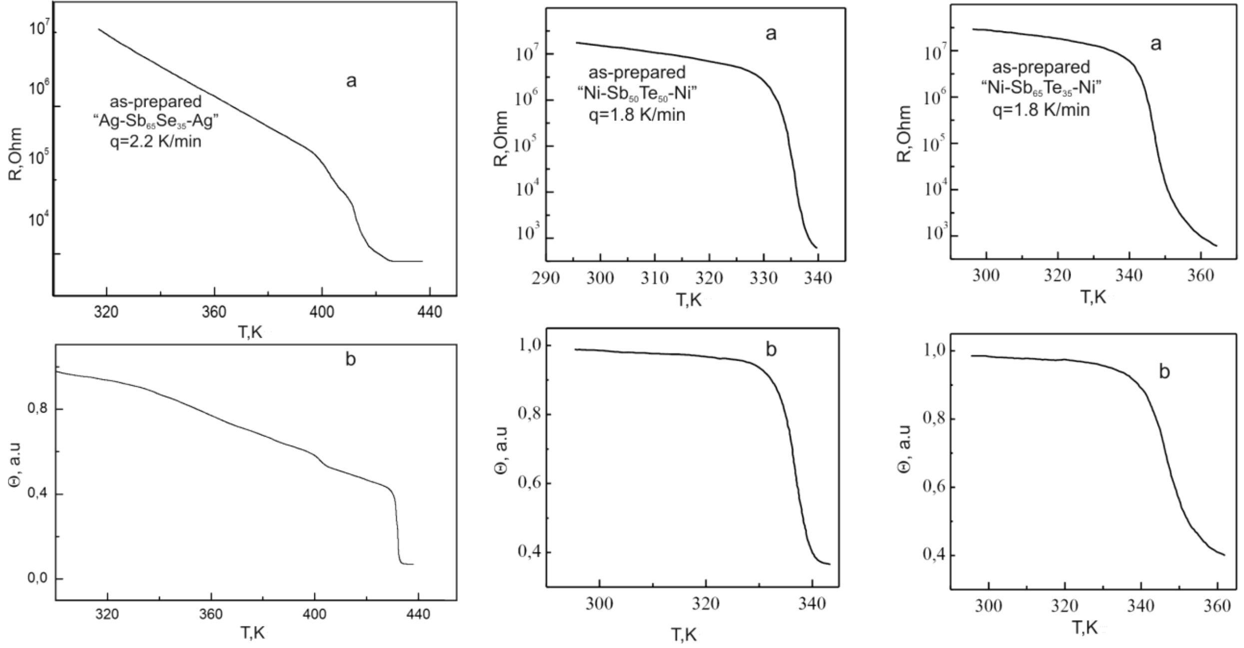

Fig. 3. Temperature dependencies *R* (*a*) and θ (*b*) of "Ag(Ni) layer-Sb-Se(Te) film- Ag(Ni)-layer" samples

The influence of natural ageing and annealing on the phase transition parameters were investigated. The resistance change increases (~2 order) at transition "as-prepared – aged in natural conditions – annealed" sample. Such changes can be associated with structural transformations that occur in amorphous films during aging and annealing.

These results shows the possibility of using Sb_xSe_{100-x} and Sb_yTe_{100-y} films for the manufacture of memory cells and temperature sensors.

OPTICAL CUBIC NONLINEARITY OF THIN FILMS OF PALLADIUM OXIDE: VALUE, DYNAMICS AND NATURE

V. Liakhovetskyi[1], A. Brodin[2], V. Rudenko[1], M. Brodyn[1], V. Styopkin[1]

[1] Institute of Physics of the NAS of Ukraine, 46, Nauky avenue, Kyiv, 03028, Ukraine
[2] National Technical University of Ukraine "Igor Sikorsky Kyiv Polytechnic Institute",

Palladium oxide is a non-magnetic semiconductor of p-type [1] with tetragonal crystalline structure, space group D^9_{4h} [2]. PdO is widely used as an effective catalyst. It is a promising material for energy conversion applications of the photovoltaic and electrocatalytic types. We have showed that it also is an effective nonlinear optical material and thus may find use in modern optoelectronics

We investigated linear and nonlinear optical properties of thin polycrystalline PdO films on silica and glass substrates. In particular, linear absorption spectra in the interval of 1.5 to 6 eV are similar to the imaginary part of the dielectric function polarized spectra of PdO monocrystals, obtained by Weber et al. [3]. It suggests that microcrystals in our films are predominantly oriented with the *C* axis orthogonal to the substrate surface. The bandgap, as revealed by an apparent absorption edge at 2.5 eV, is $E_g = 2.3$ eV.

Nonlinear optical properties were investigated, utilizing 800 nm 180 fs laser radiation. The films exhibit relatively high positive cubic nonlinear susceptibility Re $\chi^{(3)} = +1.1\times10^{-6}$ esu ($n_2 = 5.6\times10^{-9}$ cm^2/W) and nonlinear absorption coefficient $\beta \approx 5\times10^{-5}$ cm/W due to two-photon absorption. A positive sign of Re $\chi^{(3)}$ implies the following two mechanisms of refractive nonlinearity: intraband carrier dynamics and optical Kerr effect.

Time-resolved absorption measurements within 2.5 eV absorption band under 800 nm excitation revealed subtle changes of the absorption that exhibit two-step relaxation with relaxation times of 2 ps and 1 ns. We associate the fast time with intraband carrier (predominantly holes) relaxation dynamics, the latter also responsible for the refractive nonlinearity, whose relaxation time is thereby in the picosecond range.

Relatively fast and strong refractive nonlinearity of polycrystalline PdO films along with relatively low nonlinear absorption make them attractive candidates for optoelectronics applications.

1. Rogers D.B., Shannon R.D. and Gillson J.L., Crystal growth and semiconductivity of palladium oxide, *J. Solid State Chem.* **3** (2) (1971) 314.
2. Waser J., Levy H.A. and Peterson S.W., The structure of PdO, *Acta Crystallogr.* **6** (7) (1953) 661.
3. Weber W.H., Remillard J.T., McBride J.R., and. Aspnes D.E, Optical dielectric response of PdO, *Phys. Rev. B* **46** (1992) 15085.

SYNTHESIS AND CHARACTERIZATIONS OF COLLOIDAL Ag_2ZnSnS_4 AND Cu_2ZnSnS_4 NANOCRYSTAL THIN FILMS DEPOSITED BY SPIN-COATING

Mazur N.V., Dzhagan V.M., Havrylyuk Ye.O., Valakh M.Ya., Kapush O.A., Hreshchuk O.M., Yukhymchuk V.O.

V. Lashkaryov Institute of Semiconductor Physics NAS of Ukraine, 41 pr. Nauky, 03028 Kyiv, Ukraine

The growing consumption of electricity worldwide stimulates the search for environmentally friendly sources of electricity. One of the most promising alternative sources is solar energy. Today, more than 80% of solar panels use Si as an absorbing layer. However, since Si has an indirect-bandgap, it is not possible to achieve sufficiently large absorption in truly thin-film devices. Also, the production of Si-based solar cells on an industrial scale is harmful to the environment. The alternatives to silicon for use in third-generation thin-film photovoltaics must have a direct-bandgap, be cheap, and environmentally friendly. One of such materials are compounds of the Cu_2ZnSnS_4 (CZTS) family. The bandgap of about 1.3 eV is almost ideal for efficient absorption of solar radiation, the direct-bandgap provides a high absorption coefficient (up to 10^5) even on thin films, all components are widespread and non-toxic. The possibility of environmentally friendly low-temperature colloidal synthesis of CZTS nanocrystals (NCs) in aqueous solutions provides further advantages and makes this material very promising as a potential thin-film absorber of the new-generation solar cells.

However, there are certain issues with these relatively complex compounds that need to be overcome for their effective use in industrial solar cells. One of the main factors that hinder the high values of the conversion efficiency is the high concentration of antisite defects (Cu_{Zn} and Zn_{Cu}). The energy of the formation of these defects is very low, due to the close ionic radii of Zn and Cu. One of the ways to reduce the concentration of this type of antisite defects is suggested to be a partial or complete replacement of Cu atoms by Ag atoms.

In this work, NCs of Cu_2ZnSnS_4 and Ag_2ZnSnS_4 (AZTS) were obtained by methods of low-temperature colloidal synthesis in aqueous solutions. Raman spectroscopy was chosen as the characterization method. Its advantage over other methods in the study of compounds of the CZTS family is that it allows us to detect not only the presence of antisite defects Cu_{Zn} and Zn_{Cu}, but also the possible manifestation of secondary defective phases, the appearance of which is due to multicomponent basic compound. Besides, it's possible to measure both thin films, powders, and colloidal solutions of the NCs. Our study was aimed at finding optimal synthesis conditions for the formation of highly crystalline and stable CZTS NCs of targeted composition.

ELECTROPHYSICAL PROPERTIES OF POLYMER COMPOSITES BASED ON CARBON NANOTUBES AND GRAPHENS

Makhno S.M, Lisova O.M., Gunya G.M, Gorbik P.P., Sementsov Yu.I., Kartel M.T.

Інститут хімії поверхні ім. О.О. Чуйка НАН України,
вул. Генерала Наумова, 17, Київ, 03164, Україна, E-mail: stmax@ukr.net

The electrophysical properties of the systems polychlorotrifluoroethylene – carbon nanotubes (PCTFE – CNT) and polychlorofluorofluoroethylene - carbon nanotubes@graphene nanoplates (PCTFE – CNT@GNP) were investigated by the method of ultrahigh - frequency interferometry and the two-contact method at low frequencies. It was found that the system with CNT@GNP has higher electrophysical characteristics, in particular reaches the percolation threshold at 0.011 by volume of the filler, against 0.013 for the system with CNT, due to a more uniform distribution of the conductive component in the polymer. Obviously, the reason is that the initial suspension of CNT@GNP is stable for a long time and does not stratify into fractions, unlike suspensions of individual materials.

The use of polymer composite materials (PCM) is promising in various industries, aerospace, for supporting structures, etc. Electrically conductive fillers increase the range of use due to the wide range of their electrical and electromagnetic properties [1]. Recently, intensively developing areas related to the creation and use of carbon nanotubes (CNTs). CNTs are widely used for the manufacture of composites for shielding from electromagnetic radiation, protection against radio interference and antistatic coatings [2]. The development of temperature, pressure, humidity sensors, etc. deserves attention. It has been shown [3] that sensors based on polymer composites and CNTs are stable only with sufficient grinding of CNT agglomerates.

The ball, planetary vibration, jet mills, disintegrators, etc. are used for dispersion of CNTs in industry and in laboratory conditions. To obtain stable suspensions, a large number of methods of chemical surface modification of CNTs [1, 3] and surfactants are used. The dispersion of CNTs can be performed in dry form by contactless grinding of materials using air jets of different configurations also [4].

Particular attention is paid to hybrids of carbon materials, in particular such as CNT@GPN (carbon nanotubes@graphene nanoplates) [5], and structural modifications and methods of their production are diverse [5-9]. This is three-dimensional grids, textile materials, nanostructured inclusions, etc. Most often, such materials with additional components [5-7] and without them, are used as electrode material for high-capacity capacitors, organic LEDs (OLED) and cathodes of vacuum elements [8].

The aim of the work is to study the concentration dependences of the electrical conductivity of the systems polychlorotrifluoroethylene – CNT and polychlorofluorofluoroethylene – CNT@GNP, to establish the patterns of structural processes.

Multilayer CNTs were obtained by CVD method [4], GNP - by electrochemical deposition from graphite foil [10]. Crystal amorphous polymer of polychlorotrifluoroethylene (PCTFE) F-3M grade A was used to make PCTFE – CNT and PCTFE – CNT@GNP composites. Then dispersed with an ultrasonic dispersant (USDN-A) for 2 minutes Dried to constant weight, ground and pressed at a temperature of 513 K and a pressure of 2 MPa.

The study of the real (ε′) and imaginary (ε″) component of the complex dielectric permittivity and the real (μ′) and imaginary (μ″) component of the complex magnetic permeability of composites was carried out in the ultrahigh-frequency (UHF) range of 8-12 GHz using a meter-based interferometer of phase difference RFK2-18 and standing wave coefficient and attenuation P2-60 electrodeless method, and electrical conductivity at low frequencies 0.1; 1 and 10 kHz two-contact method using an E7-14 immittance meter [11].

Dispersion of carbon nanotubes, as well as GNP in water by the ultrasonic method is accompanied by stratification of the obtained suspension over time, stabilization of suspensions requires the use of a significant amount of surfactants. It was observed that the compatible suspension of CNT and graphene is stable for a significant time without the use of surfactants, so CNT and graphene are surfactant and stabilizing components relative to each other.

The dependences of the electrical conductivity of the PCTFE -– CNT and PCTFE – CNT@GNP systems are similar (Fig. 1), the values of the electrical conductivity of the PCTFE – CNT@GNP system are slightly higher in comparison with PCTFE – CNT, in general by 1-2 orders. The percolation threshold for the system with CNT is observed at 0.013 volume fractions, for the system containing CNT@GNP – 0.011, due to a more uniform distribution of the conductive component in the polymer. As the filler content increases, the systems are in a state of a branched continuous percolation cluster, which causes high values of real and imaginary components of complex dielectric constant at microwave (Fig. 2) and electrical conductivity of the order of 10^{-2} at low frequencies at 0.05 volumetric filler content. The values of ε′ and ε″ for the PCTFE – CNT@GNP system exceed the corresponding values of PCTFE – CNT by an average of 8%.

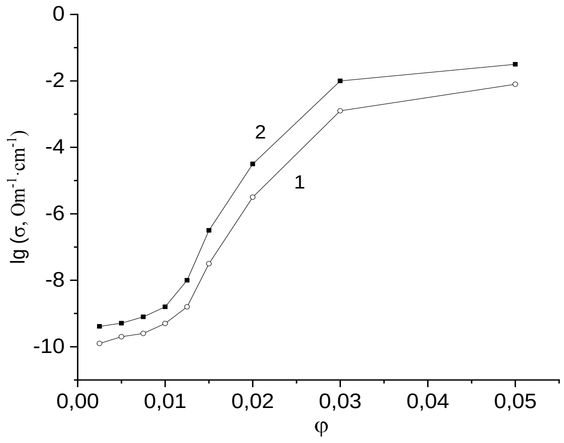

Fig. 1 – The electrical conductivity on the content of carbon filler for systems: 1 - PCTFE – CNT; 2 - PHTFE – CNT@GNP

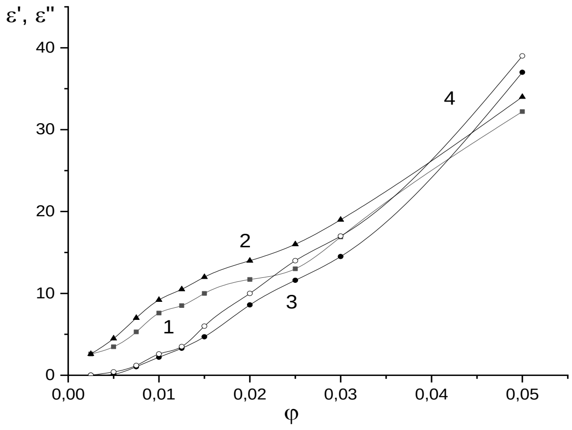

Fig. 2 – The real (ε′) 1,3 and imaginary (ε″) 2,4 components of complex dielectric drowning of relative composites on content of carbon filler for systems: 1, 2 - PCTFE – CNT; 3, 4 - PCTFE – CNT@GNP

It was found that the suspension of CNTs and graphene is stable for a long time without the use of surfactants. The electrophysical properties of PCTFE – CNT and PCTFE – CNT@GNP systems at low frequencies and in the microwave range have been studied. The percolation threshold for the systems is 0.13 and 0.11, respectively, due to the uniform distribution of the conductive filler in the polymer.

Keywords: carbon nanotubes, graphene, dielectric constant, percolation threshold, electrical conductivity, ultrahigh frequencies

1. Badamshina E.R., Gafurova M.P., Estrin Ya.I. Modification of carbon nanotubes and synthesis of polymer composites with their participation // Uspekhi khimii. – 2010.– V. 11, № 79. – C. 1027–1064.
2. *Ukrainian patent for a utility model* № 140182 від 4.07.19 Makhno S.M., Lisova O.M, Gunya G.M., Gorbik P.P. Acrylic-polyurethane nanocomposite paint coating // Bul. №3 of 10.02.20

3. Koval'ska E.A., Kartel' M.T., Prikhod'ko G.P., Sementsov Yu.I. Physicochemical methods for cleaning carbon nanotubes // Chemistry, physics and technology of surface. – 2012. –T.3, № 1. – C. 20–44.
4. Sementsov Yu.I. Formation of structure and properties of sp2-carbon nanomaterials and functional composites with their participation / Ed. Academician of the National Academy of Sciences of Ukraine M.T. Cartel - Kyiv: Chuyko Institute of Surface Chemistry NAS of Ukraine; LLC NVP Interservice, 2019.– 364 c.
5. O. Thonganantakul, S. Srinives, W. Chaiwat, K. Kerdnawee, K. Suttiponparnit, T. Charinpanitkul Temperature dependence of iron oxide-graphene oxide properties for synthesis of carbon nanotube/graphene hybrid material // Catalysis Today, 2020.– P. 1-8. https://doi.org/10.1016/j.cattod.2020.01.016
6. J. Ye, B. Hu, Y. Jin, Z. Wang, Y. Xi, L. Fang, Q. Pan Interface engineering integrates fractal-tree structured nitrogen-doped graphene/ carbon nanotubes for supercapacitors Electrochimica Acta, 2020 https://doi.org/10.1016/j.electacta.2020.136372.
7. K. Liu, Y. Yao, T. Lv, H. Li, N. Li, Z. Chen, G. Qian, T. Chen Textile-like electrodes of seamless graphene/nanotubes for wearable and stretchable supercapacitors // Journal of Power Sources 446 (2020) 227355 https://doi.org/10.1016/j.jpowsour.2019.227355
8. X. Hong, W. Shi, H. Zheng, D. Liang Effective carbon nanotubes/graphene hybrid films for electron field emission application // Vacuum 169, 2019 https://doi.org/10.1016/j.vacuum.2019.108917
9. Q. Shi, A. Zhu Interface regulation of graphene/carbon nanotube on the thermal conductivity and anticorrosion performance of their nanocomposite // Progress in Organic Coatings 140, 2020 https://doi.org/10.1016/j.porgcoat.2019.105480
10. Y. Sementsov, S. Makhno, M. Kartel, W. Bo, G. Dovbeshko, V. Styopkin and S. Nedilko Graphene Nanoparticles and Graphene Nanoparticles - Polyamide 12/12 Composites // International Journal of Innovative Science, Engineering & Technology.–2017.– Vol. 4, Issue 8.– P. 71-78.
11. Ganyuk L.M., Ignatkov V.D., Makhno S.M., Soroka P.M. Investigation of dielectric properties of fibrous material // Ukr. phys. zhurn.–1995.–T. 40, № 6.– C. 627–629.

FESEM STUDY OF SURFACE MORPHOLOGY OF ARRAYS OF NOBLE METALS NANOPARTICLES

Makar L.I.[1], Mudry S.[2], Rubish V.M.[1], Shtablavyi I.[2], Yasinko T.I.[1]

[1]*Institute for Information Recording, NAS of Ukraine,4 , Zamkovi schody St., 88000, Uzhgorod Ukraine*
[2]*Ivan Franko National University of Lviv, Kyrylo i Mephodiy 8, 79005 L'viv, Ukraine*

In [1-3] it was shown that in the presence of localized plasmon field generated light in terms of surface plasmon resonance(SPR) in composite structures “Au(Ag) NPs/chalcogenide film”, photoinduced mass transport processes in chalcogenide films can be intensified. Therefore, controlled nanostructuring of the chalcogenide film surface becomes possible. If the surface relief is known is possible and mapping the distribution of the electric field of surface plasmons. In this regard, the need to study the morphology of nanoparticles (NPs) arrays, which can be used for these purposes, as well as plasmon-active substrates for surface-enhanced Raman spectroscopy (SERS), is not in doubt.

In this report the results of investigation of the technological conditions influence of formation on the morphology of arrays of noble metals nanoparticles are given.

The formation of arrays of randomly distributed of Au and Ag nanoparticles was performed by rapid radiation heating [4] of thin (4-35 nm) films of these metals in air to temperatures of 573-693 K. For the investigations of surface morphology of noble metals nanoparticles arrays a field emission scanning electron microscopy (FESEM) analysis was performed using a Hitachi S-4100 microscope with a secondary electron detector. The scanning of the sample surface was carried out by electron beam operating at 15 kV and 10μA with the spatial resolution of 10 nm in the secondary electron image regime.

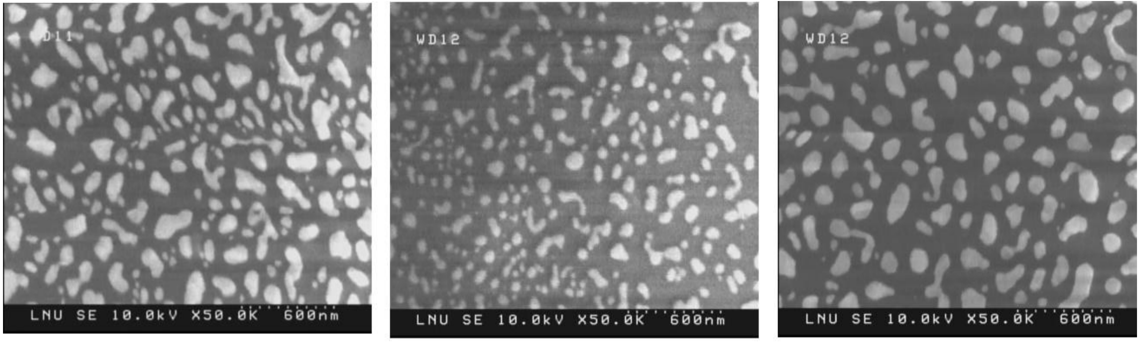

Fig. 1. SEM images of gold NPs arrays of different morphology, formed at 623 K

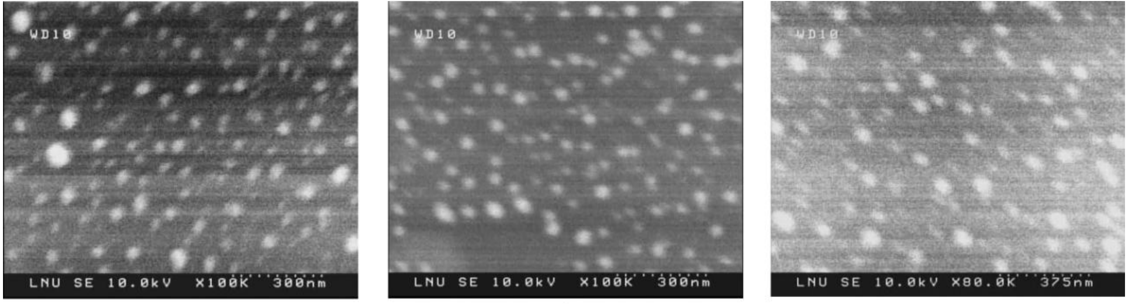

Fig. 2. SEM images of silver NPs arrays of different morphology, formed at 623 K

SEM images of some arrays of Au and Ag nanoparticles formed under different conditions are shown in Fig. 1-3. The analysis of the obtained results showed that the average size of nanoparticles in arrays ranges from several tens to several hundreds of nanometers. As the nominal thickness of deposited gold and silver decreases, the surface density of nanoparticles increases. The average size of nanoparticles is reduced.

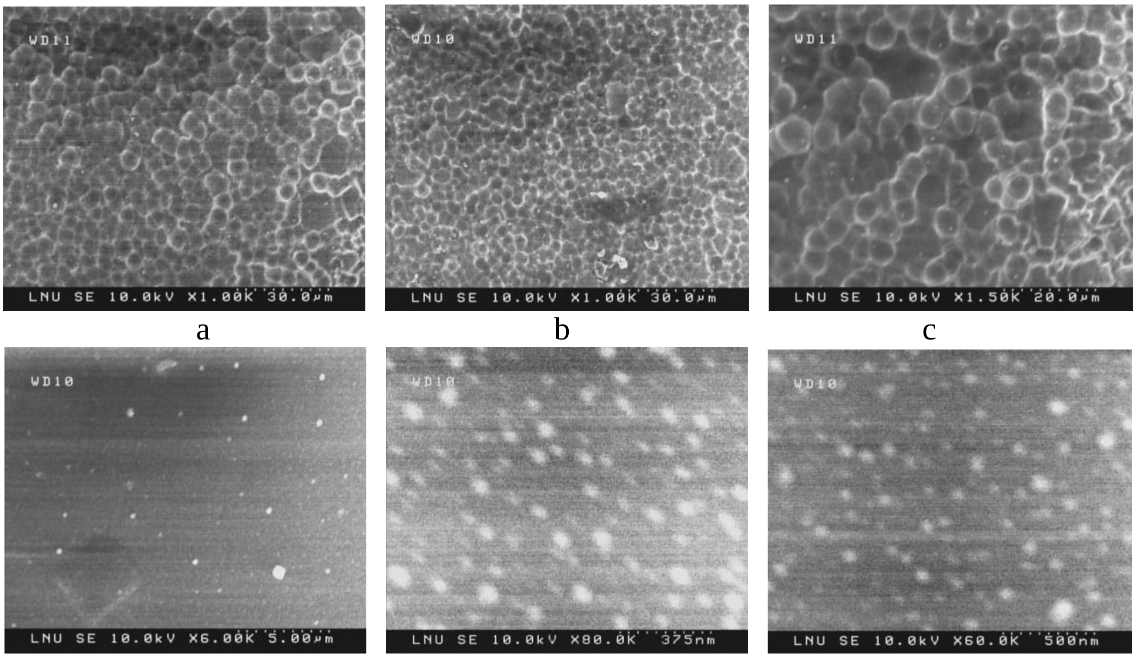

a b c

d e f

Fig. 3. SEM images of different areas of silver NPs arrays, formed at 573 K

Studies of the transmission spectra of the formed arrays of Au and Ag nanoparticles using an Ocean Optics spectrophotometer showed that the position of the maximum of the SPR band (λ_{SPR}) of Au NPs arrays is in the range of 532-597 nm, and for Ag NPs arrays – in the range of 424-509 nm. As the nanoparticle size increases, the λ_{SPR} shifts to the long-wavelength region of the spectrum.

At relatively low temperatures and annealing times the surface morphology of arrays in different areas is significantly removed. For example, in Fig. 3 are SEM images of different parts of an array of Ag NPs, formed at 573 K for 30 s (Fig. 3a – c given SEM images areas of the arrays at the edges, and Fig. 3d – f – near the middle). This is probably due to the uneven temperature distribution of the nanosized Ag film deposited on the glass substrate from the middle to the edges of the film.

Thus, the average size of Au and Ag NPs in arrays of random distributed nanoparticles formed by rapid radiation heating of nanosized films of these metals to temperatures of 573-693 K, depend on the thickness of gold and silver films and regimes of their thermal treatment. As the thickness of Au and Ag films increases, the average size of nanoparticles of these metals also increases.

Examples of practical application of the investigated NPs arrays are given.

1. Trunov M.L. Lytvyn P.M., Oberemok O.S., Durkot M.O., Tarnaii A.A., Prokopenko I.V., Rubish V.M. Light-induced mass transport in amorphous chalcogenides/gold nanoparticles composites // Semiconductor Physics, Quantum Electronics & Optoelectronics. – 2013. – V.16. – No.4. – P. 354-361..
2. Trunov M.L., Lytvyn P.M., Nagy P.M., Csik A., Rubish V.M. and Kökényesi S. Light-induced mass transport in amorphous chalcogenides: Toward surface plasmon-assisted nanolithography and near-field nanoimaging // Phys. Stat. Solidi B. – 2014. – V.251. – No.7. – P. 1354-1362..
3. Rubish V.M., Lytvyn P.M., Trunov M.L., Kyrylenko V.K., Horvat Yu.A., Yasinko T.I. Amorphous chalcogenides in nanoplasmonics // Proc. XVI Intern. conf. “Physics and technology of thin films and nanosystems (ICPTTFN-XVI). – Ivano-Frankivsk, Ukraine”. – 2017 – P. 31.
4. Durkot M.O., Kyrylenko V.K., Lytvyn P.M., Rubish V.M., Tarnaj A.A., Trunov M.L. Formation of Ag nanoparticles arrays and their optical transmittance spectra Mat. Intern. Meeting “Clusters and nanostructured materials (CNM-5)”. – Uzhgorod, Ukraine. – 2018. – P. 163-164.

GOLD NANOPARTICLES FOR BIOMEDICAL APPLICATION

Mukha Iu.[1], Vityuk N.[1], Khodko A.[2], Severynovska O.[1], Eremenko A.[1]

[1]*Chuiko Institute of Surface Chemistry, NAS of Ukraine,*
17 General Naumov Str., Kyiv 03164, Ukraine, iu.mukha@gmail.com
[2]*Institute of Physics, NAS of Ukraine, pr. Nauky, 46, Kyiv, 03039, Ukraine.*

Gold nanoparticles (Au NPs) become increasingly important in a wide range of high technology applications, especially for biomedicine, usually for sensing, imaging, drug delivery, and therapy.

To perform a variety of functions the surface of Au NPs can be modified with different agents. For the use of Au NPs in biomedicine the toxicity of metal-based nanosystem must be reduced, that can be achieved through the use of biocompatible agents during the synthesis.

Tryptophan (Trp), an essential amino acid, is suitable for the synthesis of NPs as a bifunctional reducing and stabilizing agent. Also, the mechanism of reaction in such a system could be a prototype of the interaction of Au NPs with peptides or proteins containing aromatic amino acids.

In the present work the properties of Au NPs, obtained in the presence of Trp, were compared with the properties of Au NPs, prepared with the use of typical surfactant as a stabilizer and strong reducer. Optical properties, morphology and fragmentation of Au NPs obtained in different ways were analyzed using UV-vis spectroscopy, transmission electron microscopy and laser desorption/ionization mass spectrometry.

Three different procedures to produce Au NPs from Au^{3+} ions were performed in an aqueous solution containing gold in a concentration of $C_{Au} = 10^{-3}$ M at room temperature using: 1) $NaBH_4$ (Sodium borohydride) as reducing agent and surfactant SDS (Sodium dodecyl sulfate) as a stabilizer (indicated as Au-$NaBH_4$/SDS); 2) $NaBH_4$ as reducing agent and Trp as a stabilizer (Au-$NaBH_4$/Trp); 3) Trp for both purposes (Au-Trp/Trp). The initial components interacted using the following molar ratios: 1) $\nu(NaBH_4):\nu(Au):\nu(SDS) = 1:1:15$; 2) $\nu(NaBH_4):\nu(Au):\nu(Trp) = 1:1:1$; 3) $\nu(Trp):\nu(Au) = 1:1$.

Absorption spectra of all obtained Au NPs colloids contained typical localized surface plasmon resonance (LSPR) bands of gold (fig. 1a). We observed the most intense and symmetrical LSPR band with a maximum at 540 nm for Au-$NaBH_4$/SDS colloid, while for both systems containing amino acid tryptophan LSPR bands were around 2.5 times less intense and red-shifted to 565 (Au-$NaBH_4$/Trp) and 579 nm (Au-Trp/Trp). At the same time, full width at half maximum of LSPR bands of Trp containing systems was 2-3 times bigger. Moreover, these bands had long-wavelength shoulders at around 700 nm that could be attributed to the absorbance of aggregated particles, namely chain-like structures built from previously formed gold nanoparticles as was shown in [1]. The formation of Au NPs, in this case, was accompanied by the precipitation of blue-colored powder.

According to the TEM images (fig. 2b), in Au-$NaBH_4$/SDS colloid, the size of formed Au NPs was of 20-30 nm. In Au-Trp/Trp system particles were formed of approximately the same size, 20-40 nm. In both cases, nanoparticles had a spherical shape. But in case, when Trp was used only as a stabilizer, namely in the Au-$NaBH_4$/Trp system, synthesized nanoparticles had irregular form and were the biggest among others in studied systems. The aggregation of NPs occurred via splitting along plane surfaces and was reflected as the broadest LSPR absorption band, and confirmed by TEM images.

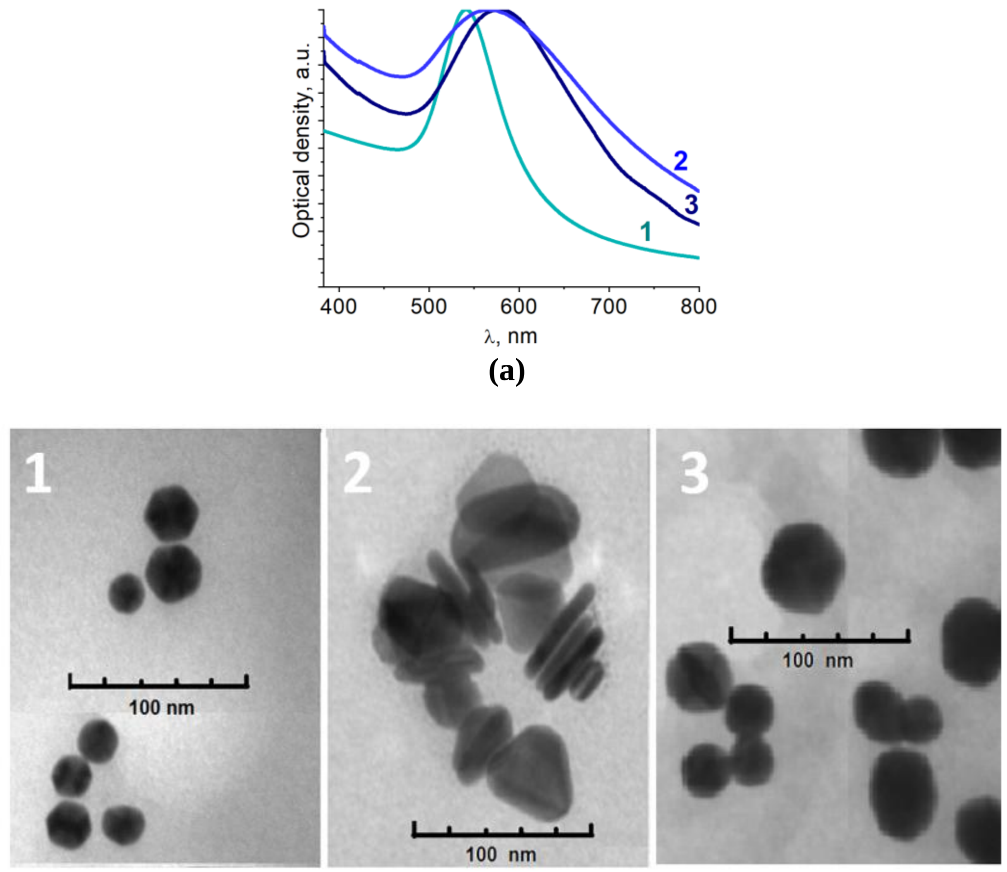

(a)

(b)

Figure 1. Normalized absorption spectra of Au NPs in colloid (a) and corresponding TEM images (b), where “1” refers to Au-$NaBH_4$/SDS, “2” – Au-$NaBH_4$/Trp, “3” – Au-Trp/Trp.

The certain type of stabilizer, that covers the surface, defines the ionization ability of gold nanoparticles. Synthesized Au NPs mostly decompose during the ionization process. For all systems in mass spectra for positive and negative ions, the series of intense single monoisotopic peaks with a pitch of 197 Da that refers to the average mass of Au were observed (fig. 2). Thus, they correspond to the ionization of “naked” metal clusters Au_x, not covered with the ligand layer. More effectively this process occurred in negative mode.

In general, for all studied systems, ion intensity decreases with increasing the size of the cluster. But there is one pronounced feature observed in the mass-spectra of nanoparticles. The intensity of Au_x signals alternate depending on the number of atoms in the cluster. Namely, signals of odd clusters Au_{2n+1} were more intense than of even ones Au_{2n}. The authors of [2. 3] observed a similar tendency for nanogold.

The electronic system of nanoparticles in Au-Trp/Trp, when amino acid used as reducing acid and stabilizer, increased their ability to ionize through the electron capture (negative mode), and especially its emission (positive mode) compare to other colloids. The most intense signals were inherent to Au_3 clusters for all systems and both modes.

For negative mode signals of gold clusters till Au_{25} for Au NPs, obtained via reduction with $NaBH_4$, were fixed, while for Au-Trp/Trp system the intense pitches were further observed. A similar trend was observed in positive mode when small clusters only till Au_9 for Au-$NaBH_4$/SDS and Au-$NaBH_4$/Trp were fixed.

The alternation of intensities and the peculiarities of Au_3 and Au_9 clusters are consistent with the stability of the cluster due to the jellium model theory, explained in the mentioned references above. The clusters correspond to magic numbers having extraordinary stability due to shell closing electron counts. In its turn clusters containing an even-number of valance electrons possess higher stability due to spin-spin coupling than those having an odd number of electrons bound in their electronic shell, and thus ionization occur harder.

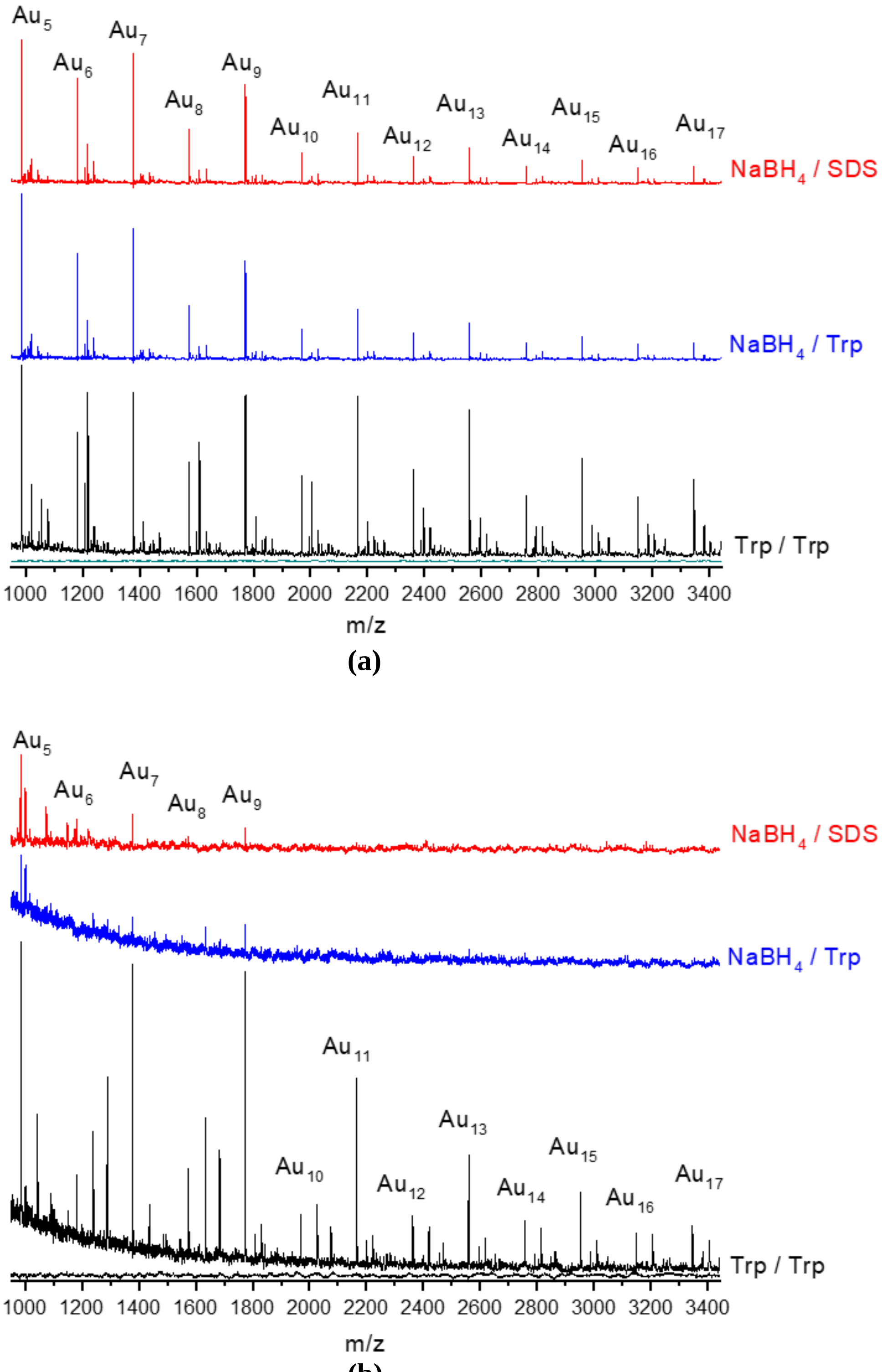

Figure 2. Representative fragment of mass spectra of gold colloids under consideration in the mass range from 1000 to 3400 Da for negative (a) and positive (b) ions.

In conclusion, it was shown that as the result of all applied synthetic methods nanosized gold was formed, confirmed by electron microscopy. All colloidal systems were characterized by absorption bands of localized surface plasmon resonance of gold. All studied nanoparticles and had a similar trend during ionization processes.

The way for improving the stability of Au NPs prepared in the presence of Trp was developed in [4]. The method was further applied for preparation of Au-containing nanosystems with anticancer effect [5, 6], that finally resulted in effective nanosystem with pronounced antitumor and antimetastatic effects *in vivo* [7].

1. Khodko A., Kachalova N., Scherbakov S., Eremenko A., Mukha Iu. Effects of Photochromic Furan-Based Diarylethenes on Gold Nanoparticles Aggregation // Nanoscale Research Letters. – 2017. – 12:271.
2. Kéki S., Nagy L., Deák G., Zsuga, M. (2004). Bimetallic silver-gold clusters by matrix-assisted laser desorption/ionization // Journal of the American Society for Mass Spectrometry. – 2004. – 15(10). – P.1455–1461.
3. Peña-méndez E.M., Hernández-fernaud J.R., Nagender R., Houška J., Havel J. The Chemistry of gold clusters in plasma generated with MALDI, Laser Desorption Ionisation and laser ablation from various precursors // Chem. Listy 102. – 2008. – P.1394−1398.
4. The pH-Dependent Stucture and Properties of Au and Ag Nanoparticles Produced by Tryptophan Reduction. Mukha Iu., Vityuk N., Severynovska O., Eremenko A., Smirnova N. // Nanoscale Research Letters. – 2016. – V. 11:101.
5. Mukha Iu, Vityuk N, Grodzyuk G, Shcherbakov S, Lyberopoulou A, Efstathopoulos EP, Gazouli M. Anticancer effect of Ag, Au, and Ag/Au bimetallic nanoparticles prepared in the presence of tryptophan. // J Nanosci Nanotechnol. – 2017. – V.12. – P.8987–8994.
6. Shmarakov I, Mukha Iu, Vityuk N, Borschovetska V, Zhyshchynska N, Grodzyuk G, Eremenko A. Antitumor activity of alloy and core-shell type bimetallic AgAu nanoparticles // Nanoscale Res Lett. – 2017. – V. 12:333.
7. Ag/Au Bimetallic Nanoparticles Inhibit Tumor Growth and Prevent Metastasis in a Mouse Model / Katifelis H., Mukha I., Bouziotis P., Vityuk N., Tsoukalas C., Lazaris A.C., Lyberopoulou A., Theodoropoulos G.E., Efstathopoulos E.P., Gazouli M. // International Journal of Nanomedicine. – 2020. – V.15. – P.6019–6032.

INVESTIGATION OF THE MORPHOLOGY AND LUMINESCENCE PROPERTIES OF MG-DOPED ZNO NANOSTRUCTURES GROWN AT DIFFERENT SUBSTRATE TEMPERATURES

Myroniuk D. V.[1], Karpyna V. A.[1], Myroniuk L. A.[1], Khranovskyy V. D.[2], Ievtushenko A. I.[1]

[1]*I. M. Frantsevich Institute for problems in materials science, NAS of Ukraine,*
3, Krhyzhanovsky st., 03142, Kyiv, Ukraine,
[2]*Department of Physics, Chemistry and Biology, Linköping University,*
S-581 83, Linköping, Sweden

Zinc oxide has a band gap at 3.37 eV at room temperature, which makes it one of most interesting materials candidates for optoelectronic devices in the UV region. The large exciton banding energy about 60 meV leads to pronounced excitonic effects in emission and absorption spectra up to room temperature [1, 2]. The key point of the semiconductor devices design is to have heterostructures that can provide a free carriers and optical confinement for example: high electron mobility transistors and light emission diodes. It is critical to have band gap engineering in order to realize a device-based material [3]. The band gap engineering of ZnO can be realized by alloying with MgO and CdO. Theoretically, the band gap of MgZnO ternary alloys can be tuned from 3.37 eV (ZnO) to 7.8 eV (MgO) [4]. Nonetheless, a high MgO content leads to phase separation. For a moderate content of MgO, the alloy keeps the wurtzite crystal structure of ZnO, providing a wide range of band gap engineering ranging from 3.37 to 4.0 eV [3]. In addition, the exciton binding energy increases in the ZnMgO/ZnO/ZnMgO quantum wells, thus being this heterostructure suitable for fabricating electronic devices, due to the increase in carrier confinement.

ZnO in nanostructure (NS) form attract attention of many researchers as perspective material. Tuned nanostrucutres like doped ZnO have major applications in laser diodes and UV optics for producing specific photon wavelength emission, solar cells, UV filters, sensors and as photocatalysts.

ZnO NS doped by Mg were deposited by metal organic chemical vapor deposition on the silicon substrates at the ~ 190-450 °C temperature range using the mixture of zinc and magnesium acetylacetonates (AA) as precursors.

Scanning electron microscope observation was carried out in order to investigate the morphologies Mg-doped ZnO NS depending on substrate temperatures. The microstructure of the ZnMgO layers were studied by a Leo 1550 Gemini scanning electron microscope (SEM) at a primary beam acceleration potential of 5 kV. $Zn_{0.95}Mg_{0.05}O$ (Fig. 1 a-d) and $Zn_{0.9}Mg_{0.1}O$ (Fig. 2 a-d) films have been grown on Si (100) substrates at temperatures from 250 to ~ 400 °C.

The surface morphology of the $Zn_{1-x}Mg_xO$ nanostructures changes with increasing substrate temperature and AA-Mg content in the obtained layers.

In the case of $Zn_{0.95}Mg_{0.05}O$ films at low substrate temperatures (250-300 °C), adatom mobility is low and basis ZnO wurtzite columns preserve the random orientations which together form the multi grained layer. Low grain boundary coarsening via diffusion also results small islands which may be fully amorphous with multiple grain orientation. The size of grains in the sample is roughly 75 nm (Fig. 1 a), and 100-150 nm (Fig. 1 b). As the substrate temperature increases to 350-400 °C, so does adatom mobility and grain boundary diffusion, leading to the formation of polycrystalline and textured layers consisting of visible hexagonal plate islands as the result of increased grain migration and grain boundary diffusion in the coalescence process. These islands act as the base for one dimensional growth via the vapor-solid mechanism which is the result of the initial constituents breaking down and forming ZnO molecules which combine at the surface of these hexagonal plates and form the nanorods. The observation of the surface showed the formation of single nano crystalline grains with hexagonal shape ~ 200-500 nm. The observed nanocolumns were short and only presented on the surface of the sample (Fig. 1 c-d).

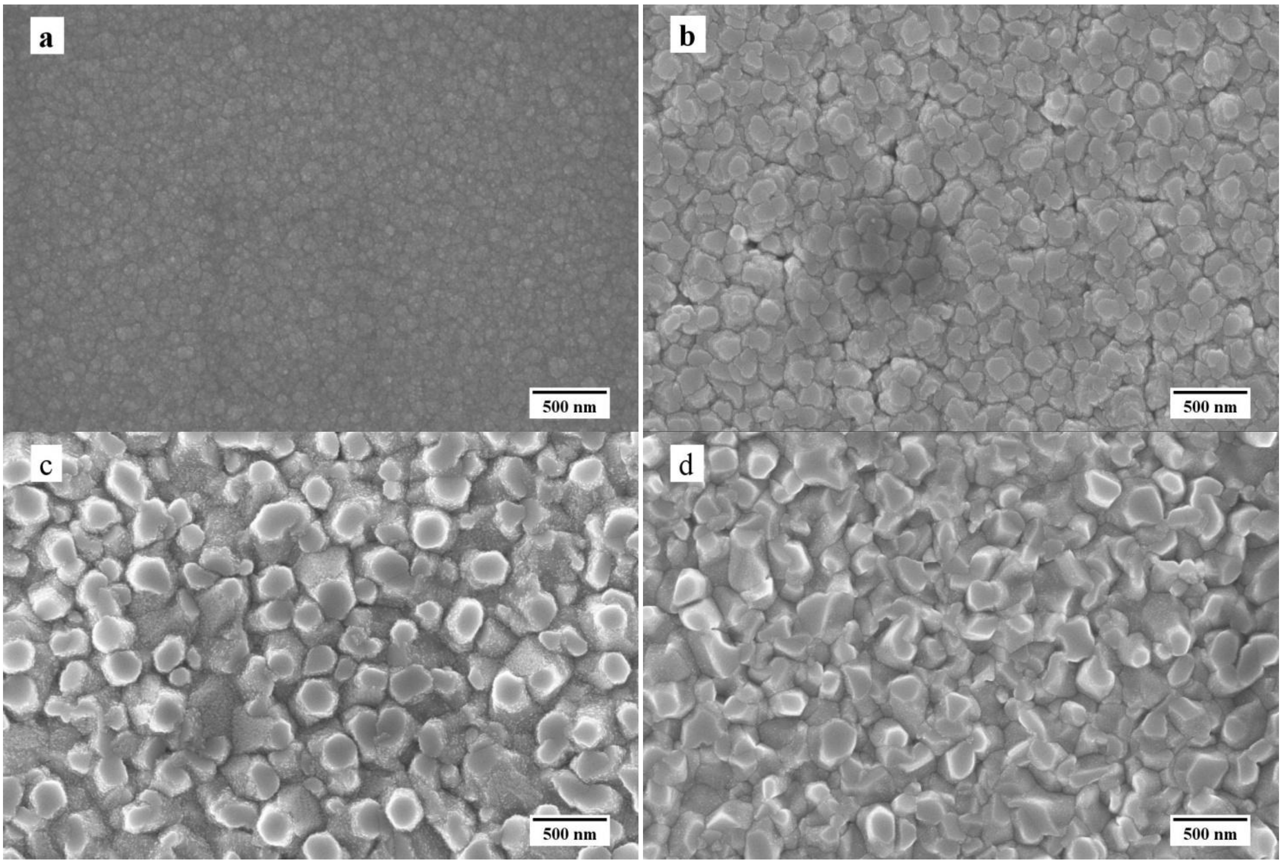

Fig. 1. SEM images of $Zn_{0.95}Mg_{0.05}O$ nanostructures obtained at different deposition temperatures: a - 250 °C, b – 315 °C, c - 350 °C, d - 390 °C.

SEM images indicating that multi-layer polycrystalline films $Zn_{0.9}Mg_{0.1}O$ start to growth at 250 °C with particle size up to 800 nm, not hexagonal informal shape and interfere with each other's due to the crystal orientation. At ~ 300-350 °C the surface morphology of the exhibit a polycrystalline and the grain have the composed of regular arrangement of the hexagonal crystallites or grain with s diameter about 850 nm (Fig. 2 b). It can be seen that the nanopillar have a hexagonal shape. The diameters of the hexagons are around 800 nm, whereas the tip has a dimension of around 200 nm (Fig. 2 c). Sample with an approximate substrate temperature of 420 °C shows a quasi-array of nicely formed hexagonal nanorods with a 200-300 nm diameter range (Fig. 2 d).

Comparison with other samples grown at different temperatures shows that 350 °C is the lowest temperature when nanorods $Zn_{1-x}Mg_xO$ were formed.

Combination between cross section and top view SEM images indicated that the grain size and thickness of $Zn_{1-x}Mg_xO$ layers (Fig. 2) increase to a certain value when the temperature increases. The reason for that is at the low growth temperature, the atoms do not have enough the kinetic energy to move the suitable position at which they connect each other to form bigger grains.

The SEM cross section image (Fig. 3 a) shows the amorphous film of $Zn_{0.95}Mg_{0.05}O$ obtained at 250 °C. With increasing temperature to ~ 300 °C cross section (Fig. 3 b) indicates columnar structure. Film is rough and uniform with a thickness ~ 700 nm. At substrate temperature ~ 400 °C the film thickness is around 1.5 μm (Fig. 3 d). With increasing the temperature, the oxidation and crystallization process becomes fast and growth rate is increased [5].

In the case of $Zn_{0.9}Mg_{0.1}O$ nanostructures are grown at relatively high temperature (350-400 °C) more grains and the film start to be crystalized and grains shape looks like a rod with a hexagonal top (Fig. 2 h). Furthermore, the thickness of these films is greater and reaches more than 2 μm. These changes can be related to the temperature effect, that can be detected for both morphology and bandgap. On the other hand, lower temperature of Si substrate is the result of amorphous or polycrystalline thin films.

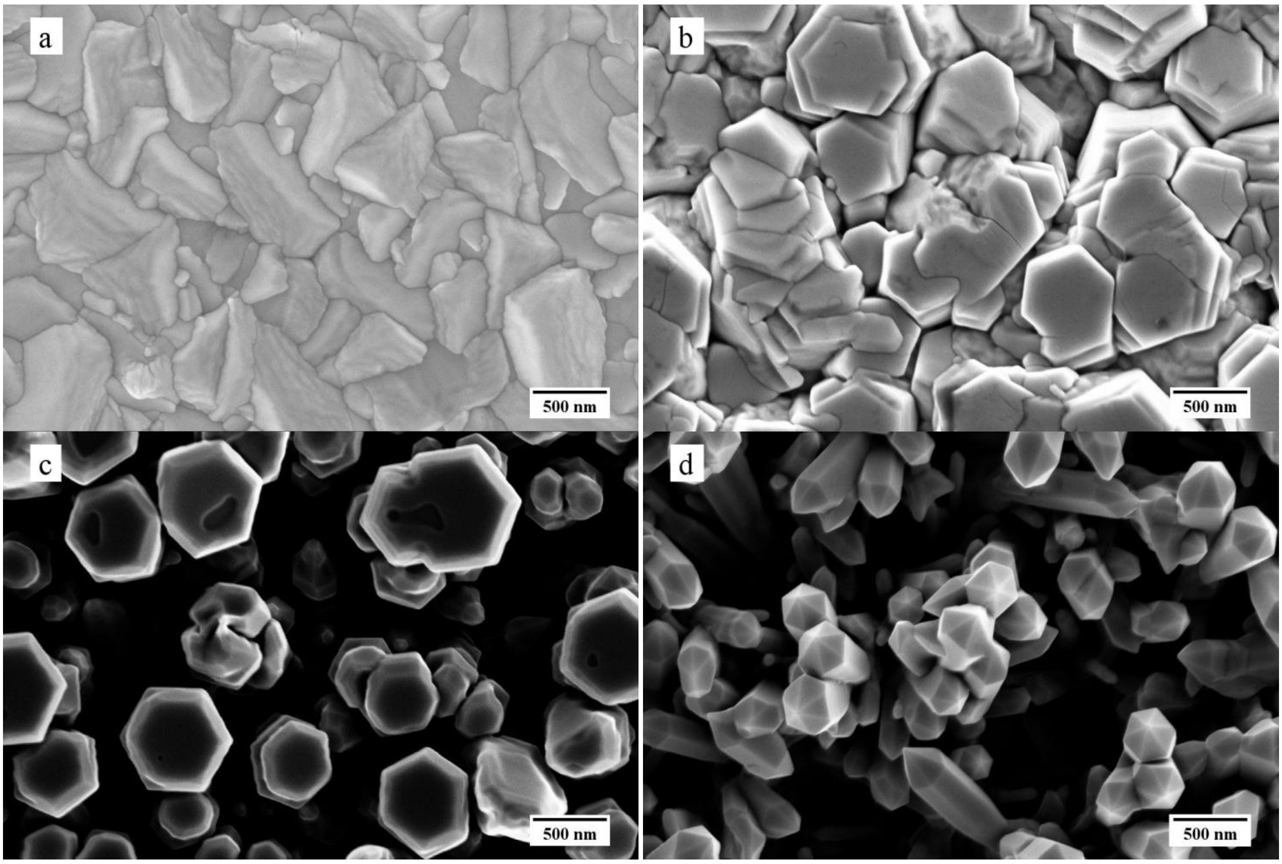

Fig. 2. SEM images of $Zn_{0.9}Mg_{0.1}O$ nanostructures obtained at different deposition temperatures: a - 250 °C, b - 320 °C, c - 350 °C, d - 420 °C.

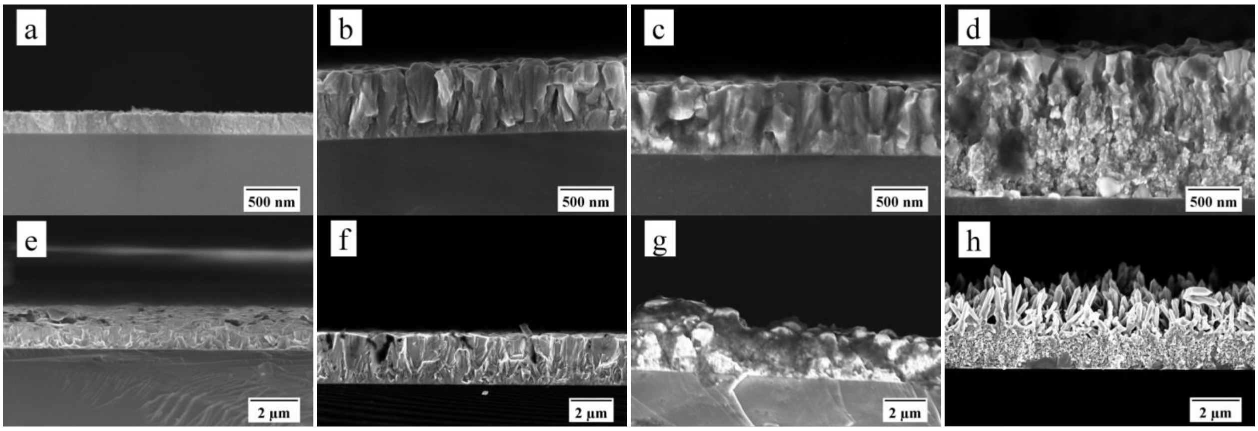

Fig. 3. Cross-section view $Zn_{1-x}Mg_{x}O$ nanostructures obtained at different deposition temperatures: a-d $Zn_{0.95}Mg_{0.05}O$ a - 250 °C, b – 315 °C, c - 350 °C, d - 390 °C; e-h $Zn_{0.9}Mg_{0.1}O$ e - 250 °C, f - 320 °C, g - 350 °C, h - 420 °C.

The main characterization technique to be used for the ZnO NS is photoluminescence spectroscopy. In this technique, a UV laser (325 nm) is used to excite the sample. As a result the photon emission with different wavelengths originating from free exciton recombination, deep level defects (DLD), is observed (Fig. 4).

Briefly, the high intense peak of near band emission (NBE) at ~376 nm caused by free exciton recombination has the full width at half maximum of peak about 14.41 nm. The emission band at a visible wavelength range (peak at ~ 470 nm) arises from radiative recombination through point defects in the ZnO lattice. The ratio of NBE and DLD spectral integral intensity emission (figure of merit) peaks was about 6 confirming that ZnO:Mg nanostructures are suitable for LED applications.

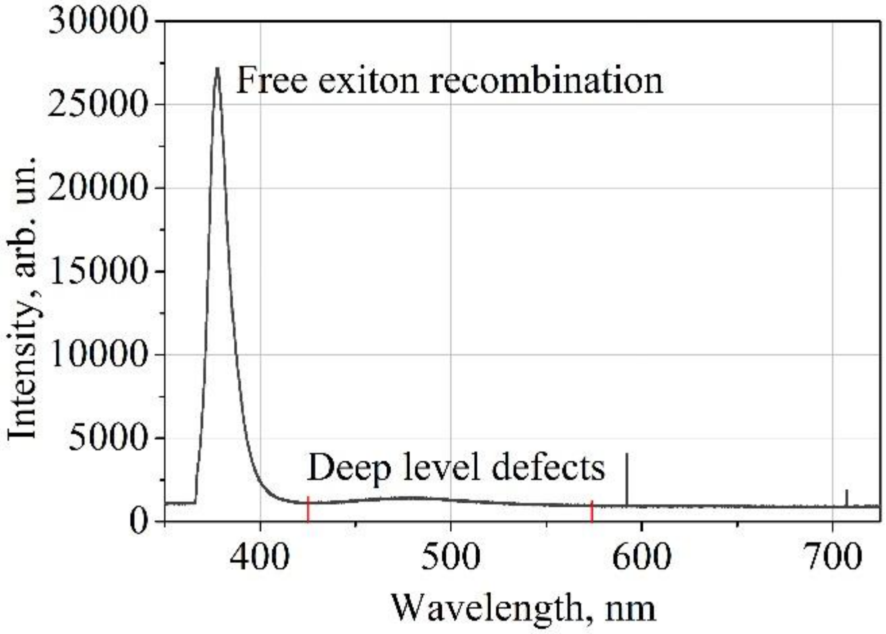

Fig. 4. PL scan of sample “hexagonal nanorods” of $Zn_{0.9}Mg_{0.1}O$ NS, grown at deposition temperature 400 °C.

Acknowledgements

This work was partially supported by the research projects of the NAS of Ukraine “The development of photocatalytic nanocomposites for viruses inactivation in the air” (№40/20-H) and “Development of innovative photocatalytic nanostructured materials based on ZnO and TiO_2” (528/IPM-11/20).

1. Lashkarev G. V., Shtepliuk I. I., Ievtushenko A. I., [et. al.]. Properties of solid solutions, doped film, and nanocomposite structures based on zinc oxide // Low temperature physics, 2015. – V. 41. – P. 129-140.
2. Look D. C. Recent advances in ZnO materials and devices // Mater. Sci. Eng. B., 2001. – V. 80 – P. 383-387.
3. Janotti A., Van de Walle C. G. Fundamentals of zinc oxide as a semiconductor // Reports Prog. Phys., 2009. – V. 72. – P. 126501.
4. Su L., Zhu Y., Zhang Q., [et. al.]. Solar-blind wurtzite MgZnO alloy films stabilized by Be doping // J. Phys. D. Appl. Phys., 2013. – V. 46. P. 245103.
5. Ahmmad B., Kanomata K. Hirose F. Controlled Morphologies of Nanostructured ZnO Films by MOCVD Method // Applied Mechanics and Materials, 2014. – V. 492 – P. 311-315.

MECHANISMS OF GEOMECHANICAL TRANSFORMATIONS OF MARINE SEDIMENTS UNDER THE INFLUENCE OF BIOCOLLOIDAL PROCESSES

Panko A.V.[1], Kovzun I.G.[1], Prokopenko V.A.[1,2], Nikipelova O.M.[3],
Tsyganovich O.A.[1,2], Oliinyk V.O.[1]

[1]F.D.Ovcharenko Institute of biocolloid chemistry of NAS of Ukraine,
42, Ak.Vernadskogo Blvd., Kyiv 03680, Ukraine
[2]National technical University of Ukraine «KPI»,
37, Peremohy Ave., building 4, Kyiv 03056, Ukraine
[3]Engineering and Technology Institute "Biotechnika" of NAAS of Ukraine,
26, Maiakska St, Khlibodarske, Odes'ka oblast, 67667

For the first time the mechanisms of geomechanical nanostructural and microstructural biocolloidal transformations, as well as layer-by-layer separation of iron-aluminosilicate turbidite-pelitic sediments were studied, taking into account the findings of specialists in various scientific fields [1-3] and experimental data (Figs. 1 and 2).

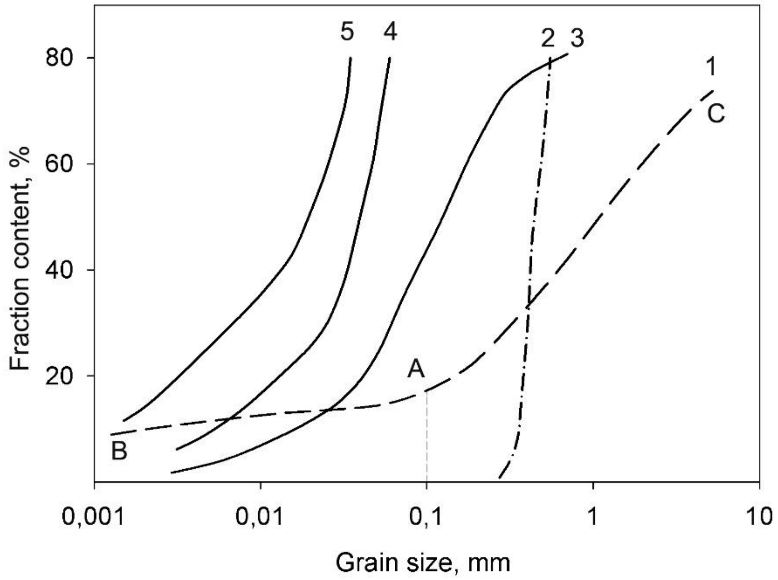

Fig. 1. Distribution of grain sizes in the most typical iron-aluminosilicate sediments:
1 – turbidite-pelitic ooze flow; 2 – sand; 3 – clays; 4 – loess; 5 – siltstone;
AB – pelitic fractions; AC – turbidite fractions

The mentioned processes significantly depend on the biocolloid transformations of sediments. These transformations combine microstructural and nanostructural geomechanical selfdispersion of sediments with their simultaneous separation into separate layers under the influence of microorganism activity as a part of biogeocenoses. The upper layer of such sediment, which forms in conditions of its rapid mixing or displacement (catastrophic processes of underwater sediments flowing at a speed up to 100 km/h) is enriched in natural conditions under the influence of microorganism metabolic products with nanostructured iron hydroxides, calcite and clay minerals – montmorillonite, hydromica, glauconite, kaolinite. Medico-biological studies have shown that such layers, separated from other sediment layers, have different particle sizes and mineral composition, as well as different biomedical properties. It is shown that the stratification of suspensions into separate layers occurs during the activation of microorganisms from biogeocenoses by nutrient media, i.e. in the conditions of biocolloid and geomechanical processes activation, which last for 5-25 days. Upon completion of these processes, the stratification of suspensions disappears. It was found that the upper layer of suspensions under the brine layer during the activation process hugely enriches with nano- and microparticles of iron and calcium compounds, and it increases the therapeutic properties of peloids separated from turbidite-pelagic marine underwater sediments in several times.

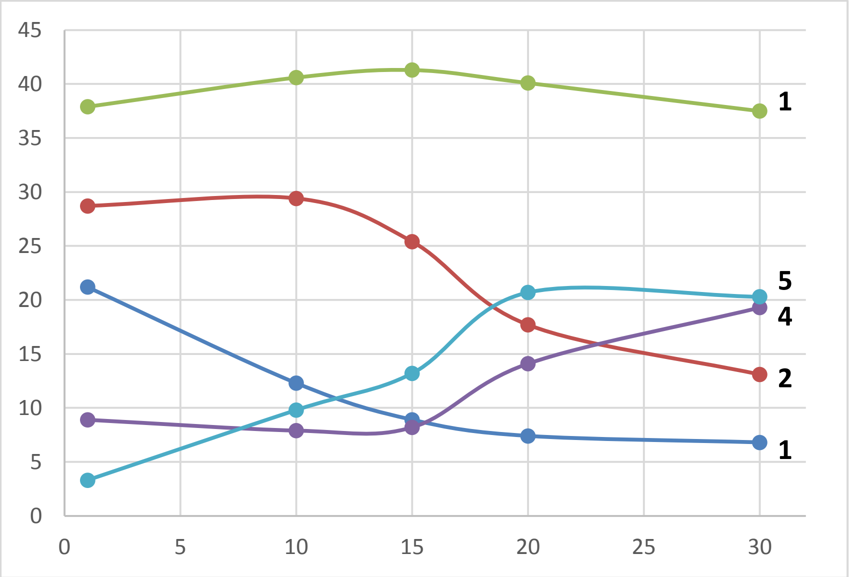

Fig. 2. Geomechanical selfdispersion of suspension (NaCl = 28 g/dm^3) of iron-aluminosilicate marine sedimentary iron ore of biocolloid origin under the action of biocolloidal processes. Fractions: 1 – 5-1 mm; 2 – 1-0.5 mm; 3 – 0.5-0.05 mm; 4 – 0.05-0.005 mm; 5 – <0.005 mm

It was also established for the first time that the biocolloid treatment of iron-aluminosilicate materials leads to stratification of suspensions into three layers during the activation process. The middle layer has a higher specific weight than the upper and lower (bottom) layer. The mechanism of such a phenomenon is considered and substantiated.

The obtained results can be used not only in medical practice, but also to improve the technologies of poor iron ores enrichment (Fig. 2), as well as theory development of many natural processes, primarily related to bio- and environmental safety.

1. Lessin G., Artioli Y., Almort-Rosell E. [et al]. Modelling Marine Sediment Biogeochemistry: Current Knowledge Gaps, Challenges, and Some Methodological Advice for Advancement // Frontiers in Marine Science, 2018. – V. 5, N. 19. – P. 1-8. https://doi.org/10.3389/fmars.2018.00019.
2. Нікіпелова О.М. Колоїдно-хімічні властивості мулових пелоїдних систем та основні принципи їх регулювання. Дис. д.х.н., Київ. – 2011.
3. Panko A.V., Kovzun I.G., Nikipelova O.M. [et al]. Nanostructural Effects in Iron Oxide Silicate Materials of the Earth’s Crust. – In: O. Fesenko, L. Yatsenko (eds), Nanophysics, Nanophotonics, Surface Studies and Applications, 2018. – Springer: Cham, 2019. – P. 367-386. https://doi.org/10.1007/978-3-030-17759-1_25

ULTRASONIC AND MAGNETIC-FIELD-ASSISTED ARRANGEMENT OF NANOSIZED CRYSTALLITES OF COBALT-CONTAINING LAYERED DOUBLE HYDROXIDES

Pashkevich Yu. G.[1], Salak A. N.[2], Vieira D. E. L.[2], Lukienko I. M.[3], Shapovalov Yu. O.[3], Fedorchenko A. V.[3], Fertman E. L.[3], Babkin R. Yu.[1], Shilin A. D.[4], Rubanik V. V.[4],Rubanik V. V. Jr.[4], Ferreira M. G. S.[2], Vieira J. M.[2]

[1]O. O. Galkin Donetsk Inst. for Phys. and Eng. of NASU, Kyiv 03680, Ukraine
[2]Department of Materials and Ceramics Engineering, CICECO – Aveiro Institute of Materials, University of Aveiro, Aveiro 3810-193, Portugal
[3]B.Verkin Inst. for Low Temp. Phys. and Eng. of NASU, Kharkiv 61103, Ukraine
[4]Institute of Technical Acoustics of NASB, 210023 Vitebsk, Belarus

The anions clay family - layered double hydroxides (LDHs) consist of the positively-charged octahedral layers of the double metal hydroxides $[M^{2+}_{1-x}M^{3+}_{x}(OH)_2]^{x+}$. The interlayer space is intercalated by water molecules and by anions $(A^{y-})_{x/y}$ which compensate the layer charge. The LDH short notation, namely $M^{2+}_{n}M^{3+}$-A^{y-}, where $n=(1-x)/x$ is the M^{2+} and M^{3+} in the layer, is commonly used. The weak, mostly hydrogen-bond, interlayer coupling allows easy exchange of the internal LDH anions into some external anions from the solution. The LDH ability for anion exchange reactions (AER) presents most attractive features for applications.

In this report we demonstrate that high – power sonication sufficiently accelerates the synthesis of Co-Al LDH by hydration of nanopowders of the sol-gel mixed metal oxides and the process of anion exchange with various organic and inorganic anions. Particularly, the time duration of the nitrate to carbonate anion exchange for the Co-Al LDH under sonication reduces from 7 days to 7 min [1]. We show that combining both ultrasonic and magnetic field action produce highly oriented de-agglomerated layers of Co-Al LDH flake-like nanocrystallites. Fig. (a) illustrates the magnetic field action on the precipitation process of a hexagonal crystallite of $Co_2Al\ NO_3$. A fragment of the octahedral layer is only shown. The red arrows represent magnetic moments $\boldsymbol{m}=g_{\perp}\mu_B\boldsymbol{H}$ of Co^{2+} cations. The directional anisotropy arises due to g-factors anisotropy $g_{\perp}>>g_{\parallel}$ caused by the local environment of cobalt ions. Fig. (b) and (c) are SEM images (cross section views) of layers of the Co_2Al-NO_3 crystallites deposited on glass substrates without (b) and with (c) application of magnetic field [1]

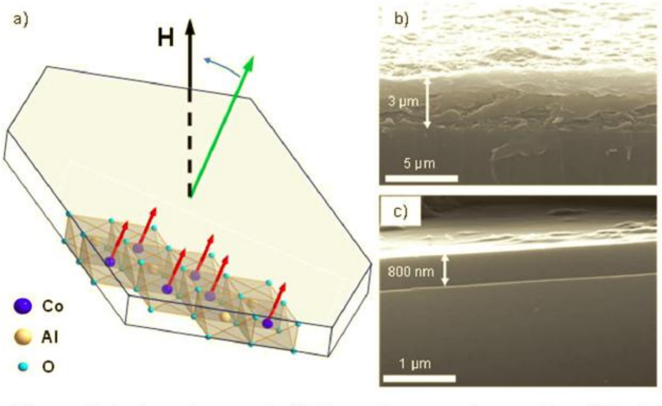

This work was supported by the Ukraine – Belarus bilateral project 2020-2021.

1. Salak A.N., et al ChemEngineering, 2019, **3**, 00062.

STUDY OF THE STRUCTURAL FEATURES OF ULTRADISPERSED DIAMOND IN A SUPERCRITICAL FLUID UPON NANOSECOND PULSED LASER ANNEALING

Prudnikov A.M.[1], Liedienov N.A.[1,2], Pashchenko A.V.[1,2,3,4], Dmitrenko V.Y.[1], Pas'ko M.[5], Pashkevich Yu.G.[1]

[1]Donetsk Institute for Physics and Engineering named after O.O. Galkin of the National Academy of Sciences of Ukraine, 46. Nauky Av., Kyiv, 03028, Ukraine
[2]State Key Laboratory of Superhard Materials, International Center of Future Science, Jilin University, 130012 Changchun, China
[3]Ivano-Frankivsk National Technical University of Oil and Gas, MESU, 76019 Ivano-Frankivsk, Ukraine
[4]Institute of Magnetism, NAS of Ukraine and MES of Ukraine, Kyiv 03142, Ukraine
[5]Donetsk National Medical University, Lyman 84404, 27 Pryvokzalnaya Str., Ukraine

Recently, in the world practice of creating new materials, the acceleration of synthesis processes has been widely employed due to use of laser annealing of a target in a liquid. The ablation - evaporation of target particles under the action of a laser pulse is a main process. Using this process, diamond nanoparticles were obtained while using graphite as a target. A significant drawback is the limitation by the laser plasma (ablation torch near the target surface) and the formation of a mass of the obtained material with an increase in the intensity of laser irradiation.

The main task and goal of this work is the synthesis of superdense carbon and carbon nitride phases upon nanosecond laser irradiation of nanocolonar carbon nitride films located in a liquid solution with the presence of ultradispersed diamond (UDD). In this case, the intensity of the laser pulse does not exceed the ablation threshold, but is sufficient to transform the liquid into a supercritical state. Therefore, the synthesis of new phases occurs directly on the surface of the target (film) with the participation of the liquid and UDD nanoparticles. Nanocolonar carbon nitride films were used as a precursor target.

The economic significance of this method is in the fact that it is aimed at finding and developing cheaper, simplified and at the same time more efficient technologies for the synthesis of new multifunctional film nanomaterials.

Structural changes in the nanocolonar nitride carbon films under the action of laser irradiation were investigated using high-resolution transmission electronic microscopy (HRTEM) and Raman spectroscopy. In the Raman spectra, there are carbon D, A, G and G' bands at 1343, 530, 1590 and 2704 cm^{-1}, respectively. The most noticeable changes are observed in the region of Raman scattering of the A band. More than a fivefold increase in the integrated intensity of the A band is observed with an increase in the laser irradiation intensity, which correlates well with the data obtained in the quantitative analysis of carbon and nitrogen. With an increase in the intensity of laser irradiation, the concentration of nitrogen sharply increases.

The studies of low-intensity laser irradiation of nanocolonar carbon nitride films by the HRTEM method allow us to conclude that the carbon shells around UDD nanoparticles are not closed (such as fullerene structures), but are formed from imperfect fragments of bent carbon sheets less than 10 nm in size. Additional laser treatment in isopropanol increases both the size of UDD nuclei and the thickness of the carbon nitride coating with increasing nitrogen concentration. The size of nitride carbon fragments is increased and their ordering in the lateral and transverse directions increases.

The work has been carried out within the Target program of fundamental research of the NAS of Ukraine «Promising basic research and innovative developments nanomaterials and nanotechnologies for industry, health and agriculture» (Project № 14/20-H)

VI-B GROUP METALS SILICIDES NANOPOWDERS PRODUCTION BY MELTS ELECTROLYSIS

Shakhnin D.B., Malyshev V.V., Gab A.I., **Prykhodko O.A.**

Open International University of Human Development “Ukraine”, 26, Lvivska St., 03115 Kyiv, Ukraine

Silicon compounds of VI-B group metals belong to an important class of inorganic compounds with a range of valuable properties. Their powders can be converted into construction materials with desired electrophysical, fire resistance, corrosion resistance, and wear resistance properties which makes them promising inorganic materials for new developing areas of technology.

Disilicides MSi_2 (M = Cr, Mo, W) are the most studied and practically important ones. The most common method for their preparation is synthesis from elementary substances under inert gas atmosphere at temperature 1273-1373 K. Other known methods include thermal reduction by magnesium and alumininium from oxides at temperature 1873-2573 K, chemical vapor deposition of halides, and finally electrolysis of molten salt, which is of the most promising ones. Information regarding obtaining Cr, Mo, and W silicides by electrolysis of molten salts is scarce. Method for chromium silicides obtaining in silicate (borate)-fluoride melts and for molybdenum silicides obtaining in alkali metal fluorides melts are described in literature.

Development of practical applications of method of synthesis by electrolysis of melts was hampered by the data lack on electrochemical behavior of compounds used as sources of metal and silicon.

For synthesis of Cr, Mo, and W silicides, their oxygen compounds were used dissolved in KCl-KF and $NaCl\text{-}Na_3AlF_6$ mixtures. It enables us to realize large current densities and to use graphite as anode material without risk of anode effect.

Deposition of fine powders by electrolysis was carried out in a quartz reactor. Anode was graphite crucible MPG-7, and cathode was tungsten rod. Product was extracted together with the working cathode, mechanically separated from it, and ground.

Silicides are separated by consecutive leaching of salts with hot water and with 10% solution of H_2SO_4 heated up to 50-60 ºC. Then, precipitate was washed with distilled water, filtered, and dried to constant weight at 100-105 ºC.

Bulk properties were determined by analytical methods, and surface ones were controlled by physical methods: X-ray diffraction, thermogravimetric analysis, and low-temperature adsorption of argon. Phase composition of the powders was determined using DRON-2 device and Cu Kα radiation, and specific surface area - by BET method through low-temperature adsorption of argon. Contents of Cr, Mo, and Si, and also of main impurities, were found in powders by atomic absorption spectroscopy method using Pye-Unicam spectrometer; tungsten was determined by the gravimetric method.

Synthesis of silicides of molybdenum and tungsten. Preliminary experiments on electrolysis of chromium (molybdenum, tungsten) and silicon containing melts make it possible to generalize findings (Table 1).

In current-voltage curves for chloride-cryolite melts, under joint presence of sodium molybdate and silicon oxide, two waves are observed. The first of them is caused by electroreduction of molybdenum oxyfluoride complex, and the second one – by oxyfluoride complex of silicon. Difference between half-wave potentials is 0.8-0.9 V. Similar situation is observed in presence of sodium tungstate, with the only difference that difference of half-waves potential is 100-150 mV lower. These data confirm that silicides synthesis could be carried out by electrolysis alone in kinetic regime.

It causes the following sequence of steps for electrosynthesis of silicides of molybdenum and tungsten: I - deposition of more electropositive metals (molybdenum or tungsten); II -

deposition of the second component - silicon - on the surface of Mo or W deposited earlier; III - silicon reaction diffusion into the depth of metal-salt "pear" with formation of silicides phases of different compositions up to higher silicides.

Table 1. Electrochemical systems and melt electrolysis conditions for synthesis of VI-B group metals silicides

Electrolyte	Refractory metal containing component	Silicon containing component	*U*, V	*T*, K	Cathode product
Na_2SiF_6 (K_2SiF_6)	Cr_2O_3, Cr fluorides	Na_2SiF_6 (K_2SiF_6)	1.9-2.1	1273	$CrSi_2$
Li, Na, K / F	Mo Fluorides	K_2SiF_6	1.9-2.2	1273	$MoSi_2$
NaCl-Na_3AlF_6	Na_2MoO_4 (Na_2WO_4)	SiO_2	1.8-2.2	1173	Mo_3Si_5, $MoSi_2$, W_3Si_5, WSi_2
NaCl-Na_3AlF_6	K_2CrO_4	SiO_2	2.5-3	1173	Cr_3Si, CrSi, Al compd.
KCl-KF	K_2CrO_4	K_2SiF_6 (SiO_2)	3.0-4.0	1173	Cr_3Si, $CrSi_2$

Silicides synthesis process can be described by the following electrochemical and chemical equations:

at cathode:

$$MO_3F_2^{2-} + 6\bar{e} \to M + 3O^{2-} + 2F^-, \qquad (1)$$

$$SiO_2F_2^{2-} + 4\bar{e} \to Si + 2O^{2-} + 2F^-, \qquad (2)$$

$$M + zSi = MSi_z\,; \qquad (3)$$

at anode:

$$2O^{2-} - 4\bar{e} + C \to CO_2\,. \qquad (4)$$

Duration of the first stage of synthesis depends on amount of refractory metal in system and on cathode current density. To obtain molybdenum or tungsten in form of fine powder, current density should be the maximum possible one.

The second stage begins with exhausting of electropositive component. Synthesis of silicides can be carried out only under conditions that molybdenum or tungsten powders deposit at cathode surface in form of metal-salt "pear" of such size and shape which allow it to be held firmly at the cathode without breaking. In case of the metal (W or Mo) powders falling out to the electrolyzer bottom, synthesis components are not in contact with each other, and silicides synthesis does not occur.

Temperature of electrochemical synthesis of molybdenum and tungsten silicides is 850-900 ºC. Gain in energy of interaction compared with known synthesis processes is provided by interaction of deposited at cathode fine powders of Mo (W) and silicon at atomic level.

Optimization of process of electrochemical synthesis of silicides of molybdenum or tungsten is reduced to determination of concentration ratio, current density and temperature values, and also of process duration.

Choice of concentration ratios of components was guided by the following considerations. According to literature, silicon dioxide has a limited solubility in molten cryolite (8.82 wt.%) at 1010 ºC. Addition of sodium chloride to cryolite results in lower mixture melting temperature and higher solubility of SiO_2. In eutectic melt (737 ºC; 68.5 wt.% NaCl and 31.5 wt.% Na_3AlF_6), its solubility is about 1.0 wt.%. Maximal content of cryolite in binary system NaCl-Na_3AlF_6 which allow to carry out electrolysis at 900 ºC is 70 wt.% with the SiO_2 solubility in melt of such composition 2.0 wt.%. Concentration of sodium molybdate (tungstate) is determined by value of SiO_2 solubility which provide for stoichiometric composition silicides obtaining. Choosing the concentration of the refractory metal oxysalt, one should also take into account the first stage of electrochemical synthesis. The first stage is formation of metal-salt "pear", and process of deposition of silicon starts after salt exhaustion. Salt concentration in melt (with i_k = const) defines duration of metal deposition at cathode and size of metal-salt "pear". For complete siliconizing of deposited molybdenum or tungsten, content of Na_2MO_4 in melt should not exceed 2 wt.%.

Essential role in electrochemical synthesis of silicides of Mo and W is played by temperature and current density values. Lowering the temperature below 850 ºC does not ensure completeness of interaction of Mo(W) and Si, and temperature rise above 950 ºC reduces stability of metal-salt "pear" due to which silicides are not formed. With optimal melt composition, pure products were obtained with current density 0.5-1.2 A/cm^2 for $MoSi_2$ and 0.5-1.5 A/cm^2 for WSi_2. With $i_k < 0.5$ A/cm^2, obtained product is contaminated with Mo or W. Within the range of current density 0.5-1.5 A/cm^2, with current density increase, dispersity of Mo and W silicides increases.

During electrochemical synthesis of silicides of Mo and W, as well as during direct interaction of simple substances, main process is silicon diffusion through metal layer. In such a case, metal is weakly involved in diffusion, and higher silicides are formed in such a system from lower ones. Therefore, obtained products composition is influenced significantly by process duration. Thus, melt having a composition wt.%: NaCl - 49; Na_3AlF_6 - 49.0; Na_2MoO_4 - 1.0; SiO_2 - 1.0, at 900 ºC and with current density 1.0 A/cm^2, depending on electrolysis duration, different products are produced:

Duration, min:	10	20	30	45	60
Phase composition:	Mo	Mo, Mo_5Si_3	Mo_5Si_3, $MoSi_2$	$MoSi_2$	$MoSi_2$, Si

Similar dependence of phase composition on electrolysis duration is observed in NaCl-Na_3AlF_6- Na_2WO_4-SiO_2 system. Thus, optimal electrolysis duration is 45-50 min.

Washed free of salts and silicon and dried silicides of Mo and W are fine powders with particle size of 0.1-5 μm. The main parameters characterizing experimental samples are presence of free silicon and impurities content, as well as specific surface area of samples.

According to X-ray analysis data, in some cases products contained free silicon which was removed by treatment with hot sodium hydroxide solution. Degree of free silicon removal was controlled by x-ray diffraction data. Washed free from silicon molybdenum and tungsten disilicides have content of impurities (Si, Na, Al) at level of hundredths of a percent. Specific surface of Mo_2Si and WSi_2 is 6-15 m^2/g.

It is known that Group VI silicides are highly chemically stable compounds, and $MoSi_2$ is the most oxidation-resistant one among oxygen-free compounds. Temperature of beginning of active oxidation of $MoSi_2$ is 1600, and of WSi_2 – 1400 ºC. However, fine powders of $MoSi_2$ are oxidized in air at about 370 °C to form MoO_2, MoO_3, SiO_2.

Electrochemical synthesis of chromium silicide. Initially, high-temperature electrochemical synthesis of chromium silicide is carried out from a mixture of molten NaCl-Na_3AlF_6 - K_2CrO_4 - SiO_2. Voltammetric curves show reduction waves of oxyfluoride complexes of Cr and Si at significantly different potentials, - (0.7-0.9) V and - (1.6-1.9) V, respectively. Depending on composition and electrolysis parameters, Cr_2O_3, higher silicide $CrSi_2$, and silicide Cr_3Si phases were obtained as a mixture with aluminum compounds.

To optimize synthesis conditions for chromium silicides containing no aluminum compounds, electrochemical synthesis was carried out in KCl-KF-K_2SiF_6- K_2CrO_4 system. The resulting current-voltage dependences show reduction waves for oxyfluoride complexes of Cr and Si at significantly different potentials.

Depending on electrolyte composition and electrolysis parameters, both individual phases Cr_2O_3, Cr_3Si, and $CrSi_2$, and also mixtures of these phases with low silicon content were obtained

(Table 2). Choosing concentrations of CrO_4^{2-} and SiO_2 (K_2SiF_6), it should be taken into account that, at the first stage of electrolysis, Cr_2O_3-salt "pear" is formed which starts to become siliconized during exhaustion of the refractory metal. Unlike high-temperature electrochemical synthesis of silicides of molybdenum and tungsten, during this synthesis, one of components are not deposited in elementary form but rather in oxide form, and the other acts as a reducing agent of the mentioned oxide to form binary compounds.

Table 2. Phase composition of electrolysis products of system KCl-KF(25wt.%)-K_2SiF_6(1wt.%) - SiO_2-K_2CrO_4 (t = 900ºC, U = 3-4 V)

K_2CrO_4, wt.%	The duration of electrolysis, min.				
	5	10	15	30	60
0.5	Cr_2O_3	Cr_3Si; Si	Cr_3Si; $CrSi_2$	$CrSi_2$	$CrSi_2$; Si
1.0	Cr_2O_3	Cr_3Si; Si	Cr_3Si; Si	Cr_3Si; $CrSi_2$	$CrSi_2$; Si

Thus, during electrolysis of chromium (molybdenum, tungsten) and silicon containing melts, high temperature electrochemical synthesis of powders of silicides of chromium, molybdenum, and tungsten was implemented.

METAL NANOPARTICLES IN TECHNOLOGY OF VETERINARY VACCINES' MANUFACTURING

Rieznichenko L.[1,2], Dybkova S.[1], Tiutiun S.[2], Gruzina T.[1], Zhovnir O.[2]

[1]F.D. Ovcharenko Institute of Biocolloidal Chemistry NAS of Ukraine, Vernadskogo Av., 42, Kyiv, 03142, Ukraine
[2]Institute of Veterinary Medicine NAAS of Ukraine, Donetska Str., 30, Kyiv, 13151, Ukraine

Nanomaterials, particularly metals nanoparticles, have broad prospects for using in humane and veterinary medicine as part of veterinary immunobiological means (VIM), means of targeted delivery of active substances, antimicrobial, antifungal and antiviral agents, etc.

Thus, the modification of existing VIM with various metal nanoparticles provides a significant increasing in their effectiveness and a spectrum of positive effects on the animals' organism due to the unique biological properties of nanoparticles, like expressed antianemic activity, the ability to stimulate hematopoietic function, antimicrobial activity, etc.

The purpose of the work was substantiating experimentally the use of metal nanoparticles in veterinary medicine as part of the VIM and stimulating tissue preparations.

Colloidal solutions of spherical nanoparticles of gold with an average size of 30 nm, silver 30 nm, iron 40 nm and copper 40 nm were synthesized to use in research. The researches were carried out using preparative methods of biochemistry, microbiology, electron microscopy, determination of antibiotic resistance, working on plasmid DNA, safety assessment of nanopreparations according to the Methodological Guidelines of the Ministry of Health of Ukraine "Assessment of the safety of nanopreparations", determination of toxicity, etc.

Conducted fundamental researches *in vitro* and *in vivo* have made it possible to determine the optimal nature, size and concentration of metal nanoparticles for their effective use in biotechnological schemes for the manufacturing of veterinary vaccines and stimulating tissue preparations.

It has been proven that the introduction of metal nanoparticles into the nutrient medium stimulates the growth of bacterial mass. Thus, the introduction of silver nanoparticles at concentration range of 0.1-2.0 μg/ml or iron nanoparticles at concentration range 0.007-0.080 mg/ml to the medium during the cultivation of *Escherichia coli* provides a 2-fold increase in biomass growth. By the cultivation of microorganisms of *Clostridium* genus, an effective increase in the bacterial mass growth (1.2-3 times) was established at the presence of copper nanoparticles at a concentration range of 0.01-0.05 mg/ml and iron nanoparticles at concentration range (0.02-0.1 mg/ml). The introduction of gold nanoparticles into the VIM's composition promoted an increase in the immunogenicity of vaccines. Modified experimental veterinary immunobiological means (vaccines) "Velshicolisan+AuNP" and "Velshicolisan+AgNP" were characterized as safe according to the results of genotoxicity and cytotoxicity tests. The introduction of gold or silver nanoparticles in a living organism can lead to the losing of plasmid-associative antibiotic resistance in representatives of probiotic and transient microflora of animals.

The optimal concentrations of metal nanoparticles and the conditions for modifying the vaccines "Velshisan", "Multibovisan", "Actinokolisan", "Actinosan" have been determined. A number of experimental VIM with iron, copper, gold and silver nanoparticles have been created: "Velshisan + FeNP", "Velshisan + CuNP", "Velshisan + AuNP", "Velshisan + AuNP-stimulus", "Velshisan + AgNP", "Multibovisan + AgNP (1%)" and "Multibovisan + AgNP (0.5%)", "Actinokolisan + AgNP", "Actinosan + AgNP". Conducted veterinary vaccines were characterized as safe in terms of genotoxicity and cytotoxicity.

The stimulating tissue preparation "STP" was modified with iron nanoparticles. The safety in terms of cytotoxicity and genotoxicity of "STP" and "STP" modified with iron nanoparticles were investigated. *In vitro* the stimulating effect of the means "STP" for the test eukaryotic cells of the piglet testicle line (ST) was established. It has been shown that both "STP" and "STP" modified with 40 nm iron nanoparticles at a concentration of 1.0 mg/ml per metal are safe in terms of cytotoxicity and genotoxicity.

Methodological Guidelines of the use of metal nanoparticles in the biotechnologies produced by VIM for the specific prevention of infections in farm animals with the aim of their introduction into the practice of veterinary medicine have been developed and approved.

The results obtained have been successfully implemented in utility model patents and an invention patent.

INVESTIGATION OF THE SHORT-RANGE ORDER STRUCTURE OF NANOSIZED CHALCOGENIDE FILMS BY SERS-METHOD

Rubish V.M.[1], Durkot M.O.[1], Hreshchuk O.M.[2] , Makar L.I.[1], Pop M.M.[1,3], Studenyak I.P.[3],
Yasinko T.I.[1], Yukhymchuk V.O.[2]

[1] *Institute for Information Recording, NAS of Ukraine,4 , Zamkovi schody St., 88000, Uzhgorod Ukraine*
[2] *V. Lashkaryov Institute of Semiconductor Physics, NAS of Ukraine, Prospekt Nauky, 41, Kyiv 03028, Ukraine*
[3]*Uzhgorod National University, 3, Narodna sq., 88000, Uzhgorod, Ukraine*

Raman spectroscopy is widely used to analyze the structure of thin films of chalcogenide vitreous semiconductors (ChVS), namely crystallinity, vibrational structure, composition, existence of defects etc. ChVS are widely used in different fields like optoelectronics, photonics, recording systems, due to their unique semiconductor properties [1]. However, it's quite complicated to characterize them due to low thickness of the films. In this regard, the SERS method (surface-enhanced Raman spectroscopy) could resolve this problem. SERS enhancement based on the phenomenon of surface plasmon resonance (SPR), which appear in the nanostructured arrays of Au or Ag nanoparticles (NPs) under resonant laser excitation. And it's allow to study nanosized ChVS films. SERS also used to detect ultralow quantities of biologically active substances [2-5]. It should be noted that chalcogenide materials have not been studied yet by the SERS-method. This paper is devoted to the study of the structure of nanosized arsenic sulfide films by surface-enhanced Raman spectroscopy.

Thin films of arsenic sulfide with thickness of 30, 50 and 60 nm were deposited by the method of thermal evaporation from quasi-closed diffusion cells -on glass substrates and on the surface of arrays of randomly distributed gold nanoparticles with different average NPs size (d) and maximum position of SPR band (λ_{SPR}) therefore composite structures of "Au NPs/As_2S_3 film" were formed. As_2S_3 films were obtained at a deposition velocity of 1-5 nm/s. Arrays of Au NPs A1 (d=20-35 nm, λ_{SPR}=532 nm), A2 (d=30-40 nm, λ_{SPR}=538 nm) and A3 (d=40-60 nm, λ_{SPR}=574 nm) were used for the experiments. Investigations of Raman spectra of as-prepared and annealed As_2S_3 films and composite structures "Au NPs/As_2S_3 film" were carried out at room temperature on the Horiba Jobion-Yvon spectrometer. For excitation, a red laser was used (λ_{exc}=671 nm).

Fig. 1a shows the Raman spectra of as-prepared nominally pure As_2S_3 films with a thickness of 60 and 30 nm (curves 1 and 2) and the same films deposited on arrays of gold nanoparticles A3 (curves 3 and 4). It can be seen that Raman signal is almost absent for ChVS films on glass substrate (Fig.*1a*, curve 1, 2), also there is no Raman signal for nominally pure As_2S_3 film with a thickness of 50 nm, annealed for 1 hour at a temperature of 450 K (Fig.*1b*, curve 1).

As can be seen from Fig. 1*a* (curves 3 and 4), the reliable Raman signal was obtained for As_2S_3 films of the same thicknesses (60 and 30 nm), but deposited on Au NP arrays. It is worth mentioning that Raman spectra for As_2S_3 films of both thicknesses applied to the array 3 are almost identical. They contain an intense wide band with a maximum at 343 cm^{-1}, a number of weak bands at 108, 135, 168, 188, 232, 260 and 486 cm^{-1} and peculiarities (in the form of a small shoulder) at 221, 308-310 and 362 cm^{-1}. As for glass and "thin" film of As_2S_3 [1], the main band in Raman spectrum of the composite structure "Au NP/As_2S_3 film" is caused by vibrations of As and S atoms in AsS_3 trigonal pyramid. The shoulder at 308-310 cm^{-1} is caused by deformation vibrations of S-As-S bonds of AsS_3 pyramids, with the participation of which the matrix of films is constructed. A weak band at 168 cm^{-1} can be attributed to As-S-As vibrations, and a band at 486 cm^{-1} is due to sulfur-sulfur bonds. Sufficiently intense bands at 188 and 232 cm^{-1} and a number of less pronounced bands and peculiarities at 108, 135, 221, 362 cm^{-1} indicate the presence in the structural network of As_2S_3 films of a significant number of molecular fragments As_4S_4 with homopolar As-As bonds. A weak band at 260 cm^{-1} can be attributed to fluctuations of atoms in structural groups As_4S_3. The analysis of the obtained results allows making a conclusion about the nanoheterogeneous structure of as-prepared As_2S_3 films. Their structural network is a mixture of pyramidal structural groups AsS_3 and partially polymerized disordered molecules As_4S_4, As_4S_3 and fragments of rings and chains of sulfur.

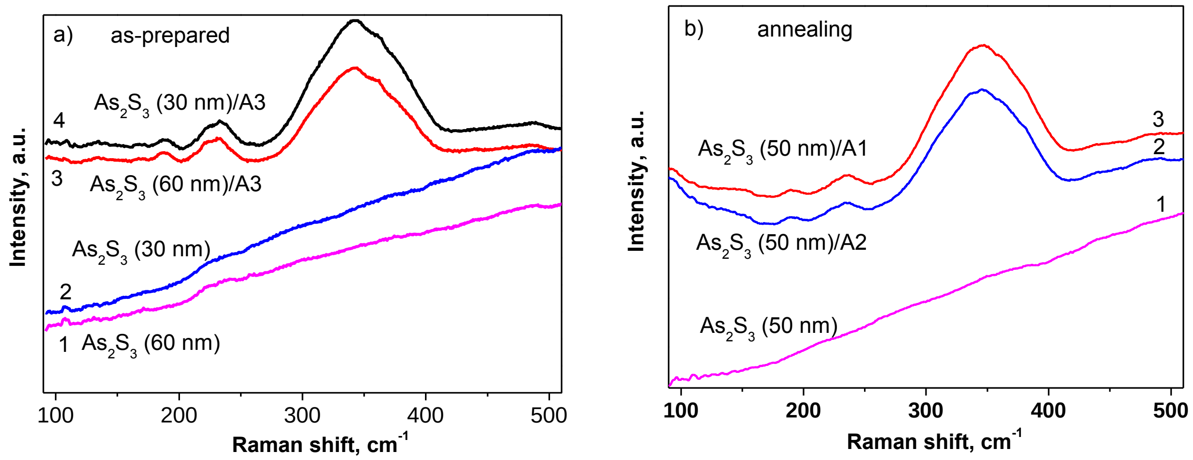

Fig.1. Raman spectra of as-prepared (a) and annealed (b) nominally pure and deposited on of Au NPs arrays As_2S_3 films.

Fig. 1b (curves 2 and 3) shows Raman spectra of annealed composite structures based on As_2S_3 films with thickness of 50 nm and Au NPs arrays A1 and A2. Attention is drawn to the similarity of the obtained spectra with the spectrum of glassy As_2S_3. Compared to spectra of composite structures with as-prepared As_2S_3 films, Raman spectra of plasmon structures with annealed As_2S_3 films contain fewer peculiarities associated with the presence of molecular fragments with homopolar As-As bonds in their structural network. This is evidenced by the absence of bands in the spectra of annealed films at 135, 221 and 260 cm^{-1} and less pronounced band character at 188 and 235 cm^{-1}. After annealing of films, the homopolar chemical bonds breaks and switch in the corresponding molecular fragments, which in turn leads to their polymerization into the structural network of pyramidal AsS_3 groups. In Raman spectra this process manifests itself in a significant reduction in the intensity of bands caused by homopolar bonds (or even their disappearance) and changes in the angles of As-S-As bonds. Changing the angles of such bridgings, in turn, is manifested in a significant change in the frequencies of deformation vibrations. This can explain the presence of weak band at 148 cm^{-1} in the Raman spectrum of As_2S_3 annealed film. Let us remind that for as-prepared film, a band caused by As-S-As vibrations was detected at 168 cm^{-1} (Fig. *1*a, curves 3 and 4). Based on the obtained results, it can be concluded that in annealed As_2S_3 films the concentration of molecular fragments with homopolar bonds is significantly lower than that of as-prepared ones, but it also remains significant.

Therefore, experimental studies have shown that glass substrates with arrays of randomly distributed gold nanoparticles formed on their surface with an average size of 20-60 nmand position of maxima of SPR bands in the range of 520-575 nm (with large half-width up to near IR), can be used as effective SERS-substrates (with a high efficiency of Raman signal amplification) for the investigation of Raman spectra and, accordingly, the structure of nanosized chalcogenide films.

1. Petrov V.V., Kryuchin A.A., Rubish V.M. Materials for Perspective Optoelectronic Devices. Kiev: Naukova dumka-Verlag, 2012. – 336 p.
2. Chang R.K., Furtak T.E. Surface enhanced Raman scattering // New York: Plenum Press. – 1982. – P. 379.
3. Moskovits M. Surface-enhanced spectroscopy // Rev. Modern Phys. – 1985. – V.57. – P.783-826..
4. Nabiev I.P, Efremov R.G., Chumanov G.D. Giant Raman scattering and its application to the study of biological molecules // Advances in physical sciences – 1988. – V.154. – No. 3. – P.459–496.
5. Yukhymchuk V.O. Hreshchuk O.M., Dzhagan V.M. et. al. Experimental studies and modeling of “starlike” plasmonic nanostructures for SERS application // Phys. Stat. Solidi B. – 2018. – P. 1800280 (1-8).

PONDEROMOTIVE FORCES AS A REASON FOR DESTRUCTION OF VIRUS INTERACTING WITH NANOPARTICLES

V. Lozovski[1,2], **N. Rusinchuk**[1] and V. Lysenko[2]

[1] Institute of High Technologies Taras Shevchenko National University of Kyiv, 56 Volodymyrska str., 01602 Kyiv, Ukraine
[2] V.Lashkariov Institute of Semiconductor Physics, National Academy of Sciences of Ukraine, 45 Nauki ave., 01000 Kyiv, Ukraine

The interaction between nanoparticles and viruses can be the reason of a lost by the virus its infectiviy, e.g. [1-3]. However, the mechanism of this action is not known. There are different suppositions for this mechanism. We would like to discuss, to extend and to improve the model of influence of nanoparticle on the virus infectivity based on the local-field enhancement effect proposed earlier in [3]. The main feature of proposed model is the arising of the domains of high local field (hot spots) at the virus surface. It was shown that the higher the local field gradient is, the higher antiviral action is without explanation of this dependence. Here we would like to consider this dependence and try to explain it via the action of ponderomotive forces.

The most human viruses have the quasi-spherical shape with linear dimension about 100 nm. The characteristic dimensions of the nanoparticles are about few nanometers. Then, we can use the model when the virus is spherically shelled solid nanoparticle where core is characterized by dielectric constant and the virus shell is characterized by its own dielectric constant. As is was mentioned, in the system there are the high local field on the virus surface. The domains of high field mean the existance of gradients of the local field at the surface of virus shell. The molecules at the surface of virus contain the polar sites. Then, the dipole moments of the polar sites are under action of the inhomogeneous field. It means that the forces acting to the molecule-receptors arises (ponderomotive forces): $F = -P_i \cdot \partial E_j / \partial x_i$.

The action of the forces leads to damage the virus surface molecules (up to destruction of virus shell) which can lead to the loose the infection ability of the virus. Sketch of the main stages of the mechanism are shown in Fig. 1.

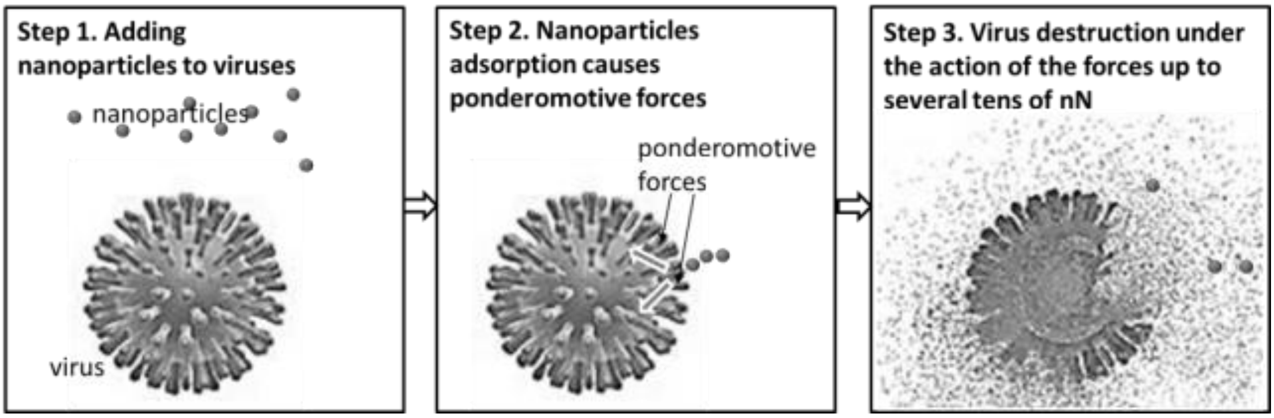

Fig. 1. Sketch of the proposed mechanism of nanoparticles action on the virus

Using approach described in [4] we calculated the adsorption potential in the system, defined the distance between nanoparticles. Then, for this system of two nanoparticles we calculated the local field distribution and the ponderomotive forces distribution. The maximum force acts at nearly the 1 nm inside the virus from its surface. Direction of forces is schematically shown in Fig. 1 and maximum force value is presented in Table 1.

Table 1. System parameters and results of calculation.

Parameter	**System 1**	**System 2**
Virus	Influenza virus H1N1	
Outer radius, nm	60	
Inner radius, nm	50	
Dielectric constant of the virus core	2	
Dielectric constant of the virus shell	4	
Nanoparticle material	Au	
Nanoparticle radius, nm	5	20
Nanoparticle dielectric constant	$10.5+1.3i$	
Ponderomotive force max value, nN	75	5

It can be seen, that for smaller nanoparticle the maximum force value is rather high. If we compare this value with experimental results of study of mechanical properties of viruses, we can see that the maximum ponderomotive force is higher than the force needed for irreversible virus deformation [5]. Consequently, these forces may lead to the virus particle destruction, which can be seen on micrographs of viruses with nanoparticles, e.g. in [2]. Compare of the calculation results, existed experimental results of mechanical properties of viruses, and results of virological experiments with nanoparticles indicate that ponderomotive forces may lead to the destruction of the virus particle. Thus, for example maximum force value in the system with smaller nanoparticle prevails over the forces value for irreversible virus deformation, while in the system with bigger nanoparticle the force is much lower.

1. L. Lu, R.W.Y. Sun, R. Chen, C.K. Hui, C.M. Ho, J.M. Luk, G.K.K. Lau, C.M. Che, Silver nanoparticles inhibit hepatitis B virus replication, *Antiviral Therapy*, Vol. 13, Issue 2, 2008, pp. 253-262.
2. N.A. Mazurkova, Yu.E. Spitsyna, Z.R. Ismagilov, S.N. Zagrebel’nyi, E.I. Ryabchikova, Interaction of titanium dioxide nanoparticles with influenza virus, *Nanotechnologies in Russia*, Vol. 5, 2010, pp. 417-420.
3. V. Lozovski, V. Lysenko, V. Piatnytsia, O. Scherbakov, N. Zholobak, M. Spivak, Physical point of view for antiviral effect caused by the interaction between the viruses and nanoparticles, *Journal of Bionanoscience*, Vol. 6, Number 2, 2012, pp. 109-112.
4. V. Lozovski, N. Rusinchuk, T. Vasiliev, Repulsive Interaction between Two Different-Sized Nanoparticles due to Self-consistency, in *2019 IEEE 39th International Conference on Electronics and Nanotechnology, ELNANO 2019*, Kyiv, Ukraine, 16-18 April 2019, pp. 253-256.
5. P.J. de Pablo, M. G. Mateu, Mechanical properties of viruses, in *Structure and Physics of Viruses*, 2013, pp. 519-551.

ELECTRICAL PROPERTIES OF MERCURY MODIFIED AMORPHOUS SELENIUM

Kyrylenko V.K.[1], **Rubish V.M.**[1], Nykyruy L.[2], Pisak R.P.[1], Durkot M.O.[1], Zapukhlyak Z.R.[2], Fedelesh V.I.[3], Uvarov V.N. [4]

[1] *Institute for Information Recording, NAS of Ukraine,4 , Zamkovi schody St., 88000, Uzhgorod Ukraine*
[2] *Vasyl Stefanyk Precarpathian National University, Ivano-Frankivsk, Ukraine*
[3] *Uzhgorod National University, 3, Narodna sq., 88000, Uzhgorod, Ukraine*
[4]*G.V. Kurdumov Institute of Metal Physics, NASU, 36, Academican Vernadsky Blvd., 036680, Kyiv, Ukraine*

The synthesis and study of semiconductor materials based on II-VI thin films (Zn, Cd and Hg chalcogenides) have attracted considerable attention due to their unique properties. Mercury chalcogenides are technologically attractive materials that can be used in IR detectors, ultrasonic transducers, catalysts, electrostatic reflective materials and solar cells. Limited information about the features of the synthesis and properties of film materials of mercury chalcogenides is explained by the difficulties that arise during their production. Therefore, the development of a simple and reproducible technique for the synthesis of mercury selenide films is an urgent task.

This paper presents the results of studies of the effect of mercury vapor on the electrical resistance *(R)* of amorphous selenium (*a*-Se) thin films.

Studies of the dependences of resistance on the exposure time in mercury vapor were performed in special air-tight boxes on planar structures «Cr layer–*a*-Se – Cr layer» at *T*=288-293 K. *a*-Se with a thickness of 300-700 nm were obtained by vacuum evaporation of vitreous selenium from quasi-closed effusion cells on to unheated glass substrates with a semi-transparent layer of chromium applied.

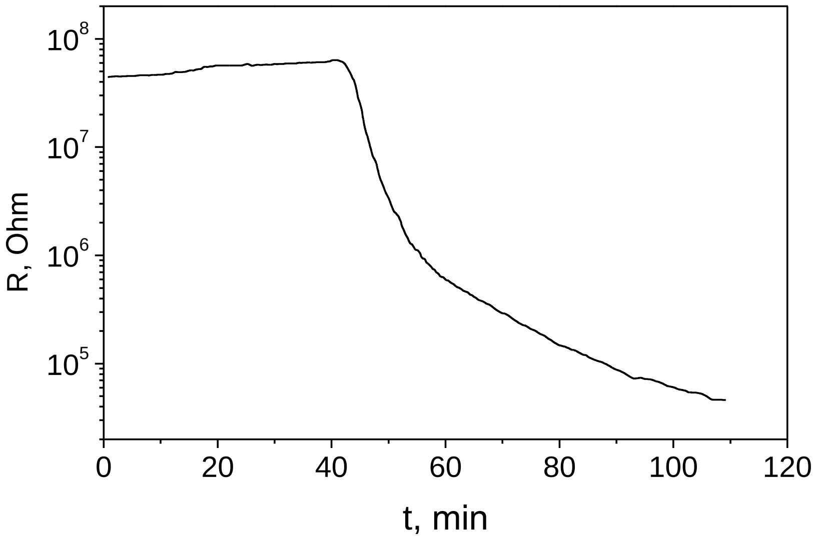

Fig.1. The dependence of the electrical resistance of the sample «Cr layer – *a*-Se – Cr layer» on the exposure time in mercury vapor (explanation in text)

In Fig. 1 the typical dependence of the electrical resistance of the planar sample "Cr layer – *a*-Se –Cr layer" on the exposure time with Se film thickness of 700 nm in vapor of Hg at normal pressure and temperature 288 K for all studied samples is presented. The mercury concentration was 12 mg/m^3 (partial pressure $1.2 \cdot 10^{-3}$ mm Hg). From Fig. 1 it is seen that there is a latent period during which the resistance of the sample remains almost unchanged. Its duration is ~ 40 min.

Further the resistance decreases sharply, with an average rate of change of $3.8 \cdot 10^6$ Ohms/min., by about 2-3 orders of magnitude. In the third part of the curve *R(t)* the rate of change of resistance decreases to 10^3 Ohms/min. The resistance of the sample after 3 hours of exposure time in Hg vapor is $2 \cdot 10^3$ Ohms. Note that the type of dependences *R(t)* and, in particular, the magnitude of the resistance jump depends on the Se film thickness. In addition, modification of Se films with mercury leads to their darkening.

To find out the reason for some increase in the resistance of the sample at the initial stage of measurements (the first 40 minutes), changes were made to the measurement method. The measuring system was connected to the sample only for the time of resistance measurement (approximately 1 s) every 5 minutes. The film thickness of Se was ~ 350 nm. Using this measurement method changes in the resistance of the sample during the latent period are not observed (Fig. 2). The obtained data allow to assume that the measured current, which averages 10^{-12} A, makes some adjustments when measuring samples in a continuous mode (Fig. 1). However, these adjustments make a small contribution to the dependence of the resistance of the samples on the modification time of amorphous selenium by mercury vapor. The main result is the detection of a sharp decrease in the resistance of the sample for a certain exposure time in Hg vapors. In this case, the change in *R* is almost 6 orders of magnitude.

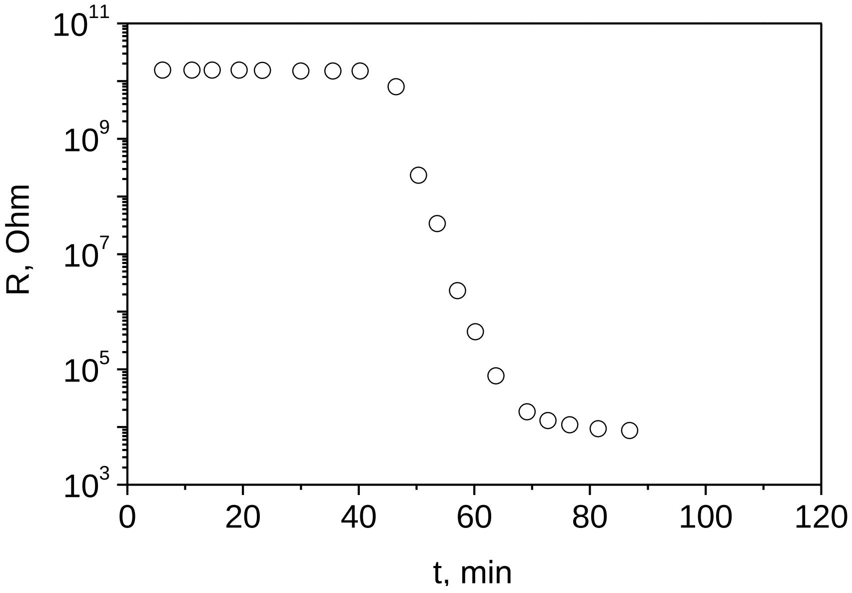

Fig. 2. The dependence of the electrical resistance of the sample «Cr layer – *a*-Se – Cr layer» on the exposure time in mercury vapor (explanation in text)

It is most likely that the main reason for the significant decrease in the electrical resistance of amorphous selenium films during their modification by mercury is the formation in their matrix of nanocrystalline inclusions of mercury selenide.

The obtained results indicate the possibility of using these structures to create highly sensitive mercury vapor sensors.

A STUDY OF REGULARITY THE CLUSTER METAL FORMATION IN OLIGOPHENOLATE

Savchenko D.A., Pashchenko E.A., Kukharenko C.A., Kaidash O.N.

V. Bakul Institute for Superhard Materials of the NAS of Ukraine,
2 Avtozavodska Str., Kyiv, 04074, Ukraine

New generation of composite materials for extreme conditions of operation can be expected from the polymers having gained of curing complex compounds of oligophenylenes with some metals. The structure and properties of oligomers determine the structure and properties of polymers. The highest mechanical properties are characterized by metal polymers for which metal compounds are used, and as anions – sulfates, chlorides, and acetates – are served. It was showed that the nature of the anion affects on the form in which the metal is present in the material — in cluster or ionic form, or in both forms simultaneously. In their opinion, in terms of mechanical properties, the most promising are materials containing the metal in cluster form.

The processes of oligomeric systems formation, containing nanoscale clusters of vanadium, iron, and copper, were studied. In the manufacture of metal-polymer materials, aqueous solutions of vanadium, iron, and copper chlorides, nitrates, acetates, and sulfates (with a salt concentration of 15 g/l) and an oligophenylene solution (100 g/l) were used as starting components. Solutions containing the corresponding anion and metal cation were merged with a solution of hydroquinone at a temperature of 323 K (50 °C), after this an abundant precipitate formed for 10 min, which was filtered off from the residues of the initial compounds that did not react and then dried.

A qualitative assessment of the state of a metal in ionic and cluster form in the oligomer is possible using UV spectroscopy. Its results for vanadium are presented in Figure. It follows from the figure that the use of different types of anions leads to a different ratio of the ionic and cluster forms metals in the material. The results of the study of the proportion of metal contained in cluster form are presented in the Table. The presented data indicate that a decrease in the polarizability of the anion leads to an increase in the amount of metal in cluster form in the oligomer.

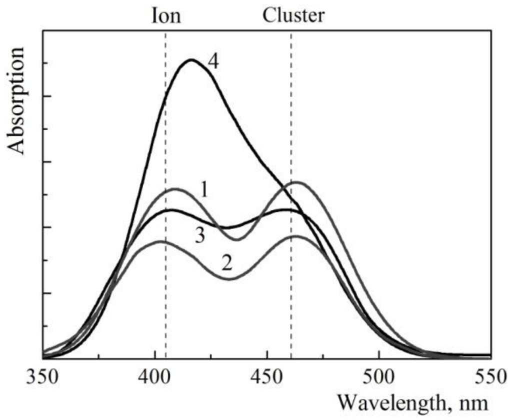

Figure – The content of vanadium in cluster and ionic form in oligophenolate made from: *1*-chloride–, *2*-nitrate–, *3*-sulfate–, *4*-acetate–anion

Table – Proportion of the metal in cluster form in metal-oligomer (in brackets – the anions of the ionic polarizability known from literature)

Metal in the oligo-mer	Type of the anion entering in the initial metal compound:			
	chloride- (2,18 Å^3)	nitrate- (4,67 Å^3)	sulfate- (7,1 Å^3)	acetate- (44,43 Å^3)
V	0.56	0.53	0.51	0.24
Fe	0.67	0.48	0.44	0.11
Cu	0.55	0.50	0.49	0.44

The conditions for their preparation have been optimized, allowing to increase the yield of the reaction product by 1.2–1.6 times. It was shown that the physicochemical nature of the anion in the composition of metal salts determines the equilibrium position between ions and clusters form of metal in the composition of the synthesized oligomers, and anion decrease in the polarizability of the anion by 11.3 times leads to an increase of 2.3–3.2 times in the cluster form metal particles located in the oligomer.

OBTAINING TECHNOLOGY OF HYBRID NANOMATERIALS CARBON NANOTUBES - GRAPHENE NANOPARTICLES

Sementsov Yu.I.[1,2], Ivanenko K.O.[3], Grebelna Yu.V.[2], Kartel M.T.[1,2], Karachevtseva L.A.[1,4], Makhno S.M.[2], Zhuravskyi S.V.[1,2], Wang Bo[1], Yang Weiyou[1]

[1]*Ningbo University of Technology, 201 Fenghua Road, Ningbo, 315211, China*
[2]*O. Chuiko Institute of Surface Chemistry, National Academy of Sciences of Ukraine, 17 General Naumov Str., Kyiv, 03164, Ukraine*
[3]*ISTC "Surface Chemistry" NAS of Ukraine, 17 General Naumov Str., Kyiv, 03164, Ukraine*
[4]*Department of Photonic Crystals, V. Lashkaryov Institute of Semiconductor Physics, NAS of Ukraine, Kyiv, Ukraine*

Graphene, with a high specific area and conductivity, has great potential in many areas, such as electronic devices, solar panels, sensors, supercapacitors and hydrogen storage [1]. However, the practical application of graphene materials is significantly constrained by the agglomeration of graphene sheets due to their strong Van der Waals interactions. One of the best approaches to realize the great potential of graphene for different applications is to add some space between the folded graphene sheets to avoid such rearrangement and agglomeration. At the same time, the filler should contribute to the overall large surface area and electrical conductivity of whole materials [1]. CNTs are an ideal candidate due to their high conductivity, large specific surface area, and, most importantly, their interaction with graphene sheets due to their similar carbon structure [2–5]. By bonding graphene sheets, CNTs can significantly reduce the internal electrical resistance and improve the overall electrical conductivity. Therefore, the production of graphene/CNT hybrids has aroused great interest. In [1] there are three possible structures of hybrids: CNTs lie in the plane of the GNPs, perpendicular to it, and CNTs are wrapped in the GNP. Such structures are formed by different methods [6–11]: “folding” layer by layer, growing CNTs on the surface of GNPs, “unpacking” CNTs on nanobands, etc. However, all methods are quite complex, not always controlled and it is far from technological implementation.

This study proposes an effective cheap technological method for obtaining graphene nanoparticles with controlled size distribution by the anodic oxidation of condensed expanded graphite. And when as a precursor carbon-carbon composite material EG-CNTs [12, 13] using are obtained dispersions of the hybrid composite CNTs-GNPs.

Multiwall carbon nanotubes (MWCNTs) due to their unique mechanical properties and large aspect ratio (length to diameter ~10^3) are the best nanofillers for matrices of various natures. By sacrificing one or more layers of nanotubes, it is possible to modify them by the hetero atoms of various elements by regulating the chemically reactivity of the MWCNTs, i.e. the interaction with the matrixs. To obtain CNTs modified with oxygen by anodic oxidation in sulphuric acid according to the scheme described in [14], were used MWCNTs synthesized by the method of catalytic pyrolysis (CCVD), according to [15], conformed to the requirements of the standard TU U 24.1-03291669-009:2009. According to TEM, X-ray diffraction, and Raman spectroscopy data, the noticeable amount of amorphous carbon was not detected. The state of the CNTs surface was monitored by the XPS method (spectrometer Thermo scientific K-Alpha). Large-scale production of MWCNTs, as a rule, is a CVD-method, which gives CNTs agglomerates in the form of tubes entangled with each other, with the size of 20–500 μm in diameter. We investigated a possibility of deagglomeration of MWCNTs in an ultrasonic disperser UZDN-M900T and universal homogenizer using shear deformation together with the effect of cavitation in an aqueous dispersion in the presence of surfactants. The analysis of the agglomerates was carried out by means of laser correlation spectroscopy (LCS). The particle size distribution function was determined with laser photon correlation spectrometer «Zetasizer-3» (Malvern Instrument, UK).

Effective deagglomeration agent for CNTs are strong acids and oxidizing agents, as reported e.g. in [16]. Therefore, our idea was, to use a simultaneous process of deagglomeration CNTs and intercalation of natural graphite. This procedure was performed by the chemical [14] or electrochemical (anodic) oxidation as in [17]. The obtained product was washed with water to a pH ≈ 6–7 and dried. The dried product is heated to a temperature of 850–1250°C in the thermal shock mode. A composite carbon material was obtained with composition, CNTs 0.1–3.0 wt. %; expanded graphite (EG) is the rest [18, 19]. After cooling, the composite carbon material was rolled into a foil. Under EG anodic oxidation, namely, insertion of anions between crystal layers of graphite, intercalation does not take place. In this case a diffusion of the anions to the structure defects dominates; we call this process as a secondary "intercalation". Thus, the GNP has been prepared by the secondary "intercalation" of the electrodes from EG foil and EG + CNT foil in the alkaline electrolyte (KOH) of low concentration at an electric current ranging of 6–60 mA/cm^2 by the scheme of anodic oxidation (Fig. 1).

As expected, the anodic oxidation in sulphuric acid with a transmission of 80–120 A·h/kg led to efficient deagglomeration of multiwall CNTs. The Fig. 2 shows the distribution of CNTs agglomerates according to the sizes determined by the LCS method. Water dispersion of the composition is stable over time: the average particle size is 50 nm; two fractions – from 20 to 100 nm, the amount – 99.9%, weight – 10%; from 250 to 500 nm, the amount of 0.1%, weight – 90%; high polydispersity ranges from 0.35–0.4, that is, the particles are close enough to spherical shape.

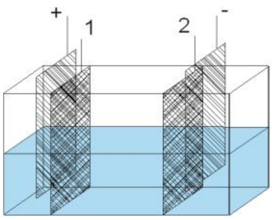

Fig. 1. The scheme of EG anode oxidation: (+) – anode, (-) – cathode, 1 and 2 – polypropylene membranes.

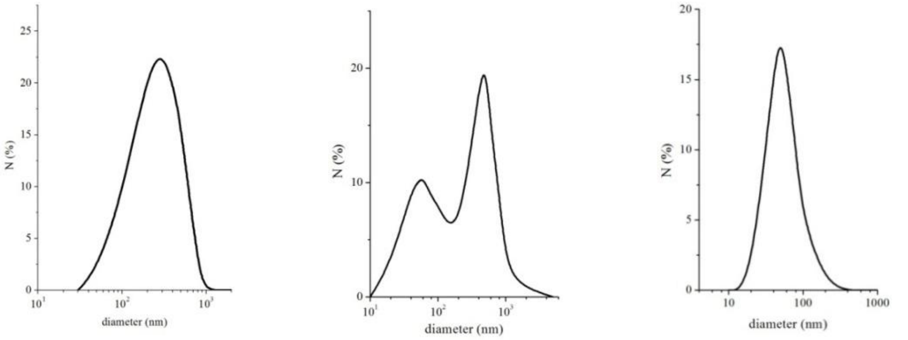

Fig. 2. Averaged particle size distributions in a suspension of CNTs: a – "mono-modal" mode; b – "poly-modal" mode, particle volume distribution (mass if density is constant); c – "poly-modal" mode, particle distribution by number.

According to [17], the transmission the 80–120 A·h/kg of electricity leads to the formation the first stage of an intercalated graphite compounds, which provides a coefficient of expansion of more than 300 times and high-quality roiling material from EG. According to the results of XPS analysis, the chemical state of the surface of samples EG and EG + CNT had the following composition (Table 1). As can be seen from the data in Table 1, the simultaneous oxidation of graphite with CNTs reduces the oxygen content on the surface of the composite material compared to EG.

Table 1. Chemical state of the surface of samples EG and EG + CNT, at. %

Samples	C 1s	O 1s	S 2p
EG	95.15	4.63	0.22
EG+1 % CNT	97.27	2.5	0.22

The structural features of EG of various genesis and EG-CNT nanocomposites were characterized by Raman spectroscopy, the results of which are shown in Table 2. Note that a comparison of the EG spectra obtained from chemically and anodically oxidized graphite (Table 2) shows that EG chemically oxidized graphite has a more defective structure. The G range is biased towards higher frequencies; doubled the ratio of I_D/I_G. Apparently, this is due to peroxidation of graphite matrix. According to Raman spectroscopy (Table 2), the least defective are samples of EG, which was obtained from anodic oxidized graphite. CNTs do not significantly change the Raman spectra of the composition of the material EG-CNTs, which can be explained by their low content ~ 1% wt. For rolled materials EG and TEG + CNTs, the thermal diffusivity was determined according to the method described in [20]. This value was commensurable to the thermal diffusivity of pyrolytic graphite and slightly increases at low CNTs content (Table 3).

In Fig. 3 shows the TEM image of the sample EG-CNTs. As it is well visible CNTs "built in" in a matrix of EG. According to the scheme shown in Fig.1, anodic oxidation was performed

Table 2. The main parameters of the characteristic bands manifested in the micro-cattle spectra of EG of different genesis, CNTs and EG-CNT composites

Samples, synthesis condition	EG		EG + CNTs		Initial CNTs
	Chemical oxidized, $K_2Cr_2O_7$	Anodic oxidized, 55% H_2SO_4	Chemical oxidized, $K_2Cr_2O_7$	Anodic oxidized, 94 % H_2SO_4	
D, см$^{-1}$	1378	1374	1377	1375	1348
G, см$^{-1}$	1602	1598	1598	1597	1573
2D, см$^{-1}$	2794	2752	2748	2737	2706
D_{FWHM}, см$^{-1}$	89	-	-	51	51
G_{FWHM}, см$^{-1}$	53	18	22	23	53
I_D, від. од.	8,1	3	14	5,0	9,0
I_G, від. од.	11,1	117	126	33,6	10,4
I_D/I_G	0,73	0,03	0,11	0,15	0,86

Table 3. Thermal diffusivity of carbon materials samples, m^2/s

Samples	EG, ρ, g/cm^3		EG+1%CNTs, ρ, g/cm^3		Pyrolytic graphite layers [21]	
	1.0	1.4	1.0	1.4	normal	parallel
α, m^2/s	$1.14{\cdot}10^{-4}$	$1.81{\cdot}10^{-4}$	$2.45{\cdot}10^{-4}$	$1.82{\cdot}10^{-4}$	$3.6{\cdot}10^{-6}$	$1.22{\cdot}10^{-3}$

and graphene nanoparticles were obtained. LCS particle size analysis (Fig. 4) showed that the GNP sample contains two types of particles – large particles (13 microns), which soon precipitate, and smaller ones of about 450 nm in size being more stable. In the approach of spherical particles, minimal sizes for small particles fraction is 8–12 nm, maximum size is 130–300 nm and the dominant size is 35–55 nm depending on the anodic oxidation conditions. For the big size particles fraction these values are 130–300, 3200–70000 and 640–16500 nm, respectively. This result shows the possibility of controlling the particle size due to the technological parameters of oxidation and by controlling the structure of the EG itself. In the case of using foil filled with carbon nanotubes, the size of such particles is different, see Fig. 5. The resulting particles can be precipitated and obtain films of graphene nanoparticles (Fig. 6).

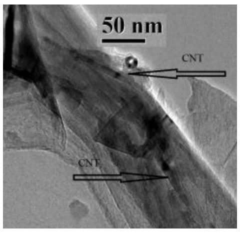

Fig. 3. TEM images of EG + CNTs samples

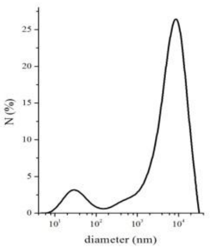

Fig. 4. The particle size distribution in suspension of GNPs.

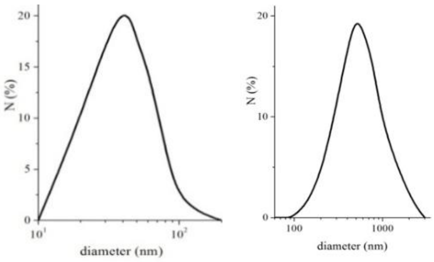

Fig. 5. Particle size distribution: left GNPs, right GNPs + CNTs

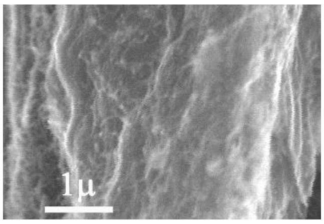

Fig. 6. Films of GNPs + CNTs

The measurement of thermal diffusivity and thermal conductivity of such films is the next task. In Fig. 7 shows typical Raman spectra of EG samples and GNP films. Structural differences are obvious. The intensity of the 2D band for GNP film samples exceeds the G band intensity (1.12 times), which unequivocally confirms that these samples belong to multilayer graphene nanoparticles.

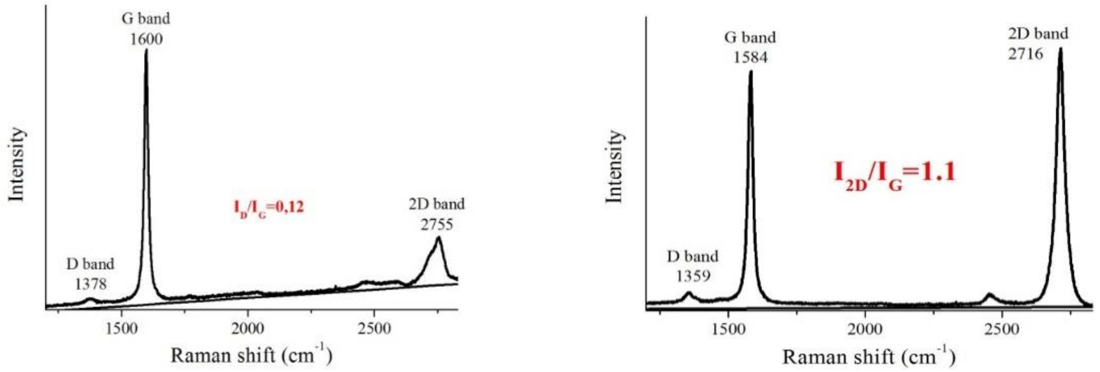

Fig. 7. Raman spectra of EG samples and GNP films

The results of the study of frequency conductivity in the range of 10^{-2}–10^{5} Hz of the GNP disperse system, which indicates its linear increase in frequency. This means the main contribution of electrons to conductivity and the absence of an ionic conductivity component. Thus, modification of multiwall CNTs with oxygen simultaneously with anodic oxidation of natural dispersed graphite allowed to create for the first time a carbon-carbon composite EG-MWCNTs with improved physical and mechanical characteristics without additional use of binders. The cheap technology for the production of GNP by anodic oxidation of solid EG with controlled parameters and particle size distribution from tens to thousands of nanometers and a thickness of ten or more layers of graphene was developed. GNP particles obtained by the developed technology have a good graphite structure and metallic properties. Anodic oxidations for the developed technique allow to obtain composite stable dispersions of nanoparticles of multilayer graphene with carbon nanotubes, which are promising materials for filling matrices of different nature.

1. Fan W, Zhang L, Liu T 2017 Graphene-Carbon Nanotube Hybrids for Energy and Environmental Applications. Springer Briefs in Molecular Science. doi:10.1007/978-981-10-2803-8
2. Nardecchia S, Carriazo D, Ferrer M L, Gutierrez M C, del Monte F 2013 Three-dimensional macroporous architectures and aerogels built of carbon nanotubes and/or graphene: synthesis and applications *Chem Soc Rev* **42** 794
3. Kong H X 2013 Hybrids of carbon nanotubes and graphene/graphene oxide. *Curr Opin SolidState Mater Sci* **17** 31
4. Mani V, Chen S M, Lou B S 2013 Three-dimensional graphene oxide-carbon nanotubes and graphene-carbon nanotubes hybrids. *Int J Electrochem Sci* **8** 11641
5. Lee W J, Maiti U N, Lee J M, Lim J, Han T H, Kim S O 2014 Nitrogen-doped carbon nanotubes and graphene composite structures for energy and catalytic applications *ChemCommun* **50** 6818
6. Shakir I 2014 High energy density based flexible electrochemical supercapacitors from layer-by-layer assembled multiwall carbon nanotubes and graphene. *Electrochim Acta* **129** 396
7. Wang S C, Yang J, Zhou X Y, Li J 2013 Layer-by-layer assembled sandwich-like carbon nanotubes/graphene oxide composite as high-performance electrodes for lithium-ion batteries *Int J Electrochem Sci* **8** 9692
8. Liu Y, Liu Y, Feng H B, Wu Y M, Joshi L, Zeng X Q, Li J H 2012 Layer-by-layer assembly of chemical reduced graphene and carbon nanotubes for sensitive electrochemical immunoassay *Biosens Bioelectron* **35** 63
9. Kim Y K, Min D H 2009 Durable large-area thin films of graphene/carbon nanotube double layers as a transparent electrode *Langmuir* **25** 11302

10. Hong T, Lee D W, Choi H J, Shin H S, Kim B 2010 Transparent, flexible conducting hybrid multilayer thin films of multiwalled carbon nanotubes with graphene nanosheets *ACS Nano* **4** 3861
11. Yu D S, Dai L M 2010 Self-assembled graphene/carbon nanotube hybrid films for supercapacitors *J Phys Chem Lett* **1** 467
12. CN Patent No ZL 2015 1 0372161.8 (26 April, 2017)
13. CN Patent No ZL 2015 1 0372162.2 (03 May, 2017)
14. Sementsov Y I et al. 2019 Expanded graphite and its composites. Akademperiodyka
15. Melezhik A V, Sementsov Y I, Yanchenko VV 2005 Synthesis of Fine Carbon Nanotubes on Coprecipitated Metal Oxide Catalysts *Russ J Appl Chem* **78** 917
16. Wang Z, Shirley M D, Meikle S T, Whitby R L D, Mikhalovsky S V 2009 The surface acidity of acid oxidised multi-walled carbon nanotubes and the influence of in-situ generated fulvic acids on their stability in aqueous dispersions *Carbon* **47** 73
17. Kartel M, Sementsov Y, Makhno S, Weijun Zhang, Xiaochen Zhang, Li Vei Gen, Bo Wang 2017 Electrochemical reactor and process conditions for the continuous oxidation of natural graphite with a capacity of 10 kg/hour *Intern. Journal of Innovative Science, Engineering & Technology* **4** 203
18. CN Patent application No 201911247529.2 (09.12.2019)
19. CN Patent application No 201911247536.2 (09.12.2019)
20. Sun J G 2010 Thermal Conductivity Measurement for Thermal Barrier Coatings Based on One- and Two-sided Thermal Imaging Methods *AIP Conference Proceedings* **1211** 458
21. https://www.engineersedge.com/heat_transfer/thermal_diffusivity_table_13953.htm

This work was supported by the Target Program of Basic Research of the National Academy of Sciences of Ukraine "Prospective Basic Research and Innovative Developments of Nanomaterials and Nanotechnologies for the Needs of Industry, Health Care and Agriculture".

THE MECHANISMS AND DYNAMICS OF ANTIOXIDANT ACTION OF NANOCERIA AND CERIA-BASED NANOPARTICLES

Vladyslav Seminko, Pavel Maksimchuk, Ganna Grygorova, Elena Okrushko, Yuri Malyukin

Institute for Scintillation Materials NAS of Ukraine, 60 Nauky ave, Kharkiv, Ukraine

Reactive oxygen species (ROS), such as O_2^- (superoxide anions), H_2O_2 (hydrogen peroxide), and $^{\cdot}OH$ (hydroxyl radicals) are biologically active molecules formed inside the mitochondria of living cells during cellular respiration. ROS play an important role as cell signalling molecules, and are indispensable during immune response. However, an increase in ROS concentration can lead to cell damage known as oxidative stress. Prevention of oxidative stress is usually provided by internal cell systems such as enzymes (superoxide dismutase and catalase) and antioxidant molecules (such as ascorbic acid). For instance, the content of hydrogen peroxide can be regulated by catalase which decomposes it to water and molecular oxygen. Catalase-like redox activity of ceria nanoparticles allowing them to decompose hydrogen peroxide via the same way as catalase ($2H_2O_2 \rightarrow 2H_2O + O_2$) was shown recently in the number of studies. At the same time, the mechanisms of ROS decomposition by ceria nanoparticles proposed by different authors are sufficiently different [1].

The methods of optical spectroscopy were used to study the mechanisms of formation of defect centers in cerium oxide nanocrystals and mixed oxides. The influence of defect structure on the mechanisms of antioxidant activity of nanocrystals was revealed, and possible ways to control both the defect structure and antioxidant properties of nanoparticles were shown. Several types of defect centers (Ce^{3+} - V_o -Ce^{3+} complexes, F^0- and F^+-centers) were observed, the ratio of which in cerium oxide nanocrystals depends on the atmosphere of heat treatment, the size of the nanocrystals, and concentration of impurity ions [2].

The antioxidant activity of ceria and ceria-based mixed (CeO_2 - Re_2O_3 (Re = Y, Eu, Tb), CeO_2-ZrO_2) colloidal nanoparticles depends strongly on the temperature, size of nanoparticle, type and concentration of doped ions, and laser irradiation. The key role of Ce^{3+}-V_o-Ce^{3+} complexes in H_2O_2 decomposition by ceria-based nanoparticles was revealed. While for CeO_2-ZrO_2 nanoparticles the rate of H_2O_2 decomposition was higher than in CeO_{2-x} nanoparticles, for other mixed nanocrystals the sufficient slowing-down of H_2O_2 decomposition was observed. This effect was explained by the main role of Ce^{3+}-V_o-Ce^{3+} complexes in the processes of hydrogen peroxide decomposition, which role is similar to the role of active sites of enzymes. The number of Ce^{3+}-V_o-Ce^{3+} complexes increases at Zr^{4+} incorporation due to increase of the content of oxygen vacancies, but decreases at incorporation of isovalent ions (Y^{3+}, Eu^{3+}, Tb^{3+}) leading thereby to higher or lower rate of H_2O_2 decomposition, respectively. On the contrary, for hydroxyl radicals ($^{\cdot}OH$) and superoxide anions (O_2^-) the antiradical activity of ceria nanoparticles is determined not by the content Ce^{3+}-V_o-Ce^{3+} complexes, but merely by Ce^{3+}/Ce^{4+} ratio on the nanoceria surface. The continuous laser irradiation with specific wavelengths leads to formation of additional oxygen vacancies, and so, of additional Ce^{3+}-V_o-Ce^{3+} complexes providing better antioxidant activity of pre-irradiated ceria nanoparticles [3].

1. Reed K., Cormack A., Kulkarni A. [et al.]. Exploring the properties and applications of nanoceria: is there still plenty of room at the bottom? // Environmental Science: Nano, 2014. – V. 1. – N. 5. – P. 390-405.
2. Seminko V., Maksimchuk P., Bespalova I. [et al.]. Defect and intrinsic luminescence of CeO_2 nanocrystals // Phys. Status Solidi B., 2017. – V. 254.– P. 1600488:1-6.
3. Klochkov V.K., Malyukin Yu.V., Grygorova G.V. [et. al.] Oxidation-reduction processes in CeO_{2-x} nanocrystals under UV irradiation // Journal of Photochemistry and Photobiology A: Chemistry, 2018. – V. 364.– P. 282-287.

INFLUENCE OF MELTS ELECTROLYSIS CONDITIONS ON THE PHYSICAL AND CHEMICAL PROPERTIES OF MOLYBDENUM CARBIDE NANOSTRUCTURED POWDERS AND COATINGS

Gab A.I., Malyshev V.V., Shakhnin D.B., **Shiray Zh.V.**

Open International University of Human Development “Ukraine”, 26, Lvivska St., 03115 Kyiv, Ukraine

To date, the processes of electroplating of VI-B group metals from ionic melts are sufficiently well developed. Their preparation as cathodic deposits of a definite form is determined by the electrolyte composition and the choice conditions for the electrolysis. Many electrodeposition processes are still in the stage of their introduction into industry and semi-industrial tests. Present work is logical continuation of this new promising trend in industrial electrochemistry.

Experiments were performed in a hermetic electrolytic cell. Na_2WO_4-3mol%MoO_3, Na_2WO_4-5mol%WO_3 and Na_2WO_4-Li_2WO_4-10mol%WO_3 molten mixtures were used as electrolytes, respectively. The coatings were investigated metalographically. The grain size was observed by MIM8M and Hitachi 800 microscopes on the cross-section at 40-50 μm from the substrate. The microhardness was measured with PMT-3 device by applying 100 g indenter on the cross-section. The texture of coatings was studied by DRON-2 and X-ray diffractometers. The faceting of coating surfaces was determined by an optical goniometer.

Atmosphere above the bath for deposits obtaining from melts. The change of atmosphere from air to argon over the bath does not influence practically on the grain size. In both cases coatings are non-textured or possess very low <111> texture. The only difference was the formation of more smooth surface with argon atmosphere over the bath. Such similarity could arise because, in the equilibrium with the melt, the metal exists in the form of oxygen-containing anions within the highest oxidation state, and oxygen solubility in such melts appears to be low. Therefore, air-to-argon replacing does not change the melt composition and, practically, does not influence the electrodeposition process.

On the contrary, introduction of CO_2 into the electrolytic cell strongly influences the molybdenum (tungsten) deposits structure, particularly decreasing grain size. Increase of CO_2 partial pressure during the electrolysis of Na_2WO_4-Li_2WO_4-10mol% WO_3 melt at 1023K leads to co-electrodeposition of tungsten powder and carbon powder on cathode.

At 1173 K, compact deposits of molybdenum and tungsten were obtained with CO_2 concentration up to 100 vol %. However, at the same temperature, carbon appears at the cathode (up to 1 wt %) from Na_2WO_4-WO_3 melt with CO_2 content more than 25 vol % . It could be related to a higher basicity of the melt containing sodium tungstate. In such a melt, activity of oxygen ions at the same WO_3 concentration is higher than that for Na_2WO_4– Li_2WO_4 melt.

Both of molybdenum and tungsten deposits keep columnar structure up to 60-70vol% CO_2. The microhardness of deposits increases with increasing CO_2 content in atmosphere of electrolytic cell.

Addition of CO_2 to atmosphere over tungstate-molybdate melts changes deposits structure. For example, at 1123 K and, as it is especially visible, at 1273 K, under 10-40 vol% CO_2, obtained coatings are mainly oriented with <100> direction perpendicular to substrate. Under CO_2 containing atmosphere, grain size decrease allows to obtain molybdenum and tungsten coatings with thickness up to 1-1.5 mm.

The current impulse. Besides CO_2 atmosphere application, another possibility for grain size decrease is to use current impulses at the beginning of electrolysis or during whole process. Pulse electrodepositions have been performed from both Na_2WO_4-3 mol% MoO_3 and Na_2WO_4-5 mol % WO_3 melts. Nickel plate has been used as a substrate. Current impulses were created by special A-quad-B pulse generator. Cathode direct current density was 7.5×10^{-2} A/cm^2 in all experiments.

In the case of cathode impulse applying at the beginning of electrolysis procedure, decrease of grains size has been observed. For example, at 30A/cm^2 impulse amplitude and 40-50 ms duration, their size decreases from 10-14 μm down to 3-5 μm. Such a grain size decrease is, possibly, a cause of minor increase of coating microhardness from 220 up to 280 kG/mm^2 for molybdenum and from 380 up to 440 kG/mm^2 for tungsten.

X-Ray investigations have shown that starting impulses up to 30A/cm^2 do not influence on coating particles orientation. Regardless of starting impulses application, molybdenum and tungsten coatings have prevailing <110> orientation. Applying current impulses up to 30A/cm^2 increases layers defectiveness only which can be explained by arising of new metal crystallization centres on each coating grain. Using impulses with amplitude more than 50 A/cm^2, obtained coatings become spongy with a weak cohesion to the substrate. Possibly, it is typically for the conditions of practically complete disappearing of dimolybdate and ditungstate ions from cathode region. Coating type may depend on realization of secondary reduction of $M_2O_7^{2-}$ ions by sodium atoms primarily forming on cathode and then diffusing from its surface into near-electrode area.

For applied electrochemistry, it is convenient to use such inexpensive, non-aggressive, non-hygroscopic solvents as equimolar KCl-NaC1 and NaCl-Na_3AlF_6 melts. Stability in air, compatibility with aluminium oxide and electrolytic cell constructional materials allowing electrolysis realization in open cell with dissolving tungsten (molybdenum) anodes, and also relative environmental safety are advantages of such melts. In these electrolytes, refractory metals can be deposited onto graphite, copper, and nickel. However, in case of steel substrate, inadherent, complicated composition coatings appear.

Electrolysis conditions and parameters. An important condition of a strong coating-to-substrate cohesion is that the corrosion potential should be more positive than deposition potential. Therefore, for evaluation of the possibility of tungsten coatings deposition onto different substrates, standard potentials of copper, nickel, steel 3, stainless steel, and titanium relative to KCl-NaCl-2.5mol % $PbCl_2$ | Pb, NaCl-5mol % Na_2WO_4 | O_2, Pt and Na_2WO_4-20 mol % WO_3 | O_2, Pt half-cells were measured. The potential of tungsten deposition is more negative than copper and nickel corrosion potential in KCl-NaCl-Na_2WO_4-$NaPO_3$ and NaCl-Na_3AlF_6-Na_2WO_4 melts, which causes a possibility of successful coating deposition. However, this potential is still more positive than steel corrosion potential, and tungsten deposits under such conditions as inadherent powder. In Na_2WO_4-B_2O_3, Na_2WO_4-$NaPO_3$, and Na_2WO_4-$Na_2S_2O_7$ melts, standard potentials of all electrodes are more positive than potential of tungsten deposition, and coatings appear to be coherent. These rules relate completely to the same molybdates melts and molybdenum electrodeposition.

Tungsten electrodeposition has been performed from halide-oxide (KCl-NaCl-Na_2WO_4-$NaPO_3$, NaCl-Na_3AlF_6-Na_2WO_4(WO_3)) and oxide (Na_2WO_4-B_2O_3, Na_2WO_4-$NaPO_3$, and Na_2WO_4-$Na_2S_2O_7$) electrolytes. We have investigated influence of tungstate and oxygen ions concentration, temperature, cathode current density, and time of electrolysis on coatings composition and structure. Optimal deposition parameters have been selected. Standard electrodes KCl-NaCl-2.5 mol % $PbCl_2$ | Pb at 1023 K in halide-oxides melts and Na_2WO_4 - 0.2 mol % WO_3 | O_2, Pt at 1173 K in oxide melts were used.

Influence of tungstate and oxygen ions concentration. Tungsten coatings can be deposited from KCl-NaCl-Na_2WO_4-$NaPO_3$ melts with $0.02<[PO_3^-]/[WO_4^{2-}]<0.18$ ratio. At Na_2WO_4 concentrations lower than 0.1 mol %, inadherent coatings with traces of phosphides were formed; at Na_2WO_4 concentrations higher than 10 mol %, powders were obtained with tungsten oxides peaks on X-ray patterns. At $[PO_3^-]/[WO_4^{2-}]\geq0.18$ ratio, tungsten and their phosphides were obtained, and no coherent coating was formed. Tungsten coatings were deposited from NaCl-Na_3AlF_6- Na_2WO_4 melts with sodium tungstate concentration within 1-15 mol % range. At higher concentrations, tungsten dioxide and tungsten bronzes appeared. From Na_2WO_4-B_2O_3 electrolyte, tungsten was deposited at B_2O_3 concentration below 10 mol %. At higher boron concentrations, powders were formed with tungsten oxides and tungsten bronzes appeared on X-ray patterns. From

Na_2WO_4-$NaPO_3$ melts, tungsten coatings were obtained at phosphate concentration within 0.5-15.0 mol % range. At higher concentrations, tungsten bronzes appeared simultaneously with tungsten, and coating was quickly transformed to dendrites. From Na_2WO_4 - 2.5-12.5 mol % $Na_2S_2O_7$ melts, tungsten was deposited. With higher $Na_2S_2O_7$ concentrations, deposited coatings contained tungsten dioxide and tungsten sulphides as by- products.

Electrolysis temperature. Compact tungsten coatings were obtained from halide-oxide melts at 973-1073 K with current density up to 0.25 A/cm^2. At higher temperatures, melt becomes unstable and more volatile. At temperatures lower than 973 K, only thin (up to 5 μm) tungsten layers can be obtained, and coating was quickly transformed to powder. At higher current densities, only disperse tungsten powders can be obtained.

In the case of oxide melts, compact tungsten coatings were obtained at 1023-1123 K with current density up to 0.40 A/cm^2. At temperatures lower than 1023 K, thin tungsten layers (up to 15-20 μm) can be obtained. At current densities higher than 0.40 A/cm^2, thin tungsten powders with specific surface up to 40-50 m^2/g were obtained.

Cathode current density and electrolysis duration. Influence of cathode current density and electrolysis duration on deposits structure was studied in KCl-NaCl-2.5 mol % Na_2WO_4 -0.35 mol % $NaPO_3$, NaCl-Na_3AlF_6-7.5 mol % Na_2WO_4, Na_2WO_4-5 mol % $NaPO_3$, and Na_2WO_4-5 mol % $Na_2S_2O_7$ electrolytes. Compact coatings with good adherence to substrate were obtained at 923-1173K with current densities values within 0.01-0.15 and 0.03-0.25 A/cm^2 range from halide-oxide and oxide electrolytes, respectively. Coating grains sizes decrease with increasing of current density. However, at current density higher than 0.25 A/cm^2, substantial increase in grain size and roughness was observed, which leads to coating-to-dendrites transformation. At current density values lower than 0.025 A/cm^2, corrosion rate exceeds that of coating formation, and no coherent coating was formed. Tungsten deposition rate within studied interval of current densities was 5-15 μm/h for halide-oxide melts and 20-45 μm/h for oxide electrolytes, and current yield of tungsten in coating form appears to be up to 60 % and 95 %, respectively. With increase of electrolysis period, the current yield drops down.

Using reverse regime of deposition. Profile measurements results show that coatings thickness increase leads to increase in grain size. It was desirable to decrease grain size using reverse deposition regime. Cathode processes duration was changed within 15-50 s range, anode period duration was 0.5-3.0 s, and current density was 0.2-0.5 A/cm^2. For example, optimal conditions for Na_2WO_4-5 mol % $NaPO_3$ electrolyte at 1173 K were as follows: i_c = 0.15 A/cm^2, i_a = 0.30 A/cm^2, τ_c = 25 s, τ_a = 1.5 s. As a result, relatively smooth cathode coatings with thickness up to 0.5 mm have been obtained.

CONCLUSIONS.

Electrodeposition of molybdenum and tungsten coatings from halide-oxide and oxide melts was studied, and coatings structure control methods were proposed.

Replacement of air atmosphere by inert one over electrolytic bath does not practically influence deposits structure and grains size. Carbon dioxide introduction into electrolysis atmosphere significantly alters coatings structure toward deposit grains size decrease and co-deposition of carbon powder and W(Mo) powder.

Possibility of deposits grains size decrease and microhardness improve during current impulses application both at the beginning and during the whole electrolysis process was demonstrated. Current impulses up to 30 A/cm^2 do not affect deposit orientation. With impulses amplitude more than 50 A/cm^2, deposit becomes dendritic and loosely coherent with substrate.

Conditions (melt composition, electrolysis temperature, cathode current density and process duration) of continuous coherent coatings obtaining were defined.

Method of coatings structure improvement towards finer grains formation by means of reverse deposition mode was proposed.

PHOTOCHEMICAL SYNTHESIS OF METAL-SEMICONDUCTOR COMPOSITES BASED ON CRYSTALLINE GRAPHITIC CARBON NITRIDE FOR PHOTOCATALYTIC HYDROGEN PRODUCTION

Shvalagin V.V., Korzhak A.V., Kutsenko O.S., Kuchmiy S.Ya.

L.V. Pisarzhevskii Institute of Physical Chemistry of the National Academy of Sciences of Ukraine,
Prospect Nauki 31, Kyiv 03028, Ukraine; e-mail: vitaliy.shvalagin@gmail.com

By photoreduction of metal ions on the surface of crystalline graphite carbon nitride (CGCN) [1] under visible light, a series of metal-semiconductor nanocomposites (CGCN/Au, CGCN/Pd, CGCN/Pt) with the size of the metal nanoparticles of ca. 10 nm was obtained (Fig. 1). The structure and optical properties of the obtained nanocomposites were investigated. It was shown that the obtained composite materials, unlike the mechanical mixture of semiconductor-metal, exhibit high photocatalytic activity in the process of hydrogen evolution from aqueous solutions of alcohols under visible light. It was established that this feature of the composites may be related to the change in the chemical composition of the semiconductor during metal particles photo-deposition. It was shown that the activity of the obtained composite photocatalysts depends essentially on the nature of the metal, its content, and electron donor solution. For the most active CGCN/Pt nanocomposite under optimal conditions, the "Apparent quantum yield" of hydrogen production at 405 nm was about 54%.

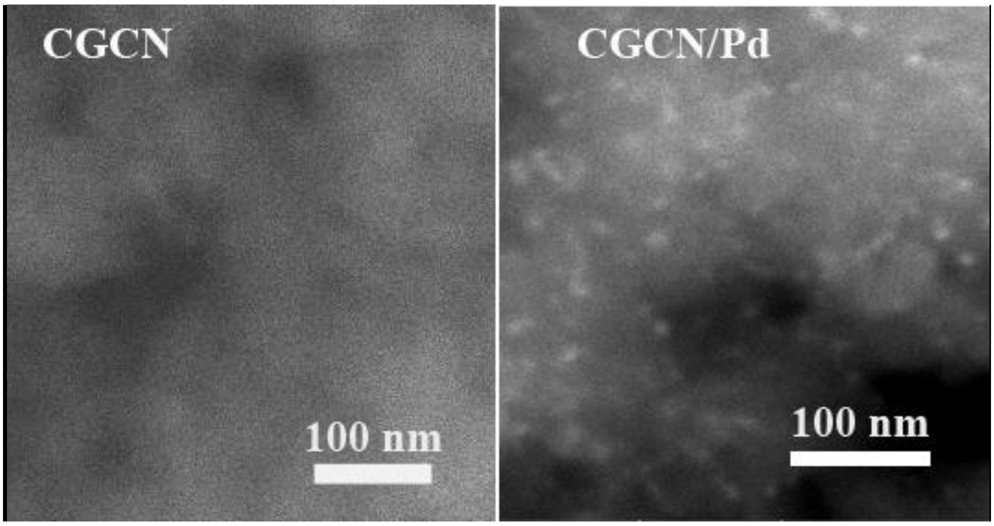

Fig. 1 SEM image of CGCN and CGCN/Pd(0.6%) nanocomposite. Light Dots - Pd Nanoparticles.

Acknowledgments

This research was supported by the General Research Project of the L.V. Pisarzhevskii Institute of Physical Chemistry NAS of Ukraine (funded by the National Academy of Sciences of Ukraine) (project No IPC-A-3-2020) and target program of basic research of NAS of Ukraine «Promising basic research and innovative development of nanomaterials and nanotechnologies for the needs of industry, health care and agriculture» (project No 26/20-N).

1. V. Shvalagin, G. Korzhak, S. Kuchmiy, M. Skoryk, O. Selyshchev, D. Zahn, J. Photochem. Photobiol. A Chem. 390 (2020) 112295.

SAPATIALLY MODULATED PHASES IN ANTIFERRODISTORTIVE MULTIFERROICS

Anna N. Morozovska[1,2], Eugene A. Eliseev[3], Deyang Chen[4], **Vladislav Shvetz**[2],
Christopher T. Nelson[5], and Sergei V. Kalinin[5]

[1] *Institute of Physics, National Academy of Sciences of Ukraine, 46, pr. Nauky, 03028 Kyiv, Ukraine*
[2] *Taras Shevchenko Kyiv National University, Physics Faculty, Kyiv, Ukraine*
3 Institute for Problems of Materials Science, National Academy of Sciences of Ukraine, Krjijanovskogo 3, 03142 Kyiv, Ukraine
[4]*Institute for Advanced Materials and Guangdong Provincial Key Laboratory of Optical Information Materials and Technology, South China Academy of Optoelectronics, South China Normal University, Guangzhou 510006, China*
5 The Center for Nanophase Materials Sciences, Oak Ridge National Laboratory, Oak Ridge, TN 37831

The physical understanding what is the nature of spatially modulated phases (SMP) in rare earth doped antiferrodistortive multiferroics and how they behave close to surfaces and interfaces are still absent. The emergence of SMP in the vicinity of morphotropic phase transition in $La_xBi_{1-x}FeO_3$ (x~0.2) is explored on the atomic level using high resolution Scanning Transmission Electron Microscopy [1].

The suppression, or “melting”, of the SMP in the vicinity of the domain wall surface junction is observed experimentally in $La_{0.22}Bi_{0.78}FeO_3$ (BFO:La) films and simulated in the framework of thermodynamic Landau-Ginzburg-Devonshire (LGD) theory.

We consider a BFO:La film of thickness h placed in a perfect electric contact with conducting bottom electrode that mechanically clamps the film at the surface $x_2 = 0$. The top surface of the film ($x_2 = h$) is mechanically free and partially electrically open, e.g. it can be separated from the top electrode by an ultra-thin gap, or covered with the surface screening charge.

The system of coupled Euler-Lagrange equations allowing for Khalatnikov relaxation of the oxygen tilt and polarization components, Φ_i and P_i , is:

$$\frac{\delta G_{LGD}}{\delta P_i} = -\Gamma_P \frac{\partial P_i}{\partial t}, \qquad \frac{\delta G_{LGD}}{\delta \Phi_i} = -\Gamma_\Phi \frac{\partial \Phi_i}{\partial t}. \qquad \text{(1a)}$$

Here i=1, 2, 3. Equations (1a) are supplemented by the boundary conditions of zero generalized fluxes at the film boundaries,

$$\left. b^{(S)}\Phi_i + v_{ijkl}\frac{\partial \Phi_j}{\partial x_k} n_l \right|_{x_2=0,h} = 0, \quad \left. a^{(S)} P_i + g_{ijkl}\frac{\partial P_j}{\partial x_k} n_l \right|_{x_2=0,h} = 0. \qquad \text{(1b)}$$

Elastic problem formulation is based on the modified Hooke's law obtained using the thermodynamic relation $u_{ij} = -\frac{\delta G_{ELS}}{\delta \sigma_{kl}}$, where u_{ij} are the components of elastic strain tensor. Mechanical equilibrium conditions are $\partial\sigma_{ij} / \partial x_j = 0$. The film-substrate interface is strained, because misfit strain close to -1% corresponds to BFO:La/STO pair.

Distributions of nonzero tilt components Φ_1 and Φ_2 AFD order parameter**,** FE polarization components P_1 and P_2, elastic stress and electric potential were simulated by FEM near the 109°twin-wall surface junction in BFO: La by LGD-approach. We superposed a random seeding at a regular 109° twin-wall and studied the system relaxation to an equilibrium state. We imposed natural boundary conditions for polarization components, and regarded that tilts are zero at both surfaces. Results of FEM are shown in **Fig. 1,** where we showed the final equilibrium state.

FEM simulations for BFO:La exhibit spatially modulated distributions of tilts and polarization components throughout the entire film**.** The modulation period (about 0.4 nm) is conditioned by the system tendency to minimize the imbalance between the gradient and depolarization energies. Since the period coincides with a lattice constant, the SMP mimic AFE phase. Φ_1 has the same sign, while Φ_2 has different sign on opposite sides of the wall (compare **Figs. 1a** and **1b**). Elastic stress is concentrated in the modulation rather than at domain wall (see **Fig. 1c**). With respect to Φ the SMP is rippled, because a nonzero background dominates. Since P_1 and P_2 (as well as φ) have different signs on opposite sides of the wall (see **Figs. 1d**-**f**), the SMP is complete with respect to **P**, because any background is absent.

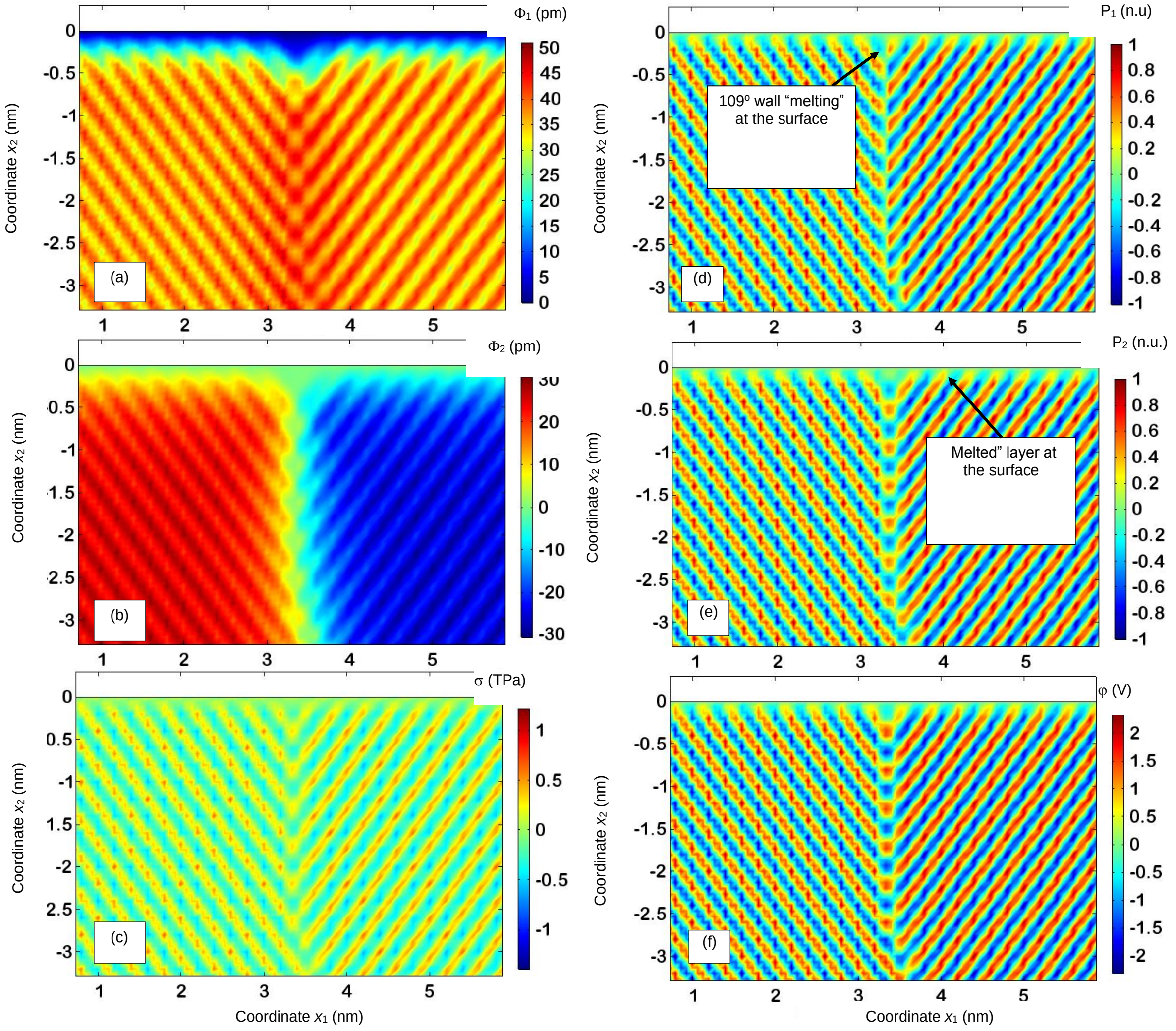

Fig 1. Distribution of tilts **Φ (a-b**, in pm**),** hydrostatic pressure σ **(c**, in TPa**),** polarization **P (d-e**, in normalized units), and electrostatic potential φ **(f,** in Volts**)** near the twin-wall surface junction in a 10-nm BFO:La film. Here we supposed natural boundary conditions for polarization components and zero tilts at the surfaces. BFO:La parameters are listed in Ref.[1].

The spatial modulation of polarization "melts" across the AFD-FE wall, and the melting effect becomes more pronounced when the wall approaches the surface**.** The origin for the melting effect is the system tendency to reach optimal balance between the gradient-correlation and electrostatic energy of the long-range stray electric fields outside the film and related depolarization effects inside it. The observed behavior provides insight to the origin of SMPs in antiferrodistortive multiferroics.

1. N. Morozovska, E. A. Eliseev, D. Chen, V. Shvetz, C. T. Nelson, and S. V. Kalinin. Melting of Spatially Modulated Phases in La-doped $BiFeO_3$ at Surfaces and Surface-Domain Wall Junctions (http://arxiv.org/abs/1910.05730)

FEATURES OF PHOTOELEKTRON SPEKTRUM OF As(Sb)-S-J COMPOUDS IN THE ENERGY RANGE OF 5,0-11,3 eV

Spesyvykh O.O.

Uzhgorod Netional Universiti, Kapitulna st. 13, 88000 Uzhgorod, Ukraine

In this work, we study the energy distribution curves of photoelectrons (EDCP) of compounds As_2S_3, AsSJ, $As_1Sb_{1-x}J$, SbSJ in the amorphous state and for SbSJ -k, S_8 - k in the crystalline state in the energy range 5-11.3 eV. EDCP obtained by the method of delay potential, the accuracy of determining the position of the levels is not worse than ± 0.1 eV. At EDCP, the peculiarities of the density of electronic states of both the valence and conduction bands are observed. Conditionally, they are denoted by A_i for the valence band, and by P_i - the conduction band. For the possibility of comparison, all compounds are summarized relative to the Fermi level E_F. Data on S_8 are taken from [1]. The level W corresponds to the position of the top of the valence band relative to the vacuum level (photoelectrons threshold). The research results are presented in Table 1.

Table 1. Energy levels of compounds S_8, As_2S_3, AsSJ, $As_1Sb_{1-x}J$, SbSJ

Compound	E_F, eV	P_1, eV	P_2, eV	P_3, eV	P_4, eV	P_5, eV	P_6, eV	-W, eV	$-A_1$, eV	$-A_2$, eV	$-A_3$, eV	$-A_4$, eV	$-A_5$, eV	$-A_6$, eV
S_8 – к [1]	5,6					6,2		7,5	1,9			3,1		4,6
As_2S_3	4,4			5,5		6,3		6,2	1,8			3,2	3,95	4,7
AsSJ	4,4	4,8	5,1	5,5	5,8	6,3		5,8	1,85	2,2	2,65	3,15	3,90	4,7
As_1 Sb_{1-x} SJ	4,4	4,6	5,0	5,3	5,6	6,4		5,9	2,0		2,50	3,50	4,10	
SbSJ	4,6		5,0		5,7	6,4		5,7		2,3	2,50	3,55		
SbSJ –к	4,6		5,1		5,7		6,6	5,7	1,85		2,55	3,55	4,0	

The introduction of As atoms into sulfur leads to a significant reduction in the Fermi level and the work function, which is due to a decrease in the band gap from 2.6 eV to 2.36 eV, respectively, an increase in conductivity and a decrease in possible surface charging. The introduction of iodine atoms to As_2S_3 reduces the work function W to 5.8 eV. The introduction of AsSJ (10-30)% of Sb atoms leads to a slight shift in the features of EDCP in the conduction band and a decrease in the level of A_3 by 0.4 eV of the valence band. For crystalline SbSJ, the level of P_5 is observed, with an energy of 6.6 eV.

The investigated compounds are similar chain structures in which the role of chalcogen, as can be seen, is decisive. For all tested compounds, the energy levels of sulfur within the accuracy of the experiment are maintained. No A_6 level was detected in compounds As_x Sb_{1-x} SJ and SbSJ.

1. Nelsen P. Photoemission studies of sulfur. - Phys. Rev. B., 1974, v.10, № 4, p.1673-1682.

STUDY OF PHOTOELECTRON SPECTRA As (Sb) -Se-J SYSTEMS

Spesyvykh O.O.

Uzhgorod National University, str. Kapitulna 13, 88000 Uzhgorod, Ukraine

The paper presents a study of the peculiarities of photoelectron spectra in the region of incident photon energies 5-11.3 eV, obtained by the method of delay potential, of some compounds based on As (Sb) -Se-J in the crystalline and vitreous state, respectively, denoted by letters (k) and (a). All the presented compounds crystallize into similar structures in the form of -As (Sb) -Se- chains with a similar type of bonds between atoms, which makes it possible to trace the influence of atoms in the construction of the electronic structure of compounds.

The results of the research are shown in Table 1 for the excitation levels of the conduction band, which are denoted by the letters P_i, and Table 2 for the energy levels of the valence band, which are denoted by the letters A_i, respectively. Energy counts were performed from the Fermi level E_F. The accuracy of energy level determination is not worse than ± 0.1 eV.

Table 1 Features of energy levels of the conduction band of compounds As (Sb) -Se-J

Сполуки	E_F, eV	Енергії зони провідності, eV							
		P_1	P_2	P_3	P_4	P_5	P_6	P_7	P_8
As_2Se_3-a [1]	4,8	-	5,30	5,55	6,00	-	-	-	-
As_2Se_3-a	4,8	5,20	5,40	5,50	6,05	-	-	6,90	-
As_2Se_3-к	4,8	5,20	5,30	5,60	6,00	6,20	6,70	6,90	7,00
Sb_2Se_3-a [2]	4,8	-	-	-	5,90	-	-	6,90	7,40
Sb_2Se_3-к [2]	4,8	-	5,30	-	6,10	-	6,70	-	-
AsSeJ-a	4,8	-	5,40	5,50	6,05	-	-	-	-
SbSeJ-a	4,8	-	5,40	-	-	-	-	-	-

Table 2. Features of energy levels of the valence band of compounds As (Sb) -Se-J

Сполуки	E_V, eV	Енергії зони провідності, eV						
		$-A_1$	$-A_2$	$-A_3$	$-A_4$	$-A_5$	$-A_6$	$-A_7$
As_2Se_3-a [1]	1,0	-	-	3,10	-	-	-	-
As_2Se_3-a	1,0	2,60	2,95	3,20	3,60	3,75	3,90	4,50
As_2Se_3-к	1,0	2,60	3,00	3,35	3,60	3,80	3,90	4,55
Sb_2Se_3-a [2]	-	2,30	-	-	-	-	-	-
Sb_2Se_3-к [2]	1,1	2,70	-	-	-	3,70	-	4,40
AsSeJ-a	1,0	-	-	-	-	-	-	-
SbSeJ-a	1,0	-	-	-	-	-	-	-

Analysis of the presented data shows that the replacement of As atoms by Sb and the introduction of J atoms does not lead to a change in the position of the detected levels, but only to a decrease in the density of states, both conduction band and valence band. For AsSeJ and SbSeJ, the energy distribution curves of photoelectrons by energy represent the peak of scattered electrons on which no features of the electronic structure of the valence band were observed. The same Fermi level is observed for all the presented compounds, which may indicate a special contribution to the formation of the energy structure of the upper valence band and the conduction band by Se atoms. The change in the states of the compounds does not lead to significant changes in the position of the energy levels and is within the accuracy of the experiment ± 0.1 eV. The conduction band of the investigated compounds is more structured. The paper uses data from works [1, 2] for comparison, which are in good agreement with the obtained results

Levels E_V are determined from the curves of the spectral distribution of photoemission - correspond to the position of the top of the valence band. As can be seen from Table 2, the position of the top of the valence band in all investigated compounds is formed at one energy close to 5.8 eV, only in Sb_2Se_3-k shifted by 0.1 eV below. The study of the spectral distribution of photoelectrons in the threshold region made it possible to estimate the value of the "tails" of the density of localized states in the band gap ΔE for As_2Se_3-a, they are ≈0.4 eV, for Sb_2Se_3-a ≈0.7 eV, for AsSeJ-a ≈0.4 eV. The accuracy of determining ΔE is not worse than ± 0.1. The value of ΔE for vitreous compounds largely depends on the production technology. Indirect optical transitions are possible in the threshold region of photoemission**.**

1. Коломиец Б.Т., Корнев К.П.,Коченмировский А.С. Фотоэмиссионные исследования стеклообразных полупроводниковых систем As-Se-Te, As-Sb-Se, As-S-Se/ - Физика и Химия стекла. 1982, т. 8, № 6, с.736-739.
2. Hurych Z., Davis D., Burek D., at al. Photoemission studies of crystalline and amorphous Sb_2Se_3. – Phys. Rev. 1974, 9, № 10, p.4392-4404.

INNOVATIVE NANOLAYER VACUUM ARC COATINGS FOR SURFACE HARDENING OF PRODUCTS THAT OPERATE IN DIFFICULT CONDITIONS

Stolbovoy V.A., Andreev A.A., Voevodin V.N., Serdiuk I.V., Dolomanov A.V.

National Science Center “Kharkov Institute of Physics and Technology”, NAS of Ukraine,
1, Akademicheskaya St., Kharkov, 61108, Ukraine

Modern industrial development dictates new requirements for hardening and reducing the degree of wear of machine parts and assembly units, mechanisms and tools. For steel parts, surface nitriding or wear-resistant protective coatings are mainly used. At present, the traditional furnace nitriding of steels is widely used, but it has a number of disadvantages: a long process time (~ 60 hours) and the impossibility of hardening steels with a low tempering temperature. Therefore, technologies are being developed that are free from such disadvantages. In addition to nitriding, wear-resistant vacuum-arc coatings based on nitrides of simple elements (such as TiN) or multicomponent ones, for example TiAlN, are usually used to harden the surface of tool and structural materials, due to their good physical and mechanical characteristics. However, single-layer coatings do not meet the technical requirements, and the price of the multicomponent material and the complexity of its manufacture require the development of alternative coatings. Therefore, some types of nanolayer coatings have been developed, which are better than single-layer coatings in their functional properties [1,2].

To solve the problem of hardening the surface of steels, an integrated approach is required. For example, nitriding of steels followed by the formation of nanolayer vacuum-arc coatings in a single technological process. This makes it possible to solve the scientific and technical problem of creating fundamentally new wear-resistant, protective layers on products for mechanical engineering, aviation, and the nuclear industry.

The creation of nanolayer vacuum-arc nitride coatings on steel products subjected to preliminary ion nitriding is aimed at reducing the level of internal microstresses and preventing the formation of cracks. Cracks appearing in coatings under shock and alternating loads will be split at the boundaries of various nitride layers, after which the crack will shift in the transition layer. High internal microstresses at the coating-substrate interface lead to the formation of coating defects. The formation of hydrogen-free nitrided layers on the surface of parts creates a transition boundary between the coating and the substrate, and also improves adhesion. Production tests of high-precision tools with complex surface geometry with nanolayer coatings showed an increase in tool life up to 5-7 times. Thus, nanolayer coatings on nitrided surfaces make it possible to increase the efficiency of the cutting tool when processing difficult-to-machine materials (for example, titanium alloys). The use of the method of vacuum arc deposition of nanolayer (10-50 nm) nitride coatings in combination with ion nitriding makes it possible to obtain nanostructured superhard (> 45 GPa), heat-resistant (up to 900 ° C) coatings with a thickness of more than 4 μm with increased adhesive properties. Ionic nitriding in the gas plasma of an arc discharge allows creating a transition layer (9-11 GPa) on hardened steel with a hardness of 5 ... 7 GPa. The nitriding process at a high potential (-1100V) on the parts also leads to a better cleaning of the surface from oxides, thereby improving adhesion. Nano-layer vacuum-arc nitride coatings are suitable for use on carbide and high-speed steel cutting tools and machine parts operating for wear in a wide temperature range.

1. Sobol’ O.V., Andreev A.A., Gorban’ V.F., Postelnyk H.O., Stolbovoy V.A., Zvyagolsky A.V., Dolomanov A.V., Kraievska Z.V. The use of negative bias potential for structural engineering of vacuum-arc nitride coatings based on high-entropy alloys. PAST. 2019. №2(120), p. 127-135.
2. Столбовой В.А. Влияние толщины слоев многослойного покрытия TiN/MoN и глубины азотирования на структурные и механические характеристики стали 12Х18Н10Т. Журнал физики и инженерии поверхности, 2017, том 2, № 2, с. 80–85.

$A^{II}B^{VI}$ SEMICONDUCTOR QUANTUM DOTS AND THEIR BIOCONJUGATE WITH ALBUMIN: INTERACTION AND BIOIMAGING PROPERTIES

Stolyarchuk I. D.[1], Klepach H. M.[2,3], Gunyak A. I.[1], Stolyarchuk A. I.[1]

[1]*Department of Physics, Drohobych Ivan Franko Padagogical University, 24 I. Franko Str., 82100 Drohobych, Ukraine*
[2]*Department of Analytical Biotechnology, Institute of Cell Biology, National Academy of Sciences of Ukraine, Drahomanov Street 14/16, 79005 Lviv, Ukraine*
[3]*Department of Biology and Chemistry, Drohobych Ivan Franko Pedagogical University, 24 I. Franko str., 82100 Drohobych, Ukraine*

Semiconductor nanoparticles or quantum dots (QDs) have been extensively explored for biomedical applications. Due to unique size dependent optical properties, semiconductor quantum dots can be successfully used as a novel probes in biosensors as well as bioimaging and biolabeling [1-3]. The $A^{II}B^{VI}$ based QDs are particularly interesting from the biomedical applications point of view, due to the size dependent optical properties, broad absorption spectra, narrow photoluminescence (PL) spectra, long luminescence lifetime or high sensitivity which enable to use them as effective imaging markers. In addition, II-VI semiconductor compounds have another functionality as a basic matrix for diluted magnetic semiconductors (DMSs). Among DMSs Mn-doped II-VI semiconductor based nanostructures are the promising because of their chemical stability, strong fluorescence in visible region and high sensitively to the applied magnetic field.

In the present work, we report on comparative studies of interactions between CdTe, CdS and CdMnS nanoparticles and model proteins type of HSA. To probe this interaction, in addition to conventional UV-Vis absorption and photoluminescence spectroscopic methods we have used micro-Raman spectroscopy and technique of magneto-optical Faraday rotation, which is important for case of nanoparticles with magnetic impurities. For the evaluation of optical properties of pure QDs, pure HSA and QDs + HSA complex OA, PL, FTIR spectra are recorded and analyzed. An addition of HSA to the colloidal QDs leads to a gradual decrease of optical density and broadening of exciton structure was observed. It was proved that, in all cases, the fluorescence quenching of HSA by the QDs depends on the size and temperature. In the steady-state fluorescence studies, the interaction parameters including binding constants, number of binding sites, quenching constants were determined. The Stern-Volmer plots for the $A^{II}B^{VI}$ based QDs under interaction with HSA are analyzed. Obtained results suggest existence of static mechanism of fluorescence quenching in the interaction between HSA and QDs. The results of oscillation spectra can give important information about the processes occurring during bionanocomplex formation and indicate a slight reduction of α-helical folding protein type. The results on Faraday rotation spectra are more informative for diluted magnetic semiconductor QDs. In this case, influence of the added proteins on spin exchange interactions can be extracted.

Obtained data enable us to find optimal QDs concentration in QDs-HSA bionanocomplex (bionanoconjugates) useful for cancer cells bioimaging. However, in case of CdMnS QDs - HSA bionanocomplex using for labeling this cells, the concentration of QDs should be higher. The low toxicity as well as high stability of the QDs - HSA bionanoconjugates in the case of their using as bio-imaging probes has been demonstrated.

1. Smith B.R., Gambhir S.S. Nanomaterials for In Vivo Imaging // Chem. Rev. 2017, 117, 901–986
2. Hong T., Liu W., Li M., Chen C. Recent advances in the fabrication and application of nanomaterial based enzymatic microsystems in chemical and biological sciences // Analytica Chimica Acta, 2019 – V. 1067. – P. 31-47.
3. Sharifi M., Avadi M. R., Attarb F. [et al.]. Cancer diagnosis using nanomaterials based electrochemical nanobiosensors // Biosensors and Bioelectronics, 2019 – V. 126. – P. 773–784.

NSC KIPT PERSPECTIVE DEVELOPMENTS OF NANOSTRUCTURAL CARBON DIAMOND-LIKE COATINGS FOR INDUSTRIAL APPLICATIONS

Strel’nitskij V.E., Vasiliev V.V., Kalinichenko O.I., Luchaninov O.A., Reshetnyak E.N.

National Science Center "Kharkiv Institute of Physics and Technology",
1 Akademichna Str., Kharkiv, 61108, Ukraine
e-mail: strelnitskij@kipt.kharkov.ua

A brief overview of promising developments of NSC KIPT in the field of equipment and processes of vacuum-arc synthesis of carbon diamond-like coatings for industrial applications is given. Ways to improve the properties of coatings deposited from filtered plasma are discussed. It is substantiated that the deposition in the conditions of high - voltage pulse bias potential on the substrate allows flexible control the nanostructure and properties of the coatings. Improving the adhesion to the substrate, as well as improving the tribological and protective properties of the coatings is achieved through the formation of a layered structure.

Vacuum-arc coatings based on diamond-like carbon are multifunctional and widely used to modify the surface of parts and tools used in metalworking, mechanical engineering, aerospace, medicine, micromechanics and other industries due to the unique combination of properties. High-quality coatings are characterized by high hardness, low coefficient of friction, chemical inertness, biocompatibility, high radiation resistance and thermal conductivity [1, 2]. Development of equipment and processes for the synthesis of high-quality diamond-like coatings (DLC) on a large area is an urgent and important task, the solution of which will increase the productivity of the process, as well as expand the range of processed products. In addition, there is a need in deposition DLC on the surfaces of products of complex shape, spherical, etc. (such as friction joints of endoprostheses). In the vacuum-arc method, the coating is deposited from the directed flow of plasma, so to form on such surfaces the equal thickness coatings, it is necessary to look for new technical solutions. Improving the characteristics and functional properties of DLC is impossible without deepening the knowledge of the physical mechanisms that determine the processes of formation of the structure and phase composition of the coating material. That is why it is important to theoretically study the mechanisms of DLC synthesis, to identify the role of bombardment of the growth surface with ions of high energy (several keV) in the activation of radiation-stimulated phenomena, and the effect of coating deposition temperature.

In the National Science Center "Kharkov Institute of Physics and Technology" (NSC KIPT) laboratory of superhard coatings for many years are conducted research on the synthesis and study of the characteristics and properties of diamond-like coatings (DLC) [2]. One of the tasks of the laboratory is to develop equipment and processes for the synthesis of high-quality protective antifriction carbon coatings. Based on the results of one of the areas of scientific and technical research, an installation for vacuum-arc synthesis of high-quality DLC coatings by deposition from filtered carbon plasma by PIIID method (deposition from plasma with simultaneous implantation) was created [3]. Existing equipment includes a high-performance vacuum-arc plasma source with a filter of macroparticles of cathode material (graphite) and a pulse generator to supply high-voltage bias potential to the processed products. Due to plasma filtration, homogeneity of the coating material composition in volume and reduction of surface roughness is achieved. During the action of high-voltage pulse bias potential, carbon ions are accelerated and deposited with increased energy, which ensures their periodic implantation in the subsurface coating layer. This leads to the intensification of radiation-stimulated processes in the deposited material, one of the consequences of which is a decrease in the level of residual compressive stresses in the coatings, which improves their adhesion to the substrate.

Experimental results of many researchers from various literature sources show that with increasing pulse amplitude, the level of internal compressive stresses in the DLC coating decreases monotonically [4]. The same dependence follows from the theoretical consideration in the framework of the model of the nonlocal thermoelastic peak of the carbon ion [5, 6] (Fig. 1a). Experiments conducted in our laboratory showed that the hardness of the coating also decreases (Fig. 1b).

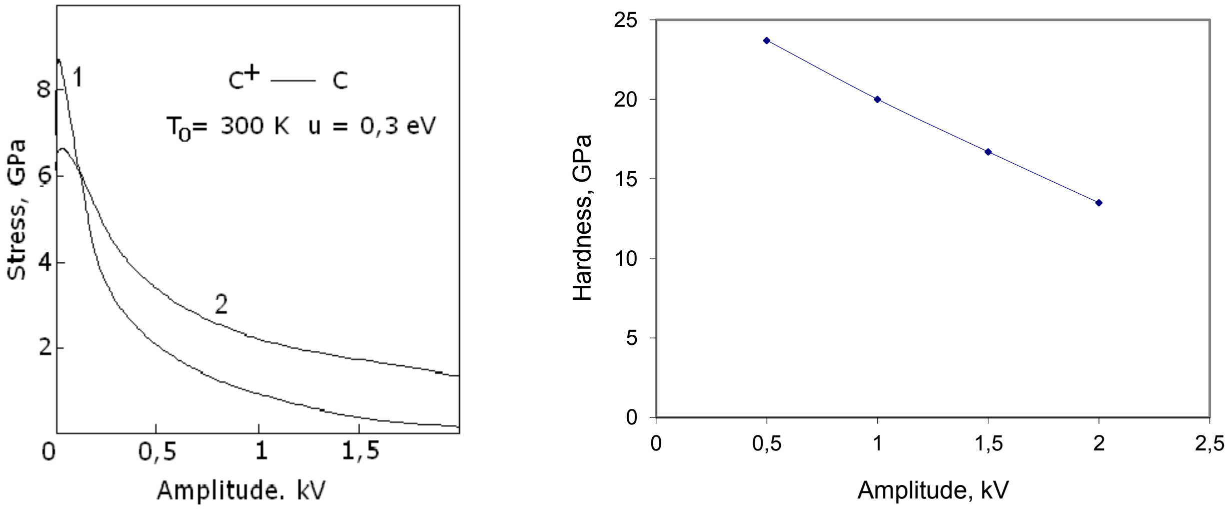

а б

Fig.1. The level of internal stresses (a), theoretical calculation in the mode of DC bias potential (curve 1) and pulsed one (curve 2), and experimental data on the hardness of DLC depending on the amplitude of the pulse bias potential on the substrate (b).

In traditional industrial technologies, the deposition of DLC is preceded by the deposition of a plastic intermediate layer, usually of carbide-forming metal (Ti, Cr). In our studies, we found experimentally the modes of vacuum surface treatment using the pulsed bias potential, which provide a high level of adhesion of the DLC without deposition of such intermediate layer. This technique is currently being tested on stainless steel and silicon carbide [7].

Another option to ensure the required level of adhesion of the DLC to the base was to create coatings of multilayer architecture, in which hard stressed layers of DLC are combined with layers with lower hardness and, accordingly, a lower level of internal stresses [8]. The laboratory has developed the deposition of multilayer DLC of various architectures: with periodically repeated soft and hard DLC layers, as well as quasi-gradient coatings, in which the hardness changes monotonically in each subsequent layer (Fig. 2, a, b). Typical process parameters are: arc current 70-100 A, argon pressure $1\cdot10^{-4}$ Torr, amplitude of pulse bias potential in the range of 0.5-2 kV, duration 5-20 µs, repetition frequency 12 kHz.

The coatings were tested for abrasion resistance according to the scheme: the rotating abrasive disk - the plane of the sample, the wear of the samples was assessed by visual optical and interference microscopy [8].

Based on the test results, conclusions can be drawn. Thicker coatings, of course, have a longer margin of operation under friction. Thus, increasing the thickness of the DLC on silicon carbide to 6 microns due to the use of a multilayer architecture of coatings with periodically repeated soft and hard layers leads to improved abrasion resistance. However, the adhesion of such coatings deteriorates compared to quasi-gradient, smaller thickness. Thus, it can be expected that the best set of functional properties will be characterized by DLC with the optimal thickness, which should be determined by testing results.

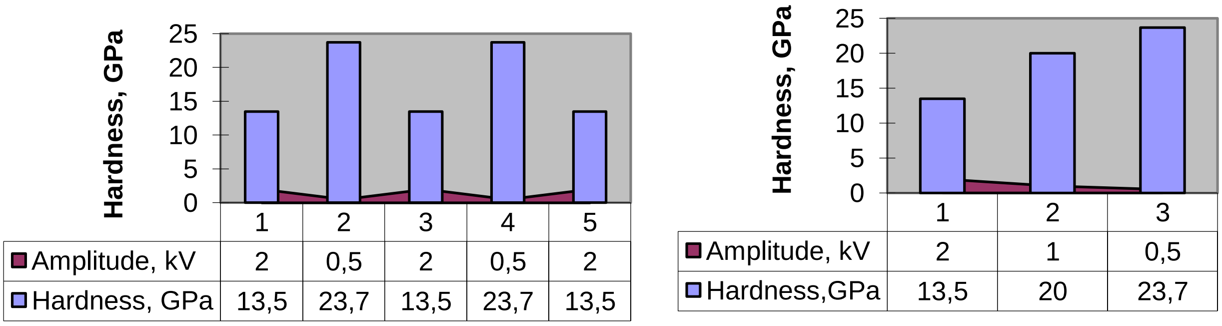

	1	2	3	4	5
🟥 Amplitude, kV	2	0,5	2	0,5	2
🟦 Hardness, GPa	13,5	23,7	13,5	23,7	13,5

	1	2	3
🟥 Amplitude, kV	2	1	0,5
🟦 Hardness,GPa	13,5	20	23,7

а б

Fig.2. DLC architecture: coating with five periodically repeating hard and soft layers (a) and quasi-gradient coating (b).

Today, the industrial use of laboratory developments is carried out on the basis of cooperation with the native company Grace Engineering, Sumy, which is a leader in Ukraine in the production of compressor and pumping equipment.

Gas sealing in dry gas dynamic sealing (GDS) of compressors is realized between two rotating rings with flat polished surfaces and should provide reliable protection of friction surfaces at pressure of the gases pumped up to 200 atm and above. Therefore, the coating must have a high quality mirror surface. Such requirements are met by coatings deposited from filtered vacuum-arc carbon plasma, which are characterized not only by a low coefficient of friction, but also high hardness, thermal and abrasive resistance. This method is used in NSC KIPT for deposition protective DLC on elements of GDS. Figure 3 shows a view of silicon carbide sealing rings with diamond-like coatings for GDS, which is used by Grace Engineering company in the production of high pressure compressors.

Fig.3. Batch of silicon carbide rings, with diamond-like coatings, intended for use in the GDS of high-pressure compressors.

At this stage of laboratory research, the main task is to improve the properties of DLC and their performance on parts of complex shape and large size up to 300 mm in diameter. Solving this problem on the one hand requires experimental and theoretical study of physical processes in the synthesis of DLC, on the other - the modernization of equipment to expand its technical capabilities and the implementation of deposition processes on products of a wider range of purposes.

It is planned to improve the quality of the existing diamond-like coatings (DLC), which are currently deposited by proven processes, by forming a layered or composite nanostructure by optimizing radiation-stimulated synthesis processes and nitrogen doping. The formation of nanoscale inclusions of graphite-like or nitride phases in the DLC is expected, which will help reduce brittleness, improve tribological and protective properties of coatings.

1. V.E. Strel’nitskij, I.I. Aksenov. Diamond-like Carbon Films. Kharkov.: «Contrast», 2006, 344p (in Russian).
2. I.I. Aksenov, A.A. Andrejev, V.A. Belous, V.E. Strel’nitskij, V.M. Khoroshikh. Vacuum arc: plasma sources, coatings deposition, surface modification. Kijev: Naukova dumka, 2012, 727 p. (in Russian).
3. V.A. Belous, V.M. Vojevodin, B. V.E. Strel’nitskij, S.J. Didenko, A.V. Rybka, A.V. Mazilov, V.V. Vasyliev, A.A. Luchaninov, E.N. Reshetniak, M.I. Ilchenko, V.E. Kutnij, A.A. Veriovkin, L.O. Shpagina, V.M. Borisenko, D.G. Pshenichnyj, Yu.V. Plisak, O.P. Kuznetsov.
4. Experimental technological complex for fabrication and testing products from DLC and metal layered composites for main branches of industries // Science and innovations, 2014, Vol.10, N4, p. 5-21 (in Russian).
5. M.M.M. Bilek, D.R. McKenzie, R.N. Tarrant, S.H.M. Lim, D.G. McCulloch. Plasma-based ion implantation utilizing a cathodic arc plasma // Surface and Coatings Technology. 2002, v. 156, p. 136-142.
6. A.I. Kalinichenko, S.S. Perepelkin, V.E. Strel’nitskij. Dependence of intrinsic stress and structure of ta-C film on ion energy and substrate temperature in model of the non-local thermoelastic peak. Diamond Relat. Mater. 19 (2010) 996-998.
7. A.I. Kalinichenko., S.S. Perepelkin, V.E. Strel’nitskij, Calculation of intrinsic stresses in the diamond-like coatings produced by plasma ion deposition in modes of DC and pulse bias potentials, IOP Conf. Series: Materials Science and Engineering 81 (2015) 012049.
8. V.V. Vasyliev, A.A. Luchaninov, V.E. Strel’nitskij. Deposition of DLC coatings on silicon carbide rings for gas dynamic sealing of high pressure compressors. VANT. 2018. N1(113), p.88-92 (in Russian).
9. V.V. Vasyliev, A.A. Luchaninov, V.E. Strel’nitskij. Investigation of the abrasive durability of the multilayer diamond-like coatings for the ring-shaped dry gaseous seals made of SiC. Problems of atomic science and technology. 2019, № 1. Series: Plasma Physics (25), p,. 216-218.

EQUIPMENT FOR PLASMA SPRAYING

Zhiguts Yu.Yu., Legeta Ya.P., **Strukov B.M.**

Uzhhorod National University, 46, Pidgirna Str., Uzhhorod, Ukraine, 88000

While investigating the opportunities of synthesis of materials with the help of metal-thermic reactions was conducted micromelting, on the basis of which the process of interaction of aluminium with K (or Na) powder caliche's lies.

Strong exothermic of the reaction was directed to the warming up of the excessive aluminium, which is added into the composition and thus it made it possible to get it in a liquid state.

This liquid metal may be easily separated from dross and can used not only for casting, but also for the welding of the aluminium conductor wires using a special device.

The optimal compositions of the exothermically reactions are worked out output value of aluminium ingot from charge are established (depending upon the quantity of Al powder); changes in microstructure of Al are discovered for the expense of the modification of Na (or K) that gets into the metal from the exothermically charge; the attributes of Al, which is received by the metallothermical way are investigated; the part of Al is proposed in order to increase the economy of the process of changing on aluminium wastes.

Keywords: metallothermy, mechanical properties, micromelting, technology.

Introduction. Advances in mechanical engineering, advancing development of new forms of production, conditions of single and small-scale production, modern repair and restoration technologies require the use of technologies that give the alloy surfaces the necessary complex of physical, mechanical and operational characteristics.

Analysis of the literature data showed that one of the promising ways to improve the technological and service properties of materials, expanding their functional purpose is to create surfaces of materials with a composite structure obtained through combined processes that combine self-propagating high-temperature synthesis (SHS) and aluminothermic processes or plasma spraying.

To date, improvements in material properties are achieved mainly through the use of traditional materials technologies and subsequent thermal, chemical-thermal and other processing methods. But their high energy consumption, the need to combine several technological steps, compliance with environmental requirements lead to the need to find other ways to provide the required properties of materials surfaces and the synthesis of new materials, sometimes with unique properties that can avoid these shortcomings [1-3]. For the implementation of the combined technologies requires a whole set of equipment, which allows to provide high quality of coating of parts surfaces [4]. One such promising complex is the development and use proposed in this work of a theoretically designed and experimentally tested device for dusting and surface doping, which can be used even in small-scale production in the processing of individual parts and workpieces.

The purpose of the work was to develop a means of dust protection for technological equipment in the processes of ion alloying and SHS in the plasma sputtering of the surfaces of the parts and use it to form on the surface of the part of the wear-resistant high-hard coating.

The methodology of the tests. Checking the presence of the clamp (contact) of the protective earth and its condition was checked visually. The clamping of the protective grounding was controlled by the absence of paint and rust. The electrical resistance was checked with the milliometer according to the instructions on this device (the electrical resistance between the protective earth clamp and the control unit housing, the fan control panel in turn) was measured, with the electrical resistance not exceeding 0,1 ohms. The insulation resistance of the chambers was checked by the megometer according to the instructions on this device with the insulation resistance being at least 1 MOm. The electrical strength of the insulation was tested by the universal punching device according to the instructions for this device, as shown in fig. 1. All measurements controlled for the absence of breakdown of the insulation and its surface overlap.

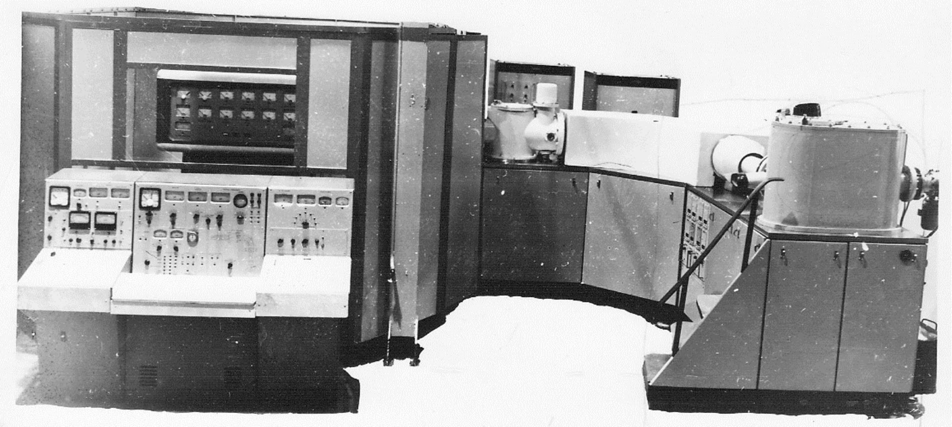

Fig. 1. The appearance of the complex

Measurement of air velocity was measured by an anemometer with a manual winged under the centres of each filter at a distance of 150 mm from the air distributor 3 times at each point, followed by calculation of the arithmetic mean of the air velocity.

Measure the concentration of dust particles in the working volume of the chambers to perform after 3 hours of operation of the fans at maximum revolutions under the center of each filter at a distance of 150 mm from the air distributor at an average air flow rate of 0,3-0,4 m/s. For all measurements, the concentration of dust particles in the working volume of the chambers did not exceed 4 particles with a size of 0,5 μm or more in 1 litre of air. The illumination was checked by a 1,2-meter light meter at the lamp of the working volume of the cameras. The values of electrical power consumed by the cameras are measured by the kit according to the instructions for this unit when the fans are running at maximum speed and all the lamps are switched on.

Design development of the complex. The developed equipment is intended for providing by means of dust protection of technological equipment for the processes of alloying in the production of parts in serial and small-scale production. Dust cameras create an air environment in the loading area for complex spraying and alloying devices. The equipment is designed to work in industrial premises.

Dust chambers are collapsible structures that consist of ceiling dusting units mounted on racks. The working volume is limited by walls made of transparent fire-resistant hardened glass. Doors are provided for access to the work volume. The floor of the cameras is the floor of the room in which they are installed. The camera is controlled by the control panel mounted on the rack. The dust extraction unit is a frameless welded structure with a fan and filters installed.

The principle of operation of the cameras consists in the continuous supply to the working volume of a uniform vertical stream of purified air. The stream of purified air moves in the working space from top to bottom, capturing in its path the suspended particles formed during the technological operations and takes these particles out of the working volume. The chambers have high-performance filters for fine air purification with a filter cloth, which allows to ensure the purity of air in the working volume, which corresponds to I class of purity. Wedge separators used in filters increase their reliability and durability. The centrifugal fan used in the chambers is compact, low noise and provides a capacity of up to 2000 m^3/hour. To reduce noise and vibration, the fan is mounted on spring shock absorbers with a high cushioning ratio. In terms of technical level and quality of equipment, it is at the level of the best foreign samples similar to the destination and above the level of domestic products close to the destination. The equipment thus developed is intended to create an air environment in the loading area of alloying devices and SHS. The use of equipment in such complex technological processes increases the percentage of output of suitable products by 0,6%. Technical characteristics of the equipment: Concentration of dust particles in the working volume amount of 4 particles/litre of air, particle size of 0,5 μm, air flow rate entering the working volume of 0,3-0,4 m/s, power consumption 1,5 kVA, overall dimensions of the working volume 1400x1010x2300 mm.

Experimental work on the use of the complex for the manufacture of products by combined technologies. In plasma surface sputtering (PSS), SHS mixes virtually all W through oxygen-free combustion with carbon to form WC carbide. Excess carbon and a very small amount of tungsten alloy iron, forming a liquid steel of eutectoid composition, which under rapid cooling conditions turns into a cane in layers up to 80 microns thick. The thickness of the doped layer is ~500 µm. This layer consists of ~50% WC particles and ~50% (by volume) metal bond (steel "У8А"). The same figure shows that in the zone of intense thermal influence, the microstructure of the steel has acquired a very small columnar structure with a slight inclination of thin dendrites (which have almost no branches) to the opposite direction of the plasma advance. High-solid (~2000 HV) WC carbides, which occupy up to 50% of the volume of the entire carbidostal layer, are visible in the semi-floodplain. Studies have shown that the microhardness of WC carbides is almost ten times higher than that of steel. Thus, it was possible to organize the SHS process in a relatively thin layer due to the use of PNP technology at the same time to solve the following problems: for heating, melting and carbonization of iron; for melting W particles and burning them in carbon to form WC carbides.

It is important to note that no non-metallic phases and their inclusions are formed during the specified oxygen-free combustion. The hardening of the hardened layer to the base alloy is also obtained by metallurgical means.

Conclusions. As a result of the experimental design, the authors conducted a number of search works, worked out the design documentation of the experimental complex for dust protection and doping of parts in the process of plasma spraying, made prototypes and conducted their operational tests, as well as carried out experimental work on the study of samples use of complex technologies.

The combination of PSS and SHS in one operation allows to solve a whole set of technical problems for obtaining high-strength carbidostal-type materials and solid alloys on the alloy surface. The new complex technological process allows to increase the worn surfaces of parts of machines, devices and devices to a depth of up to 500 microns with materials having high mechanical, service and technological properties.

1. Zhiguts Yu.Yu., Legeta Ya., Golovka Yu. Development of SHS technology / Prospects of world science: XV intern. scientific and practical conf., 30 July 2019 - 7 August 2019: Materials of the conf. – Sheffield: Science and education LTD, 2019. – №. 8. – P. 61 - 63.
2. Zhiguts Yu.Yu., Levdar K. Thermite foundry profit for supply of high-alloyed steels / Areas of scientific thought: XIII intern. scientific and practical conf., 30 December 2017 - 7 January 2017: Materials of the conf. – Sheffield, S Yorkshire, England: Science and education LTD, 2017. – V. 11. – P. 7 - 9.
3. Zhiguts Yu.Yu., Antalovskyy V.V., Hom'ak B.Ya. The possibility of synthesis of hard alloys / Prospects of world science: 12 international scientific and practical konf., 30 july – 07 august 2016.: V. 3. materials conf. – Sheffield UK: "Science and Education" LTD, 2016. – V. 22. – P. 56 - 59.

TUNNELING AS A POSSIBLE MECHANISM OF SELF-ORGANIZATION OF DISLOCATION AND IMPURITY SUBSYSTEMS

Raransky M.D., Oliynych-Lysiuk A.V., Tashchuk O.Yu., **Tashchuk R.Yu.**, Lysiuk O.V.

Yuri Fedkovich Chernivtsi National University, Chernivtsi
M. Kotsyubinsky street, 2, Ukraine
Тел.: +38 0955074333 E-mail: romatastshcuk@gmail.com

It is well known that the processes of self-organization are realized in open thermodynamic systems, far from equilibrium, if the control parameter of the system exceeds some critical value. The emergence of order in a previously disordered system occurs abruptly, as in phase transformations, giving it unique properties, which makes such a system attractive to both scientists and engineers working in the field of new technologies [1]. However, the mechanisms of such nonequilibrium phase transformations, as well as the conditions for the stabilization of ordered phases, are not always clear today, especially when it comes to real (defective) crystalline solids.

Studies of the spatiotemporal evolution of the elastic and inelastic properties of such crystals, deduced from the state of thermodynamic equilibrium by temperature-force action, magnetic field, or irradiation, have shown that bright oscillations are observed in the time dependences of these characteristics. Their appearance is explained by the self-organization of dislocation-impurity structures in destabilized crystalline solids.

We hypothesized that self-organization in the studied dislocation-impurity systems may arise due to quantum diffusion of both point defects-defecton in the dislocation atmosphere and kink on the dislocations (topological solitons) in the case when the defective subsystem is in an unstable state after irradiation, magnetic action or thermocycling.

Found that

- In the studied aluminum, india, beryllium topological solitons can occur at both cryogenic and room temperatures (for example, in beryllium). The probability of their occurrence depends both on the height of the Pierrels barrier and on the magnitude and sign of the Poisson's ratios ν.
- The probability of tunnel transition also depends on the speed of dislocations in comparison with the speed of sound V_{sound}^{l},, on the magnitude of the applied external mechanical stress and internal thermal stresses in polycrystalline materials. Thus, the slow motion of kinks at edge dislocations (with a velocity of $0.01\, V_{sound}^{l}$,) in Be with a high probability can be below the barrier for both normal (ν = 0.03) and auxetic (ν = -0.08) states. But the rapid movement of kinks on the dislocation ($0.1\, V_{sound}^{l}$) is possible only for auxetic beryllium
- It is shown that in Be another type of defects - defectons - is a quantum motion of carbon impurities near the edge dislocations. Estimation of the de Boer parameter for carbon atoms in the vicinity of the geometric inflection at the edge dislocation $L \sim \frac{h}{a\sqrt{m_C E_{\text{Вз}}}} = 0{,}349$ showed a significant probability of inclusion of their quantum diffusion in this metal. Quantum delocalization of carbon impurities in magnesium-thermal condensate (MTC) Be near dislocations allows to explain the anomalous behavior of Kinetic Dependences of Internal Friction (KDIF) curves in the range of 300–500 K (see Fig. 1), which was reported in [3].

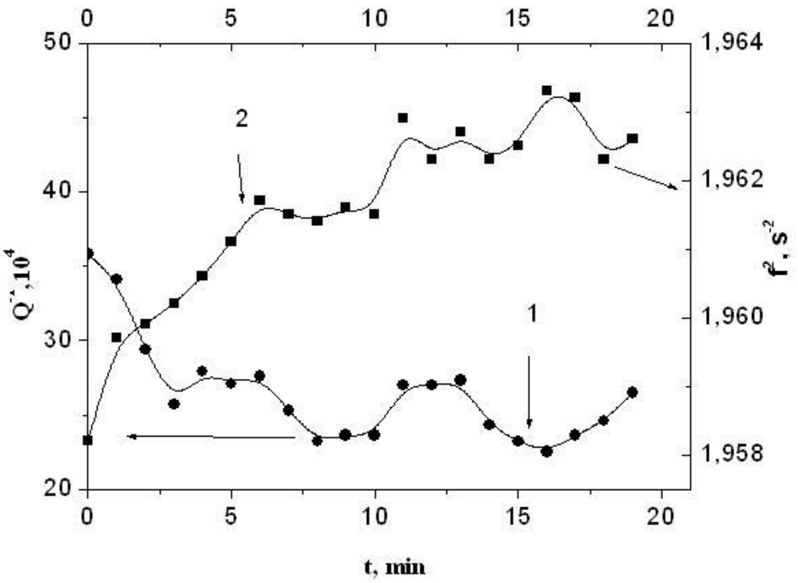

Fig.1. Kinetic dependences of internal friction (KDIF) (1) and the square of the frequency of natural torsional oscillations f^2 (2) of MTC Be after thermal cycling and cyclic deformation at 10^{-5} (5 min) at 260oC. (Fig. accommodated from work [3])

1. I.R. Prigogine, D. Kondepudi. Modern thermodynamics. From heat engines to dissipative structures. (Mir, Moscow, 2002). - 461 p.
2. Alona Valyavska, Alla Oliynich-Lisyuk, Mykola Raranskiy. Self-organization of defects in highly uneven alloys of aluminum // Journal of Physical Doslidzhen. 2019.– Vol. 23, No. 2.– C.2998-12–2998-13.
3. Oleinich–Lysyuk A.V., Gutsulyak B.I. Oscillating nature of time dependences of internal friction in nonequilibrium systems // Condensed media and interphase boundaries.– 2008. – Volume 10, No. 1. - P. 47 - 49

CONVERSION OF AUXETICS INTO AN ORDINARY CRYSTAL IN THE PROCESS OF PLASTIC DEFORMATION OF THE INDIUM-NANOLAYERS

Raransky M.D., Oliynych-Lysiuk A.V., Kurek I.G., **Tashchuk O.Yu.**, Tashchuk R.Yu.

Yuri Fedkovich Chernivtsi National University, Chernivtsi
M. Kotsyubinsky street, 2, Ukraine
**Тел.: +38 0955074333 E-mail: romatastshcuk@gmail.com*

Widespread use of auxetics materials (natural substances and artificial formations with a negative Poisson's ratio ν) in the manufacture of seismically stable structures, protective equipment that effectively absorbs impact energy, and other devices and appliance stimulates the study of changes in deformation properties of auxetics during mechanical stress (external or internal) that occur during their exploitation. This information becomes even more important when the auxetic, which has ν <0, is a component of the material in the form of crystalline structures of nanoparticles or thin layers [1], or in the form of inclusions of non-auxetic materials in ordinary ones. In this case, the deformation properties and relaxation of mechanical stresses in these inclusions are also determined by the properties of the matrix and can differ significantly from the macroscopic ones.

In modeling processes in such materials, Hooke's linear approximations are used mainly for elastic deformations [2] and do not take into account the possibility of their operation at stresses approaching the strength limit of the material σ_B. Despite considerable practical interest, there are few models that would describe the behavior of auxetics at such stresses [3]. Thus, Ciambella and Saccomandi (2014) [3] modeled the dependence of the Poisson's ratio ν on the degree of relative tensile deformation for auxetic foams and explained the experimental results obtained during the deformation of the foams, the inversion of the sign of ν with increasing tensile deformation, and the transformation of the auxetic cell into a normal non-auxetic.

We have assumed that such a transformation is also possible in crystalline auxetics with an increase in the degree of mechanical stresses up to σ_B. In natural crystalline auxetics, in contrast to artificial foams, in addition to areas with a correct crystal structure, the deformation of which can be successfully described in a linear approximation, there are defects in the crystal structure. It is the defects in the periodic arrangement of atoms that mainly determin σ_Be the deformation properties of natural crystals during plastic deformations. With this in mind, scientists and engineers need to have information about the properties of almost ideal crystalline layers of auxetic in a wide range of temperatures, including cryogenic, and its properties in the vicinity of defects (linear, planar, volumetric and their combinations) depending on temperature and distances in the process of increasing mechanical stresses [4].

As a model auxetic, we chose indium, which is a known non-axial auxetic, the Poisson's ratio ν of which varies in different directions in the crystal in a wide range from -1 to +1.3, which is widely used in the form of thin contact layers and various inclusions [5].

During thermal cycling in the interval 2 ÷ 300 K in thin layers In, we observed inversion of the sign of total dilatation ε_{ii} of the 2D layer at 80 - 100 K, double inversion of the sign of deformation in the direction perpendicular to the plane of the layer ε_{zz} [6] with increasing external mechanical stresses in auxetic and non-auxetic crystallographic directions.

As a continuation of these studies in this paper we studied the behavior of mechanical and thermal components of deformation of indium nanolayers in a wide temperature range from cryogenic to room with increasing mechanical stresses up to σ_B in auxetic and non-auxetic directions in the crystal in order to identify the possibility of transformation of auxetic directions into ordinary non-auxetic in thin 2D-layers of indium.

The short results can be summarized as follows

- The mechanical component of the deformation ε_m, which occurs in 2D nanolayers of indium in the direction perpendicular to the plane of the layer, depends on the magnitude of the external mechanical stress σ in the non-auxetic and auxetic directions in the crystal in fundamentally different ways (Fig. 1, Fig. 2).

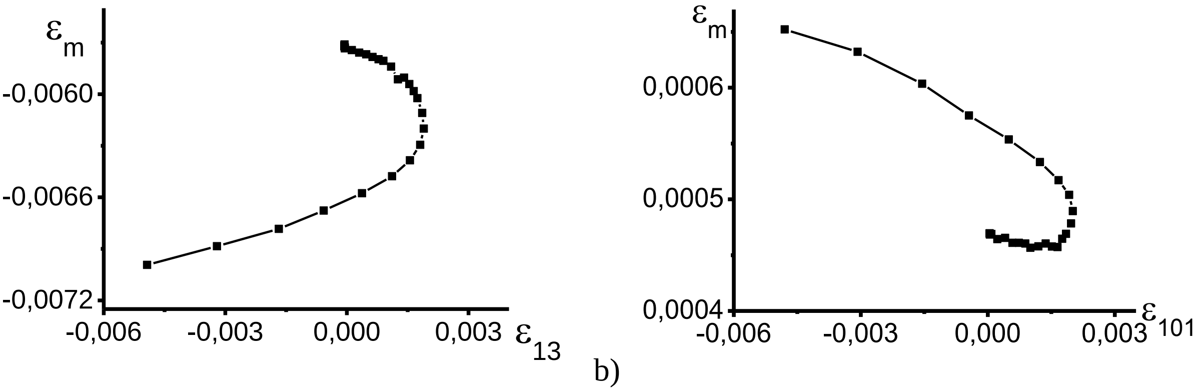

a) b)

Fig. 1. Dependences of the mechanical component of deformation in the non-auxetic (a) and auxetic (b) direction in the indium layer on the degree of deformation in the plane of the layer at an external mechanical compressive stress of 10^6 Pa.

- At mechanical stresses of the order of 10^6 Pa, the dependence ε_m (ε_{zz}) has a nonlinear character (Fig. 1): in non-auxetic directions ε_m first increases with increasing ε_{zz}, and then continues to grow with decreasing ε_{zz} (Fig. 1a), in contrast to auxetic directions , in which ε_m decreases with increasing ε_{zz} (Fig. 1b). In this case, the value of ε_m in the non-auxetic direction remains almost an order of magnitude larger than in the auxetic direction.

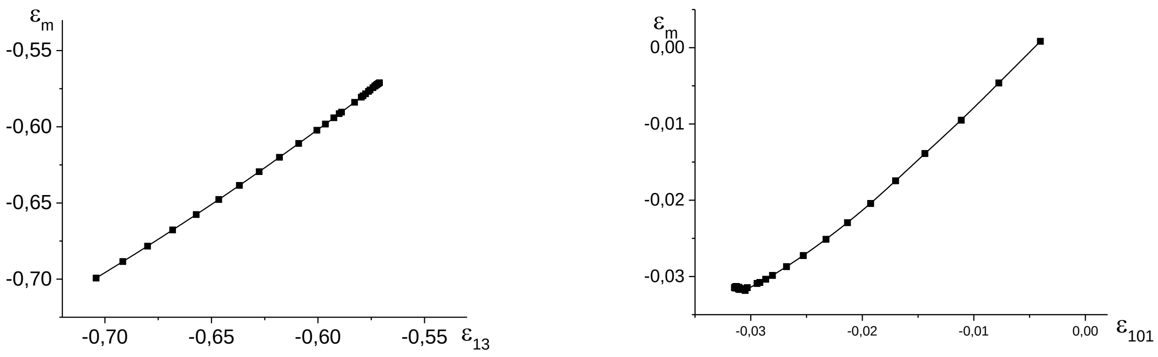

a) b)

Fig. 2. Dependences of the mechanical component of deformation in the non-auxetic (a) and auxetic (b) direction in the indium layer on the degree of deformation in the plane of the layer at an external mechanical compressive stress of 10^8 *Pa*

- At $\sigma \sim 10^8 Pa$, the nature of the dependence ε_m (ε_{zz}) fundamentally changes to almost linear in both non-auxetic and auxetic directions (Fig. 2a and Fig. 2b), which can be interpreted as a transition to the same deformation mechanisms, i.e. transformation of auxetic directions into crystals in ordinary, but the difference between the levels of $\varepsilon_m$in the auxetic and non-auxetic directions in the crystal remains and even slightly increases.

1. Lisovenko DS. Auxetic mechanics of isotropic materials, crystals and anisotropic composites / Dissertation for the degree of Doctor of Physical and Mathematical Sciences. Moscow, 2019 .-- 392 p.
2. Teik-Cheng Lim. Auxetic Materials and Structures/ Engineering Materials: Springer 2015. –587 p
3. Ciambella J, Saccomandi G () A continuum hyperelastic model for auxetic materials.// Proc Roy Soc A. – 2014. – 470(2163).– P. 20130691
4. Raranskiy N.D., Oliynich-Lysyuk A.V., Tashchuk R.Yu, Lysyuk A.V., Tashchuk A.Yu. Peculiarities of deformation in In crystals in a wide temperature range // MFinT.– T.40, v.11.– P.1453-1463.
5. Raransky M.D., TashchukR.Yu., Kurek I.G., Oliynich-Lysyuk A.V. Thermoplastic Properties of Quasi-Isotropic Indium Layers//Abstractbook XVII International Freik Conference on Physics and Technology of Thin Films and Nanosystems. Ivano-Frankivsk, May 20-25, 2019. – P. 257.
6. Raranskiy M.D., Oliynich-Lisyuk A.V., Kurek I.G., Tashchuk R.Yu., Tashchuk O.Yu. About the inversion of the deformation sign in balls In. // Functional materials for Innovative Energy, FMIE-2020, Kyiv 25-27 May 2020. - S. 49.

INCLUSION COMPLEX FORMATION OF BENZENE AND PHENOL WITH β-CYCLODEXTRIN IN AQUEOUS SOLUTIONS

Trofymchuk I.M., Belyakova L.A.

Chuiko Institute of Surface Chemistry of NAS of Ukraine, 17, General Naumov St., 03164 Kyiv, Ukraine

Cyclodextrins (*CDs*) are well known cyclic oligosaccharides formed of 6 or more glucopyranose units. *β-CD* is one of the most common member of cyclodextrin family, consisting of seven glucopyranose units linked by α-(1,4)-glycosidic bonds. Molecule of *β-CD* is torus-liked macro-ring with all secondary hydroxyl groups situated on one of the two edges of the ring, whereas all primary ones are placed on the other edge. The cavity of *β-CD* molecule is lined by the hydrogen atoms and ether oxygens and as consequence is thought to be hydrophobic. Due to these structural features of molecule, *β-CDs* can form supramolecular inclusion complexes of “host”–“guest” type with inorganic and organic compounds, both in the solid state and in the solution [1]. The driving forces for the complex formation between *β-CD* “host” molecule and “guest” molecules have been attributed to the release of entropy-rich water molecules from the cavity, van der Waals and hydrophobic interactions, hydrogen bonding, release of ring strain in *CD* molecule, and changes in solvent-surface tension [2].

The aim of this study was to investigate an inclusion complex formation of benzene (*Benz*) and phenol (*Phen*) with *β-CD* in aqueous solutions.

From the results of geometry optimization of *Benz, Phen* and *β-CD* molecules using Hyper Chem program, it is obviously that the size of “guest” aromatics is appropriate with the size of “host” hydrophobic cavity (Figure 1). Benzene and its derivative form inclusion complexes with *β-CD* in aqueous solutions that was proved by means of UV spectroscopy. An increased bands intensity of UV absorption spectra of benzene and phenol aqueous solutions was observed after adding *β-CD*. The spectroscopic data are consistent with a binding model that assumes formation of 1 : 1 “*β-CD–Benz*” and “*β-CD–Phen*” inclusion complexes.

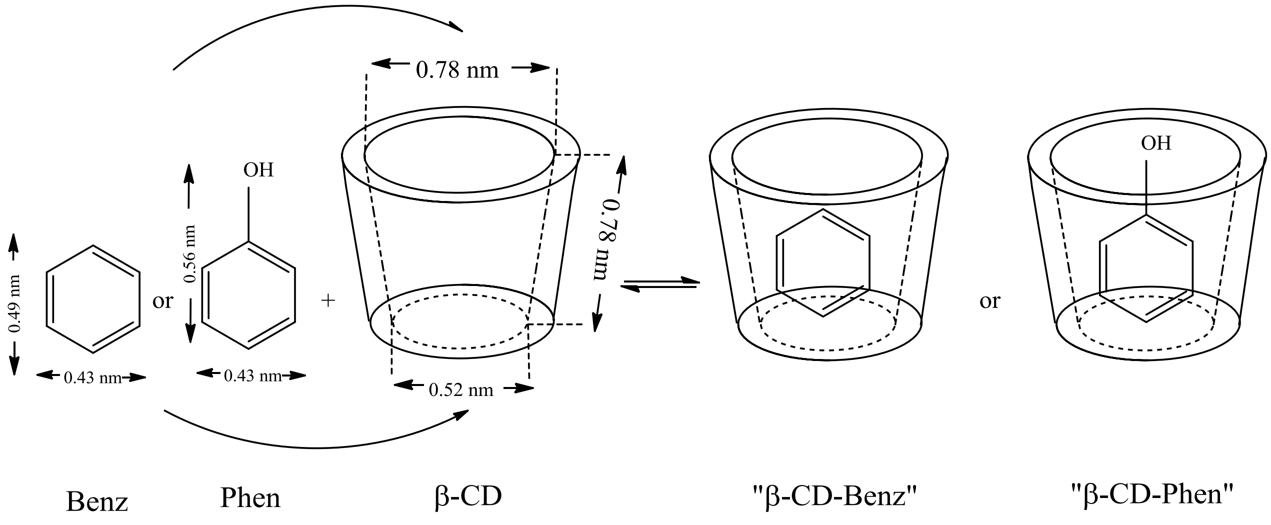

Fig.1. Geometry of aromatic and oligosaccharide molecules and the formation of their inclusion complexes.

Stability constant for 1 : 1 inclusion complexes of *Benz* and *Phen* with *β-CD* at 290–307 K and thermodynamic parameters of their formation were calculated by Ketelar and Van’t Hoff equations, respectively (Table 1).

Table 1. The formation constants of "*β-CD–Benz*" and "*β-CD–Phen*" inclusion complexes and thermodynamic parameters for the binding of benzene and phenol to *β*-cyclodextrin

Inclusion complexes	T, K	K_S, l·mol^{-1}	ΔG°, kJ·mol^{-1}	ΔH°, kJ·mol^{-1}	ΔS°, kJ·mol^{-1}
"*β-CD–Benz*"	291	116	–11.5	–32	–72
	298	86	–11.0		
	303	68	–10.6		
"*β-CD–Phen*"	290	94	–11.0	–56	–157
	293	57	–9.8		
	299	45	–9.5		
	307	23	–8.0		

The values of stability constant K_s for 1 : 1 inclusion complex at different temperatures are rather small in both cases, and stability constant increases with diminishing of temperature. Such weak interactions are typical for non-specific forces or inclusion complexes with volatile compounds. It was shown that formation of 1 : 1 "*β-CD–Benz*" and "*β-CD–Phen*" inclusion complexes is spontaneous and thermodynamically profitable exothermal process, which is accompanied with energy release and decrease of enthalpy ΔH and entropy ΔS.

Given the possibility of inclusion complex formation between benzene or its derivative and *β-CD* in aqueous solutions, we might expect that oligosaccharide immobilized on solid surfaces could be promising for separation and removing of aromatics from water.

1. Szejtli J. Introduction and general overview of cyclodextrin chemistry // Chemical Review, 1998. – V. 98. – N. 5. – P. 1743-1752.
2. Huang M.J., Watts J.D., Bodor N. Theoretical studies of inclusion complexes of α-and β-cyclodextrin with benzoic acid and phenol // International Journal of Quantum Chemistry, 1997. – V. 65. – N. 6. – P. 1135-1152.

JOINT ADSORPTION OF METHANE AND WATER ON HYDROPHOBIC AND HYDROPHILIC SILICA ADSORBENTS

Turov V.V., Gun'ko V.M., Krupska T.V.

Chuiko Institute of Surface Chemistry, General Naumov Street 17, 03164 Kyiv, Ukraine;

Adsorption features of gases, vapors or liquids are defined by a ratio of changes in the Gibbs free energies (ΔG) of an adsorbate at a surface and far from it (*i.e.* in bulk liquid or vapor/gas phase). A more negative value of ΔG for an adsorbate in the adsorption layer corresponds to stronger adsorption; *i.e.*, interaction energy between adsorbed molecules and surface sites is greater than that between neighboring molecules of the adsorbate. However, phase state features of adsorbed substance *vs*. temperature are often unknown or poorly defined due to strong effects of confined space in pores onto bound compounds. The adsorption theory considers that on a surface or in pores of adsorbents, adsorbate fluid forms with the density intermediate between ones of a gas and a liquid.

Despite numerous publications on fumed oxides, interfacial phenomena at a surface of blends with unmodified and hydrophobized nanosilicas were poorly studied; however, similar systems can be of interest from practical point of view. Therefore, the aim of this work was to study the interfacial phenomena and mentioned above effects with polar (water) and nonpolar (methane) adsorbates at a surface of a blend with hydrophilic (A-300) and hydrophobic (AM1) nanosilicas in comparison with that for A-300 alone.

Hydrophilic nanosilica A-300 ($S_{BET} \approx 290$ m^2/g, initial bulk density $\rho_b \approx 0.05$ g/cm^3 and after wetting (by water at content $h = 0.5$ and 3.0 g/g) and drying (at 433 K for 8 h) bulk density grows to 0.1 and 0.25 g/cm^3, respectively) and hydrophobic AM1 (A-300 modified by dimethyldichlorosilane (DMS) cross-linkable due to formation of two OH groups per hydrolyzed DMS molecule) (Pilot plant of Chuiko Institute of Surface Chemistry, Kalush, Ukraine) were used in the study. A mixture with treated A-300 (water-wetted-died, $\rho_b \approx 0.25$ g/cm^3, labeled here as dense A-300) and AM1 (hexane-wetted-dried) (1 : 5) with added (to A-300) water (at $h = 0.1$ g per gram of both dry silicas) was weakly (with no strong mechanical loading) or strongly stirred. Note that water was added to dense A-300 ($h = 0.6$ g/g), which was then mixed with AM1 (1:5) that gave $h = 0.1$ g/g. These samples were used to study the adsorption of methane. Upon the methane adsorption, 5 mm NMR ampoule with a sample (100-200 mg) was connected to a rubber vessel with methane (freezing point $T_f = 90.7$ K) at 1.1 atm. The value of $h = 0.1$ g/g corresponding to maximal adsorption of methane onto nanosilica was selected for this study.

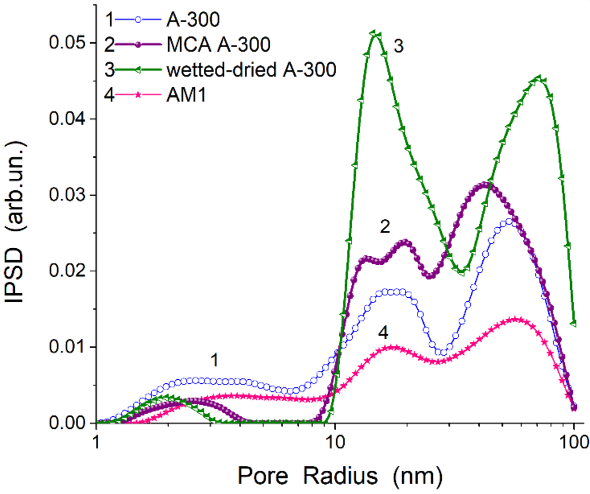

Fig. 1. Incremental pore size distributions of A-300 initial and differently treated (mechanochemical activation (MCA) for 2 h in a ball-mill, and wetted and dried) and chemically modified by dimethyldichlorosilane (AM1) calculated using DFT method with a model of pores as voids between nonporous spherical nanoparticles).

The pore size distributions (PSD) of nanosilicas (determined from nitrogen adsorption-desorption isotherms using a model of voids between NPNP in the secondary particles) (Fig. 1) demonstrate a larger contribution of broad pores in the range of R = 10-100 nm than that of narrow pores at $R < 10$ nm.

Besides liquid organic solvents, adsorption of methane (at pressure 1.1 bar) onto nanosilicas was studied but with pre-adsorbed water (h = 0.1 g/g) (Fig.2). An adsorbent blend of hydrophilic (dense A-300) and hydrophobic (AM1) (at 1:5 w/w) was used as initial one (mixed without strong mechanical loading for 5 min) and strongly stirred (after addition of water to A-300) to form uniform blend to compare with dense A-300 alone (Fig. 2). Since the amount of water in samples is precisely known, the ratio of integral intensity of ^{1}H NMR signals of water and methane at each temperature allows us to estimate their quantity being in a mobile state registered in the ^{1}H NMR spectra of high resolution.

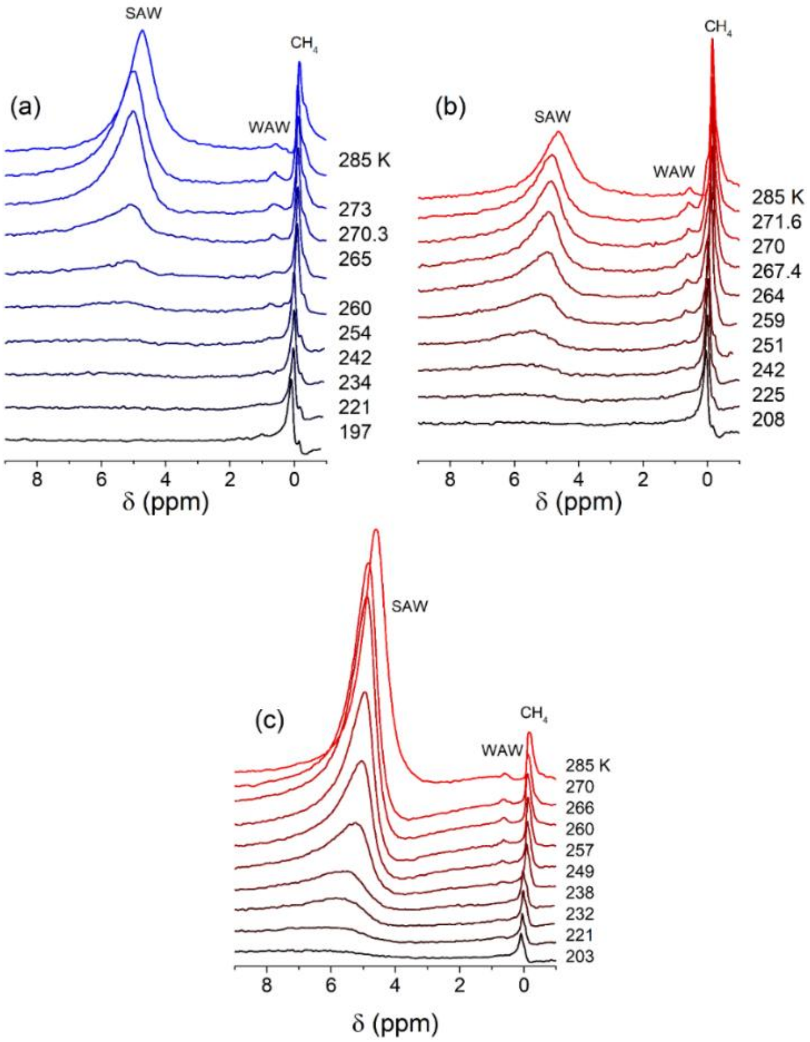

Fig.2. ^{1}H NMR spectra recorded at different temperatures of water (h = 0.1 g/g) and methane adsorbed onto (a) initial blend of treated A-300 and AM1; (b) this blend after strong stirring of the mixture; and (c) dense A-300.

Water is observed in the spectra (Fig. 2) as ^{1}H NMR signals at $\delta_H \approx$ 4.5-5.5 and 1 ppm corresponding to strongly (SAW) and weakly (WAW) associated waters, respectively [15]. Signal intensity of SAW strongly decreases with decreasing temperature due to partial freezing of bound water at $T < T_f$ of water. Highly mobile methane molecules are characterized by a relatively narrow signal at $\delta_H \approx 0$ ppm. Signal intensity of methane weakly changes with decreasing temperature because $T >> T_f$ of methane. Spectral contribution of methane being in the gas phase is relatively low (this is also clear from comparison of the amounts of adsorbed methane for different samples, *vide infra*).

Minimal adsorption of methane (2.5 mg/g) is observed for hydrophilic dense A-300 at *h* = 0.1 g/g (Fig. 3a). It increases up to 10 mg/g for the composite weakly treated and becomes maximum (25 mg/g) for the strongly stirred composite. These differences can be explained by several factors. First, silicas are characterized by different PSD (Fig. 1). Second, pre-adsorbed water fills narrow voids, and if the volume of these voids decreases (*e.g.* in dense A-300) that secondary porosity caused by bound water clusters (Figs. 3c,d) can be less appropriate for the adsorption of methane. Upon strongly stirring of A-300/AM1, dense structures of A-300 can be partially destroyed. A major fraction of water is remained in state bound to A-300 since AM1 can adsorb small amounts of water (Fig. 3). Therefore, conditions for the adsorption of methane become more appropriate than that for dense A-300 alone that leads to maximal adsorption of methane.

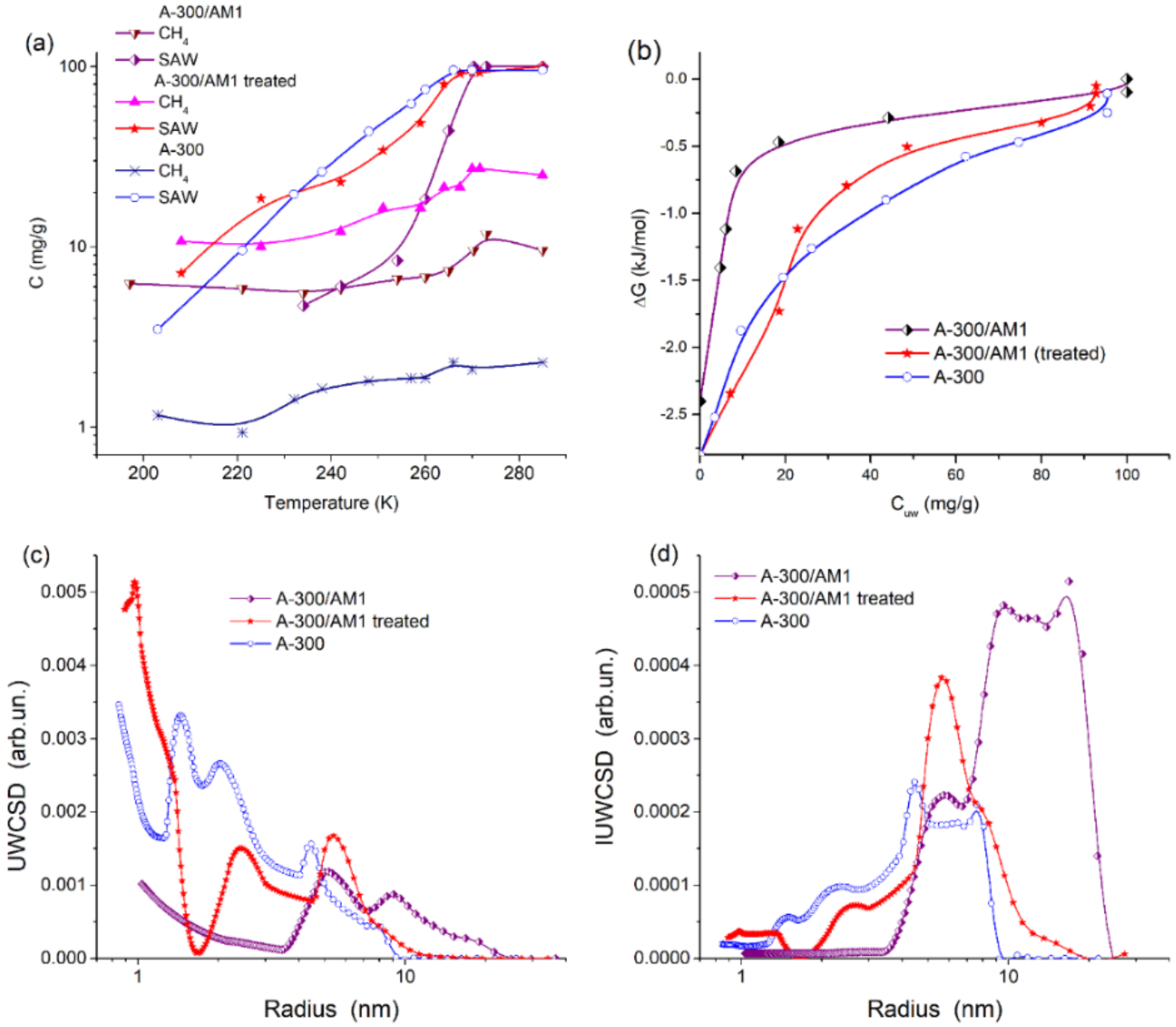

Fig. 3. (a) Temperature dependences of concentration of mobile phases of water and methane, (b) relationship between changes in the Gibbs free energy; and (c, d) unfrozen water cluster size distributions (UWCSD) differential (c) and incremental (d) for initial and stirred blends of dense A-300/AM1 (1:5) and dense A-300 calculated using NMR cryoporometry.

In the case of the weakly treated blend with A-300/AM1, the adsorption conditions for methane are worse than that for the strongly treated blend because of the difference in the particle organization. Since water was added to A-300, which was then mixed with AM1 (1:5) and then weakly treated, a fraction of hydrated A-300 can form certain shells around secondary particles with hydrophobic NPNP of AM1. However, the amount of water is relatively low (0.6 g per gram of A-300 or 0.1 g per gram of both silicas), as well as A-300 in the A-300/AM1 blend, to form core-shell secondary structures at a microscale level upon strong decomposition of large secondary particles of AM1. Therefore, the adsorption of methane onto the weakly treated blend is higher than that for the dense A-300 alone at the same h = 0.1 g/g. Upon strongly stirring, the core (AM1) – shell (A-300 + water) structures were destroyed that resulted in the increase in the adsorption of methane. A certain increase in signal intensity of methane (Figs. 2 and 3a) with increasing temperature can be due to increased mobility of bound molecules, which were practically immobile at low temperatures. Thus, the adsorption of methane depends on the presence of hydrophobic AM1 and treatment type of the A-300/AM1 blend.

RESEARCH AND DEVELOPMENT OF NANOSTRUCTURAL MATERIALS IN ISSPMT OF NSC KIPT

Victor Voyevodin

Institute of Solid State Physics, Material Science and Technologies of NSC KIPT,
Kharkiv, Ukraine
voyev@kipt.kharkov.ua

The structure of materials determines their properties, which, in turn, determine the scope of their application. Research and development of nanostructured materials can lead to the creation of new materials with unique properties, such as ODS (oxide dispersion-strengthened) steels, High Entropy Alloys, MAX phases etc. and the discovery of new properties in already widely used materials.

The state of development, the main achievements and prospects of development and investigation carried out in ISSPMT NSC KIPT NASU of Ukraine in the field of functional nanomaterials and nano technologies are presented.

The technology of production of nanostructurized ODS steels for production of radiation-tolerant materials is developed and discussed.

The method for production of ultra-dispersed (including also the nano-sized) powder of compositions Al_2O_3 – $ZrO_2(Y_2O_3)$, is developed; the method is based on the saturation of Al_2O_3 by water solutions of Zr and Y nitrates. It is used on lengthy isolation of controlled storage of radiation wastes.

Firstly were carried out the investigations of bio-compatibility of magnesium and iron materials of stents for treatment of patients with heart-vascular illness. The high efficiency of magnesium stents on their dissolving after 3-4 months exposure in blood vessel is shown. The negative reactions of tissues on the presence of stents were not detected.

Process of synthesis of nano-structurized diamond coatings alloyed by nitrogen with specific resistance into the range from 10^6ohms×cm to 10^{-1}ohms×cm is developed. It is provided at the expanse of milling of diamond grain size to 12…15 nm and effective change of the structure of grain boundaries on increase of nitrogen concentration in gaseous mixture to 40%.

Nanostructured coatings (crystallite size~30 nm, H=35 GPa, thickness ~7 mkm) with high mechanical, corrosion and radiation resistance are deposited on zirconium alloy Zr1Nb; such coatings will provide the safety and guaranteed life of claddings for fuel elements during their operation into nuclear reactor and will maintain their integrity in an accident on heating to temperature of 1100°C during 3600 sec.

Experimental-industrial method of catalytic gaseous-phase synthesis of carbon nanotubes and nanofibers (dimension 34-67 nm, strength – 9 - 10 GPa) is developed; this method allows the use of carbon materials in medicine (for filling of damaged tissues).

A new kind of vacuum-arc coatings on the base of high-entropy alloys (HEA), especially Ti-V-Zr-Nb-Hf-N is developed. The maximum values of hardness on the level of 60 GPa with modulus of elasticity 600-650 GPa were observed for these coatings. Vacuum annealing at temperature 1000°C or radiation exposure with argon ions with dose 1×10^{16}ions/cm^2 and energy 1,8 MeV doesn`t induce the change of physical-mechanical characteristics HEA due to the formation of nanostructure with sphere-like clusters with the size 3…5 nm.

A series of technological processes of vacuum-arc deposition of nanostructured two-component coatings based on different metals has been developed. Metal coatings Zr_xTi_{1-x}, Zr_xNb_{1-x}, Zr_xCr_{1-x}, Zr_xY_{1-x} with a concentration of alloying elements from 0 to 100% were formed from the filtered plasma. It is shown that nanostructured coatings are more radiation resistant compared to microstructured bulk metal of the same composition up to 80 dpa irradiation doses at 500 °C.

According to the results of studies of the composition, structure, mechanical characteristics of coatings based on systems Ti-N, Cr-N, Ti-Al-N and Ti-Cr-N, deposited from the filtered vacuum-arc plasma, the optimal conditions for the formation of coatings with high protective properties were determined. It is experimentally established that the nanostructured coatings TiN, CrN, (Ti,Al)N, (Ti,Al)N+1%Y and (Cr,Ti)N synthesized within the project have high radiation resistance when irradiated with He^+ ions with energy 500 keV doses up to 10^{17} ions/cm^2. That significantly exceeds the stability of massive materials with a microcrystalline structure. The main type of destruction of coated nitrides when irradiated with He^+ ions is flaking at depths close to the average projective range of ions. It is theoretically shown that coating materials with lower coefficients of thermal expansion are more stable, for which the mechanism of thermoacoustic activation of defect migration is inefficient and does not promote flaking. In addition, flaking can be difficult due to the amorphous-crystalline structure. Theoretical conclusions agree with the experimental data.

Fusion energy requires new materials with high resistance to sputtering, blistering and irradiation. The creation of nanostructured materials can significantly accelerate the development of these technologies. Using a gas plasma source series of W, Ta, and W-Ta coatings with crystallite size from 16 to 30 nm and tantalum content from 0 to 38 at.% were deposited. Introduction of Ta (5 38%) in the W coating leads to the columnar growth suppression and formation of a condensate with more equiaxial elements. Coatings with such a structure possess high mechanical properties. This is extremely important for choosing a material for fusion reactors.

Vacuum deformation technology for radiation-protective multilayer three-component laminates of the Ti-Fe-W system has been developed, which are potentially competitive in comparison with Al-Pb system composites due to the higher melting point of their components. With the same value of the attenuation coefficient, the weight of the composites can be 30 - 40% less than the weight of the equivalent aluminum. A characteristic feature of composites is the inherent emergence of radiation protective properties due to the presence of interfaces between layers of dissimilar metals.

To improve durability of tools and machine parts, protective coatings characterized by high hardness and adhesion, corrosion and abrasion resistance, high temperature strength and chemical stability are required. Mechanical or chemical properties of two-component nitride coatings are not always sufficient. By adding a third element or creating multilayer structure in the nitride coating microstructure and various properties can be improved.

A series of oxynitride vacuum-arc coatings with thickness ~ 10 μm based on titanium and chromium has been developed. The grain size decrease from 109 nm for CrN to 11 nm for CrON is observed. It is shown that coatings based on CrON system due to high hardness (30 GPa), low coefficient of friction (0.48), low wear rate (6.7×10^{-8} mm^3/Nm) can replace the widely used chromium nitride (coefficient of friction (0.65) and wear rate (4×10^{-6} mm^3/Nm), both to increase the working capacity of the processing tool and to protect machine parts. It is shown that nanostructured oxynitride titanium coatings TiN_xO_y have high values of nanohardness (34 GPa), corrosion resistance in saline solution and good decorative properties.

The properties, structural features and tribological tests of complex-doped $Cr_xV_{1-x}N$ and multilayer (thickness of one layer – λ=25 nm) CrN/VN coatings with thickness ~ 7 μm were investigated. The addition of the third element (vanadium) leads to a decrease in crystallite sizes from 100 nm to 36 nm or the creation of a nanolayer structure, which causes a significant improvement in the properties of the coatings. Due to the low coefficient of wear (2×10^{-7} mm^3/Nm) and friction (0.4). The obtained nanostructured multilayer (λ=25 nm) coatings VN/MoN have exceptional properties in comparison with single-layer mono nitrides VN and MoN: high hardness (35 GPa), good abrasion resistance, low friction coefficient (0.35), resistance to high temperatures and chemical inertness. These coatings also can be used as self-lubricating coatings in tribological contacts operating at high temperatures.

By the vacuum-arc method, using a MAX phase (Ti_2AlC) cathode were deposited coatings with the composition $Ti_{65}Al_7C_{28}$ and a structure containing phases TiC and α-Ti (Al) with a crystallite size of 12 and 8 nm, respectively. Coatings are characterized by a small number of macroparticles on the surface and the absence of a columnar structure. The cavitation resistance of

$Ti_{65}Al_7C_{28}$ coatings is 3 times, and the abrasion resistance is 30 times higher than that of Ti_6Al_4V alloy and 1.5 times higher than for TiN coating. This indicates the prospects of studying the processes of synthesis of protective nanostructured coatings using cathodes based on MAX-phases for protecting turbine blades from cavitation and erosion wear.

Thus, it is shown that by creating a nanostructure in various materials and coatings, new properties can be obtained or performance characteristics can be significantly improved.

INTEGRATED DIFFUSION SATURATION OF THERMITE STEEL SURFACE BY POLYMERS

Zhiguts Yu.Yu., **Zub I.M.**

Uzhhorod National University, 46, Pidgirna Str., Uzhhorod, Ukraine, 88000

Introduction The development of modern technology requires the creation of new materials to ensure reliable operation of machine parts and tools in various conditions. In solving this problem, considerable attention should be paid to the introduction of effective methods of chemical-thermal treatment (CTT) into production. The synthesis of termite materials, given the advantages of the technology, is booming. At the same time, the use of diffusion coatings in various industries solves a number of important national economic problems, the relevance of which is confirmed by the increasing attention both in Ukraine and abroad.

The solution of these tasks is carried out as a result of the development of fundamentally new highly efficient diffusion saturation technologies. The wide possibilities for this are revealed by the use of diffusion coatings of termite alloys with a complex of elements. Complex diffusion coatings have high strength, viscosity, heat resistance, corrosion resistance, wear resistance, that is, they provide high operational properties of the machined parts.

Therefore, the creation of new highly efficient saturating media for complex saturation, which allows obtaining coatings with special properties and contributing to the intensification of the diffusion processing process, is an urgent task [1].

Analysis of patent and literature data has shown the promise of using compounds of organic nature, in particular polymers, to intensify the processes of nitrocarburizing termite alloys [1-4].

Purpose of the study. The research is aimed at finding new active saturating media and methods for intensifying the processes of thermo-chemical treatment of termite alloys.

Materials and methods of experimental research. The studies were carried out on samples of “Ст 3” carbon termite steels and on “P6M5” alloyed termite high-speed steel. Diffusion saturation of the samples was carried out by heating with industrial high frequency currents and electrical resistance at a speed of 323-423 K/s. The processes of thermal degradation of polymer compositions were studied on a PAULIK-ERDEY system derivatograph (Hungary). In this case, differential thermal and thermogravimetric analyses were carried out.

The structure and phase composition of the diffusion layers were studied using metallographic, x-ray phase, and X-ray microanalysis. Metallographic studies were performed using an MIM-7 optical microscope, X-ray diffraction analysis was performed using a DRON-3.0 diffractometer, and X-ray microanalysis was performed using a scanning electron microscope and KAMEBAKS X-ray microanalyzer from KAMEKA (France).

The thickness and quality of diffusion coatings were determined using an optical system on a PMT-3 device according to the distribution of microhardness and contact thermo-EMF. To measure the value of contact thermo-EMF, we used a special installation mounted on the basis of the “ПМТ-3” microhardness tester, in which the diamond pyramid was replaced by a reference electrode.

Mechanical properties - impact strength was determined on a pendulum headstock MK-30; tensile strength characteristics on a tensile testing machine 2161P; hardness on Brinell and Rockwell hardness testers; electrochemical studies at the potentiostat “П-5827”.

Experimental studies began with the selection of the optimal components for the nitrocarburizing process of termite steels.

The selection of effective organic media was carried out on the basis of a comparison of the thermodynamic factors of the decay of molecules. Carbonitride organic compounds were analyzed by the temperature and energy of breaking the chemical bonds of the functional groups: amide ($-CO-NH_2$); amino ($-NH_2$); cyano ($-CN$); isocyanate- ($-NCO$); nitroso ($-N=O$); nitro ($-NO_2$); isooxy- ($-NON_2$); azo ($-NN$); azido- ($-NNN$); heterocyclic compounds containing tertiary nitrogen, in comparison with those of the day nitrogen (N_2) and ammonia (NH_3) traditionally used components of media for nitrocarburizing.

The analysis showed that organic compounds with low bond breaking energies up to 350 kJ/mol (nitro-, nitroso-, azooxy-, diazo-, azido) compounds during heating to saturation temperatures of 773-1373 K (optimal temperature for nitrogen diffusion in α, γ, δ-phases of iron) decompose with the formation of a weakly active molecular nitrogen, which has not been used as an effective medium for saturation, due to the high dissociation energy of its molecules – 942 kJ/mol.

The study of the saturating ability of compounds with bond cleavage energies above 435 kJ/mol (nitriles and cyanides) is of less interest for several reasons. The most promising components containing carbon and nitrogen for nitrocarburizing processes turned out to be compounds with a chemical bond breaking energy of 350-420 kJ/mol (amides, amines, heterocycles). These compounds have increased thermal stability, decompose at temperatures above 473-573 K with the formation of various active low molecular weight compounds with a low dissociation energy of molecules.

The high saturating ability of polymers is explained by the peculiarities of their decomposition under the influence of a number of factors: high temperatures, high-speed heating, and the electromagnetic field as a result of thermal and electrochemical reduction degradation, which proceed with the formation of low molecular weight volatile products on the surface of thermite steel that can actively adsorb and diffuse deep into the alloy.

Studies have led to optimization of the composition of the UF resin (urea-formaldehyde) relative to variable factors of the saturating medium: viscosity, concentration of UF resin and its saturation time. The optimization criteria were the thickness of the nitrocarbon layer, which characterizes the rate of CTT processes and the maximum microhardness of the coating, which characterizes the quality of diffusion processing. The calculation results showed that the compositions of CF resin with a dynamic viscosity of more than 200 Pa·s and a concentration of 60-100% have the maximum saturating ability. At a treatment temperature of 1223 K and a saturation time of 60-300 s on “P6M5” steel, they provide the formation of a nitrocarbon layer 130-280 μm thick with a surface microhardness of 7–7.5 GPa (fig. 1), which is 5–10 times faster compared to commonly used industrial media (nitrocarburizing at 1223 K for 60 min and cyanidation at 1223 K for 30 min).

The results of the study of the temperature-time parameters of the saturation process showed that, depending on the temperature and processing time, the structure and properties of the nitrocarbonized layer vary over a wide range. At low temperatures 793-973 K is mainly the saturation of steel with nitrogen, when 1033-1133 K – nitrogen and carbon and 1133-1323 K – carbon. For example, the phase composition of samples of steel “P6M5” treated at 1223 K, regardless of the time of saturation, consists mainly of solid solution of nitrogen and carbon in γ-iron solid solution on the basis of nitride $Fe_{2\text{-}3}N$. The value of the lattice γ-phase is practically constant and is a=0,3635±0,0003 nm, which corresponds to the limit content of nitrogen and carbon of 2.14 wt. %.

The study of physical and mechanical properties of the samples showed that the cyanide in the UF resin increases the tensile strength by 20-60% in static tensile testing and reduces the impact strength of the samples to 10 %, which is within the permissible values for commonly used methods, cyanidation of low-carbon steels.

Nitrocarburizing in the composition based on UF resin can significantly increase the hardness of steel, for example, for low-carbon “Cт 3” – 4,0 GPa, for alloyed “P6M5” – 11,5 GPa (table 1).

Table 1

The results of diffusion saturation of steels in UF resin (concentration – 90%)

Steel grade	Processing mode		Layer thickness, microns	The microhardness of the layer, GPa
	temperature, K	time, min		
Cт 3	1223	3	100	4,0
P6M5	833	5	50	11,5

Tests of steel samples “P6M5” after nitrocarburizing in UF resin (1233 K for three minutes) under sliding friction conditions showed an increase in wear resistance by 2,5-3 times compared to untreated samples. In fig. 1 shows the change in microhardness and wear resistance over the cross section of a sample of “P6M5” steel under dry friction.

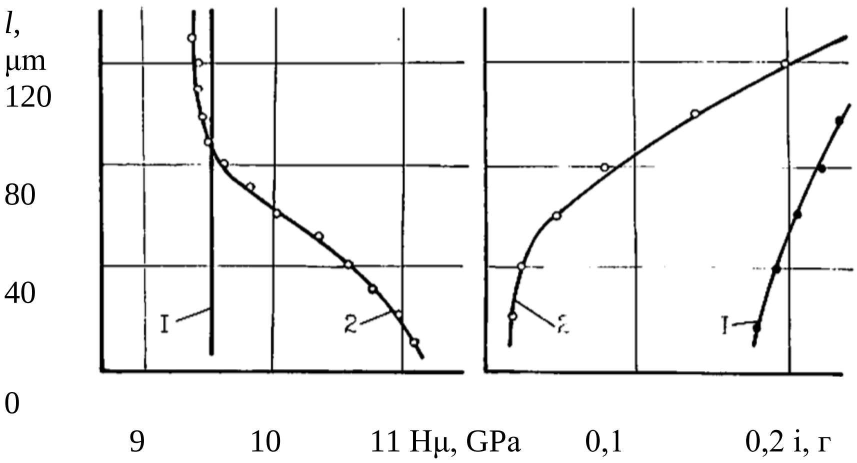

Fig. 1. Change in microhardness (Hµ) and wear resistance (i) over the cross section of a sample of “P6M5” steel under dry friction conditions: 1 – initial sample, 2 – sample after nitrocarburizing in UF resin in the form of a coating at a temperature of 560^0C for 5 min

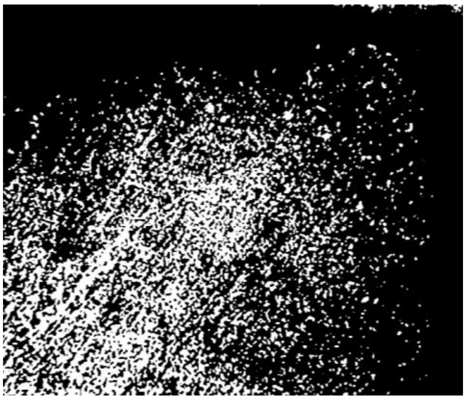

Fig. 2. The microstructure (x200) of the nitrocemented layer of steel “P6M5” after processing in UF resin in the form of a coating at a temperature of 560^0C for 5 min

Table 2

№	Index	Departure		After nitrocarburizing in UF resin	
		without treatment	“ГОСТ 380-71”	150^0C, 3 min	950^0C, 3 min
1	Layer thickness, microns	-	-	40-60	75-100
2	Hardness HB, MPa	1310	1240	2170	4010
3	Hardness HRC	-	-	20	42
4	Tensile strength, MPa	513	372-480	600	817
5	Elongation at tension,%	27	26-27	9	4
6	The relative narrowing in tension,%	60	-	25	17
7	Impact strength, kJ/m^2	993	784	809	817

The values of impact strength, strength indicators of samples “Cт 3” after processing differs little from those for samples after nitrocarburizing, which allows us to recommend the developed compositions for industrial use.

Physical and mechanical properties of thermite steel analogue of “Ст 3” are shown in table 2. The technological scheme of industrial use of the developed compounds is proposed.

Thus, the results of the studies showed the feasibility and prospects of the implementation of CTT processes of termite steels in polymer-containing media, made it possible to develop technological compositions and technology of steel nitrocarburizing processes.

Conclusions. 1. Resin-based polymer-containing compositions have been developed that provide high rates of CTT processes for termite alloys. These compositions can increase the rate of nitrocarburization up to 20 times in comparison with commonly used industrial environments. At the same time, high-quality diffusion layers with a high hardness of 4000-11500 MPa are formed, allowing 2-3 times to increase the wear resistance of the machined parts.

2. A method is proposed for choosing the most effective components for the process of nitrocarburization of thermite steels, which made it possible to develop compositions with high saturation ability.

3. It has been established that under the same temperature-time conditions of saturation, polymers have a greater saturating ability compared to commonly used low molecular weight substances. For example, at a temperature of 1223 K and a cyanidation time of 60 s, a urea-formaldehyde resin provides a large thickness of 145 μm and a microhardness of 7.5 GPa.

4. The activating effect of polymers in the processes of diffusion saturation of steels is caused by the formation in the treatment zone of a high concentration of active low molecular weight products, various radicals of the pyro-polymer residue capable of interacting with the metal surface and diffusing deep into the alloy. Compositions based on UF resins are highly adaptable, which is explained by good adhesion of UF resins to a metal surface, and the absence of corrosive effects on the materials of workpieces and equipment.

1. Жигуц Ю. Ю., Лазар В. Ф. Технології отримання та особливості сплавів синтезованих комбінованими процесами // Ужгород: Видавництво «Інвазор», 2014. – 388 с.
2. Жигуц Ю. Ю., Лазар В. Ф., Хом’як Б. Я. Перспективні технології засновані на комбінованих процесах // Науковий вісник Мукачівського державного університету. Журнал наукових праць. – № 22 (17). Мукачево. 2017. – С. 29 - 40.
3. Zhiguts Yu. Yu., Vivtharskuj O. V. Using SHS for synthesis of nanostructures in hard alloys and karbidostal’s // Clusters and nanostructured materials (CNM-4’2015) Комплексне забезпечення якості технологічних процесів та систем: 4 international meeting, 12-16 October 2015.: materials conf. – Uzhorod: Ukraine, 2015. – С. 141.
4. Zhiguts Yu. Development of SHS technology / Yu.Zhiguts, Ya.Legeta, Yu.Golovka // Prospects of world science –2019: XV intern. scientific and practical conf., 30 July 2019 - 7 August 2019: Materials of the conf. – Sheffield: Science and education LTD, 2019. – № 8. – P. 61 - 63.

POSTERS

EFFECT OF Se-CONTENT DOPING ON ELECTRONIC, DYNAMICAL AND MECHANICAL PROPERTIES OF $TlInS_2$ LAYERED CRYSTAL

T. Babuka[1,2], O.O. Gomonnai[3,4], K.E. Glukhov[1], L.Yu. Kharkhalis[1], A.V. Gomonnai[3,5],
D.R.T. Zahn[6], M. Makowska-Janusik[2]

1- Institute for Physics and Chemistry of Solid State, Uzhhorod National University, 54 Voloshin St., 88000 Uzhhorod, Ukraine
2- Institute of Physics, Faculty of Mathematics and Natural Science, Jan Dlugosz University in Czestochowa, Al. Armii Krajowej 13/15,
42-200 Czestochowa, Poland
3- Uzhhorod National University, 46 Pidhirna Str., 88000 Uzhhorod, Ukraine
4- Vlokh Institute of Physical Optics, 23 Dragomanov Str., 79005 Lviv, Ukraine
5- Institute of Electron Physics, Ukr. Nat. Acad. Sci., 21 Universytetska Str., 88017 Uzhhorod, Ukraine
6- Semiconductor Physics, Chemnitz University of Technology, D-09107 Chemnitz, Germany

Recently layered crystals have attracted research interest due to their promising structural and physical properties. A possibility to create new multifunctional artificial materials obtained through the arrangement of several layered crystals has become a new subject of studies. Therefore, at this stage in the search for new materials, extensive investigation is carried out on the structural and physical properties of layered semiconductors, which can be promising materials for heterostructures. One of such materials is $TlInS_2$ crystal, which belongs to the $A^{III}B^{III}C^{VI}_2$ group of chalcogenide semiconductors – ferroelectrics [1], and is regarded to be one of the highly anisotropic crystals [2,3]. In the row of $TlIn(S_{1-x}Se_x)_2$ crystalline solid solutions, the crystal structure changes from C_{2h}^6 to D_{4h}^{18} symmetry at a Se content x near 0.7–0.75 [2,3]. It was concluded that in the (x, T) phase diagram of the $TlIn(S_{1-x}Se_x)_2$ crystals a Lifshitz type point can exist [4] and polycritical phenomena in the (p, T)-phase diagram of these materials [5].

For our investigations $TlIn(S_{0.75}Se_{0.25})_2$ single crystals were grown by the Bridgman technique [6]. The crystal quality and chemical composition were checked by methods described in Ref. [6]. The lattice parameters were determined by X-ray diffraction study and compared to known data for $TlInS_2$ crystal. Additionally, the absorption spectra were measured. The energy band gap for $TlIn(S_{0.75}Se_{0.25})_2$ crystal was obtained $E_g = 2.17$eV.

The electronic and vibrational properties of the $TlIn(S_{0.75}Se_{0.25})_2$ crystal were calculated taking into account the GGA approximation implemented in the Quantum-ESPRESSO package. Since the $TlInS_2$ crystal possesses a layered structure with the vdW gap we applied the DFT-D approach, taking into account the Tkatchenko and Scheffler (TS) correction of the dispersion interaction. In the results, the values of the band gap were obtained equal to 2.14 eV that is good correlated with experimentally measured data.

Calculated vibrational parameters were compared with available experimental data of Raman scattering and good agreement was demonstrated. Elastic anisotropy (directional dependence of the Young moduli) of these compounds was modeled and analyzed for the first time. In the result, next values of the elastic constants were obtained: C_{11}=45.23685 GPa, C_{22}=42.93885 GPa, C_{33}=54.29495 GPa, C_{44}=3.12360 GPa, C_{55}=-20.09220 GPa, C_{66}=24.1507 GPa, C_{12}=32.69328 GPa, C_{13}=31.93395 GPa, C_{15}=-10.18002 GPa, C_{23}=20.87000 GPa, C_{25}=4.60690 GPa, C_{35}=17.42128 GPa, C_{46}=0.93285 GPa. Using the Christoffel equation the sound velocities of $TlInS_2$ and $TlIn(S_{0.75}Se_{0.25})_2$ crystals were calculated. For a detailed study of the effect of doping on the physical properties of the considered material, obtained results were compared with known experimental data for pure $TlInS_2$ crystal [7].

1. V. Grivickas, P. Scajev, V. Bikbajevas, O. V. Korolik, A. V. Mazanik, Carrier dynamics in highly excited $TlInS_2$: evidence of 2D electron-hole charge separation at parallel layers Phys. Chem. Chem. Phys., 21, pp. 2102-2114 (2019).
2. Panich, A. M. Electronic properties and phase transitions in low-dimensional semiconductors. Journal of Physics: Condensed Matter, 20, pp. 293202 (2008).
3. K. R. Allakhverdiev, T. G. Mamedov, B. Akmoğlu, S. S. Ellialtioğlu, Phase transitions in ternary layered $A^3B^3C_2^6$ group ferroelectric semiconductors. Tr. J. Phys. 18, pp. 1-66. (1994).
4. Sheleg A U, Hurtavy V G, Shautsova V V, Aliev V A. Dielectric properties and phase transitions in crystals of $TlInS_xSe_{2-x}$ solid solutions. Phys. Solid State 54, pp 622–625. (2012).
5. Guranich P P, Rosul R R, Gomonnai O O, Slivka A G, Roman I Y, Gomonnai A V. Ferroelastisity of $TlInS_2$ crystal. Solid State Commun. 184 pp. 21-24. (2014).
6. Gomonnai A V, Petryshynets I, Azhniuk Yu M, Gomonnai O O, Roman I Yu, Turok I I, Solomon A M, Rosul R R, Zahn D.R.T. Growth and characterisation of sulphur-rich $TlIn(S_{1-x}Se_x)_2$ single crystals. J. Cryst. Growth. 367, pp 35-41. (2013).Martynyuk-Lototska, I.
7. Trach, O. Kokhan, R. Vlokn, Efficient acousto-optic crystal, $TlInS_2$: acoustic and elastic anisotropy, Applied Optics, Vol. 56, No. 11 (2017).

DEVELOPMENT OF HIGH-EFFICIENT SOLAR CELLS WITH PYRAZOLINE LUMINOPHOR COATING LAYER

Ie.V. Beliak, D.Yu. Manko

Institute for Information Recording, NAS of Ukraine, Shpak str., 03113 Kyiv, Ukraine
e-mail: beliak1312@gmail.com

Solar cell systems has been found to be a promising green energy source with strong support by both government and customers which recently got significant delivery infrastructure development [1-3]. Nevertheless large scale use of solar energy is still not possible due to its low efficiency caused by substantial mismatch between the solar radiation and photo-electrical transducer optical absorption spectra [4-6]. It should be also mentioned that solar energy which cannot be absorbed by photo-electrical transducer will overheat it structure which causes solar element lifetime decrease. The typical approach to solve mentioned problem is development multi-junction photovoltaic element by combining several p-n junctions of subcells structure which has to combine different a bandgap fully covering solar radiation spectrum [7-9]. Unfortunately multi-junction solar cell cannot be considered as a green energy source while it characterized by:

- complicated fabrication process which leads to high cost;
- use of toxic compounds during fabrication process;
- high cost of solar cell's safe disposal procedure.

It was proposed to develop solar based on polycrystalline silicon photoelectric transducer with nanostructured pyrazoline luminophor coating layer [10]. Luminophor coating is used to absorb shorter wavelengths of the solar radiation spectrum (280-510 nm) and transmits longer wavelengths radiation (according to the photoluminescence process and spectral Stocks shift) which can be absorbed by photoelectric transducer (550-630 nm). Nanostructured pyrazoline luminophor class was synthetized in order to meet following parameters [11-16]:

- high quantum yield (samples of pyrazoline luminophor coating have shown 75-85% of quantum yield)
- spectral Stocks shift which allow to cover mismatch between spectra (samples of pyrazoline luminophor coating have shown $\Delta\lambda_{SS} = 150 - 310$ nm);
- possibility of an luminescence and absorption bands variation of the material (samples of pyrazoline luminophor coating have shown band variation of $\Delta\lambda_{\mathrm{LUM}} = 12 - 70$ and $\Delta\lambda_{\mathrm{ABS}} = 10 - 30$ nm);
- stability of optical properties of the (samples of pyrazoline luminophor coating have shown stability of optical properties under sunlight exposure within luminescence and absorption 2% rate level during 20 years of exploitation);
- low cost and fabrication process simplicity (samples were fabricated by mixing of pyrazoline dye, white zeolite and UV lacquer with further UV exposure).

Luminescent irradiation is not collimated which cases loss of half of the converted energy by luminophor coating layer. It was noticed that non-flat structure of the solar cell elements [10] could increase absorption rate of converted radiation by photoelectric transducers. Let's consider periodic structure with horizontal element, element angled by α and connected with the first one, and element angled by $(\pi - \alpha)$ and connected with the second one. When we determine every element length as L than width of the three elements group as a combined element of periodic structure is $\left(L + 2L \cdot cos(\alpha)\right)$ and whole structure relief height is $L \cdot cos(\pi/2 - \alpha)$. If we know angle of incident light β_{IL} and wavelength λ_{IL}, reflection coefficient of relief photoelectric transducer is calculated as function $\varepsilon(\beta_{\mathrm{IL}}, \lambda_{\mathrm{IL}})$. It allows determining optimal structure parameters of solar cell and properties of luminophor coating layer it is necessary to develop proper mathematical model of the absorption process.

Luminescent light intensity gain caused by application of the relief structure of photoelectric transducer can be calculated as integral by $\lambda_{\mathrm{IL}} \in \left[\lambda_{\mathrm{IL}}^{\min}; \lambda_{\mathrm{IL}}^{\max}\right]$ of three integral functions sums by $l \in [0; L]$:

$$\left[\begin{array}{c} \Delta I_{\mathrm{LUM}} = \int_{\lambda_{\mathrm{IL}}^{\min}}^{\lambda_{\mathrm{IL}}^{\max}} \left(\int_{0}^{L} (I_{\mathrm{LUM}} \cdot \varepsilon) dl + \int_{0}^{L \cdot cos(\alpha)} (I_{\mathrm{LUM}} \cdot \varepsilon' + I_{\mathrm{LUM}} \cdot \varepsilon'') dl \right) d\lambda_{\mathrm{IL}} \\ I_{\mathrm{LUM}} = I_{\mathrm{IL}} \cdot \eta \cdot k_{ABS} \end{array}\right.,$$

where

- I_{LUM} is intensity of luminescent signal;
- I_{IL} is intensity of incident light;
- ε, ε' and ε'' are reflection coefficient function by l and λ_{IL} for three type elements
- η is quantum yield
- k_{ABS} is luminophor absorption coefficient.

Synthesized nanostructured luminophor class is based is based on organic pyrazoline dye with addition of polymethylmethacrylate or polystyrene, white zeolite which forms nanoporous structure and UV lacquer “Rengolux PRO”. Computer simulation was provided for solar cell based on polycrystalline silicon photoelectric transducer. It allowed determining optimal linear parameters of photoelectric transducer elements and choosing luminophor coating material with proper optical properties. Basically estimated parameters could be demonstrated as a list of methodological recommendations of solar cell development which include chemical components of luminophor coating dye and optimal angle value of photoelectric transducer elements:

- 53SM pyrazoline luminophor based on pyrazoline UV dye with 5% addition of polymethylmethacrylate (optimal angle value is 30°);
- 59HM pyrazoline luminophor based on pyrazoline orange-red dye with 5% addition of polymethylmethacrylate (optimal angle value is 40°);
- 59M pyrazoline luminophor based on pyrazoline orange-red dye (optimal angle value is 40°);
- 53SC pyrazoline luminophor based on pyrazoline UV dye with 5% addition of polystyrene (optimal angle value is 35°);
- 59HC pyrazoline luminophor based on pyrazoline orange-red dye with 5% addition of polystyrene (optimal angle value is 45°).

Thereby computer simulation of the photoelectric transducer relief structure coated with luminophor layer allowed understanding physics of the process and calculating optimal parameters of the solar cell.

1. Conley, K. A. (2017). *Solar energy*. Minneapolis, MN: Core Library, an imprint of Abdo Publishing.
2. Sohn, E., & Ohlenroth, P. (2020). *Solar energy*. Chicago, IL: Norwood House Press.
3. Felix, R., & Craig, D. (2019). *Solar energy*. Minneapolis, MN: Sandcastle, an imprint of Abdo Publishing.
4. Boer, W. D., & Gregorkiewicz, T. (2012). Enhancing solar cell efficiency by tailoring the spectrum. *SPIE Newsroom.* doi:10.1117/2.1201202.004136
5. Dorodnyy, A., Shklover, V., Braginsky, L., Hafner, C., & Leuthold, J. (2014). Spectrum splitting double-cell scheme for solar photovoltaics. *2014 IEEE 40th Photovoltaic Specialist Conference (PVSC).* doi:10.1109/pvsc.2014.6925365.
6. Lorentzen, J. R., Scheiman, D. A., Hoheisel, R., Walters, R. J., & Jenkins, P. P. (2015). Impact of solar simulator spectrum on multi-junction solar cell measurement. *2015 IEEE 42nd Photovoltaic Specialist Conference (PVSC).* doi:10.1109/pvsc.2015.7355847

7. Emery, K., & Osterwald, C. (2013). Better measurement of multijunction solar cell efficiency. *SPIE Newsroom*. doi:10.1117/2.1201311.005201
8. Fraas, L. M. (2014). The Story of the 40% Efficient Multijunction Solar Cell. *Low-Cost Solar Electric Power*, 97-115. doi:10.1007/978-3-319-07530-3_8
9. Rabeya, R., & Hakim, F. (2018). Design and Performance Analysis of Multijunction Organic Solar Cell Exceeding 14% Efficiency. 2018 10th International Conference on Electrical and Computer Engineering (ICECE). doi:10.1109/icece.2018.8636785
10. Kryuchyn, A.A., & Beliak, Ie.V. (2014). Development of nanostructured luminophor coating for broadening of solar cell absorption spectrum. *Next Generation Technologies for Solar Energy Conversion V*. doi:10.1117/12.2060832
11. Beliak Ie.V. Luminescence of the pyrazoline dye in nanostructured zeolite matrix / Ie.V. Beliak, V.G. Kravets, A.A. Kryuchyn. // *Semiconductor Physics, Quantum Electronics & Optoelectronics*. – 2007. – V.10, N.1. – P. 33-35.
12. Beliak Ie.V. Development of Fluorescent Multilayer Disc Structure / Ie. Beliak, L. Butenko // Proc. SPIE. – 2011. – Vol. 8011. – pp. 80112-80120
13. V.V. Petrov, Zichun Le., A.A. Kryuchyn, Ie.V. Beliak. A.S. Lapchuk, E.M. Morozov. Long-term storage of digital information July 2018 DOI: 10.15407 Akademperiodyka. 360.148ISBN: 9789663603605.
14. Petrov, V., Kryuchyn, A., Beliak, I., & Lapchuk, A. (2016). Multi-Photon Microscopy and Optical Recording. doi:10.15407/akademperiodyka.311.156.
15. Anikin, P., & Beliak, I. (2019). Development of multispectral recording media for multilayer photoluminescent information recording. *Electronics and Information Technologies, 12*. doi:10.30970/eli.12.11.
16. Beliak, I. V., Petrov, V. V., Manko, D. Y., & Kryuchyn, A. A. (2014). Synthesis of Recording Medium for Multilayer Photoluminescent Disc. *Advances in Materials Science and Applications, 3* (1), 6-12. doi:10.5963/amsa0301002.

MIXING AND SELF-ORGANIZATION OF THE STRUCTURE OF MATERIALS UNDER SEVERE PLASTIC DEFORMATION

Beygelzimer Y.[1], Kulagin R.[2], Davydenko O.[1], Dmitrenko V.[1]

[1]*Donetsk Institute for Physics and Engineering named after O.O. Galkin of the National Academy of Sciences of Ukraine, 46. Nauky Av., Kyiv, 03028, Ukraine*
[2]*Institute of Nanotechnology, Karlsruhe Institute of Technology, 76344 Eggenstein-Leopoldshafen, Germany*

The report presents results of studies on a mixing of metals during the formation of nanostructured metal compositions by the severe plastic deformation (SPD) technique. When creating new materials, the starting components are combined with each other, usually in a liquid state. Solid-phase synthesis by joint plastic deformation of the components under high pressure opens up completely new possibilities in this regard. The guiding principle was proposed by the Nobel Prize winner Percy Williams Bridgman. He suggested an innovative technique based on the torsion of samples in the form of thin disks between two anvils, and used it to create alloys and polymers in his first experiments [1, 2]. The sample was compressed between the anvils during the deformation under an applied pressure of tens of thousands of bars. Today the technique is known as High Pressure Torsion (HPT).

Since the late 1980´s, HPT has been widely used to create ultrafine-grained metals and alloys with remarkable physical and mechanical characteristics [3]. In addition to HPT other techniques were developed, based on the Bridgman´s idea to stimulate phase transformation by applying large deformations. This approach has a common name of SPD [4].

A key step in the materials synthesis during SPD is the delivery of atoms of different components to specific locations in the sample. It is carried out due to the mixing process in the solid phase. One can distinguish the mixing at different spatial scales. We can outline the synthesis during the SPD as follows. The starting material has rather large structural characteristic size of tens or hundreds of micrometers and can be used in various shapes, such as wires, tapes, plates, powder particles, etc. During SPD, they are thinned to micron and submicron scale, fragmented into small pieces and mixed together. In parallel, crystal lattice defects including vacancies, dislocations, and grain boundaries are formed, leading to the mechanical activation of the material and acceleration of the diffusion processes. High hydrostatic pressure in the deformation zone prevents the failure of the material. All this creates the conditions for the formation of solid solutions, new phases, and chemical compounds, even those that cannot be obtained by liquid-phase approach.

The scheme of SPD synthesis looks rather understandable and was already presented by P. Bridgman in his first works [1, 2]. However, the details of the process are still largely unexplained in microstructural terms. This hinders the employment of the enormous potential of SPD synthesis, since without the knowledge of the process details it is impossible to gain the desired result. In particular, without understanding the mechanisms of solid-phase mixing, it is not possible to ensure the necessary distribution of substances throughout the sample volume.

In order to quantitatively study the mixing process, a parameter characterizing the degree of mixing is introduced in the work. This is done as follows. Let us consider schematically the process of mixing two substances, A and B. They are completely separated in the initial state, and their volume fractions are equal to a and b respectively $(a + b = 1)$ (Fig. 1).

Fig.1. Scheme of mixing two components (a – initial, b – after deformation)

During the mixing, regions with two substances are formed (Fig. 1b). We define a parameter that would characterize the degree of mixing of substances in such areas. In the study of mixing, first of all, it is necessary to determine the size of the averaging area, which allows introducing such concepts as the concentration of components and field characteristics of mixing. This area plays the role of a representative volume in the mechanics of continuous media. Its characteristic size should be determined by the physics of the process. In the study of mixing, the averaging area will be considered a point, similar to material points in the mechanics of continuous media.

We will consider only two scale levels, each of which is associated with its determinative mechanisms of mixing. For the lower scale level, where mixing is due to diffusion, the characteristic sizes satisfy the condition $l < l_d$, where l_d is the characteristic size of the diffusion zone ($l_d = \sqrt{2D_{eff}\tau}$, where τ is the characteristic diffusion time and D_{eff} is the effective diffusion coefficient). According to preliminary estimations $l_d \sim 1\ \mu m$.

The upper scale level is characterized by the lengths $l_d \ll l < L$, where L is the size of the sample (the area that the components originally occupy). At this level, mixing is due to the mechanisms of advection mass transfer. Studies of mixing at the upper and lower scale levels will be performed according to their respective methods. Below we describe the technique proposed for the mixing at the upper scale level.

At the upper level, we introduce the concepts of concentration of components $\xi_a(\mathbf{r})$ and $\xi_b(\mathbf{r})$, by which we mean the volume fractions of components A and B in the averaging zone, centered at a point $\mathbf{r}$. Obviously, $\xi_a(\mathbf{r}) + \xi_a(\mathbf{r}) = 1$. The numbers $\xi_a(\mathbf{r})$ and $\xi_b(\mathbf{r})$ are determined by EDX analysis, with a spot size $\sim l_d$. As a measure of mixing $\omega(\mathbf{r})$, we take a value that satisfies the following conditions:

(1) in areas where there is no mixing, when $\xi_a = 0$ and $\xi_a = 1$, $\omega = 0$;
(2) for perfect mixing, when $\xi_a = a$, the value ω reaches a maximum of 1.

A variety of expressions can satisfy these conditions, of which we take the simplest:

$$\omega = \begin{cases} \dfrac{\xi_a}{a}, \ when\ \xi_a \le a \\ \dfrac{1-\xi_a}{1-a}, \ when\ \xi_a > a \end{cases}$$

As an example, Fig. 2 shows the distribution of the ω value for the workpiece of two layers of copper and aluminum of equal thickness under the HPT deformation.

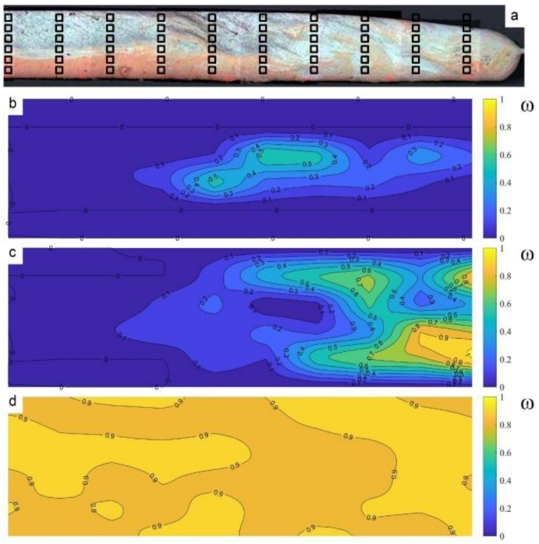

Fig. 2. Scheme of the ω index distribution through the sample cross section
(a – scheme of samples with points of XRD analysis, b, c, d – distribution of ω index for beginning, middle and complete intermixed stages two layers respectively)

The aim of the experiment was to restore the ω(r) field in the sample volume according to the results of its measurements in various sections of the sample. In the experiment, we have studied the dependency of ω(r) on the properties of the materials, the geometric characteristics of the initial sample, the number of the anvil rotations, and the deformation temperature.

The work is carried out within the Target program fundamental research of the NAS of Ukraine (Project № 41/20-H).

1. Bridgman P.W. Effects of High Shearing Stress Combined with High Hydrostatic Pressure // Phys. Rev., 1935. – V. 48. – P. 825-847.
2. Bridgman P.W. Polymorphic Transitions up to 50,000 Kg/Cm of Several Organic Substances // Proceedings of the American Academy of Arts and Sciences, 1938. – V. 72. – N.6. – P. 227-268.
3. Valiev R.Z., Estrin Y., Horita Z. [et al.]. Producing Bulk Ultrafine-Grained Materials by Severe Plastic Deformation: Ten Years Later // JOM, 2016. – V. 68. – P. 1216-1226.
4. Estrin Y., Vinogradov A. Extreme grain refinement by severe plastic deformation: A wealth of challenging science // Acta. Mater., 2013. – V. 61. – P.782-817.

ELECTROCHEMICAL SYNTHESIS OF NANOCRYSTALLINE Mo-RICH SUPERALLOYS

Bersirova O.L., Kublanovsky V. S.

V.I. Vernadsky Institute of General & Inorganic Chemistry of National Academy of Sciences of Ukraine,
Academic Palladin Avenue, 32/34, Kyiv, 03142, Ukraine,
e-mail: bersibol@ukr.net

1. Introduction

Metallic molybdenum coatings and its alloys can be prepared using mechanical alloying, powder metallurgy, spark plasma sintering and laser cladding.Though the electrodeposition is one of the most promising techniques for producing these materials because of its relative low cost compared to the other methods and easy control of composition, structure and properties by operating electrolysis parameters such as bath pH, temperature, its chemical composition.

Molybdenum electrodeposits can be obtained by using non-aqueous and molten salt electrolytes. Unfortunately, pure molybdenum deposits cannot be obtained from aqueous molybdate solutions. In this case pure molybdenum deposits possibly are hindered by the formation of the mixture of polyvalent molybdenum oxides and/or hydroxides on the cathode during electrodeposition and it cannot be directly reduced to metallic molybdenum, due to a very low overvoltage for hydrogen evolution. Whereas metallic Mo from aqueous electrolytes can be successfully co-deposited with iron group metals (Ni, Co, Fe) with obtaining the corresponding alloys with high content of refractory element in the composition. This type of reaction was described as induced co-deposition. Generally, the molybdate ions are reduced to molybdenum oxide or hydroxide that in the presence of iron group metal (Ni, Fe or Co) allows formation of the corresponding binary alloy deposits. However, the addition of an appropriate complexing agent is necessary in order to improve the quality of the obtained coatings.

The Mo alloys with iron group metals have been successfully electrodeposited from a citrate, citrate–ammonia, pyrophosphate-ammonium chloride and glycinate baths.

Ammonium containing baths a can be used in order to increase the deposition rate and current efficiency of electrolysis but the addition of ammonium also results the decrease of molybdenum content in the alloy composition. Its percentage in the electrodeposit can be increased by increasing molybdate concentration in the plating bath. Generally the Mo content in the alloy coatings is influenced by pH of electrolyte as well. It is known that as the pH of the different baths for Ni-Mo electrodeposition increases, the deposition rate of Ni increases. That means at higher pH values alloys contain lower percentage of Mo (< 30 wt.%) but they are deposited with higher current efficiency and deposition rate. It was shown that the content of Mo in Ni-Mo decreases with increasing the pH of pyrophosphate electrolyte from 8.5 to 10 while current efficiency becomes lower. The further increase of pH neither deposition rate nor current efficiency did not change significantly. In contrast, an increase of pH of citrate-ammonia plating bath leads to the gradual increase of Mo amount in Ni-Mo alloy coatings up to 50.4 wt.% at pH 7. Below this value Mo percentage considerable decreases up to 13.9 wt.% at pH 10. Important to mention that at this pH value electrodeposition process was the most efficient (about 80%). Finally it was shown that an increase of citrate-ammonia electrolyte pH above 10 influences neither the deposition rate nor current efficiency.

2. Experimental

The series of baths containing a high concentration of acetate, phosphate, formate and chloride salts (up to 10 M) were tested in order to develop an electrolyte for deposition of the thick pure molybdenum coatings. But only the acetate baths allowed preparing thicker than 1 μm shiny Mo deposits. Accordingly, based on [1], Ni-Mo alloy coatings in this work were prepared from an ammonia-acetate electrolyte containing nickel sulfate heptahydrate, potassium acetate, ammonium acetate and ammonium molybdate. All solutions were prepared from chemicals of analytical grade purity dissolved in distilled water. The electrodeposition of the coatings was conducted at 30 °C at the different current densities varied from 10 to 300 mA cm^{-2} under magnetic stirring condition. The pre-experimental Cu substrate preparation consisted of chemical degreasing, washing, cleaning in an ultrasonic bath for 6–7 min and etching in HNO_3:CH_3COOH:H_3PO_4 (1:1:1) solution at temperature of 60 °C. A three electrode system with Cu substrate as a working electrode, Pt sheet (3x7 cm) as a counter electrode and saturated Ag/AgCl electrode as the reference was used for electrodeposition. All potentials are presented vs. saturated Ag/AgCl reference.

Table 1. Composition of bath used for Ni-Mo coatings deposition (concentrations are given in mol l^{-1}).

Bath	CH_3CO_2K	$CH_3CO_2NH_4$	$(NH_4)_2MoO_4$	$NiSO_4{\cdot}7H_2O$	pH
1	10,2	10,4	0.004	0.001	8.2
2				0.002	8.2
3				0.004	8.2

Surface morphology of the deposits was examined using scanning electron microscopy (SEM: Philips XL-30). The chemical composition of the prepared coatings was investigated using energy dispersive X-ay spectroscopy (EDS) at accelerating voltage of 20 kV. After determining the composition of obtained alloys by EDS technique, the current efficiency (CE) was calculated according to the Faradays' law. The thickness of the electrodeposits was calculated from gravimetric and elemental analysis data and varied from 10 to 30 μm.

3. Results and discussions

The influence of the concentration of $NiSO_4{\cdot}7H_2O$ on the chemical composition of Ni-Mo deposits was examined at a constant content of CH_3CO_2K – 10.2 M, $CH_3CO_2NH_4$ – 10.4 M and $(NH_4)_2MoO_4$ – 0.004 M, containing the variable concentrations of Ni(II) ions from 0.001 M to 0.004 M. The influence of Ni(II) ion concentration on the alloy composition and current efficiency (CE) at three different molar ratios of Ni(II)/Mo(VI) (0.25; 0.5; 1) and three different current densities (10, 30 and 300 mA cm^{-2}) is given in Fig. 1.

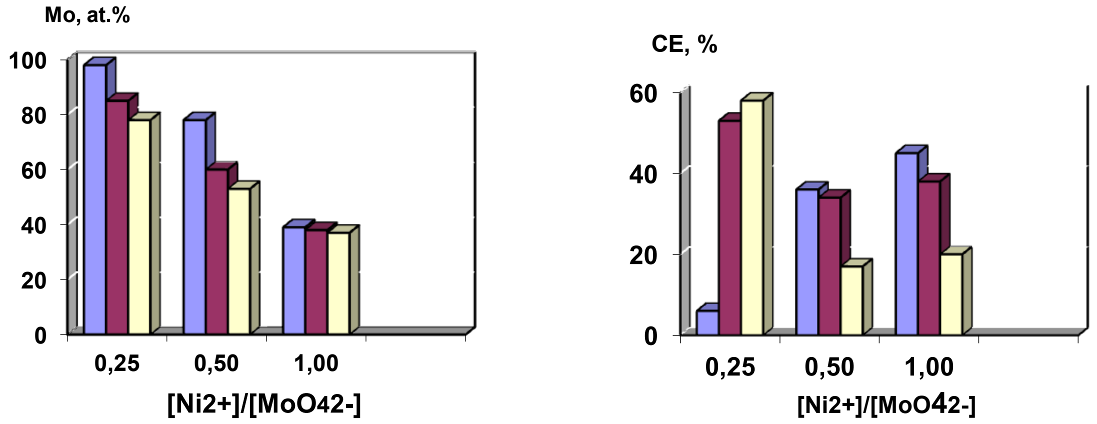

Fig. 1. The dependence of molybdenum content of the Ni-Mo deposit (a) and current efficiency (b) on $[Ni^{2+}]/[MoO_4^{2-}]$ concentration ratio in ammonia-acetate plating solution: 1 – 30; 2 – 100; 3 – 300 mA cm^{-2}.

As shown in this figure, the chemical composition of Ni-Mo alloy depends on both Ni(II)/Mo(VI) ratio and on the applied current density. Previously it was reported that by increasing the Ni(II)/Mo(VI) molar ratio in the plating bath from 0.38 to 2.29 (this means higher Ni content in solution), the content of molybdenum in Ni-Mo alloy dramatically decreases from 38 to 1-2 wt.%, respectively. In our particular case, it can be clearly seen that the amount of molybdenum in alloys' composition decreases with an increase in Ni(II) concentration in electrolyte from 0.001 M to 0.004 M when Mo(VI) concentration remains a constant (0.004 M). Accordingly, the highest content of molybdenum in Ni-Mo deposits (more than 80 at.%) in this study was obtained from the plating bath having the lowest Ni(II) ion concentration in the electrolyte (0.001 M) at 30 mA cm^{-2} when Ni^{2+} and MoO_4^{2-} ions concentration ratio in solution is 1:4. It can be clearly seen that at this ratio a slight decrease of Mo content in the deposit with increasing the current density has been observed from 92 wt.% at 30 mA cm^{-2} to 79 wt.% at 300 mA cm^{-2}. The similar tendency was observed even at ratio 0.5 when the concentration of Ni^{2+} in the solution was 2 times higher than MoO_4^{2-}(Fig.2). Moreover in this case the Mo content in the deposits at higher current densities (>100 mA cm^{-2}) was practically the same (about 55-56 wt.%) [2, 3]. Interestingly, in other authors' works it was indicated that at low mass ratio (0.59) the increase of current density led to the slightly higher molybdenum content in Ni-Mo alloy, from 24 wt.% at 42 mA cm^{-2} to 29 wt.% at 140 mA cm^{-2}. In contrast a slight decrease of Mo content against the applied current density has been observed for higher Ni^{2+}/MoO_4^{2-} ratio (2.29) [4]. Meanwhile in our study at higher ratio when the Ni^{2+} concentration is the same as MoO_4^{2-}, the increase of current density does not show significant influence on molybdenum percentage in Ni-Mo alloy composition and in all cases it did not exceed ~38-40 wt.% (Fig.2).

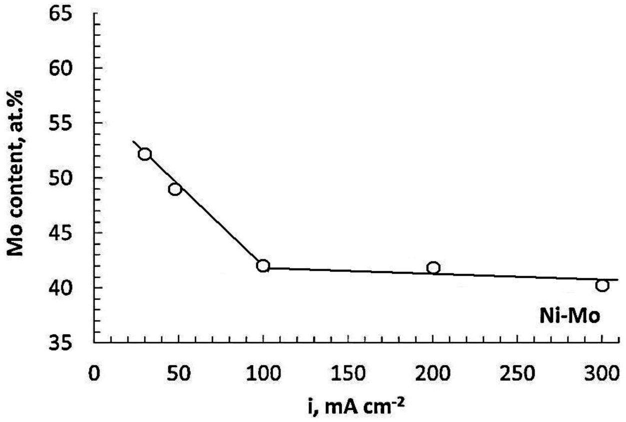

Fig. 2. The dependence of molybdenum content of the Ni-Mo deposit on cathodic current density. Concentration ratio in ammonia-acetate plating solution $[Ni^{2+}]/[MoO_4^{2-}]=0.5$.

It is known that the main side reaction of the induced co-deposition of Mo with iron group metals (Ni, Co, Fe) is related to the hydrogen evolution reaction. Accordingly, the current efficiency (CE) in all cases is lower than 100 %. In our study with an increase of Ni(II) concentration in the electrolyte from 0.001M to 0.004M current efficiency of deposition increases (Fig. 1b). Though this tendency is more pronounced at lower current density (30 mA cm^{-2}) where the CE increases constantly from 5 % to 41 % when Ni(II) concentration in the plating bath increases from 0.001 M to 0.004 M, respectively. Accordingly, the maximum current efficiency (~ 41 %) was observed at the higher Ni(II)/Mo(VI) concentration ratio when the solution consists of equal concentrations of $NiSO_4$ and $(NH_4)_2MoO_4$ (0.004 M) and deposition occurs at was 30 mA cm^{-2}. With an increase in the current density the influence of Ni(II) concentration on CE becomes negligible.

Acknowledgment. This work was carried out in the framework of the target research program of the NAS of Ukraine "Promising basic research and innovative development of nanomaterials and nanotechnologies for the needs of industry, health and agriculture", project №28/20-H, 2020.

1. Morley, T.J. et al. The deposition of smooth metallic molybdenum from aqueous electrolytes containing molybdate ions // Electrochem. Commun. 2012, 15, 78–80.
2. Design of Highly Active Electrodes for Hydrogen Evolution Reaction Based on Mo-Rich Alloys Electrodeposited from Ammonium Acetate Bath / E.Vernickaitė, O.Bersirova, H.Cesiulis, N.Tsyntsaru // Coatings. – V.9, №2. – 2019. – P.85-101.

3. Electrocatalytic properties of electrodeposited molybdenum alloys for hydrogen evolution reaction / E.Vernickaite, O.Bersirova, M.Lelis, H.Cesiulis // International Conference of Lithuanian society of Chemistry “CCT-2016“, 28-29 April 2016, Vilnius, Lithuania, - p.108.
4. S. Costovici, et al. Investigation of Ni-Mo and Co-Mo alloys electrodeposition involving choline chloride based ionic liquids // Electrochim. Acta. – 207. – 2016. – P.97–111.

INDENTATION SIZE EFFECTS AND MECHANICAL PROPERTIES OF SUPERIONIC MIXED CRYSTALS WITH ISOVALENT CATION SUBSTITUTION

Bilanych V.S., Skubenych K.V., Babilya M.I., Pogodin A.I., Studenyak I.P.

Uzhhorod National University, 46, Pidhirna Str., 88000 Uzhgorod, Ukraine

Due to the high ionic conductivity, superionic crystals with the argyrodite structure are of practical interest, in particular, for solid-state ionics. One of the main characteristics of such crystals is the capability to atomic substitution and formation of solid solution rows. During the growth of mixed crystals, the level of defects, as well as homogeneitie, can be estimated by measuring their hardness. Using standard indenters and measuring the microhardness at different depths of imprints give an opportunity to analyze the process of plastic deformation in these crystals. The study of the influence of a load P on the indenter on the hardness $H(P)$ makes it possible to find an interval of loads in which these parameter remains almost constant. This is the so-called true hardness, a value that can be used to compare with the properties of other materials or when studying the influence of various factors on the properties of the test material such as the cationic isovalent substitution. The study of the dependence of hardness on the indenter penetration depth can provide information on the gradient of mechanical properties with depth in the material under study, in particular, the concentration of defects and the presence of various phases and impurities. The states of the surface layer and the sample volume are not necessarily identical. The dependence of hardness on the depth of imprint is the phenomenological scale effect (ISE - indentation size effect). In most homogeneous materials, the hardness increases with decreasing indentation depth. The most common approach to the physical interpretation of ISE is provided by the theory of strain gradient plasticity, which uses the idea of geometrically necessary dislocations that ensure the continuity of an unevenly deformed material. The aim of this paper is to study the dependence of microhardness for $(Cu_xAg_{1-x})_7SiS_5I$ mixed crystals with argyrodite structure on the imprint depth, as well as on their chemical composition.

$(Cu_xAg_{100-x})_7SiS_5I$ mixed crystals, grown by Bridgman-Stockbarger methods, were used to measure microhardness. Measurements of the microhardness H of these materials were carried out at room temperature using the Vickers indenter. The dependences of microhardness H on the depth h of the imprint for $(Cu_xAg_{100-x})_7SiS_5I$ mixed crystals at room temperature were obtained by variation the load on the indenter from 0.02 N to 2 N.

Figure 1 presents the dependences of normalised microhardness H on the depth h of the imprint for $(Cu_xAg_{100-x})_7SiS_5I$ mixed crystals at room temperature. It can be seen that with increasing depth of imprint h, the microhardness H decreases. Thus, the direct dimensional effect is observed for $(Cu_xAg_{100-x})_7SiS_5I$ mixed crystals. This can be explained by the fact that with the increase in the load P on the indenter and its deepening, the deformations zones under indenter extend in the depth of the investigated sample, their volumes grow. The dimensional effect is a consequence of the induced, i.e. created during the indentation, gradient of plastic deformation in the microcontact zone, which can be interpreted in a model of geometrically necessary dislocations (GND). According to GND model, the indentation of crystals is accompanied by the formation of circular loops of geometrically necessary dislocations with Burgers vectors perpendicular to the plane surface of the crystal. In this case, the dependence $H(h)$ should be described by the equation:

$$\frac{H}{H_0} = \sqrt{1+\frac{\rho_G}{\rho_S}} = \sqrt{1+\frac{h^*}{h}},$$

where H is the hardness for a given depth of imprint h; H_0 is hardness in the absence of geometrically necessary dislocations (i.e., for $h >> h^*$, when the deformation gradient under the indenter does not affect the hardness value), ρ_G is the density of geometrically necessary dislocations, ρ_S is the density of statistically accumulated dislocations, h^* is the characteristic depth of the imprint, which depends on the form of the indenter, the displacement module and the hardness.

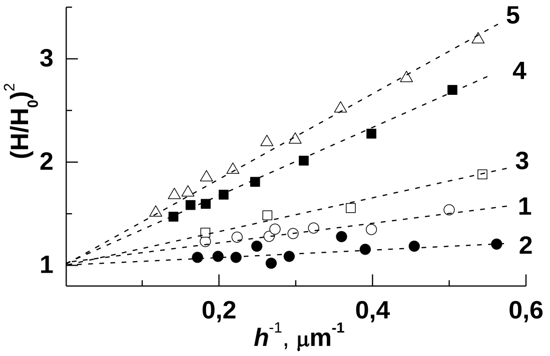

Fig.1. Dependences of the normalised microhardness of $(Cu_xAg_{100-x})_7SiS_5I$ mixed crystals on the depth of the imprint and their approximation in the GND model: x=100 (1), x=75 (2), x=50 (3), x=25 (4), x=0 (5).

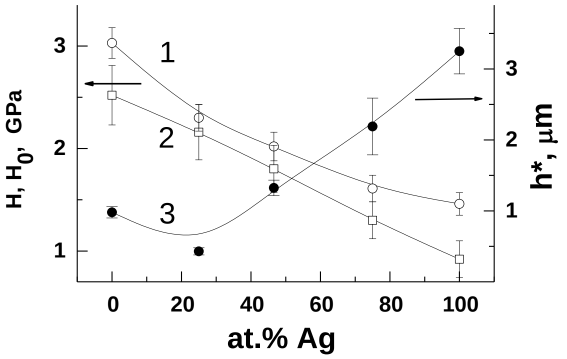

Fig.2. Compositional dependences of microhardness H (curve 1) (at P = 0.5 N) and parameters of the model of the GND model H_0 (curve 2) and h^* (curve 3) for $(Cu_xAg_{100-x})_7SiS_5I$ mixed crystals.

The analysis of the normalized microhardness dependence on the depth of the indenter immersion showed to establish a correspondence between the experimental data and the mechanism of deformation of $(Cu_xAg_{100-x})_7SiS_5I$ mixed crystals based on the theory of strain gradient plasticity (SGP). The parameters of GND model for the investigated crystals were determined and showed in Fig.2. It was established that at isomorphic substitution of Cu atoms by Ag atoms, the microhardness of the investigated mixed crystals decreases, which may be caused by the growth of the ionic radius of the cation. The minimal density of statistically distributed dislocations is revealed in Ag_7SiS_5I crystal.

ELECTRONIC STRUCTURE OF Na_2GeSe_3 CRYSTALS

Bletskan D.I., Vakulchak V.V., Studenyak I.P.

Uzhhorod National University, Voloshyn Str. 54, 88000 Uzhhorod, Ukraine
crystal_lab457@yahoo.com

Currently, an intensive work on finding electrode materials for sodium-ion batteries, which could potentially replace lithium-ion batteries has been under way. A significant advantage of sodium-ion batteries compared to lithium ones is that there is much more sodium on Earth than lithium, therefore, sodium batteries could be cheaper than lithium ones. Solid electrolytes are also needed to create sodium batteries. Promising materials with high ionic conductivity on sodium cations at room temperature are glassy germanium dichalcogenides modified by sodium chalcogenides [1]. For the presence of ionic conductivity, it is necessary to have “tunnels” in the crystal lattice of the matrix along which alkali metal ions move. Among these materials is sodium selenogermanate Na_2GeSe_3.

In the present paper, using the density functional method in LDA+U approximations, we calculated the energy band structure, the total and local partial densities of states and the spatial distribution of the electron density of Na_2GeSe_3 crystal.

Crystal structure. Na_2GeSe_3 crystallizes in a monoclinic structure, the symmetry of which is described by $P2_1/c$ space group. The unit cell contained four formula units (Z = 4) with lattice parameters a = 7.097, b = 16.068, c = 6.073 Å [2]. Ge atoms were in a tetrahedral environment with selenium atoms. The framework of the crystalline structure is formed by endless chains $(GeSe_3)_n^{2n-}$ elongated along c axis, between which there are channel voids. The motif from which the chains are built is formed by two tetrahedra [$GeSe_4$], interconnected by common vertices, having α-cis mutual orientation, which determines the zigzag nature of chains (Fig. 1). The unit cell contains two types of nonequivalent chains that differ in the opposite direction of twisting. In the voids between the chains, there are Na atoms in two nonequivalent positions: octahedral (NaI) and pentagramal (NaII). This polyhedron can be described as a distorted trigonal bipyramid.

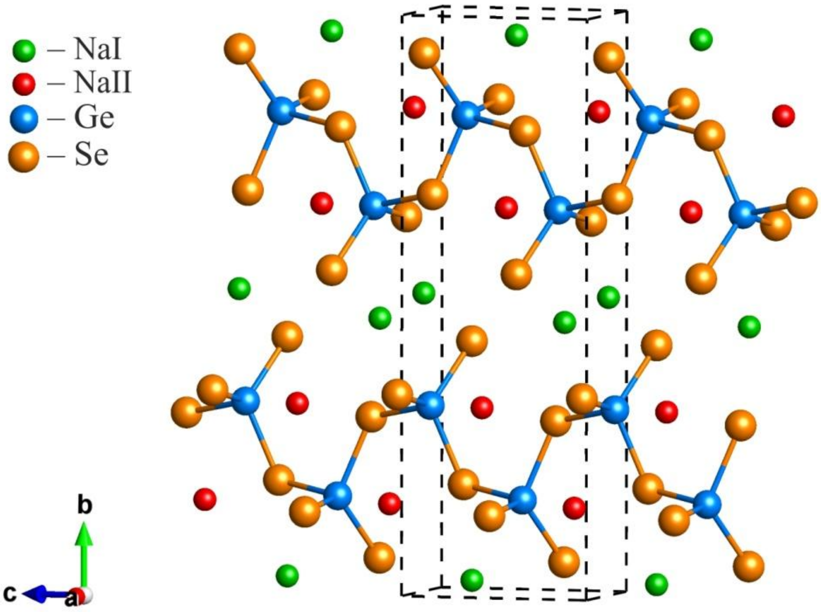

Fig. 1. The crystal structure of Na_2GeSe_3.

Electronic structure and nature of the electronic states. The band structure of Na_2GeSe_3 calculated in LDA+*U* approximation is shown in Fig. 2, *a*. The position of the top of the valence band located in the center of the Brillouin zone (BZ) at point Γ was selected as the starting point of the energy scale. The bottom of the conduction band also lies in the center of the BZ, therefore sodium selenogermanate is a direct-gap crystal with the calculated band gap E_{gd} = 2.61 eV, which is close to the experimental value of 2.56 eV determined from the analysis of the optical absorption edge [3].

Valence bands have a weak dispersion and form three energetically isolated bundles of bands. Information on the contributions of atomic orbitals to the crystalline states of Na_2GeSe_3 is provided by calculations of the total and local partial densities of states. The distribution profiles of the total density of states, as well as the contributions from the individual states of various atoms for Na_2GeSe_3 are shown in Fig. 2, *b*. It follows from the analysis of the energy distribution of local partial densities of states of sodium, germanium and selenium that in each of the three bundles of occupied bands of *s*- and *p*-states they give unequal contributions differ in value from each other. In the valence band of Na_2GeSe_3, the 4*s*- and 4*p*-states of selenium predominate, and their energy position is significantly different.

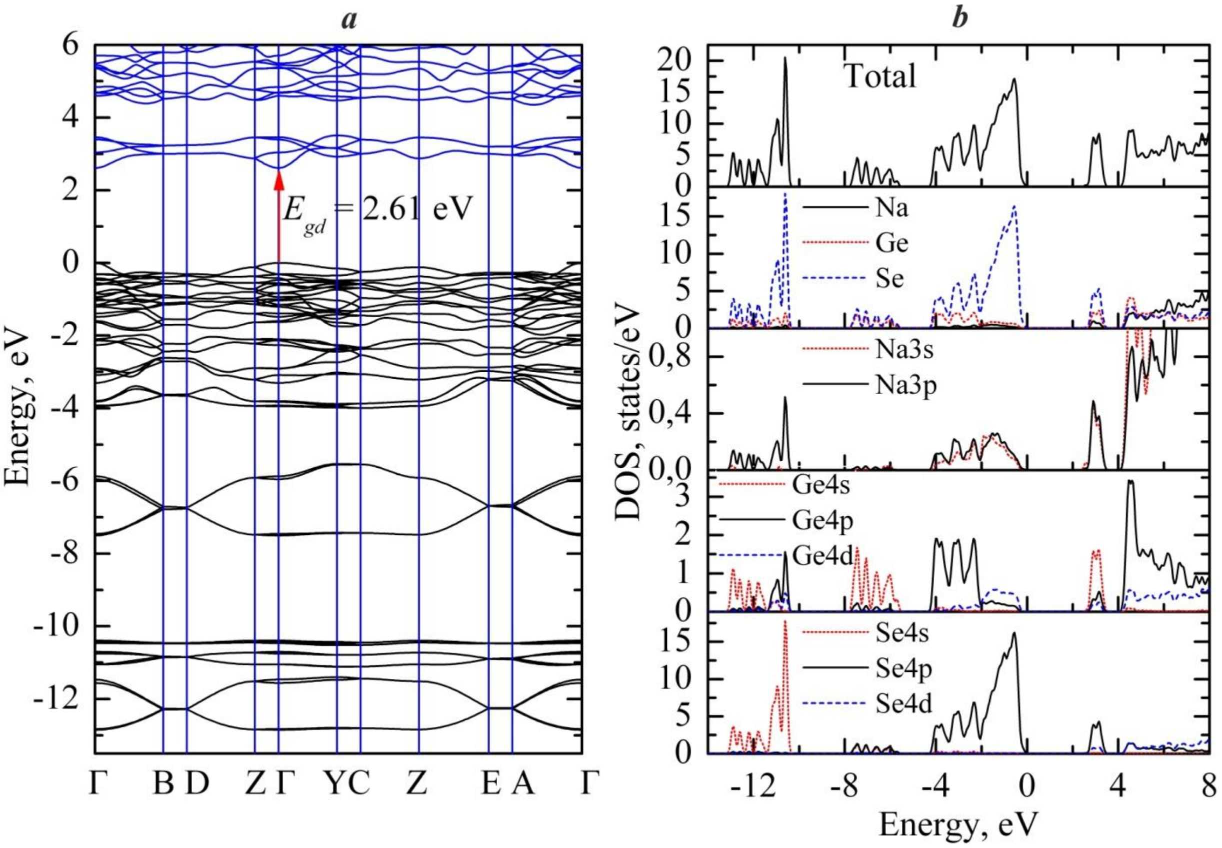

Fig. 2. The electronic structure (*a*), total and local partial densities of electronic states (*b*) of monoclinic Na_2GeSe_3 crystal.

The lowest energy bundle of valence bands, located in the energy range from –13.73 to –10.99 eV, is formed mainly by 4*s*-states of selenium atoms. Despite the prevailing nature of 4*s*-states of selenium, the hybridization effects of Ge and Se atoms states for this valence subband are noticeable, and it is leads to the appearance of contributions of 4*s*-states of germanium atoms, which are mainly localized in the energy region of the lower four bands, and contributions of Ge4*p*-states into the next bundle of 6 zones having a weak dispersion.

The average bundle of 4 bands following the *s*-bands of selenium is separated from them by the energy range of 3.20 eV, and it had a width of 2.07 eV and did not overlap with the upper valence subband, thus it had formed an isolated subband. This filled subband had a hybrid character and is formed as a result of the overlapping of Ge4*s*- and Se4*p*-states, thus played a significant role in the formation of Ge – Se covalent bonds in [$GeSe_4$] tetrahedra forming infinite chains.

The upper bundle of occupied zones can be conditionally divided into two parts: the lower part (–4.42 ÷ –2.18 eV) of 12 zones, which had a mixed character with the participation of hybridized 4*p*-states of selenium and 4*p*-states of germanium with a slight admixture of *s*- and *p*-states of sodium; the upper one (–2.18 ÷ 0 eV) containing 20 zones, that is formed mainly by non-bonding 4*p*-orbitals of selenium and wich are filled with two electrons (a lone pair), with admixture of *p*-, *d*-states of germanium and *s*-, *p*-states of the alkali metal. The top of the valence band at point Γ is formed exclusively by non-bonding $4p_{\pi}$-states of selenium.

A characteristic feature of Na_2GeSe_3 electronic spectrum is the presence of one isolated unoccupied subband, separated by a forbidden energy interval of 0.84 eV width from subsequent unoccupied zones. The low-energy electronic structure of unfilled electronic states of sodium selenogermanate is mainly formed by the “mixing” of free *p*-states of selenium with *s*- and *p*-states of germanium and sodium.

Spatial distribution of the electron charge. Studying the distribution of the total valence electron charge density $\rho(\boldsymbol{r})$ in the form of contour maps allows us to obtain useful information about the nature of chemical bonds in Na_2GeSe_3 both within the same chain and between chains, which is rather difficult experimentally for such complex crystal structure. Also, additional information on the nature of ionic conductivity can be obtained from electron density maps.

The electron density distribution $\rho(\boldsymbol{r})$ between a germanium atom and two selenium atoms belonging to a separate [$GeSe_4$] tetrahedron is illustrated by the electron density map shown in Fig. 3, *a*. It can be seen from this figure that the maximum electron density $\rho(\boldsymbol{r})$ is concentrated in [$GeSe_4$] tetrahedra near the positions of selenium atoms. The presence of common contours $\rho(\boldsymbol{r})$, covering the electron density maxima on selenium and germanium atoms, characterizes the covalent component of the chemical bond. The ionic component is determined by the partial transfer of charge density from germanium and sodium atoms to more electronegative selenium atoms.

The spatial distribution of the valence charge density shows that there is a strong covalent-ionic bond between germanium and selenium atoms, which are in the same chain, and the atoms belonging to two neighboring chains interact extremely weakly (Fig. 3).

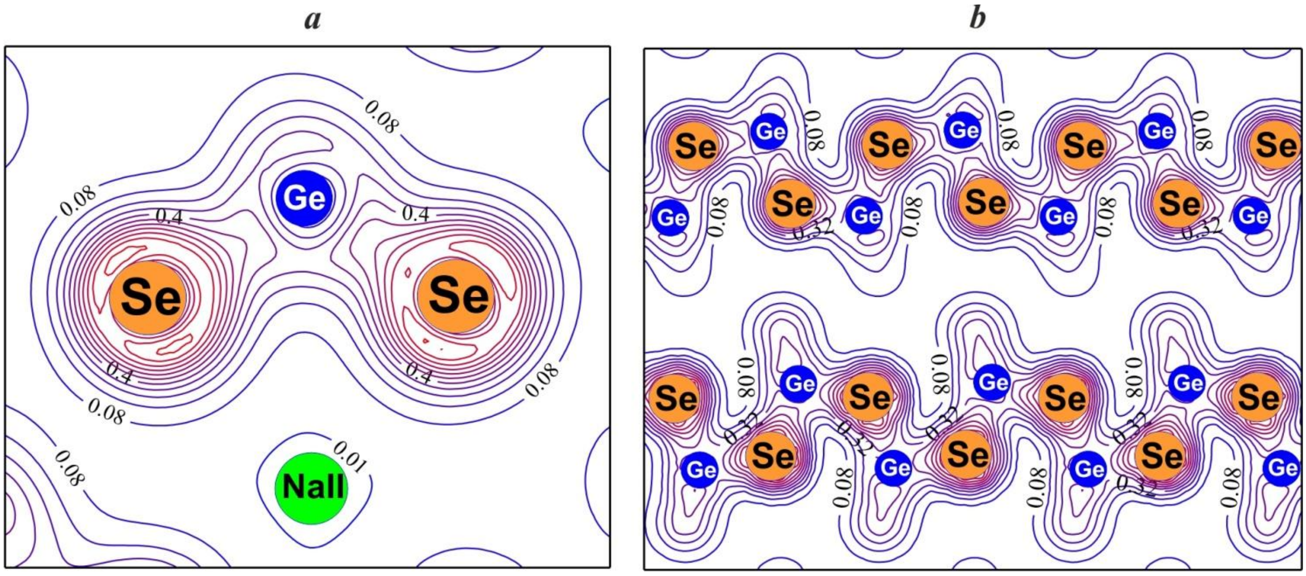

Fig. 3. Maps of the spatial distribution of the charge density in Na_2GeSe_3 crystal at the plane passing, along Se–Ge–Se bonds in endless chains (*a*) and in the plane through atoms of selenium, germanium, and sodium (*b*).

Sodium atoms localized in an interchain space do not have common electron density contours ρ(***r***) with neighboring anions (selenium atoms). It can be seen from the electron density contour maps of Na_2GeSe_3 crystal (Fig. 3) that between endless chains of [$GeSe_4$] tetrahedra linked by common vertices there are “tunnels” of minimal electron density, which serve as the channels for the movement of Na^+ ions. Thus, a weak participation of sodium atoms in the formation of electronic states (low charge density around Na^+ ions) and the presence of through “tunnels” between endless chains $(GeSe_3)_n^{2n-}$ with a very low charge density along the *c* axis provide a high mobility of sodium ions along these channels, and as a result high ionic conductivity.

1. Barrau B., Ribes M., Maurin M., Kone A., Souquet J. -L. Glass formation, structure and ionic conduction in the Na_2S–GeS_2 system // J. Non-Cryst. Sol., 1980. – V. 37, № 1. – P. 1–14.
2. Eisenmann B., Hansa J., Schaefer H. Zur Kenntnis der Selenidosilikate und -germanate $Na_4Si_4Se_{10}$, Na_2GeSe_3 und $Na_8Ge_4Se_{10}$ // Zeitschrift für Naturforschung B, 1985. – V. 40, № 4. – P. 450–457.
3. Podyachaya Ye.N., Gnidash N.I., Gapochenko S.D. Methods of preparation and study of the optical properties of $Na_2Ge_2Se_5$ and Na_2GeSe_3 thin films // Proceedings of the 3-th International Symposium «Vacuum Technologists and Equipment», Kharkov, Ukraine, September 22–24, 1999. – V. 2. – P. 262–263.

THIN FILMS OF SAMARIUM VANADATE NANOPARTICLES FOR ENHANCED LIGHT HARVESTING OF NEAR UV AND VISIBLE LIGHT

Chukova O.V.[1], Dorofeeva A.I.[1], Nedilko S.A.[1], Nedilko S.G.[1], Voitenko T.A.[1], Paszkowicz W.[2], Rahimi Mosafer H.S.[2], Manousaki M.[3], Savva K.[3], Stratakis E.I.[3]

[1]*Taras Shevchenko National University of Kyiv, Volodymyrska Str., 64/13,*
01601, Kyiv, Ukraine
[2]*Institute of Physics, Polish Academy of Sciences, al. Lotników, 32/46,*
02-668, Warsaw, Poland
[3]*Institute of Electronic Structure & Laser (IESL) of Foundation for Research & Technology*
Hellas (FORTH), Heraklion 711 10, Crete, Greece

Thin oxide films are widely used for optical material science needs; in particular, as luminescent converters for adaptation of incident solar light to spectral sensitivity of silicon solar cells and for transformation of violet and blue LED radiation into green-red light. All the noted applications require development of compounds with enhanced light harvesting from ultraviolet (UV) and violet spectral range (300 – 450 nm). Oxides doped with rare-earth (RE) ions are perspective candidates for the role of UV light absorbers due to their excellent thermal, mechanical and optical properties. In particular, vanadate nanoparticles were recently proposed as promising materials for spectrum conversion for improved energy harvesting by silicon solar cells. Visible-light photocatalytic activity of vanadates has been known for more than twenty years. The $BiVO_4$ was widely considered as catalyst in oxidative dehydrogenation of ethyl benzene to styrene and as photocatalyst for oxygen extraction from aqueous silver nitrate solution under visible-light irradiation. Photocatalytic applications also require nanostructured materials with increased light harvesting from near UV and visible spectral range.

At the last years a lot of compositions were synthesized over the world and considered for the noted purposes [1-3]. There are bismuth, cerium and lanthanum orthovanadates, magnesium, copper, argentum and strontium vanadates and many others. Up to now mainly extensive approach to new compositions development was applied. We propose to develop common models predicting changes of characteristics of vanadate films with modification of their compositions. With this aim we have grown vanadate films by various methods: evaporation from solution, spin-coating, and pulsed laser deposition.

The films were made from $La_{1-x}Sm_xVO_4$ and $La_{1-x-y}Sm_xCa_yVO_4$ vanadate nanoparticles those were synthesized for this purpose by sol-gel method. The details of synthesis can be found in [3]. Crystal lattice structure of the initial nanoparticles was determined using x-rays Shimatzu-2000 diffractometer (CuKa-radiation with a Ni filter) as monazite or zircon dependently on sample compositions. The substrates were chosen taking into account possible practical applications of the developed luminescent films. There are glass and silicon substrates. The latter are amorphous silicon plates those are used for production of silicon solar cells.

Microstructure of the samples was studied with optical microscope and scanning electron microscope (SEM) JEOL JSM-7000F. Thin film metrology was carried out using a tabletop reflectometer (FTPadv, SENTECH Instruments GmbH) coupled to an optical microscope. Reflectance spectroscopy of the samples was performed using Perkin Elmer Lambda 950 spectrometer. The powder samples were pressed in sample holder and then spectra of diffuse reflection were measured. In the used mode, the monochromator is placed before the samples and the light reflected from the powder samples is collected by photometric sphere. Luminescence spectra excited with 325 nm laser were registered using ACTONi (500) monochromator with grating 150 grooves/mm (blaze @ 300 nm), slit on 50 micron and liquid N2 - cooled CCD camera. Luminescence spectra excited with 405, 478 and 532 nm laser or powerful Xenon lamp 325 nm radiation were registered using DFS-12 monochromator with grating 600 grooves/mm, slit on 50 micron and FEU-79 photomultiplier

As a result of the carried out investigation, it was found that morphology, optical characteristics and luminescent properties of the vanadate films depend on method of their deposition. Comparing the results of microscope investigations of the films obtained by three different methods, we clearly see that films obtained by pulsed laser deposition and spin-coating are characterized by a more homogenous thickness and by a lower rate of agglomeration of the deposited vanadate nanoparticles and this fact evidences a higher quality of these films (Fig. 1).

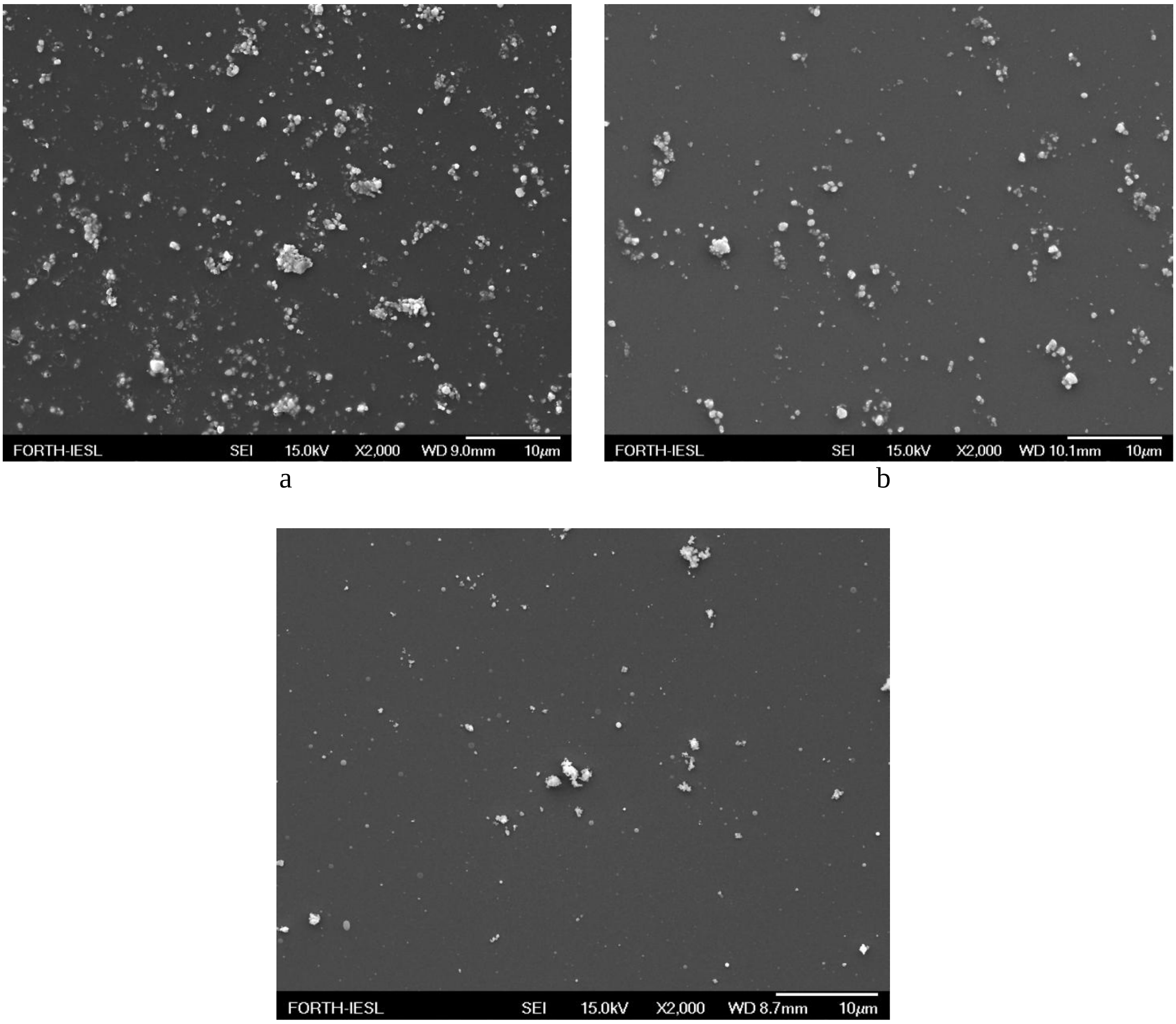

a b

c

Fig.1. SEM images of the $La_{0.8}Sm_{0.1}Ca_{0.1}VO_4$ films prepared by various methods: a - solution evaporation of silica gel containing colloid; b – spin-coating; c – pulsed laser deposition

From the other hand, content of the incorporated nanoparticles is higher for the films prepared by solution evaporation carried out with silica gel colloidal solvent. This increases luminescence intensity of the films prepared by solution evaporation method. Luminescence spectra of the investigated films consist of narrow lines caused by f-f transitions in the Sm^{3+} ions. Intensity of the Sm^{3+} emission is also higher for the films deposited on silicon substrates compared to the films on glass substrates. For the samples made on the glass substrates the wide bands of glass emission are also contributed to the spectra. Besides, the pulsed laser deposited vanadate films on silicon substrates have demonstrated arise of antireflection properties as a result of laser-induced random nanostructured profile. At the same time, used experimental conditions in the pulsed laser deposition method are not enough to obtain films on glass substrates with luminescent characteristics of the films sufficient for their applications, whereas the films deposited on silicon substrates have demonstrated promising luminescent characteristics.

Therefore, we should conclude that luminescent vanadate films are characterized by distinctive dependence of their morphological and optical properties on the method of deposition and type of substrate. The best methods for the films deposition can be chosen taking into account expected application and required morphological and optical parameters for this application.

This work has received funding from Ministry of Education and Science of Ukraine under bilateral grant agreement No 43-2020 and from the EU-H2020 research and innovation program under grant agreement No 654360.

1. Krumpel A.H., Kolk E., Cavalli E., Boutinaud, Bettinelli M., Dorenbos P. Lanthanide 4f-level location in $AVO_4:Ln^{3+}$ (A = La, Gd, Lu) crystals // J. Phys.: Condens. Matter, 2009. – V.21. – P. 115503-8.
2. Nakajima T., Isobe M, Tsuchiya T., Ueda Y., Manabe T. Correlation between Luminescence Quantum Efficiency and Structural Properties of Vanadate Phosphors with Chained, Dimerized, and Isolated VO_4 Tetrahedra // J. Phys. Chem. C, 2010. – V. 114. – P. 5160–5167.
3. Chukova O., Nedilko S.A., Nedilko S.G., Papadopoulos A., Slepets A., Stratakis E.I., Voitenko T., Structure and spectroscopy characterization of $La_{1-x}Sm_xVO_4$ luminescent nanoparticles synthesized co-precipitation and sol-gel methods // Optical Materials, 2019. – V.95. – P. 109248-11.

PROXIMITY-INDUCED TRIPLET SUPERCONDUCTIVITY IN $Bi_2Sr_2Ca_2Cu_3O_{6+x}$:$La_{2/3}Sr_{1/3}MnO_3$ NANOCOMPOSITES

Dmitrenko V.Yu., Krivoruchko V.N., Tarenkov V.Yu.

Donetsk Institute for Physics and Engineering named after O.O. Galkin of the National Academy of Sciences of Ukraine, 46. Nauky Av., Kyiv, 03028, Ukraine

Random binary nanocomposites of half-metallic ferromagnet (hmF), $La_{2/3}Sr_{1/3}MnO_3$, *nano*particles and *d*-wave superconductor (SC), $Bi_2Sr_2Ca_2Cu_3O_{6+x}$, *micro*particles have been prepared and their superconducting state has been studied. Superconductivity of the samples with the hmF component up to 30% of the volume fractions ratio has been directly detected. Unconventional symmetry of the nanocomposites' superconducting state order parameter has been experimentally studied by a point-contact (PC) spectroscopy technique. The experimental results get natural and qualitative explanation within the scenario of *p*-wave spin-triplet superconducting correlations induced in the nanocomposite due to the proximity effect.

Samples. The samples were prepared by using a traditional cold-pressed technique. The components were mixed according to their volume ratios. Composites containing submicron (~5÷10μm) Bi2223 ($Bi_2Sr_2Ca_2Cu_3O_{6+x}$) particles and LSMO ($La_{2/3}Sr_{1/3}MnO_3$) nanoparticles (~20÷30nm) have been produced. Bismuth strontium calcium copper oxide Bi2223 has a transition temperature $T_{C0} \approx 110$ K, the highest among cuprate high-T_C SCs. The coherence length $\xi_S(T = 0)$ is anisotropic with $\xi_{ab} \approx 2$ nm in the *ab*-plane, which is a typical value for Cu oxide SCs, and along the *c*-axis direction less than 0.02 nm. Therefore, the grains of the superconducting material have been large then the superconducting coherence lengths. The superconducting gap in Bi2223 is estimated to be 30.0÷35.0 meV [1]. The compacted Bi2223 samples display transparent boundaries and strong links among grains that is typical for high-T_C SCs, (see, e.g., [2] and references therein).

Details of the LSMO nanoparticles preparation can be found in Refs. [3,4]. Comparative investigations of the nuclear magnetic resonance and the nuclear spin-spin relaxation of ^{55}Mn nuclei of the nanopowders and polycrystalline samples with the same composition confirmed a ferromagnetic state and a double exchange mechanism of the magnetic interaction (and thus, half-metallic properties) for nanoparticles of the size we used [5].

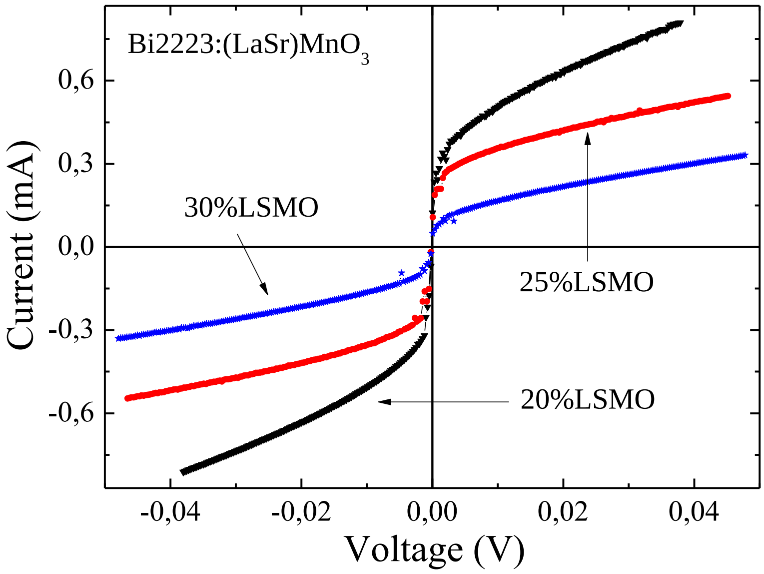

Fig.1. Current-voltage characteristic of Bi2223:$La_{2/3}Sr_{1/3}MnO_3$ nanocomposites with 20, 25 and 30 vol.% of LSMO, $T = 4.2$ K

Bulk characteristics. Figure 1 illustrates current-voltage (I-V) characteristic of the samples with 20, 25 and 30 vol.% of LSMO measured at 4.2 K. We observe a clear zero-resistance supercurrent branch, with an excess current I_{exc} of 0.32 mA, 0.27 mA and 0.12 mA, respectively. For more details of the bulk sample's transport characteristics see Ref. [6].

Point-contact spectroscopy. We used the PC spectroscopy technique for measuring directly superconducting state characteristics for the heterostructures under consideration. Figures 2 and 3 illustrate representative dynamic conductance spectra, $G(V) = dI(V)/dV$, of the nanocomposite Bi2223:LaSrMO(30%) - Ag point contact at $T = 4.2$ K. Two limiting cases are shown here: a junction with metallic-type conductivity, Fig. 2, so-called Andreev reflection (AR) contact, and a junction with the tunnel-type conductivity, Fig. 3. Typical for the d-wave cuprate SC conductance structure has been observed on both contacts.

In Fig. 2, the AR conductance spectrum demonstrates a dip at 26.8 meV that is recognized as a Bi2223 gap feature [1]. The second conductance dip at 6.5 meV is attributed to the proximity induced triplet superconducting pairing gap in LSMO. Pronounced zero-bias conductance peak has been clearly detected in the conductance spectra. The zero-bias conductance peak was predicted theoretically and detected experimentally for unconventional p-wave spin-triplet pairing as well as with a d-wave symmetry of the order parameter, and reflects the internal phase symmetry of the pair potential (see, e.g., [7-12] and references therein).

In Fig. 3, typical results for a tunnel contact of the Ag tip with the samples Bi2223:LSMO with 30 vol.% of LSMO are shown. The conductance peak at ≈ 34.7 meV representing the Bi2223 gap is detected. The conductance peak at 6.2 meV, respectively, is attributed to the intrinsic triplet superconducting pairing energy in LSMO. The pronounced zero-bias conductance dip determined by the d-wave symmetry of the order parameter has been clearly detected in the conductance spectra as well.

Thus, contrary to the half-metallic properties (spin-polarized current) of LSMO, the transport PCs measurements performed on Bi2223:LSMO nanocomposite demonstrate features typical for a mixture of d-wave and p-wave superconducting symmetries of the order parameter.

Discussion. As expected, a critical temperature of the proximity-induced triplet superconducting state is determined by T_{C} of a superconducting partner. That is why interplay between magnetism and superconductivity in hybrid structures involving high-T_{C} superconducting oxides and metallic ferromagnet with a spin-polarized current has attracted considered interest. Various experiments have provided convincing arguments for unconventional proximity effect in proximity-coupled high-T_{C} SC/hmF structures [8-12]. Promising example of hetero-structured SC/hmF systems with tunable inhomogeneity of the magnetic partner is composites. Being experimentally accessible with controllable parameters, such random hetero-structures offer unique testing ground for studying superconducting proximity effect in systems with a variable scale of magnetic disorder. Superconductivity in a granular mixture of superconductor-insulator films was extensively studied, both experimentally and theoretically, in a framework of the percolation theory. Proximity effects are explored in composites of s-wave SC/normal metal [12] and s-wave SC/hmF [13] structures. Superconducting proximity effect and transport properties of random binary nanocomposites of hmF and d-wave SC have been still less discussed [6].

In this work, the Bi2223:LSMO nanocomposites were prepared and their transport properties have been experimentally studied. Observed superconducting state's distinctive features, most probably, are due to two different effective length scales reflecting two-level scale interaction in the system. One is determined by the geometric difference between constituent components while another arises due to the proximity effect. For a three-dimensional composite with roughly the same geometrical size of components, the three-dimensional lattice percolation model predicts $f_{\mathrm{C}} \sim 0.16$ for the percolation threshold of the volume fraction, f, of a superconducting component [13]. Yet, in our case, the classical percolation theory is strongly affected (i) by a large geometrical disparity between components and (ii) by the superconducting proximity effect. In the nanocomposites, the superconducting triplet component of a Cooper pair with parallel spins arises due to the unconventional AR at the SC/hmF nanointerfaces. An additional channel, the so-called crossed AR can be realized as well.

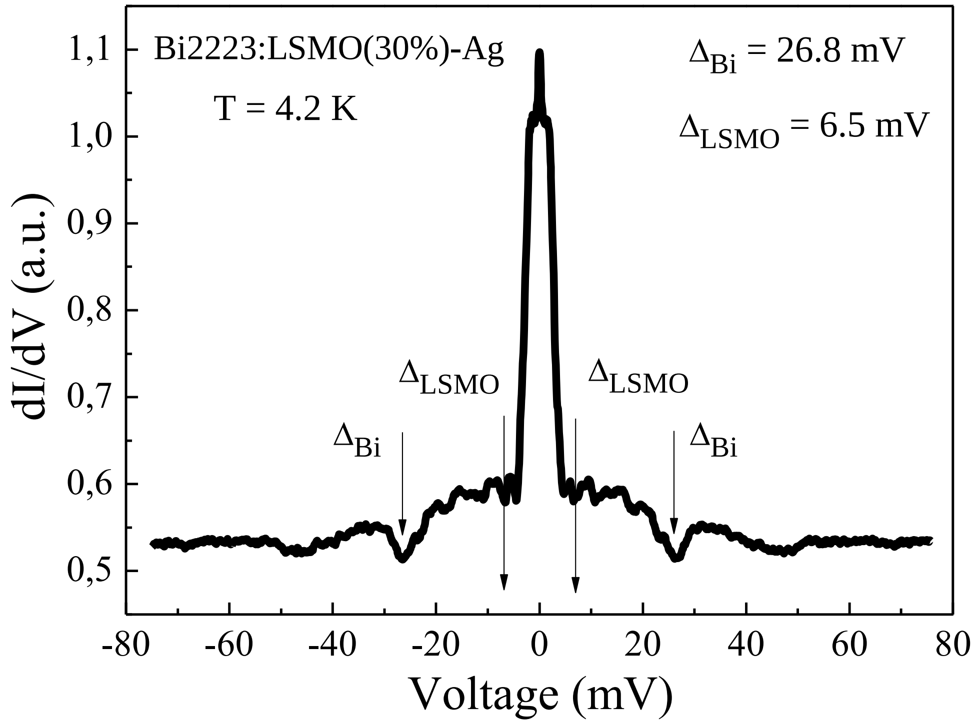

Fig.2. Andreev reflection spectra of the nanocomposite $Bi2223{:}La_{2/3}Sr_{1/3}MnO_3(30\%)$ - Ag point contact

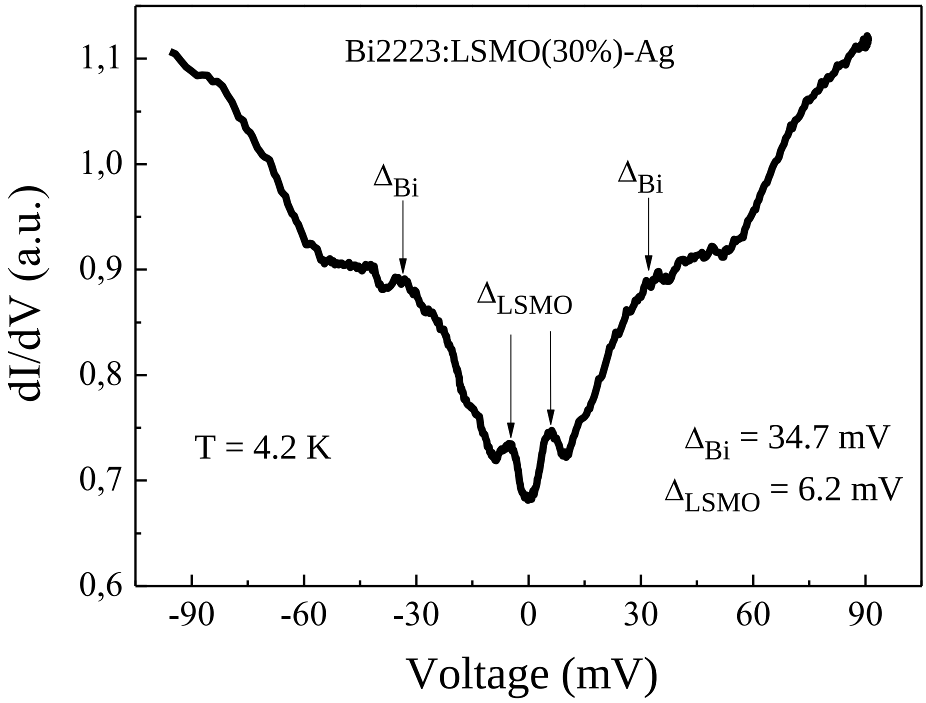

Fig.3. Tunneling spectra of the nanocomposite $Bi2223{:}La_{2/3}Sr_{1/3}MnO_3(30\%)$ - Ag point contact

Summarizing, we have prepared and studied Bi2223:(nano)$La_{2/3}Sr_{1/3}MnO_3$ composites. Superconductivity in samples below 30 vol.% concentration of LSMO has been observed. The basic attributes (critical temperature, current-voltage dependence, percolation threshold, etc.), most probably, cannot be quantitatively explained within the framework of a conventional percolation scenario. Tunnel and AR spectroscopies point that, most probably, in the nanocomposites under consideration we deal with a mixture of *p*-wave and *d*-wave superconducting states. Besides its fundamental interest, designing ways for raising the transition temperature of a triplet superconducting state is an important goal of condensed-matter research and is expected to play crucial roles for applications in superconducting spintronics [14].

The work has been carried out within the Target program of fundamental research of the NAS of Ukraine “Promising basic research and innovative developments nanomaterials and nanotechnologies for industry, health and agriculture” (Project № 17/20-H).

1. Hashimoto M., Vishik I.M., He R.-H. [et al.]. Energy gaps in high-transition-temperature cuprate superconductors // Nature Physics, 2014. - V.10. – P. 483-495.
2. Hilgenkamp H., Mannhart J. Grain boundaries in high-Tc superconductors // Rev. Mod. Phys., 2002. – V. 74 - N.2. – P.485-549.
3. Savosta M.M., Krivoruchko V.N., Danilenko I.A., [et al.]. Nuclear spin dynamics and magnetic structure of nanosized particles of $La_{0.7}Sr_{0.3}MnO_3$ // Phys. Rev. B, 2004. – V.69. – N.2. – P. 024413.
4. Krivoruchko V., Konstantinova T., Mazur A. [et al.]. Magnetic resonances spectroscopy of nanosize particles $La_{0.7}Sr_{0.3}MnO_3$ // J. Magn. Magn. Mater., 2006. – V.300. – N.1 - P. e122-e125.
5. Mazur A.S., Krivoruchko V.N., Danilenko I.A. Phase separation in nanosize samples of $(LaSr)MnO_3$ // Low Temp. Phys., 2007. – V.33. – N. 11 – P. 931-934.
6. Krivoruchko V.N., Tarenkov V.Yu. Percolation transitions in d-wave superconductor-half-metallic ferromagnet nanocomposites // Low. Temp. Phys., 2019. – V. 45. – N. 5. – P. 476-481.
7. Daghero D., Tortello M., Ummarino G.A. [et al.]. Strong-coupling d-wave superconductivity in $PuCoGa_5$ probed by point-contact spectroscopy // Nature Comm., 2012. – V. 3. – P. 1785.
8. Kalcheim Y., Kirzhner T., Koren G. [et al.]. Long-range proximity effect in $La_{2/3}Ca_{1/3}MnO_3$/(100)$YBa_2Cu_3O_{7-\delta}$ ferromagnet/superconductor bilayers: Evidence for induced triplet superconductivity in the ferromagnet // Phys. Rev. B, 2011. – V. 83. – N. 6. – P. 064510.
9. Millo O., Koren G. What can Andreev bound states tell us about superconductors? // Phil. Trans. R. Soc. A., 2018. – V. 376. – P. 20140143.
10. Eschrig M., Löfwander T., Triplet supercurrents in clean and disordered half-metallic ferromagnets // Nature Phys. 2008. - V. 4. - N. 1 – P. 138-143.
11. Satapathy D. K., Uribe-Laverde M. A., Marozau I. [et al]. Magnetic proximity effect in $YBa_2Cu_3O_7/La_{2/3}Ca_{1/3}MnO_3$ and $YBa_2Cu_3O_7/LaMnO_{3+\delta}$ superlattices // Phys. Rev. Lett., 2012. – V. 108. - N. 19. – P. 197201.
12. Keizer R.S., Goennenwein S.T.B., Klapwijk T.M. [et al]. A spin triplet supercurrent through the half-metallic ferromagnet CrO_2 // Nature (London), 2006. – V. 439. – P. 825-827.
13. Sternfeld I., Shelukhin V., Tsukernik A. [et al.]. Proximity effect in granular superconductor-normal metal structures. // Phys. Rev. B, 2005. – V. 71. – N.6. – P. 064515.
14. Tao Y.C., Hu J. G., Superconducting spintronics: Spin-polarized transport in superconducting junctions with ferromagnetic semiconducting contact // J. Appl. Phys., 2010. – V. 107. – P. 041101.

SURFACE MORPHOLOGY AND OPTICAL CHARACTERISTICS OF ARRAYS OF RANDOMLY DISTRIBUTED GOLD NANOPARTICLES

Durkot M.O.[1], Kyrylenko V.K.[1], Tarnaj A.A.[1], Vlaykov G.G. [2],
Kremenitsky V.V.[2], Novichenko V.M.[2]
[1] Institute for Information Recording, NAS of Ukraine,4 , Zamkovi schody St.,
88000, Uzhgorod Ukraine
[2] Technical Centre NAS of Ukraine, Pokrovskaya, 13 str., Kyiv-04070, Ukraine

In the present work we describe technological conditions for the formation of arrays of randomly distributed gold nanoparticles (NPs) with controlled parameters by the method of rapid radiation heating of thin gold films in the air and results of investigations their surface morphology and optical properties.

The arrays of randomly distributed gold nanoparticles are formed by the method of rapid (20-25 K/s) radiation heating to temperatures 623-723 K in the air of thin (8-35 nm) gold films deposited on glass substrates. The design of the device allows us to continuously monitor the dynamics of change the transmission spectrum of the film during heat treatment with fiber Ocean Optics spectrophotometer. Use of spectrophotometer in the process of heat treatment gold films allowed to control changed in the maximum spectrum of the surface plasmon resonance (SPR) (λ_{SPR}) at the formation of nanoparticles and stop annealing when they of the preset sized. Using this method, arrays of gold nanoparticles with different NP sized and optical characteristics were formed.

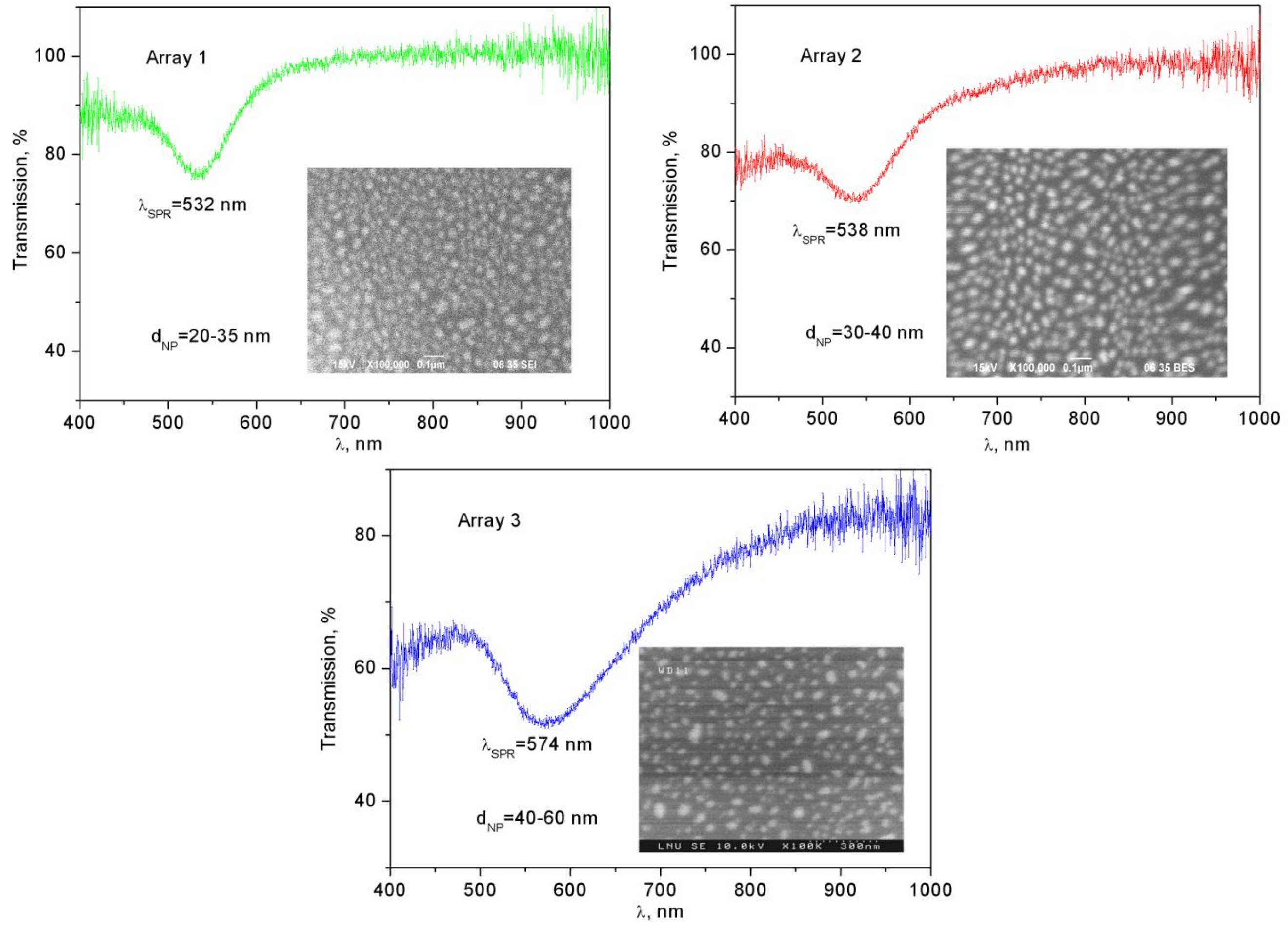

Fig.1. Transmission spectra and SEM images (inserts) of arrays of randomly distributed gold nanoparticles A1, A2 and A3

For the investigations of the surface morphology of the arrays a scanning electron microscopy (SEM) analysis was performed using a JSM 6064-LV (JEOL) microscope. The scanning of the sample surface was carried out by electron beam operating at 15 kV and 0,1 nA with the spatial resolution of 10 nm in the secondary electron image regime.

Fig.1 shows the transmission spectra of some arrays of gold NPs (A1, A2 and A3). The value λ_{SPR} of these arrays is at 532 (A1), 538 (A2) and 574 (A3) nm. Studies of the surface morphology of arrays A1, A2 and A3 by scanning electron microscopy showed that the average size of nanoparticles in these arrays is 20-35, 30-40 and 40-60 nm, respectively. As the nominal thickness of the deposited gold decreases, the surface density of nanoparticles increases, and their average sizes decrease. The values of λ_{PPR} also decrease.

Studies have shown that by the method of rapid (30-300 s) radiation heating of thin (4-20 nm) gold films in air at temperatures of 623-723 K, arrays of randomly distributed Au NPs with the size of nanoparticles 20-80 nm, the maximum position of the SPR band which are in the spectrum range 520-597 nm. It was found that the average size of nanoparticles depends on the thickness of gold films, temperature and annealing time.

It is shown that the obtained arrays of gold nanoparticles can be used as substrates for studying the structure of nanosized chalcogenide films by surface-enhanced Raman spectroscopy (SERS).

The authors express their gratitude for assistance in the formation of NPs arrays and measurement of transmission spectra to researcher Trunov M.L. of Uzhgorod laboratory of optoelectronics and photonics materials of the Institute for Information Recording of the NAS of Ukraine.

DIELECTRIC PROPERTIES OF $Cs_2Ag_2P_2Se_6$ CRYSTALS

Molnar A., **Gal D.**, Ban H., Haysak A.

Department of the Physics of Semiconductors, Uzhhorod National University,
Voloshina str. 54, 88000, Uzhhorod, Ukraine

Over the last few years, a large number of promising 2D materials have been investigated in order to find compounds with different band gap for the needs of modern electronics [1]. Previously, there was intensive research amid 3D materials for functional electronics devices [2]. Among the 2D and 3D crystals the family of the $Me_2P_2S(Se)_6$ stand out as a special class [3]. However, for a long time, this type of compounds lacked crystals of a one-dimensional or chain structure. Therefore, it was interesting to begin researching of the electrophysical properties of $Cs_2Ag_2P_2Se_6$ crystals, which has a chain, 1D structure.

$Cs_2Ag_2P_2Se_6$ were synthesized by the molten alkali polyselenophosphate flux technique [4]. It's melt congruently at 594 ^{o}C. Yellow/brown rod-like crystals of $Cs_2Ag_2P_2Se_6$ crystallize in the monoclinic space group $P2_1/n$ with $a = 6.807(3)$ Å, $b = 12.517(3)$ Å, $c = 8.462(3)$ Å, $\beta = 95.75(3)^{o}$, V = 717.3(8) Å^3, and Z = 2 [4]. In addition to the structure, practically the only one known parameter of this material was the band gap, which is $E_g = 2.55$ eV.

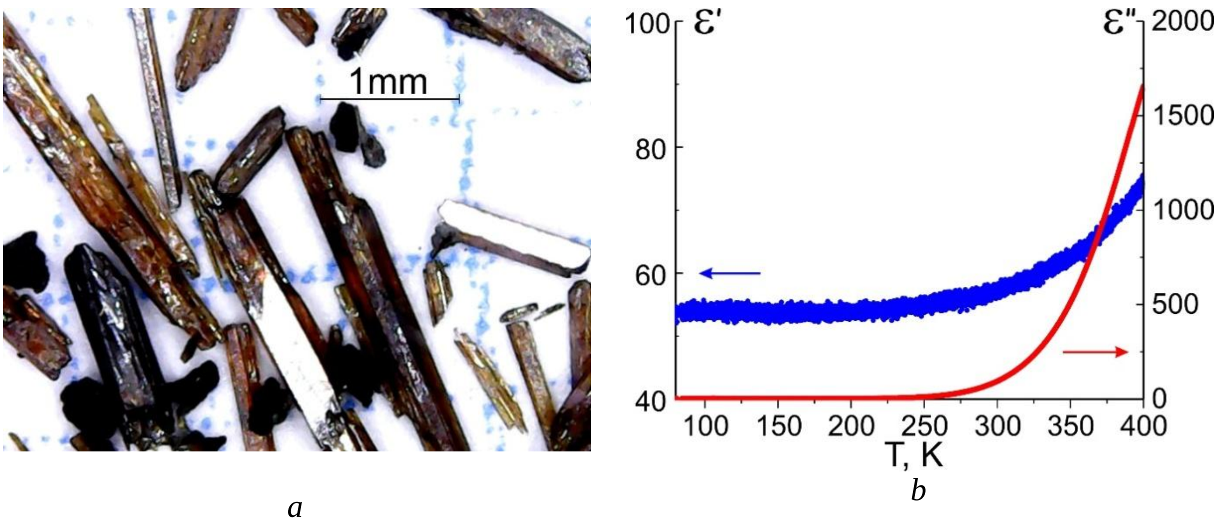

a

b

Fig.1. The appearance and size of $Cs_2Ag_2P_2Se_6$ crystals, and temperature dependency of its dielectric constant.

We have investigated the temperature dependence of the dielectric constant of crystals at a frequency of 10 kHz and a temperature range of -200 ÷ +120C. The electrodes in the form of a silver paste were applied to the opposite ends of the "needle" of a crystal 5 mm long and 1×1 mm^2 in cross section. To measure electrophysical parameters, we used a Goodwill digital LCR meter (LCR-819).

Unfortunately, no phase transitions were found in the indicated temperature range. As we can see in graph 1b, the temperature dependence of both the real and the imaginary parts of the dielectric constant show's activation behavior, which once again indicates that these crystals are semiconductors. Noteworthy is the relatively high dielectric constant of the samples, which may indicate the presence of additional mechanisms of polarization in these crystals at low frequencies. A significant increase in dielectric constant and especially dielectric losses is observed starting from 250K. The activation energy obtained by us from the temperature dependence of the conductivity of $Cs_2Ag_2P_2Se_6$ crystals is 2.5 eV, which is in good agreement with the value of 2.55 eV obtained in [4] from optical absorption spectra.

As the experience of mechanical processing of $Cs_2Ag_2P_2Se_6$ crystals has shown, they prick quite easily and grow in the form of thin needles, which can be successfully used to create one-dimensional nanostructures for nanowire electronics [5].

1. Susner M.A., Chyasnavichyus M., McGuire M.A., Ganesh P., Maksymovych P. Metal Thio- and Selenophosphates as Multifunctional van der Waals Layered Materials // Advanced Materials, 2017. – V. 29, I. 38. – P. 1602852(39).
2. Воронин Б.М., Приходько Г.П., Кириллов С.А. Слоистые соединения в системах металл-фосфор-халькоген // Киев: Наукова думка, 1992. – 208 с.
3. Vysochanskii Yu.M., Janssen T., Currat R., Folk R., Banys J., Grigas J., Samulionis V. Phase Transitions in Ferroelectric Phosphorous Chalcogenide Crystals // Vilnius University Publishing House, 2006. – 453 p.
4. Timothy McCarthy J., Mercouri Kanatzidis G. Synthesis in Molten Alkali Metal Polyselenophosphate Fluxes: A New Family of Transition Metal Selenophosphate Compounds, $A_2MP_2Se_6$ (A = K, Rb, Cs; M = Mn, Fe) and $A_2M'_2P_2Se_6$ (A = K, Cs; M' = Cu, Ag) // Inorganic Chemistry, 1995. – V. 34. – p. 1257-1267.
5. Guozhen Shen, Yu-Lun Chueh Nanowire Electronics // Springer Singapore, 2019. – 393p.

THERMOKINETICS OF FORMATION AND OXIDATION OF CARBON NANOFORMS

Garbuz V.V.,* Silinska T.A., Kuzmenko L.M., Petrova V.A.

Institute of Problems of Materials Science named after I.M. Frantsevich NAS of Ukraine,
Krzhyzhanovskogo str., 3, Kyiv, Ukraine, 03142 Email: Garbuz.v1950@gmail.com*

Layered carbon nanoform (LNC) generate in nature on acceptor surfaces during fuel combustion, with insufficient oxygen content and at temperature range of 820 to 1070 K for CO disproportion. The fact of creation of heat-resistant LNCs was appeared as resistance for system C – O – (H) in the local reducing environment to total combustion.

A thermokinetic model of formation and decomposition of layered carbon nanoforms (LCNs) is proposed. The model is based on the fundamental regularity of the temperature discrete component of the CO (Boudoir – Mayer) disproportion reaction. It has the form of a superposition of a package of reversible redox reactions of individual LCN in the temperature range of 820 − 1070 K. The superposition of the reaction package has two thermokinetic components: fast (discrete) and slow (continuous). The rate of continuous process, formation and decomposition of carbon mud, $v_{red\,/\,ox}$ C $\approx 10^{-8}$–10^{-7} mol / s.

The activation parameter of the reaction (decay) of the first order $E_{a\ ox}$ is defined as 35 ± 5 kJ/mol. The intensity of rapid oxidation processes has an exponential temperature dependence in the region of 1073 – 1473 K is $v_{red\,/\,ox}$ C $\approx 10^{-6}$–10^{-5} mol / s. The activation energies of oxidation (combustion) of most nanoforms are in the range of ~ 173 ± 5 kJ / mol.

The oxidation temperatures of carbon nanoforms have been established. Thus, at 823 K in the environment of CO or oxygen mainly formed or oxidized nano-inions, at 873 K – graphite nanopackages, 923 K – cross-layered, 973 K – conical-layered, 1013 K – scroll-like nanofibers, 1033 K – multiwall, and at 1073 K – single-walled nanotubes [1].

The mechanism of carbon polymerization is free-radical. The catalytic basis of polymerization is a set of three types of primary paramagnetic carbon radicals with 1 – 3 free electrons. Concentrations of radicals have the form of a superposition of Gaussian curves on the acceptor surface of the promoter in the temperature range 820 – 1070 K. They form a prototype of the above package of reactions. Primary radicals give rise to three types of nanoforms: spherical, lamellar-fibrous and tubular.

The reactions are reversible depending on the environment and temperature. When the equilibrium of LNC deposition and carbon mud is reached, the reaction package over time turns into a Ƨ-shaped curve, symbatic of the temperature dependence of the CO partial pressure. The chemical properties of nanoforms combine two types of topological interaction: peripheral hydrophilic and surface hydrophobic.

Peculiarities of synthesis and “up-stop-up” oxidation procedure at attestation and selective determination of carbon nanoforms in mixtures are discussed. If there is only one type of equipment for thermal analysis or carbon analyzer, it is possible to perform preliminary certification: identification and measurement of the composition of the finished carbon products in the view of nanoforms.

The thermokinetic model [2] gives an idea of the reversible processes of transformation of carbon nanoforms in the C – O− (H) system according to the Boudoir – Mayer reaction. It confirms several ideas about:

1) the temperature line of the acceptor surface of the promoter in the range of 820 – 1070 K;
2) superpositions of processes of fast and discrete, continuous and slow redox reactions of CO decomposition in the region of 820 – 1070 K;
3) the mechanism of polymerization of layered carbon nanoforms as free radical;
4) the type of polymerization reactions of nanoforms - chain, branched in the planes of pseudo-sp2 hybridization of carbon;

5) three types of primary free radical catalysts on the acceptor surface of the promoter with 1-3 free electrons;

6) three types of reproducible carbon nanoforms: spherical, planar-fibrous and tubular in the range of 820 − 1070 K;

7) free (macro) radicals, which are essentially all the polymerization products of layered carbon;

8) two types of carbon atoms in the nanoforms: saturated internal and paramagnetic peripheral;

9) two types of interaction of carbon nanoforms: hydrophobic surface and hydrophilic peripheral;

10) dimensional dependence of hydrophilicity and hydrophobicity, as well as the concentration of peripheral oxygen of C – O groups on the diameter of planar elements of nanoforms in the range from 1 to 40 nm;

11) the potential formation of the mechanism of combustion (oxidation) of carbon nanoforms above 234 K in an environment containing oxygen, in addition to the final act - thermal desorption of peripheral CO pairs;

12) constant temperature of formation and oxidation of thermodynamically stable carbon nanoforms.

The model explains the phenomena that occur during the production and oxidation of materials based on carbon nanoforms.

1. Garbuz V.V., Kuzmenko L.M., Petrova V.A., Silinskaya T.A., Terentyeva T.M. Kinetics of thermal oxidation of multilayer carbon nanotubes in an oxygen stream // Powder metallurgy, 2019. – № 3/4. – P. 33 – 40.
2. 2. Scientific modeling Science Learning Hub (https: // www.sciencelearn.org.nz/ resources / 575-scientific-modeling).

FIRST PRINCIPLES STUDY OF FERROELECTRIC AND ANTIFERROMAGNETIC STATES IN MIXED M1M2$P_2S(Se)_6$ CRYSTALS

Glukhov K.E., Babuka T.Ya., Kharkhalis L.Yu., Vysochanskii Yu.M.

Institute for Physics and Chemistry of Solids, Uzhhorod National University 54, Voloshyn St., 88000 Uzhhorod, Ukraine

The layered crystals of the M1M2$P_2S(Se)_6$ (M1, M2 metal cations) family are promising materials for functional electronics [1]. Especially of great interest are multiferroics materials in which dipole and spin ordering can coexist and influence each other. One such material is $CuCrP_2S_6$ known to have ferroelectric and antiferromagnetic phase transitions [1,2]. Obviously, conditions for utilizing such complex functional material could be elaborated only on the basis of known and clearly described physical properties of electronic and spin subsystems of the crystal, thus in our work, we considered the main physical properties of the $CuCrP_2S_6$ crystal from first principles.

In the presented work, using *ab initio* approach the structural, electronic, and magnetic properties of $CuCrP_2S_6$ crystal were simulated. Simulation were carried out using DFT-D approach which gave us an opportunity to perform correct geometry optimization of the considered layered structure. The energy band spectrum for this material was calculated in spin-polarized approach. With GGA-D functional taken into account the value of the band gap of $CuCrP_2S_6$ crystal found to be equal to 0.55 eV. To disclose the nature of chemical bonding existing in layered chalcogenide crystals DOS, orbitals and spatial distribution of valence electron density were calculated.

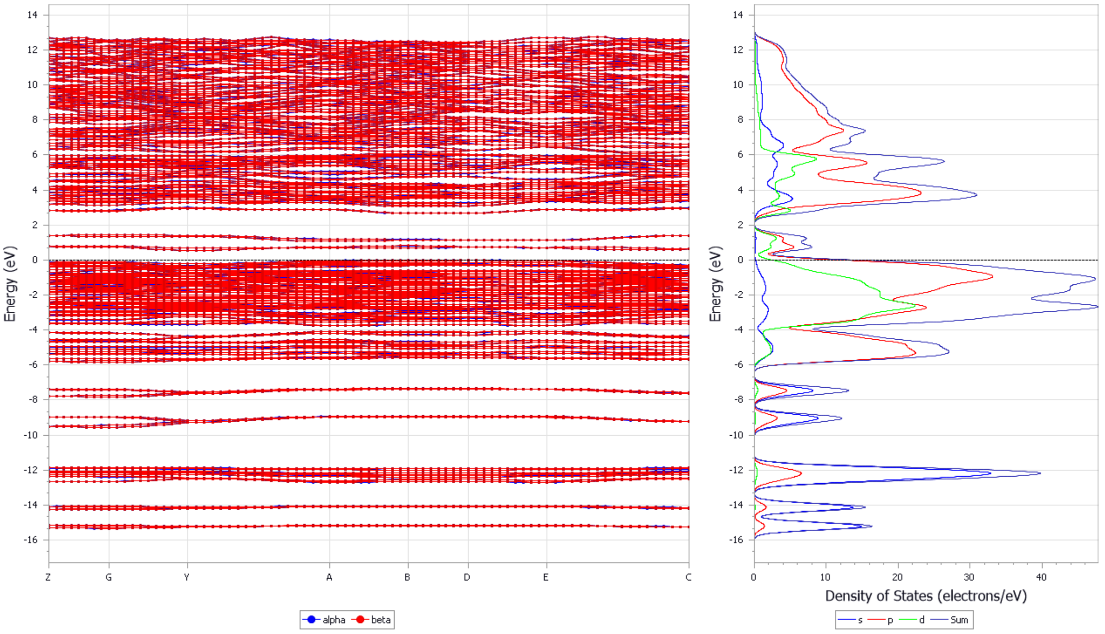

Fig.1. Calculated band structure and DOS for $CuCrP_2S_6$ crystal in antiferromagnetic state

Additionally, by means of DFT simulation, it was shown the preferable spin ordering and charge density distribution (see Figure 2.) in the vicinity of Cr atoms.

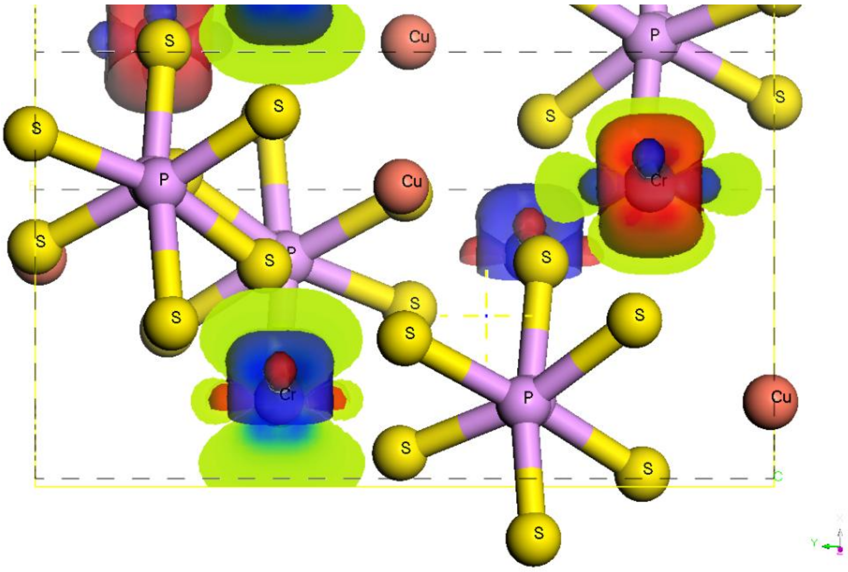

Fig.2. Spatial distribution of spin density in $CuCrP_2S_6$ crystal

The results of our investigation confirm that $CuCrP_2S_6$ crystal has an antiferromagnetic spin ordering at low temperatures. Also, it was shown that the application of an electric field can switch the magnetic state in this layered crystal making it promising functional material for electronic device applications.

1. Youfang Lai, Zhigang Song [et al.]. Two-Dimensional Ferromagnetism and Driven Ferroelectricity in van der Waals $CuCrP_2S_6$ // Nanoscale, 2019. – V. 11. – P. 5163-5170.
2. Banys J., Samulionis V., Cajipe V.B., and Vysochanskii Yu. Dielectric properties of ferroelectrics CuInP2Se6 and CuCrP2S6 // Ferroelectrics, 2001. – V. 257. – N. 1. – P. 163-168.

DETERMINATION OF TOXICITY OF HYBRID NANOCOMPLEXES COMPRISING NANOPARTICLES OF GADOLINIUM ORTHOVANADATE AND CHOLESTEROL

Goltsev A.M.[1], Malyukin Yu.V.[2], Bondarovych M.O.[1], Babenko N.M.[1], Gayevska Yu.O.[1],
Dubrava T.G.[1], Volkova N.O.[1], Klochkov V.K.[2], Ostankova L.V.[1]

[1]Institute for Problems of Cryobiology and Cryomedicine of the National Academy of Sciences of Ukraine, Kharkiv, Ukraine, Pereyaslavska str. 23, Kharkiv, Ukraine 61015
[2]Institute for Scintillation Materials of the National Academy of Sciences of Ukraine, Kharkiv, Ukraine, Nauky ave. 60, Kharkiv, Ukraine, 61001

Targeted therapy of oncology diseases when using various nanomaterials is one of the modern means of a combined therapy of malignant tumors. In experimental conditions in vivo using Ehrlich carcinoma, the possibility of applying the nanocomplexes (NCs) of $GdYEuVO_4$ containing cholesterol to identify and inhibit the growth of cancer cells has been substantiated [Goltsev A.N., 2015., Goltsev A.N., 2016, Goltsev A.N. 2017]. To successfully implement an antitumor ability of NC their penetration and intracellular accumulation, depending on incubation time and causing the impairment of mitochondria function with the subsequent induction of apoptotic and necrotic changes have been established to be necessary. In addition, the antitumor effect of NC can be realized by inhibiting the pluripotency genes in them [Goltsev A.N., 2015.], primarily this is *nanog*, which is key in determining the self-maintenance of cancer stem cells (CSCs), the functional activity of those determines the tumorigenesis intensity [Goltsev A.N., 2015]. However, the question on a possible negative effect of NCs on the function of normal cells of the body when using them is significant. Based on this, the aim of this research as to study the toxic effects of hybrid NCs on healthy animals when an acute toxicity was induced.

The study was performed in 8-month-old healthy females of BALB / c mice weighing 20-22 g, kept in standard animals' house conditions of the Institute for Problems of Cryobiology and Cryomedicine of the National Academy of Sciences of Ukraine (Kharkiv). All manipulations with animals have been approved by the Bioethics Committee of the Institute and carried out in accordance with the General Principles of Animal Experiments approved by the First National Congress in Bioethics (Kyiv, 2004) and agreed with the provisions of the European Convention for the Protection of Vertebrate Animals and Other Scientific Purposes"(Strasbourg, 1986).

Hybrid NCs were synthesized by the staff of the Institute for Scintillation Materials of the National Academy of Sciences of Ukraine, Kharkiv [Klochkov V.K., 2015]. Solutions of NCs contain 1.3 g / l of nanoparticles of $GdYVO_4$: Eu^{3+} spherical and cholesterol (0.02 g / l) in 5% glucose solution. Briefly: cholesterol ("Acros organics", Belgium) was dissolved in ethyl alcohol and an aqueous solution of 2-3 nm nanoparticles (NPs) was added to the mixture, followed by vacuum removal of alcohol and the addition of 5% glucose solution [Klochkov V.K. 2015]. To study the acute toxicity of NCs, they were intraperitoneally administered to animals of the experimental groups once in different volumes of the synthesized solution of NCs: 0.1 ml (0.13 mg NPs), 0.5 ml (0.65 mg NPs), 1 ml (1.3 mg NPs), 2 ml (2.6 mg NPs) per animal (n = 6 in each group). Only 5% glucose solution in the same volume was intraperitoneally administered to the control animals (n = 6).

In accordance with the principles of an acute toxicity assessment [Khabriev R.U., 2005] clinical signs of intoxication: animal behavior, intensity and nature of motor activity, hair and skin condition, food and water consumption, dynamics of body weight change and recorded the percentage of death animals were daily determined. On days 1, 7 and 14 after the NCs introduction the mass of internal organs (liver, spleen, inguinal lymph nodes, kidneys), followed by calculation of mass coefficients, clinical blood test, and the total number of myelokaryocytes in the bone marrow was also determined. On day 14, all the animals were taken out from the experiment by means of euthanasia, and the number of stem cells ($CD34^+CD38^-$) in their bone marrow was examined by flow cytometry using monoclonal antibodies (BD Biosciences, USA). The activity of γ-glutamyl transferase (GGT) and γ-glucose-6-phosphate dehydrogenase (G-6-PDG) in the supernatants of liver homogenates was spectrophotometrically determined according to the manufacturer's instructions. In addition, the internal organs of experimental and control groups of animals were histologically examined. To do this, the material was fixed in a 10% solution of formalin, dehydrated, paraffinized and made histological sections, which were stained with hematoxylin-eosin and studied with a light microscope Primo Star (Carl Zeiss, Germany).

It was found that with a single intraperitoneal administration of a solution of NCs at a concentration of 0.1 ml, 0.5 ml, 1 ml per animal, as well as glucose solution at appropriate concentrations, no fatalities were reported among animals. Daily examination did not reveal any symptoms of animal intoxication in any of the above groups during the experiment. The effect of the above concentrations of NCs, as well as glucose, on the body weight of mice during the experiment was not detected.

But the introduction of 2 ml NCs solution from the first time of observation led to hypodynamics, shortness of breath, tremor of the whole body and rumpled hair of animals of this group. Symptoms of intoxication increased during the first day of observation and on the 2nd day after the introduction of NCs there was detected 50% death of animals in this group. Moreover, in an animal survived for 14 days after administration of 2 ml of NCs at autopsy, a significant solid tumor in spleen, a significant decrease in the number of myelokaryocytes and an rise in the number of $CD34^{+}CD38^{-}$ stem cells in the bone marrow, corresponding to the published data were revealed [Grin S.A., 2012, Zwolak I., 2013]. No changes in behavior were observed in the animals after administration of the maximum volume of glucose (2 ml), however, the death of one of 6 animals was noted 4 days after administration of the solution. The number of myelokaryocytes and stem cells in the bone marrow of animals with the introduction of appropriate glucose solutions did not differ significantly from similar indices for intact animals.

On day 14 the animals of all experimental groups showed a dose-dependent increase in GGT, the only enzyme that destroys glutathione. This indicates the development of oxidative stress, which reached its peak in the group with the introduced 2 ml NCs. A sharp increase in GGT in the animals of this group was accompanied with significant pathomorphological changes in the structure of liver with signs of hepatocyte necrosis. Administration of glucose solutions in different concentrations did not affect the morphological characteristics of liver and the activity of GGT enzyme.

In all experimental groups on day 14 we found a compensatory increase in the activity of antioxidant system enzymatic link, judging by the concentration of G-6-PDG. This indicates the body's ability to remove excess concentrations of free radicals, by maintaining their concentration at a constant level. Only in the group with the introduction of 2 ml of NC revealed a decrease in the activity of G-6-PDG, which against the background of a sharp increase in GGT in animals of this group confirms the deregulatory state of the pro- and antioxidant system. In control groups with the introduction of the appropriate concentration of glucose, the activity of G-6-PDG did not differ from that of intact animals.

Thus, there was determined the potential semi-lethal dose of nanoparticles in the composition of NCs, which causes 50% mortality when administered intraperitoneally, that was 2.6 mg per animal, exceeding the therapeutic (0.13 mg) 20 times. The introduction of such an amount of NP can lead to the induction of tumor formation, and significant changes in hematological and biochemical parameters. The introduction of a therapeutic dose (0.1 ml) and a dose exceeding 10 times did not lead to pathological changes in the studied parameters.

In general, the findings supplement the understanding of the mechanisms of antitumor therapy by nanomaterials based on orthovanadates of rare earth elements and emphasize the need to study biologically safe doses of NCs when used in animals in vivo.

INVESTIGATION OF RADIOPROTECTIVE ACTIVITY OF CERIUM OXIDE CeO_{2-x} AND ORTHOVANADATE $Gd_{0.9}Eu_{0.1}VO_4$ NANOPARTICLES *IN VIVO*

Grygorova G.V., Klochkov V.K., Yefimova S.L.

Institute for Scintillation Materials NAS of Ukraine, 60 Nauky ave., 61072 Kharkiv, Ukraine

Redox-active nanomaterials, which are able to generate or scavenge free radicals and reactive oxygen species (ROS), are of growing interest in modern technologies ranging from catalysis, photovoltaic cells, UV protective screens to nanomedicine including cancer diagnosis and treatment. In our previous papers, we reported on biological activity of rare-earth orthovanadate nanoparticles and cerium oxide (pro- / antioxidant properties, effects on bioenergy processes in cell mitochondria, selective accumulation in cell nuclei, etc.) that makes such redox nanomaterials very prospective for biomedical applications and requires deep understanding the mechanisms of their redox activity [1-3].

In this work, we report on the effectiveness of CeO_{2-x} and $Gd_{0.9}Eu_{0.1}VO_4$ nanoparticles in radioprotection in model animals during radiation exposure. In the experiments, colloidal solutions of nanoparticles with average sizes of 10 nm for CeO_{2-x} and 8×20 nm for $Gd_{0.9}Eu_{0.1}VO_4$ were used. Nanoparticles were injected per os by two different schemes – once and during 15 days. For the 15-days scheme of $Gd_{0.9}Eu_{0.1}VO_4$ nanoparticles injection during 30 days of observation the survival of animals irradiated with a dose of 6.0 Gy was 100 %; for ceria it was 90 % for CeO_{2-x} nanoparticles (Table 1). Control groups were irradiated without injection of nanoparticles. The following parameters were analyzed: 30-day survival rate (% mortality); the average life duration; integral indicators (cumulative frequency). In addition to the analysis of the 30-day survivability, different signs of acute radiation sickness were monitored, such as a ruffled fur (a common indicator for the state of the body), bloating, diarrhea, swelling of mouth and eyes. By all these characteristics a protective effect of the nanoparticles was observed in the case of per os injection of both types of nanoparticles and irradiation by 6.0 Gy. It was revealed that 7.0 Gy radiation dose is lethal. For an irradiation by 7.0 Gy the signs of acute radiation sickness did not differ from those of the controls.

Table 1 Mortality and lifetime of rats after 30 days after X-ray irradiation procedure by 6 and 7 Gy

№ group	Type of nanoparticles	Dose of irradiation, Gy	Scheme	n	n_1	n_2	Animals died, %	Compared groups
1		6.0	control 1	10	6	79	60	
2	CeO_2	6.0	1	10	1	11	10	1-2
3	$GdVO_4$: Eu	6.0	1	10	0	0	0	1-3
4		7.0	control 2	20	19	161	95	
5	CeO_2	7.0	2	10	9	96	90	4-5
6	$GdVO_4$: Eu	7.0	2	10	6	47	60	4-6
7	CeO_2	7.0	1	10	8	59	80	4-7
8	$GdVO_4$: Eu	7.0	1	10	10	78	100	4-8

Note: n-the total number of rats in the experiment; n_1 - number of dead rats; n_2 - the total number of the lived days of rats

Probably, the radioprotective effect of nanoparticles is related to their antioxidant action. On the example of the SOD mimetic activity model for nanoparticles we have shown, that

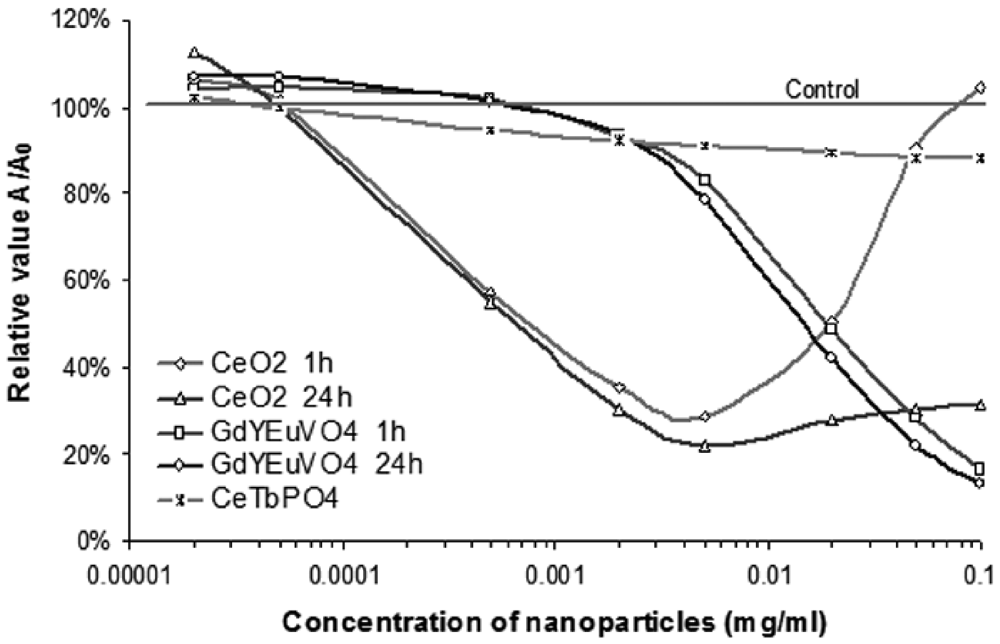

nanoparticles based on $ReEuVO_4$ (Re=Gd, Y) at particle concentration more than 0.0005 mg/ml, as well as CeO_{2-x} nanoparticles inactivate superoxide radicals in a model system (Fig.1).

Fig.1 Inhibition of $O^{2-\bullet}$ in the presence of nanoparticles at the epinephrine autoxidation

But one cannot exclude the possibility of induction of own protective functions of the organism at injection of nanoparticles. The mechanism of radioprotective action of considered types of nanoparticles requires further more in-depth research. But these results can serve as a motivation to consider inorganic nanoparticles as the basis for new drugs possessing by radioprotective effect. In general, the radioprotective effect of considered nanoparticles corresponds to, and even possibly exceeds the level of protection provided by conventionally used organic radioprotectors.

1. G. Grygorova, V. K. Klochkov, Ye. Mamotyuk, Yu.V. Malyukin, Cerium Dioxide CeO_{2-x} and Orthovanadate ($Gd_{0.9}Eu_{0.1}VO_4$) Nanoparticles for Protection of Living Body from X-Ray Induced Damage // in: Nanomaterials for Security, Springer. - 2016. – p. 289–296.
2. V.K. Klochkov, A.V. Grigorova, O.O. Sedyh, Yu.V. Malyukin, The Influence of Agglomeration of Nanoparticles on Their Superoxide Dismutase-Mimetic Activity // Colloids Surf. A: Physicochem. Eng. Aspects. – 2012. – V.409. – P. 176–182.
3. K. Hubenko, S. Yefimova, T. Tkacheva, P. Maksimchuk, I. Borovoy, V. Klochkov, N. Kavok, O. Opolonin, Yu. Malyukin, Reactive oxygen species generation in aqueous solutions containing $GdVO_4$:Eu^{3+} nanoparticles and their complexes with methylene blue //Nanoscale Res. Lett. – 2018. – V.13. – p. 100.

EFFECT OF INCREASING THE THERMAL CONDUCTIVITY OF SOME MOLECULAR CRYSTALS

Yu.V. Horbatenko, O.O. Romantsova, A.I. Krivchikov, O.A. Korolyuk

B.Verkin Institute for Low Temperature Physics and Engineering of NAS of Ukraine,
Prospekt Nauky, 47, Kharkiv 61103, Ukraine
horbatenko@ilt.kharkov.ua

In present work, we have been analyzed the temperature dependences of the thermal conductivity of molecular crystals – benzophenone and its derivatives, derivatives of nitrobenzene and some freons, which are demonstrated an increase in thermal conductivity with temperature increasing at temperatures above the phonon maximum. It was found this effect occurs in both ordered and disordered phases of molecular crystals. It is shown the increase in thermal conductivity with temperature can be represented by the Arrhenius equation, which describes the some thermoactivation process. Thus, the increase in thermal conductivity is associated with the manifestation of the thermoactivation mechanism of heat transport. It was established the observed effect in thermal conductivity is due to the influence of intramolecular vibrations on phonon heat transport.

Yuliia V. Horbatenko, Olesia O. Romantsova, Oksana A. Korolyuk, Andrzej Jeżowski, Daria Szewczyk, Joseph Ll Tamarit, Alexander I. Krivchikov, *Journal of Physics and Chemistry of Solids* 127, 151–157 (2019).

DIELECTRIC PROPERTIES CHANGES IN AGED GLASSY SELENIUM

Horvat A.A.[1], Mikla V.V.[2], Minkovich V.V.[1], Molnar A.A.[1], Solomon A.M.[3], Rubish V.M.[4]

[1] *Faculty of Physics, Uzhhorod National University,*
A. Voloshin str., 54, 88000 Uzhhorod, Ukraine
[2] *Ukrainian-Hungarian Education and Scientific Institute, Uzhhorod National University,*
Universytetska str., 14, 88017 Uzhhorod, Ukraine
[3] *Institute of Electron Physics, National Academy of Science of Ukraine,*
Universytetska str., 21, 88017 Uzhhorod, Ukraine
[4]*Institute for Information Recording, National Academy of Science of Ukraine,*
Zamkovi skhody str., 4, 88000 Uzhhorod, Ukraine

Selenium is almost the only elemental substance that is easily obtained in the form of bulk glass, i.e. which has a high ability to glass forming. Based on it alloys photosensitive elements, switching and optical recording devices, etc. was developed [1]. More over recently even ferromagnetic or ferroelectric (multi-ferroic) behavior was found [2]. At the same time, it is known that the vitreous state is metastable and has excess internal energy relative to the corresponding crystal. Structural relaxation and modification of dielectric properties by the introduction of impurities have been studied in detail in vitreous selenium, but such studies have been conducted in a limited temperature range [3] and time [4, 5]. In this regard, we compare the dielectric properties of aged and freshly synthesized samples of vitreous selenium, including the crystallization temperature range.

Initially, bulk samples of vitreous selenium were obtained several tens (30-35) years ago by the quenching technique by using high purity Se (99.999***%).*** Obtained glassy selenium ingots were stored at room temperature in the dark and on the air for decades. For rejuvenation, the aged vitreous selenium was re-melted and kept for several days prior to measurements to avoid high speed relaxation processes. The amorphous nature of both aged and rejuvenated selenium alloys is confirmed by the results of X-ray phase analysis and by a characteristic conchoidal fracture of the glass.

Measurement of dielectric response in the frequency range 10 Hz - 50 kHz was carried out using our automated measuring system based on impedance meters LCR-819 from Good Will company (GW Instek). Dielectric constants temperature and frequency dependences of the rejuvenated and aged sample of vitreous selenium was investigated. As examples at Fig. 1 temperature dependences was shown At a certain temperature close to the glass transition temperature Tg, the values of ε' and ε" begin to increase. The dependence of ε'(T) in the region of Tg at several frequencies is shown in the insert to Figs. 1 a. The most significant difference in the behavior of dielectric constant in aged and rejuvenated samples is observed in the crystallization region of glasses. In the same temperature range, the dielectric dispersion becomes quite noticeable. It should be noted that in the temperature range T <Tg the values of ε' and ε" for aged samples of vitreous selenium are much higher than in rejuvenated glass even ten times depending on the frequency of the measuring field.

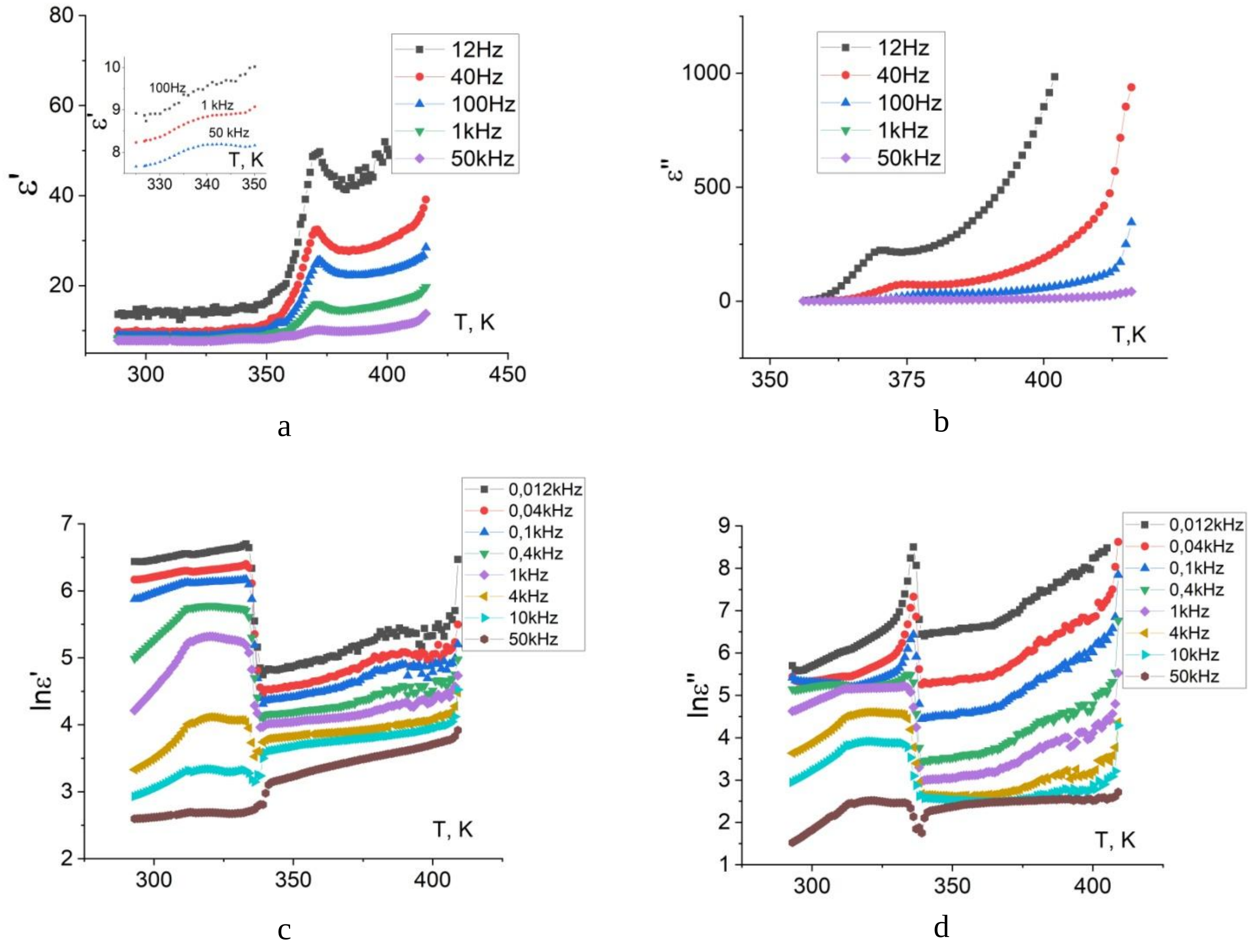

a

b

c

d

Fig. 1. The real ε'(a, c) and imaginary ε" (b, d) parts of the complex dielectric constant ε* temperature dependences obtained in rejuvenated (a, b) and aged (c, d) sample of vitreous selenium at different frequencies (the first heating cycle).

This result indicates the presence an additional mechanism of polarization due to the processes of long-term structural relaxation in the vitreous state, which makes a significant contribution to the dielectric constant and confirmed by the constructed Cole-Cole diagrams shown on Fig. 2.

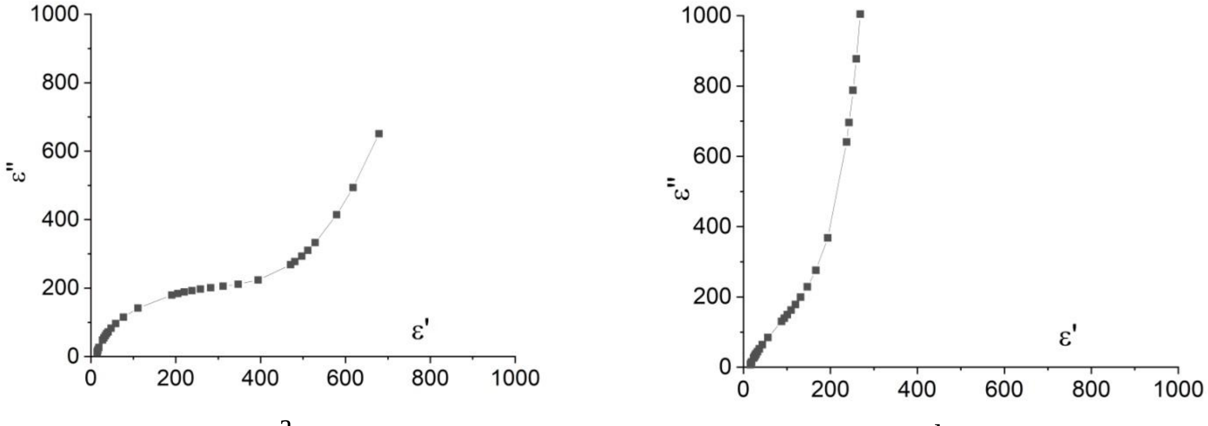

a

b

Fig. 2. Cole–Cole plots before (a – 330K) and after (b-335K) crystallization for aged selenium glass.

Cole-Cole diagrams appear only before the crystallization of the glass and with increasing temperature are masked, especially at low frequencies, due to the increase of electrical conductivity and, accordingly, dielectric losses. The parameters of relaxation polarization at 320 K estimated from the Cole-Cole diagrams are as follows: relaxation depth $\Delta\varepsilon \sim 500$, average relaxation time $\tau \sim 2.3 \cdot 10^{-4}$ s, distribution parameter of $\alpha \sim 0.3$. Of course, the values of these parameters are temperature dependent, but the correct selection of the contribution to the total complex dielectric constant of observed relaxers is problematic. Nevertheless, we can assume that the observed effects are associated with Maxwell-Wagner relaxation, i.e. the formation of space charges. In micro-heterogeneous systems, charge carriers can accumulate at the boundaries between clusters, which leads to polarization at the "interface". This occurs only when the clusters differ in the values of dielectric constant or conductivity. The main cause of polarization at the "interface" is usually the difference in conductivity, because the dielectric constant varies from cluster to cluster much less than the conductivity.

Thus the temperature-frequency investigation of the complex dielectric constant components in aged and rejuvenated by re-melting vitreous selenium shown that as a result of structural relaxation appears an additional mechanism of polarization and the corresponding dielectric dispersion, which is probably due to the micro-heterogeneity of the structure and associated with the transition regions between the vitreous matrix and crystalline phase nuclei. Their presence causes a significant difference in the behavior of dielectric parameters during crystallization of aged and rejuvenated glassy selenium.

1. Springer Handbook of Electronic and Photonic Materials. Editors: S. Kasap, P. Capper, (Eds.) 2017, XXXVI, 1536 p. (https://doi.org/10.1007/978-3-319-48933-9)
2. Anirban Pal, Sharmila N. Shirodkar, Smita Gohil, [et al.]. Multiferroic Behavior in Elemental Selenium below 40 K: Effect of Electronic Topology // Sci. Rep., 2013. 3:2051. (https://doi.org/10.1038/srep02051)
3. A. Sharma and N. Mehta. Analysis of dielectric relaxation in glassy Se and $Se_{98}M_2$ (M = Ag, Cd and Sn) alloys. A study of metal-induced effects // Eur. Phys. J. Appl. Phys., 2012. – V. 59: 10101. (https://doi.org/10.1051/epjap/2012120184)
4. S. Dash, P. Chen, and P. Boolchand. Molecular origin of aging of pure Se glass: Growth of inter-chain structural correlations, network compaction and partial ordering // J. Chem. Phys., 2017. – V. 146. – Issue 22. (https://doi.org/10.1063/1.4983480)
5. A. Dwivedi, R. Arora, N. Mehta, N. [et al.]. Choudhary, A. Kumar. Dielectric relaxation in $Se_{80}Ge_{20}$ and $Se_{75}Ge_{20}Ag_5$ chalcogenide glasses // Semiconductor Physics, Quantum Electronics & Optoelectronics, 2005. – V. 8. – № 3. – P. 45-49.

SYNTHESIS AND CRYSTAL STRUCTURE OF NEW MIXED ORTHOVANADATES $Pr_{0.5}R_{0.5}VO_4$ (R = Sm, Gd, Dy, Er, Yb)

Hreb V.M., Tupys A.M., Vasylechko L.O.

Lviv Polytechnic National University, 12, Bandera St., 79013 Lviv, Ukraine

Rare earth (R) orthovanadates RVO_4 are widely used as catalysis, gas sensors, laser host, phosphors and unusual magnetic materials. Tuning of their unique properties such as electronic, optical, luminescent, interfacial and catalytic properties allow expanding branch of application. Previous crystal structure investigations show that rare earth orthovanadates adopt monoclinic monazite-type structure for $LaVO_4$ and tetragonal zircon-type structure for other RVO_4 compounds. In continuation of our previous investigations of the mixed vanadates $R_{1-x}R_xVO_4$, the present work is devoted to evaluation of the influence of heat treatment temperature on the formation of single phase materials in the $PrVO_4$–RVO_4 systems and detail studies of their crystal structure.

The powders of the mixed orthovanadates $Pr_{0.5}R_{0.5}VO_4$ (R = Sm, Gd, Dy, Er, Yb) were prepared by solid-state reaction technique. Stoichiometric amounts of ammonium metavanadate NH_4VO_3, praseodymium oxide Pr_6O_{11} and rare earth oxides R_2O_3 (R = Sm, Gd, Dy, Er, Yb) were carefully mixed in agate mortar. The mixtures were initially heat treated at 900ºC in air two times for 5h with intermediate grinding of the product. Thorough phase and structural analysis of as-obtained powders revealed that $Pr_{0.5}Sm_{0.5}VO_4$ adopts single phase tetragonal structure after first stage of annealing (900 ^{o}C, 5+5h). Additional heat treatment at 1000 ^{o}C in air for 5h is required to obtain single phase materials of $Pr_{0.5}Gd_{0.5}VO_4$ and $Pr_{0.5}Dy_{0.5}VO_4$. More difficult is phase formation of $Pr_{0.5}R_{0.5}VO_4$ orthovanadates with smaller R-cations, such as Er and Yb. The single phase purity of these materials was achieved only after their 6-hours annealing in air at 1200 ^{o}C and 1400 ^{o}C for $Pr_{0.5}Yb_{0.5}VO_4$ and $Pr_{0.5}Er_{0.5}VO_4$, respectively.

Full profile Rietveld refinement of $Pr_{0.5}R_{0.5}VO_4$ structures was performed in space group $I4_1/amd$ using cell dimensions and atomic coordinates of tetragonal $PrVO_4$ as initial structure model. Graphical results of that refinement (on the example of $Pr_{0.5}Gd_{0.5}VO_4$) are presented on Fig. 1. The insert to the Figure illustrates chains of edge-sharing RO_8 dodecahedra (greenish) and VO_4 tetrahedra (bluish) in zircon-type $Pr_{0.5}R_{0.5}VO_4$ structure. The microstructural parameters of the $Pr_{0.5}R_{0.5}VO_4$ powders, such as average grain size $<D_{ave}>$ and microstrains $<\varepsilon>$ of crystallites, which were evaluated from angular dependence of the Bragg's maxima peak broadening, show that increasing treatment temperature and its duration lead to growing size of crystallites and reduction microstrains caused by reduction of dispersion of interplanar distances in corresponding structures. The LaB_6 external standard was used for the correction of instrumental broadening. Corresponding value of $<D_{ave}>$ and $<\varepsilon>$ of crystallites for $Pr_{0.5}R_{0.5}VO_4$ (R = Sm, Gd, Dy, Er, Yb) single phase materials are collected in Table 1.

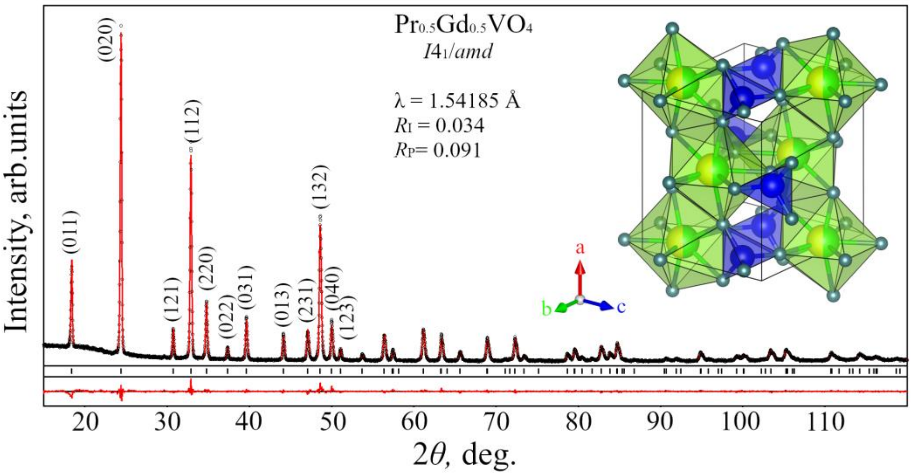

Fig. 1. Graphical results of Rietveld refinement of tetragonal $Pr_{0.5}Gd_{0.5}VO_4$ synthesised at 1200 ^{o}C.

The derived unit cell dimensions of $Pr_{0.5}R_{0.5}VO_4$ (R = Sm, Gd, Dy, Er, Yb) are in good agreement with the lattice parameters of $PrVO_4$ and RVO_4 compounds, thus proving formation of the continuous solid solution with tetragonal structure in the $PrVO_4$–RVO_4 pseudo-binary systems (Fig. 2). Value of a, c parameters and unit cell volume V are collected in Table 1.

Table 1. Structural and microstructural parameters of $Pr_{0.5}R_{0.5}VO_4$ (space group $I4_1/amd$)

	a, Å	c, Å	V, Å^3	$\langle D_{ave} \rangle$, nm	$\langle \varepsilon \rangle$, %
$Pr_{0.5}Sm_{0.5}VO_4$	7.3151(2)	6.4271(2)	343.92(3)	198	0.0546
$Pr_{0.5}Gd_{0.5}VO_4$	7.2906(2)	6.4104(3)	340.73(4)	115	0.0880
$Pr_{0.5}Dy_{0.5}VO_4$	7.2575(3)	6.3891(3)	336.52(4)	84	0.1853
$Pr_{0.5}Er_{0.5}VO_4$	7.2305(2)	6.3719(3)	333.12(4)	266	0.1257
$Pr_{0.5}Yb_{0.5}VO_4$	7.2047(1)	6.3584(2)	330.05(2)	472	0.0961

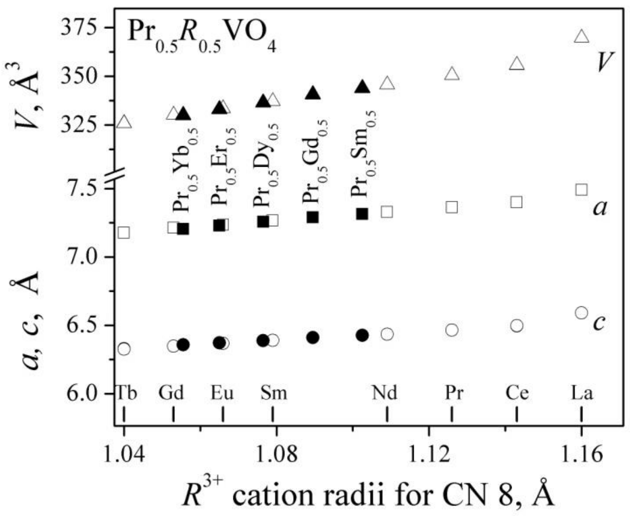

Fig. 2. Lattice parameters and unit cell volumes of tetragonal $Pr_{1-x}R_xVO_4$ series in a comparison with the literature data for the parent RVO_4 compounds as a function of the radii of R^{3+} ions.

Acknowledgements. The work was supported in parts by the Ukrainian Ministry of Education and Science under Project N 0118U000264 and ICDD Grant-in-aid program.

ORTHOVANADATE $GdYVO_4:Eu^{3+}$ NANOPARTICLES WITH SWITCHABLE REDOX-ACTIVITY

Hubenko K. O., Yefimova S. L., Maksimchuk P. O., Kavok N. S., Klochkov V. K., Malyukin Yu. V.

Institute for Scintillation Materials of NAS of Ukraine,
60 Nauky Ave., Kharkiv, 61072, Ukraine
**e-mail: gubenko@isma.kharkov.ua*

Nanoparticles (NPs), which promote generation of reactive oxygen species (ROS) and stimulate the onset of oxidative stress responsible for the development of a variety of adverse conditions, are of great prospect for various nanomedicine applications. ROS generation in semiconducting NPs is a complex process, the efficiency of which is governed by both NPs characteristics (size, morphology, etc.) and external conditions, such as type of irradiation. On the other hand, in NPs characterized by high amount of structural defects, for instance, oxygen vacancies (V_O) in oxide NPs, such defects could serve as traps for charge carriers and are responsible for ROS production in NPs even without UV irradiation (in the dark). In our previous works, we have shown that $GdYVO_4:Eu^{3+}$ NPs exhibit photo-catalytic activity (ROS production) at both UV-light irradiation [1, 2] and in the dark condition [3].

In this work, we report switchable redox activity of small (d=2nm) $GdYVO_4:Eu^{3+}$ nanoparticles (NPs) in aqueous solutions and biological environment. It has been revealed that depending on pre-treatment conditions (exposure to UV light or storage in the darkness) the same NPs exhibit pro- or anti-oxidant properties.

Pro-/anti-oxidant activity in aqueous solutions was evaluated by UV-vis spectroscopy by the ascorbic acid (AA) oxidation test, and hydroxyl radical ($^{\bullet}OH$) and superoxide anion ($O_2^{\bullet-}$) generation analysis. Lipid oxidation and cell viability estimation under the effect of NPs have been also analyzed.

Multi-functional $GdYVO_4:Eu^{3+}$ NPs with switchable redox activity are assumed to be a new theranostic agent in radiotherapy.

1. S.L. Yefimova, P.O. Maksimchuk, V.V. Seminko, N.S. Kavok, V.K. Klochkov, K.A. Hubenko, A.V. Sorokin, I.Yu. Kurilchenko, Yu.V. Malyukin, J. Phys. Chem. C., 123, 15323 (2019).
2. K. Hubenko, S. Yefimova, T. Tkacheva, P. Maksimchuk, I. Borovoy, V. Klochkov, N. Kavok, O. Opolonin, Yu. Malyukin, Nanosc. Res. Lett., 13, 101 (2018).
3. P. O. Maksimchuk, S. L. Yefimova, K. O. Hubenko, V. V. Omelaeva, N. S. Kavok, V. K. Klochkov, A. V. Sorokin, Y. V. Malyukin. Phys. Chem. C., 124, 3843 (2020).

TEMPERATURE DEPENDENCE OF SURFACE-DOPED TiO_2 EMISSION

O. F. Isaieva[1,3], V.I. Dzhagan [1], V. Shymanovska[2], D.R.T. Zahn[4], G.Yu. Rudko[1,3]

[1]*Lashkaryov Institute of Semiconductor Physics, NAS of Ukraine, Kyiv, Ukraine*
[2]*Institute of Physics, NAS of Ukraine, Kyiv, Ukraine*
[3]*National University "Kyiv-Mohyla Academy", Kyiv, Ukraine*
[4]*Semiconductor Physics, Chemnitz University of Technology, D-09107 Chemnitz, Germany*
E-mail: oksana.isaieva@isp.kiev.ua

TiO_2 is known for its ample applications in various fields. The most important ones are solar cells fabrication and photocatalysis for high-yield hydrogen production. TiO_2 is very efficient in utilizing the energy of UV light**,** however, since TiO_2 is transparent in the visible range, pure material is not applicable for harvesting energy in wider spectral range. Various methods were tested to surmount this drawback, among them surface doping has been proven to be an efficient method to achieve absorption of visible light by TiO_2 and to make the material good for both UV and visible ranges. Beside the transparency variation, this type of treatment causes concomitant changes of other properties of the material which are far from being completely described. In the present study we analyze the influence of surface doping with phenothiazine (PTZ) on the light emitting properties of TiO_2 powders.

The initial undoped powders of TiO_2 have been synthesized by thermal hydrolysis of titanium tetrachloride ($TiCl_4$) in hydrochloric acid solutions (100 °C). The precipitate was calcined at 200 °C for 5 h. After washing of the powder with double-distilled water (until a pH of ~7 was reached) the powder was thermally annealed in air at 300 °C. Surface doping of the powders with phenotiazine (PTZ) was done by mechanical grinding of TiO_2 powder with 5 wt% admixture of granular PTZ in an agate mortar at ambient conditions. During the grinding the white powder of undoped initial TiO_2 changed its color from white to dark-blue, almost black. Investigations of photoluminescence spectra and Raman scattering were carried out using of LabRam HR spectrometer. Luminescence was excited by light with the photon energy 3.8 eV. Power of the exciting light is 4,05 mW.

Both initial and surface-doped TiO_2 powders were characterized by various methods. It has been shown earlier [1] that the grains of TiO_2 powders have crystalline anataze structure and the average size of the grains is 10nm. In the present study we measured Raman spectra of the initial and surface-doped TiO_2 powders. The data obtained corroborated earlier results on anatase structure of the grains in undoped powder. Moreover, it was shown that Raman spectra of surface-doped TiO_2 powders are almost identical to the ones of initial TiO_2 which supports the conclusion that surface doping does not deteriorate the structure of grains.

Light emitting properties of surface-doped TiO_2 powders were probed by temperature-dependent photoluminescence spectroscopy, and the experimental spectra were compared with the results for the undoped TiO_2 and PTZ. The photoluminescence measurements at room temperature demonstrated that the emission of undoped TiO_2 at band-to-band excitation close to the band edge (the excitation wavelength 325 nm) is dominated by very wide band of self-trapped excitons recombination. Transformations of the emission spectra after surface doping with PTZ were assumed to be a result of overlapping of the emissions from undoped TiO_2 and PTZ molecules on the surface. This interpretation was corroborated by measuring temperature dependence of luminescence. It was shown that despite different behavior of the intensities of spectral components both of them can be clearly seen in the luminescence spectra of the surface-doped samples in the whole temperature range under study.

1. Kernazhitsky L. Dark-blue titanium dioxide: Effect of phenothiazine on structural and optical properties of nanocrystalline anatase TiO2/ L. Kernazhitsky, V. Shymanovska, T. Gavrilko, V. Naumov, L. Fedorenko, J. Baran// Journal of Physics and Chemistry of Solids, 126 (2019).

THE DIELECTRIC FUNCTION OF THE COMPOSITE WITH THE METAL-GRAPHENE NANORODS

Karandas Ya.V.[1], Korotun A.V.[1], Titov I.M.[2]

[1]*National University “Zaporizhzhia Politechnic”, 64, Zhukovskogo St., 69063 Zaporizhzhya, Ukraine*
[2]*UAD Systems, 84 Alexandrovska St., 69002, Zaporizhzhya, Ukraine*

The relation for the effective dielectric function for the composite with the metal-graphene nanorods has been obtained in the frameworks of the renormalized Maxwell-Garnett theory. One calculates the dielectric function for the metallic core to Drude approximation. One uses Kubo formalism in order to calculate the dielectric function for the graphene shell. The numerical results have been obtained for the nanocomposite based on the rods Ag@G with the different radius with the different thickness of the graphene shell.

The use of the surface plasmons for the control of the interaction between the light and the matter on the subwave scale has the vast application [1]. This is due to the fact that the shape and the location of the peak of the plasmonic resonance depend both on the size and the shape of the particles [2], and, hence, can be adjusted with the help of the choice of the synthesis conditions, what is of particular importance for the construction of the data-processing devices, for the development of the subwave optical devices, the plasmonic antennas, the nanolasers, the elements of the optical layouts and the photosensitive devices [3].

Among the different shapes of the nanoparticles one pays the great attention to the nanorods and the cylindrical shells due to their high spectral tunability in the biological spectral windows, and due to the existence of the great number of the new synthesis methods, which give the opportunity to control the size, the morphology and the area of the surface of such nanoparticles. But the use of the monometallic structures is limited by the persistency of their properties.

From this viewpoint, the most advanced is the use of the layered structures such as “core – shell” (A@B), in which, for example, the metallic core of the material A is covered with the shell of the material B, where the material B can be both the dielectric and the other metal. Such systems give an opportunity to tune up the position and the profile of the plasmonic resonance by means of the variation of the spacing and by means of the sorting of the different types of the atoms in more effective way.

An alternative material for the coating of the metallic 1*D*-structures can be graphene – 2*D*-carbon material, in which the surface plasmons can be excited in the middle and far IR zones. In this context the graphene plasmonics stimulates the essential progress in the nanophotonic technologies. In particular, the metallic nanocylinders, covered with graphene, have the vast application in the photon devices, the nonlinear devices, the lasers, and in the other fields [4]. That is why the study of the optical properties of the composites with metal-graphene nanorods is actual.

Let us consider the composite, which consists of the bilayered metal-graphene nanorods, placed in the matrix with the dielectric permittivity т_{m}. In order to describe the optical properties of such heterogeneous systems one makes good use of the different modifications of the effective-medium theory.

One of the most popular models of the effective medium is Maxwell-Garnett theory. But this theory is unusable in the case when the filling factor is high and it is necessary to take into account the dipole-dipole interaction between the nanoinclusions. Hence, the starting point for our calculations is the formula for the effective dielectric permittivity of the composite. This formula has been obtained with the help of the renormalized Maxwell-Garnett theory [5]:

$$\frac{\mathrm{T}_{\mathrm{eff}}-\mathrm{T}_{\mathrm{m}}}{\mathrm{T}_{\mathrm{eff}}+2\mathrm{T}_{\mathrm{m}}}=\frac{1}{3}\beta\tilde{\alpha}^{*}, \qquad (1)$$

where β – the volume fraction of the composite; $\tilde{\alpha}^*$ – the renormalized averaged polarizability, which is determined by the relation

$$\tilde{\alpha}^* = \frac{2}{\beta\bar{\tilde{\alpha}}_@}\left(1-\sqrt{1-\beta\tilde{\alpha}_@^2}\right); \qquad (2)$$

$$\tilde{\alpha}_@ = \frac{1}{3}\left(2\tilde{\alpha}_@^{\perp}+\tilde{\alpha}_@^{\parallel}\right). \qquad (3)$$

Here $\tilde{\alpha}_@^{\perp}$ and $\tilde{\alpha}_@^{\parallel}$ – the transversal and longitudinal components of the polarizability tensor of the metal-graphene nanorod, which are determined by the relations

$$\tilde{\alpha}_@^{\perp} = 2\frac{\left(\varepsilon(\omega)-\varepsilon_G\right)\left(\varepsilon_G-\varepsilon_m\right)+\beta_c\left(\varepsilon(\omega)-\varepsilon_G\right)\left(\varepsilon_G+\varepsilon_m\right)}{\left(\varepsilon(\omega)+\varepsilon_G\right)\left(\varepsilon_G+\varepsilon_m\right)+\beta_c\left(\varepsilon(\omega)-\varepsilon_G\right)\left(\varepsilon_G-\varepsilon_m\right)}, \qquad (4)$$

$$\tilde{\alpha}_@^{\parallel} = \frac{\varepsilon(\omega)-\varepsilon_m-\beta_c\left(\varepsilon(\omega)-\varepsilon_G\right)}{\varepsilon_m}. \qquad (5)$$

From the expression (1) for the effective dielectric function one can obtain

$$\varepsilon_{\text{eff}} = \varepsilon_m\frac{1+\frac{2}{3}\beta\tilde{\alpha}^*}{1-\frac{1}{3}\beta\tilde{\alpha}^*}. \qquad (6)$$

In the frameworks of Drude theory the dielectric function of the metallic core

$$\varepsilon(\omega)=\varepsilon_1(\omega)+i\varepsilon_2(\omega)=\varepsilon^{\infty}-\frac{\omega_p^2}{\omega^2+\gamma_{\text{eff}}^2}+i\frac{\omega_p^2\gamma_{\text{eff}}}{\omega\left(\omega^2+\gamma_{\text{eff}}^2\right)}, \qquad (7)$$

where ε^{∞} is the contribution of the ion core, ω_p is the frequency of the volume plasmons, γ_{eff} is the effective electron relaxation rate, which can be represented in the form

$$\gamma_{\text{eff}} = \gamma_{\text{bulk}}+\gamma_s+\gamma_{\text{rad}}. \qquad (8)$$

Here γ_{bulk} is the relaxation rate in the 3*D*-metal; γ_s is the relaxation rate, which is resulting from the scattering of the electrons on the surface. In the case of the radial electron motion in the nanocylinder this relaxation rate can be determined as

$$\gamma_s = \frac{27\pi}{128\left(\varepsilon_m+1\right)}\left(\frac{\omega_p}{\omega}\right)^2\frac{v_F}{R_c}, \qquad (9)$$

where v_F is the Fermi velocity of the electrons, R_c is the radius of the metallic core.

The radiation relaxation rate can be determined as follows

$$\gamma_{\text{rad}} = \frac{3}{128}\frac{V}{\sqrt{\varepsilon_m\left(\varepsilon^{\infty}+\varepsilon_m\right)}}\left(\frac{\omega_p}{c}\right)^3\left(\frac{\omega_p}{\omega}\right)^2\frac{v_F}{R_c}, \qquad (10)$$

where $V=\pi R_c^2 l$ is the volume of the metallic core, l is the length of the rod.

The dielectric function of the graphene shell

$$\varepsilon_G = 1+i\frac{\sigma_G}{\varepsilon_0\omega t}, \qquad (11)$$

where t is the thickness of the graphene shell ($t=Nt_G$, N – the number of the layers of graphene, $t_G=0.335$ nm is the thickness of the monoatomic layer of graphene); $\sigma_G=\sigma_{\text{intra}}+\sigma_{\text{inter}}$ is the conductivity of graphene, the interband and intraband components of which can be determined as

$$\sigma_{\text{inter}} = \frac{e^2}{4\hbar}\left[\frac{1}{2}+\frac{1}{\pi}\operatorname{arctg}\left(\frac{\hbar\omega-2\mu_c}{k_{\text{B}}T}\right)-\frac{\text{i}}{2\pi}\ln\left(\frac{\left(\hbar\omega+2\mu_c\right)^2}{\left(\hbar\omega-2\mu_c\right)^2+\left(2k_{\text{B}}T\right)^2}\right)\right];$$

$$\sigma_{\text{intra}} = \frac{2\,\text{i}\,k_{\text{B}}T}{\pi\hbar^2\left(\omega+\frac{\text{i}}{\tau}\right)}\ln\left[2\operatorname{ch}\left(\frac{\mu_{\text{c}}}{k_{\text{B}}T}\right)\right]. \qquad (12)$$

In the formulas (12) μ_{c} is the chemical potential; T is the temperature.

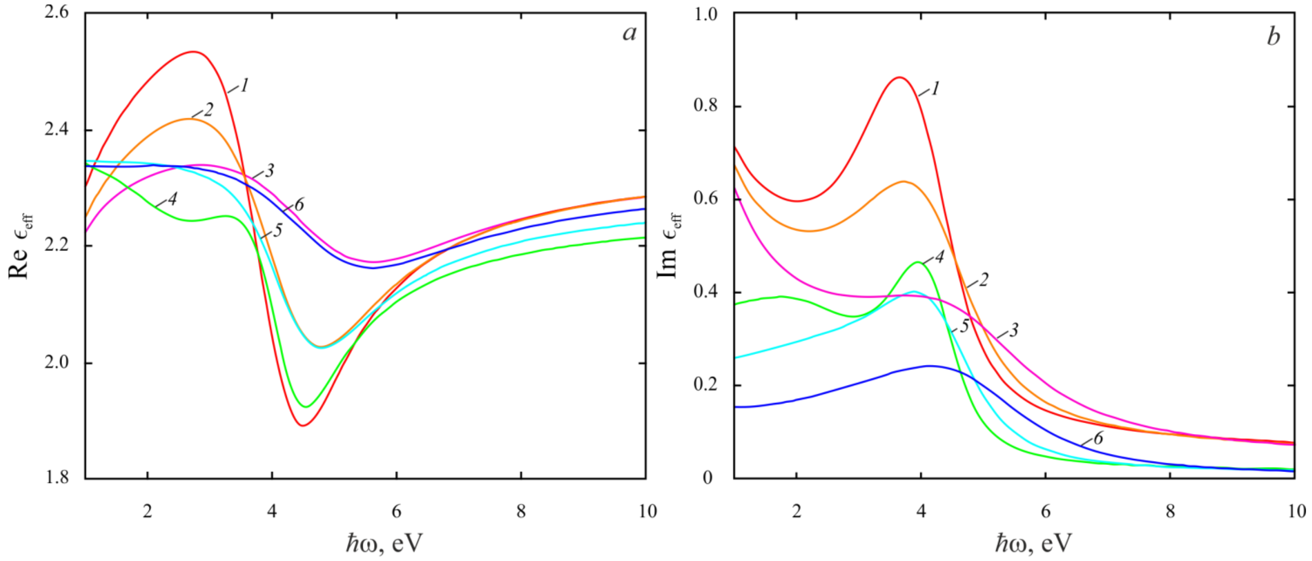

Fig.1. The frequency dependences of the real (*a*) and imaginary (*b*) parts of the effective dielectric function of the composite (the curves *1 – 3*: $N=1$, $R_{\text{c}}=10$, 20, 50 nm; the curves *4 – 6*: $N=10$, $R_{\text{c}}=10$, 20, 50 nm)

The figure 1 shows the calculations for the frequency dependence of the real and imaginary parts of the effective dielectric function of the nanocomposite in the case of the silver nanorods with the different radius, which are covered with the graphene layer of the different thickness. It should be pointed out that the thickness of the graphene coating has the significant effect on τ_{eff} of the composite. If the number of the graphene layers becomes greater than the smoothing of the dependences $\operatorname{Re}\tau_{\text{eff}}(\hbar\omega)$ (fig. 1, *a*) and $\operatorname{Im}\tau_{\text{eff}}(\hbar\omega)$ (fig. 1, *b*) happens, the maximums $\operatorname{Re}\tau_{\text{eff}}(\hbar\omega)$ disappear, and the maximums $\operatorname{Im}\tau_{\text{eff}}(\hbar\omega)$ become mild. As well, the changes of the real and imaginary parts of the dielectric function of the nanocomposite in the case when the thickness of the shell is 10 monolayers are small in comparison with the case of one monolayer. The fact of the smoothing of the maximums $\operatorname{Re}\tau_{\text{eff}}(\hbar\omega)$ and $\operatorname{Im}\tau_{\text{eff}}(\hbar\omega)$ under the increase of the radius of the nanorod core seems to be paradoxical, but it can be explained by the attenuation of the dipole-dipole interaction in this case.

The relation for the effective dielectric function of the nanocomposite with the metal-graphene cylinders has been obtained with the help of the renormalized Maxwell-Garnett theory.

It has been established that the character of the frequency dependences of the real and imaginary parts of the effective dielectric function of the composite depends on the number of the graphene layers. If this number becomes greater than the maximums of the real part disappear, and the maximums of the imaginary part become mild. The smoothing of the maximums of the curves under the increase of the radius of the metallic core results from the attenuation of the dipole-dipole interaction between the nanocylinders.

1. Ma R.M., Oulton, R.F., Sorger, V.J. [et al.]. Plasmon lasers: Coherent light source at molecular scales // Las. Photon. Rev., 2012. – V. 7. – P. 1-21.
2. Maier S.A. Plasmonics: fundamentals and applications (Springer Science & Business Media, 2007).
3. Korotun A.V., Koval’ A.O., Kryuchyn A.A. [et al.]. Nanophoton technologies. Modern state and prospects (Uzhgorod: PE Sabov A.M., 2019).
4. Teng, D., Wang, K., Li, Z. [et al.]. Graphene-coated nanowire dimers for deep subwavelength waveguiding in mid-infrared range // Opt. Expr., 2019. – V. 27. – P. 12458-12469.
5. Barrera R.G., Monsivais G., Mochán W.L. Renormalized polarizability in the Maxwell Garnett theory // Phys. Rev. B, 1988. – V. 38. – N. 8. – P. 5371-5379.

MECHANISMS OF FORMATION AND PHYSICAL PROPERTIES OF 2D-STRUCTURES Al and In

Karbivska L.I., Smolyak S.S., **Karbivskyy V.L.,** Romansky A.A.

G.V. Kurdyumov Institute for Metal Physics, N.A.S. of Ukraine, 36, Academician Vernadsky Boulevard, 03142, Kyiv, Ukraine

The formation mechanism of indium nanostructures on the Si (111) and Si (110) silicon single crystal surfaces during multi-stage thermal deposition has been studied experimentally and theoretically. The growth of metal structures on a semiconductor substrate without its cooling and the presence of inert gases in the working volume leads to complex mechanisms of nucleation and growth of indium nanostructures, which differ from well-known mechanisms. By changing the technological deposition parameters, it is possible to obtain various pictures of self-ordered nanostructures.

Nanotribological parameters of subroughness R_a, R_q, R_{zjis}, R_z, S_{ratio} for indium surfaces have been established. It is shown that under multistage deposition there is an increase in the size of clusters with the general preservation of the trend of increasing the maximum difference between ridges and valleys (Fig.1).

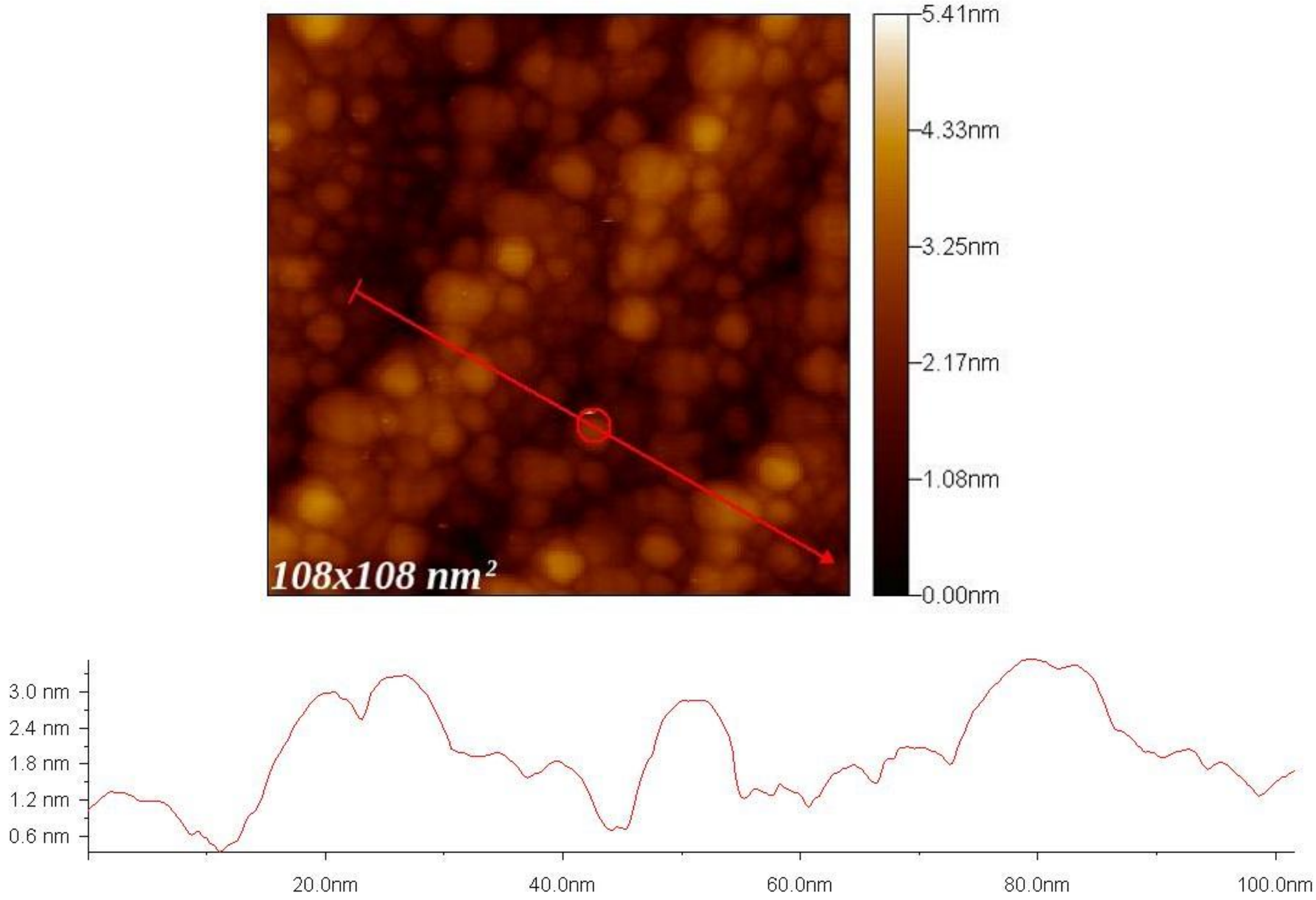

Fig.1. Roughness profile of indium on the Si(111) surface.

It is noteworthy that the roughness profile is characterized by a spread in heights from 0.6 to 3.0 nm and at the same time, there is a periodic substructure of the relief in the form of bunch lines.

For both silicon surfaces during thermal deposition, the formation of indium clusters of regular cubic shape is observed, which indicates the formation of metal nanocrystals. The transformation of the density of electronic states of In is established from an individual cluster (~ 10 nm in size) on the Si (111) surface to a bunchy coating of the single crystal surface with a coating thickness of no more than 30 - 40 nm, characterized by the absence of a band gap for a massive sample (Fig. 2).

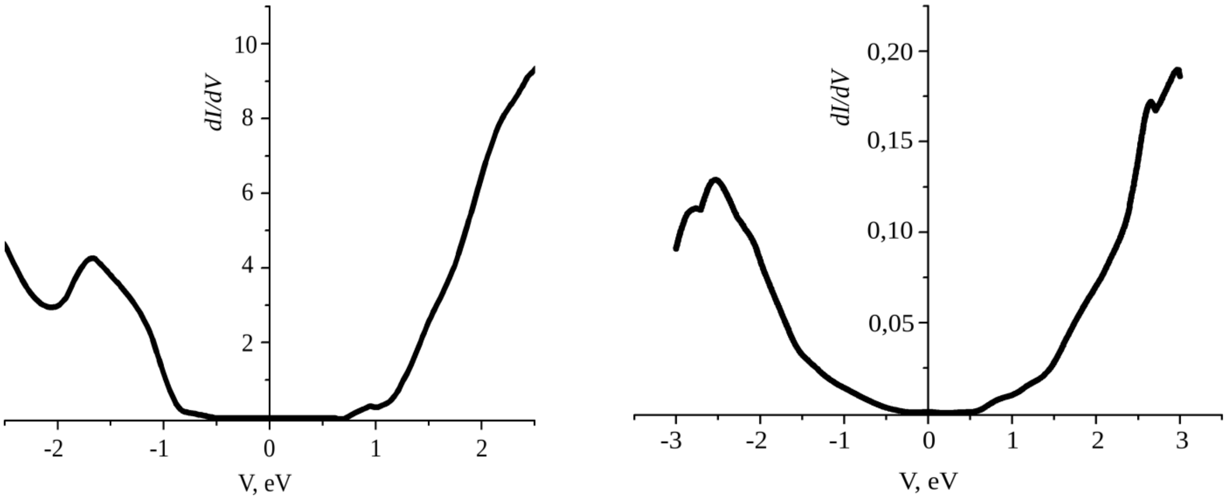

a)

b)

Fig. 2. Densities of electronic states: fig. 2, a - separate cluster and
fig. 2, b - continuous coating.

The curve in Fig. 2, *a* characterizes the density of electronic states of one of the clusters. As can be seen, the curve of the density of electronic states characterizes a not quite metallic cluster, taking into account the presence of a certain gap at the "Fermi level". It can be assumed that energy bands are not fully formed in In clusters with a size of ~ 10 nm. The transition to the surface morphology completely filled with bunches of clusters leads to the transformation of the density of electronic states shown in Fig. 2, b. The curve of the density of electronic states is much closer to that of metallic In. The first peaks in the region of occupied states characterize the *p*-states of indium. In the case of an individual cluster, they have a narrow peak and are localized at ~ 1.8 eV, and upon passing to coating, this maximum shifts to the region of high binding energies and has an almost nonzero value in the region of zero binding energies. The area of free states has the same transformation tendencies of the state curve.

TECHNOLOGICAL APPROACH TO ZnO NANOSTRUCTURES GROWTH FROM METALORGANIC COMPOUNDS FOR PHOTOCATALYTIC APPLICATIONS

Karpyna V.A., Myroniuk L.A., Myroniuk D.V., Bykov O.I., Zahornyi M.M., Ievtushenko A.I.

I. M. Frantsevich Institute for problems of materials science, NAS of Ukraine,
3, Krhyzhanovsky st., 03142, Kyiv, Ukraine

ZnO is considered as a good candidate for photovoltaic applications because of its characteristics, such as direct and wide band gap that allow strong absorption in the near UV spectral region. There is new approach to build high efficient ZnO UV photodetectors multilayered structures [1]. A large exciton binding energy ~60 meV could provide excitonic emission at room temperature that favors to build optoelectronic device and random nanolasers that is still investigated [2]. The observation of feeble ferroelectricity and giant piezoelectricity in doped II–VI ZnO binary semiconductor open the doors to develop small ferroelectrics and flexible piezoelectric nanogenerators [3]. In recent years, ZnO is also considered as efficient and promising candidate for photocatalitic applications in green environmental management system because of its strong oxidation ability and good photocatalytic activity compared to TiO_2 [4].

A method for growing ZnO nanostructures from chemical vapors by decomposition of metalorganic compounds at atmospheric pressure (APMOCVD - atmospheric pressure metal organic chemical vapor deposition) has been proposed and developed. The deposition process in the APMOCVD method takes place in a tubular furnace with a temperature gradient between two zones: high temperature zone is used for substrate placing while low temperature zone for precursor evaporator. A feature of the process is the supply of a mixture of argon and oxygen carrier gases, which provides additional vapor distribution in order to form homogeneous nanostructure films at relatively low process temperature. Zinc acetylacetonate was used as metalorganic precursor for growing ZnO nanostructures on silicon, glass and sapphire substrates.

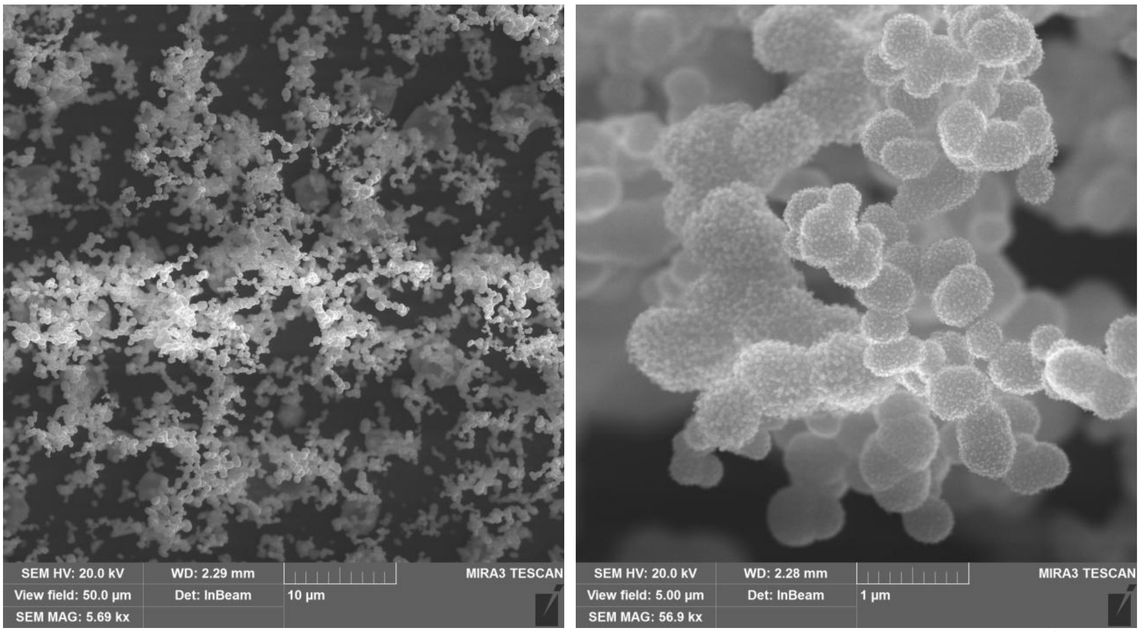

Fig.1 SEM images of ZnO nanostructures deposited on sapphire substrates at 350 ^{o}C.

An X-ray diffraction analysis of the deposited nanostructures was performed, which confirmed the formation of a crystalline phase of wurtzite ZnO with the most intense reflexes from plane (100), (002) and (101). Fig. 1 demonstrates the SEM images of ZnO nanostructures grown by the APMOCVD method on sapphire substrates. We can see the formation of spherical nanostructures with average sizes of 200 nm. We perform the series of experiment with different amount of source material loaded in evaporator and with distinct substrate temperature. The distance between evaporated boat and a substrate holder is sufficiently influence on the kind of formed nanostructure. Photocatalytic activity of obtained ZnO nanostructures will be tested. The obtained results will be presented and discussed.

Acknowledgements

This work was partially supported by the research project of NAS of Ukraine "The development of photocatalytic nanocomposites for viruses inactivation in the air" (№40/20-H) and was partially supported by the research projects of NAS of Ukraine "Development of innovative photocatalytic nanostructured materials based on ZnO and TiO_2" (528/IPM-11/20).

1. Ferhatia H., Djeffal F. Enhanced performance of ultraviolet photodetector based on sputtered ZnO/Au/ZnO multilayer structure // Superlattice and Microstructures, 2019. – V. 134. – P. 106225.
2. Fadzliana N., Samsuri S.A.M., Chan S.Y., Hsu H.C., W. Maryam. Influence of Al doping on random lasing in ZnO nanorods // Optics & Laser Technology, 2020. – V. 124. – P. 106004.
3. Goel S., Kumar B. A review on piezo-/ferro-electric properties of morphologically diverse ZnO nanostructures // J. Alloys and Compaunds, 2020. – V. 816. – P. 152491.
4. Samadi M., Zirak M., Naseri A. [et. al.] Recent progress on doped ZnO nanostructures for visible-light photocatalysis // Thin Solid Films 2016. – V. 605. – P. 2-19

TOPOLOGY OF BAND STRUCTURE AND SPATIAL DISTRIBUTION OF ELECTRON DENSITY IN SEMICONDUCTORS OF In-Se SYSTEM

Kharkhalis L.Yu., Liakh M.V., Glukhov K.E. , Babuka T.Ya.

Institute of Physics and Chemistry of Solid State, Uzhhorod National University,
54 Voloshin St., 88000 Uzhhorod, Ukraine

It is known the A^{III}–B^{VI} (A-In, Ga, B- Se, Te) system contains many compounds, in particular InSe (GaSe), In_2Se_3, In_4Se_3, In_6Se_7. Recently, these materials have been intensively studied in connection with the prospects of their practical application. Due to the layered structure in combination with other crystals, the InSe crystal is widely used for the formation of heterostructures, which leads to almost ideal heterocontact. This InSe crystal, like In_2Se_3 with a defective structure, can be used as a cathode material in solid-state batteries, as well as for the formation of nanostructured type capacitors. A high coefficient of a thermoelectric quality factor was found in the In_4Se_3 crystal [1], this opens up new possibilities in thermoelectricity [2,3]. There is some information in the literature about the physical properties (thermoelectric, kinetic, and optical) of the In_6Se_7 crystal [4], as well as the new In_3Se_4 crystal (In_3Te_4), which is very little studied today. Therefore, it is of interest to study the structural and electronic properties of the considered group of crystals. The obtained information on the topology of the band structure and spatial distribution of electron density for materials of the In–Se system can be used to explain existing physical properties, as well as to predict new effects, such as non-trivial topological phase transitions in indium selenides.

In the present work, we aimed at the establishing of some regularities in the evolution of the elementary energy bands topology and determination of the actual Wyckoff position issued from *ab initio* calculations of the electronic band spectra and partial distribution of electron density in the crystals of β-InSe, In_2Se_3, In_4Se_3, and In_6Se_7. To select the Wyckoff position for these crystals of the In–Se system, we use the elementary energy band concept based on the theoretical group methods and the empty lattice approximation. It is shown that the energy spectra are formed from the minimal complexes with the determined symmetry and the maximum of electron density is localized in the actual Wyckoff position that is suggested by the topology of the spatial distribution of the valence electron density. The results of our analysis in the main directions of the Brillouin zone are presented in the Table. As it follows from Table the actual Wyckoff positions are the lines and planes which intersect the In–Se bonds. This fact indicates the dominance of the covalent type of bonding in the considered compounds.

Thus, utilizing only the structural data, the space symmetry group, and the information about the existence of the forbidden gap of crystals we can predict the symmetry and topology of the energy states and verify the first principle calculation of the band spectrum and also obtain the information about the origin of the chemical bonds in the indium selenides.

Table. Symmetry, lattice parameters, minimal band complexes, and actual Wyckoff positions

	Compounds	Symmetry	Minimal band complexes	Wyckoff position
1.	In_4Se_3	$D_{2h}^{12}\,(Pnnm)$ $a = 15.296\overset{0}{A},$ $b = 12.308\overset{0}{A}$ $c = 4.0806\overset{0}{A}$	$12(\Gamma_1 \oplus \Gamma_4 \oplus \Gamma_6 \oplus \Gamma_7)+$ $3(\Gamma_2 \oplus \Gamma_3 \oplus \Gamma_5 \oplus \Gamma_8)$	$g(x, y, 0)$
2.	β-InSe	$D_{6h}^{4}\,(P6_3/mmc$ $)$ $a = b = 4.048\overset{0}{A},$ $c = 16.930\overset{0}{A}$	$\Gamma_1 \oplus \Gamma_4 \oplus \Gamma_5 \oplus \Gamma_8 \oplus \Gamma_9 \oplus$ $\Gamma_{10} \oplus \Gamma_{11} \oplus \Gamma_{12} -$ $2H_1 \oplus 2H_2 \oplus 2H_3$ $\Gamma_1 \oplus \Gamma_4 \oplus \Gamma_5 \oplus \Gamma_8 - H_2 \oplus H_3$ $\Gamma_1 \oplus \Gamma_8 - H_2$	$k(x, 2x, z)$ $f(1/3, 2/3, z)$ $d(1/3, 2/3, 3/4)$
3.	γ-InSe	$C_{3v}^{5}\,(R3m)$ $a = b = 4.002\overset{0}{A}$ $c = 24.946\overset{0}{A}$	$13\Gamma_1 \oplus 7\Gamma_3 - 13Z_1 \oplus 7Z_3 -$ $20D_1 \oplus 7D_2 - 20A_1 \oplus 7A_2$	$a(\nu\vec{a})$ $b(\nu(\vec{a}_1 + \vec{a}_2) + \mu\vec{a}_3)$
4.	ε- InSe	$D_{3h}^{1}\,(P\overline{6}m2)$ $a = b = 3.743\overset{0}{A}$ $c = 15.919\overset{0}{A}$	$7(\Gamma_1 \oplus \Gamma_4) + (\Gamma_5 \oplus \Gamma_6) -$ $7(A_1 \oplus A_4) + (A_5 \oplus A_6) -$ $9(R_1 \oplus R_4)$	$g(0, 0, z)$ $i(4/3, 2/3, z)$
5.	α- In_2Se_3	$C_{6}^{6}\,(P6_3)$ $a = b = 4.00\overset{0}{A}$ $c = 19.24\overset{0}{A}$	$8(\Gamma_1 \oplus \Gamma_4) + 2(\Gamma_2 \oplus \Gamma_5) +$ $2(\Gamma_3 \oplus \Gamma_6)$	$a(0, 0, z)$ $b(2/3, 1/3, z)$
6.	γ-In_2Se_3	$C_{6}^{2}\,(P6_1)$ $a = b = 7.11\overset{0}{A},$ $c = 19.34\overset{0}{A}$	$12(\Gamma_1 \oplus \Gamma_2 \oplus \Gamma_3 \oplus \Gamma_4 \oplus \Gamma_5 \oplus \Gamma_6)$	$a(x, y, z)$
7.	In_6Se_7	$C_{2h}^{2}\,(P2_1/m)$ $a = 9.43\overset{0}{A}, b = 4.063\overset{0}{A}$ $c = 18.378\overset{0}{A},$ $\beta = 109.34^0$	$25(\Gamma_1 \oplus \Gamma_4) + 5(\Gamma_2 \oplus \Gamma_3) -$ $25(Y_1 \oplus Y_4) + 5(Y_2 + Y_3) -$ $15(Z_1 + Z_2 + Z_3 + Z_4)$	$e(\alpha_1\vec{a}_1 + \alpha_2\vec{a}_2)$

1. Rhyee J.-S., Lee K.H., Lee S.M., [et al.]. Peierls distortion as a route to high thermoelectric performance in In_4Se_{3-2d}//Nature. - 2009 No.18, 459.- Pp. 965-968
2. 2 Lim Y.S., Jeong M., Seo W.-S., Lee J.-H., Park C.H., Sznajder M., Kharkhalis L.Yu., Bercha D.M., Jang J. Condenson state and its effects on thermoelectric properties in In_4Se_3// J.Phys.D.: Appl.Phys.- 2013. V. 46. - Pp. 275304-275308.
3. Jeong M., Lim Y.S., Seo W.-S., Lee J.-H., Park Ch.-H., Sznajder M., Kharkhalis L.Yu., Bercha D.M., Yang J. Condenson-related thermoelectric properties and formation of coherent nanoinclusions in Te-substituted In_4Se_3//Journ. of Materials Chemistry A., 2013, V.1.- Pp. 15342-15347.
4. Nasr T.B., Abdallah H.B, and [et al] First-principle study of the electronic and the optical properties of In_6Se_7 compound// Physica B.-2010.- **405.-** P.3427-3432

AB INITIO INVESTIGATION OF STRUCTURAL AND ELECTRONIC PROPERTIES OF THE InSe DILUTED MAGNETIC MATERIALS

Kharkhalis L.Yu., Glukhov K.E., Babuka T. Ya., Korolevych O.O..

Institute of Physics and Chemistry of Solid State, Uzhhorod National University,
54 Voloshin St., 88000 Uzhgorod, Ukraine

Owing to the peculiar crystal structure and anisotropic physical properties the quasi two-dimensional crystals of indium selenide are very interesting and perspective materials for spintronic investigations. The existence of the van der Waals coupling between the layers allows easily to intercalate the InSe crystal by various magnetic impurities and thus influence on its magnetic properties. Recently, in the experimental investigations [1-4] it was shown that the intercalation of the these crystals by transition metal impurities with an unclosed d-shells (Mn, Fe, Co, Ni) leads to the ferromagnetic order appearance. To understand the mechanism of magnetic properties of the intercalated layered materials, it is of interest to carried out the first principle study of the structural data and electronic spectra of diluted by magnetic impurities indium selenide With the purpose we considered the different models of the intercalated β-InSe crystal by the way of 2x2x1 and 3x3x1 supercells construction. It is shown that the impurities of 3d- metals can enter both in the structure of the layers and in the van der Waals space. In the Figure 1 the supercells for β-InSe:Mn are presented.

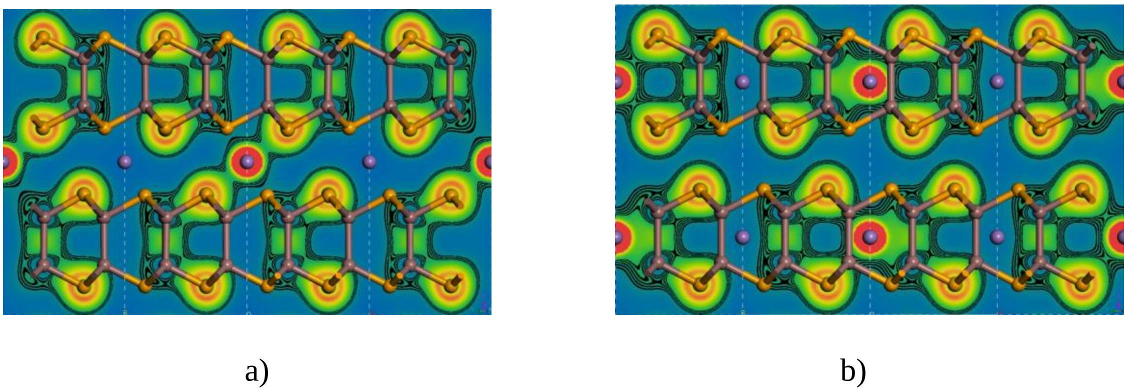
a) b)

Fig.1.Supercell 2x2x1 -β-InSe with inter layer Mn (a) and
with intra layer Mn (b)

In this report, utilizing first-principles pseudopotential method within density-functional theory the electronic and magnetic properties of the β -InSe layered crystal doped with 3d-elements of Mn have been investigated.

The band spectra, the total and partial spin densities (Figure 2) for a β-InSe crystal with different concentrations of Mn have been calculated.

It was established that diamagnetic structures of β-InSe intercalated with 3d elements of Mn become magnetically ordered. We obtained the estimates for the magnetic moment for the considered models of intercalated crystal of indium selenide. It is shown that the local magnetic moment for Mn is changed in dependence on structure of the intercalated β-InSe. In particular, the value of local moment of the Mn impurity atom is equal to $\mu=6.19541\ \hbar/2$ for 2x2x1 - β-InSe with inter layer Mn; $\mu=5.07087\ \hbar/2$ for 3x3x1 -β-InSe with inter layer Mn; $\mu=5.86415\ \hbar/2$ for 2x2x1 β-InSe with intra layer Mn.

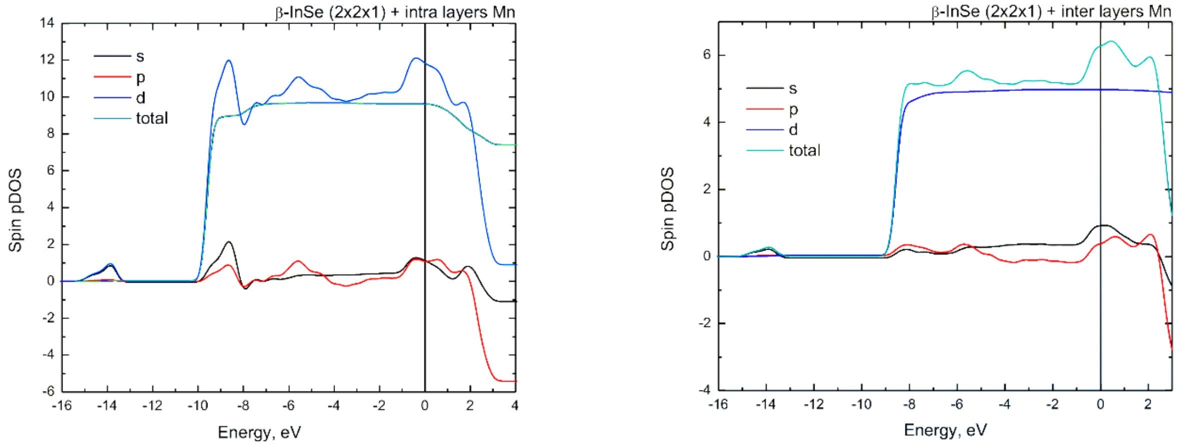

Fig.2. Spin pDOS for different models of 2x2x1 supercell of β-InSe:Mn

We performed the calculations of the spin-polarized spectra and partial charge densities for spin subsystems and also analyzed their evolution induced by magnetic dopants of Mn in layered indium selenide. The calculated electronic properties correctly explain the origin of the ferromagnetic ordering in the *β*-InSe intercalated crystals.

1. Kaminskii V.M., Kovalyuk Z.D., Ivanov V.I. Structure and physical properties of In_2Se_3<Mn>, InSe<Mn> and InSe<Fe> layered crystals//Physics and chemistry of solid state.- 2015.- V. 16, № 1.- P. 44-48.
2. Boledzyuk Z.B., Kovalyuk Z.D, Kudrinskyi Z.R., B.V.Kushnir [et al]. The effect of the introduction of Ni^{2+} ions on the properties of InSe layered crystal//Physical engineering of surface. - 2014.-V. 12, № 2.- P.184-189.
3. Boledzyuk V.B, Kovalyuk Z.D, Kudrynskyi Z.R. [et al.]. Structure and magnetic properties of cobalt-intercalated layered InSe crystals//Technical Physics.- 2014.-V. 84, N10.- P.44-47.
4. Bakhtinov A.P., Boledzyuk V.B, Kovalyuk Z.D. [et al.]. Magnetic properties and surface morphology of layered In_2Se_3 intercalated with cobalt//Physics of the Solid State.- 2013.- V.55. - P.1063-1070.

CNTS FORMATION BY PRODUCTS OF METHANE AIR CONVERSION AT MODERATE TEMRERATURES

Khovavko A.[1], Nebesniy A.[1], Svyatenko A.[1], Filonenko D.[1],
Kotov V.[1], Bondarenko B.[1], Nie G[2]

[1]*Department of Thermo-chemical Processes and Nanotechnologies, Gas Institute of the National Academy of Sciences of Ukraine. Degtyarivska 39, Kyiv-03113, Ukraine.*
[2]*School of Physics and Telecommunication Engineering, Yulin Normal University, Yulin 537000, China.*
E Mail: ahova2005@ukr.net

The process of carbon nanotubes (CNTs) forming by a CVD (chemical vapor deposition) method at different hydrodynamic and temperature modes using various catalysts was investigated on the created laboratory and pilot equipment. A new plate-type catalyst has been developed and successfully tested. The efficiency of its use is confirmed by the quality and quantity of the obtained carbon nanomaterial.

The most common carbon-containing gaseous source – natural gas was used as the feedstock for CNTs synthesis. Natural gas was pre-converted on a nickel catalyst, whereupon the resulting conversion products were used to synthesize CNTs. There were developed some decisions to improve the aggregate for CNTs synthesis. It's proposed to apply consistently sluice chambers in different zones of the reactor. The distinctive feature – supporting different gas composition atmospheres in functional zones.

It is advisable to recirculate spent gases to increase carbon nanomaterial yield. The use of gas recirculation increases the specific yield of carbon material, but in this case, due to the accumulation of nitrogen in the gas phase, the recirculation rate is limited and cannot exceed n = 0.8-1.0. Proposed technological solutions allow increasing the yield of CNTs per volume unit of carbonaceous atmosphere. The best result of CNTs yield in the carbon material was approximately 95%.

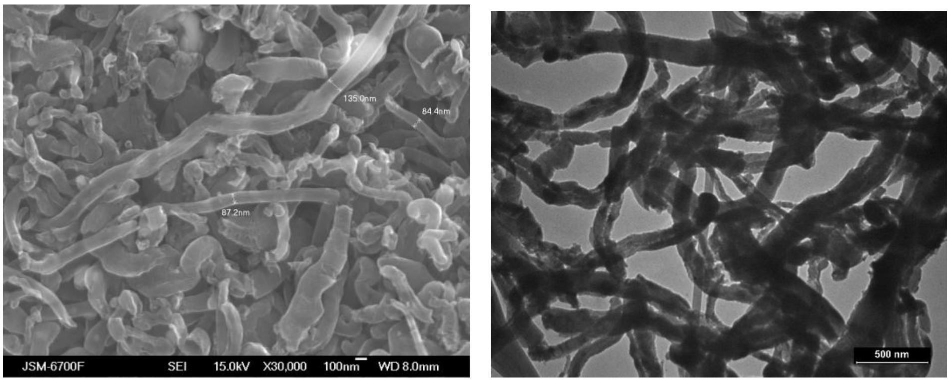

a) b)

Fig. 1. View of CNT_S obtained as a result of fresh-reduced iron processing by converted natural gas at T = 650°C; a) - SEM photo, b) - TEM photo.

The mechanism of carbon nanomaterial formation at moderate temperatures while processing of fresh-reduced iron by products of air conversion of natural gas is considered. It is shown that under given conditions the size and the shape of the resulting carbon are dependent on the temperature and the size of microscopic iron grains formed during reduction. These iron grains are the catalyzer of the reaction of carbon monoxide disproportionation. It is concluded that the formation of nucleus of the new carbon phase occurs at the contact boundaries of neighboring grains of newly reduced iron with the subsequent formation in these places of ring-shaped carbon cups. Nanotubes are forming as a result of further carbon crystallization and separation of iron particles from the main mass is occurring i.e., there is a fragmentation of the substance of the catalyst. Our researches allow making the conclusion that in the temperature range below 700° C carbonization-decarbonation cycles in the Feγ- Fe_{α}-Fe_3C system can play a crucial role in CNTs formation.

1. NEBESNYI A., KOTOV V., SVIATENKO A., FILONENKO D., KHOVAVKO A., BONDARENKO B. Carbon nanomaterial Formation on Fresh Reduced Iron by Converted Natural Gas. Nanoscale Research Letters (2017).
2. BONDARENKO B., SVIATENKO O., KOTOV V., KHOVAVKO A., FILONENKO D., NEBESNIY A., VISHNEVSKY A. Research of the technology of carbon nanotubes production in gas mixtures contained CO. International Journal of Energy for a Clean Environment (2013) 14(2–3):177–182.

STRUCTURE AND MECHANICAL PROPERTIES OF VACUUM ARC V-O-N COATINGS

Klimenko I.O., Belous V.A., Kolodiy I.V., Vasilenko R.L., Kuprin A.S., Ovcharenko V.D., Tolmachova G.N. , Gilewicz A., Warcholinski B.

1-National Science Center "Kharkov Institute of Physics and Technology", Kharkov, Ukraine
2-Koszalin University of Technology, Institute of Technology and Education, Koszalin, Poland

Transition-metal (TM) nitrides are refractory ceramics with exceptional properties, including high hardness, good wear and abrasion resistance, low friction, high-temperature stability, and chemical inertness. Owing to the good thermal and catalytic properties and good tribological features of vanadium nitride, a low wear rate and friction coefficient, thin coatings can be used in a wide range of applications. The oxidation of vanadium nitride to vanadium oxides including V_2O_5 and Magnéli phases from the series V_nO_{2n-1} allows their usage as self-lubricating coatings in tribological contacts working at high temperatures [1]. Now, attention is paid to the three-component compounds of Me-O_x-N_y type [2, 3] transition metals. Structure and properties of V-O-N vacuum arc coatings depending on the concentration of nitrogen and oxygen are not studied.

The goal of this study was to investigate V-O-N coatings deposited using vacuum arc evaporation with different relative oxygen concentration $O_2 = O_2/(N_2 + O_2)$.

The V-O-N coatings were deposited using unfiltered vacuum arc plasma method in a "Bulat" system equipped with a V (99.99%) cathode of 60 mm diameter. Samples of 32 mm in diameter and 3 mm in thickness were taken from HS6-5-2 steel. A reactive gas a gas mixture ($N_2 + O_2$) with different relative oxygen concentrations, $O_2(x) = O_2/(N_2 + O_2)\%$, was used where x equals 0, 10, 20, 30, 50, 70 and 100%. The arc current was 80 A. The deposition process was performed at a substrate bias voltage of −150 V. The thickness of all deposited coatings was about 5÷6 μm.

The surface morphology, microstructure and chemical composition of V-O-N coatings were investigated using Scanning Electron Microscopy (SEM), X-ray Diffraction (XRD) and Energy Dispersive X-ray Spectroscopy (EDS). The mechanical properties of coatings were characterized using nanoindentation.

XRD analysis showed that, depending on the oxygen concentration, the phase composition of the coatings changes from pure nitride to a mixture of nitride and oxide and to a pure oxide.

According to scanning electron microscopy data VN coatings have nanostructured columnar grains with width 20-30 nm; V-O-N coatings are quasiamorphous and VO_x coatings have columnar grains with width 500-1000 nm.

Nanohardness and Young's modulus for V-O-N coatings are strong depends on the oxygen concentration. Pure VN coatings have nanohardness ~ 40 GPa, and the Young's modulus ~ 500 GPa, introduction of 10 at.% of O_2 causes decreasing of nanohardness to 25 GPa, and the Young's modulus to 295 GPa, a further increase in the oxygen concentration leads to a monotonic decrease in the nanohardness and Young's modulus, and for coatings deposited in pure oxygen it is 2 and 80 GPa, respectively.

1. R. Franz, C. Mitterer. Vanadium containing self-adaptive low-friction hard coatings for high-temperature applications: A review // *Surface and Coatings Technology* 228 (2013) p. 1–13.
2. B. Warcholinski, A. Gilewicz, O. Lupicka, A.S. Kuprin, G.N. Tolmachova, V.D. Ovcharenko, I.V. Kolodiy, M. Sawczak, A.E. Kochmanska, P. Kochmanski, T.A. Kuznetsova, T.I. Zubar, A.L. Khudoley, S.A. Chizhik. Structure of CrON coatings formed in vacuum arc plasma fluxes // *Surface and Coatings Technology* 309 (2017) p. 920–930.
3. B. Warcholinski, A. Gilewicz, A.S. Kuprin, G.N. Tolmachova, V.D. Ovcharenko, T.A. Kuznetsova, T.I. Zubar, A.L. Khudoley, S.A. Chizhik. Mechanical properties of Cr-O-N coatings deposited by cathodic arc evaporation // Vacuum 156 (2018) p. 97–107.

IMPACT OF ABERRATIONS AND DEFOCUSING ON SPECKLE SUPPRESSION EFFICIENCY IN LASER PICO PROJECTORS WHEN USING NANO-STRUCTURAL DOE BASED ON THIN FILM

Kliuieva T.Yu.

Institute for Information Recording of NAS of Ukraine, Shpak Str. 2, Kiev 03113, Ukraine

Projection technologies have recently been actively used in various industries. The pico projectors provide an easy way to project the contents of these devices on the surfaces such as notebooks, portable projection screens, walls, and others. Active use of projection technology in mobile devices requires the search for new solutions when creating projectors. Laser diodes are small and create high-power light beams with a small diameter. This allows you to create on their basis optical systems for projectors with small size and weight. Besides, laser scanning provides high resolution and much higher color saturation.

However, the use of laser sources in projection systems creates speckle noise in the image on the screen. This phenomenon can significantly reduce the image quality, creating a granulation of image intensity in the human eye (subjective speckle). Therefore, the reduction of speckle noise is an urgent problem in the design of laser projectors. Since the real optical system has aberrations and there is always a certain shift of the image plane relative to the screen (defocusing), it is important to know how aberrations and defocusing will affect the reduction of speckle noise.

It is well known that a fully developed speckle is not sensitive to aberrations in the imaging system [1-2] (human eye). The statistics of the speckle field created by a moving beam of coherent light were studied [1]. However, all analyzes in this work were performed for use in barcode scanners, and the effects of aberration and defocusing of the scanning beam were not considered. The effect of optical aberrations on laser speckle in the projection system was studied [3]. This study examined partially developed specimens and an aberration imaging system, such as a camera lens or the lens of the human eye. However, neither the optical projection system that transmits the beam to the screen nor its aberrations have been studied.

This report investigates the effect of aberrations and defocusing the projector lens on the efficiency of reducing speckle noise in a laser projector system with simultaneous reproduction of 2D images containing a moving nano-structural diffractive optical element (DOE).

Hardware methods for reducing speckle noise are based on noise averaging. In turn, the averaging of the speckle noise is based on the reduction of the coherence of the laser beam. One of the most promising methods of reducing speckles is the use of DOE, located inside the optical system. The use of DOE allows you to accurately control the parameters of the optical system, which facilitates the development of optical systems with the required characteristics. The DOE structure is based on binary pseudorandom sequences, such as Barker code, on thin transparent film.

It is shown that shifting the screen by a distance h from the image plane only leads to the renormalization of the argument of the autocorrelation function. Renormalization in this case leads to the same result as refocusing the lens to a new screen position, ie the module of the autocorrelation function does not depend on the defocusing of the lens.

Thus, the contrast of speckles does not depend on the presence of defocusing it is a function of the numerical aperture $NA_{OUT} = \sin(\theta_{OUT})$of the lens, where θ_{out} half the angle at which the lens is visible from the plane of the screen (Fig. 1).

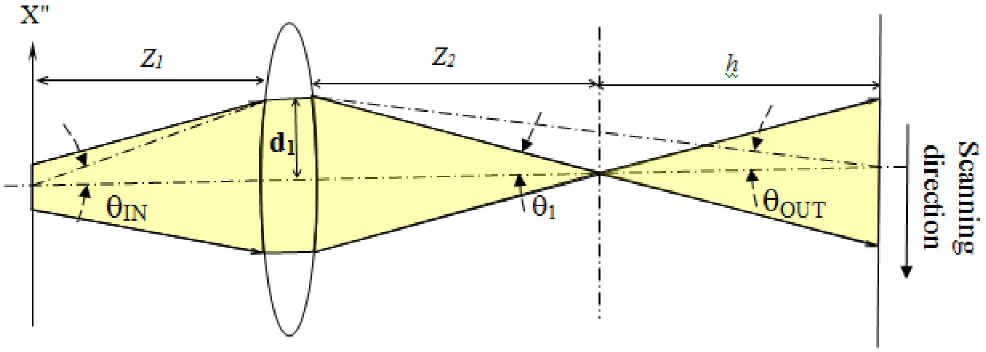

Fig.1. Depiction of scanning beam and definition of numerical aperture: $NA_{IN} = \sin\theta_{IN} \approx d_1/ Z_1$ and $NA_{OUT} = \sin\theta_{OUT} \approx d_1/ (Z_2+h)$ [4]

It was established that application of the method of reducing speckle noise when scanning a laser display using a small subpixel structure, such as Barker code or other approaches, should not require increasing the screen resolution of the projection system compared to normal values. Resolution is determined solely by image quality requirements.

The optimal shape of the beam for optimal reduction of speckle-noise was studied. It is shown that the problem of optimizing the shape of the scanning beam to obtain the maximum reduction of speckle noise can be reduced to the problem of minimizing the autocorrelation function. Numerical optimization with a 6-component Fourier series was performed for the case $NA_{OUT} / NA_{EYE} = 6.18$, where NA_{OUT} is the output of the NA projection lens (Fig. 1), and NA_{EYE} is the numerical aperture of the human eye. Numerical simulation has shown that even for smaller NA ratio (NA_{OUT}/NA_{EYE} ~1) where the optimization should provide the most effect the beam shape optimization could provide only to 8.5% decrease in speckle contrast ratio relatively to homogeneous spatial spectrum.

So, in the case of a real optical system with a finite numerical aperture (NA), a beam with a uniform filling of the projection lens aperture would provide the best reduction of speckle noise. This conclusion is consistent with the known fact that the contrast of the speckles in the scanning beam depends mainly on the original NA lens.

The impact of aberrations and the defocusing of optical systems on the noise reduction efficiency for two different DOE locations inside the projector optical systems is analyzed. A thin lens model based on the Fresnel diffraction theory with preservation of a square term in the plane of the object was used for modeling, which is important in the study of coherent optical systems.

It is shown that small aberrations change only the phase of the wavefront of the diffraction orders and therefore do not change the number of diffraction orders that illuminate a given area of the screen, and therefore do not affect the contrast of the speckles [Fig. 2]. But larger aberrations cause a reversal of the direction of propagation of the rays that have passed through the lens. The angle of rotation of the rays is greater for peripheral rays (rays of higher diffraction orders). Depending on the sign of the aberration coefficient, the direction of rotation can be directed either to or from the optical axis.

Rotation of light beams of diffraction orders leads to an uneven change of angles between them (only defocusing leads to a uniform change of angles between adjacent diffraction orders). This effect will affect the efficiency of reducing the speckle noise only when the distance between the diffraction orders decreases to a value less than the decorrelation angle of the speckle structures. Therefore, in the paraxial region of the screen, only large aberrations will have some effect on the efficiency of reducing speckle noise. However, at the periphery of the optical beam, the number of diffraction orders illuminating this area can be changed by aberrations due to their rotation relative to the optical axis. Therefore, large aberrations in this area should cause an abrupt increase in the contrast of speckles with a simultaneous decrease in light intensity.

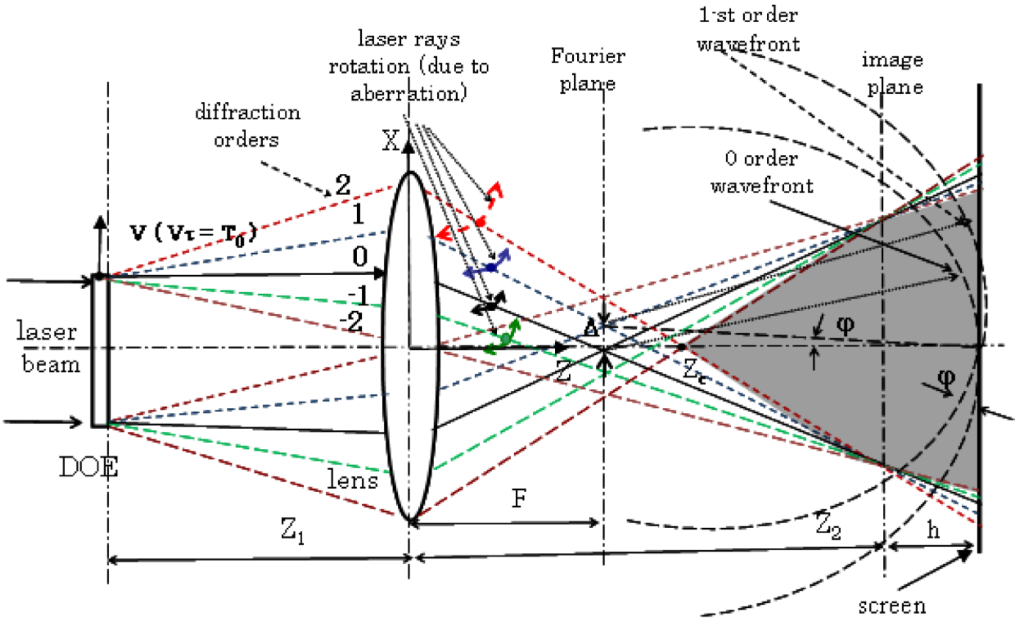

Fig. 2 Optical scheme of laser beam propagation from DOE to the optical modulator [2]

Thus the reduction of speckle noise based on moving nano-structural DOE placed in a plane conjugate to the optical modulator has a low sensitivity to aberration until the aberration changes the number of diffraction orders that illuminate the screen. The contrast of speckles on the periphery of the world spot has a stepwise behavior if the aberrations change the number of diffraction orders that illuminate the area. In the optical circuit with DOE located in front of the optical modulator, the contrast of the speckles is not sensitive to the distance between the optical modulator and DOE, if the optical modulator is illuminated by all diffraction orders.

1. J.W. Goodman, Speckle Phenomena in Optics, Roberts and Co., 2006.
2. Lapchuk, A., Yurlov, V., Pashkevich, G.A., Prygun, A., Kryuchyn, A.A., & Shylo, S. (2016). Impact of aberrations on speckle suppression efficiency on moving a DOE inside the optical system. *Displays*, *43*, 1-8.
3. P. K. Murphy, J. P. Allebach, and N. C. Gallagher, “Effect of optical aberrations on laser speckle”, J. Opt. Soc. Am. A, Vol. 3, No. 2, February 1986.
4. V. Yurlov, A. Lapchuk, S.-K. Yun, J.-H. Song, I. Yeo, H. Yang, and S.-D. An, Speckle suppression in scanning laser displays: aberration and defocusing of the projection system, Appl. Opt. 48 (2009) 80–90.

MAGNETICALLY SENSITIVE NANOCOMPOSITES WITH CARBON-CONTAINING SURFACE

Gorbyk P.P.[1], Petranovska A.L.[1], Dzyubenko L.S.[1], Oranska O.I.[1], Abramov M.V.[1], Palyanytsya B.B.[1], Kulyk T.V.[1], **Korniichuk N.M.**[1], Kusyak A.P.[2], Kusyak N.V.[2]

[1]*Chuiko Institute of Surface Chemistry, NAS of Ukraine, 17 General Naumov str., Kyiv 03164, Ukraine*
[2]*Ivan Franko Zhytomyr State University, 40 V. Berdychevska str., Zhytomyr 10008, Ukraine*

Carbon-containing nanomaterials and nanocomposites (NC) including core–shell type nanoparticles with magnetically sensitive, are used demand in engineering, biotechnology, medicine, environmental protection etc. Magnetically sensitive NC with carbon components and a developed surface are used in the development of new types of media for targeted delivery of drugs, medical hyperthermia, magnetically controlled adsorbents for various functional purposes; components of electrically conductive, sound and heat insulating and antifriction materials; protective shields and absorbers of electromagnetic radiation, catalysts, sources of electric energy etc. Carbon-containing coatings in NC are able to perform unique functions and protect it from the aggressive action of acidic and alkaline environments.

The result of the formation of carbon-containing coating is a decrease in aggregation, increase in specific surface area, improvement of adsorption properties, including in relation to drugs.

In addition, by changing the carbon content on the oxide surface, can control its hydrophilic-hydrophobic properties. The most common one-step method for the synthesis of carbon-containing NC is hydrothermal (solvothermal). The disadvantage of this method is the formation of a mixture of intermediate products of thermolysis of organic compounds on the surface of the magnetic nanoparticle (MNPs). No less well-known method is when pre-synthesized (MNPs) are mixed with a carbon source (eg, glucose, dopamine and ethylene glycol) followed by a carbonization process. This method can control the carbonization process by changing the conditions and reaction medium.

Among the nanodisperse magnetically sensitive materials used to create multifunctional NCs, magnetite (Fe_3O_4) and its modified forms occupy an important place due to their unique physicochemical and biological properties.

The use of modified magnetite to create magnetically controlled carriers of drugs, immunosorbents for purification of blood products from viruses etc is promising, from a scientific and practical point of view.

Such NCs, detecting a high adsorption capacity, can be controlled by a magnetic field, and the stage of separation of the spent adsorbent can be performed by the method of magnetic separation.

In this work, nanoscale single-domain Fe_3O_4 was used as a mineral magnetosensitive matrix for the synthesis of NC with a carbon surface. Sucrose and starch were chosen as the carbon source.

The aim of the work is the synthesis of new magnetosensitive nanocomposites based on magnetite with a carbon shell and the determination of their adsorption activity, which is relevant in the context of the development of new teranostics drugs and adsorption post-therapeutic detoxification of the body.

Magnetite was synthesized by the Elmore reaction:

$Fe^{2+} + 2Fe^{3+} + 8NH_4OH \rightarrow Fe_3O_4 + 4H_2O + 8NH_4^+$.

The cristal structure of nanoparticles was determinated by X-ray diffraction (XRD). XRD measurements were perfomed using DRON-4-07 diffractometer with Cu/Kα radiation (λ = 0.1542 nm) and Ni filter.

Specific surface area and pore size were determined by the method of nitrogen thermal desorption using KELVIN 1042 Sorptometer.

The size (MNPs) was estimated by the formula $D_{\mathrm{BET}} = 6/(\rho S_{\mathrm{BET}})$, where ρ –is the density, S_{BET} – the value of the specific surface area calculated by the theory of polymolecular adsorption of Brunauer, Emmett and Teller (BET).

The synthesized ensembles NPs Fe_3O_4 were characterized by sizes 3–23 nm; the average particle size was 8–12 nm. The specific surface area (S_n) of the synthesized magnetite is 100 $m^2 \cdot g^{-1}$.

The magnetization of the samples was measured using a vibrating magnetometer at a frequency of 228 Hz at room temperature. Samples for research were dry demagnetized polydisperse materials. For comparing Ni sample and Fe_3O_4 (98%) nanoparticles ("Nanostructured & Amorphous Materials Inc", USA) were used. The measurement error did not exceed 2.5%.

Magnetic measurements on Fe_3O_4 nanoparticles indicate that the particles are superparamagnetic at room temperature with a coercivity (H_c) of 55,0 Oe. The measured saturation magnetization (σ_s,) is 56,2 $emu \cdot g^{-1}$. Determination of the magnetic properties of the synthesized MNPs showed that the samples had narrow hysteresis loops. It indicate low energy losses during magnetization and can be used as a magnetically sensitive carrier for targeted delivery of biologically active compounds in a biological environment.

In order to protect the magnetite from oxidation during pyrolysis, since the high temperature necessary for of carbonization of the shell, was carried out chemical modification of magnetite an intermediate layer of aluminia oxide. Aluminum isopropylate was selected as a modifier. Modification was carried out by applying two layers of aluminia oxide, followed by heat treatment.

Carbon-containing shells on the surface of NCs Fe_3O_4/Al_2O_3 were obtained by impregnation in solutions of sucrose or starch at the rate of 0.45 g of carbohydrate per 1 g of NC. Carbonization of the carbohydrate shell and obtaining NCs $Fe_3O_4/Al_2O_3/C$ was carried out in a special furnace with programmable heating at a temperature of 500 ° C for 2 h in a stream of argon. The heating rate to T = 500 ° C was 10^0 C min.

Determination of the products of thermal destruction of the organic phase of the modifier on the surface of NC, carried out by the method of temperature-programmable desorption mass spectrometry, on a monopoly mass spectrometer MX-7304A (Sumy, Ukraine). The mass of the sample for the study 10-20 mg, pressure ~ $5 \cdot 10^{-5}$ Pa, programmable linear heating of the sample at a rate of 0.17 °C per second was carried out to a temperature of ~ 750 ° C. Registration of mass spectra in the range of 1-210 m/z. and analysis of curves of dependence of pressure of volatile products of thermolysis on temperature of sample (R/T) were carried out by the automated system of registration and data processing.

In the mass spectra of composites heat-treated at 500° C, there are no furan derivatives and other products that are characteristic of thermal destruction of carbohydrates. According to the results of research, CO_2, CO and water are recorded, which indicates the efficiency of the carbonization process of the carbohydrate coating under these conditions.

The method of differential thermal analysis (DTA) in combination with differential thermogravimetric analysis (DTGA) was used to study transformations in NCs. Registration of thermograms was carried out using a derivatograph Q-1500D (Hungary) in the temperature range of 20-1000 ° C at a heating rate of 10 ° $C \cdot min^{-1}$.

Studies of the magnetic properties of the obtained NCs showed that the magnetic characteristics of the composites do not decrease due to treatment at a temperature of 500° C for 2 hours.

The adsorption capacity of nanostructures was evaluated by the adsorption of methylene blue (MB). The adsorption characteristics of the $Fe_3O_4/Al_2O_3/C$ composite (g = 30 mg, V = 5 ml, pH = 7.0, t = 3 h) were investigated in static mode in the concentration range: 0.002 - 0.150 $\text{мг} \cdot \text{мл}^{-1}$ at room temperature, then the composite was separated by decantation on a permanent magnet. The amount of adsorbed substance on the surface of the composites was determined by measuring the concentration of contact solutions before and after adsorption (λ = 590 nm, l = 1 cm, Spectrofotometer Lambda 35 UV/Vis Perkin Elmer Instruments).

The adsorption capacity was calculated using equation: $A = (C_0 - C_p) \cdot V/g$, where A ($mg \cdot g^{-1}$) is the amount adsorbed. Co and Cp ($mg \cdot ml^{-1}$) are the initial and equilibrium concentration of the

MB solution. *V* (ml) is the volume of the solution, *g* (g) is the mass of absorbent used. The removal efficiency of MB (*R*) was obtained with equation: R, % = $[(C_0 - C_p)/\ C_0]\cdot 100$. According to the results of kinetic studies was establish , a difference in the rate of adsorption equilibrium was established during carbonization with sucrose (45 minutes, A = 4.7 $mg\cdot g^{-1}$) and starch (2 hours, A = 3.5 $mg\cdot g^{-1}$).

Studies of the adsorption isotherm on the surface of $Fe_3O_4/Al_2O_3/C$ were performed in the concentration range Co = 0.028 – 0.148 $mg\cdot ml^{-1}$ (sucrose precursor), and Co = 0.0024 – 0.021 $mg\cdot ml^{-1}$, (starch precursor) (g = 0.03 g, V = 5 ml).

Increasing the concentration of MB leads to sorption saturation of the surface of $Fe_3O_4/Al_2O_3/C$ composites. When used as a precursor of sucrose, the value of the adsorption capacity (A = 18.9 $mg\cdot g^{-1}$) is higher than for composites carbonized with starch (A = 2.8 $mg\cdot g^{-1}$).

Experimental results of MB adsorption on the $Fe_3O_4/Al_2O_3/C$ surface used to construct isotherms and analyzed for compliance with Langmuir and Freundlich models.

The calculated values of the parameters A_∞, r^2 indicate the possibility of using both models to describe the adsorption processes for the $Fe_3O_4/Al_2O_3/C$, sample carbonized by sucrose (r^2 = 0.977 Langmuir model and 0.982 Freundlich model). For the $Fe_3O_4/Al_2O_3/C$, sample carbonized with starch, only the Freundlich model is optimal (r^2 = 0.970).

Conclusions

The synthesized ensembles of single-domain NPs Fe_3O_4 are characterized by sizes 3–23 nm, specific surface area S_n = 100 $m^2\cdot g^{-1}$, coercive force Hc = 55.0 Oe, saturation magnetization σs = 56.2 Gs · $cm^3\cdot g^{-1}$, relative residual magnetization Mr / Ms =0.2. To give NPs Fe_3O_4 sufficient thermal stability, they were modified with alumina and NCs Fe_3O_4/Al_2O_3 were obtained. Carbonization of the surface of NC Fe_3O_4/Al_2O_3 was carried out using carbohydrates - chemically pure of sucrose and starch. New magnetically sensitive NCs $Fe_3O_4/Al_2O_3/C$ of the core-shell type based on single-domain magnetite were synthesized and their magnetic and adsorption properties were investigated. It was found that the saturation magnetization of $Fe_3O_4/Al_2O_3/C$ is sufficient for their use as a means of targeted delivery of drugs and adsorption materials. The value of the relative residual magnetization indicates that the removal of the field will not lead to magnetic aggregation of the NPs in the liquid.

THE MAPS OF THE ELECTROMAGNETIC WAVES IN THE NANOCOMPOSITE WITH METALLIC 1D-INCLUSIONS

Korotun A.V., Pavlishche N.I.

[1] *National University "Zaporizhzhia Politechnic", 64, Zhukovskogo St., 69063 Zaporizhzhya, Ukraine*

The frequency dependences for the effective dielectric function of the composite with metallic 1D-inclusions in the cases of the low and high concentrations have been obtained. The charts of the electromagnetic waves, which propagate in such mediums, have been constructed. The possibility of the propagation of the surface plasmon-polaritons on the "composit-air" boundary has been studied.

It is known that the necessary condition for the propagation of the surface plasmon-polaritons on the boundary between two mediums is the presence of the material with the negative real part of the dielectric permittivity. The metals in the visible and infrared regions of the spectrum, some dielectrics and the semiconductors in the frequency range between the longitudinal and transverse optical mode, and also the artificial materials, such as the nanocomposites "metal – dielectric", possess such properties [1]. The propagation of the surface plasmons on the "metal – dielectric" boundary has been studied theoretically and experimentally in the works [2] and [3] correspondingly. The propagation of the surface plasmons in the layered structures has been studied in [4]. In spite of the fact that the surface plasmons in the disordered nanocomposites have been observed experimentally [5], the systematic analysis of the dispersion relations and the other characteristics of the electromagnetic waves has been completed only for some types of the nanocomposites – glass-metal mediums with the spherical metallic particles [6], and such analysis for the composites with the inclusions of the other shape has not been performed.

The main idea of this article is the obtaining of the dispersion relations for the electromagnetic waves on the "dielectric - composite" boundary with the chaotically arranged metallic nanowires for the cases of the low and high concentrations of 1D-inclusions.

Let us consider the composite with the chaotically arranged metallic cylinders. Let us assume that the direction of the electric field coincides with the axes of the cylinders. An effective dielectric function of such composite has the form

$$\varepsilon_{\mathrm{eff}}=\varepsilon_{\mathrm{m}}\left[1+\beta\frac{\varepsilon(\omega)-\varepsilon_{\mathrm{m}}}{\varepsilon(\omega)+\frac{1}{2}(1-\beta)\left(\varepsilon(\omega)-\varepsilon_{\mathrm{m}}\right)}\right], \tag{1}$$

where ε_{m} – the dielectric permittivity of the matrix; β – the volume content of the metallic fraction; $\varepsilon(\omega)$ – the dielectric function of the metal. Under the condition of the loss of the attenuation this function can be given in the following form

$$\varepsilon(\omega)=1-\frac{\omega_p^2}{\omega^2}. \tag{2}$$

Here $\omega_p^2=e^2n_e/\varepsilon_0m^*$ – the frequency of the volume plasmons in the metal.

Let us consider the case of the low concentration of the metallic inclusions ($\beta\ll 1$). In this case

$$\varepsilon_{\mathrm{eff}}=\varepsilon_{\mathrm{m}}\frac{\varepsilon(\omega)+\frac{1}{2}(1-\beta)\left(\varepsilon(\omega)-\varepsilon_{\mathrm{m}}\right)+\beta\left(\varepsilon(\omega)-\varepsilon_{\mathrm{m}}\right)}{\varepsilon(\omega)+\frac{1}{2}(1-\beta)\left(\varepsilon(\omega)-\varepsilon_{\mathrm{m}}\right)}=\varepsilon_{\mathrm{m}}\frac{\omega^2+\omega_{\mathrm{TO}}^2}{\omega^2+\omega_{\mathrm{LO}}^2}\frac{\varepsilon_{\mathrm{m}}-1-\frac{1}{2}(1+\beta)}{\varepsilon_{\mathrm{m}}-1-\frac{1}{2}(1-\beta)},$$

where ω_{TO} and ω_{LO} – the frequencies of the transverse and longitudinal optical modes, the corresponding expressions for which are given below

$$\omega_{\mathrm{TO}}^2 = \frac{\omega_p^2\left(3+\beta\right)}{2\varepsilon_{\mathrm{m}} - 3 + \beta}; \qquad \omega_{\mathrm{LO}}^2 = \frac{\omega_p^2\left(3-\beta\right)}{2\varepsilon_{\mathrm{m}} - 3 - \beta}. \tag{3}$$

Finally, the dielectric function for the rarefied composite with the nanocylinders under the condition of the loss of the attenuation has the form:

$$\varepsilon_{\mathrm{eff}} = \varepsilon_{\mathrm{m}} \frac{\left(3+\beta\right)\omega_{\mathrm{LO}}^2\left(\omega^2 + \omega_{\mathrm{TO}}^2\right)}{\left(3-\beta\right)\omega_{\mathrm{TO}}^2\left(\omega^2 + \omega_{\mathrm{LO}}^2\right)}. \tag{4}$$

The condition of the plasmonic resonance in the composite is $\varepsilon_{\mathrm{eff}}\left(\omega_{sp}\right) = -1$, that is why

$$\varepsilon_{\mathrm{m}} \frac{3+\beta}{3-\beta} \frac{\omega_{\mathrm{LO}}^2}{\omega_{\mathrm{TO}}^2} \frac{\omega_{sp}^2 + \omega_{\mathrm{TO}}^2}{\omega_{sp}^2 + \omega_{\mathrm{LO}}^2} = -1. \tag{5}$$

The relation (5) can not be satisfied at any condition, because the left-hand side of this expression is positive. That is why the propagation of the surface plasmons on the boundary between the composite and the environment is impossible. It can be explained by the fact that the properties of such composite are close to the properties of the dielectric medium due to the low concentration of the metallic nanocylinders.

The formula for the effective dielectric function of the composite with the high content of the metallic fractions can be obtained by means of the substitution $\varepsilon_{\mathrm{m}} \to \varepsilon\left(\omega\right)$ and conversely in the relation (1). By reason of this we obtain

$$\varepsilon_{\mathrm{eff}} = \delta \frac{\omega^2 - \omega_p^2}{\omega^2} \frac{\omega^2 + \omega_{\mathrm{TO}}^2}{\omega^2 + \omega_{\mathrm{LO}}^2},$$

with the designation

$$\delta = \frac{\left(3+\beta\right)\varepsilon_{\mathrm{m}} - \left(1+\beta\right)}{\left(3-\beta\right)\varepsilon_{\mathrm{m}} - \left(1-\beta\right)}, \tag{6}$$

and the frequencies of the transverse and longitudinal optical modes are equal to

$$\omega_{\mathrm{TO}}^2 = \frac{\omega_p^2\left(1-\beta\right)}{\left(3+\beta\right)\varepsilon_{\mathrm{m}} - \left(1-\beta\right)}; \qquad \omega_{\mathrm{LO}}^2 = \frac{\omega_p^2\left(1-\beta\right)}{\left(3-\beta\right)\varepsilon_{\mathrm{m}} - \left(1-\beta\right)} \tag{7}$$

correspondingly.

Taking into account the condition of the plasmonic resonance $\varepsilon_{\mathrm{eff}}\left(\omega_{sp}\right) = -1$ we have

$$\delta \frac{\omega^2 - \omega_p^2}{\omega^2} \frac{\omega^2 + \omega_{\mathrm{TO}}^2}{\omega^2 + \omega_{\mathrm{LO}}^2} = -1,$$

from which we obtain the biquadratic equation for the frequency of the surface plasmonic resonance

$$\left(\delta+1\right)\omega_{sp}^4 + \left(\omega_{\mathrm{TO}}^2 + \omega_{\mathrm{LO}}^2 - \omega_p^2\right)\omega_{sp}^2 - \omega_{\mathrm{TO}}^2\omega_p^2 = 0, \tag{8}$$

the positive solution of which is

$$\omega_{sp}^2 = \frac{-\omega_{\mathrm{TO}}^2 - \omega_{\mathrm{LO}}^2 + \omega_p^2 + \sqrt{\left(\omega_{\mathrm{TO}}^2 + \omega_{\mathrm{LO}}^2 - \omega_p^2\right)^2 + 4\left(\delta+1\right)\omega_{\mathrm{TO}}^2\omega_p^2}}{2\left(\delta+1\right)}. \tag{9}$$

The figure 1 shows the dependences $\varepsilon_{\mathrm{eff}}\left(\omega/\omega_p\right)$ for the composites with the low and high content of the metallic inclusions in teflon $\varepsilon_{\mathrm{m}} = 2.3$. As mentioned above, the propagation of the surface plasmon-polaritons on the boundary between the composite with $\beta \square 1$ and the air is impossible ($\varepsilon_{\mathrm{eff}} > 0$), and TEM-waves propagate in the frequency domains $\omega < \omega_{\mathrm{TO}}$ and $\omega > \omega_{\mathrm{LO}}$.

These domains are separated by the “band gap” $\omega_{\mathrm{TO}} < \omega < \omega_{\mathrm{LO}}$ (fig. 1, *a*). Hence, the optical properties of such composite are close to the properties of the dielectric matrix.

The situation is more complicated for the composite with the high content of the metallic nonoconductors. In this case TEM-waves propagate in the frequency domains $\omega_{\mathrm{TO}} < \omega < \omega_{\mathrm{LO}}$ and $\omega > \omega_p$, the “band gaps” are $0 < \omega < \omega_{\mathrm{TO}}$ and $\omega_{sp} < \omega < \omega_p$, and the surface plasmon-polaritons propagate in the domain $\omega_{\mathrm{LO}} < \omega < \omega_{sp}$ on the “composite - air” boundary.

As well, the values of the frequencies of the transverse and longitudinal optical modes are essentially different for the composites with the low and high content of 1*D*-inclusions. Namely, $\omega_{\mathrm{TO}}, \omega_{\mathrm{LO}} > \omega_p$ in the case of the composite with $\beta \ll 1$, and $\omega_{\mathrm{TO}}, \omega_{\mathrm{LO}} < \omega_p$ for the composites with $\beta \to 1$.

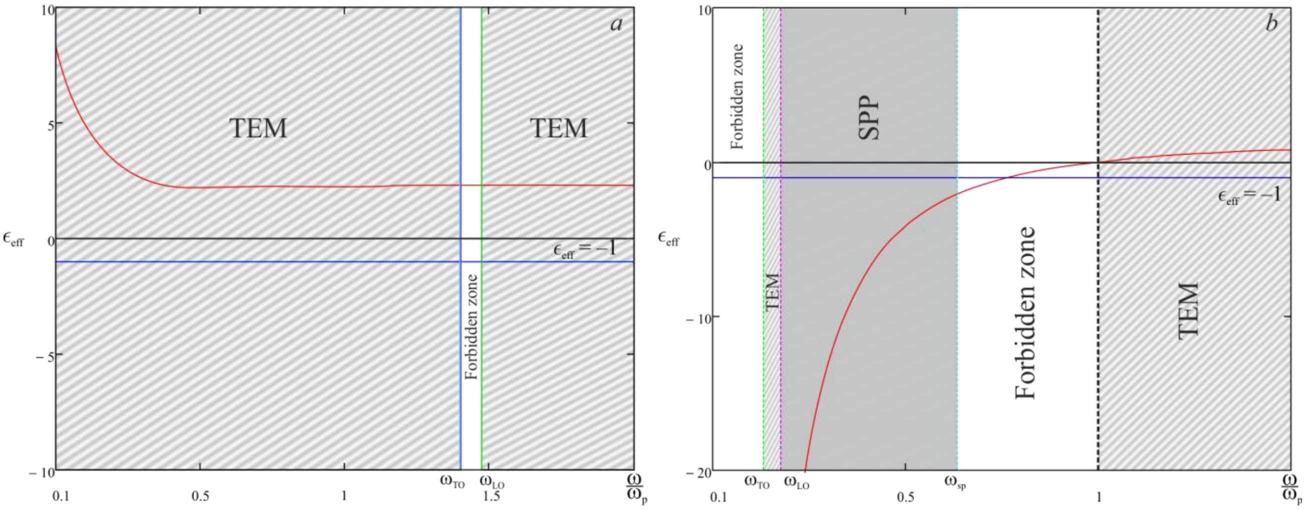

Fig.1. The frequency dependence of the effective dielectric permittivity of Drude-composite with 1*D*-inclusions for $\beta = 0.15$ (*a*) and $\beta = 0.85$ (*b*).

The plasmonic properties of the nanocomposite with the chaotically arranged nanowires in the case when the direction of the electric field coincides with the axes of the conductors have been considered in the work.

One considers the dielectric function of the metallic 1*D*-structures to Drude approximation without due regard to the attenuation.

The cases of the low and high content of the metallic fraction have been studied.

It has been established that the propagation of the surface plasmon-polaritons on the boundary between the composite with the low concentration of the metallic inclusions and the air is impossible, and inside the composite only TEM-waves can propagate. It shows that the properties of such composite and the properties of the standard dielectric are close. There exist the band gaps (with respect to the frequency) and the domains with the electromagnetic TEM-waves inside the composite with the high content of the metallic fraction. The propagation of the surface plasmon-polaritons is possible on the boundary between the composite and the environment in the frequency domain from the frequency of the longitudinal optical mode to the frequency of the surface plasmons.

6. Drachev V.P., Chettiar U.K., Kildishev A.V. [et al.]. The Ag dielectric function in plasmonic metamaterials // Opt. Exp., 2008. – V. 16. – N. 2. – P. 1186-1195.
7. Pitarke J.M., Silkin V.M., Chulkov E.V. [et al.]. Theory of surface plasmons and surface-plasmon polaritons // Rep. Prog. Phys., 2007. – V.70. – P.1-87.
8. Economou E.N. Surface plasmons in thin films // Phys. Rev., 1969. – V.182. – N.2. – P. 539-554.

9. Schuchinsky A.G., Yan X. Surface plasmons in layered structures with semiconductor and metallic films // Eur. Phys. J. Appl. Phys., 2009. – V.46. – id. 32605.
10. Sardana N., Heyroth F., Schilling J. Propagating surface plasmons on nanoporous gold // J. Opt. Soc. Am. B, 2012. – V.29. – P.1778-1783.
11. Sokolov K.S., Zhurikhina V.V., Kazantsev D.Yu. [et al.]. Studies of copper-silver glass-metal nanocomposites // Surf. Interface Anal., 2013. – V.45. – P.366-368.

THE MECHANISM OF FORMATION OF POROUS STRUCTURE OF THE DERMIS COLLAGEN MODIFIED ECOSAFETY DIFFERENT CRYSTALS OF NATURAL MINERALS

Kozar Oksana

Mukachevo State University, 26, Uzhhorodska street, 89608 Mukachevo, Ukraine

To achieve the required complex of operational properties of leather materials for the top of the footwear in the production of a large number of multi-functional materials. The bulk of them are used in liquid furnish processes and are conditioned by the need to create a highly-formed structure of the dermis and the operational properties appropriate to the target skin. Reducing the quality of leather raw material, significant damage to the facial layer, loose structure, uneven density in topographical areas complicate the possibility of qualitative skin formation and require the use of an increased amount of tannins, additions, fillers and fissuring materials, which increases the cost price of finished products. A rational and thorough approach to the selection of the above-mentioned chemical materials will help to regulate the qualitative indices of the finished skin.

The promising development of modern technologies in the production of leather materials is the application in the processes of liquid decoration of mineral fillers that are capable of correcting and regulating the effectiveness of forming the dermis structure and corresponding operational properties. In this case, the positive influence of mineral fillers is maintained by combining traditional treatments and the use of minerals with different crystalline and chemical structures, which increases the efficiency of technological influences and creates the prerequisites for achieving the necessary complex of operational properties of the skin of various intended uses.

The aim of the work was to determine the influence of mineral fillers of different crystalline and chemical structures in the composition of acrylic-mineral compositions on the formation of the structure and operational properties of leather materials.

The structure of collagen of dermis of natural skins, modified with composition of natural minerals on the basis of zeolite and montmorillonite and cationic polyelectrolyte polyhexamethylene guanidine hydrochloride (PHMG) was investigated. The mechanism of formation of the porous structure of the dermis on the level of fibrils and primary fibers with fine particle minerals of different crystalline-chemical structures is proposed. The influence of the type of mineral filler on the operational and antibacterial properties of leather materials has been determined.

X-RAY LUMINESCENCE OF CADMIUM-MODIFIED THIN FILMS OF ARSENIC DISULFIDE

Krasilinets V.M.[1], Loya V.Yu.[1], Chychura I.I.[2], Birov M.M.[1], Popovich K.P.[1], Edinak O.V.[2]

[1]*Institute of Electron Physics, Ukranian National Academy of Sciences, Universytetska Street 21, 88000, Uzhhorod, Ukraine, e-mail: kvn7@i.ua*
[2]*National Universiry of Uzhhorod, Engineering department, Universytetska Street 14, 88000, Uzhhorod, Ukraine*

Cadmium concentrations in the *As– S – Cd* system were chosen in the glass formation region according to [1]. The synthesis was performed by heating in a flame of oxygen-gas burner at temperatures above the melting points of the respective glasses_with further homogenization within 72 hours. Cadmium-modified thin chalcogenide films were obtained by thermal vacuum evaporation from a closed tantalum evaporator (Knudsen effusion cell) on the glass substrates. The deposition rate was 3–5 nm/s, at ~ 10^{-4} Pa vacuum. At this speed, the main parameters of the film do not change during deposition process [2]. Batch based on the As - S matrix was evaporated from Knudsen effusion cells at constant temperature of the evaporator. Developed effusion cells of the evaporator ensured the preservation of the source material and the film stoichiometry. Due to the change of constant control parameters (evaporation temperature, condensation rate) the necessary flow of the modifying component (*Cd*) was created. This type evaporators provide high stability of film growth rate, optical quality of a surface and exclude microparticles loss. Depending on evaporator temperature, the growth rate of the structure changed from 50 to 200 Å / s. Spraying was carried out at substrate temperatures of 293-393 K. The distance from the substrates to the evaporator was chosen in the range of 0.250 ÷0.265 m. The thickness of the obtained films was measured on the Linnik MII-4 interferometer and it was (1.12–1.58) μm. Analyzing the obtained experimental results, we concludes that when the cadmium content in the studied films increases to 3A%, the degree of ionicity of covalent bonds decreases (Fig. 1). These changes are associated with the restructuring of the type of bonds and strengthening of the film structure. In the *As-S-Cd* system, the impurity injection leads to a decrease in the degree of ionicity, which indicates to a disorder of the structure of the films and the rearrangement of short-range bonds, which leads to an increase in the intensity of X-ray luminescence of these films.

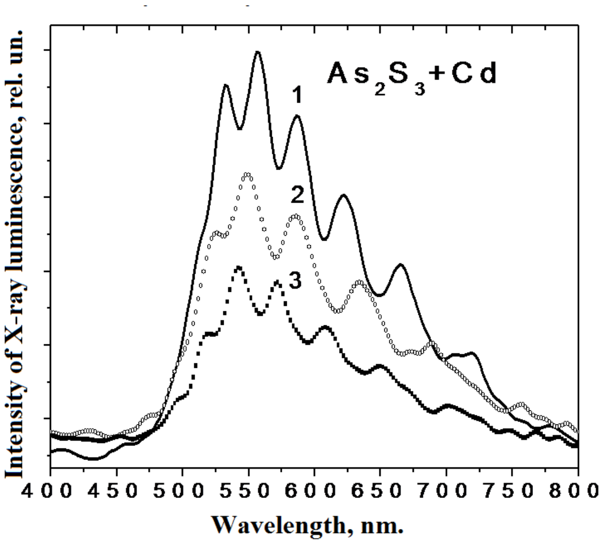

Fig. 1. X-ray luminescence spectrum of As_2S_3 thin films depending on the Cd concentration: 1-1A%, 2-2A%, 3-3A%.

1. Г.З. Виноградова, Стеклообразование и фазовые равновесия в халькогенидніх системах. Наука, М. 127 с. (1984).
2. В.М. Жихарєв, В.Ю. Лоя, А.М. Соломон, Я.В. Грицище. Швидкість вакуумного осадження та оптична якість плівок As_2S_3. // Вісник Ужгородського національного університету. Серія фізика. – 2015. – №37. – С.51-56.

ELECTROCHEMICAL PARAMETERS OF THIN TIN FILMS IN CYCLING IN LITHIUM-ION BATTERIES

Kublanovsky V.[1] , Globa N.[2], Nikitenko V.[1], Babenkov E.[1], Shmatok Yu.[2], Bersirova O.[1]

[1]*V. I. Vernadsky Institute of General & Inorganic Chemistry of National Academy of Sciences of Ukraine,*
Academic Palladin Avenue, 32/34, Kyiv, 03142, Ukraine,
[2]*Joint Department of Electrochemical Energy Systems of NAS of Ukraine,*
Vernadskogo blvd, 38a, Kyiv, 03680, Ukraine
e-mail: kublan@ukr.net

ABSTRACT. Thin fine tin electrodeposits were obtained from pyrophosphate electrolyte under different electrolysis conditions and duration. It was found that tin films with minimal masses, obtained from a pyrophosphate electrolyte, are characterized by a high specific capacity, durability, and the ability to reversibly cycle in lithium-ion batteries (LIB). With prolonged cycling, the stabilization of the specific capacity of tin films is observed in the range of 470-710 $mA{\cdot}h{\cdot}g^{-1}$. The coulomb efficiency of tin films in the first cycle is practically independent of the mass of the tin film and amounts to 70%; further it increases to 90%. The obtained tin films are capable of providing a high charge/discharge current density without mechanical destruction.

INTRODUCTION. The development of new anode materials, characterized by high specific capacitances and density of discharge currents, is an important task. Alloy-forming materials are considered as an alternative to replacing carbon anodes, among which the most promising are tin, and tin-containing composite coatings, in particular alloys of tin with nickel, cobalt, copper, zinc, antimony [1, 2]. One of the simplest and most easily controlled methods for producing coatings with metals and alloys, which makes possible to control their structure and functional properties, is electrochemical deposition from aqueous complex electrolytes [3, 4]. The authors of [5–10] substantiated the criteria for the selection of ligands for complex electrolytes.

Earlier [11–14], we obtained the results of studies of thin tin films electrodeposited from tartrate, citrate, and citrate-trilonate electrolytes. It has been shown that the nature of the ligand determines such electrochemical characteristics as the specific capacitance value and cycling efficiency. The more stable charge/discharge characteristics were obtained for tin films deposited from citrate electrolyte [14]. The process of electrodeposition of tin (II) from a pyrophosphate electrolyte is limited by the previous chemical reaction of dissociation of the complexes $[Sn(HP_2O_7)(P_2O_7)]^{5-}$ or $[Sn(P_2O_7)_2]^{6-}$ [5, 15]. This allows controlling the slowdown of the electrode process and, therefore, the morphology, structure and properties of the obtained tin films, in particular their porosity.

This work is devoted to the study thin tin film electrodeposition from pyrophosphate electrolyte, and to analyze electrochemical parameters (specific capacity, corrosion resistance, and cycling efficiency in LIB) such deposits as anode materials for LIB.

EXPERIMENTAL PART. Tin deposits were obtained on a copper foil substrate with a surface of 2 cm^2 from a pyrophosphate electrolyte of the composition, $g{\cdot}l^{-1}$: $SnCl_2{\cdot}2H_2O$ – 90, $K_4P_2O_7{\cdot}3H_2O$ – 425, NH_4Cl – 50, at pH 7.2. Electrolysis was carried out at current densities of 1.0 and 1.5 $mA\ cm^{-2}$ and temperature of 25 °C for 15, 30 and 45 min. Platinum was used as the anode. The electrolysis was carried out under conditions of natural convection. The mass of tin deposit was determined on an analytical balance ”ADV-200M”. Electrochemical studies of the obtained tin deposits were carried out in disk cells of size 2016. A 1 M solution of lithium *bis*-(trifluoromethane)sulfonimide (LiTFSI) in a mixture of fluoroethylene carbonate and dimethyl carbonate solvents taken in a mass ratio of 1:3 was used as an electrolyte. As an counter electrode and a reference electrode lithium metal was used. Celgard 2400 polypropylene film with thickness of 25 μm was used as a separator. Working electrodes with tin deposits immediately before assembling the cells were dried in vacuum at a temperature of 100 °C. All operations related to the preparation of electrodes, electrolytes and cell assembly were carried out in dry glove boxes.

Voltammograms were recorded at a sweep speed of 0.5 mV·s^{-1}, a temperature of 25 ± 2 °C, and a voltage range of 0.01–1.20 V. For galvanostatic tests Neware Battery Testing System was used with the appropriate software. The cycling was carried out in the voltage range of 0.01-1.1 V at currents from 100 to 500 μA·cm^{-2}. The impedance curves of the two electrodes cells with tin and lithium electrodes in initial state and fully discharged (after the first lithiation) state were obtained at the frequency range 0.08 Hz – 50 kHz and amplitude of applied voltage of 10 mV. The experiment was carried out after establishing a constant value of the open circle potential (OCP) in the cells.

RESULTS AND DISCUSSION. The mass of tin deposit obtained from pyrophosphate electrolyte, and the electrolysis parameters are presented in table 1.

Table 1. Parameters of electrolysis and mass of tin deposit obtained from pyrophosphate electrolyte

№ sample	J_k , mA·cm^{-2}	t , min.	m_{Sn} , mg·cm^{-2}	Current efficiency, %	$Q_{discharge}$	Q_{charge}	$Q_{charge}/Q_{discharge}$ %
					mA·h·g^{-1}		
1	1,0	15	0,25	44,7	860	602	70
3		30	0,51	45,7	928	588	63
5		45	0,78	46,7	1087	737	68
2	1,5	15	0,27	33,0	1029	733	71
4		30	0,53	31,8	1151	802	70
6		45	0,87	34,8	1158	830	72

The process of incorporation of lithium into tin proceeds according to the mechanism of alloy formation and is characterized by multi-stage processes [16]. The galvanostatic charge/discharge curves of Sn films, obtained in the first cycle, are shown in Fig. 1a. The real potentials corresponding to phase transitions are determined not only by thermodynamics, but also by kinetic constraints, depending on the conditions for obtaining deposit and the conditions of the cathodic process.

The profile of charge/discharge curves changes significantly in comparison with the curves of the first cycle (Fig. 1). The kinks observed on the corresponding curves of the first cycle at the end of the cycle are smoothed. These differences are associated with a change in the structure of tin deposits and the release of the electrode to a more stable cycling mode. This is confirmed by a decrease in capacity loss during cycling in later charge/discharge cycles.

The discharge specific capacity analysis indicates an increase in specific capacity with increasing mass of deposit. The relatively low value of coulombic efficiency (63–72%) in the first cycle of lithium incorporation and extraction is associated with side processes caused by the formation of SEI and the decomposition of electrolyte [17]. However, already from the second cycle, the coulombic efficiency increases to 90%.

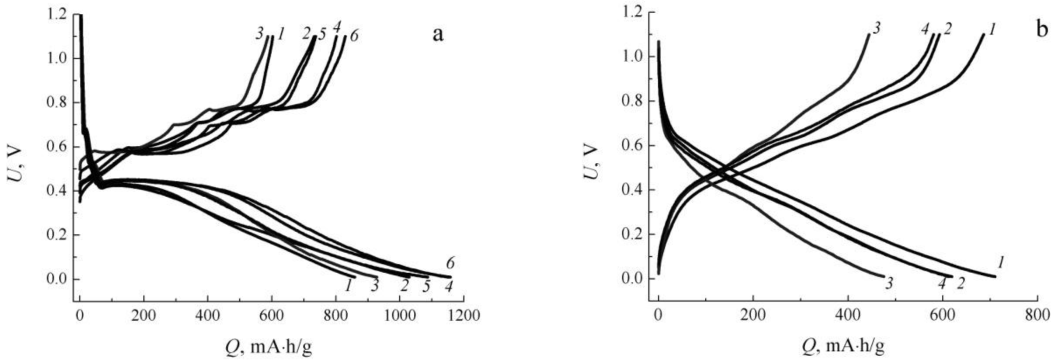

Fig. 1. Discharge/charge curves of the first (a) and 60th (b) cycle at the cycling current density of 100 μA·cm^{-2} for Sn-electrodes. The numbers on the curves correspond to the numbers of samples.

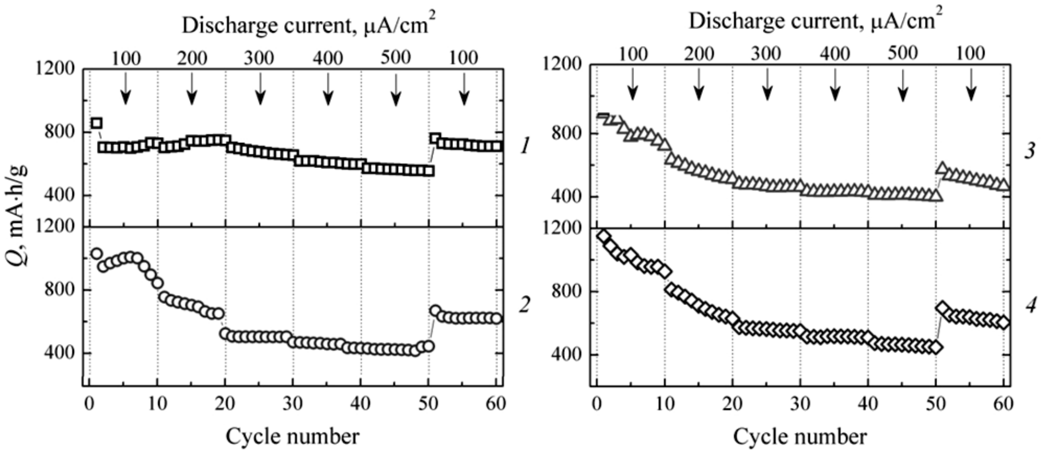

Fig. 2. Cycling performance of Sn-electrodes at different discharge currents (charge current – 100 μA·cm^{-2}). The numbers on the curves correspond to the numbers of the samples in Table 1.

Figure 2 shows the dependence of the specific capacity of tin deposits obtained at electrolysis currents of 1.0 and 1.5 mA·cm$^{–2}$ during the first lithiation on their mass. The obtained dependences in both cases are not linear, which implies a decrease in the utilization coefficient of the tin deposit when a certain mass (thickness) is reached at different cyclic current densities.

The results of galvanostatic cycling of tin electrodes (samples 1-4) are presented in Fig. 2. The minimum loss of specific capacity both within one discharge current and with its increase from 100 to 500 μA·cm$^{–2}$ was obtained for sample 1 which is characterized by a minimum mass (0.25 mg·cm$^{–2}$). Sample 2 with the same mass of the tin film (0.27 mg·cm$^{–2}$), is characterized by a larger loss of specific capacity during prolonged cycling. This is apparently due to the different morphology, structure and properties of tin films, primarily their porosity. For the remaining samples, an increase in the rate of decrease in specific capacity with an increase in the mass of deposits is observed. At the same time, in all cases, at later stages of cycling, relative stabilization of the specific capacity is observed, which after the 60 cycles is in the range from 470 to 710 mA·h·g$^{–1}$.

The impedance spectra of electrochemical cells after the first cycle of lithiation of Sn-electrodes are significantly different from the initial ones, both in nature and in the resistance of the active and reactive parts of the impedance curve (Fig. 3). The semicircle in the high-frequency region is characteristic for many lithium systems in which a passive film is formed on the lithium electrode, the nature and character of which depend on the composition of the electrolyte and the state of the electrodes [18 - 20].

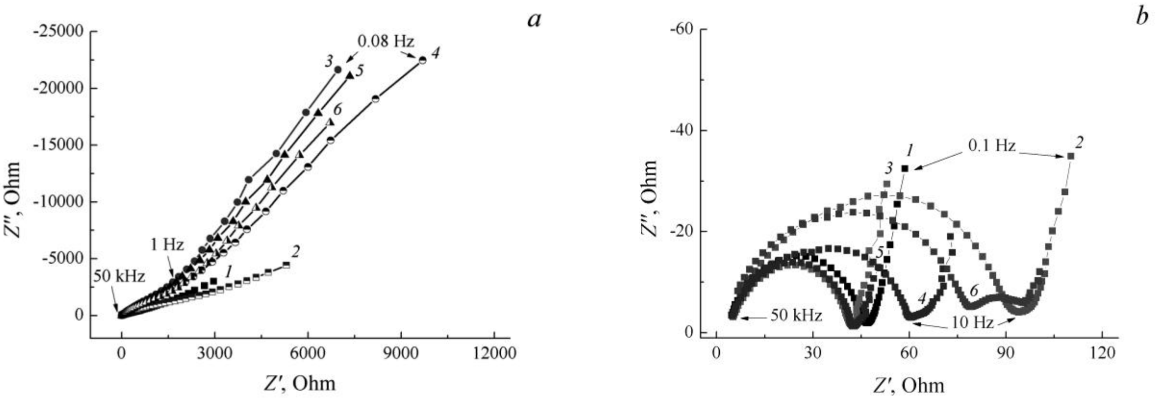

Fig. 3. Impedance spectra of the Li-Sn system in Nyquist coordinates before cycling (a) and after the first discharge (b)

The tin films obtained at a current density of 1 mA·cm^{-2} (1, 3, and 5) are characterized by lower resistance of the active part of the impedance than the electrodes obtained at a current density of 1.5 mA·cm^{-2} (2, 4, and 6), with almost the same mass of tin deposits. All the studied electrodes after the first lithiation cycle are characterized by an increase in resistance at a frequency of 50 kHz, which may be due to a change in the porosity and thickness of the deposit because of the introduction of lithium. This is in good agreement with the fact that with the introduction of lithium into tin and the formation of the $Li_{4,4}Sn$ alloy its volume increases to ~300% [21].

This work was carried out in the framework of the target research program of the NAS of Ukraine «New Functional Substances and Materials of Chemical Engineering», project №7–20, 2020.

1. Pridatko K.I., Churikov A.V. Anode non-carbon lithium-accumulating composite materials. Elektrokhimicheskaya Energetica. 2005. **5** (1): 16.
2. Kamali A.R., Fray D.J. Tin-based materials as advanced anode materials for lithium ion batteries. Rev. Adv .Mater. Sci. 2011. **27:** 14.
3. Hadsoun J., Pacero S., Scrosati B. Electrodeposited Ni-Sn intermetallic electrodes for advanced lithium ion batteries. J. Power Sources. 2006. **160:** 1336.
4. Huang L., Wei H.B., Ke F.S., Fan X.Y., Li J.T. Electrodeposition and lithium storage performance of three-demension porous reticular Sn-Ni alloy electrodes. Electrochem. Acta. 2009. **54:** 2693.
5. Orekhova V.V., Andryushchenko F.K. Issledovanie kineticheskih zakonomernostei electrodnyh reakcii v poliligandnyh electrolitah. Electrohomiya. 1974. **10** (3): 363.
6. Orekhova V.V., Andryushchenko F.K. Polyligand electrolytes plating. (Kharkov: Vishcha shkola, 1979).
7. Bersirova O., Bruk L., Dikusar A., Karaman M., Sidelnikova S., Simashkevich A., Sherban D., Iapontseva Iu. Thin films of titanium and tin oxides and semiconductor structures on their basis obtained by pyrolytic pulverization: preparation, characterization, and corrosion properties. Surface Engineering and Applied Electrochemistry. 2007. **43** (6): 443.
8. Cesiulis H., Bersirova O., Valiuniene A., Prosycevas I., Baltrunas G. Structural and Morphological Study of Silver Electrodeposits. Materials Science (Medziagotyra). 2004. **10** (2): 142.
9. Bersirova O., Krolikowski A., Kublanovsky V. Deposition conditions and corrosion characteristics of galvanic silver coatings for microelectronics. Ochrona przed korozja. 2002. **11A**: 149.
10. Bersirova O., Kublanovsky V., Cesiulis H., Electrochemical Formation of Functional Silver Coatings: Nanostructural Peculiarities. ECS Transactions. 2013. **50** (52): 155.
11. Kublanovsky V.S., Nikitenko V.N. Mechanism of the electrodeposition of palladium coatings from glycinate electrolytes. J. Electroanal. Chem. 2013. **699:** 14.
12. Kublanovsky V.S., Nikitenko V.N. Electrochemical properties of palladium(II) trans- and cis-diglycinate complexes. Electrochim. Acta. 2011. **56:** 2110.
13. Kublanovsky V.S., Nikitenko V.N., Globa N.I. Electrochemical Deposition of Corrosion-Resistant Coatings from Tin-Nickel Alloys. Mater. Sci. 2017. **52:** 687.
14. Kublanovsky V.S., Nikitenko V.N., Globa N.I. Effect of the nature of a ligand on electrochemical characteristic of tin films in cycling in lithium-ion batteries. Russ. J. Appl. Chem. 2015. **88:** 407.
15. Shmatok Yu., Globa N.I., Nikitenko V.N., Babenkov T.A., Kublanovsky V.S., Electrochemical characteristics of tin films in cycling in lithium-ion batteries. Ukrainian Chemistry Journal, 2019. **85**(10): 67.
16. Idota Y., Kubota T., Matsufuji A., Maekawa Y., Miyasaka T. Tin-based amorphous oxide: a high-capacity lithium-ion-storage material. Science. 1997. **276:** 1395.
17. Globa N.I., Shmatok Y.V., Milovanova O.I., Sirosh V.A., Kirillov S.A. Electrolytic Double-Layer Supercapacitors Based on Sodium-Ion Systems, with Activated-Carbon Electrodes. Russ. J. Appl. Chem. 2018. **91:** 187.
18. Churikov A.V., Nimon E.S., Lvov A.L. Impedance of Li—Sn, Li—Cd and Li—Sn—Cd alloys in propylene carbonate solution. Electrochim. Acta. 1997. **42:** 179.
19. Churikov A.V., Gamayunova I.M., Shirokov A.V. Ionic processes in solid-electrolyte passivating films on lithium. J. Solid State Electrochem. 2000. **4:** 216.
20. Churikov A.V., Pridatko K.I., Ivanishchev A.V., Ivanishcheva I.A., Gamayunova I.M., Zapsis K.V., Impedance spectroscopy of lithium-tin film electrodes. Russ. J. Electrochem. 2008. **44** (5): 550.
21. Aravindan V., Lee Y.S., Madhavi S. Research progress on negative electrodes for practical Li-ion batteries: beyond carbonaceous anodes. Adv. Energy Mater. 2015. 5: 1402225.

ACID TREATED CRYSTALLINE GRAPHITIC CARBON NITRIDE, A NEW MATERIAL FOR VISIBLE LIGHT SELECTIVE ORGANIC COMPOUNDS PHOTO-OXIDATION

Kuchmiy S.Ya.[1], Shvalagin V.V.[1], Kompanets M.O.[1,2]

[1]L.V. Pisarzhevskii Institute of Physical Chemistry of the National Academy of Sciences of Ukraine, Prospect Nauki 31, Kyiv 03028, Ukraine; e-mail: kuchmiy@inphyschem-nas.kiev.ua
[2]L.M. Litvinenko Institute of Physical-Organic Chemistry and Coal Chemistry of the National Academy of Sciences of Ukraine, Kharkivske Shose, 50, Kyiv 02160, Ukraine

The development of photocatalytic systems for the partial oxidation of various organic substrates, in particular alcohols, to the corresponding carbonyl compounds is a promising area of research that allows the process to be carried out at room temperature and atmospheric pressure using molecular oxygen or air as an oxidizing agent. Of particular interest are photocatalysts sensitive to visible light, including the use of solar radiation initiating the process as an energy source.

One of the promising semiconductor photocatalysts is graphite-like carbon nitride (g-C_3N_4) which, in addition to sensitivity to visible light, has several other advantages: non-toxicity, low cost, ease of preparation, convenient arrangement of energy levels, which allows initiating practically important oxidative and reductive processes.

Recently, materials based on g-C_3N_4 obtained by its additional treatment in molten salts have been widely studied, as a result of which it is possible to obtain carbon nitride with increased crystallinity (CGCN), improved optical characteristics, and high photocatalytic activity in the reaction of molecular hydrogen evolution. In some cases, such materials showed high activity only in the presence of organic or inorganic acids [1]. Information on the effect of acids on the course of other redox processes is very limited.

In this regard, the aim of this work was to study the effect of acids on the composition, morphology, and optical properties of carbon nitride samples activated in molten salts, as well as the photocatalytic properties of such materials during the selective oxidation of organic substrates under the influence of visible light.

CGCN samples were prepared by known method [2] by heat treatment of g-C_3N_4 in KCl and LiCl melt at 550 °C for 4 h followed by washing of the obtained products with water. The original g-C_3N_4 was synthesized by melamine annealing at 550 °C and atmospheric pressure for 2 h. To study the effect of acid, the obtained CGCN samples were additionally treated in aqueous lactic acid with stirring for 1 hour followed by washing with water (AT-CGCN).

As can be seen from the SEM images (Fig. 1a), the initial g-C_3N_4 consists mainly of layered particles of several micrometers in size. The additional heat treatment of g-C_3N_4 in the salt melt leads to a significant change in its morphology, namely, the formation of elongated nanoparticles of several hundred nanometers in length and about 50 nm wide (Fig. 1b). The thickness of the formed particles is small enough, as evidenced by their low contrast. This indicates that the additional treatment of the original carbon nitride in the melt of lithium and potassium salts leads to its delamination and decrease of lateral sizes to the nanometer range. In this case, the acid treatment of CGCN does not significantly change the morphology of the AT-CGCN sample (Fig. 1c).

The photocatalytic activity of the obtained samples was studied in the reaction of gas-phase partial oxidation of ethanol with oxygen by irradiation with visible light (λ>400 nm).

It was found that the consumption of ethanol (Fig. 2a), as well as the formation of the photo-oxidation product, acetaldehyde, when used as a photocatalyst, CGCN at the initial stage proceeds more than an order of magnitude faster than g-C_3N_4 (curves 1 and 2).

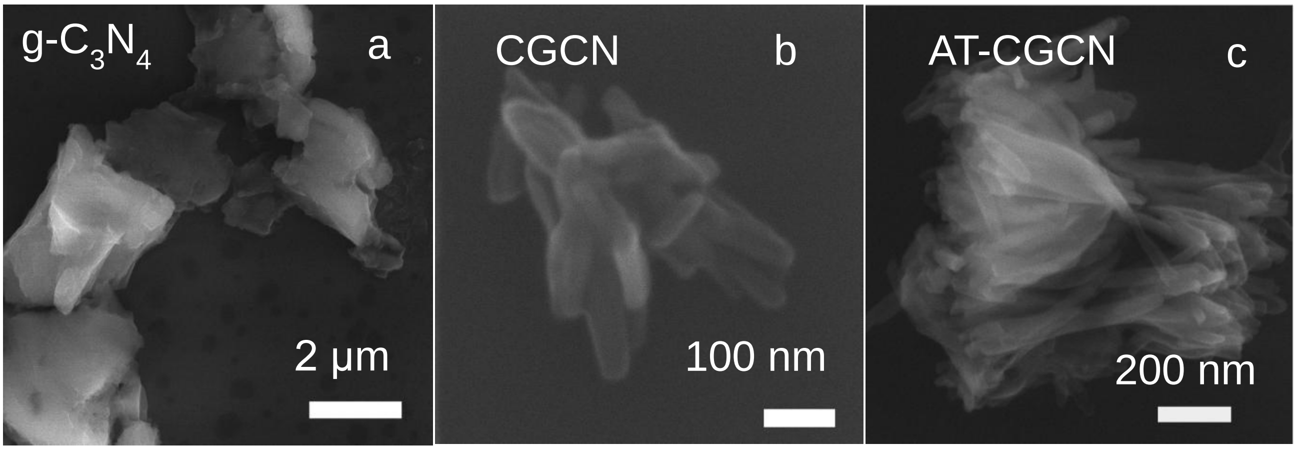

Fig. 1 SEM image of the original g-C_3N_4 (a), crystalline graphite carbon nitride (CGCN) (b) and CGCN after treatment with lactic acid solution (AT-CGCN) (c).

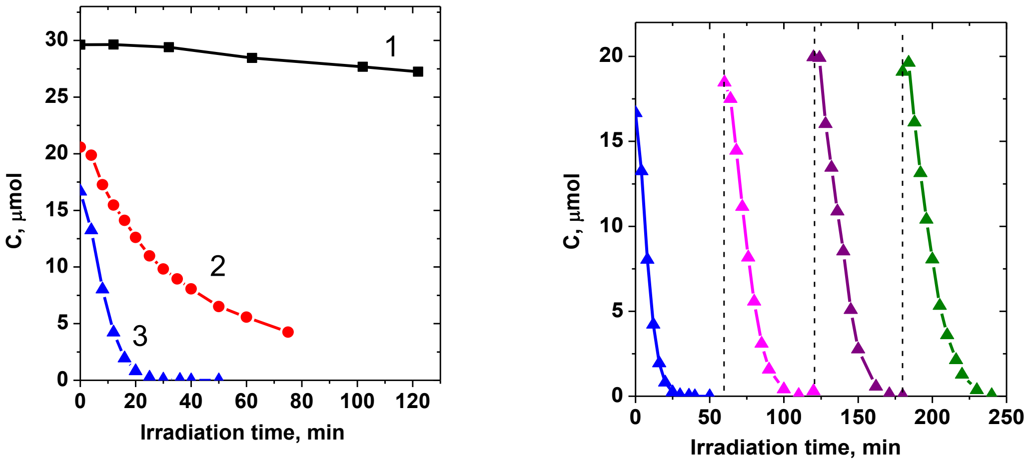

a b

Fig. 2 (a) Kinetic curves of photocatalytic oxidation of ethanol using samples g-C_3N_4 (1), CGCN (2) and AT-CGCN (3) under visible light ($\lambda > 400$ nm). (b) Stability test of ethanol photo-oxidation for AT-CGCN under visible light.

During CGCN irradiation in the presence of ethanol vapor, a darkening of the sample occurs, and a decrease in the rate of the photoprocess is observed (Fig. 2a, curve 2). This behavior of the photocatalyst can be associated both with its destruction during irradiation, and with the blocking of the active centers of the surface of the photocatalyst by-products of photo-oxidation - “sample carbonization”.

When using an AT-CGCN sample pretreated in an acid solution as a photocatalyst, the rate of ethanol oxidation is significantly higher than in the case of CGCN (Fig. 2a, curves 2 and 3). The rate of ethanol oxidation remains virtually unchanged during the photoprocess (Fig. 2a, curve 3). Also, during the photoprocess, the color change of the photocatalyst is not observed. These results indicate that the treatment with CGCN by an acid solution not only leads to a significant increase in the photocatalytic activity of the obtained material during the oxidation of ethanol with atmospheric oxygen, but also contributes to its increased stability to degradation.

To determine the stability of the photocatalytic system with the participation of AT-CGCN, the sample was irradiated with visible light for several complete oxidation cycles of both the starting ethanol and acetaldehyde. As can be seen from those presented in Fig. 2b results, after four series of irradiation, the activity of the system in the studied process decreases insignificantly, which indicates its high stability.

Using the photocatalysts obtained in this work, we also studied the photocatalytic oxidation of a number of other organic substrates, in particular, isopropanol, benzyl alcohol. With the participation of AT-CGCN, benzyl alcohol is oxidized with high selectivity to benzaldehyde (96%) with a conversion of more than 80% (see Fig. 3).

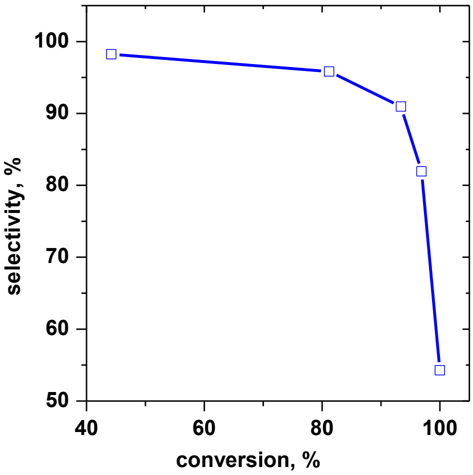

Fig. 3 Benzaldehyde selectivity versus benzyl alcohol conversion over AT-CGCN photocatalysts.

The activity of the nanostructured AT-CGCN material was investigated in the reaction of photocatalytic aerobic aromatization of substituted 1.4-dihydropyridines under visible light ($\lambda > 400$ nm). It was established that initial substituted 1.4-dihydropyridines can be easily aromatized to the corresponding aromatic product with a high conversion and selectivity level. The presence of the nanostructured photocatalyst increased rate of the investigated process twice compared to solely photolysis.

Thus, as a result of the study, it was found that CGCN obtained by heat treatment of g-C_3N_4 in a molten potassium and lithium salt exhibits more than an order of magnitude higher photocatalytic activity in the oxidation of alcohols under visible light in comparison with the initial photocatalyst. It was shown that the treatment of CGCN in aqueous solutions of lactic acid leads not only to a significant increase in the photocatalytic activity of the obtained material in the process of ethanol oxidation with atmospheric oxygen, but also contributes to its increased stability to degradation. The process of photocatalytic oxidation of alcohols in the systems studied can be carried out both to complete and partial oxidation of substrates to produce the corresponding aldehydes or ketones, which can be used in the synthesis of other organic compounds. The high photoactivity of the nanostructured AT-CGCN can be attributed to the intense absorption of visible light, the small particle size and developed surface.

Acknowledgments

This research was supported by the General Research Project of the L.V. Pisarzhevskii Institute of Physical Chemistry NAS of Ukraine (funded by the National Academy of Sciences of Ukraine) (project No IPC-A-3-2020) and target program of basic research of NAS of Ukraine «Promising basic research and innovative development of nanomaterials and nanotechnologies for the needs of industry, health care and agriculture» (project No 26/20-N).

1. N. Andryushina, V. Shvalagin, G. Korzhak, G. Grodzyuk, S. Kuchmiy, M. Skoryk, Appl. Surf. Sci. 475 (2019) 348.
2. V. Shvalagina, G. Korzhak, S. Kuchmiy, M. Skoryk, O. Selyshchev, D. Zahn, J. Photochem. Photobiol. A Chem. 390 (2020) 112295.

THE INFLUENCE OF HEATING CONDITIONS ON ELECTRICAL AND OPTICAL CHARACTERISTICS OF Sb-Se AND Sb-Te AMORPHOUS FILMS

Durkot M.O.[1], **Kyrylenko V.K.**[1], Kryuchyn A.A.[1], PetrovV.V. [1], Pisak R.P.[1],
Pop M.M.[1,2], Rubish V.M[1]

[1] *Institute for Information Recording, NAS of Ukraine,4 , Zamkovi schody St., 88000, Uzhgorod Ukraine*
[2]*Uzhgorod National University, 3, Narodna sq., 88000, Uzhgorod, Ukraine*

This paper presents the results of investigations of electrical resistence and optical transmission temperature dependences of $Sb_xSe(Te)_{100-x}$ ($x \geq 50$) thin films under thermal cycling and heat conditions changes.

Crystallization of $Sb_xSe(Te)_{100-x}$ ($x \geq 50$) thin films (thickness ~ 100-200 nm) was investigated by the method, which allows simultaneously measurements of electrical resistance R and optical transmission θ on the one sample. Amorphous films were obtained by the method of vacuum evaporation of the corresponding composition crystalline alloys from quasiclosed effusion cells. Investigations of $R(T)$ and $\theta(T)$ dependences were carried out on planar structures “Cr layer-$Sb_xSe(Te)_{100-x}$ film- Cr layer” in the temperature range 293-493 K both in continuous mode at heating rates (q) 3 and 6 K/min, in thermal cycling regime and in heating mode with temperature scanning stops at selected stabilization temperatures (T_{st}) for a certain temperature stabilization time (t_{st}). The accuracy of temperature measurement was ±0.5 K. Registration of $\theta(T)$ change was carried out at a wavelength 880 nm.

Nonisothermal crystallization of $Sb_xSe(Te)_{100-x}$ ($x \geq 50$) amorphous films is accompanied by a sharp decrease in resistance and transmission. On the basis of dependences $R(T)$ and $\theta(T)$ the transition parameters (the transition starting temperature (T_{ph}) from amorphous to crystalline state, temperature range of transition (ΔT_{ph}), resistance (ΔR) and transmission ($\Delta\theta$)changes) are determined. As the heating rate increases T_{ph} and ΔT_{ph} shift to higher temperatures.

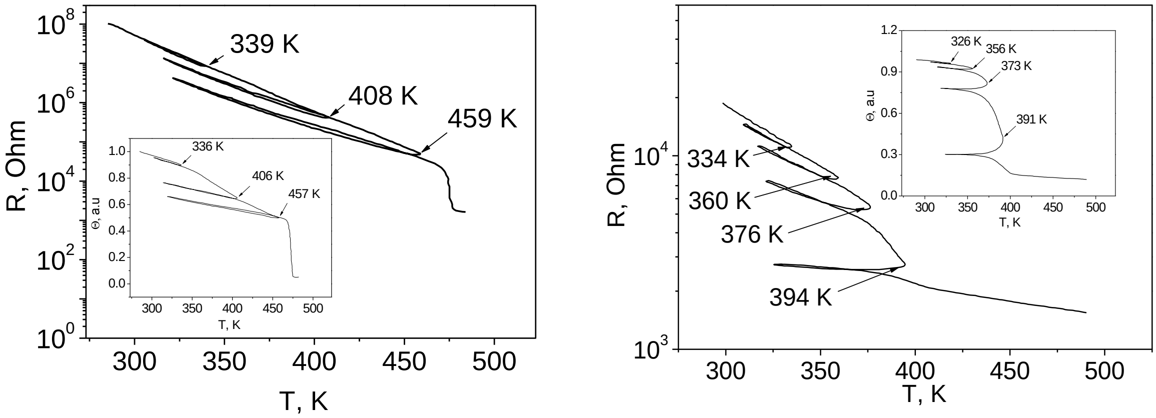

Fig.1. $R(T)$ and $\theta(T)$ changes of “Cr –$Sb_{65}Se_{35}$ film- Cr” (a) and “Cr –$Sb_{50}Te_{50}$ film–Cr” (b) samples during thermal cycling (q=6 K/min)

Fig. 1 shows typical for all studied samples temperature dependences of R and θ of planar samples “Cr-chalcogenide film-Cr” during thermal cycling (heating↔cooling). The heating of the samples was carried out at a given heating rate, and cooling – in the off mode of the heating element.

Fig. 2 shows dependences $R(T)$ and $\theta(T)$ of samples “Cr-chalcogenide film-Cr” in heating mode with temperature scanning stops for a certain time. In this mode at selected T_{st} temperature controller for a certain t_{st} was transferred to the regime of temperature stabilization. From the above data it is seen that hysteresis effects are observed on the temperature dependences R and θ, and they are more pronounced for telluride samples. Decreasing by step of resistance and transmission indicates the partial crystallization of chalcogenide films, while the change in θ is significant. Analysis of the obtained data shows that the fraction of crystallized volume Δ*V* depends on the heat treatment mode.

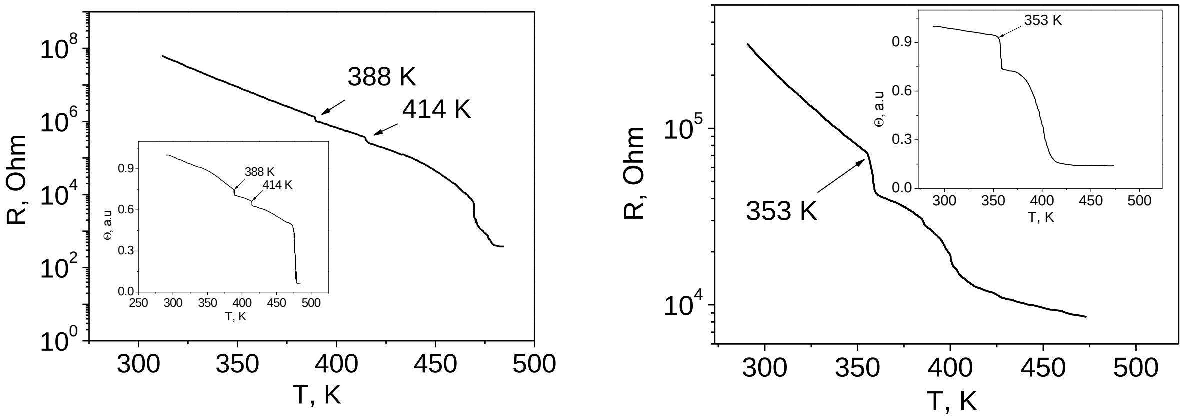

Fig.2. *R*(*T*) and θ(*T*) (insert) dependences of the sample “Cr –$Sb_{55}Se_{45}$ film–Cr” (*q*=6 K/min) with temperature scanning stop for 30 min. at 388 and 414 K (a) and “Cr–$Sb_{50}Te_{50}$ film–Cr” (*q*=3 K/min) with temperature scanning stop for 60 min. at 353 K (b)

Thus it was fond that the thin films $Sb_xSe(Te)_{100-x}$ with $x \geq 50$ crystallize under certain heating conditions. The phase transition from the amorphous state to the crystalline sate is accompanied by a sharp decrease in electrical resistance and transmission. The transition parameters (T_{ph}, ΔT_{ph}, ΔR, $\Delta\theta$, ΔV) depend on the chemical composition of the films and the conditions of heating and thermal cycling, i.e., the crystallization process can be controlled by changing the thermal modes of film treatment.

EFFECT OF SILVER BY COPPER SUBSTITUTION ON FERRIELECTRIC PROPERTIES IN $CuInP_2X_6$ LAYERED COMPOUNDS

Liubachko V.[1,2], Oleaga A.[2], Salazar A.[2], Vysochanskii Yu.[1], Kohutych A.[1], Pogodin A.[1]

[1] *Institute for Solid State Physics and Chemistry, Uzhhorod University, Pidgirna Str. 46, 88000 Uzhhorod, Ukraine*
[2] *Departamento de Física Aplicada I, Escuela de Ingeniería de Bilbao, UPV/EHU, Plaza Ing. Torres Quevedo 1, 48013 Bilbao, Spain*

Over the last decades various scientific efforts have been conducted in order to study dielectric, thermal, optical, elastic and acoustic properties of $CuInP_2X_6$ phosphorus chalcogenides. These materials are promising candidates for functional electronics and piezoelectronics because they demonstrate a rich set of physical properties. The substitution of certain chemical elements allows to obtain new compounds demonstrating a rich variety of physical properties, photosensitivity etc.

$CuInP_2S_6$ is the main compound of the family of 2D layered phosphorus semiconductors which shows a well-defined first-order order–disorder ferrielectric phase transition at $T_c \approx 315$ K. As the off centering of the Cu ions is much greater than that of In, the result is an uncompensated two-dimensional ferrielectric arrangement with total polarization along the *c*-axis. [1]. Compounds of $CuInP_2Se_6$ are very similar to those of $CuInP_2S_6$ which also have high and low temperature structures (the reduction in symmetry takes place at a much lower temperature (236 K vs. 315 K)) [2].

The substitution of Cu by Ag alters completely this scenario. At low concentrations the transition is shifted to lower temperatures and it is less sharp and wider; moreover, from our results it turns out that the character of the phase transition has changed to second order for $Ag_{0.1}Cu_{0.9}InP_2S_6$, as it was also observed with ultrasonic measurements in [3]. At full substitution the transition is frustrated, there is no hint of any transition down to 30 K. The detailed comparison of the evolution at the substituting Ag by Cu is given in fig. 1 a. The reduction of the phase transition temperature is not so pronounced in $Cu_{0.9}Ag_{0.1}InP_2Se_6$ but the transition is severely smeared. At full substitution of Cu by Ag in $AgInP_2Se_6$ the transition is also completely frustrated as it happens with sulphide compounds (fig. 1 b).

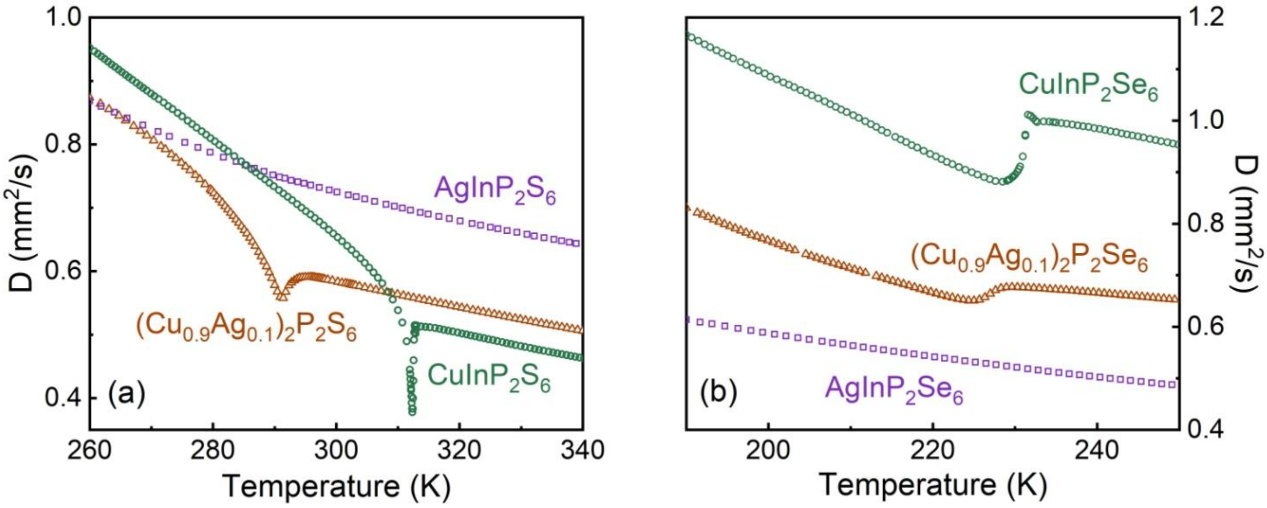

Figure 1. Temperature dependence of thermal diffusivity for sulphides (a) and selenides (b), measured in the direction parallel to the layers

As the transition in $CuInP_2(S,Se)_6$ can be explained on the basis of a second order Jahn Teller effect induced by the local dynamic hopping of Cu^+ ions [1], it is important to establish what happens when Cu is substituted by Ag. The presence or absence of this effect is severely dependent on the covalency of the bonds and the hybridization of the s and d orbitals of the $(Cu, Ag)^{1+}$ cation. The latter is more efficient in silver doped compounds in the paraelectric phase, leading to a bigger covalency of the Ag–$[P_2S_6]$ bonds; these properties make the silver compounds more stable. Besides, silver ions have a bigger size which implies that the freezing of the hopping motion of the Cu^+ ions which leads to the ordered, ferrielectric phase is much more difficult to happen [4, 5]. All these reasons add up to explain the lowering of the ferrielectric phase transition temperature with small amounts of silver and its full frustration when the substitution is completed.

1. V. Maisonneuve, V.B. Cajipe, A. Simon, R. Von Der Muhll, J. Ravez. Ferrielectric ordering in lamellar $CuInP_2S_6$ // Physical Review B, 1997. – V. 56. – P. 10860-10868.
2. X. Bourdon, V. Maisonneuve, V.B. Cajipe, C. Payen, J.E. Fischer. Copper sublattice ordering in layered $CuMP_2Se_6$ (M = In, Cr) // Journal of Alloys and Compounds, 1999. – V. 283. – P. 122-127.
3. V. Samulionis, J. Banys, Y. Vysochanskii. Ultrasonic and Piezoelectric Studies of Phase Transitions in Two-Dimensional $CuInP_2S_6$ Type Crystals // Ferroelectrics, 2009. – V. 379. – P. 69-76.
4. M. Gave, D. Bilc, S. Mahanti, J. Breshears, M. Kanatzidis. On the Lamellar Compounds $CuBiP_2Se_6$, $AgBiP_2Se_6$ and $AgBiP_2S_6$ // Inorganic Chemistry, 2005. – V. 44. – P. 5293-5303.
5. T. Babuka, K. Glukhov, Y. Vysochanskii, M. Makowska-Janusik. Structural, electronic, vibration and elastic properties of the layered $AgInP_2S_6$ semiconducting crystal – DFT approach // RSC Advances 2018. – V. 8. – P. 6965(1-13).

FORMATION OF HgSe NANOCYSTALLINE INCLUSIONS IN THE MATRIX OF AMORPHOUS SELENIUM FILMS

MakarL.I.[1], Mudry S.[2], Nykyruy L.[3], Pisak R.P.[1]., Rubish V.M.[1], Shtablavyi I.[2], Bespalov S.A.[4], Solomon A.M.[5], Yavorskyi R.S.[3]

[1]*Institute for Information Recording, NAS of Ukraine,4 , Zamkovi schody St., 88000, Uzhgorod Ukraine*
[2]*Ivan Franko National University of Lviv, Kyrylo i Mephodiy 8, 79005 L'viv, Ukraine*
[3]*Vasyl Stefanyk Precarpathian National University, Ivano-Frankivsk, Ukraine*
[4]*Presidium of NAS of Ukraine, 54, Volodymyrska st., 01030, Kyiv, Ukraine*
[5]*Institute of Electron Physics, NAS of Ukraine, 21, Universytetska St., 88017, Uzhgorod, Ukraine*

In paper presents the results of studies of the structure and surface morphology of mercury-modified amorphous selenium films by X-ray diffractometry and scanning electron microscopy, accordingly.

Amorphous Se films with a thickness 700 nm were obtained by vacuum evaporation of vitreous selenium from quasi-closed effusion cells on to unheated glass substrates. Selenium films modification was carried out in special hermetic boxes by keeping them in mercury vapor for 0.5-48 hours at 293 K.

Investigations of X-ray diffraction patterns for studied materials were carried out on «ДРОН-3» X-ray apparatus (λ=1.5418 Å). For the investigations of the microstructure of the samples (modified selenium films) a field emission scanning electron microscopy (FESEM) analysis was performed using a Hitachi S-4100 microscope with a secondary electron detector. The scanning of the sample surface was carried out by electron beam operating at 15 kV and 10μA with the spatial resolution of 10 nm in the secondary electron image regime.

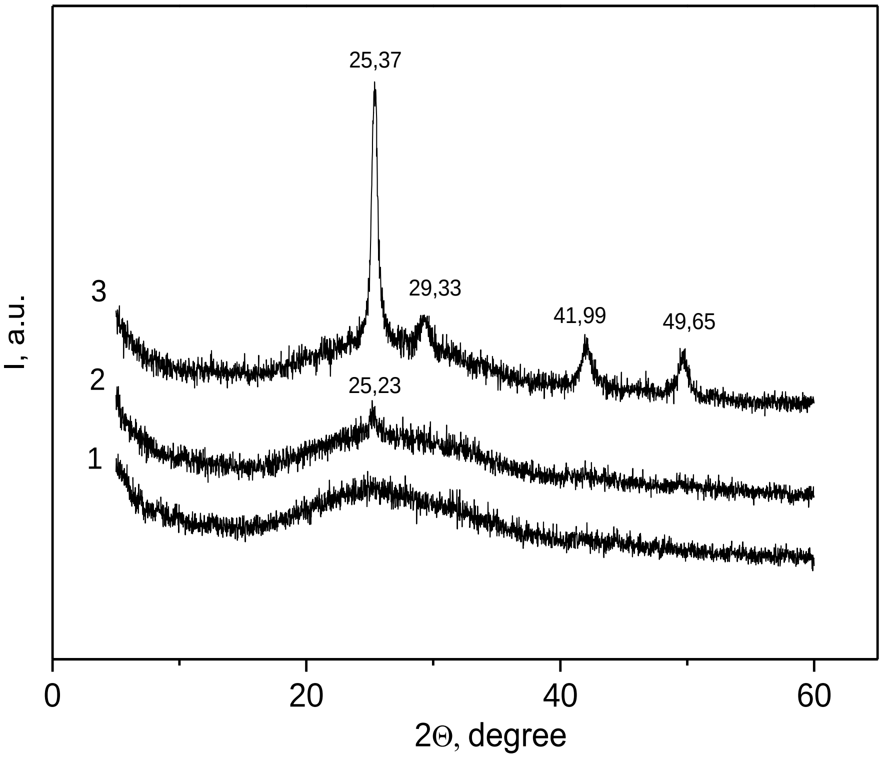

Fig. 1. Diffractograms of as-deposited amorphous Se films modified with mercury vapor for 1 hour (1), 24 hours (2), and 48 hours (3).

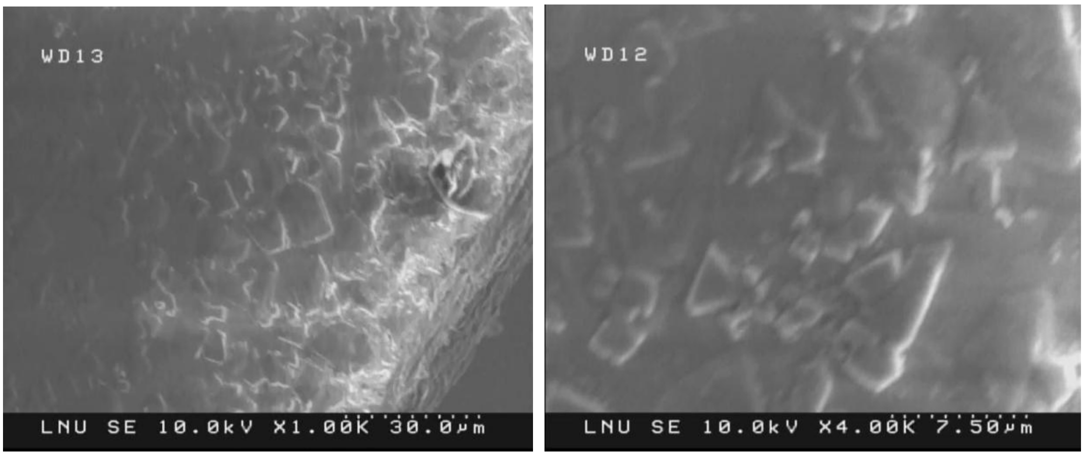

Fig. 2. SEM image of different places on the surface of amorphous film Se, with exposure for 30 minutes in mercury vapor, with different magnification.

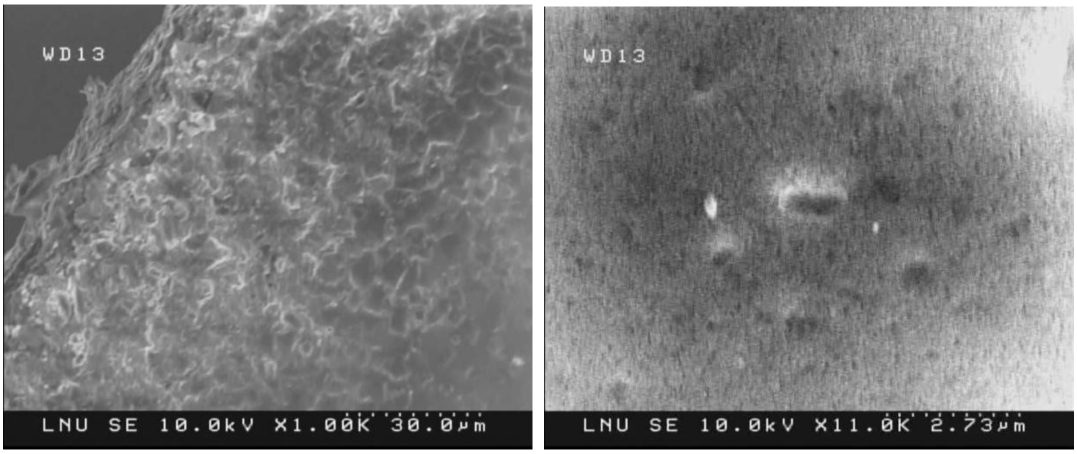

Fig. 3. SEM images of different places on the surface of amorphous Se film, with exposure for 1 hour in mercury vapor, with different magnification.

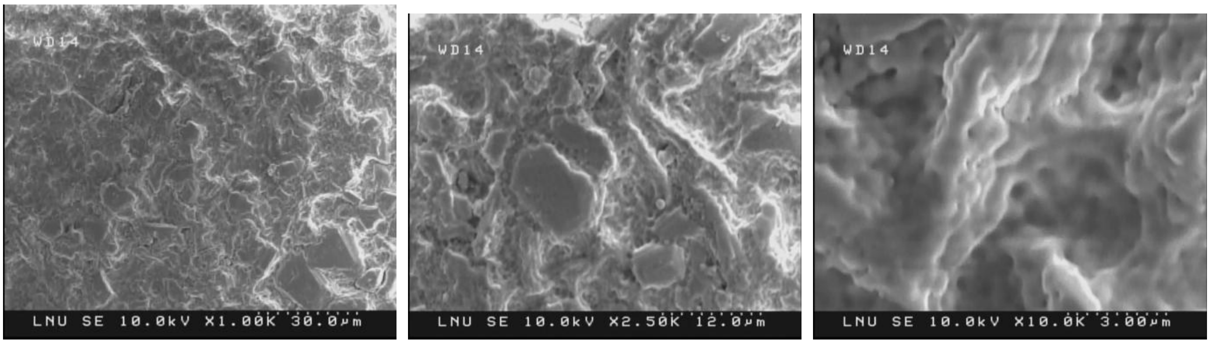

Fig. 4. SEM image of different places on the surface of amorphous Se film, with exposure for 1.5 hours in mercury vapor, with different magnification.

In fig. 1 shows the diffraction patterns of amorphous Se films with a thickness of 700 nm, exposure in mercury vapor at 293 K for 1 hour (curve 1), 6 hours (curve 2), and 48 hours (curve 3). Note, that the diffraction pattern of the modified mercury for a relatively short period of the time of Se film (curve 1) is practically indistinguishable from the diffraction pattern of the nominally pure amorphous selenium film. Exposure of films in mercury vapor for a long time leads to the formation in the amorphous matrix the nanosized HgSe inclusions in the cubic modification, which accompanied by the appearance on the diffractograms of weakly expressed reflexes. As the exposure time increases, the reflexes become pronounced, and their position agrees well with the position of intense reflexes on the diffractograms of crystalline mercury selenide obtained by the hydrochemical method using aqueous solutions of various substances: $HgCl_2$, $SeCl_4$ and ($N_2H_4H_2O$) [1], $Hg(CH_3COO)_2$ and $SeCl_4$ in the presence of $N_2H_4H_2O$ [2].

FESEM studies of mercury-modified amorphous selenium films (Fig. 2-4) confirm the conclusion based on the analysis of diffractograms that the phase structure formed during the modification of amorphous selenium films corresponds to the structure of crystalline HgSe.

The formation mechanism of the crystalline inclusions of mercury selenide in amorphous selenium films during their modification by mercury vapor is discussed.

1. Esmaeili-Zare M., Salavati-Niasari M., Sobhani A. Simple sonochemical synthesis and characterization of HgSe nanoparticles // Ultrasonics Sonochemistry. – 2012. – V.19, – Is. 5, P. 1079-1086.
2. Salavati-Niasari M., Esmaeili-Zare M., Sobhani A. Cubic HgSe nanoparticles: sonochemical synthesis and characterisation // Micro & Nano Letters. – 2012. – V.7, No.12, P.1300-1304.

IMPROVING HYDROXYL RADICAL SCAVENGING PROPERTIES OF CeO_{2-x} NANOCRYSTALS BY DOPING AND UV PRE-IRRADIATION

Maksimchuk P.O., Seminko V.V., Sedyh O.O., Aslanov A.V., Malyukin Yu.V

Institute for Scintillation Materials of NAS of Ukraine,
60 Nauky Ave., Kharkiv, 61072, Ukraine
e-mail: pmaksimchuk@isma.kharkov.ua

The ability of CeO_{2-x} nanoparticles (nanoceria) to effective antioxidant defense of the living cells have been discussed in the number of publications since the first observation of their ROS-protective action in 2006 [1]. The unique enzyme-like action of nanoceria enables long-term protection of the cells against excessive concentrations of superoxide (SOD-like activity [2]) and hydrogen peroxide (catalase-like activity [3]).

Hydroxyl radicals ($^{\bullet}OH$) are usually considered as the most dangerous type of reactive oxygen species formed inside the living cells that leads to increasing demand for antioxidant nanomaterials able to effective $^{\bullet}OH$ elimination. Nanoceria has recommended itself as the one of the most potent $^{\bullet}OH$ scavengers due to high content of Ce^{3+} ions and easy $Ce^{3+}\leftrightarrow Ce^{4+}$ switching making possible effective redox cycling.

In this paper we consider both the interconnection between $^{\bullet}OH$ scavenging and Ce^{3+}/Ce^{4+} ratio in nanoceria, and the ways of improving $^{\bullet}OH$ scavenging ability by increase of Ce^{3+} content. The influence of doping nanoceria by non-isovalent (Y^{3+}) or smaller (Zr^{4+}) ions and pre-irradiation of nanoparticles on the Ce^{3+} content and $^{\bullet}OH$ scavenging properties of nanoceria is discussed.

The influence of Y^{3+}- and Zr^{4+}-doping, and pre-irradiation on the $^{\bullet}OH$ scavenging properties of nanoceria was studied using spectroscopic techniques. The dependence of $^{\bullet}OH$ scavenging properties on the content of Ce^{3+} ions in nanoceria was confirmed by the simultaneous study of luminescence spectra and nanoceria - $^{\bullet}OH$ interaction processes. Incorporation of doped ions as well as 325 nm laser pre-irradiation of nanoceria water solutions led to sufficient increase of the content of Ce^{3+} ions accompanied by corresponding improvement of $^{\bullet}OH$ scavenging characteristics. While Y^{3+}-doping provided increase of Ce^{3+} content due to formation of Ce^{3+}-O_v-Y^{3+} complexes, Zr^{4+}-doping and pre-irradiation led to formation of additional oxygen vacancies and Ce^{3+}-O_v-Ce^{3+} complexes by lowering the energy required for oxygen release from nanoceria lattice. Overall, remarkable $^{\bullet}OH$ scavenging properties and reversible redox characteristics make Y^{3+}- and Zr^{4+}-doped and pre-irradiated ceria nanocrystals the potent materials for $^{\bullet}OH$ scavenging in living cells.

1. B. A. Rzigalinski, *Technology in cancer research & treatment*, 4, 651-659 (2005).
2. E. G. Heckert, A. S. Karakoti, S. Seal, W. T. Self, *Biomaterials*, 29, 2705-2709 (2008).
3. T. Pirmohamed, J. M. Dowding, S. Singh, B. Wasserman, E. Heckert, A. S. Karakoti, W. T. Self, *Chemical communications*, 46, 2736-2738 (2010).

ATOMIC FORCE SPECTROSCOPY FOR SORPTION PROPERTIES ESTIMATIONS OF FILMS IN SENSOR APPLICATIONS

Malyuta S.V.[1,2]**,** Rusavsky A.V.[1,2], Nazarov O.M.[1,2], Lytvyn P.M.[1]

[1] *V. Lashkaryov Institute of Semiconductor Physics NAS of Ukraine, 41, Nauky pr., 03028 Kyiv, Ukraine,*
[2] *National Technical University of Ukraine "Igor Sikorsky Kyiv Polytechnic Institute", 37, Peremohy pr., 03056 Kyiv, Ukrainee-mail: serhiy.malyuta@gmail.com*

Control of the sensor elements adhesive properties is an important task for development of reliable and efficient electronic devices. Increasing the sensor surface adhesion may indicate an enhancement in its sorption properties and improvement of the total sensitivity of device. The implementation of nano-probe technique for testing of carbon based sensor elements adhesive properties is described.

The work of surface adhesion can be measured directly at the nano-scale by force spectroscopy technique realized in atomic force microscope (AFM). This technique based on the recording of the distance-dependent interaction forces between AFM tip and investigated surface (so called force-distance curves) [1]. The measurements consists of three stages: approaching the AFM tip to surface, "capturing" tip by surface and tip withdrawing from a surface.

In this study, hundreds of force-distance curves were recorded at various surface positions of investigated carbon films. The magnetron plasma enhanced CVD method used to obtain these highly porous thin carbon films [2]. AFM probes made of Si_3N_4 with the tip radius of 20 nm and spring constant of the cantilever of 0.32 nN / nm as well as the silicon probes of 1000 nm tip apex radius and spring constant of 2.8 nN / nm were used.

The AFM tip detaches from the surface with a higher force $F_{pull\text{-}off}$ than was captured. This effect is caused by surface adhesion. The absolute value of adhesion work W_a defined as:

$$W_a = F^2_{pull-off} \big/ 2k,$$

where k is a spring constant of a tip cantilever. To compare the data obtained by different AFM probes, the adhesion energy was characterized by the value of critical force according to the Johnson-Kendall-Roberts model (JKR) [3, 4]:

$$W_{adh} = F_{pull-off} \big/ 1.5\pi R,$$

where R is the tip apex radius. The measured adhesion produced, mainly, by capillary and van der Waals forces.

Surface adhesion energies values for the plasma-threated carbon films shown in Fig. 1. Data obtained by two different tips illustrated. Higher values of adhesion energy to the surface detected for samples that were treated with plasma containing nitrogen, and this regularity does not depend on the size of AFM tip apex. The obtained values for the surfaces treated by different types of plasma correlate with the study [5]. The difference in the absolute values of the adhesion energy obtained by probes of different sizes and materials is due to the peculiarities of capillary interactions at the nano-scale level.

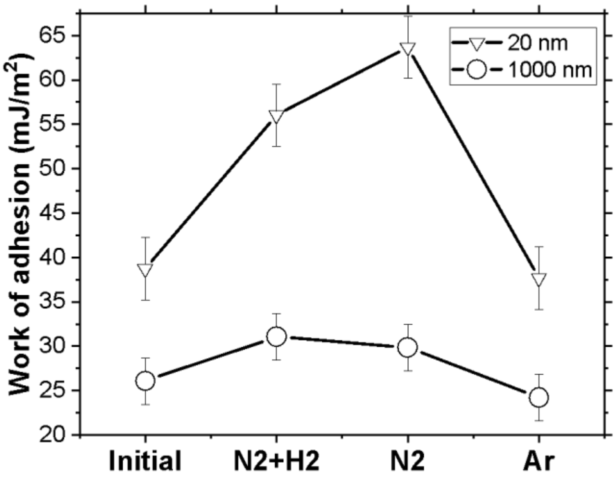

Fig.1 Adhesion energies of carbon film surfaces, after plasma treatments, obtained by atomic force spectroscopy by probes of different tip radii.

Thus, it is shown that the proposed method for assessment the adhesive properties of the sensor surface is applicable for the characterization of nano-porous carbon films. Plasma caused transformations of film's sorption properties were successfully detected at various scales by AFM tips of different radii. The same approach is applicable to the diagnosis of surfaces of other materials, where roughness does not exceed a few tens of nm. The surfaces of higher roughness could be characterized as well but the effect of rough surface should be taken into account in appropriate manner.

1. Cappella B., Dietler G. Force-distance curves by atomic force microscopy // Surface Science Reports. 1999. Vol. 34, no. 1–3. p. 1–104.
2. Slobodian O. M., Gomeniuk Y. V., Vasin A. V., [at. al.] Graphitic Nanoporous Carbon Thin Films: Fabrication Method, Structural, Electrical and Gas Sensor Properties // ECS Transactions, 2020. 97(5), 151.
3. Johnson K. L., Kendall K., Roberts A. Surface energy and the contact of elastic solids. //Proceedings of the Royal Society of London. A. Mathematical and Physical Sciences 1971. Vol. 324, no. 1558. p. 301–313.
4. Jiang T., Zhu Y. Measuring graphene adhesion using atomic force microscopy with a microsphere tip // Nanoscale. 2015. Vol. 7, no. 24. p. 10760–10766.
5. Polaki S.R., Kumar N., Krishna N.G., [at. al.] Microwave plasma induced surface modification of diamond-like carbon films // Surface Topography: Metrology and Properties. 2017. Vol. 5, no. 4. p. 045005.

ELECTRICAL AND MAGNETIC PROPERTIES OF POLYMER NANOCOMPOSITES BASED ON NICKEL FERRITE MODIFIED WITH COPPER SULFIDE

Mazurenko R.V., Prokopenko S.L., Abramov M.V., Gunja G.M., Makhno S.M., Gorbyk P.P.

Chuiko Institute of Surface Chemistry, NAS of Ukraine,
17 General Naumov Str., Kyiv 03164, Ukraine E-mail: r.v.mazurenko@gmail.com

The radiation absorbing nanocomposites have attracted much attention due to their applications in the number of electronic products and devices in the means of wireless communication, local area networks and other communication equipment. Considerable interest was directed to materials that absorb electromagnetic radiation with greater efficiency over a wide range of frequencies. The combination of magnetic and electrical components enables the possibility of regulating their electromagnetic characteristics, which can be used in the absorption of electromagnetic radiation. Ferromagnetic materials can be promising in this direction. The electroconductive component may be copper sulphide. Permeability of the magnetic materials is decrease at microwave range. To create the nanomaterials that effectively interact with electromagnetic radiation were synthesized of the nanocomposites $CuS/NiFe_2O_4$.

Nickel ferrite was synthesized via the sol-gel autocombustion method. A solution of cetyltrimethylammonium bromide (CTAB) was used to chemically modify the surface of nickel ferite. The concentration of CuS on a surface of ferrite was 0.32 and 0.38 volume fractions. Polymer filled composites were prepared by mechanical milling of the polychlorotrifluoroethylene powder with modified ferrite $CuS/NiFe_2O_4$ until homogeneous mixture, which thereafter was compressed at the polymer melt temperature of 513 K and a pressure of 2 MPa.

The obtained materials were studied by X-ray diffraction, transmission electron microscopy, immittance meter and vibration magnetometer. The real (ε') and imaginary (ε'') components of the complex permittivity in microwave range were measured using the interferometer at a frequency of 9 GHz. As shown in fig. 1*a* nickel ferrite nanoparticles have a size of about 50 nm. After modification of CuS ferrite nanoparticles, TEM images show finer nanoparticles (approximately ~ 15-20 nm), presumably corresponding to copper sulfide (fig. 1*b*). The presence of diffraction peaks is assigned to spinel-type of cubic $NiFe_2O_4$ (JCPDS card No. 86-2267). The average crystallite size of the $NiFe_2O_4$ is found to be 35-40 nm. For samples modified of copper sulfide, the diffraction patterns show reflections that refer to the hexagonal phase of CuS (JCPDS 78-0877). The average crystallite size of copper sulfide is 20-25 nm. Electroconductivity at low frequencies of $NiFe_2O_4$ is $\sim 10^{-5}$ Om^{-1} cm^{-1}. The nanocomposites $CuS/NiFe_2O_4$ ($0.32 \leq CuS \leq 0.38$) is shows an increase values of the electroconductivity, almost in four orders of magnitude when compared with electroconductivity of $NiFe_2O_4$. The introduction of $CuS/NiFe_2O_4$ into PCTFE ($0.035 \leq CuS \leq 0.15$) leads to an increase in the values of ε ', ε '' 5-8 times.

The magnetization of the ensemble of nickel ferrite nanoparticles is 37.4 emu/g and decreases in proportion to an increase in the concentration of copper sulfide on the surface of ferrite nanoparticles to 25.9 emu/g.

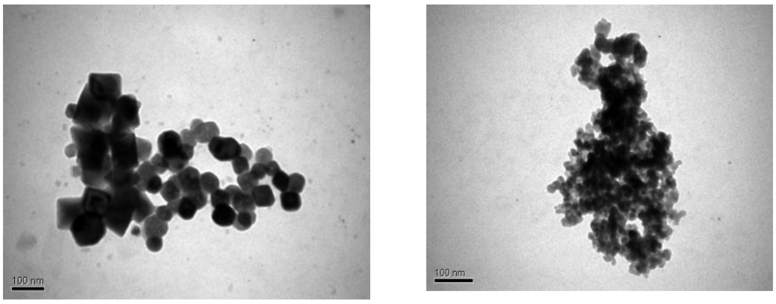

a *b*

Fig 1. TEM images of synthesized nickel ferrite and corresponding modified ferrite: *a* - $NiFe_2O_4$, *b* – $0.32CuS/NiFe_2O_4$

GOLD NANOPARTICLES-COATED OPTICAL FIBRE-TIP PROBES FOR COMMON AND ULTRAFAST SERS

Morozov Ye.M.

Institute for Information Recording, NAS of Ukraine, 2, Shpaka St., 03113 Kyiv, Ukraine

Raman spectroscopy is a powerful technique for revealing intrinsic local chemical information in different type of systems, and is important in physics, material science, chemistry, biology, and medicine. As spontaneous Raman signal is inherently weak, different types of Raman spectroscopy have been proposed and developed, such as surface-enhanced, tip-enhanced, femtosecond-stimulated, femtosecond time-resolved impulsive stimulated, polarized, and shifted excitation Raman spectroscopy. Recently, in surface-enhanced Raman spectroscopy (SERS), nanoparticles-coated optical fibre-tip probes have garnered significant interest [1,2]. Hutter et al. [2] provided a systematic study of gold nanoparticles-coated optical fibre-tip probes by means of a two-dimensional (2D) numerical simulation. However, 2D analysis gives only qualitative insight into a process or device and cannot provide a full description. Moreover, the ultrashort pulse delivery capability of such Raman probes remains unclear. In [2], the model used for analysis contained an “ideal” arrangement of NPs that is impossible to achieve in experiment. From this ideal arrangement, it is unclear whether the NPs behave like a coupled chain or like separate NPs. In this study [3], we report a novel 3D computational experiment on ultrashort pulse (2.11 fs at the FWHM intensity level) propagation through an optical fiber-tip probe decorated with gold nanoparticles using a constant structure of the probe’s dielectric taper but different configurations of the arrangement of NPs, and reveal parameters such as electric field enhancement and temporal ultrashort pulse characteristics. Moreover, we eventually identified a new structure consisting of only six terminal NPs and demonstrate its potential in practical applications.

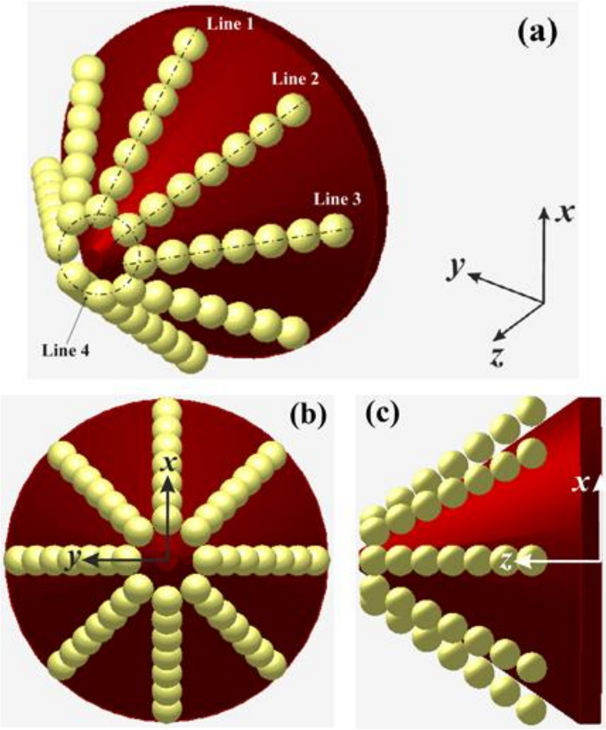

Fig. 1. (a) Perspective, (b) front and (c) side views of a schematic illustration of the initial optical fibre-tip probe structure.

In Fig. 1, the initial (“ideal”) optical fibre-tip probe model used for simulation is presented. The NPs were arranged to form eight lines (chains). However, due to the symmetry of the structure with respect to planes $x = 0$ and $y = 0$, and the axis of rotation, we are interested only in three chains of gold nanoparticles intersected in Fig. 1 by Lines 1, 2, and 3. This initial configuration is extremely convenient to perform such an analysis as it allows – by gradually removing certain nanoparticles – to track the position and behaviour of the hot spots and establish their ultrafast characteristics. At the same time, from the experimental point of view, this initial NP arrangement can be considered as an averaged arrangement of NPs on the optical fibre-tip probe surface, while all other configurations can be attributed to inaccuracies in the manufacturing of such structures.

Fig. 2 shows the normalized electric field amplitude distribution along Line 4 for five configurations; Config4 is a configuration with only six terminal NPs (see Fig. 3). The starting point of Line 4 in Fig. 2 was defined as the center of nanoparticle NP-1_1 with anti-clockwise bypass (dependence of the coordinates x and y on the distance along Line 4 is shown in the Figure's inset).

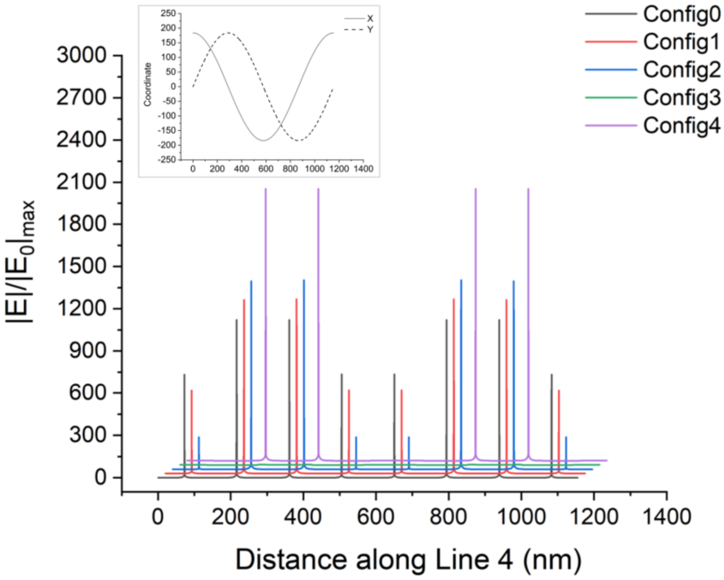

Fig. 2. Normalized electric field distribution along Line 4 for five configurations (inset shows dependence of the coordinates *x* and *y* on the distance along Line 4). Note: For convenience, the curves are offset relative to one another by 20 units along the abscissa and by 30 units along the ordinate.

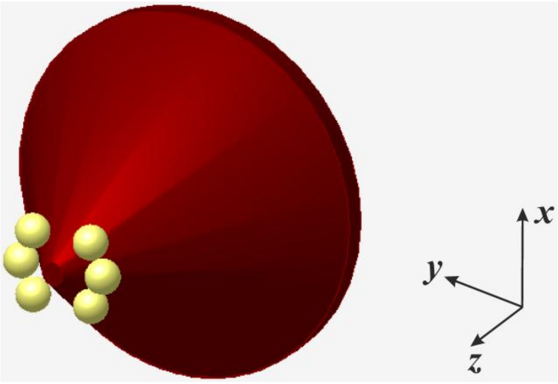

Fig. 3. Perspective view of a schematic illustration of Config4 of the optical fibre-tip probe structure.

From Fig. 2, it is clear that the distribution of electric field amplitude enhancement is almost identical for Config0–Config2. For Config3, there is no hot spot due to the absence of the corresponding NPs. Config4 is characterized by the presence of four hot spots only between the corresponding nanoparticles (between NP-2_1 and NP-3_1, NP-3_1 and NP-4_1, NP-6_1 and NP-7_1, and NP-7_1 and NP-8_1) and higher normalized amplitudes than other configurations (increasing from 1121.73 for Config0 to 1934.54 for Config4). Such an increase in the electric field amplitude enhancement for Config4 can be explained by the fact that more energy of the fundamental HE_{11} mode reaches the tip of the probe, which lead to a more intense excitation of the corresponding coupled LSPs. For Config4, the electric field enhancement is as high as 2,000.00; that is, the intensity at these points increases by $\approx 4.0\times10^6$ times. It is also worth noting that Config4 could potentially provide a higher spatial resolution the other configurations because it has more localized hot spots, while effective SERS area will be smaller. However, this smaller effective SERS area can be balanced by a more intense SERS signal in this case. Therefore, this increased spatial resolution can be useful for practical applications because the SERS signal is highly sensitive to the location of the SERS fibre-tip probe in a living cell [4].

In this way, we performed a 3D computational experiment on ultrashort pulse propagation through gold nanoparticles (NPs)-coated optical fibre-tip probes with a constant structure of the probe’s dielectric taper but different configurations of the arrangement of the NPs. A hot spot with the highest amplitude of the electric field was found not along the same chain of the NPs but between terminal NPs of neighbouring chains at the probe’s tip (the amplitude of the electric field in the hot spots between the NPs along the same chain was of the order of 10^1, while that between terminal NPs of neighbouring chains was of the order of 10^3). Consequently, we identified a configuration with only six terminal nanoparticles (Config4 in the main text) which shows the advantage of the highest enhancement in the electric field amplitude and holds potential to provide the highest spatial resolution during the SERS analysis of the object of interest (such as a live cell).

As for the ultrashort optical pulse characteristics of the considered structure, the temporal responses of the hot spots for all configurations were characterized by relatively strong pulse elongation (relative elongation was greater than or equal to 4.3%). At the same time, due to the reflection of the incident pulse and consequent interference, the temporal responses of most hot spots contained a few peaks for all configurations except for Config4. This shows that an in-depth preliminary optimization of the structure and different laser pulse shaping techniques is needed to obtain single-peak and unextended pulse responses. However, due to inaccuracies in the manufacturing of such structures (especially the size of nanoparticles and the distances between them), their use for ultrafast analysis presents certain difficulties. Nonetheless, the ultrashort temporal responses of all hot spots for Config4 were characterized by a single peak, albeit with a relatively large pulse elongation (absolute elongation of 4.94 fs and relative elongation of 234.1%).

These results suggest the need for further theoretical analysis and numerical optimization as well as the experimental verification of the structure with only six terminal nanoparticles (Config4). This will help us develop a deep understanding of the parametric behaviour of the structure to improve its ultrashort characteristics. In addition, these efforts need to be complemented by the development of experimental means for realization of the proposed geometry. Up to now, focused ion beam etching has been mostly used for structuring of the apex of optical fibre tips coated with a thin metallic layer. However, more recently a rich toolbox for the preparation of plasmonic nanostructures resembling the proposed geometry become available based on the self-assembly. So far it has been utilized in techniques including colloidal lithography and DNA origami used for nanoscale control of docking of chemically synthesized metallic nanoparticles. These techniques can be in principle used for direct structuring the optical fibre-tip probes as well as on substrates followed by a transfer of the prepared structures to a fibre tip by template stripping.

1. Liu M. [et. al]. Plasmonic tip internally excited via an azimuthal vector beam for surface enhanced Raman spectroscopy // Photon. Res., 2019. – Vol. 7. – P. 526-531.
2. Hutter T., Elliott S. R. and Mahajan S. Optical fibre-tip probes for SERS: numerical study for design considerations // Opt. Exp., 2018. – Vol. 26. – Article ID 15539.
3. Morozov Ye.M., Lapchuk A.S., Prygun A.V., Kryuchyn A.A. and Dostalek J. Investigation of optical fiber-tip probes for common and ultrafast SERS // New J. Phys., 2020. – Vol. 22. – Article ID 033027.

Vitol E. A. [et. al]. In situ intracellular spectroscopy with surface enhanced Raman spectroscopy (SERS)-enabled nanopipettes // ACS Nano, 2009. – Vol. 3. – P. 3529–3536.

AB INITIO CALCULATIONS OF CRYSTAL AND ELECTRONIC STRUCTURE OF SOLID SOLUTIONS BASED ON LEAD CHALCOGENIDES

Nykyruy L.I.[1], **Naidych B.P.**[1], Kostyuk O.[1, 2]

[1]*Vasyl Stefanyk Precarpathian National University, Shevchenko Str., 57, Ivano-Frankivsk, 76018, Ukraine*
[2]*Ivano-Frankivsk National Medical University, Halytska Str. 2, Ivano-Frankivsk, 76018, Ukraine*

The growing requirements of materials science and industry create ever higher demands on new materials. The use of binary compounds is no longer sufficient to meet the requirements. Obtaining fundamentally new materials with excellent properties is possible using solid solutions, layered structures, quantum dots etc. The widespread use of II-VI and IV-VI compounds based solid solutions is due to their high efficiency as thermoelectric and detector materials [1-3]. The study should begin with an analysis of the microstructure at the junction of two materials.

Ab initio calculations of equilibrium positions of atoms in the structure, electron density distribution, total energy and frequencies and oscillation spectra of binary lead chalcogenides and ternary compounds on its base are performed using the Becke-Lee-Yang-Parr exchange correlation functional (B3LYP) [4] and Stevens-Basch-Krauss-Jasien-Cundari (SBKJC) basic set [5].

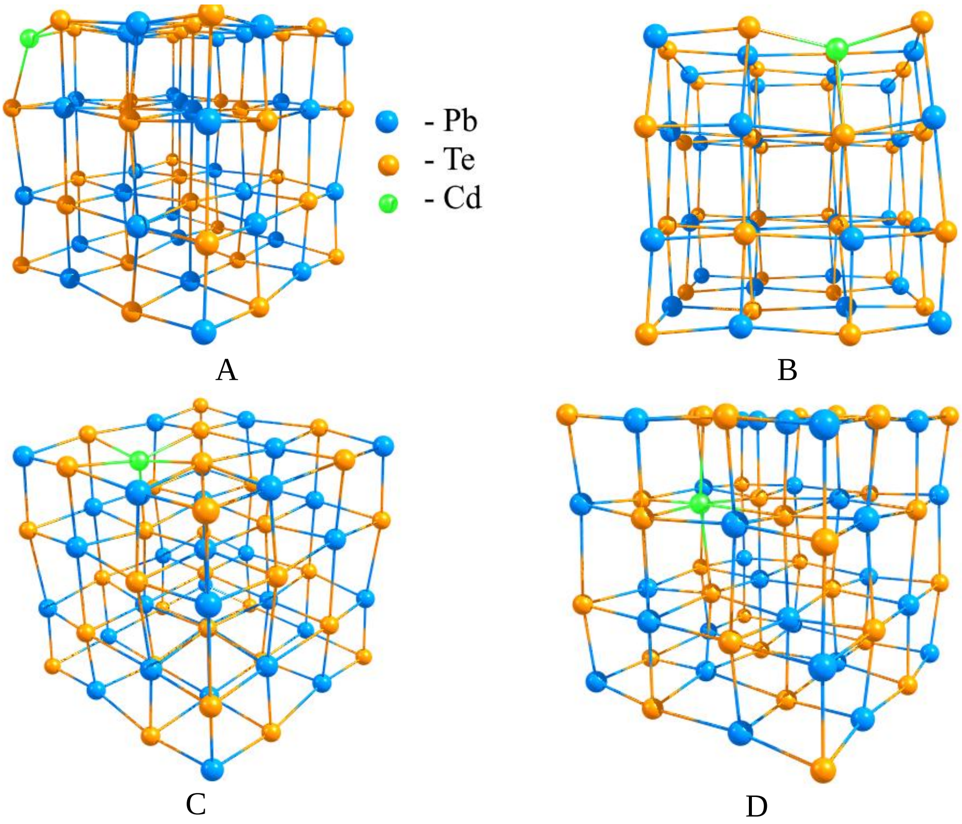

Fig. 1. Cluster models for $Pb_{0.97}Cd_{0,03}Te$ solid solution when placing a cadmium atom in the crystal lattice point: A) three-, B) four-, C) five- and D) six-coordinated lead atoms.

The equilibrium positions of atoms in the alternate placement of cadmium atoms in the position of lead on the surface and inside the model cluster were calculated. The clusters for the calculation of the studied properties consisted of 64 atoms. The calculation is performed by constructing a Hessian matrix of the second derivatives of the total energy for determination the equilibrium positions of atoms in the structure as the minima on the surface of the potential energy of the clusters. Next step was the calculation of the energy parameters for the optimized structure.

The distribution of the partial contributions from metal and chalcogen atoms is analyzed for assessing the modification of the electron spectrum. Visualization of the obtained calculations results is carried out in the Chemcraft.

The introduction of cadmium atoms in the crystal lattice with an ionic bond type, which form mixed ion-covalent bonds with tellurium, leads to a change in the intensity of isolines on the charge distribution map. The increase in electron density is due to the contribution of the covalent component of the Cd-Te bonds.

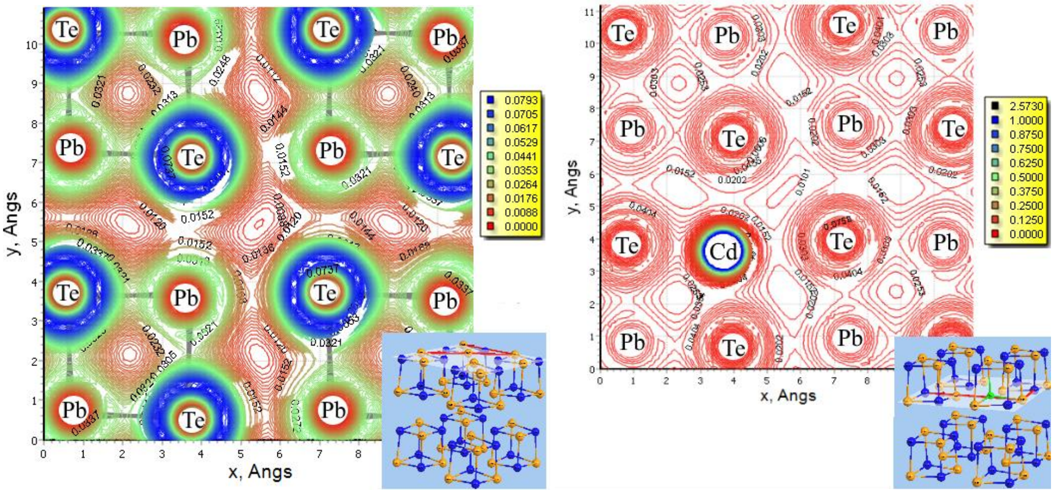

Fig. 2. Spatial maps of electric charge distribution in model clusters.

The electron density distribution in a cluster consisting of lead and tellurium atoms is qualitatively different from the case when in the base compound the cadmium atom is located in the position of one of the lead atoms (Fig. 2). The minimum electron density in a binary compound is 0.0088 and the maximum value is 0.0793. Substitution of metal atoms leads to an increase in the minimum value of density to 0.125 and in the maximum value to 2.573. Comparison of the electron density distribution of solid solutions makes it possible to analyze the nature of the chemical bonds in these compounds. The similarity of the electron density distribution around metal and chalcogen atoms and the presence of electron cloud deformation along the bond line in lead telluride indicate the predominance of the ionic bond type. A marked increase in the intensity of the lines around the cadmium is the result of a much lower electronegativity, and therefore the bonds will have higher percentage of covalence.

The density functional theory allows to model the crystallographic positions of atoms and study the change of the main crystallographic parameters due to the formation of solid solutions of multicomponent chalcogenide crystals. The formation of a solid solution of $Pb_{0.97}Cd_{0.03}Te$ leads to a decrease in the crystal lattice parameter comparing to the basic structure of PbTe. Cluster with cadmium substituted six-bonded lead atom has the lowest energy. The cadmium atom in the lead vacancy causes a local change in the electron density distribution due to the presence of a covalent component in the Cd-Te bond.

This study was supported by the Ministry of Education and Science of Ukraine as the project for young scientists “Technology of thin-film thermoelectric micromodules based on multicomponent compounds with quantum-size effects”(0119U100062).

1. M. Bukała, P. Sankowski, R. Buczko, P. Kacman, Physical Review B: Condensed Matter 86, 085205 (2012).
2. S. Kumar, Z.H. Khan, M.M. Khan, M. Husain, Current Applied Physics 5, 561 (2005).
3. K. Ahn, K. Biswas, J. He, I. Chung, V. Dravid, M. G. Kanatzidis, Energy & Environmental Science. (2013).
4. A.D. Becke, Journal of Chemical Physics 98, 5648 (1993).
5. M.S. Gordon, M.W. Schmidt, in *Theory and Applications of Computational Chemistry, the first forty years*, Chapter 41, eds. by C. E. Dykstra, G. Frenking, K. S. Kim, G. E. Scuseria (Elsevier, Amsterdam, 2005) pp. 1167-1189.

PHONON SPECTRA OF THE Cu_7SiS_5I AND Ag_7SiS_5I CRYSTALS

Nebola I.I., Katanytsia A.F., Shteyfan A.Ya., Sidey V.I., Ochkay I.I., Studenyak I.P.

Uzhhorod National University, Voloshin Str., 54, 88000 Uzhhorod, Ukraine
e-mail: ivan.nebola@uzhnu.edu.ua

Nowadays the crystalline systems with high ionic conductivity, namely the title superionics Cu_7SiS_5I and Ag_7SiS_5I, are of serious interest for both experimenters and theorists. The attention paid to these systems within the researchers' community is primarily due to the increasing possibilities of their practical use as solid electrolytes in capacitors and batteries, as well as in the membranes of fuel cells. Of particular interest are the superionic crystalline conductors characterized by the presence of a high-temperature phase with high conductivity, the current carriers of which are ions. Physicochemical properties of the superionic crystalline Cu_7SiS_5I and Ag_7SiS_5I conductors are actually determined by their crystal structure.

The main goal of the present theoretical study of the lattice dynamics of the above superionic crystals was to carry out the (3+d)-dimensional description of the argyrodite structures within the framework of the superspace symmetry concept and also to calculate the dispersion of the phonons for these structures [1-3].

The compositional features of the realization of complex crystals and systems of solid solutions by the mechanism of filling the translationally equivalent positions (prescribed by a given basis of the protocrystal) with different atomic species and vacancies are covered by the superspace symmetry concept. Different combinations of protocrystal bases and real crystal formations can be taken into account together with all possible variants of compositional filling of crystallographic positions. The use of a complete set of modulation vectors allows one to determine the amplitudes of mass modulation functions and, on their basis, to generate a generalized dynamic matrix of a real physical object and a mass perturbation matrix: the first matrix is given as a superposition of dynamic protocrystal matrices defined at different Brillouin zone's (BZ) points associated with the modulation vectors, while the second one is described by the amplitudes of mass modulation functions [4, 5].

Within the framework of the superspace symmetry concept, the dispersion curves of a phonon spectrum of a given crystalline formation are defined as solutions of the matrix equation (under the condition of zero equality of the determinant) of the form:

$$\left|D_{\alpha\beta}(k+q_i)-\omega^2\delta_{\alpha\beta}\delta_{ij}-\omega^2\rho_{(i-j)}\delta_{\alpha\beta}\right|=0, \qquad (1)$$

where $D_{\alpha\beta}(k+q_i)$ are the dynamic matrices of a monoatomic protocrystal, defined at the $(k+q_i)$ points of the BZ, $\rho_{(i-j)}=\rho_i\left(q_i,\Delta^* b^*_{ij}\right)$ are the amplitudes of the mass modulation function given for the (q_i-q_j), modulation vector, k is the wave vector, q_i are the modulation vectors, and α,β are the coordinates x,y,z. The solution of the matrix equation with respect to $\omega^2(k)$ allows one to determine the dispersion dependences of a given phonon spectrum, while taking into account different variants of compositional filling makes possible to trace from their genesis [5].

The dynamic matrices $D_{\alpha\beta}(k+q_i)$ of the protocrystal are determined from the relationship (2):

$$D_{\alpha\beta}(k+q_i)=\sum_{(n\neq 0)}\alpha_n\frac{n_\alpha n_\beta}{n^2}\left(1-e^{i(k+q_i)n}\right), \qquad (2)$$

where α_n is the force constant of the interaction between the atom in the 0th position and the nth neighboring atom, n_α and n_β are the projections of the vector n on the axes α,β.

In the equidistant approximation taken for the model, the force characteristic depends only on the distance between the atoms, and then the interaction of different varieties of atoms in equidistant positions is the same. This approach allows one to build a dynamic matrix in the quasi-diagonal form. In the non-equidistant approximation, α_n is determined by the distance between the positions and also by the difference in physical characteristics of the objects that occupy these positions.

The values of the amplitudes of the mass characteristics $\rho(q_j)$ are obtained by solving a system of equations (3) with respect to the amplitudes of the mass modulation functions $\rho(q_j) = \rho_j$:

$$m(r_k) = \sum_{j=1}^{s^3} \rho(q_j) e^{iq_j r_k}, \tag{3}$$

where s is the number of possible positions of atoms in the superlattice, $m(r_k)$ are the mass characteristics in these positions, q_j is the array of modulation vectors, the number of which is equal to the number of positions in the superlattice.

Here we describe some members of the argyrodite family in the superspace symmetry concept, based on the model of the natural FCC (8*a*,8*a*,0) superlattice, by using the equidistant approximation of the force field.

Representatives of the argyrodite family belong to the crystal structures characterized by the partial occupations of certain crystallographic orbits by the atoms of one sort. The crystal structures of the members of this family, the Cu_7SiS_5I and Ag_7SiS_5I superionics [6], consists of a rigid anionic framework and a disordered cationic sublattice formed by the Cu(Ag) atoms, which is typical for the argyrodite crystals. In the Paterson projections of the above structures, the electron density peaks specify the following crystallographic positions of the atoms: 24-fold position (*g*), 48-fold position (*h*), 16-fold position (*e*), and two of the four 4-fold positions (*a*), (*b*), (*c*), (*d*). Accordingly, the following atomic positions were chosen: Cu1(Ag1) in 24(*g*), Cu2(Ag2) in 48(*h*), 16 of 20 S in 16(*e*) with $x = 3/8$, and 4 S in 4(*c*), I in 4(*a*), Si in 4(*b*) [5].

To calculate the phonon spectra of the Cu_7SiS_5I and Ag_7SiS_5I crystals, the model structures featuring the atomic coordinates and occupancies given in Table 1 were chosen.

An attempt to take into account the partial occupancy of the Cu2(Ag2) position requires a transition to a model taking into account the 512-fold multiplication of the unit cells of the protocrystal with the FCC basis (*a*, *a*, 0), (*a*, 0, *a*), (0, *a*, *a*) and the superlattice with the FCC basis (8*a*, 8*a*, 0), (8*a*, 0, 8*a*), (0, 8*a*, 8*a*), *i.e.* 8 × 8 × 8 = 512-fold multiplication.

Table 1. **Atomic positions and occupancies of the model Cu_7SiS_5I and Ag_7SiS_5I argyrodite structures**

Atom	**Coordinates by [6]**	**Occu-pancy by [6]**	**Coordinates by [7]**	**Occu-pancy by [7]**	**Coordinates by this work**	**Model occu-pancy [this work]**
Cu1 (Ag1)	(0.02362, 1/4, 1/4)	0.624	(0.01747, 0.25, 0.25)	1.0	(0, 1/4, 1/4)	5/6
Cu2 (Ag2)	(0.01914, 0.30918, 0.30918)	0.376		0.0	(0, 5/16, 5/16)	2/12
Cu3 (Ag3)	(0.0116, 0.1917, 0.1917)	0.376		0.0		0.0
I	(0, 0, 0)	0.989	(0,0,0)	1.0	(0, 0, 0)	1.0
S1	(1/4, 1/4, 1/4)	0.989	(1/4, 1/4, 1/4)	1.0	(1/4, 1/4, 1/4)	1.0
S2	(0.62183, 0.62183, 0.62183)	1.0	(0.62183, 0.62183, 0.62183)	1.0	(5/8, 5/8, 5/8)	1.0
Si	(1/2,1/2,1/2)	1.0	(1/2, 1/2, 1/2)	1.0	(1/2, 1/2, 1/2)	1.0

The array of 512 possible positions of atoms covers 30 orbits, and the set of 512 modulation vectors is divided into 30 stars (Table 2).

Table 2. **Arrays of positions gathered in orbits and of modulation vectors gathered in stars for the Cu_7SiS_5I and Ag_7SiS_5I argyrodite structures with the (8a×8a×0) superlattice used for taking into account the partial occupancy of the Cu2 (Ag2) position**

Atoms	**No. of orbit (position)**	**Atomic positions gathered in orbits**	**No. of star (multiplicity)**	**Modulation vectors gathered in stars**
I	1(1)	$[0,0,0]$	1(1)	$[0,0,0]$
	2(2-13)	$[a,a,0]$	2(12)	$[\pi/8a, \pi/8a, 0]$
	3(14-19)	$[2a,0,0]$	3(6)	$[\pi/4a, 0, 0]$
	4(20-43)	$[2a,a,a]$	4(24)	$[\pi/4a, \pi/8a, \pi/8a]$
	5(44-55)	$[2a,2a,0]$	5(12)	$[\pi/4a, \pi/4a, 0]$
	6(56-79)	$[3a,a,0]$	6(24)	$[3\pi/8a, \pi/8a, 0]$
	7(80-87)	$[2a,2a,2a]$	7(8)	$[\pi/4a, \pi/4a, \pi/4a]$
	8(88-135)	$[3a,2a,a]$	8(48)	$[3\pi/8a, \pi/4a, \pi/8a]$
	9(136-141)	$[4a,0,0]$	9(6)	$[\pi/2a, 0, 0]$
Cu2(Ag2)(2/12)	10(142-153)	$[3a,3a,0]$	10(12)	$[3\pi/8a, 3\pi/8a, 0]$
	11(154-177)	$[4a,a,a]$	11(24)	$[\pi/2a, \pi/8a, \pi/8a]$
	12(178-201)	$[4a,2a,0]$	12(24)	$[\pi/2a, \pi/4a, 0]$
	13(202-225)	$[3a,3a,2a]$	13(24)	$[3\pi/8a, 3\pi/8a, \pi/4a]$
	14(226-249)	$[4a,2a,2a]$	14(24)	$[\pi/2a, \pi/4a, \pi/4a]$
	15(250-297)	$[4a,3a,a]$	15(48)	$[\pi/2a, 3\pi/8a, \pi/8a]$
	16(298-321)	$[5a,a,0]$	16(24)	$[5\pi/8a, \pi/8a, 0]$
	17(322-369)	$[5a,2a,a]$	17(48)	$[5\pi/8a, \pi/4a, \pi/8a]$
Cu1(Ag1)(5/6)	18(370-375)	$[4a,4a,0]$	18(6)	$[\pi/2a, \pi/2a, 0]$
	19(376-399)	$[4a,3a,3a]$	19(24)	$[\pi/2a, 3\pi/8a, 3\pi/8a]$
	20(400-411)	$[5a,3a,0]$	20(12)	$[\overline{3\pi}/8a, 3\pi/8a, 0]$
	21(412-423)	$[4a,4a,2a]$	21(12)	$[\pi/2a, \pi/2a, \pi/4a]$
	22(424-429)	$[6a,0,0]$	22(6)	$[3\pi/4a, 0, 0]$
	23(430-453)	$[5a,3a,2a]$	23(24)	$[\overline{3\pi}/8a, 3\pi/8a, \pi/4a]$
	24(454-477)	$[6a,a,a]$	24(24)	$[3\pi/4a, \pi/8a, \pi/8a]$
	25(478-489)	$[6a,2a,0]$	25(12)	$[3\pi/4a, \pi/4a, 0]$
S2	26(490-497)	$[6a,2a,2a]$	26(8)	$[3\pi/4a, \pi/4a, \pi/4a]$
S1	27(498)	$[4a,4a,4a]$	27(1)	$[\pi/2a,\pi/2a,\pi/2a]$
	28(499)	$[-4a,-4a,-4a]$	28(1)	$[\bar{\pi}/2a,\bar{\pi}/2a,\bar{\pi}/2a]$
	29(500-511)	$[7a,a,0]$	29(12)	$[\bar{\pi}/8a, \pi/8a, 0]$
Si	30(512)	$[8a,0,0]$	30(1)	$[\pi/a, 0, 0]$

Description of the structure and calculations within the superspace symmetry concept were performed by solving the secular equation (1) of the order 1536×1536, involving 512 possible positions, 14 of which are occupied by the atoms of the Cu_7SiS_5I and Ag_7SiS_5I structures: I [0, 0, 0], Cu2(Ag2)(142) [3, 3, 0], Cu2(Ag2) (153) [0,–3,–3], Cu1(Ag1) (371) [4,0,4], Cu1(Ag1) (372) [0,4,4], Cu1(Ag1) (373) [–4,4,0], Cu1(Ag1) (374) [–4,0,4], Cu1(Ag1) (375) [0,-4,4], S2(490) [6, 2, 2], S2(491) [2, 6, 2], S2(492) [2, 2, 6], S2(493) [–6, 2, 2], S1(498) [4, 4, 4], Si(512) [8, 0, 0]. The dynamic matrices of the protocrystal were calculated at 512 points of BZ. By modifying the occupancies of crystallographic positions of the atoms, and by adjusting the values of the force constants in the equidistant approximation, the phonon spectra were obtained for the high symmetric directions of the Brillouin zone of the FCC lattice.

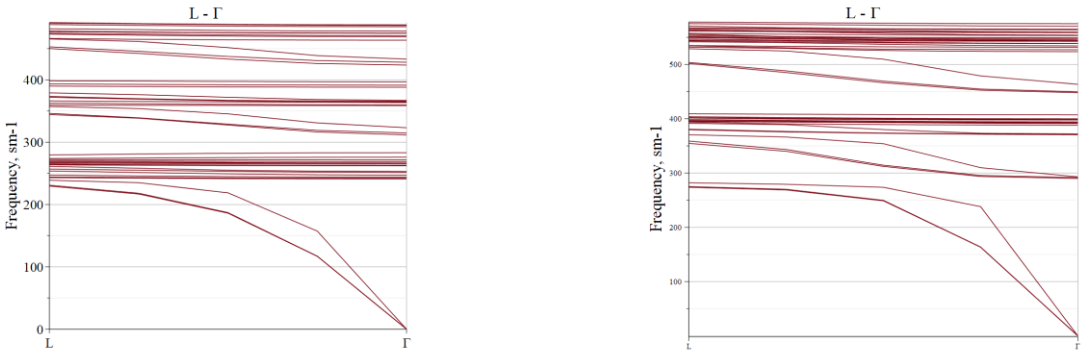

(a) Ag_7SiS_5I (b) Cu_7SiS_5I

Fig. 1. Dispersion dependences along the Γ–L direction for argyrodite crystals.

The values of the force constants α_n are given in the order of ascending distances between the position of the orbit 1(0, 0, 0) and n+1, taking into account all possible variants of the distances between the pairs of occupying atoms. The force constants were chosen in the equidistant approximation; the interaction was determined only by the distance and did not depend on the type of interacting pairs of atoms. For example, for the compound Ag_7SiS_5I, α_{26n} is the force constants describing the interaction at a distance of $4a\sqrt{3}$ and equal to 3 N/m, so the others are, correspondingly, powerConstants := [52.1, 0, 0, 0, 0, 0.01, 9, 0.01, 1, 1, 0, 0, 0, 0, 0.7, 0, 7, 5, 0, 0, 0, 2, 0, 0, 0.08, 3, 1, 23.5]. For the Cu_7SiS_5I compound, the calculations are analogous: powerConstants := [82.1, 0, 0, 0, 0, 3.1, 2.2, 1.7, 0.6, 1, 0, 0, 0, 0, 0.7, 0, 1, 5, 0, 0, 0, 2, 0, 0, 10.0, 53, 0.6, 19]. The dispersion dependences for the Γ–L direction of the BZ are shown in Fig. 1 (a, b).

As a result of the model analysis of the structures of Cu_7SiS_5I and Ag_7SiS_5I taking into account the occupancy of the orbit of the Cu2(Ag2) atom in the metric of the protocrystal with the FCC basis (a, a, 0), (a, 0, a), (0, a, a) and the superlattice with the FCC basis (8a, 8a, 0), (8a, 0, 8a), (0, 8a, 8a), the rearrangement of the phonon spectrum of the Cu_7SiS_5I and Ag_7SiS_5I crystals was observed, which is caused by the change of the corresponding mass characteristics of the Cu and Ag atoms and by a certain expected correlation between the power constants. The results of the calculations performed in this work are in a satisfactory agreement with the experimental data obtained for the frequency range of ~150-550 cm^{-1} at the Γ point [8]. The wide frequency ranges of values obtained here can indicate the effective possibility of their changes by changing the occupancy of the Cu2(Ag2) atoms (*i.e.* by a "jump" of atoms between the considered orbits), which is accompanied by the high ionic conductivity in the superionic Cu_7SiS_5I and Ag_7SiS_5I crystalline phases.

1. Koptsik V.A. Teoretiko-gruppovyie metody v fizike realnyh kristallov i teorii fazovykh perekhodov (Group theoretical methods in the physics of real crystals and in the phase transitions theory). In: "Teoretiko-gruppovyie metodyi v fizike: Trudyi mezhdunarodnogo seminara". – M.: Nauka. – 1980. – pp.368–381 (in Russian).
2. Janssen T. On the lattice dynamics of incommensurate crystal phases. Journal of Physics C: Solid State Physics 12 (1979) 5381–5392.
3. Nebola I.I., Ivanyas A.F., Kindrat V.Ya. The genesis of the structure and vibrational spectra of crystals with the ($Sa\times Sa\times Sa$) superlattice. Solid State Physics. 35 (1993) 1852–1866 (in Russian).
4. Nebola I.I., Shkirta I.M. Katanytsia A.F., Dolynai A.-K.V. 3+D Dimensional bases for the complex crystals lattice dynamics modeling. In: "The 19th Small triangle meeting on theoretical physics. Mezdilaborce, Slovakia. October 15–18, 2017", pp. 141–148.
5. Nebola I.I., Shteyfan A.Ya., Sidey V.I., Katanytsia A.F., Studenyak I.P., Shkyrta I.M. Model research of phonon spectra of argyrodites family. Semiconductor Physics, Quantum Electronics & Optoelectronics. 21 (2018) 134–138.
6. Nilges T., Pfitzner A.A. structural differentiation of quaternary copper argyrodites: Structure – property relations of high temperature ion conductors. *Z. Kristallogr. 220* (2005) 281–294.
7. Haznar A., Pietraszko A., Studenyak I.P. X-ray study of the superionic phase transition in Cu_6PS_5Br. Solid State Ionics 119 (1999) 31–36.
8. Studenyak I.P., Rushchanskii K.Z., Buchuk R.Yu., Stephanovich V.O. Phonon spectra of Cu_6PS_5Br superionic ferroelastic: experimental and theoretical studies. Condensed Matter Physics 10 (2007) 11–16.

PECULIARITIES OF DOUBLE ELECTRON-PHONON RESONANCE IN RAMAN SPECTRA OF GRAPHENE AND SINGLE-WALLED CARBON NANOTUBES

Nikolenko A.S.[1], Strelchuk V.V.[1,2], Stubrov Yu.Yu.[1] and Gubanov V.O.[2]

[1]*V. Lashkaryov Institute of Semiconductor Physics National Academy of Sciences of Ukraine, 41 Nauky pr., 03028 Kyiv, Ukraine*
[2]*Kyiv National Taras Shevchenko University, Department of Physics, 64 Volodymyrska str., 01601 Kyiv, Ukraine*

Double electron-phonon resonance (DR) is the key mechanism, which significantly influences first- and second-order Raman scattering in graphene and single-walled carbon nanotubes (SWCNT), and allows for registration of acceptable micro-Raman signal even from individual carbon nanotubes [2] or monoatomic layer of graphene [1]. Specific wave vector selectivity of DR mechanism allows only phonons with wave vector q = 2k, where k is an electron wave vector, to participate in electron-phonon scattering, and making it possible to study the structure of electron bands from analysis of Raman spectra. In case of graphene, two π-orbitals form dispersive bonding and anti-bonding orbital states, which correspond to valence and conduction bands, which touch each other and have linear dispersion near K-point of Brillouin zone. Quantum states of graphene transform into 1D states of SWCNT leading to the appearance of van Hove singularities in a density of electron states, which determine the electronic properties of SWCNTs and resulting in modification of the selection rules for the DR process.

This report reviews the peculiarities of double electron-phonon resonance in the Raman spectra of graphene, individual SWCNTs, and a mixture of SWCNTs. The theory-group classification of involved in DR electron and phonon states is carried out according to projective irreducible representations of wave vector groups and the forms of stationary elastic waves in SWCNTs, single-layer graphene and bulk graphite are analytically calculated. The dispersion behavior of second-order 2D bands is analyzed taking into account the peculiarities of electron and phonon energy structure of the studied carbon allotropes. The fine structure of the 2D band for the mixture of SWCNTs is related to incoming and outgoing electron-phonon resonances, and trigonal warping effect. The nature of the doublet behavior of 2D bands in the Raman spectra of individual SWCNTs is explained by DR involving phonons participating in intravalley electron transitions. To confirm these mechanisms the forms of vibrations for these specified phonons are also analyzed. The similarity of dispersion behavior of 2D phonon bands in single-walled carbon nanotubes, one-layer graphene, and bulk graphite is discussed.

1. Strelchuk V.V., Nikolenko A.S., Gubanov V.O. [et. al.]. Dispersion of electron-phonon resonances in one-layer graphene and its demonstration in micro-Raman scattering // Journal of Nanoscience and Nanotechnology, 2012. – V. 12. – P. 8671-8675.
2. Stubrov Y., Nikolenko A., Gubanov V. [et. al.]. Manifestation of Structure of Electron Bands in Double-Resonant Raman Spectra of Single-Walled Carbon Nanotubes // Nanoscale Research Letters, 2016. -V. 11. – P 2.

PHOTOLUMINESCENT AND STRUCTURAL PROPERTIES OF THIN ZnO FILMS DOPED WITH RARE EARTH METALS

Oberemok O.S., Dubikovskyi O.V, Sabov T.V, Kosulya O.V, Melnik V.P, Kladko V.P,
Romanyuk B.M, Popov V.G, Gudymenko O.Yo.

Lashkarev Institute of Semiconductor Physics NAS of Ukraine, 41Prospect Nauky, Kyiv 03028, Ukraine. e-mail: ober@isp.kiev.ua

The wide bandgap (Eg =3.37 eV) semiconductor ZnO have a high transparency from the visible to near-infrared region and high exciton binding energy (60 meV) at room temperature [1]. In this connection ZnO based heterojunctions [2] are attracted considerable attention for creation of solar cell, ultraviolet (UV) detector and laser-light emitting diode. Naturally, ZnO is an n-type semiconductor because of a deviation from stoichiometry due to the presence of intrinsic defects such as oxygen vacancies and zinc interstitials that obviously form donor levels [3]. As a rule, ZnO is doped by the IIIA group elements to obtain a layer with modified properties. Aluminum is the most suitable for this purpose because Al dopant atoms can replace a Zn atom in the structure and release a free electron that increases the free carrier concentration [4]. Besides, the optical band gap of ZnO films is changed as a function of aluminum content. It is known that the initial growth of ZnO films occurs in the form of columns of a certain orientation. The addition of Al during the film growth leads to an increase in conductivity, a change in the band gap, and densification of the ZnO film. At the same time, doping of ZnO with optically active rare-earth elements (REE) makes to expand the radiation range spectrum from the intrinsic band gap of the semiconductor to infrared radiation. Tuneable wavelength light emission lines are possible from the thin film device due to a combination of several suitable dopants [5]. The REEs will also make it possible to intelligently implement a solid-state 4-level laser system at the nanoscale. The dopants in the thin film are utilized as light emitters, which can reach the population inversion required for gain at low pumping levels due to the long life times of the excited levels. This approach can resolve the disadvantages of undoped semiconductor nanolasers, since the population inversion of a quasi-four-level laser system is achieved only at very high pump intensities. The optical emissions of rare earth elements originate from intra-shell transitions. REEs interact weak with the host matrix due to the strong shielding of the 4f-shell by the $5s^2$ and $5p^6$ orbits. As result, all REEs have a very similar chemical behavior in ZnO and the optical emission of each luminescence center occurs almost independently of the state of other centers and is determined only by its probability.

The purpose of this work was investigation of the structural and photoluminescence properties of the Al-doped ZnO (ZnO:Al) thin film system doped different REE.

ZnO:Al thin films with thickness of 70 nm were deposited on p-Si(100) substrate by DC reactive magnetron sputtering of the ZnO target with Al content of 1% at the room temperature. The film modifications were carried out by Ho^+, Tm^+, Sm^+, Er^+, Hf^+ and Nd^+ implantations with energies of 75 keV and doses of $3.1x10^{13}$ cm^{-2}. The prepared films were annealed in the temperature range from 300 to 850 ºC by furnace thermal annealing. The modified films were studied using X-ray diffraction (XRD), Photoluminescence spectroscopy (PL) and Time-of-Flight Secondary Ion Mass Spectrometry (ToF-SIMS).

Figure 1 shows the photoluminescence spectra of ZnO thin films undoped and REE-implanted after annealing at the temperature $850^{O}C$ during 30 min in the argon ambient. It’s seen that the emission band at a visible wavelength range of the undoped ZnO film arises. It’s connected with a radiative recombination through point defects in the ZnO lattice, such as oxygen vacancy, zinc vacancy, oxygen interstitial, zinc interstitial, and other. At the same time, annealing of the implanted films suppresses the radiative recombination of intrinsic film defects and leads to the appearance of new radiative lines in the spectrum. Knowing the behavior of these lines during thermal treatments, it is possible to simulate the desired wavelength of radiation to create laser diodes. The change in the structural properties of REE implanted thin ZnO films with an increase of the annealing temperature is shown in the XRD spectrum for neodymium as an example (Fig. 2). It can be seen that the annealing temperature increase leads to a shift of the 002 reflection to the region of large angles and an increase in the integral signal intensity when the annealing temperature reaches 600^{O}C.

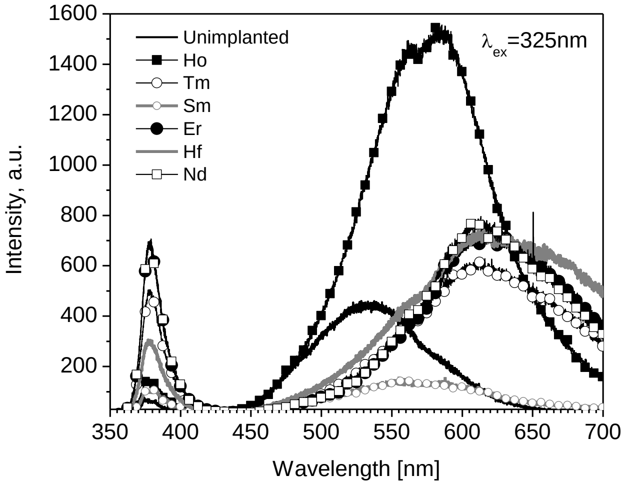

Fig.1. Room temperature PL spectra of undoped and REE-doped ZnO films after annealing at 850^{O}C in Ar ambient.

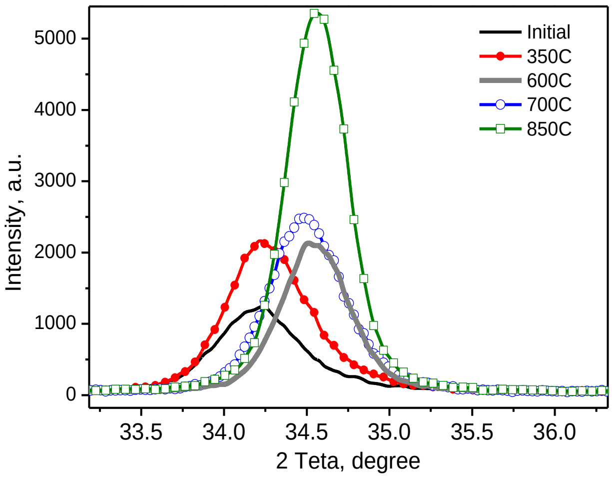

Fig.2. XRD spectrum of Nd^{+} doped ZnO films after annealing in Ar ambient.

To determine the effect of point defects on the photoluminescence and structural properties of ZnO films, the implantation of an inert krypton gas was also investigated.

1. S.J. Pearton, D.P. Norton, K. Ip, Y.W. Heo, T. Steiner, Recent progress in processing and properties of ZnO // Progress in materials science, v. 50 (3), p. 293-340 (2005).
2. M. Purica, E. Budianu, and E. Rusu, Heterojunction with ZnO polycrystalline thin films for optoelectronic devices applications // Microelectronic Engineering, v. 51–52, p. 425-431 (2000).
A. Janotti, C.G. Van de Walle, Fundamentals of zinc oxide as a semiconductor // Reports on Progress in Physics, v. 72, 126501, 29p. (2009).
3. K. Ellmer, A. Bikowski, Intrinsic and extrinsic doping of ZnO and ZnO alloys // Journal of Physics D: Applied Physics, v. 49 (41), 413002, p. 1-33 (2016).
4. N. Korsunska, L. Borkovska, L. Khomenkova, T. Sabov, O. Oberemok, O. Dubikovsky, Z. Ya. Zhuchenko, A. Zolotovsky, I.N. Demchenko, Y. Syryanyy, C. Guillaume, C. Labbe, X. Portier , Redistribution of Tb and Eu ions in ZnO films grown on different substrates under thermal annealing and its impact on Tb-Eu energy transfer // Applied Surface Science (2020), doi: https://doi.org/10.1016/j.apsusc.2020.146913.

MASS SPECTROMETRY STUDY OF CLUSTERS FORMATION BETWEEN DIMETHYL SULFOXID AND ANTIBIOTICS

Pashynska V.A.[1], Kosevich M.V.[1], Gomory A.[2]

[1] B. Verkin Institute for Low Temperature Physics and Engineering of the National Academy of Sciences of Ukraine, Nauky Avenue 47, 61103 Kharkiv, Ukraine
[2] Institute of Organic Chemistry of Research Centre for Natural Sciences, Magyar tudosok korutja 2, Budapest, H-1117, Hungary

Drugs delivery and understanding the role of clusters and nanobicomplexes formation in molecular mechanisms of facilitating the transdermal and transmembrane drugs transfer are urgent problems of the modern nanobioscience and molecular medicine. Having a significant experience in the soft ionization mass spectrometry technique usage for study of intermolecular interactions of biologically active compounds with targeting biomolecules [1], we consider the idea that a mechanism of action of agents, facilitating the drug delivery, may include formation of stable noncovalent complexes (formally considered as clusters) with the drug molecules to be transported through the cell membrane. To verify this idea experimentally we performed the electrospray ionization mass spectrometry (ESI MS) study devoted to examining the clusters formation between dimethyl sulfoxide (DMSO), which known as transdermal penetration enhancer in drug delivery [2], and a number of antimicrobial drugs: antibiotics chloramphenicol (CAP), levofloxacin (LEF) and anti-tuberculosis agent cycloserine (CYS).

Formation of stable noncovalent clusters of DMSO with the molecules of antibiotics LEF and CYS in the polar solvent methanol has been revealed by ESI MS probing of binary model systems of the DMSO with the drugs with 1:3 molar ratio, on the basis of recording the protonated DMSO•drug•H^+ complexes in the mass spectra (Fig. 1 and Fig. 2). At the same time the complexation of DMSO with CAP is not revealed in the similar model system DMSO:CAP (1:3 molar ratio), which points to existence of selectivity in DMSO-drug binding.

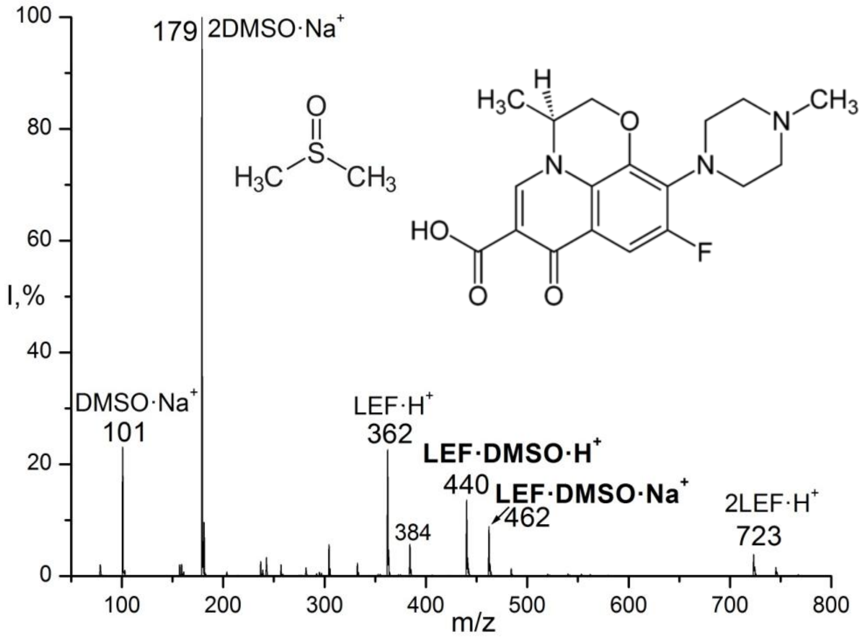

Fig. 1. ESI mass spectrum of the (DMSO+LEF) system (1:3 molar ratio).

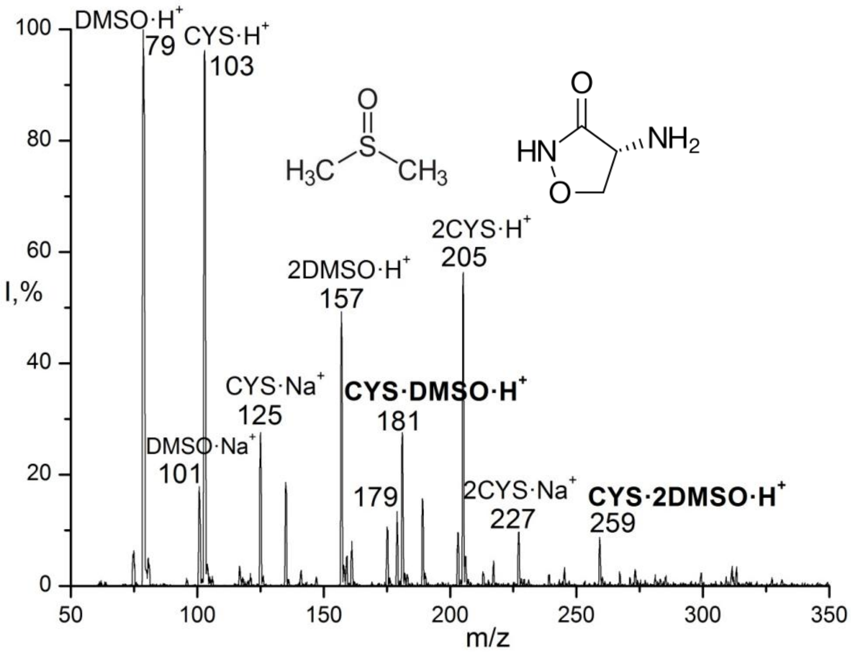

Fig. 2. ESI mass spectrum of the (DMSO+CYS) system (1:3 molar ratio).

The types of clusters observed depend on the composition of the systems. Thus, in the (DMSO+CYS) system preferentially protonated clusters are formed (Fig. 2), including DMSO dimers 2DMSO•H$^+$ and a cluster of the drug with two DMSO molecules CYS•2DMSO•H$^+$. Presence of sodium ions in the (DMSO+LEF) system (Fig. 1) is reflected in domination of the Na$^+$ cation-containing clusters of DMSO - DMSO•Na$^+$, 2DMSO•Na$^+$, and presence of LEF•DMSO•Na$^+$ cluster.

The correlation between the drugs structure features and the noncovalent complexes formation ability with DMSO molecules is discussed.

The results obtained confirm the ESI MS method applicability to study the DMSO complexation with the drugs molecules and biomolecules.

Acknowledgment. Authors acknowledge the Program of cooperation between Ukrainian and Hungarian Academies of Sciences for the financial support of the visits of the scientists from B. Verkin Institute for Low Temperature Physics and Engineering of the NAS of Ukraine to the Research Centre for Natural Sciences in Budapest, where the mass spectrometry experiments were carried out. Grant N 0120U100157 of NAS of Ukraine is appreciated.

1. Pashynska V.A., Kosevich M.V. Biophysical investigations of molecular mechanisms of action of chemotherapeutic agents. 2. Antimicrobial and antimalarial agents (Review) // Biophysical Bulletin, 2012. – V. 42. – P. 28-48.
2. Capriotti K., Capriotti J.A. Dimethyl sulfoxide: history, chemistry, and clinical utility in dermatology // J Clin Aesthet Dermatol., 2012. – V. 5. – N. 9. – P. 24-26.

OPTICAL PROPERTIES OF X-RAY IRRADIATED $(Ga_{0.4}In_{0.6})_2Se_3$ FILMS

Studenyak I.P.[1], **Pop M.M.[1]**, Kranjčec M.[2], Solomon A.M.[3], Suslikov L.M.[1]

[1]Uzhhorod National University, 46, Pidhirna St., 88000 Uzhhorod, Ukraine
[2]University North, 33 J. Križanića St., 42000 Varaždin, Croatia
[3]Institute of Electron Physics, 10 Universytetska St., 88000 Uzhhorod, Ukraine

$(Ga_xIn_{1-x})_2Se_3$ mixed crystals with $0.02<x<0.55$ belong to the defect wurtzite structure with hexagonal symmetry. The main feature of abovementioned semiconductors is the high concentration of vacancies that can form spirals along the optical axis c of the crystal. Alternation of cations and vacancies results in random fluctuations of lattice electric potential which, in turn, affects physical processes in these materials. Here we report on the ellipsometric studies of optical constants, the influence of X-ray irradiation on the optical transmission spectra, Urbach absorption edge parameters and refractive indices in $(Ga_{0.4}In_{0.6})_2Se_3$ films.

$(Ga_{0.4}In_{0.6})_2Se_3$ films were deposited onto a quartz glass substrate by thermal evaporation, their thickness being 2.8 μm. The X-ray diffraction spectra show the $(Ga_{0.4}In_{0.6})_2Se_3$ films to be amorphous. X-ray irradiation was performed for the different exposure times (30, 60 and 120 min) using wideband radiation of Cu-anode X-ray tube with approx 400 W of power applied (33 kV, 13 mA). Spectroscopic ellipsometer Horiba Smart SE was used for the measurements of the optical constants of $(Ga_{0.4}In_{0.6})_2Se_3$ films. Measurements were carried out in the spectrum region from 440 nm to 1000 nm at an incident angle of 70^0. Optical transmission spectra of $(Ga_{0.4}In_{0.6})_2Se_3$ films were measured by using LOMO KSVU-23 grating monochromator.

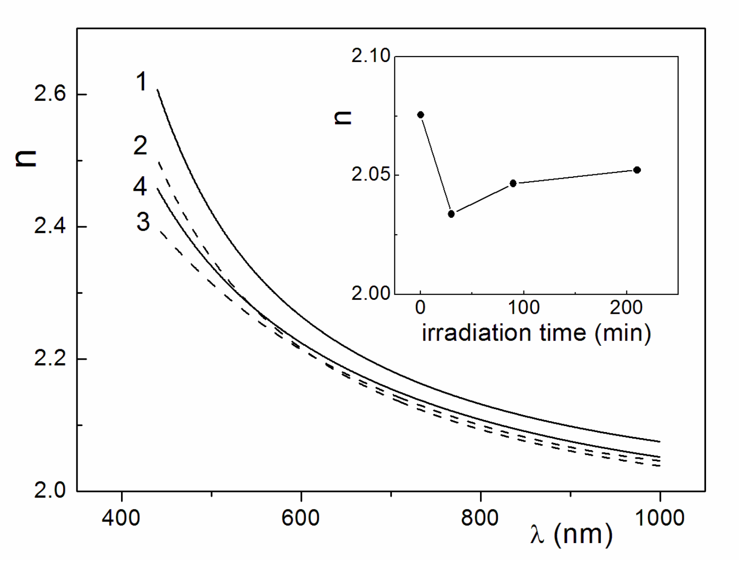

Fig.1. Spectral dependences of refractive indices n for non-irradiated (1) and X-ray irradiated $(Ga_{0.4}In_{0.6})_2Se_3$ films at various irradiation time: (2) 30, (3) 90 and (4) 210 min. The inset shows the dependence of refractive index on X-ray irradiation time.

Dispersion dependences of the refractive index for the X-ray irradiated $(Ga_{0.4}In_{0.6})_2Se_3$ films at various irradiation time are presented in Fig.1. In the transparency region a slight dispersion of the refractive index for the X-ray irradiated $(Ga_{0.4}In_{0.6})_2Se_3$ films is observed, increasing with approaching the optical absorption edge. With irradiation time increase the nonlinear variation of the refractive index in the X-ray irradiated $(Ga_{0.4}In_{0.6})_2Se_3$ films is revealed (inset in Fig.1). During first 30 min of the X-ray irradiation the refractive index decreases from 2.076 to 2.034, and further, with increasing the irradiation time this index increases nonlinearly to the value of 2.052.

Figure 2 presents the optical transmission spectra at various irradiation time at room temperature for X-ray irradiated $(Ga_{0.4}In_{0.6})_2Se_3$ films. During first 30 min of the X-ray irradiation a blue shift of the short-wavelength part of transmission spectra is observed. Then with irradiation time increase up to 90 min the shift of the short-wavelength part of transmission spectra into low-energy region occurs. After that one more small shift into high-energy region is observed (Fig. 2).

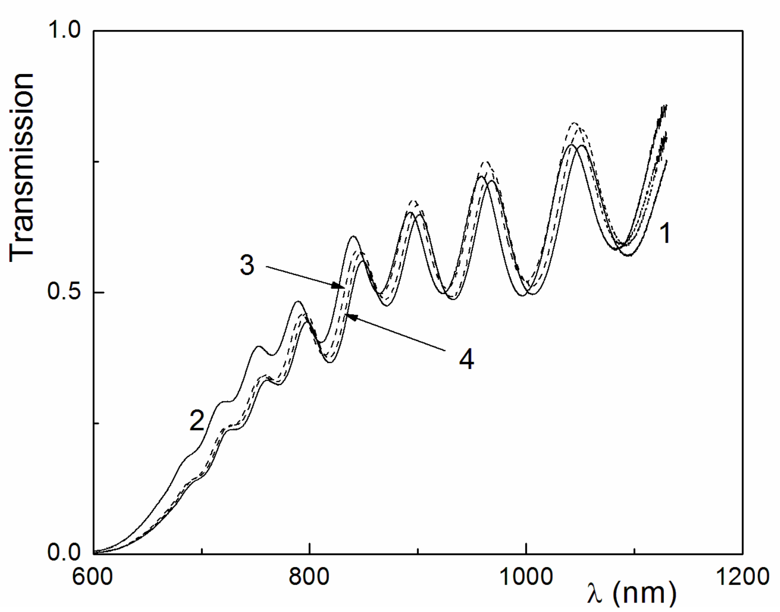

Fig.2. Optical transmission spectra of non-irradiated (1) and X-ray irradiated $(Ga_{0.4}In_{0.6})_2Se_3$ films at various irradiation time: (2) 30, (3) 90 and (4) 210 min.

Spectral dependences of absorption coefficient in the range of their exponential behavior at various irradiation time for X-ray irradiated $(Ga_{0.4}In_{0.6})_2Se_3$ films are analysed. During first 30 min of the X-ray irradiation the increase of the energy pseudogap as well as the decrease of the Urbach energy have been observed. With further irradiation time increase the nonlinear increase of the Urbach energy is revealed. The behavior of energy pseudogap of X-irradiated $(Ga_{0.4}In_{0.6})_2Se_3$ films with irradiation time increase is more complex: with irradiation time increase up to 90 min energy pseudogap value decreases, after that its small increase is observed.

X-RAY AND FESEM STUDY OF MERCURY MODIFIED CRYSTALLIZED SELENIUM FILMS

Rubish V.M.[1], Makar L.I.[1], Mudry S.[2], **Pisak R.P.**[1], Shtablavyi I.[2],
Solomon A.M.[3], Katanova L.[4]

[1]*Institute for Information Recording, NAS of Ukraine,4 , Zamkovi schody St.,*
88000, Uzhgorod Ukraine
[2]*Ivan Franko National University of Lviv, Kyrylo i Mephodiy 8, 79005 L'viv, Ukraine*
[3]*Physics, NAS of Ukraine, 21, Universytetska St., 88017, Uzhgorod, Ukraine*
[4]*Vasyl Stefanyk Precarpathian National University, Ivano-Frankivsk, Ukraine Institute of Electron*

This paper studies the effect of mercury vapor on the structure of crystallized selenium films.

Amorphous Se films with a thickness 700 and 1000 nm were obtained by vacuum evaporation of vitreous selenium from quasi-closed effusion cells on to unheated glass substrates. Crystallization of amorphous Se films was performed by their heating to a temperature of 423 K at a heating rate 6 K/min. Selenium films modification was carried out in special hermetic boxes by keeping them in mercury vapor for 1 hour at 298 K.

Investigations of X-ray diffraction patterns for studied materials were carried out on "ДРОН-3" X-ray diffractometer (λ=1.5418 Å). For the investigations of the microstructure of the samples (modified selenium films) a field emission scanning electron microscopy (FESEM) analysis was performed using a Hitachi S-4100 microscope with a secondary electron detector. The scanning of the sample surface was carried out by electron beam operating at 15 kV and 10μA with the spatial resolution of 10 nm in the secondary electron image regime.

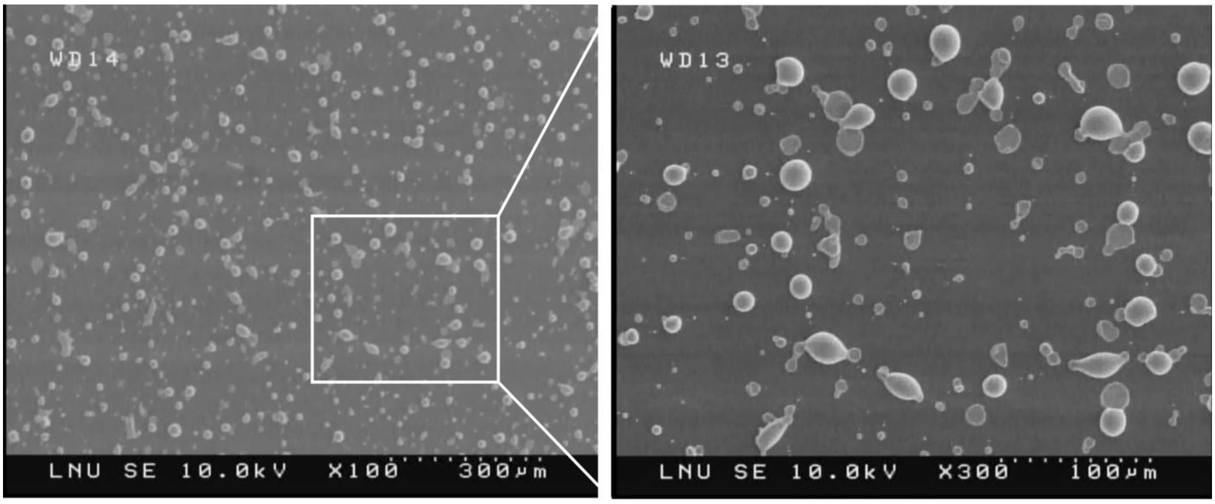

а *б*

Fig. 1. SEM image of the surface of the crystallized Se film (700 nm), after exposure to mercury vapor for 1 hour. Zoom: 100X (a) and 300X (b).

SEM images of the surface of the mercury-modified crystallized selenium film shown in Fig. 1. It shown that a significant part of mercury occur on the surface of the film in the form of individual drops. In this case, there is a certain orderliness due to the structure of trigonal selenium.

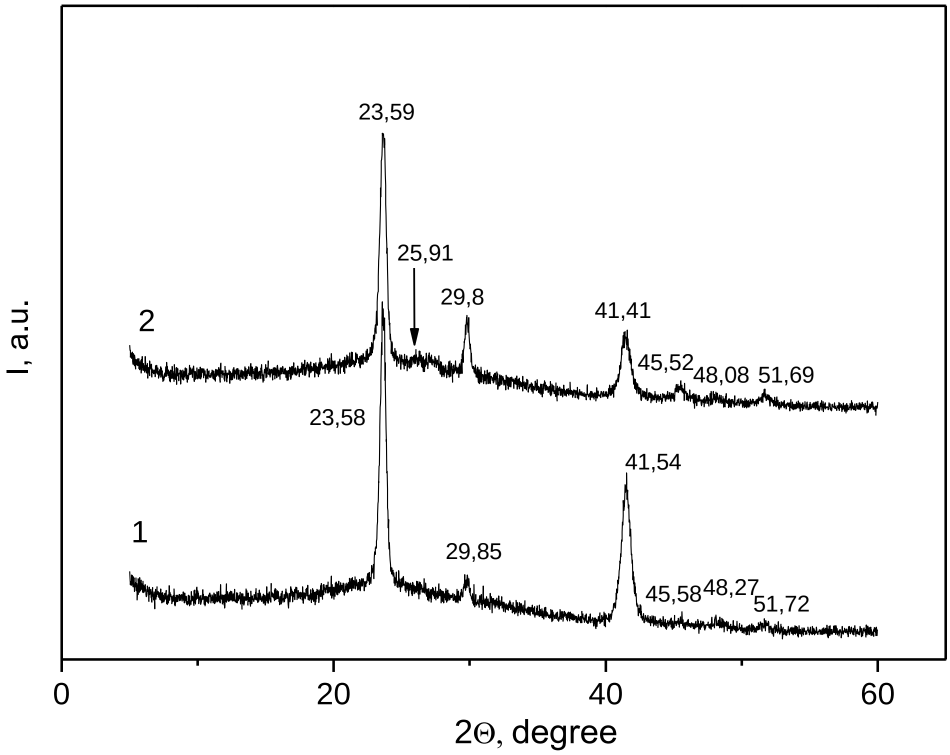

Fig. 2. Diffractograms of crystallized Se film (1000 nm) (1) and modified by mercury vapor for 1 hour crystallized Se film (1000 nm) (2).

However, X-ray studies showed (Fig. 2, curve 2) the presence of the selenium crystalline phase HgSe in the cubic modification in the mercury-modified crystallized films. For comparison, the same figure shows the diffraction pattern of nominally pure crystallized Se film (Fig. 2, curve 1). It is seen that the diffraction pattern of the mercury-modified film shows weak reflexes, the positions of which agree satisfactorily with the position of intense reflexes on the diffractograms of crystalline mercury selenide obtained by the hydrochemical method [1, 2].

The formation mechanism of HgSe crystalline inclusions in crystallized selenium films during their exposure to mercury vapor is discussed.

1. Esmaeili-Zare M., Salavati-Niasari M., Sobhani A. Simple sonochemical synthesis and characterization of HgSe nanoparticles // Ultrasonics Sonochemistry. – 2012. – V.19, – Is. 5, P. 1079-1086.
2. Salavati-Niasari M., Esmaeili-Zare M., Sobhani A. Cubic HgSe nanoparticles: sonochemical synthesis and characterisation // Micro & Nano Letters. – 2012. – V.7, No.12, P.1300-1304.

ELECTRICAL CONDUCTIVITY OF SUPERIONIC CERAMIC BASED ON Ag_7SiS_5I NANOPOWDER

Pogodin A.I., **Shender I.O.**, Filep M.J., Kokhan O.P., Studenyak I.P.

Uzhhorod National University, 46, Pidgirna Str., 88000 Uzhhorod, Ukraine

Ceramic materials are widely used due to their unique properties (structural, mechanical, chemical, functional ones, etc.). High values of elastic modulus, hardness and low thermal expansion of ceramic materials do not limit the scope of their use by engineering problems, but also significantly expand them [1]. Presently, ceramic materials are actively used in medicine, biochemistry, optics, thermoelectricity, electronics and electrochemistry [2]. The argyrodite-type superionic conductors are characterized by high values of ionic conductivity [3] and belong to the promising ceramic materials. The purpose of this study is to obtain and carry out electrical investigation of ceramic samples based on nanocrystalline powders of Ag_7SiS_5I compound.

Synthesis of Ag_7SiS_5I was carried out using elementally silver (99.995%), silicon (99.99997%), sulfur (99.999%) and pre-synthesized binary argentum (I) iodide, taken in stoichiometric ratios in evacuated (0.13 Pa) quartz ampoules. The synthesis of Ag_7SiS_5I included step heating up to 1230 K with exposure at 723 K. The as-synthesized Ag_7SiS_5I was used for the preparation of ceramic samples by solid-phase sintering of pressed nanocrystalline powders.

Nanocrystalline powder was obtained using the planetary ball mill PQ-N04 (average particle size – 150 nm). Pressing of sample was carried out at a pressure of ~ 400 MPa, annealing - at 973 K during 36 hours. Ceramic sample of Ag_7SiS_5I was obtained in the form of disk (d=8 mm, h=3-4 mm). After re-crystallization, the average size of crystallites for ceramic sample is ~ 5 µm.

Measurements of electrical conductivity of ceramic sample based on Ag_7SiS_5I were carried out by impedance spectroscopy method in frequency $10 – 2\times10^6$ Hz and temperature 292-383 K ranges using high-precision LCR meters Keysight E4980A and AT-2818. The amplitude of the alternating current constituted 10 mV. Measurements were carried out by a two-electrode method on blocking (electronic) gold contacts. Gold contacts for measurements were applied by chemical precipitation from solutions.

The ceramic sample of Ag_7SiS_5I compound is characterized by the increase of the total electrical conductivity with increasing frequency (Fig. 1), which is typical for the materials with ionic conductivity in the solid state. Based on the obtained results, the compositional dependence of the total electrical conductivity at a frequency of 100 kHz was constructed.

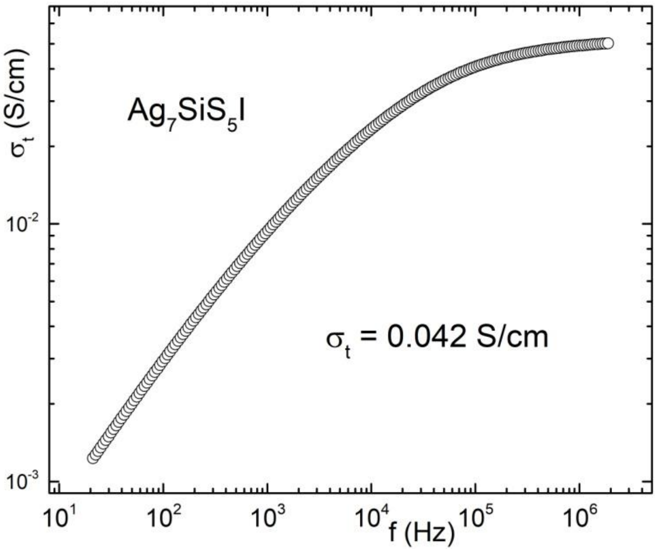

Fig.1. Frequency dependence of total electrical conductivity at temperature 298 K for ceramic sample based on Ag_7SiS_5I.

The detailed studies of frequency behaviour of total electrical conductivity, its separation into ionic and electronic components was performed by a standard approach including the use of electrode equivalent circuits and their analysis on Nyquist plots [4]. The parasitic inductance of the cell (~2×10^{-8} H) was taken into account during the analysis of a sample.

According to the results of the analysis of impedance spectra, the temperature dependences of ionic and electronic components of electrical conductivity of ceramic sample based on Ag_7SiS_5I were studied. Established, that the ionic component of electrical conductivity exceeds the electronic one by more than 60000 times.

The temperature dependences of ionic and electronic components of electrical conductivity in Arrhenius coordinates shows, that they are linear and are described by the Arrhenius law. This testifies to the thermoactivating character of conductivity. Further, the values of activation energy for the ionic and the electronic components of electrical conductivity were determined (Fig. 2).

It should be noted that the prepared ceramic sample based on Ag_7SiS_5I compound is characterized by complex and disordered structure. This is caused, primarily, by the different sizes of crystallites, the nature of their distribution and the complex process of recrystallization during the annealing of samples. Recrystallization process involves the enlargement of crystallites due to solid-phase diffusion processes, and it is accompanied by the emergence of microstructural heterogeneities that contribute to the emergence of micro- and macrodefects. This additionally leads to the appearance of internal voltage of the ceramic material. The combination of the abovementioned features causes corresponding changes not only in the overall electrical conductivity, but also in the ionic and electronic components.

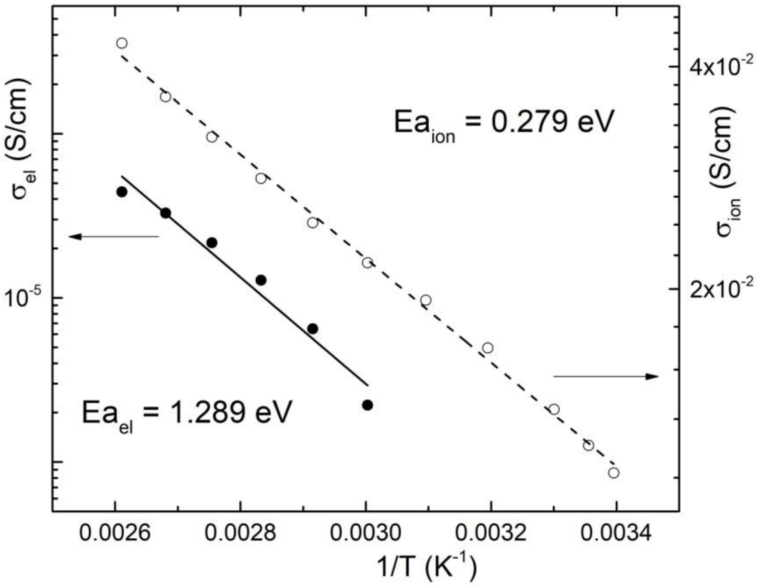

Fig.2. Temperature dependences of ionic and electronic components of electrical conductivity for ceramic sample based on Ag_7SiS_5I.

Thus, Ag_7SiS_5I compound was synthesized and based on it ceramic sample was prepared by pressing and sintering nanocrystalline powder. According to the results of micro-structural analysis, it was established that, as a result of recrystallization, the average size of crystallites for ceramic sample constitutes ~ 5 μm. On the obtained ceramic sample, the total electrical conductivity was measured by impedance spectroscopy method in the frequency range 10 – 2×10^{6} Hz and in 292 – 383 K temperature range. Based on the frequency dependence of total electrical conductivity, corresponding Nyquist plots were build, which were further analyzed using electrode equivalent circuits. Using this approach, the total electrical conductivity was divided into ionic and electronic components. It is shown that the temperature dependences of ionic and electronic components of total electrical conductivity of ceramic sample based on Ag_7SiS_5I are described by Arrhenius law, which confirms the thermoactivation nature of electrical conductivity.

1. Matizamhuka W.R. Advanced ceramics - the new frontier in modern-day technology: Part I // J. S. Afr. Inst. Min. Metall., 2018. – 118. – P. 757-764.
2. Xiao Z., Yu S., Li Y. [et al.]. Materials development and potential applications of transparent ceramics: A review // Mater. Sci. Eng. R. Rep., 2020. – 139. – № 100518.
3. Nilges T., Pfitzner A. A structural differentiation of quaternary copper argirodites: Structure – property relations of high temperature ion conductors // Z. Kristallogr., 2005. – 220. – P. 281–294.
4. Huggins R.A. Simple method to determine electronic and ionic components of the conductivity in mixed conductors a review // Ionics, 2002. – 8. – P. 300-313.

USING MECHANICAL ALLOYING FOR MAX PHASES FORMATION AS PRECURSORS OF GRAPHENE-LIKE CARBIDES OF MXENES TYPE

Solonin Yu.M.[1], **Savyak M.P.**[1], Korablov D.S.[1]

[1]*Frantsevich Institute for Problems of Materials Science, NAS of Ukraine,*
Krzhyzhanovsky str.,3, 03142, Kyiv, Ukraine

MXenes or two-dimensional (2D) transition metal carbides similarly to graphene are finding their way to a wide variety of applications [1]. The utilization of MXenes is promising for energy storage, electromagnetic interference shielding, for development of gas sensors, electrocatalysis and many other uses. MXenes can be obtained by the selective etching of A-element layers from the MAX phases. The treatment, which occurs in hydrofluoric acid, results in a particular layered structure of MXene nanosheets.

MAX phases with the general formula $M_{n+1}AX_n$ (M is a transition metal; A is an element from groups IIIA and IVA as well as P, Si, As, Cd; X is C and/or N) combine the properties of metals and ceramics [2]. MAX phases have a layered hexagonal structure. Such materials possess low density, high values of thermal and electrical conductivity, as well as strength, lowered modulus of elasticity, excellent corrosion resistance in aggressive environments, resistance to high temperature oxidation and thermal shock. Synthesis of MAX phases is carried out mainly by methods of hot isostatic pressing, spark plasma sintering and by the method of self-propagating high-temperature synthesis (SHS). These processes are quite complex and non-technological, while in order to obtain MXenes it is desirable to synthesize MAX phases in the form of a dispersed powder to improve metal etching. One of the techniques to prepare MAX phases is high-energy milling of the initial components in a planetary mill, where MAX phases can be formed owing to the reaction of mechanically activated self-propagating synthesis, as well as at low-temperature processing of pre-activated mixture of the starting components.

As reactants in the present investigation were used titanium powder (Zaporizhzhya Titanium and Magnesium Plant), soot P705, high-purity graphite OSCH-8-4 (GOST 23463-79), crystalline silicon, amorphous silicon semiconductor-grade (Crystal), aluminium powder PA-4, chrome metal X97,5. The milling was performed in argon atmosphere in a planetary mill AIR-015M. The phase composition of the samples was examined by XRD using a diffractometer "DRON 3" (Cu Kα radiation).

By applying the reaction of mechanically activated self-propagating synthesis, Ti_3SiC_2, Ti_3AlC_2, and Ti_2AlC MAX phases were synthesized. The phases Ti_3AlC_2, Ti_2AlC, and Cr_2AlC were obtained by low-temperature treatment of the pre-activated mechanical mixture.

1. Verger L., Xu C., Natu V. [et al.]. Overview of the synthesis of MXenes and other ultrathin 2D transition metal carbides and nitrides // Curr. Opin. Solid State Mater. Sci., 2019. – V. 23. – N. 3. – P. 149-163.
2. Sokol M., Natu V., Kota S. [et al.]. On the chemical diversity of the MAX phases // Trends Chem, 2019. – V. 1. – N. 2. – P. 210-223.

MODEL CALCULATIONS OF THE LAWS OF DISPERSION OF THE PHONON SPECTRUM OF BaTiO$_3$ CRYSTALS WITH PARTIAL INHABITANCE OF DIFFERENT CRYSTALLOGRAPHIC POSITIONS

I.M. Shkyrta[1], I.I. Nebola[2]

[1] *Mukachevo State University, 89600, Mukachevo, Uzhhorodska St., 26*
e-mail: I.Shkyrta@mail.msu.edu.ua
[2] *Uzhhorod National University, 88000, Uzhhorod, Voloshin St., 54*
e-mail: ivan.nebola@uzhnu.edu.ua

The study of the dynamic properties of real crystals and systems of solid solutions involves, along with a detailed analysis of experimental data, theoretical analysis. The inability in some cases to quantify their lattice dynamics analytically stimulates the development of numerical calculation methods in the framework of correct microscopic models.

Numerical modeling of phonon spectra opens up prospects for predicting the physical properties of new synthesized materials, which is especially important in studying the lattice dynamics of disordered objects with various disturbances in both structure and chemical composition.

The compositional features of the realization of complex crystal structures by the mechanism of filling with translational atoms and vacancies translationally equivalent positions given by the basis of the protocrystal are covered by the concept of superspace symmetry. At the same time various combinations of bases of a protocrystal and a real crystal (system) together with all possible options of compositional filling of crystallographic positions can be considered. The use of a complete set of modulation vectors allows to determine the amplitudes of mass modulation functions and on their basis to generate a generalized dynamic matrix of a real physical object, given as a superposition of dynamic protocrystal matrices defined at different points of the Brillouin zone. the mass perturbation matrix described by the amplitudes of the mass modulation functions [1,2].

A number of families of crystal structures are characterized by a combination of several crystallographic orbits with their partial filling with atoms of the same variety. Consider this situation based on the model of crystal structures of the perovskite family, which is characterized by equidistant arrangement of different atoms. In the concept of superspatial symmetry, the class of perovskite can be considered as a natural $(2a\times 2a\times 2a)-$lattice [1].

Since we are interested in the analysis of the situation with the partial filling of different crystallographic orbits with atoms of the same variety, we describe the structure of perovskite in the basis of the $(4a\times 4a\times 4a)-$superlattice, introducing a number of additional crystallographic orbits. Therefore, in addition to the composite superlattice obtained by modulating a monoatomic simple cubic lattice (PC) using 8 modulation vectors [1] for a $(2a\times 2a\times 2a)-$superlattice, we consider a modulated monoatomic PC using 64 modulation vectors at the base of the $(2a\times 2a\times 2a)-$superlattice.

The solution of the matrix equation with respect to $\omega^2(k)$ [2] allows to determine the dispersion dependences of the phonon spectrum, and to take into account different variants of compositional filling - to trace their genesis.

The dispersion curves of the phonon spectrum of complex crystals of the structural type of perovskite in the concept of superspatial symmetry are defined as solutions of the matrix equation under the condition of zero equality of the determinant of the form:

$$\left|D_{\alpha\beta}(k+q_i)-\omega^2\delta_{\alpha\beta}\delta_{ij}-\omega^2\rho_{(i-j)}\delta_{\alpha\beta}\right|=0, \qquad (1)$$

where $D_{\alpha\beta}(k+q_i)$ the dynamic matrices of a single-atomic protocrystal (PC) are defined at the $(k+q_i)$ points of SB for the crystal $BaTiO_3$: $(i=1,...,8)$ in the $(2a\times 2a\times 2a)-$basis ,

$(i=1,\ldots,64)-$ in the basis $(4a\times4a\times4a)-$superlattices, respectively, $\rho_{(i-j)}=\rho_i(q_i,\Delta^*b^*_{ij})$ the amplitudes of the mass modulation function given for modulation vectors (q_i-q_j), $\alpha,\beta-x,y,z$, $k-$wave vector, q_i-modulation vectors [3].

Dynamic matrices of the protocrystal $D_{\alpha\beta}(k+q_i)$ are determined from the relation:

$$D_{\alpha\beta}(k+q_i)=\sum_{(n\neq0)}\alpha_n\frac{n_\alpha n_\beta}{n^2}\left(1-e^{i(k+q_i)n}\right), \tag{2}$$

where α_n the force constant between the atom in position (0,0,0) and n neighbor, n_α, n_β the projection of the vector $\vec{n}$ on the axis α,β.

The calculation of the frequencies of phonon modes can be obtained by equating to zero the determinant written in a slightly different form [3]:

$$\left|\rho_j^{(D)}(k-q_i,\Delta^*b^*_{ij})-\omega^2\delta_{\alpha\beta}\delta_{ij}-\omega^2\rho_{(i-j)}\delta_{\alpha\beta}\right|=0, \tag{3}$$

where $\rho_j^{(D)}(k-q_i,\Delta^*b^*_{ij})=\rho_j^{(D)}$ the amplitudes of the modulation functions of the DM of a complex crystal.

Solving a system of equations

$$D^{r_k}_{\alpha\beta}(k+q_i)=\sum_{j=1}^{n}\rho_j^{(D)}(k-q_i,\Delta^*b^*_{ij})e^{iq_jr_k} \tag{4}$$

with respect to the amplitudes of the modulation functions $\rho_j^{(D)}$ of the dynamic matrix, we obtain solutions in the form of a superposition of dynamic matrices defined for each of the n positions: for $(2a\times2a\times2a)-$superstructures n = *8*; for $(4a\times4a\times4a)-$superstructures n = *64*.

A generalized description of complex cubic crystals with a $(sa\times sa\times sa)-$superlattice is laid down in the $(3+d)-$dimensional bases [1]:

$$\begin{array}{ll}
a_1=(a,0,0,-b/s,0,0); & a_1^*=(2\pi/a,0,0,0,0,0);\\
a_2=(0,a,0,\,0,-b/s,0); & a_2^*=(0,2\pi/a,0,0,0,0);\\
a_3=(0,0,a,\,0,0,-b/s); & a_3^*=(0,0,2\pi/a,0,0,0);\\
a_4=(0,0,0,b,0,0); & a_4^*=(2\pi/sa,0,0,\,2\pi/b,0,0);\\
a_5=(0,0,0,0,b,0); & a_5^*=(0,2\pi/sa,0,\,0,2\pi/b,0);\\
a_6=(0,0,a,0,0,b) & a_6^*=(0,0,2\pi/sa,\,0,0,2\pi/b).
\end{array} \tag{5}$$

Note that the dimensional description of crystals of the perovskite type with a $(2a\times2a\times2a)-$superlattice covers a set of eight modulation vectors, which can be decomposed into 4 stars: 1. $\{(0,0,0)\}-$dimension one; 2. $\{(\pi/a,\pi/a,0)\}-$dimension three; 3. $\{(\pi/a,\pi/a,\pi/a)\}-$dimension one; 4. $\{(\pi/a,0,0)\}-$dimension three. During the transition from the structure of the crystal $BaTiO_3$ with a $(2a\times2a\times2a)-$superlattice to the structure of the crystal $BaTiO_3$ with a $(4a\times4a\times4a)-$superlattice (Fig. 1), the volume of the straight lattice increases 8 times, and the volume of the Brillouin zone decreases 8 times (Fig. 2).

Based on the basis of the PC, the complete set of 64 combinations of modulation vectors can be decomposed into 10 stars [3]: 1. $\{(0,0,0)\}-$dimension one; 2. $\{(\pi/2a,0,0)\}-$dimension six; 3. $\{(\pi/a,0,0)\}-$dimension three; 4. $\{(\pi/a,\pi/a,\pi/a)\}-$dimension one; 5. $\{(\pi/a,\pi/a,0)\}-$dimension three; 6. $\{(\pi/2a,\pi/2a,\pi/2a)\}-$dimension eight; 7. $\{(\pi/2a,\pi/a,\pi/a)\}-$dimension six; 8. $\{(\pi/2a,\pi/2a,0)\}-$dimension twelve; 9. $\{(\pi/2a,\pi/2a,\pi/a)\}-$dimension twelve; 10. $\{(\pi/2a,\pi/a,0)\}-$dimension twelve.

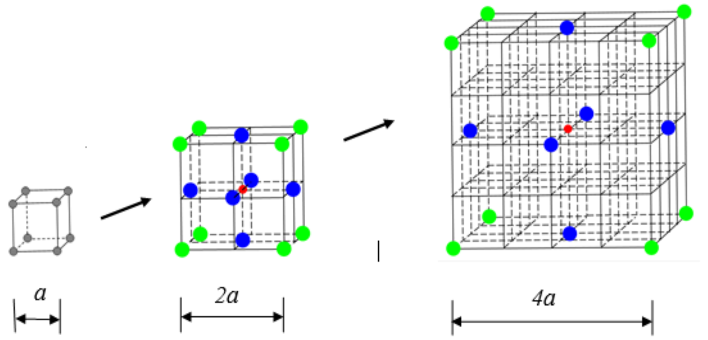

a) б)

Fig.1. Crystal structure $BaTiO_3$:
a) with $(2a\times2a\times2a)$-superlattice;
b) with $(4a\times4a\times4a)$ – lattice
● - Ba, ● - Ti, ● - O

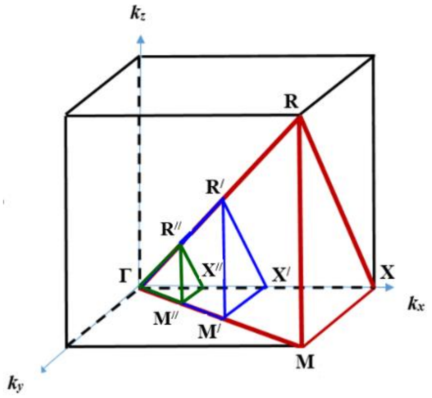

Fig..2. Transformation of PC ZB with period *a* (red lines) during the transition to $(2a\times2a\times2a)$–sublattice (blue lines), to $(4a\times4a\times4a)$ – supertrate (green lines).

In Fig.3 shows the model phonon spectrum of a $BaTiO_3$ crystal with a $(2a\times2a\times2a)$ superlattice calculated in the Maple software environment in the equidistant force field approximation along the X-Γ-M-R-Γ lines, taking into account the interaction within the first six coordination groups for an ideal structure (a) and for the case of changing the position of one oxygen atom from the position of $(0,a,0)$ to $(a,0,a)$, ie a structure with two partially filled orbits (b).

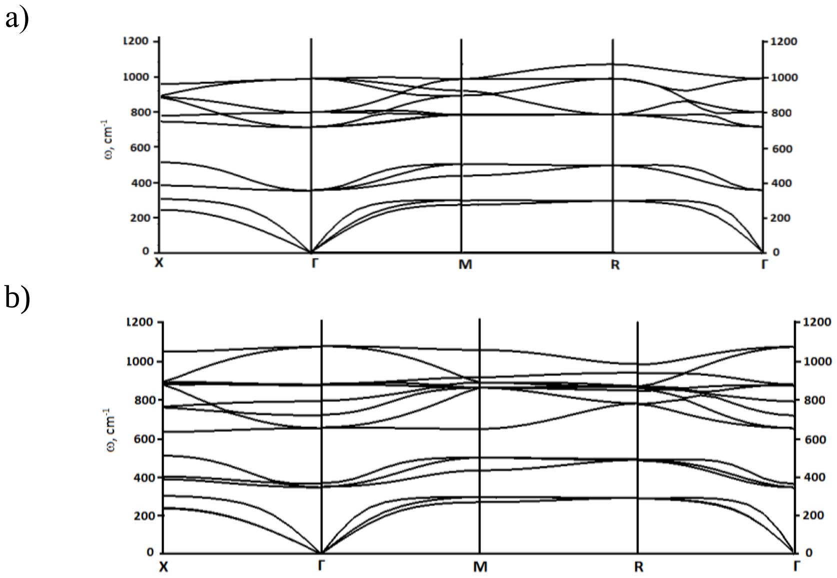

Fig.3. Model phonon spectrum of a $BaTiO_3$ crystal with a $(2a\times2a\times2a)$ superlattice ($\alpha_1=220$ N/m, $\alpha_2=110.5$ N/m, $\alpha_3=10$ N/m, $\alpha_4=5$ N/m, $\alpha_5=3.5$ N/m, $\alpha_6=2$ N/m):
a) ideal structure; b) a structure with two partially filled orbits of oxygen atoms.

Figure 4 shows the change of dispersion dependences in the direction of Γ-R SB in the $(4a\times4a\times4a)$ metric when inhabited by oxygen atoms of the orbit $(2a,2a,0)$ (ideal structure) (a), partial population of orbits (two atoms are localized in three-fold orbit $(2a,2a,0)$, and one in six-fold orbit $(2a,2a,a)$) (b) and (two atoms are localized in a triple orbit $(2a,2a,0)$, and one in a twelve-fold orbit $(2a,a,0)$) (c).

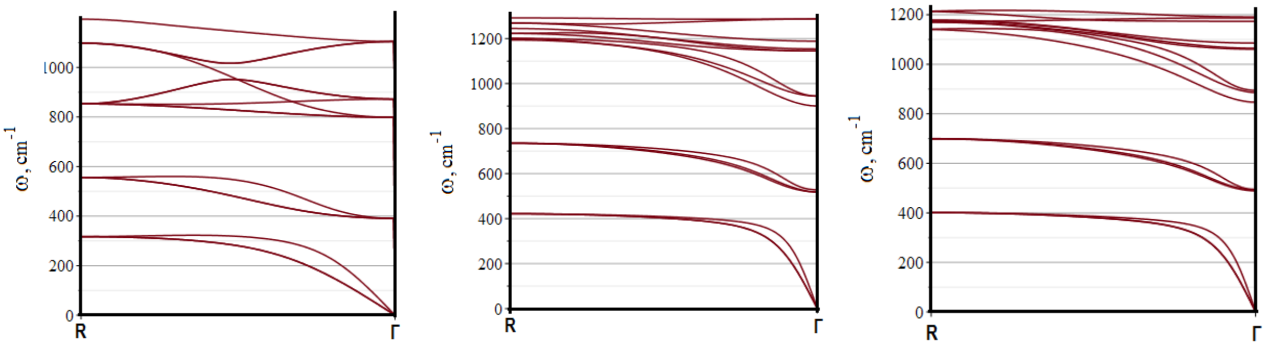

a) b) c)

Fig.4. Dispersion dependences of the phonon spectrum for the Γ-R direction of the $BaTiO_3$ crystal in the metric $(4a \times 4a \times 4a)$

a) ideal structure; b) localization of one oxygen atom in the orbit $(2a, 2a, a)$;

c) localization of one oxygen atom in the position of the orbit $(2a, a, 0)$.

The studies showed a slight rearrangement of the phonon spectrum of the $BaTiO_3$ crystal when the population changes between equivalent orbits in the $(2a \times 2a \times 2a)$ metric and a very significant rearrangement when the population changes between orbits of different multiplicity in the $(4a \times 4a \times 4a)$ metric. Note that the model calculations in the $(4a \times 4a \times 4a)$ metric are associated with the inclusion in the consideration of additional model power constants that specify the force interaction at additional distances. In the case of $(2a \times 2a \times 2a)$ metrics, additional power constants do not arise, because they are all included in the consideration of the ideal structure. Interestingly, there is almost no effect on the implementation of the low-frequency part of the spectrum in the $(4a \times 4a \times 4a)$ metric and a significant adjustment of the high-frequency branches of the phonon spectrum. In addition, the modeling in the $(4a \times 4a \times 4a)$ metric is associated with a significantly smaller value of the distance of the "jump" of oxygen atoms between the considered orbits.

1. Nebola I.I. Genezis struktury` i kolebatel`ny`kh spektrov kristallov s sverkhreshetkoj / I.I. Nebola, A.F. Ivanyas, V.Ya. Kindrat // FTT. – 1993. – V.35, No 7. – S. 1852 – 1866.
2. Ansel`m A. I. Vvedenie v teoriyu poluprovodnikov / A. I. Ansel`m. – M.: Nauka, 1978. – 616 s.
3. Shkyrta I. M. Dosli`dzhennya dispersi`jnikh zalezhnostej fononnogo spektru skladnikh kubi`chnikh kristali`v v konczepczi`yi nadprostorovoyi simetri`yi : dis.: 01.04.10 – Fi`zika napi`vprovi`dniki`v i` di`elektriki`v/ Shkyrta Ihor Mykolajovych – Uzhgorod, 2019. – 200 s.

INFLUENCE OF MONOMER STRUCTURES ON THE MORPHOLOGIES AND OPTICAL PROPERTIES OF J-AGGREGATES

Alexander Sorokin[1], Roman Grynyov[2], Irina Ropakova[1], Igor Borovoy[1], Svetlana Yefimova[1], Yuri Malyukin [1]

[1] Institute for Scintillation Materials of NAS of Ukraine, 60 Nauky ave., 61072 Kharkiv, Ukraine
[2] Ariel University, Natural Science Faculty, Physics Department, P.O.B. 3, 407000, Ariel, Israel
e-mail: sorokin@isma.kharkov.ua

Highly-ordered molecular aggregates of some organic dyes, typically, cyanines, which called J-aggregates, are a bright example of supramolecular systems due to their unique optical properties governing by excitonic nature. A specific feature of J-aggregates is an appearance of a new excitonic band (J-band) in the dye absorption spectrum, which is red-shifted with respect to the monomer one. Although, depending on the type of monomer packing in the aggregate, a blue-shifted band (called H-band) or both J- and H-bands could appear. J-aggregates spectral properties differ strongly from that of monomers and are dependent on the exciton delocalization length and, hence, the aggregate structure. The intermolecular interactions between dye molecules forming J-aggregates are rather weak and caused mainly by Van der Waals and hydrophobic forces, so the structure of aggregates strongly depends on the dye molecule structure, used solvents or their mixtures, additives, templates, etc..

In present report, we have shown the correlation between the monomer structures and the morphologies and optical properties of corresponding J-aggregates. Namely, we used the derivatives of two cyanine molecules, such as pseudoisocyanine (PIC, Fig. 1a and 1b) and 5,5’,6,6’-tetrachlorobenzimidacarbocyanine (TBC, Fig. 1c and 1c) to show how the changing in the lengths of alkyl tails of the dyes influence on the properties of PIC and TBC J-aggregates, respectively.

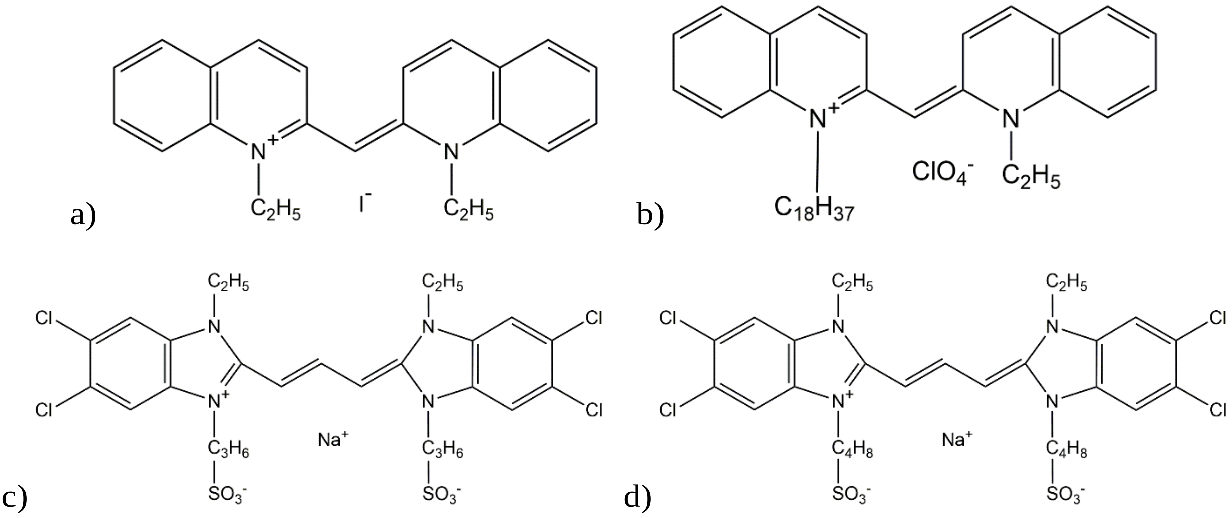

Fig. 1 Structural formula of PIC derivatives: a) PIC and b) amphi-PIC, and TBC derivatives: c) BIC and d) TDBC.

We will start the analysis for PIC derivatives, namely PIC (1,1’-diethyl-2,2’-cyanine iodide, Fig. 1a) and its amphiphilic analogue amphi-PIC (1-methyl-1’-octadecyl-2,2’-cyanine perchlorate, Fig. 1b). These dyes have the same chromophore parts (cyanine backbone), so their optical properties in the monomeric state are very similar. But the presence of different alkyl tails (two short in the case of PIC (Fig. 1a) and one very long and one short in the case of amphi-PIC (Fig. 1b)) lead to the formation in aqueous solutions J-aggregates with different structures. This is primarily due to the hydrophobic interaction. As amphi-PIC is amphiphilic, the same laws govern its aggregation as micelle formation of surfactants. As a result, the J-aggregate morphologies of PIC (Fig. 2a) and amphi-PIC (Fig. 2b) is significantly different. PIC J-aggregates (Fig. 2a) have a thread-like one-dimensional structure with a diameter of "threads" of 10 nm and more and a length of tens and hundreds of microns [1, 2]. Amphi-PIC J-aggregates have a cylindrical morphology with a cylinder diameter of ~ 4 nm and a length of up to hundreds of nanometers (Fig. 2b) [3]. It was found that the basic structural unit of these J-aggregates is a ring consisting of approximately 30 molecules, and along which the exciton excitation is localized. In solution, such rings gather into cylindrical structures due to hydrophobic interaction [3].

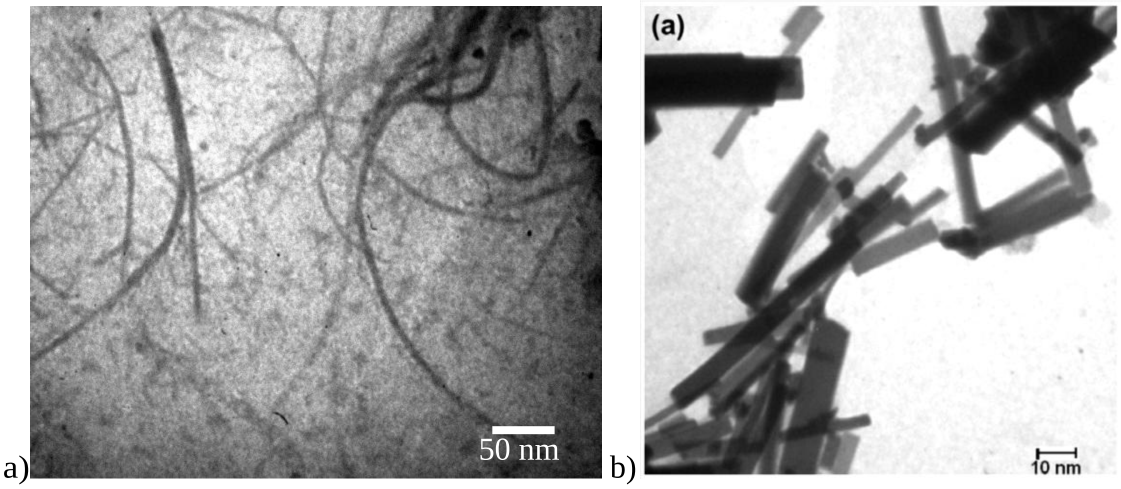

Fig. 2 TEM images of J-aggregates of a) PIC and b) amphi-PIC

The different structure of PIC and amphi-PIC J-aggregates is the reason for the significant discrepancy between their exciton characteristics. Thus, if the J-band in the case of PIC dye is one of the narrowest ($\Delta\nu_{FWHM}$ = 130 cm^{-1}) in the family of J-aggregates, then the J-band in the case of amphi-PIC dye, on the contrary, one of the widest ($\Delta\nu_{FWHM}$ = 650 cm^{-1}) (Fig. 3).

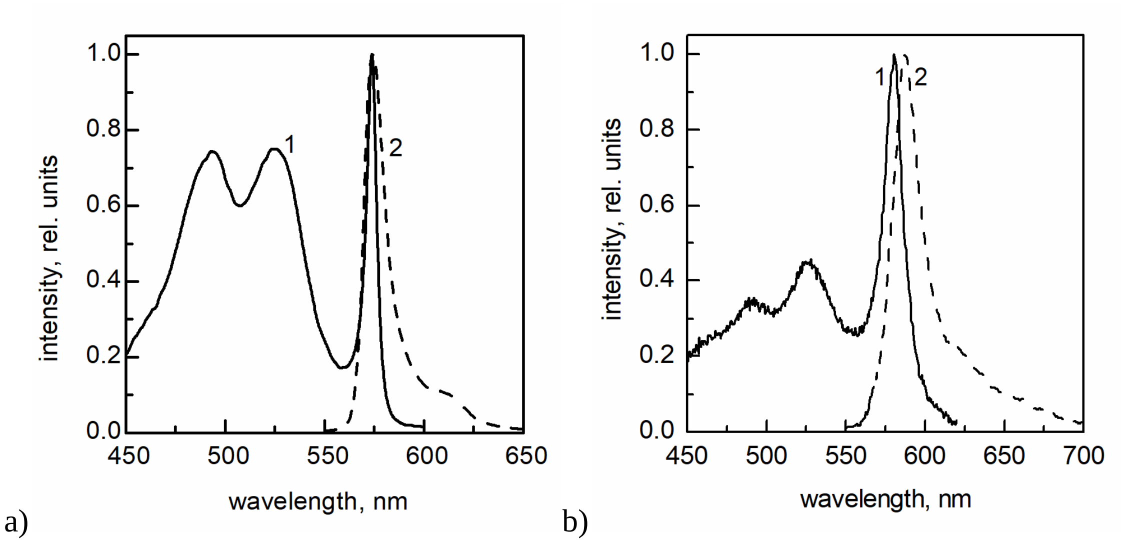

Fig. 3. The absorption (1) and luminescence (2, λ_{exc} = 530 nm) spectra of PIC (a) and amphi-PIC (b) J-aggregates in aqueous solutions.

The spectral position of the J-bands also differs: λ_{max}^{PIC} = 574 nm and $\lambda_{max}^{amphi\text{-}PIC}$ = 580 nm (Fig. 3). The significant difference in the width of J-bands for J-aggregates PIC and amphi-PIC is a consequence of different degrees of static disorder, which defines the length of exciton delocalization: for PIC J-aggregates $N_{del}^{PIC} \sim 86$ [1, 2] and for J-aggregates amphi-PIC J-aggregates $N_{del}^{amphi\text{-}PIC} \sim 4$ [3].

The luminescent characteristics of J-aggregates PIC and amphi-PIC also differ significantly, in particular, the lifetimes and quantum luminescence yields. For PIC J-aggregates the luminescence decay curve is monoexponential with a lifetime $\tau^{PIC} \sim 1.4$ ns, and for amphi-PIC J-aggregates the lifetime is very short $\tau^{amphi\text{-}PIC} \sim 35$ ps. As a result, PIC J- aggregates have a high luminescence quantum yield $\eta^{PIC} \sim 0.38$, and amphi-PIC J-aggregates, respectively, have a very low quantum yield $\eta^{amphi\text{-}PIC} \sim 0.003$.

Thus, in case of the PIC derivatives, the very long alkyl tail of amphi-PIC causes strong difference in the morphology and, hence, the optical properties of PIC and amphi-PIC J-aggregates.

However, for the other pair of the dyes, namely BIC (1,1'-disulfopropyl-3,3'-diethyl-5,5',6,6'-tetrachloro-benzimidazolylcarbocyanine sodium salt, Fig. 1c) and TDBC (1,1'-disulfobutyl-3,3'-diethyl-5,5',6,6'-tetrachlorobenzimidazolylcarbo-cyanine sodium salt, Fig. 1d), the difference in the alkyl chains is minor. Indeed, the alkyl tails of TDBC (Fig. 1c) are longer only by one group comparing with those of BIC (Fig. 1d). Despite, we have found that the morphologies and spectral properties of BIC and TDBC J-aggregates are strongly different [4].

For BIC J-aggregates, two species were found: spherical ones with the diameter within 20 – 100 nm and thick rod-like ones with the diameter of 100 nm and larger and length up to several tens of microns (Fig. 4a). Taking into account brunching structures found in some SEM images (Figure 4c) and a quite large dye concentration (10^{-3} M), we could assume that the large structures appeared to be the agglomerated ones. Contrary to BIC J-aggregates, TDBC J-aggregates exhibit rod-like structure with the rod diameter ranging within 30 – 100 nm and length up to several tens of microns (Fig. 4b). While thinner rods are rather straight, some of the thick rods are twisted around their axis (Fig. 4b). We suppose TDBC J-aggregates to be single-wall tubes, which form bundles due to the agglomeration process.

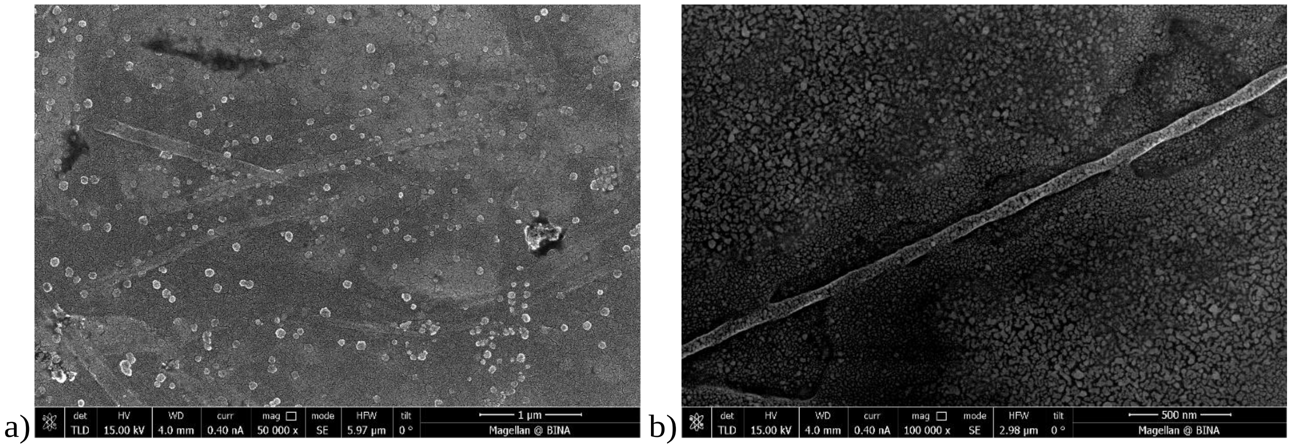

Fig. 4. XHR-SEM images of BIC (a) and TDBC (b) J-aggregates.

The optical spectra of BIC and TDBC J-aggregates are also revealing remarkable differences (Fig. 5). First, the J-bands have different shifts relatively to the monomer band and different widths: for TDBC J-aggregates λ_{max}^{J} = 584.5 nm and $\Delta\nu_{FWHM}$ = 360 cm^{-1}, while for BIC J-aggregates, λ_{max}^{J} = 592.5 nm and $\Delta\nu_{FWHM}$ = 560 cm^{-1} (Fig. 5a) [4]. Contrary to BIC J-aggregates, for TDBC J-aggregates the low-intense monomer band (λ_{max}^{H2O} = 514 nm) is clearly seen (Fig. 5a). As for BIC J-aggregates the J-band is wider, its exciton delocalization length (N_{del}^{BIC} ~ 5) is about triple less as compared to that for TDBC J-aggregates (N_{del}^{TDBC} ~ 14) [4].

Luminescence spectra of BIC and TDBC J-aggregates are very similar except the corresponding spectral positions: λ_{max} = 588.5 nm for TDBC J-aggregates and λ_{max} = 598 nm for BIC J-aggregates (Fig. 5b) [4]. At the same time, the intensity of BIC J-aggregates fluorescence is smaller (not shown) that points to smaller fluorescence quantum yield. Indeed, the fluorescence quantum yield for TDBC J-aggregates was estimated to be η^{TDBC} ~ 0.31, whereas for BIC J-aggregates this value is twice as lower η^{BIC} ~ 0.16 [4]. Such difference should be reflected in the lifetimes also. Indeed, the lifetime for BIC J-aggregates (τ^{BIC} ~ 100 ps) is about twice as higher as compared to that for TDBC J-aggregates (τ^{TDBC} ~ 60 ps) [4].

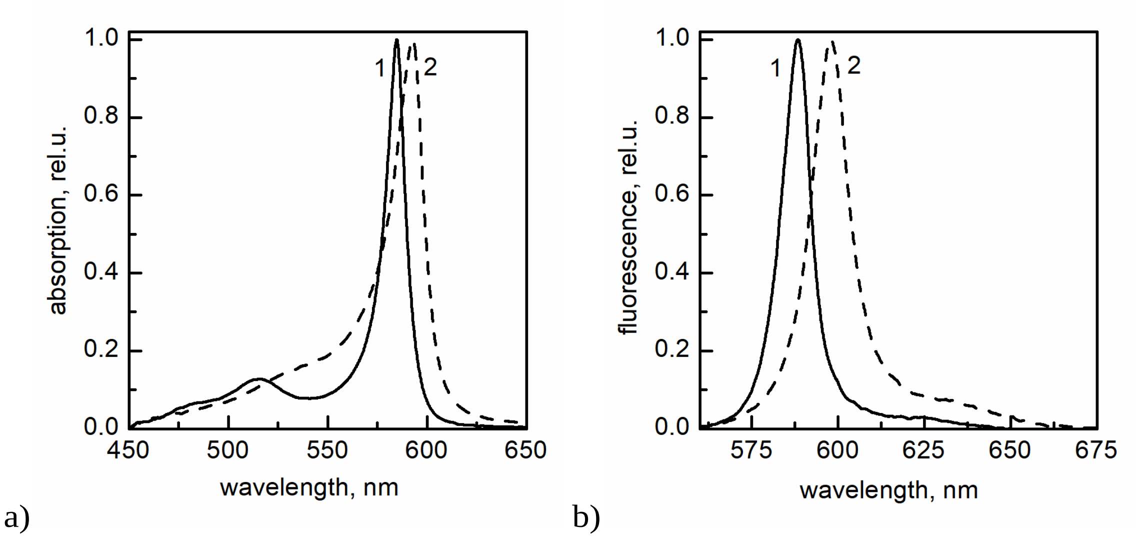

Fig. 5. Absorption (a) and fluorescence (b, λ_{exc} = 530 nm) spectra of TDBC (1) and BIC (2) J-aggregates in water (C = 10^{-4} M).

Thus, despite the minor structural difference between BIC and TDBC monomers, their J-aggregates reveal the significant difference in morphologies and, hence, in optical properties.

1. Lebedenko A. N. Pseudoisocyanine j-aggregate to optical waveguiding crystallite transition: microscopic and microspectroscopic exploration / A. N. Lebedenko, G. Y. Guralchuk, A. V. Sorokin[et al.] // Journal of Physical Chemistry B. — 2006. — Vol. 110, No. 36. — P. 17772–17775.
2. Guralchuk G. Y. Anomalous surfactant-induced enhancement of luminescence quantum yield of cyanine dye j-aggregates / G. Y. Guralchuk, I. K. Katrunov, R. S. Grynyov[et al.] // The Journal of Physical Chemistry C. — 2008. — Vol. 112, No. 38. — P. 14762–14768.
3. Sorokin A. V. Control of exciton migration efficiency in disordered j-aggregates / A. V. Sorokin, I. I. Filimonova, R. S. Grynyov[et al.] // Journal of Physical Chemistry C. — 2010. — Vol. 114, No. 2. — P. 1299–1305.
4. Sorokin A. V. Strong difference between optical properties and morphologies for j-aggregates of similar cyanine dyes / A. V. Sorokin, I. Y. Ropakova, R. S. Grynyov[et al.] // Dyes and Pigments. — 2018. — Vol. 152. — P. 49–53.

COOLING OF SUPERHEATED SURFACES BY NANOFLUIDS AND IT SIMULATION BY CFD.

Eugene Strativnov

The Gas Institute of NAS of Ukraine, 39, Degtyarivska str., 03113, Kyiv, Ukraine
e-mail: estrativnov@gmail.com

Recently, using of nanofluids (NFs) as a coolant in various fields of science and technology is rapidly developing. Because of the physical properties of the NFs differ significantly from the "classical" coolants (various liquids without adding of solid particles). It is why scientists of a world strive to find out as soon as possible the operation mechanism of NFs under various conditions of heat transfer. There are many scientific approaches and methods for studying this problem. One of these methods is computer simulation of physical processes by computational fluid dynamics (CFD). The undoubted advantage of this practice is the ability of accurately study physical phenomena at the macro and micro levels, in contrast to the technique of full-scale experiment, due to the impossibility of making the appropriate measurements in real conditions. However, computer simulation without verification of its main results by real experiment can lead to incorrect conclusions. Therefore, the main stages of a water boiling simulated in various conditions and compared with experiment and the available literature data.

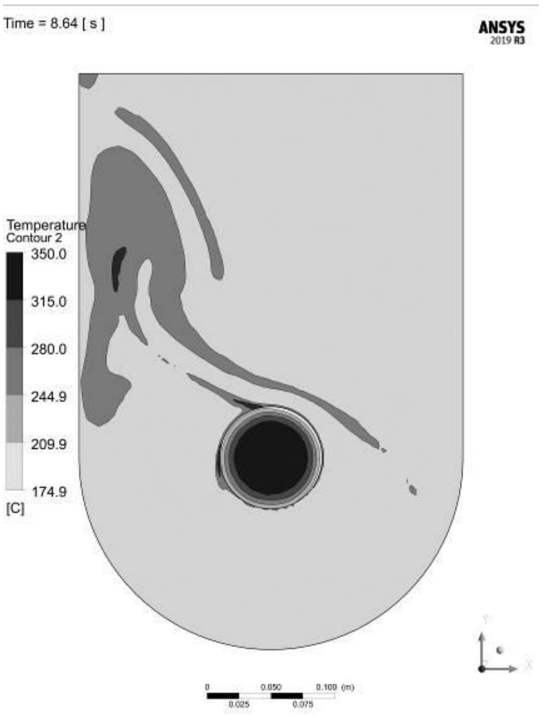

Fig. 1. CFD simulation of cooling an overheated body process.

This work includes such main points: Simulation of water heating process in conditions of natural convection (boundary conditions of the first and second kind) taking into account boiling, evaporation and condensation. Simulation of sedimentation of solids (nanoparticles: Al_2O_3 particles 70…300 nm) in still water. Simulation of cooling preheated solid body by water and NFs under natural convection conditions (third and fourth boundary conditions) taking into account boiling, evaporation, and condensation in the liquid phase and the temperature gradient in the solid. This work should be regarded as a don't completed study; it is simply a timid attempt to come a little closer to understanding the mechanism of working of NFs on the physical level.

MODIFICATION OF TEXTILE MATERIALS FOR MEDICAL PURPOSE BY NATURAL NANOTUBES

Suprun N.P[1]., Ivanov I.O.,[1,]Brichka A.V.[2], Redko Ya.V.[1]

[1]Kyiv National University of Technologies and Design (KNUTD).
Nemyrovycha-Danchenka Street, 2 Kyiv 01011, Ukraine
[2]Chuiko Institute of Surface Chemistry. National Academy of Sciences of
17 General Naumov Street, Kyiv 03164, Ukraine

Ultraviolet radiation, which is widely used in medicine. along with the positive effect, creates a number of dangers for the human body. Therefore, the problem of developing reliable, affordable and comfortable means of protection is relevant for both staff and patients. There are numerous researches aimed at creating textiles that protect against the destructive effects of ultraviolet radiation. Most often this is achieved by modification by UV absorbers, but such modification can worse the properties of materials, also used methods of processing can be not environmentally friendly. One of the perspective method of textile surface functionalization to provide protective properties against UV radiation may be the use of nanocrystalline materials, which include halositic aluminosilicate nanotubes, which can control the functional characteristics of the desired end product [1]. Aluminosilicate haloisite nanotubes (AHN) are natural materials similar to kaolinite. Nanotubes are biocompatible, resistant to biodegradation, suitable for use in biomedical materials and sanitary products [2,3], have the effect of "diffusion pump".

To verify the possibility of such functionalization was developed environmentally friendly method of nanotreating of viscose knitted fabric, which is often used as hospital linen, by aluminosilicate halositic nanotubes. Such AHN, which were synthesized by arc discharge at the Institute of Surface Chemistry, are characterized by a narrow diameter distribution, the average value of which is 1.4 ± 0.2 nm. The obtained nanomaterials were studied by a set of physicochemical methods. UV-type spectra of materials were recorded on a UV-VIS-NIR-spectrophotometer UV-3600, Shimadzu in the transmission mode in the range of 220-4000 nm with a device uncertainty of ± 1 nm. IR spectra of materials were measured at room temperature on a spectrometer IR Affinity-1, Shimadzu in the range of 4000-550 cm^{-1} using a prefix multiple disturbed full internal reflection with a diamond tip and the uncertainty of the instrument ± 2cm^{-1}.

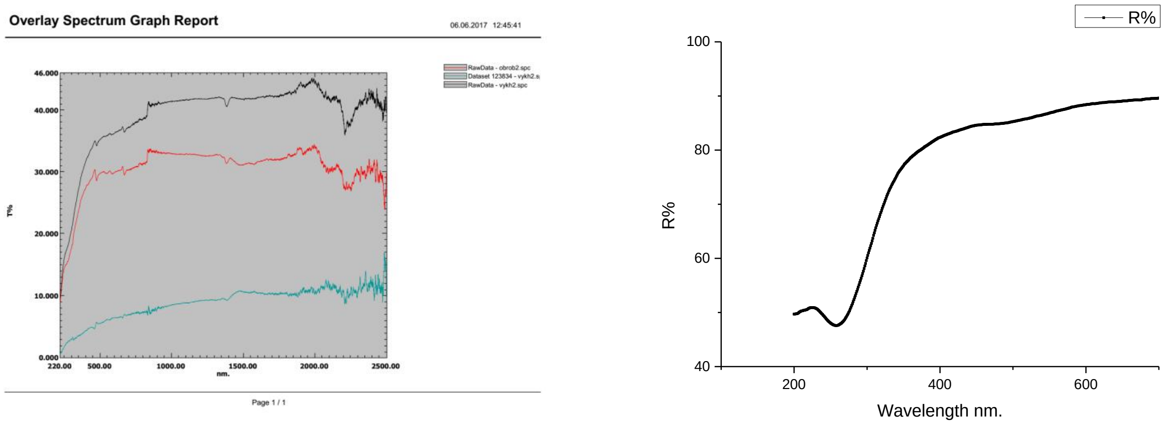

a *b*

Fig. 1. UV-type spectra: a - original (red line) and modified viscose knitted fabric (black line), b - UV spectrum of AHN in pure form

When comparing the UV spectra of the raw and treated viscose material (Fig. 1), it can be argued about its absorption capacity against ultraviolet radiation. This is evidenced by the presence of the shoulder in the range of 250 - 300 nm. The AHN is characterized by the absorption of UV radiation at 258 nm. The difference in the level of absorption of UV radiation between the treated material and the raw samples is 6 - 7%. This clearly confirms the relationship between the presence of AHN on textile material with the absorption of treated sample in the UV range. During nanoprocessing heterocoagulation (sedimentation) of AHN was occurred on the surface of textile with a simultaneous intermolecular interaction sufficient for the irreversibility of the halositic nanotubes coagulation process with the material. The stage of sorption of nanotubes in the structure of the knitted fabric is excluded, which is confirmed by the practical absence of differences in the IR spectra of the original and treated samples.

Detailed analysis of the obtained SEM images of the surface of unmodified and modified by nanotubes viscose textile materials suggests that the distribution of nanotubes on the surface of the fibers is uniform (Fig. 2), which ensures uniform properties throughout the volume of the material.

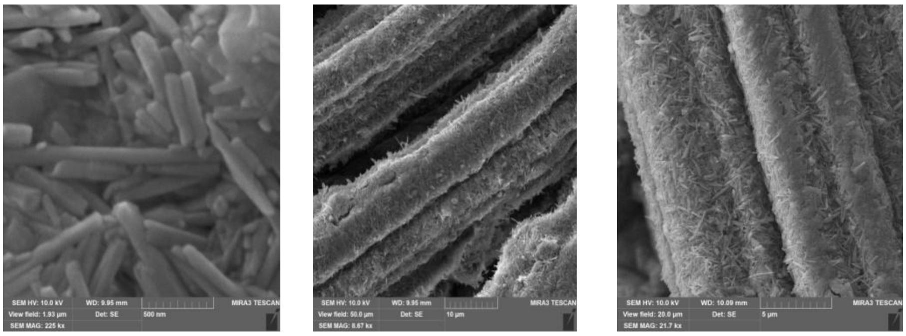

a *b* *c*

Fig. 2. SEM images of natural nanotubes (a) and viscose knitwear modified with nanotubes (b, c)

According to IR spectroscopy, after modification in the spectra, in addition to the bands characteristic of the original unmodified materials, bands belonging to the haloisite nanotubes appear (Fig. 3). That is, the chemical structure of the surface of the fibers is preserved, all the useful properties of the row material are preserved and the properties inherent to nanotubes are acquired.

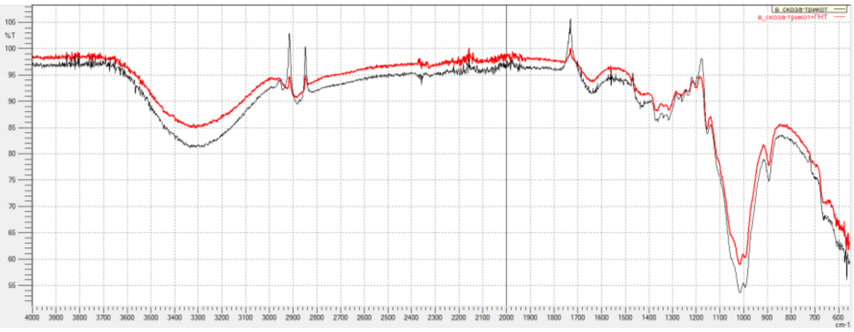

Fig. 3. IR spectra of samples of viscose knitwear row (black lines) and after nanoprocessing (red lines).

Thus, we have shown the possibility of obtaining of innovative textile materials for protection against ultraviolet radiation using cellulose-containing fibers and natural aluminosilicate nanotubes.

1. Бричка С.Я. Химия галлоизитных и имоголитных нанотрубок. Київ, Україна: Видавничий дім «Кий», 2016. 258 с.
2. Супрун Н.П., Береза-Кіндзерська Л.В., Бричка А.В., Бричка С.Я. Синтез наповнених алюмосилікатними нанотрубками агар-агарових гелів для ранових покриттів. Вісник КНУТД. 2016. №4(100). С. 49-55.
3. Бричка С.Я. Применение алюмосиликатных нанотрубок. Наноструктурное материаловедение. 2012. № 4. С. 40-60.

CRIOCHEMICAL SYNTHESIS OF $Ni_xZn_{1-x}Fe_2O_4$ NANOPARTICLES AND STUDY OF THEIR PROPERTIES

Timashkov I.P., Shlapa Yu.Yu., Solopan S.O.

Department of Solid State Chemistry, V. I. Vernadskii Institute of General and Inorganic Chemistry of the NAS of Ukraine, 32/34 Palladina ave., Kyiv, 03142 Ukraine

Magnetic nanoparticles of oxide systems are widely used in engineering, microelectronics and they also have the perspectives for application in medicine [1]. Particularly, magnetic nanomaterials are interesting in the development of inducers for the magnetic hyperthermia due to their ability to heat up in an alternating magnetic field (AMF). Magnetic hyperthermia is a method of treatment of oncological diseases by the thermal destruction (at 42 - 45 ° C) of malignant tumors with previously injected magnetic nanoparticles. However, magnetic nanomaterials for medical purposes must meet a number of important requirements: biocompatibility, small size, and the ability to heat up effectively and self-control to certain temperatures to prevent damaging the living cells.

Fe_3O_4 with a spinel structure is one of the promising materials for such purposes, because of its biocompatibility and relatively simplicity to be obtained in small sizes. However, Fe_3O_4 nanoparticles have a high temperature of the phase transition from ferromagnetic to paramagnetic state (Curie point), which makes them complicated to be used in medicine. One more alternative material, which is studied for these purposes, is the nanoscale solid solution of $(La,Sr)MnO_3$ manganite with a perovskite structure. It has the phase transition temperature that depends on the chemical composition of nanoparticles, which provide the possibility of the controlled heating of such nanoparticles in AMF to certain temperatures (43- 45 ° C). However, it is known [2] that the perovskite structure is characterized by the high value of the crystallization energy, therefore, such materials can be obtained in the crystalline state only after high-temperature treatment, which leads to the growth and agglomeration of particles [3].

As it was shown in [4], there is a possibility to obtain magnetic nanomaterials with a spinel structure with the Curie temperature in the range of 50-70 ° C, via the partial substitution of iron ions by nickel and zinc ions in the crystalline lattice. However, such nanomaterials have been synthesized at the high temperatures, whereas, it is important to develop the synthesis conditions, which will provide a possibility to obtain spinel nanomaterials with small sizes and weak agglomeration for their tests in medical applications.

Therefore, the aim of this study was the synthesis of $Ni_xZn_{1-x}Fe_2O_4$ nanoparticles by the cryochemical method, study of their crystallochemical properties and ability to heat up under the effect of an alternating magnetic field.

A set of samples with different molar ratios of nickel and zinc (1:3; 1:1; 3:1) were synthesized, where sodium hydroxide was used as a precipitator. According to X-ray diffraction analysis (XRD), an amorphous precipitate, which did not exhibit magnetic properties, was formed at the synthesis temperature. To study the formation of the crystalline structure, the precursor was treated in the range of 200-800°C. It was established that the crystalline spinel structure began to form in one stage at 300°C (Fig. 1a)

Crystalline sizes of nanoparticles as well as their level of crystallinity were estimated according to XRD data. It was shown that the formation of the crystalline spinel structure of begins at 300°C, and the level of crystallinity for nanoparticles grew with the increasing the heating temperature. The average size of nanoparticles was calculated via TEM data, which were in good agreement with the XRD results. It was found that the particle size increased and the size distribution became wider with the growth of the heating temperature.

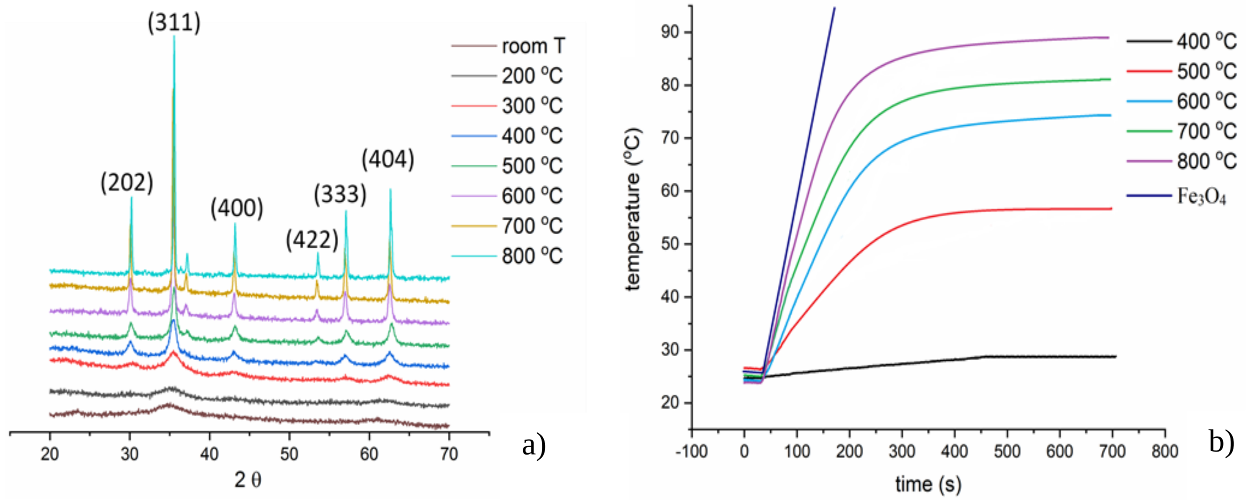

Fig. 1. XRD patterns of nanoparticles synthesized at different temperatures (a) and heating curves for magnetic fluids based on them (b)

The values of the magnetization at the room temperature was measured for a set of spinel nanoparticles with ratio of ions Ni/Zn=1:1. It was found that the magnetic properties began to appear in nanoparticles synthesized at 300°C. Obtained results are in good agreement with XRD data: magnetic properties appear during the formation of the crystalline spinel structure.

To study the heating efficiency of such nanoparticles in AMF, corresponding magnetic fluids were developed. Dependence of the heating temperature of nanoparticles on vs time of the effect of AMF are shown in Fig. 1b. Values of specific loss power (SLP) were calculated, which are in good correlation with the data of magnetic measurements. It is important to note that the maximal heating temperature of NixZn1-xFe2O4 nanoparticles saturates and does not change after some time of heating, while Fe3O4 nanoparticles with a spinel structure heat up in AMF uncontrolled to high temperatures. At the same time, crystalline nanoparticles of NixZn1-xFe2O4 with pronounced magnetic properties are formed at 500 ° C, in contrast to $(La,Sr)MnO_3$ with perovskite structure, which makes this material interesting for investigations as inducers of magnetic hyperthermia.

1. Z. Qing, Y. Zhenhua, C. Chengcheng and C. Jun “Spinels: Controlled Preparation, Oxygen Reduction/Evolution Reaction Application, and Beyond” *Chem. Rev.* 2017, 117, 10121−10211
2. O.Z.Yanchevskii, D.A.Durilin, A.I. Tovstolytkin et al. *Inorg. Mater.* 2011, *47(4)*, 431-434.
3. Yu. Shlapa, S. Solopan, A. Belous, A. Tovstolytkin "Effect of Synthesis Method of $La_{1-x}Sr_xMnO_3$ Manganite Nanoparticles on Their Properties" *Nanoscale Research Letters* (2018) 13:13 DOI 10.1186/s11671-017-2431-z
4. A.I. Tovstolytkin, M.M. Kulyk, V.M. Kalita, S.M. Ryabchenko, et. al "Nickel-zinc spinel nanoferrites: magnetic characterization and prospects of the use in self-controlled magnetic hyperthermia" *Journal of Magnetism and Magnetic Materials* (2018), doi: https://doi.org/10.1016/j.jmmm.2018.10.075

FORMATION OF SURFACE RELIEF GRATINGS IN AMORPHOUS As-Se FILMS BY POLARIZATION HOLOGRAPHY

M.L.Trunov[1,2] and V.K. Kyrylenko[1]

[1]Uzhgorod laboratory of optoelectronics and photonics materials of the Institute for Information Recording of NAS of Ukraine, Uzhgorod, Ukraine
[2]Uzhgorod National University, Uzhgorod, Ukraine

Amorphous chalcogenide-containing photosensitive thin films (CPF) show photo-induced mass transport (PMT), i.e. lateral movement of the material under band-gap light irradiation [1]. During single beam or holographic exposure with light interference patterns (IP) these films deforms following the distribution of intensity or polarization [2] of the IP resulting in the formation of so-called surface relief gratings (SRGs). It means that the structuring of the film topography occurs in a periodic manner across the film surface over the whole area of illumination. Note that despite to the light-induced softening of glassy matrix [3] the temperature of the film is ambient and the film remains to be in a sold-like state.

The process of SRG formation depends on many parameters such as irradiation intensity and polarization state of recording laser, film compositions [4] and initial film thickness, temperature of recording, polarization of additional irradiation [5] etc. For some film compositions, significant material shifts occurs even on macroscopic length scale and the amounts of transferred material were comparable with initial film thicknesses or even several times exceeded it (giant PMT) [5].

Some unique effects were also detected, e.g. inversion of surface relief [6]), low-temperature PMT (at 77 K) [7], giant ripples formation under homogeneous illumination and so on. PMT became attractive for the variety of practical application including hybrid waveguides in the integrated optics, direct optical recording of SRGs with different morphology that then may further be exploited for many applications in optics (data storage devices, diffractive optical elements, photonic crystals etc), for the control the optical response of the CPF materials due to changes in surface morphology in optoelectronics and plasmonics (e. g. trapping of light in solar cells and nanolithography). In the last case, the localized plasmon-polaritons act as a source of near-field effect producing a nanosized surface relief. *Vice versa*, when the surface relief is known, the mapping of the electric field distribution of surface plasmons is possible [8].

Although several theoretical approaches and models have been developed to describe the mechanisms of PMT [9], numerous details in the process remain unsolved until now. On a nanoscopic scale, the process driving the relief formation is the dipolar defects movement in amorphous CPF. Those dipolar defects continuously generated by the light and result in a locally preferred orientation of them with their main axis parallel to the E-field vector. Moreover the light-induced softening of glassy matrix (viscosity lowers to 10^{12} Poise, Ref.[3]) enhances their motion under the driving optical force. Latter arises due to the electric field gradient resulting from the polarized IP as local variations with respect to intensity (an intensity modulated IP) or polarization (in the case of polarization modulated IP) and triggers the dipolar defects movement in the film.

The main question is the origin and the strength of the driving force that can induce significant deformation and mechanical stresses larger than the yield point of the film far below its glass transition temperature.

Earlier [10] we have studied the overall dynamics of light induced PMT in As_xSe_{100-x} amorphous films ($0 \leq x \leq 40$ at.%) over a several main holographic schemes of recording by scalar holography with additional illumination by band-gap light polarized orthogonally to the polarization of recording beams. From the diffraction efficiencies vs time dependences of obtained SRGs we found that crossover occurs in the region of topological structural transition (4 at.% $\leq x \leq$ 5 at%.), i.e. the amorphous material change the direction of movement from “light to dark” to “from dark to light”.

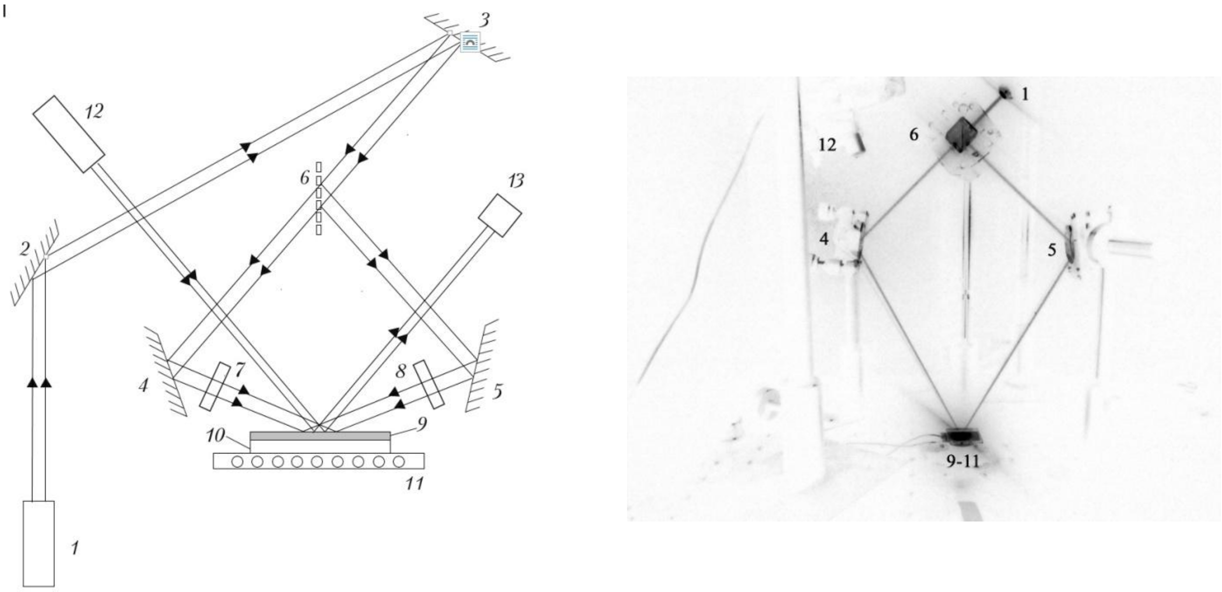

(a) (b)

Fig.1. Sketch (a) and appropriate photo (b) of experimental setup for recording of SRG formation. See text for details.

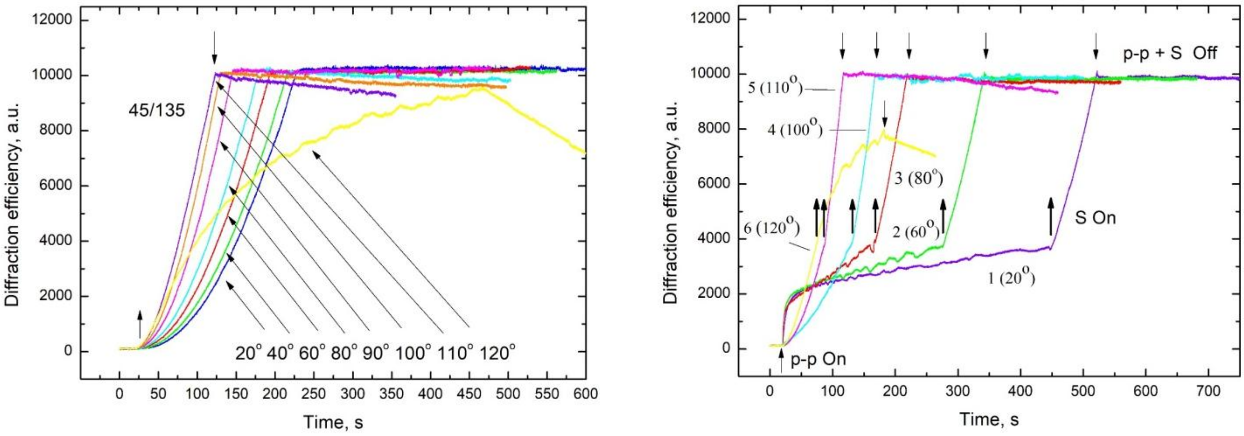

(a) (b)

Fig. 2. SRG formation and their temperature dependence (a) by polarization interference patterns (45/135) and (b) by intensity interference patterns (p-p and pp+S) in 1 μm $As_{20}Se_{80}$ film. Arrows show times when recording light (45/135 or p-p) and additional light (S) were switched on (↑) and off (↓). Temperatures and polarizations of recording and additional lasers are indicated in the figure.

Here, we report on a systematic study of SRG formation in As_xSe_{100-x} amorphous films ($0 \leq x \leq 50$ at.%) by vectorial (polarization) holography and the results were compared to the kinetic of diffraction efficiency related to the SRG obtained by scalar holography. Four different polarization configurations were used: s-s, p-p (intensity IP) and 45-135, p-s (polarization IP). In addition, we investigated the effect of P or S polarized incoherent assisting light beam.

In our experiments, to inscribe the surface relief gratings, a He-Ne laser (1) operating in a single longitudinal mode with 100-150 mW/cm^2 intensity at a wavelength of 633 nm and oscillating in horizontal linear polarization state is used (see sketch of set-up on Fig.1 a and appropriate image on Fig 1 b). The beam of laser is split into two parts of separate coherent recording beams with equal intensities using a non-polarizing beam splitter (6) and the two beams are aligned by the mirrors (4, 5) to interfere at the film surface 9 positioned on the heater. The incident angle of the two recording beams is 6.4°, which corresponds to a grating spacing of 2.8 μm. The polarization state of each beam is adjust and control with a phase wave plates (7, 8) (not shown on the Fig 1 b).

To monitor the dynamics of the formation of SRGs we used the evolution of diffraction efficiency (DE: the ratio of intensities of the first diffracted beam to the incident one). DE of the recorded SRGs was measured on a fiber spectrophotometer Optic Ocean (13) using a solid-state violet laser (12) (at wavelength of 404 nm and intensity of 10 μW) and was taken proportional to the intensity variation of the first diffraction peak in reflection mode.

The investigated samples were prepared as the structures with free surface of the film (amorphous CPF (9) - glass substrate (10)) and placed on a heater 11. High precision of the temperature measurement (± 2 C) in the range of 20 C-140 C achieved by adjusting of the current in the heater

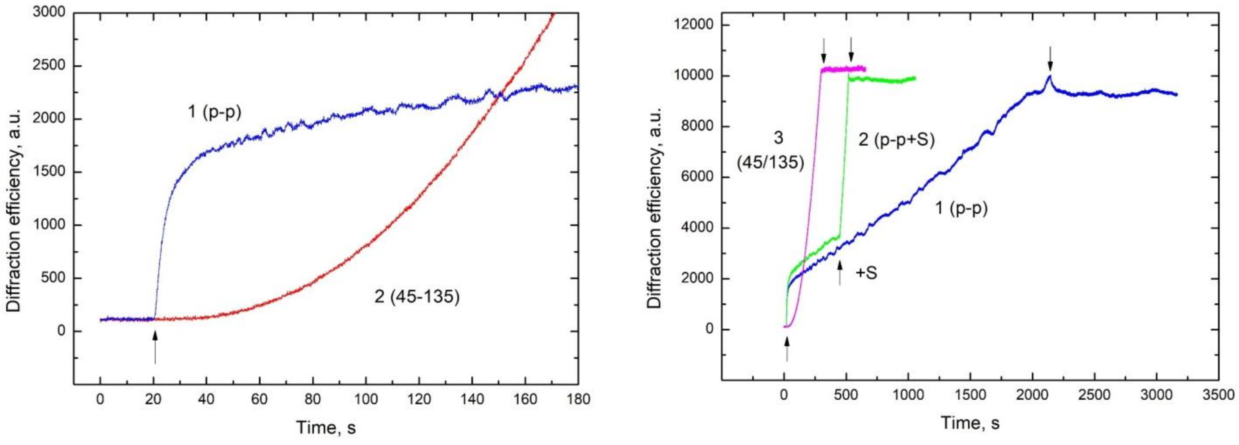

(a) (b)

Fig. 3. SRG formation (a) by polarization interference patterns (45/135) and) by intensity interference patterns (p-p and pp+S) in 1 μm $As_{20}Se_{80}$ film at ambient temperature and (b) initial part of exposure: SRG that arises due to photoexpansion of chalcogenide material is absent in case of 45/135 compared to the p-p scheme of recording. Polarizations of recording and additional lasers are indicated in the figure. Arrows show times when recording light (45/135 or p-p) and additional light (S) were switched on (↑) and off (↓).

For the first time to our knowledge, it was detected that with the increase of temperature of recording (from ambient to glass-transition temperature, Tg or even more) PMT in CPF occurs due to variation in polarization across the interference pattern with the rates, which significantly exceed those at room temperature (Fig. 2 a). Similar results were obtained very recently in p-p regime of recording [8]. We have found that the direction of the PMT depend on the direction of light polarization both recording and additional beams not only at ambient temperature but also even near the glass-transition temperature (Fig.2 b). There results have shown also that the efficiency of surface relief formation is many times higher in the case of 45/135 polarization state of the recording beams in compare to the case of p-p recording (Fig. 3 a, b) The details of compositional kinetics of recording for whole As-Se system will be presented and discussed. The mechanism of the direct recording of surface relief on amorphous chalcogenide films based on optically induced gradient force model that includes both the spatial distribution of polarization and the anisotropy of the material permittivity is discussed.

1. Saliminia A., Galstian T. V. & Villeneuve, A. Optical field-induced mass transport in As_2S_3 chalcogenide glasses // Phys. Rev. Lett. , 2000. – V. 85, 4112 (5pp).
2. Gertners U. & Teteris J. Surface relief formation in amorphous chalcogenide thin films during holographic recording // Opt. Mater., 2010.- V.32.-P. 807-810.
3. Yannopoulos S. N. & Trunov M. L. Photoplastic effects in chalcogenide glasses: A review// Phys. Status Solidi B., 2009.- V. 24. – P. 1773-1785 (2009).

4. Trunov M.L., Lytvyn P.M., Nagy P.M. [et al.]. Real time atomic force microscopy imaging of photoinduced surface deformation in As_xSe_{100-x} chalcogenide films // Appl. Phys. Lett., 2010.- V. 96.- P. 111908(3pp).
5. Trunov M.L., Lytvyn,P.M. & Dyachyns’ka O.M. Alternating matter motion in photoinduced mass transport driven and enhanced by light polarization in amorphous chalcogenide films// Appl. Phys. Lett., 2010.- V. 97. – P. 031905(3pp).
6. Kaganovskii Yu., Béke D. L., Charnovych S. [et al.]. Inversion of the direction of photo-induced mass transport in $As_{20}Se_{80}$ films: Experiment and theory// J . Appl. Phys., 2011.- V. 110. – P. 063502 (5pp).
7. Takáts V., Trunov M.L., Vad K. [et al.]. Low-temperature photo-induced mass transfer in thin $As_{20}Se_{80}$ amorphous films // Mater. Lett., 2015.- V.160. – P. 558-561.
8. Trunov, M. L., Lytvyn P. M., Nagy, P. M. [et al.]. Light-induced mass transport in amorphous chalcogenides: Toward surface plasmon-assisted nanolithography and near-field nanoimaging// Phys. Status Solidi B., 2014. - V. 251. - P. 1354-1362 .
9. Recht D. & Arnold C. Generalized Model for Photoinduced Surface Structure in Amorphous Thin Films // Phys. Rev. Lett., 2013.- V. 111. – P. 105503(5pp).
10. Trunov M.L., Lytvyn P.M. Selective light-induced mass transport in amorphous As_xSe_{100-x} films driven by the composition tuning: Effect of temperature on maximum acceleration // J. Non-Cryst. Solids, 2018. - V. 493. - P. 86-93.

DYNAMICS OF PHOTOREFRACTIVE EFFECT IN $Sn_2P_2S_6$ CRYSTALS STUDIED BY MODULATION TECHNIQUE

M. Tsyhyka, S. Hasynets, A. Кohutych, A. Grabar

Uzhhorod National University, Institute for Solid State Physics and Chemistry,
Pidhirna 46, Uzhhorod 88000, Ukraine
al_grabar@hotmail.com

A modified method for studying the dynamics of photorefractive (PR) response by the modulation method with the lock-in detection of the output amplified signal is tested. Typically, the scheme for studies the PR effect includes two coherent laser beams interacting in a crystal volume. In this case, the signal beam is amplified due to the formation of a non-local PR lattice, which is typical for the diffusion mechanism of spatial charge formation in crystals of the $Sn_2P_2S_6$ type [1]. If one of the beams is phase-modulated, that can be realized by its reflection from the mirror placed on the piezoelectric element, such phase modulation is registered by the changes in the intensity of the amplified signal beam. This scheme can be exploited as a dynamic interferometer [2]. By varying the frequency and amplitude of the phase modulation, it is possible to obtain the frequency characteristics of such a dynamic interferometer, based on the PR effect in $Sn_2P_2S_6$ crystals with different impurities (Te, Sb, Cu). The advantage of the used method is the possibility of independent detection of the first and second harmonics of the phase modulation. This is important for clarifying the mechanism of formation of the PR lattice in the studied materials. In the case of purely diffusion mechanism of the PR grating formation in these crystals, the intensity modulation at doubled frequency should be observed. But, in most of the studied doped $Sn_2P_2S_6$ samples, the first harmonic of the modulation signal is present and even dominates; besides, it is characterized by high temporal instability compared to the double-frequency signal. This result can be explained only by the fact that in these crystals is forming also a local component of the PR grating, existing due to dynamic photochromic effect. The data on modulation spectra in different doped samples and under different conditions (light intensity, PR grating spacing, light polarization, sample pre-history) were obtained. A possible model of coexistence of these two types of light-induced gratings and their interaction in $Sn_2P_2S_6$ crystals are discussed. All these data give the background for refining the existing models of the PR effect in these materials.

1. T. Bach, M. Jazbinšek, G. Montemezzani, P. Günter, A. Grabar, and Yu. Vysochanskii, J. Opt. Soc. Am. B **24**, 1535 (2007)
2. Grabar, P. Mathey, M. Tsyhyka, G. Gadrét, and I. Stoika, J. Phys.: Conf. Ser. **867**, 012027 (2017)

POLARIZATION STATES IN CORE-SHELL FERROELECTRIC NANOPARTICLES FOR ADVANCED APPLICATIONS

Morozovska A.N.[1,2], **Tulaidan V.V.** [1], Eliseev E. A.[3], Hertel R.[4], Reshetnyak V. Yu.[1], Evans D.R.[5]

[1]Taras Shevchenko National University of Kyiv, Volodymyrska Street 64, Kyiv, 01601, Ukraine
[2] Institute of Physics, National Academy of Sciences of Ukraine,
46, pr. Nauky, 03028 Kyiv, Ukraine
[3]Institute for Problems of Materials Science, National Academy of Sciences of Ukraine,
Krjijanovskogo 3, 03142 Kyiv, Ukraine
[4]Université de Strasbourg, CNRS, Institut de Physique et Chimie des Matériaux de Strasbourg,
UMR 7504, 67000 Strasbourg, France
[5]Air Force Research Laboratory, Materials and Manufacturing Directorate, Wright-Patterson Air Force Base, Ohio, 45433, USA

The fundamental question whether the structure of curled topological polarization states, such as ferroelectric vortices, can be controlled by the application of an irrotational electric field is open. Recently we studied the influence of irrotational external electric fields on the formation, evolution, and relaxation of ferroelectric vortices in spherical nanoparticles. In the framework of the Landau-Ginzburg-Devonshire approach, we performed finite element modeling of the polarization behavior in a ferroelectric barium titanate core covered with a “tunable” paraelectric strontium titanate shell placed in a polymer or liquid medium [1].

A stable two-dimensional vortex is formed in the core after a zero-field relaxation of an initial random or poly-domain distribution of the polarization, where the vortex axis is directed along one of the core crystallographic axes. Subsequently, sinusoidal pulses of a homogeneous electric field with variable period, strength, and direction are applied. The field-induced changes of the vortex structure consist in the appearance of an axial “kernel” in the form of a prolate nanodomain, the growth of the kernel, an increasing orientation of the polarization along the field, and the onset of a single-domain state.

After removal of the electric field, the vortex recovers spontaneously; but its structure, axis orientation, and vorticity can be different from the initial state. As a rule, the final state is a stable three-dimensional polarization vortex with an axial dipolar kernel, which has a lower energy compared to the initial purely azimuthal vortex. The nature of this counterintuitive result is a significant gain of the negative Landau energy in the axial region of the vortex by the formation of a kernel, which is only partly compensated by an increase in positive energy of the depolarization field, polarization gradient, and elastic stress for a vortex with a prolate single-domain kernel.

The vortex states with a kernel possess a manifold degeneracy, appearing from three equiprobable directions of vortex axis, clockwise and counterclockwise directions of polarization rotation along the vortex axis, and two polarization directions in the kernel. This multitude of vortex states in a single core is promising for applications of core-shell nanoparticles and their ensembles as multi-bit memory and logic units. A rotation of the vortex kernel over a sphere, which is possible for the core-shell nanoparticles in a soft matter medium with a controllable viscosity, may be used to imitate qubit features. This ability to control the nanoparticle’s core polarization by the shell screening, in combination with external irrotational electric fields could be attractive for new applications, such as multi-bit memory and logic units.

To imagine a multi-bit memory cell, let us consider an ensemble of non-interacting core-shell nanoparticles with a vortex polarization placed in a soft matter environment with a viscosity that is strongly temperature-dependent around the working (i.e. room) temperature [see **Fig.1(a)-(c)**]. The nanoparticles can freely rotate and move in the liquid soft matter, and are prevented from rotating when the matter becomes solid. The ferroelectric transition temperature of the particle core is much higher than the soft matter melting temperature. The core-shell nanoparticles are located between electrodes placed on opposite sides of the cell, and in any given ferroelectric core the crystallographic axes are oriented randomly. Since the equilibrium vortex axis should coincide with one of the crystallographic directions [100], [010], or [001], a given nanoparticle in the composite can be in any of three types of vortex states, with an axial kernel (two states “±1”) and without one (state “0”). The resulting polarization of a nanocomposite can be presented as a sum of these states,

$$|P\rangle = \sum_{ijk} C_{ijk}\, |ijk\rangle. \qquad (1)$$

Here C_{ijk} is a relative fraction of the state $|ijk\rangle$ in the composite, $\sum_{ijk} C_{ijk}^2 = 1$ and $0 \leq C_{ijk} \leq 1$. The first subscript i=1, 2, 3 designates the vortex axis, the second subscript j = -1, 0, +1 indicates the kernel “**color**” (i.e. polarization sign “1” or “-1” in the kernel, “0” without a kernel), and the third subscript k = “*l*” or “*r*” corresponds to the vorticity, defined as a clockwise or counterclockwise direction of the vortex polarization rotation. For a given nanoparticle the coefficients can be interpreted as probabilities. The kernel characteristic "color" introduced here is similar to the spin-flavor characteristics used to describe specific states of elementary particles in magnetic fields.

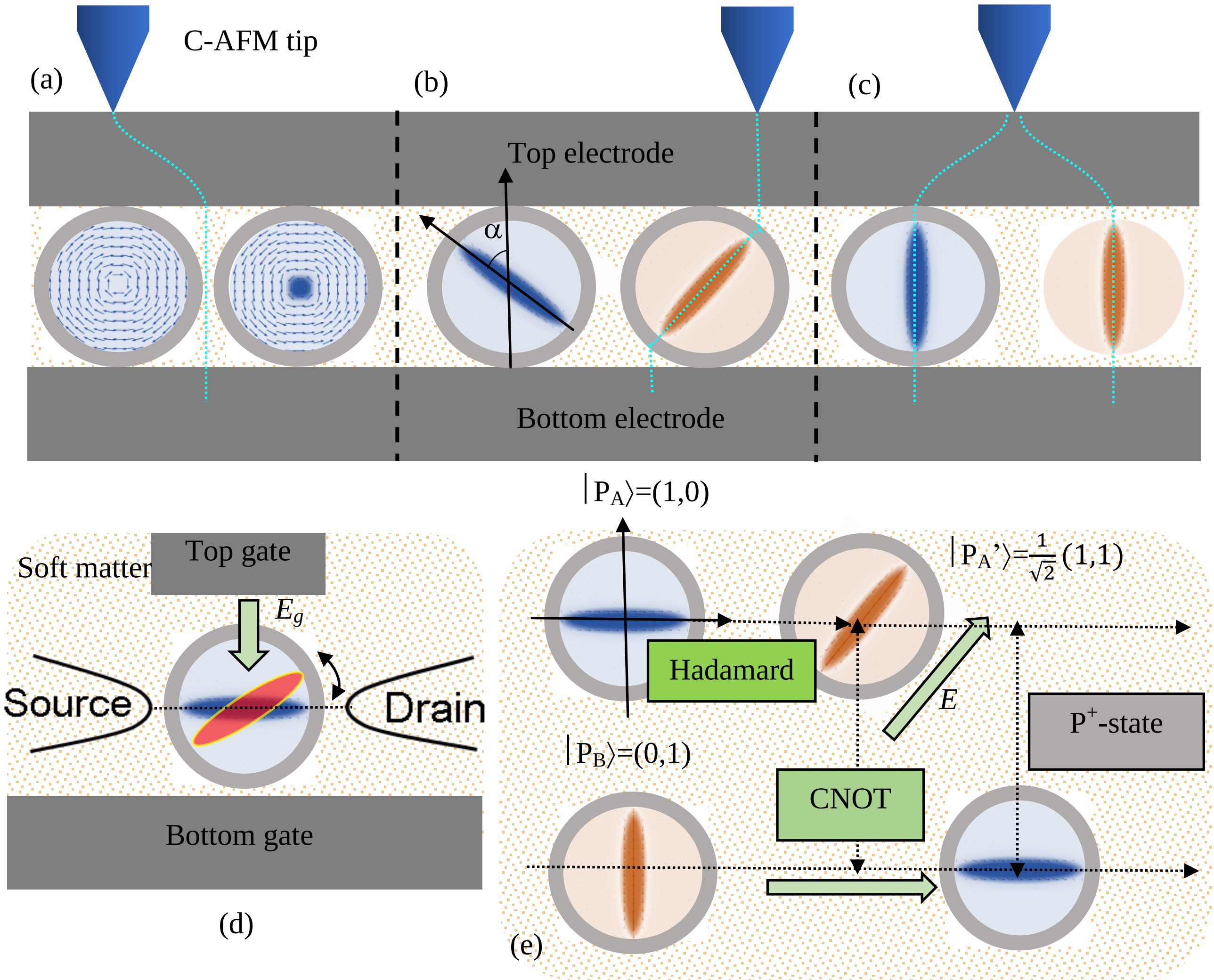

Fig. 1. Spherical core-shell nanoparticles with a vortex polarization and axial dipolar kernel placed in a plane capacitor with a thickness slightly greater than the sphere diameter. (a-c) For a conductive kernel the system can be in a low (a), intermediate (b), or high (c) conductivity state. (d) Nano-FET with a rotating channel. (e) The polarization states, $|P_A\rangle$ and $|P_B\rangle$, of two core-shell nanoparticles are labeled "A" and "B". The coupling or “entanglement” of these states occurs after the application of “Hadamard” and “CNOT” operations. Adapted from Ref.[1].

A single core-shell nanoparticle, whose polarization vortex has a dipolar kernel, placed in a soft matter environment, can be considered as a candidate for a nanosized field effect transistor (**nano-FET**) containing a “rotating” channel with an angular dependence of the local resistivity

$\rho_L(\alpha)$. Actually, the voltage applied between the FET gates can rotate or shift the particle (in order to rotate/move the kernel axis) [see **Fig.1(d)**], such that the gate field E_g can control the channel conductivity $\sigma_L(\alpha) = \frac{1}{2R[(1-cos\alpha)\rho_W+\rho_k]}$. The vortex stability and kernel rotation feasibility are advantages of the nano-FET operation. Its drawback is a relatively low operation speed due to the sluggishness of sphere rotation and/or the translational motion towards the gate.

Another interesting aspect is that the classical, behavior of the vortex axis (with or without a conductive kernel) can simulate a “qubit” at room temperature, since it formally appeared that some basic properties of qubits necessary for a quantum computation [2,3] can be simulated by the vortex states “±1” revealed in [1]. These possibilities are sketched in **Fig.1(e)**. However, one should realize that the long-range electrostatic (or magnetostatic) interaction between the core-shell ferroelectric (or ferromagnetic) nanoparticles has no similarities with “true” entanglement of e.g. photons, because the photons can be entangled at macroscopic distances [3], whereas the nanoparticles cannot be entangled at such distances due to the attenuation of electrostatic or magnetostatic fields.

Acknowledgements. A.N.M. acknowledges EOARD project 9IOE063 and related STCU partner project P751, and the Target Program of Basic Research of the National Academy of Sciences of Ukraine "Prospective basic research and innovative development of nanomaterials and nanotechnologies 2020 - 2024", Project № 1/20-H (state registration number: 0120U102306). V.Y.R. acknowledges the support of COST Action CA17139.

1. N. Morozovska, E. A. Eliseev, R. Hertel, Y. M. Fomichov, V. Tulaidan, V. Yu. Reshetnyak, and D. R. Evans. Electric Field Control of Three-Dimensional Vortex States in Core-Shell Ferroelectric Nanoparticles, submitted to Acta Materialia (http://arxiv.org/abs/2004.00962)
2. D.P. DiVincenzo, Quantum computation. Science **270**, 255 (1995).
3. M.A. Nielsen, I.L. Chuang, Quantum Computation and Quantum Information, Cambridge University Press. ISBN 978-1-107-00217-3 *(*2010)

AUTOMATATION OF FIBER OPTIC THERMOMETERS WITH GaAs NANO-POWDERS AS TEMPERATURE SENSITIVE ELEMENTS

Turianytsia I.I., Chychura I.I. Kutchak S.V.

State University "Uzhgorod National University", Universitetska St., 14, Uzhgorod 8800, Ukraine.

Basic materials of the A_3B_5 group (GaAs and GaP) are the main complex semiconductor crystals for today. They are widely used in modern optoelectronics: basic elements of IR optics, television technology and fiber optic communications. After doping, these crystals are sufficiently resistant to radiation exposure, which enables their use in areas of high background radiation and even in extreme radiation conditions. All this indicates to the prospect of using crystals of the A_3B_5 group as sensing elements of various automatic fiber-optic sensors, which can be used in extreme conditions.

In the design process of modern automatic fiber-optic information sensors the primary task is to optimize their basic optical parameters and characteristics. The initial data for such optimization are the spectra’s of optical transmission of crystals in the region of their absorption edge and theoretical functional relationships between there optical absorption values such as working wavelength of radiation and temperature. Therefore, the study of all these problems is relevant for the development of modern and effective amplitude type fiber-optic sensors of physical quantities.

In the most cited temperature measurements of the band gap of GaAs, the temperature dependence of the band gap was inferred from isoabsorption measurements in the Urbach tail region. But, the temperature dependence of the Urbach slope was not resolved. This information is essential to obtain accurate mathematical function of many variables, which would sufficiently describe the magnitude of the optical absorption of the temperature sensitive elements, which were made from these crystals. This requires an implementation of microprocessor automation devices in I.O.S. Single crystals of gallium arsenide (GaAs) have come to use in a wide range of optoelectronic applications, including the manufacture of semiconductor lasers and GaAs IC's.

Today, however, more widely are used doped GaAs crystals. It is related to their advantages over pure crystals. In the investigation, reported in this work, we used special sensitive elements. They were made by cold pressing of GaAs nano-powder. The starting material for the nano-powder was GaAs doped with Zn (impurity concentration $6{,}8 \cdot 10^{-19}$)

The edge of transmission spectra for such sensitive elements at temperature range from 250 K to 450 K were investigated experimentally. In the process of results analyzing, they were represented by one mathematical function of two arguments: the thickness of the sensitive element and its temperature. The resulting function is the basis for programming of microcontroller in the development of FOT automation system.

PROBIOTIC LACTOBACTERIA FOR CREATION OF SELENIUM CONTAINING DIETARY SUPPLEMENT

Tymoshok N.O., Bitutyky V.S., Kharchuk M.S., Kharchyshyn V.M., Lazarenko L.M.,
Kalinichenko S.V., Spivak M.Ya.

Institute of Microbiology and Virology. D.K. Zabolotny NASU, Kyiv
Email: n_timoshok@ukr.net

In recent years, it has been found that 100 million people worldwide suffer from selenium deficiency [1]. Lactic acid bacteria had proven to bind metal ions and metalloids like other microorganisms to their cells or transport and store them inside the cell [2,3].

Bacterial strains of Lactobacillus are capable of biotransformation of inorganic Se into organic forms [4,5].

According to Xia et al. [6,7] and Diowksz et al. [8] *Lactobacillus plantarum* and *L. bulgaricus* deposit elemental selenium via cell detoxification Se 4+. The creation of selenium-containing probiotic supplements is due to the trace element Se is involved in the biosynthesis of twenty-five selenoproteins, which regulate the optimal immune response of the body.

Selenium is associated with the metabolic processes of vitamins (E, C, A) and carotenoids, it plays an important role in iodine metabolism, affects the body's immune responses. Selenium is a component of glutathione peroxidase [9], thyroid reductase [10] and selenocysteine of the 21st amino acid, which is involved in the biosynthesis of cysteine (Cys) and redox reactions: humans, animals, birds and bacteria.

The aim of the study was to select probiotic strains of *Lactobacillus* are capable of biotransformation of sodium selenite into nanoselen formation to create probiotic selenium containing dietary supplement for birds.

Two strains of *Lactobacillus casei* IMB B-7280 and *L.plantarum* IMB B-7679, which are capable of transforming sodium selenite, were selected from the collection of probiotic cultures of the Department of Interferon and Immunomodulators. The selection of these strains of lactobacilli as producers of biogenic Nano-Se is due to their ability to transform sodium selenite and their ability to inhibit the reproduction of pathogenic and opportunistic microorganisms, increase the immune responses of the organism and their belonging to the category of Generally Recognized As Safe microorganisms.

Bacteria were cultured in liquid pH medium Broth (Conda) low pH, at a temperature of 30 ^{0}C for 48 h aerobically in the absence and presence of different doses of sodium selenite.

Cultivation of cultures in the presence of Na2SeO3 was accompanied by a change in the color of the medium to a reddish-brown color, which according to [11] was a characteristic feature of the formation of biogenic nanoselen (Nano-Se). Growth in the presence of Na2SeO3 at low concentrations did not affect the change in morphology and culture properties of *L. plantarum* IMB B-7679. At the same time, enrichment of the culture medium of *L. casei* IIB B-7280 with sodium selenite was accompanied by a decrease in the viability of the culture.

According to the obtained data, the optimal conditions for the enrichment culture media with Na2SeO3 in order to determine ability of *L. plantarum* IMB B-7679 and *L. casei* IMB B-7280 to produce Nano-Se were obtained.

The formation of biogenic Nano-Se was confirmed by Transmission electron microscopy (TEM) using an electron microscope JEM-1400 (Japan). Both experimental strains showed the ability to reduce Se 4+ with the formation of different sized biogenic Nano-Se. High tolerance of *L.plantarum* IMB B-7679 to significant concentrations of Na2SeO3 and synthesis of more homogeneous Nano-Se in size were established. Synthesized Nano-Se is known to be one of less toxic form of selenium than toxicity of sodium selenite with high bioavailability.

However, the size of the spherical selenium nanoparticles formed by lactobacilli was more than 100 nm. Such Nano-Se particles are called Lactomicroselenium Particles or lactomicroSel.

Culture media of *L. plantarum* IMB B-7679 were enriched with Na2SeO3 in order to determine capacity rapid formation of nanospheres with a percentage deviation from the average size of 5-20%.

The high tolerance of *L.plantarum* IMB B-7679 to Na2SeO3 and the formation of Nano-Se advised us to use the abbreviation (parts per million), ie the concentration of Se in ppm to unify the results and compare them with the literature data. It is advisable to enrich the culture medium for Bacterial strains of Lactobacillus with sodium selenite in the range of concentrations based on Se concentrations, according to the norms of the European Food Safety Authority [12].

The ability of *L.casei* IIB B-7280 and *L.plantarum* IMB B-7679 to transform sodium selenite for synthesizing Nano-Se and other organic Se compounds which are suitable for making food additives makes it possible to consider Bacterial strains of Lactobacillus as a cheap source of organic Se and Nano-Se.

1. Bañuelos, G., Lin, Z.-Q., and Yin. X. Selenium in the Environment and Human Health. London: Taylor & Francis Group eBook Published29 November 2013, DOI https://doi.org/10.1201/b15960
2. Alzate A, Cañas B, Pérez-Munguía S, Hernández-Mendoza H, Pérez-Conde C, Gutiérrez AM, Cámara C Evaluation of the inorganic selenium biotransformation in selenium-enriched yogurt by HPLC-ICP-MS. J Agric Food Chem 2007, 55(24):9776–9783.
3. Aida Verónica Quintana, Manuel Olalla-Herrera, María Dolores Ruiz-López, Miriam Moreno-Montoro, Miguel Navarro-Alarcón. Study of the effect of different fermenting microorganisms on the Se, Cu, Cr, and Mn contents in fermented goat and cow milks. Food Chemistry 2015, 188, 234-239. DOI: 10.1016/j.foodchem.2015.05.008
4. Alzate A, Fernández-Fernández A, Pérez-Conde C, Gutiérrez AM, Cámara C (2008) Comparison of biotransformation of inorganic selenium by Lactobacillus and Saccharomyces in lactic fermentation process of yogurt and kerfir. J Agric Food Chem 56:8728–8736
5. Andreoni V, Luischi MM, Cavalca L, Erba D, Ciappellano S (2000) Selenite tolerance and accumulation in the L. species. Ann Microbiol 50(1):77–88
6. Xia S.K., Chen L., Liang J.Q.: Enriched Selenium and Its Effects on Growth and Biochemical Composition in Lactobacillus bulgaricus. J. Agric. Food Chem. 2007;55:2413−2417
7. Jingpeng Yang, Jing Wang, Kun Yang, Miaomiao Liu, Yiman Qi, Tingjing Zhang, Mingtao Fan, Xinyuan Wei. Antibacterial activity of selenium-enriched lactic acid bacteria against common food-borne pathogens in vitro. Journal of Dairy Science 2018, 101 (3) , 1930-1942. DOI: 10.3168/jds.2017-13430
8. Diowksz, A.; Ambroziak, W.; Wladarezyk, M. Investigation of ability of selenium accumulation by lactic acid bacteria of Lactobacillus sp. and yeast S. cerevisiae. Pol. J. Food Nutr. Sci. 1999, 49, 17–21.
9. Burk,R.F. (1983) Biological activity of selenium. Annu. Rev. Nutr., 3, 53–70.
10. Mehdi Y, Hornick J, Istasse L, Dufrasne I. Selenium in the environment, metabolism and involvement in body functions. Molecules. 2013;18:3292-3311. DOI: 10.3390/molecules 18033292
11. Xia S.K., Chen L., Liang J.Q.: Enriched Selenium and Its Effects on Growth and Biochemical Composition in Lactobacillus bulgaricus. J. Agric. Food Chem. 2007; 55:2413−2417
12. Anon 2012 European Food Safety Authority (EFSA) Scientific opinion on safety and efficacy of selenium in the form of organic compounds produced by the selenium-enriched yeast Saccharomyces cerevisiae NCYC R646 (Selmax 1000/2000) as feed additive for all species EFSA J. 10 2778

CALIX[4]ARENE C-956 INHIBITORY ACTION KINETIC ON PLASMA MEMBRANE Ca^{2+},Mg^{2+}-ATPASE ACTIVITY OF SMOOTH MUSCLE CELL

Veklich T.O., Shkrabak O.A., Golden O.V., Kardash O.O., Kosterin S.O.

O.V. Palladin Institute of Biochemistry, NAS of Ukraine, 9, Leontovicha St., 01054 Kyiv, Ukraine

The major role in control of consentration of ions of Ca in a cytoplasm belongs to the calcic transporters, to which, beside Ca^{2+}-pump, sarcoplasmatic reticulum, uniporter of mitochondria and Na^{+},Ca^{2+}-exchanger of plasmatic membrane, calcic pump of plasmatic membrane [1] belongs as well. It, in a case of smooth muscles, executes two fundamental functions: support of low concentration of Ca^{2+} in relaxed miocytes and decrease of this cation's concentration in mioplasm after contraction during relaxation of muscles [2]. Mg^{2+}-dependent Ca^{2+}-pump uses energy of hydrolysis of one ATP molecule for transport of one ion of Ca against gradient of the latter's consentration; this transportation is electrogenic, because only one proton is being transported vice versa [1].

To research a role and partial contribution of Ca^{2+},Mg^{2+}-ATPase into regulation of inter-cell concentration of ions of Ca, it is necessary to use selective, highly-effective inhibitors, which are practically absent up to day, comparatively to calcium pump of endo(sarco)plasmatic reticulum [3]. Nevertheless, it has being demoinstrated within last years, that cyclic oligomers of phenols, calixarenes, may be effective inhibitors and activators of enzymatic, receptor and transportive membrane-connected proteins. Calix[4]arene possess anti-virus, bacterocyde anti-swelling and anti-trombotic features.

We have showed in previous researches that calix[4]arene C-956 (we give cipher), used in a consentration 100 μM, effectively (for 75 % in comparison with control meaning) inhibated enzymatic activity of Ca^{2+},Mg^{2+}-ATPase in fraction of plasma membrane of myocytes, not practically influencing the activity of Mg^{2+}-independent Ca^{2+}-dependent ATPase, Na^{+},K^{+}-ATPase and Mg^{2+}-ATPase, which are localized in the same membrane structure.

To kinetically interpret influence of calix[4]arene C-956 over enzymatic activity of Ca^{2+},Mg^{2+}-ATPase of plasma membrane of myometrium, we have studied its action over concentration dependency of the mentioned activity on ions of Ca and ATP.

Calix[4]arene C-956 (5,11,17,23-tetra(trifluoro)methyl(phenylsulfonylimi-no)methylamino-25,27-dioctyloxy-26,28-dipropoxycalix[4]arene) (Fig. 1) have been synthesized and characterized with usage of methods MRI and infrared spectroscopy in a Department of Chemistry of Phosphorants of Organic Chemistry Institute of NAS OF Ukraine (Department's Chair – corresponding member of NASU V. Kalchenko).

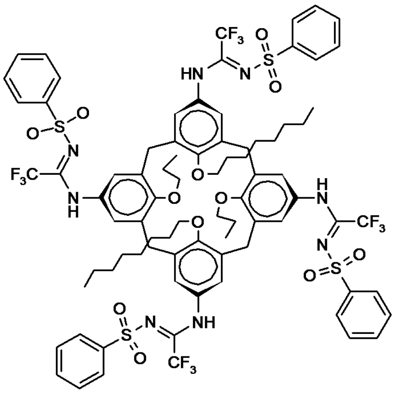

Fig.1. The structural formula of calix[4]arene C-956

Fraction of plasmatic mebranes of smooth muscles cells extracted from the myometrium of pig, as that was described earlier [4].

Content of protein in membrane fraction has been determined by method of M. Bredford [5] with usage of reaction by reagent Kumasi – G250.

It has been determined that for sarcolemma of myometrium of pig, enzymatic activity Ca^{2+},Mg^{2+}-ATPase is 3,4 ± 0,3 μmole P_i/мg of protein at 1 hour correspondently (M ± m; n = 7).

We have studied our experiments dependency of specific Ca^{2+},Mg^{2+}-ATPase activity from Ca^{2+} consentration in the incubation invironment under conditions of different consentrations of calix[4]arene C-956 (correspondently 1, 10, 30, 60 and 100 мсM). In this case, we have calculated consentration of Ca ions, taking into the account consentration of EGTA and its binding to Ca^{2+}. Enzymatic activity of Ca^{2+},Mg^{2+}-ATPase of plasma membrane of myometrium gradually increases by the level of increase of Ca ions consentration from 100 to 1000 нM, but decreases monotomously under condition of increase of inhibitor consentration (Fig. 2).

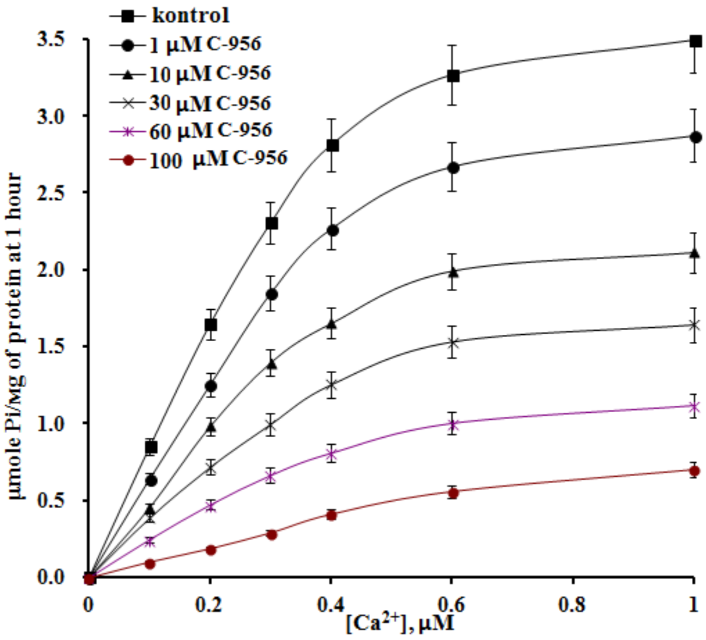

Fig.2. Influence of calix[4]arene C-956 concentration over dependence of Ca^{2+},Mg^{2+}-ATPase activity of plasma membrane of myometrium cells on concentration ions of Ca(M ± m, n = 5).

Kinetic parameters of activation by Ca ions and influence of calix[4]aren C-956 over them have been calculated. Amount of V_{max} has decreased under condition of consentration of calix[4]aren C-956 increase. Meaning of coefficient of activation of Ca^{2+},Mg^{2+}-ATPase K_{Ca} under condition of absence of calix[4]aren C-956 was 192 ± 1 nM, rate of Hill coefficient was n_H – 2,1 ± 0,1 (M ± m; n=5). Emission of calix[4]aren C-956 into the environment of incubation has increased constanta of activation by ions of Ca up to 317 ± 23 nM (under condition of presence of 100 μM C-956). Under this condition rate of Hill coefficient decreased up to 1,7 ± 0,1 (M ± m; n=5). Thus, in the range of consentration up to 50 мсM calix[4]aren C-956 practically does not influence binding of Ca^{2+},Mg^{2+}-ATPase to Ca ions, and cooperative effect of activization of enzyme by the mentioned ions.

We have studied how calix[4]aren C-956 influences binding of enzyme to ATP. Binding of Ca^{2+},Mg^{2+}-ATPase to ATP practically does not depend from consentration of calix[4]aren C-956 in the environment of incubation, what indicates absence of competition between ATP and inhibitor. That is why we may presume that substrate centre of Ca^{2+},Mg^{2+}-ATPase and hypothetic site of interaction of calix[4]aren overlap on the surface of enzyme.

Thus, data of this work may create ground for development of effective inhibitor of Ca^{2+},Mg^{2+}-ATPase of plasma membrane basedon calixaren, what will play an important role in further clarification of membrane mechnisms of cation exchange in smooth muscles, in particular, during studying of plasma membrane role in providing of electromechanic binding in them, and also in studying the regulation of ionic homeostasis in cells of smooth muscles. Besides, selective inhibitor of calcium pump of plasma membrane may be a basis for development of pharmacological means which would be able to correct inner-cell consentration of Ca ions under pathological conditions.

We are thankful to the academician of NASU V.I. Kalchenko for scientific cooperation.

1. Kosterin S.O., Babich L.G., Shlykov S.G. [et al.]. Biochemical properties and regulation of smooth muscle cell Ca^{2+}-transporting systems // К.: Science opinion, 2016. – 210p.
2. Kosterin S.O. Light-induced mass transport in amorphous chalcogenides: Toward surface plasmon-assisted nanolithography and near-field nanoimaging // Neurophysiology, 2003. – V. 35, N 3-4. – P. 215-228.
3. Veklich T.O., Mazur Iu.I., Kosterin S.O. Mg^{2+},ATP-depenent plasma membrane calcium pump of smooth muscle cells. II. Regulation of acrivity // Ukr. Biochem. J., 2015. – V. 87, N 2. – P. 5-25.
4. Kondratuk T.P., Buchenuk S.F., Prichepa A.A. [et al.]. Allocation and characterization of membrane fraction plasma membrane myometrium // Ukr. Biochem. J., 1986. – V. 58, N 4. – P. 50-56.
5. Bradford M.M. A rapid and sensitive method for the quantitation of microgram quantities of protein utilizing the prinsiple of protein-dye binding // Anal. Biochem., 1976. – V. 72, N 1-2. – P. 248-282.

THE EFFECT OF GOLD NANOPARTICLES ON SEMINIFEROUS TUBULES OF THE TESTES AFTER VITRIFICATION

Volkova N.O., Yukhta M.S., Goltsev A.M.

Institute for Problems of Cryobiology and Cryomedicine of the National Academy of Sciences of Ukraine, Pereyaslavskaya Str., 23, Kharkiv, 61016, Ukraine.

Now gold nanoparticles (AuNPs) are very attractive for usage in medical biotechnologies due to their unique properties and conventional methods of synthesis. This nanoscale metal can have different impact on both physical and chemical properties of cells, depending on its dose. AuNPs were shown to have antioxidative effects and could be helpful in regeneration processes. Warming and subsequent rehabilitation are important steps in the cryopreservation of testicular tissue. It is known that after freezing-thawing there are damages of cell membranes that reduce antioxidant protection and activate the apoptosis and necrosis in biological systems. Therefore, the involvement in cryobiological practice of nanotechnology advances, in particular, the use of nanoparticles as components of rehabilitation media, is a promising area for the restoration of testicular tissue after cryopreservation by vitrification. Thus, this study was based on the idea that the use of AuNPs as a component of rehabilitation medium can be effective for the improvement of morphofunctional state of immature testicular tissue after vitrification.

The AuNPs (Sigma-Aldrich, USA) with average size 15 nm were obtained by citrate synthesis with an initial metal concentration of 45 µg/ml. The immature testicular tissue fragments after vitrification-thawing were incubated at 22^{o}C for 30 min in Leibovitz's medium supplemented with AuNPs in concentrations of 2, 4, 6 or 10 µg/ml. Tissue fragments incubated under the same conditions without AuNPs were taken as a control. For MTT-test the samples after rehabilitation were incubated for 3 hrs at 37°C with [3-(4,5-dimethylthi azol-2-yl)-2,5-diphenyltetrazolium bromide] (Fluka, Germany) in final concentration of 0.5 mg/ml and then formazan crystals were solubilized by 100% DMSO. Absorbance was read at 570 nm on UV spectrophotometer (ERBA CHEM 7). To determine the enzymatic activity the tissue samples were homogenized and filtered, with following centrifugation (1000 g for 10 min). The activities of gamma-glutamyltransferase (GGT), glucose-6-phosphate dehydrogenase (G6PD) and total antioxidant status (TAS) were quantified by UV spectrophotometry using test kits (Randox, UK) in accordance with the manufacturer's instructions and normalized to 1 mg protein content. Histomorphology study was carried out maintaining blinding using Axio Observer Z1 inverted microscope (Carl Zeiss, Germany) with Axiovision v. 4.8 software on paraffin sections of 7 µm thickness that stained by hematoxylin and eosin. Immunohistochemical staining to MAGE-B1 were performed on deparaffinized tissue sections using monoclonal antibodies (1: 500, Invitrogen, USA). Then the relative number of positive for MAGE-B1 cells was determined. The results were processed with Student's t-test using Excel software.

The use of AuNPs in concentrations of 2-10 µg/ml did not lead to significant changes in the metabolic activity (MTT-test). There was an increase in GGT (by 1.31 and 1.35 times respectively) and TAS (by 1.22 and 1.34 times respectively) activity relative to the control in samples of testicular tissue after rehabilitation in the medium with AuNPs addition at a concentration of 4 and 6 µg/ml. The rehabilitation medium with 2-6 µg/ml AuNPs did not change the activity of G6PD. AuNPs at concentration of 10 µg/ml had a negative effect on the G6PD and TAS activity in the samples (it was decreased by 1.25 and 1.4 times respectively compared to the control).

The histological structure in control samples was characterized by moderate damage, in the form of unexpressed cell retraction, insignificant spherical cavities in the epithelial layer, its partial desquamation, pycnosis of some germinogenic cell nuclei, thickened and swollen of basement membrane. The rehabilitation of the vitrified seminiferous tubules in the medium with 2-6 µg/ml AuNPs did not have a pronounced effect on their histostructure relatively to the control, and at a concentration of 10 µg/ml even had a somewhat negative impact, increasing the degree of cell retraction and karyopyknosis. At the same time, the relative number of positive for MAGE-B1 cells did not significantly differ in all experimental groups.

Thus the AuNPs addition was the most optimal for rehabilitation of seminiferous tubules of the testes after vitrification in the concentration of 6 μg/ml. AuNPs addition at concentration of 10 μg/ml had a negative effect on the G6PD and TAS activity as well as on histological structure of seminiferous tubules. These findings relate to applied nanotechnology in its extension to reproductive medicine and can be used for development of effective rehabilitation medium for vitrified seminiferous tubules using the AuNPs.

OPTICAL PROPERTIES OF As_2S_3-Bi_2S_3 NANOCRYSTALLINE COMPOSITE

Voynarovych I.M.

Institute of Electron Physics, NAS of Ukraine, 21 Universytetska Str.,Uzhhorod 88017, Ukraine

The nano-scale semiconductor structures show a surprising variety of new interesting properties that are different from solid-state bulk materials. Reducing dimensionalities in one-, two or three directions provide new possibilities of creating materials and devices with peculiar characteristics and tuning their properties through quantum confinement phenomena. A nanocrystalline semiconductors embedded into different matrix are well known and classic object of nanomaterial science. Metal-chalcogenide nanocomposites can be promising materials in optics, electronics, opto-electronics, material science and engineering due to unique optical properties like low phonon energies, high transparency in NIR and MID infrared region, high linear and non-linear index of refraction. Combination of amorphous chalcogenide glass as a host media and bismuth sulphide nanocrystals attract our interest because the intrinsic anisotropy in the crystal structure of this material facilitates the formation of elongated nanostructures, in particular nanorods, nanoribbons, and nanowires. These nanostructures can find important applications in many nanodevices, for example field emitters, solar cells.

As_2S_3 –Bi_2S_3 nanocomposite formation was performed by the crystallization of rapidly quenched $(As_2S_3)_{1-x}$ $(Bi_2S_3)_x$ (x= 0.04, 0.06, 0.1) glasses at different conditions. Fine tuning of the annealing process of the quenched glass resulted glass-crystalline composites with different amount and distribution of 20-50 nm large Bi_2S_3 nanocrystals as well as larger, up to few micrometer long needle-like crystals.

The Raman spectra of rapidly quenched $(As_2S_3)_{1-x}$ $(Bi_2S_3)_x$ glasses and glass-crystalline composites reveal additional band at 290 cm^1 associated with oscillation of BiS_3 pyramidal structural units. The analysis of differential Raman spectra of As_2S_3 –Bi_2S_3 composites relative to pure As_2S_3 glass shows that intensity and shape of the 290 cm^1 band depends on concentration of Bi_2S_3 as well as annealing parameters. Optical absorption and the photoconductivity of bulk composite samples follow the changes of the structure in amorphous and amorphous-crystalline phase.

RAMAN SPECTROSCOPIC STUDY OF NANO-SIZED AMORPHOUS LAYERS OF SELENIUM AND PLASMON STRUCTURES “Au NPs/ Se film”

Yasinko T.I.[1], Yukhymchuk V.O.[2], Rubish V.M.[1], Minkovich V.V. [3], Mikla V.I.[3], Makar L.I.[1],
Hreshchuk O.M.[2], Horvat A.A.[3]

[1] *Institute for Information Recording, NAS of Ukraine, 4, Zamkovi schody St., 88000, Uzhgorod Ukraine*
[2] *V. E. Lashkaryov Institute of Semiconductor Physics, NAS of Ukraine, Prospekt Nauky, 41, Kyiv 03028, Ukraine*
[3] *Uzhgorod National University, 3, Narodna sq., 88000, Uzhgorod, Ukraine*

Surface-enhanced Raman scattering technique (SERS) has been developed and advanced recently. This method has been proven powerful and efficient in analyzing biological molecules, living cells and other substances of low concentration due to its unique property – enhancing of Raman signal via surface plasmon’s in nanosized metal structures. The possibility of determining of the presence and vibrational structure of low amount of molecules on SERS substances by their characteristic spectra also should be noted.

Numerous studies have shown that SERS substrates based on nanostructured Au and Ag films (prepeared by different methods of nanosized Au and Ag films) are the most convenient for this purpose. They allow efficiently increase the intensity of Raman signal by several orders of magnitude in chosen narrow spectral region [1-3]. It is necessary to accentuate that up to now the most attention was paid to biological objects. At the same time inorganic substances including nanosized chalcogenide layers were not examined at all.

In the present report we have demonstrated the results of investigation of influence of near field illumination on Raman spectra of nanosized amorphous selenium films.

Thin films of selenium with a thickness of 30, 50 and 60 nm were obtained by the method of thermal evaporation from quasi-closed diffusion cells of the corresponding composition on glass substrates and on the surface of arrays of randomly distributed gold nanoparticles (NPs) with different average NPs size (*d*) and maximum position of surface Plasmon resonance (SPR) band (λ_{SPR}). Selenium films were obtained at a deposition velocity of 1-5 nm/s. Arrays of Au NPs A1 (d=20-35 nm, λ_{SPR}=532 nm), A2 (d=30-40 nm, λ_{SPR}=538 nm) and A3 (d=40-60 nm, λ_{SPR}=574 nm) were used for the experiments. Investigations of Raman spectra of as-prepared and annealed selenium films and composite structures “Au NPs/Se film” were carried out at room temperature on the Horiba Jobion-Yvon spectrometer. For excitation, a red laser was used (λ_{exc}=671 nm).

On Fig.1 Raman spectra of amorphous Se layers (50 nm thickness) deposited on cleaned glass substrates (curve 1) and glass substrates with arrays of gold nanoparticles A2 and A3 (curves 2 and 3, respectively) are given. Raman spectra for nominally pure Se of different thicknesses are similar. For 50 nm film Raman scattering intensity was quite weak. For 30 nm thickness Raman signal is absent. As opposed, for films on arrays of Au NPs Raman signal are clearly discernible. The spectra shows intensive band at 253 cm^{-1} and weak peculiarities at 235, 185-188, 135 and 107 cm^{-1}. In [4] similar Raman spectrum was reported for nominally pure selenium films of micron thicknesses.

Here we note that Raman band located at 237 cm^{-1} dominant in spectrum of trigonal selenium and for monoclinic and glassy selenium – at 250 cm^{-1} [5]. Raman bands at 253 and 107 cm^{-1} can be assigned to vibrations in Se_8 fragments of rings, other bands – to vibration of atoms in chain-like Se_n formations. Accordingly, bands at 253 and 107 cm^{-1} can be associated with vibrations in Se_8 fragments, others – with vibration in chain-like Se_n groups.

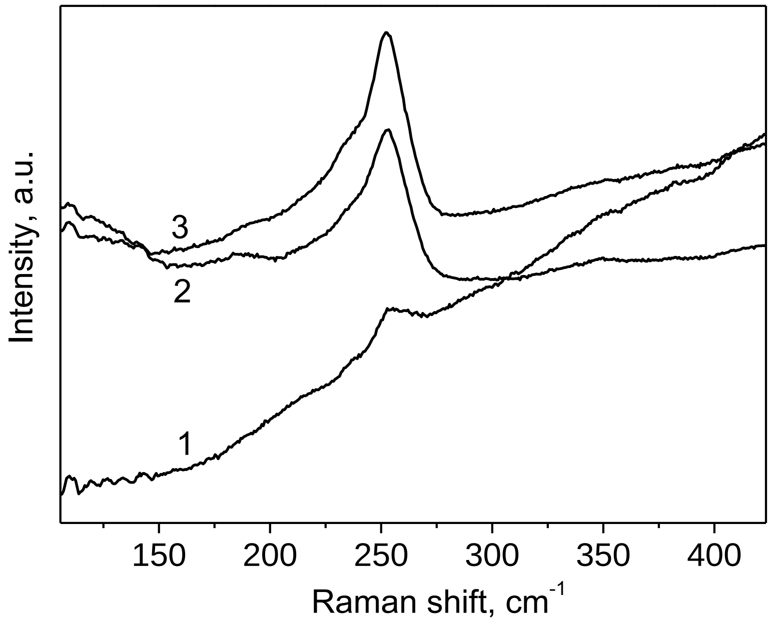

Fig.1 Raman spectra of as prepared 50 nm nominally pure selenium films (1) and deposited on arrays of Au NPs A2 (2) and A3 (3)

Thus, studies have shown that formed SERS substrates can be used to study the structure of chalcogenide nanolayers.

1. Moskovits M. Surface-enhanced spectroscopy // Rev. Modern Phys. – 1985. – V.57. – P.783-826.
2. Yukhymchuk V.O. Hreshchuk O.M., Dzhagan V.M. et. al. Experimental studies and modeling of “starlike” plasmonic nanostructures for SERS application // Phys. Stat. Solidi B. – 2018. – P. 1800280 (1-8).
3. Nabiev I.P, Efremov R.G., Chumanov G.D. Giant Raman scattering and its application to the study of biological molecules // Advances in physical sciences – 1988. – V.154. – No. 3. – P.459–496.
4. Meshalkin A., Paiuk A.P., Revutska L.A. et al. Direct surface-relief grating recording using selenium layers // Optoelectronics and semiconductor technics, 2018. – V. 54. – P. 240-247.
5. Shpak A.P. Rubish V.M., Ivanitsky V.P., Kunitska L.Yu. Non-ordering systems. P.II. Chalcogenide glasses and amorphous films – Kiev: Institute of Metal Physics, NAS of Ukraine. – 2010. – 159 C.

SURFACE NANOSCALE STRUCTURE OF SUPERCONDUCTING FILMS PROBED BY JUNCTION SPECTROSCOPY

Zhitlukhina E.S.

O.O. Galkin Donetsk Institute for Physics and Engineering, NAS of Ukraine, 46, Nauki Ave., 03028 Kyiv, Ukraine

Junction spectroscopy of superconducting films is a broad ranging term for using electrical measurements techniques conducted on superconductor-based junctions. Low-temperature scanning tunneling microscopy and spectroscopy as well as point-contact Andreev reflection experiments are widely used to reveal electronic spectra of superconductivity in studied samples and the electron-boson interaction causing its emergence. In both cases, the conductance is dominated by Andreev reflection and the well-known Blonder–Tinkham–Klapwijk (BTK) model used to extract related information. However, obtained spectra often exhibit unexpected features in the differential conductance-versus-voltage curves that cannot be appropriately explained by the BTK theory. In this contribution, we discuss physical origin one of the most frequent type of such features, local conductance dips at energies of the order of the superconductor gap, which do not follow from the conventional BTK approach.

Our explanation is based on the concept of the superconducting proximity effect that is often exploited for engineering exotic interfacial quantum phenomena requiring highly transparent interface (I) between superconducting (S) and normal (N) layers. As a rule, the nanometer-thick N sheath appears naturally due to degradation of a near-surface S-film part. If so, the BTK theory, originally applied to N′-I-S trilayers, should be generalized to the case of a four-layered N′-I-N/S heterostructure, here N′ is a non-superconducting counter-electrode, and its conclusions must be confirmed by related experiments.

Our calculations of the ballistic transport across an N′-I-N/S sample are based on a scattering formalism taking into account Andreev electron-into-hole (and inverse) reflections at N/S interfaces as well as transmission and backscattering events at the interface between N′ and N layers. Current-voltage characteristics of such devices exhibit a rich diversity of anomalous (from the viewpoint of the conventional BTK theory) features, in particular, the appearance of well-defined dips instead expected coherence peaks near the gap voltage biases.

For low-transparent interfaces I, we interpret the latter finding as emergence of a bound state inside the N nanoscale layer formed by quasi-electron and quasi-hole excitations. To understand conductance dips in samples with high-transmission interfaces I, we suggest a non-equilibrium-generated transformation of the quantum transport across the N′-I-N/S structure when the junction spectroscopy probes superconducting correlations at different positions in the N/S side, depending on the bias voltage. At small voltages, the differential conductance is dominated by the presence of proximity-induced order parameter Δ_N in the N layer and we are dealing with N′-I-S′ where S′ is an inhomogeneous superconductor where the spatially dependent gap changes from a small Δ_N value to Δ_S inside the bulk S superconductor. At larger voltage biases $V > \Delta_N/e$, hot electrons arriving into the N sheath destroy the superconducting state and we get a heterostructure formed by the S film, a normal N′-I-N counter-electrode and an interface with an unknown transmissivity. The conductance gap and a small hump are now naturally attributed to the superconducting gap edge of the S electrode. These predictions have been checked on the example of junctions based on superconducting binary Mo-Re alloy (the critical temperature was between 10 and 12 K). There were two kinds of the samples, those with a very low transmissivity (tunneling ones) and with the transmission probability about unity (point contacts). Both types of junctions have demonstrated good agreement with the proposed theory.

The study was carried out within the Target program fundamental research of the NAS of Ukraine (Project No. 17/20-H).

SOME APPLICATIONS OF NANOSTRUCTURED MATERIALS AS INTERMEDIATE LAYER FOR RESISTANCE BUTT WELDING OF HIGH TEMPERATURE ALLOYS

Ziakhor I.V., Kuchuck-Yatsenko S.I., Zavertannyi M.S., Nakonechnyi A.O., Radchenko L.M.

E.O. Paton Electric Welding Institute of National Academy of Sciences of Ukraine,
11 Kazimir Malevich Str., 03150, Kyiv, Ukraine

One of the urgent problems of design and manufacturing of aircraft gas turbine engines (GTE) is development of methods of producing sound welded joints of high temperature alloys – nickel superalloys, and intermetallic alloys, in particular, γ-TiAl titanium aluminides. Intermetallic alloy sensitivity to welding cycle is driving technologists to look for the ways to facilitate the conditions of activation of the surfaces being welded, primarily due to intensification of the process of local plastic deformation in the welding zone.

The main technique in pressure welding processes is application of interlayer from various materials. For instance, at vacuum diffusion welding (VDW) the conditions for activation of the surfaces being welded are achieved through application of intermediate layer from nanolayered foil (NF) produced by the process of electron beam evaporation and deposition of the vapour phase in vacuum. Positive influence of NF of application at VDW is associated with intensification of mass transfer processes in the welding zone, owing to running of the reaction of self-propagating high-temperature synthesis (SHS).

VDW application is limited by the need to heat the entire item being welded up to considerable temperatures in the vacuum chamber, extremely high requirements to preparation of surfaces being welded and low efficiency of the welding process. Therefore, an urgent issue is studying the applicability of pressure welding processes providing higher efficiency and possibility of sound joining of various materials without application of shielding medium or vacuum. Such pressure welding processes include resistance butt welding (RBW).

The effectiveness of application of NF of TiNi/Al and Ti/Co systems in the processes of RBW of titanium aluminide alloys was studied. In the case of direct RBW of the γ-TiAl alloy and ortho-Ti_2NbAl alloy, cracks are formed in the joint zone due to low ductility of the alloy, uneven heating along the depth and cross section of the workpieces, high level of welding stresses due to the need of significant heat input to activate surfaces to be welded.

NF of two types (Figure 1) was used as interlayer at RBW. NF thickness was as follows: TiNi/Al – 50 μm, Ti/Co NF – 73 μm. Difference in foil composition predetermines the difference in their melting temperature T_{melt}, compared to T_{melt} of the base metal (BM) of alloy being welded. Experiments were performed in K766 system, welding mode parameters were varied in the following ranges: 5 – 20 MPa pressure at heating, 20 – 100 MPa upset pressure, 3 – 8 mm upset value, and 0.5 – 2.5 s RBW process duration.

Microstructure of welded joint of γ-TiAl (Ti-47Al-2Nb-2Cr,at %) alloy made with application of TiNi/Al foil is given in Figure 2. No defects of any kind, including cracks, oxide films, and pores, were found in the joint zone. Structural changes in the joint cover a zone of total width of about 2 mm. Coarse-crystalline completely plate-like structure of BM is transformed into fine-grained bimodal $\gamma/\gamma + \alpha_2$ structure in the joint zone. The products of NF transformation at the joint are not detected.

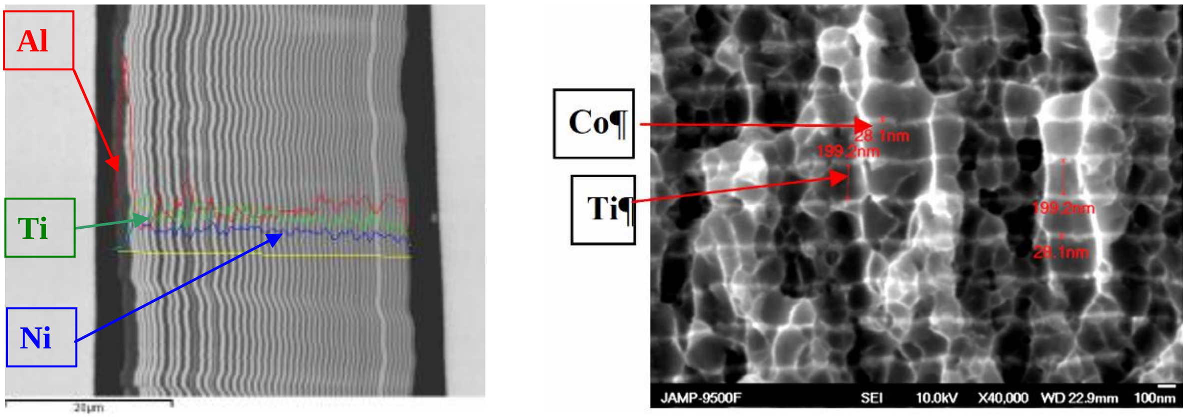

a b

Figure 1 – SEM through-thickness images in nanolayered foils Al-Ti/Ni (a), and Ti/Co (b)

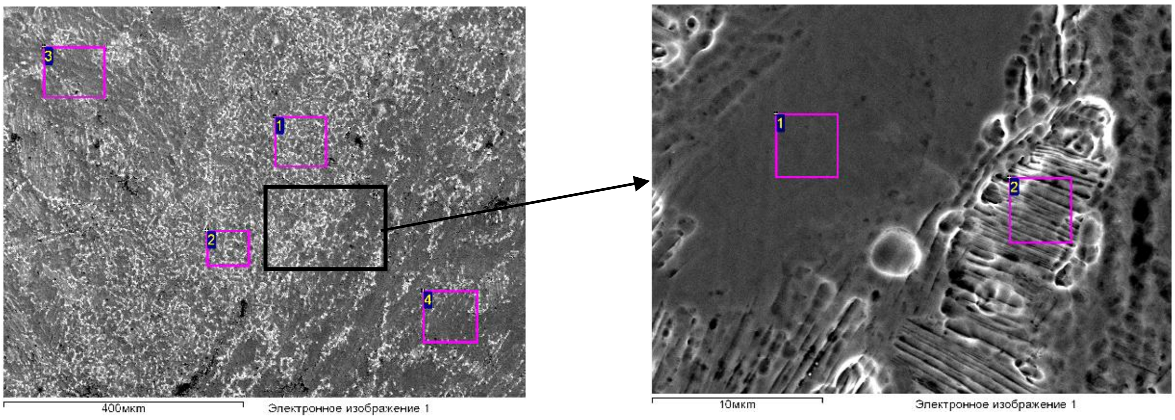

#	C	Al	Si	Ti	Cr	Nb
1	1.56	29.57	0.02	60.18	2.62	6.05
2	1.81	29.95	0.08	60.23	2.66	5.27
3	1.41	30.91	0.07	59.82	2.42	5.38
4	1.30	31.98	0.00	59.16	2.61	4.68

#	C	Al	Si	Ti	Cr	Nb
1	0.55	32.88	0.00	59.13	2.54	4.90
2	1.47	30.77	0.05	59.49	2.72	5.49

Figure 2 - Microstructure, and chemical composition, weight % (b) of the welded zone of γ-TiAl alloy made RBW with application of TiNi/Al foil as intermediate layer

At application of Ti/Co foil of eutectic composition, and at the value of upset pressure more than 6 mm chemical inhomogeneity in the welded joint is not detected. Metal structure in joining zone is fine-grained bimodal $\gamma/\gamma + \alpha_2$, irrespective of BM initial microstructure. Analysis of the results shows that joining zone of γ-TiAl alloy is narrow and uniform in cross section of the workpieces (Figure 3). This effect is due to the use of an interlayer of nanolayered foil Ti/Co system of eutectic composition, which provides localization of the processes of heat release and deformation of the contact volumes of metal during welding.

The use of Ti/Co foil interlayer ensures the formation of a defect-free joint with the indicators of mechanical properties at the level of the base metal. At rupture testing of joints, fracture runs through BM γ-TiAl alloy.

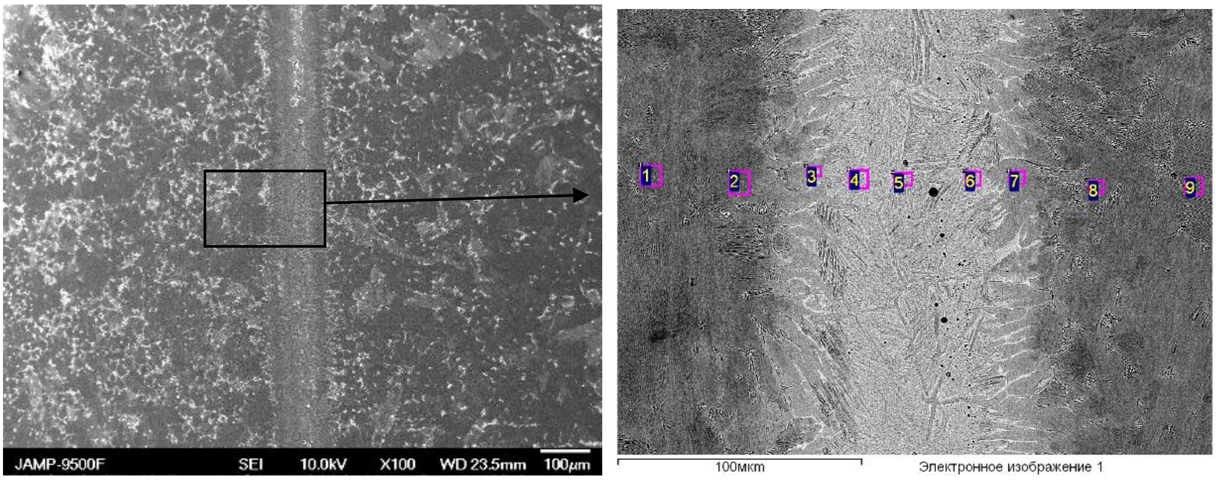

Point	C	Al	Ti	Cr	Co	Nb
1	0.53	32.90	59.23	2.36	0.00	4.99
2	0.68	31.73	59.75	2.93	0.00	4.91
3	0.95	26.66	63.02	2.68	1.53	5.16
4	0.39	22.72	67.61	1.59	3.83	3.87
5	0.62	20.20	71.12	1.41	5.58	1.07
6	0.50	24.66	66.47	1.81	2.61	3.95
7	0.95	27.64	63.41	2.47	0.64	4.89
8	0.72	31.52	60.45	2.02	0.00	5.30
9	1.01	31.46	60.52	2.26	0.00	4.74

Figure 3 – Microstructure, and chemical composition of welded zone of γ-TiAl alloy made RBW with application of Ti/Co foil as intermediate layer

Thus, it is found that application of NF of TiNi/Al and Ti/Co systems allowed an essential improvement of joint formation, reducing sample upset value and RBW process duration. The use of NF as an intermediate layer in RBW of titanium aluminides promotes rapid activation of welding surfaces with much lower energy input, and, accordingly, reduces the probability of cracking.

VACUUM DIFFUSION WELDING OF HIGH Nb CONTAINING TiAl ALLOY WITH Ni-BASED ALLOY

Petrushynets L.V., Falchenko Iu.V., **Ziakhor I.V.**, Fedorchuk V.E., Nakonechnyi A.O.

E.O. Paton Electric Welding Institute of National Academy of Sciences of Ukraine,
11 Kazimir Malevich Str., 03150, Kyiv, Ukraine

High Nb containing TiAl alloys represent an essential class of alloys that have a unique set of mechanical properties that makes them highly promising for the manufacture of gas turbine engines components. For practical use, it is important to develop a technology for welding of high Nb containing TiAl alloys with other materials, such as Ni-based alloys. Considering the significant difference in the chemical composition and properties of alloys based on TiAl and Ni, joining these two materials is a difficult task. Titanium and nickel can interact with the formation of a number of intermetallic compounds (Ti_2Ni, TiNi and $TiNi_3$). It follows that the main problem in welding high Nb containing TiAl alloy with Ni-based alloys is a strong tendency to form brittle phases in the joint zone, which can negatively affect the mechanical properties.

The object of study was heat-resistant nickel-based alloy HN77TUR (Ni–20.62–21.19Cr–2.49–2.63Ti–0.62–0.73Fe–0.57–0.88Al–0.37–0.55Si%, wt.) and high Nb containing TiAl alloy (Ti–38.42–43.85Nb–10.83–13.61Al–0.82–1.80W%, wt.). Interlayers of Al/Ni, Cu/Ti and Ni/Ti systems, produced by electron-beam physical vapour deposition (EBPVD) method were selected for investigations. Evaluation of the vacuum diffusion welding parameters influence on formation of bimetal joints of TiAl with HN77TUR was conducted in the temperature range of 950 °C, at the pressure of 5 MPa and welding time of 5 minutes.

During welding without interlayers in the joint zone there is a significant increase in the microhardness up to 11.9 GPa. This may be the result of the formation of intermetallic compounds Ni_3Nb and Ni_6Nb_7.

Application of nanolayered Al/Ni foil as an interlayer in vacuum diffusion welding of high Nb containing TiAl alloy with Ni-based alloy leads to formation of chains of pores along the interlayer/base material boundaries, as well as cracks along the interlayer/titanium aluminide boundary. Microhardness of the joint zone is on the level of 8.8 … 9.3 GPa.

Cu/Ti interlayer is more promising, compared to Al/Ni because no cracks or pores were found in the butt joint. It also ensures formation of joints with microhardness up to 8.7 GPa.

Application of Ni/Ti nanolayered foil as interlayer ensures formation of joints. Cracks are observed in some areas of the welded joint. The microhardness of the joint zone is not higher than 6.7 GPa.

The use of two-element foil as interlayer can significantly reduce the difference in microhardness values in the joint. In this case, the microhardness of the joint zone is closer to the microhardness values of TiAl alloy.

APPLICATION OF THE HILLERT METHOD FOR CALCULATION OF THREE-COMPONENT SYSTEMS USING THE GEOMETRIC THERMODYNAMICS

Zhiguts Yu., Kurytnik I.

Uzhhorod National University, 46, Pidgirna Str., Uzhhorod, Ukraine, 88000
Institute of management and production engineering, ul. M. Kolbego 8, Oswiecim, Poland, 32600

It is easy to make sure that the original Hillert equation that contains tie-line coordinates (to say nothing of great approximations needed while it was being deduced isn't used for such computation as while coming from tie-line $\alpha_0\beta_0$ to tie-line $\alpha_I\beta_I$ and then to tie-line $\alpha_{II}\beta_{II}$ these coordinates change greatly.

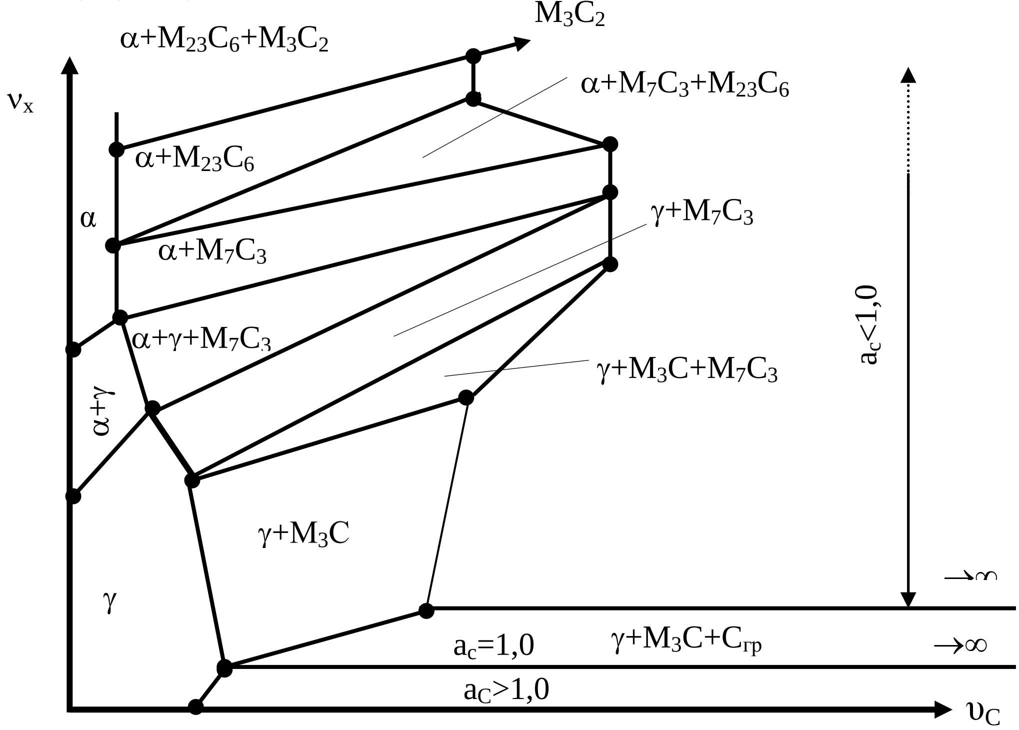

Fig. 1. Schema isothermal section of state diagram of Fe-C-X, alloys in which under $a_C>1,0$ graphite is formed (under condition that graphite is been selected as a standard state of carbon) and carbide phases M_3C (cementite), M_7C_3, $M_{23}C_6$ and M_3C_2

The triangle $\alpha+\gamma+M_7C_3$, in the inner part of which the carbon activity is constant allows to move the value a_C from the lower right tie-line of triangle to the upper tie-line and to continue computations by the equation of type in the tetragon $\alpha+M_7C_3$. Prolonging the above mentioned structure for the regions laying above the triangle $\alpha+M_{23}C_6+M_7C_3$, the tetragon $\alpha+M_{23}C_6$ and triangle $\alpha+M_{23}C_6+M_3C_2$ we can lead the computations to the region of highchrome alloys but with large degree of approximation (because the Hillert method, in principal, is perfectly designed only for deluded systems).

Conclusions. 1. The Hillert method is also spread to tie-lines of two-phase regions of triangle simplexes of tree-component diagrams of state Me-C, when these regions are removed from those sides of the mentioned triangles which in two-component under investigation in the computations of its activity. 2. The original Hillert method proved to be unserviceable to solve this problem in contrast to modified method, which uses Screinemakers orthogonal system of coordinates. 3. The reason of this lies in the fact that the modified method doesn't demand the definition and usage in the computations the coordinates of the corresponding tie-point.

Satelite conference

ACCELERATE

INVITED REPORTS

MAGNETIC PHASES IN TWO-DIMENSIONAL GEOMETRICALLY FRUSTRATED SHASTRY-SUTHERLAND SYSTEM TmB_4

Matúš Orendáč[a], Slavomír Gabáni[a], Pavol Farkašovský[a], Emil Gažo[a], Jozef Kačmarčík[a], Gabriel Pristáš[a], Konrad Siemensemeyer[b], Natalya Shitsevalova[c], and Karol Flachbart[a]

[a] *Institute of Experimental Physics, Slovak Academy of Sciences, Watsonova 47,*
SK-04001 Košice, Slovakia
[b] *Helmholtz-Zentrum Berlin für Materialien und Energie, Hahn-Meitner Platz 1,*
D-14109 Berlin, Germany
[c] *Institute for Problems of Materials Science NASU, Krzhyzhanovsky 3,*
UA-03680 Kiev, Ukraine

Systems with a geometrically frustrated Shastry-Sutherland lattice which show fractional magnetization plateaus M/M_{sat}, where M is the magnetization and M_{sat} denotes the saturation magnetization, have attracted recently a lot of attention. Among them above all TmB_4, a metallic tetraboride with strong Ising-like anisotropy along the c-axis which orders magnetically at $T_N \approx$ 11.7 K [1-3]. In the ordered phase so far three different phases are well established: - the low-field antiferromagnetic (AF) Néel phase which consists of an AF arrangement of dimers, - the half plateau phase (HPP) with M/M_{sat} = ½ in fields above about 17.5 kOe, - and the fractional plateau phase (FPP) with M/M_{sat} = 1/7, 1/8 1/9 which is located between the AF and HP phases. Recently performed studies on the FPP [4] have shown that this phase is not thermodynamically stable state, but a meta-stable variant of the basic low field AF phase.

In our contribution we present a detailed study of the ground state and stability of the AF, FPP and HPP based on magnetization and ac-calorimetric measurements. Magnetization measurements show that the FPP states are thermodynamically stable when the sample is cooled in constant magnetic field from the paramagnetic phase to the ordered one at 2 K. On the other hand, after zero-field cooling and subsequent magnetization they appear to be of meta-stable / dynamic origin. In this case the FPP states are closely associated with the HPP, mediate the HPP to the low-field AF phase and depend on the thermodynamic path / history. In this context thermodynamic paths were identified that lead to very flat fractional plateaus in the FPP. Moreover, with a further decrease of magnetic field also the low-field AF phase becomes influenced (altered) and exhibits a plateau of the order of 1/1000 M_{sat}. Parallel ac-calorimetric measurements point to corresponding entropy changes.

1. K. Siemensmeyer, E. Wulf, H.-J. Mikeska, K. Flachbart, S. Gabáni, S. Maťaš, P. Priputen, A. Efdokimova, and N. Shitsevalova, Phys. Rev. Lett. 101 (2008) 177201.
2. S.S. Sunku, T. Kong, T. Ito, P.C. Canfield, B.S. Shastry, P. Sengupta, and C. Panagopoulos, Phys. Rev. B 93 (2016) 174408.
3. Mat. Orendáč, S. Gabáni, E. Gažo, G. Pristáš, N. Shitsevalova, K. Siemensmeyer, K. Flachbart, Sci. Reports 8 (2018) 10933.
4. J. Trinh, S. Mitra, C. Panagopoulos, T. Kong, P.C. Canfield, A.P. Ramirez, Phys. Rev. Lett. 121 (2018) 167203.

INVESTIGATING THE SHORT RANGE ORDER OF CHALCOGENIDE AMORPHOUS MATERIALS BY PHOTOELECTRON SPECTROSKOPY

Matolin V.[1], Tsud N.[2], Popovych N.[3], Rizak V.[3]

[1]*Department of Surface and Plasma Science, Faculty of Mathematics and Physics, Charles University, V Holešovičkách 2, 18000 Prague 8, Czech Republic*
[2]*Elettra-Sincrotrone Trieste S.C.p.A., Strada Statale 14, km 163.5, in Area Science Park, 34149 Basovizza, Trieste, Italy*
[3]*Uzhhorod National University, Pidhirna Str., 46, 88000 Uzhhorod, Ukraine*

Amorphous chalcogenides is a class of materials with a wide range of potential applications in modern nanotechnology. These materials show a number of interesting peculiarities in their electronic and optical properties that is, first of all, related to their geometrical structure at the nanoscale. Therefore, they are interesting as model objects too, intensively studied for better understanding of ordering and self-organization in amorphous materials. The structural information that could be obtained by experimental diffraction methods on these materials is limited due to absence of long-range ordering [1]. Theoretical and experimental investigations in the last years shown that two- and three-components chalcogenide glassy semiconductors are formed in a considerably wider variety of basic structural units than their crystal analogs. The majorities consist of the middle-range ordered groups (clusters) with different geometry, depending on stoichiometry and producing technology [2]. The ordering geometry of these groups in bulk glasses and films determines its physical properties. Taking into consideration the methodical aspect the role of effective spectroscopic structural studies of complex chalcogenide glasses becomes more and more important. The photoelectron spectroscopy can provide direct structural information about local chemical order due to surface sensitivity and high resolution.

As-deposited, annealed, and *in situ* As_2S_3 nanolayers, illuminated by blue (405 nm) and red (650 nm) laser light, were studied using synchrotron radiation photoelectron spectroscopy. Changes in composition and local atomic coordination occurring in the irradiated region of As_2S_3 films were monitored by analysis of As 3d and S 2p core levels. These studies show that both the thermal treatment and the red laser illumination of As_2S_3 nanolayers decrease the concentration of homopolar (As-As and S-S) bonds. From the other hand, an increasing concentration of As-rich structural units (s.u.) with a homopolar As-As bond was observed under *in situ* blue laser illumination of As_2S_3 nanolayers.

The photoemission spectra of $As(Sb,Bi)_2S_3$ nanolayers before and after thermal annealing and laser illumination were measured using the synchrotron light source. The comparison of Sb 3d and S 2p core level spectra before and after annealing shows changes of the peak shapes and intensities what can indicate to formation of new structural units (i.e. chemical bonds) in near surface layers.

To investigate the influence of laser illumination on the surface structure we have performed the same photoelectron measurements on optically modified Sb_2S_3 sample (i.e. illuminated during 1 hour using diode laser operating at 473 nm). The analysis of Sb 3d core level spectra shows the appearing an additional shoulder what can be explained by new bonds formation under the laser illumination.

For Bi_2S non-illuminated film the wide scan was measured at the excitation photon energy of 615 eV and the positions of Bi 5d, Bi 4f, S 2p, C 1s and O 1s peaks were determined. The spectrum of Bi 5d core level region was measured in detail. The comparison Bi 5d core level before and after thermal treatment at 210°C (T_g-30°C) revealed the increasing of signal intensity and additional peak appearance at lower energy. The analyze of Bi 4f core level peaks measured after thermal annealing shows the peak shape change – the appearance of shoulder at lower energy. The peak position did not change at the same. The same measurements were carried out for laser irradiated Bi_2S_3 film ((i.e. illuminated during 1 hour using Ar-ion laser operating at 515.5 nm).

Analysis of the obtained spectra of Bi 4f core level shows a decrease in intensity and change in peak shape and position (in high energy) compared to the peak of the film before irradiation and annealing. The similar effects were observed in S 2p core level spectra of these films.

Our studies have shown that the surface of As_2S_3 nanolayers consists a network with mainly AsS_3 pyramidal rings and/or chains and contains small amount of S-S (bridges) and As-As (As4S3) bonds. The deeper As_2S_3 layers have significant amount of As-As bonds assigned to realgar-like As_4S_4 molecules. Laser irradiation leads to As oxidation and to increase the concentration of S-S bonds, to decomposition of realgar As_4S_4 molecules in deeper As_2S_3 layers and to polymerization of the structure. Similar effects were observed in surface Sb_2S_3 and Bi_2S_3 layers.

1. Feltz, Amorphous and Glassy Nonorganic Solid State (Translated from German, Ed. House “Mir”, Moscow, 1986).
2. R. Holomb, V. Mitsa, Solid. St. Commun. 129 (2004) 655.

STRUCTURAL, MECHANICAL AND THERMODYNAMIC PROPERTIES OF LITHIUM POTASSIUM TETRABORATE CRYSTALS UNDER HIGH PRESSURE: DFT CALCULATIONS AND SYNCHROTRON RADIATION X-RAY DIFFRACTION

Leonid Dubrovinsky[1], Iryna Chobal[2], Anna Pakhomova[3], Oleksandr Chobal[2], Aleksandr Kurnosov[1], Volodymyr Adamiv[4], Vasyl Rizak[2]

[1]Bayerisches Geoinstitut, Bayreuth, Germany
[2]Uzhhorod National University, Uzhhorod, Ukraine
[3]Deutsches Elektronen-Synchrotron DESY, Hamburg, Germany
[4]Vlokh Institute of Physical Optics, Lviv, Ukraine

Lithium potassium tetraborate ($LiKB_4O_7$) single crystals are a recently grown perspective nonlinear optical materials. Alongside with moderate piezoelectric coefficients, wide region of transparency and good luminescent properties these materials exhibits excellent nonlinear optical and photoelastic properties. Moreover, $LiKB_4O_7$ possesses high third-order nonlinear optical parameters and acoustooptic figure of merit when compared to other borate crystals [1,2]. Knowledge of structural, mechanical and thermodynamic properties of $LiKB_4O_7$ is important for interpretation peculiarities of chemical bonding and compression behavior of the material and thus explanation of it physical properties.

The single crystals of $LiKB_4O_7$ growth from stoichiometric melt by the Czochralski technique and belong to the space group $P2_12_12_1$ (orthorhombic system). We used an irregular-shaped crystal of $LiKB_4O_7$ (with size about 0.040 x 0.035 x 0.020 mm^3) for the synchrotron radiation X-ray diffraction study under high pressure. This experiment was performed at the Extreme Conditions Beamline P02.2 of PETRA III at Deutsches Elektronen-Synchrotron (DESY, Hamburg) using the wavelength of 0.2910 Å. Selected crystal together with small ruby crystal (for pressure estimation) were loaded into BX90-type diamond anvil cell (DAC) equipped with Boehler-Almax-designed diamonds (250 μm culet size) and rhenium gasket. The Neon gas was used as a pressure-transmitting medium. At each pressure both a wide-scan and a stepped ω-scan were collected for investigated crystal. Wide-scans consisted of 40 s exposure during rotations of ± 20° of the DAC. Step scans consisted of individual exposures taken over 0.5° intervals to constrain the ω angle of maximum intensity of each peak. Collected diffraction images were analyzed using the program CrysAlis Pro©. The SHELXL program package was used for all structural determinations.

The total energy per unit cell, electronic structure and thermodynamic properties of $LiKB_4O_7$ were calculated using the pseudopotential plane wave method, within density fictional theory (DFT) as implemented in ABINIT computer code [3]. All *ab initio* calculation were performed using the resources of the computing cluster at the V.M. Glushkov Institute of Cybernetics of the National Academy of Science of Ukraine.

In the present work, we performed careful experimental and theoretical investigations of evolution of structural, mechanical and thermodynamic properties of $LiKB_4O_7$ single crystals under application of high pressures up to 25 GPa. The hydrostatic pressure-induced volumetric changes of crystal lattice were measured using HP-XRD and described by the third-order Birch-Murnaghan equation of state (BM-EoS). The results of fitting of the BM-EoS were used to calculate bulk moduli and pressure derivatives of the bulk moduli of $LiKB_4O_7$.

We found anomalous compression behavior of axes that could be accompanied by isostructural phase transitions at pressures about 7.5 and 12 GPa with a volume drop by ~5.3% and ~2.1% respectively. Both structural changes leads to an increase in the average coordination number of boron atoms under pressure. The bulk modulus of the $LiKB_4O_7$ crystal is 32.6 GPa at ambient pressure, which is in excellent agreement with the results of other studies. Along with the increase of pressure, the value of the bulk modulus increases, which indicates that the low-pressure phase of $LiKB_4O_7$ is a bit more compressible than two high-pressure phases.

The research leading to this result has been supported by the project CALIPSOplus under the Grant Agreement 730872 from the EU Framework Programme for Research and Innovation HORIZON 2020

1. M. Sukumar, R. Ramesh Babu, K. Ramamurthi, Linear and third-order nonlinear optical properties of $LiKB_4O_7$ single crystals, Applied Physics B 121, 369 (2015).
2. O. Mys, V. Adamiv, I. Martynyuk-Lototska et al. Piezooptic and acoustic properties of $KLiB_4O_7$ crystals, Ukrainian Journal of Physical Optics 8, 138 (2007).
3. Gonze, X., Amadon, B., Antonius, G., Arnardi, F., Baguet, L., Beuken, J. M et al. The abinit project: Impact, environment and recent developments. Computer Physics Communications, 248, 107042 (2020).

NEAR AMBIENT PRESSURE XPS FOR IN OPERANDO STUDY OF GAS SENSORS

M. Vorokhta[1], I. Khalakhan[1], T. Skála[1], J. Vlček[2], P. Fitl[2], M. Vrňata[2], J. Lančok[3], A. Kozma[4], I. Matolínová[1], V. Matolín[1]

[1]*Department of Surface and Plasma Science, Charles University, Prague, Czech Republic*
[2]*Department of Physics and Measurements, Institute of Chemical Technology, Prague, Czech Republic*
[3]*Institute of Physics, Academy of Sciences of the Czech Republic, Prague, Czech Republic*
[4]*Department of Physical and Colloid Chemistry, Uzhhorod National University, Uzhhorod, Ukraine*

In this study we would like to present an application of laboratory-based near ambient pressure x-ray photoelectron spectroscopy (NAP-XPS) for in operando characterizations of gas sensors. We show that this tool can be successfully used for study of different (SnO_2, CuOx, ZnO) nanostructured chemiresistors which exhibit large surface-to-volume ratio with high concentration of active surface sites for chemisorption. The SnO_2 nanostructured layers were prepared by pulsed laser deposition, CuO_x nanowires were obtain by the thermal oxidation method, while ZnO nanowires were synthesized by hydrothermal method. Scanning and transmission electron microscopies (SEM, TEM) and atomic force microscope (AFM) were used to characterize the morphology of the as-prepared oxides. A simple gas sensors were realized by depositing the nanostructures on special fused silica substrates. Then, chemical analysis was performed on their surfaces in operational conditions by means of NAP-XPS, i.e. under exposure to different reactive atmospheres at high temperatures while following the resistivity of the films. The unique combination of thin film resistivity measurement and photoelectron study under higher pressure brought a new insight into sensoric properties and catalytic processes on the surface of studied sensors and helped better understand the gas sensing mechanism by studied materials.

STRUCTURE AND PROPERTIES OF CHALCOHALODENIDE GLASSES AND COMPOSITIES ON THEIR BASIS

Bih.L.[1], Guranich P.P.[2], Mykaylo O.A.[3], Pisak R.P.[3], Rizak I.M.[3], Rubish V.M.[3], Solomon A.M.[4], Spesyvykh O.O. [2], Tsiple M.[5], Yurkin I.M.[2]

[1] *UFR – PCMI – Ceramiques et Verres, Faculte des Sciences et Techniques Errachidia, B.P 509, Boutalamine, Errachidia, Morocco*
[2] *Uzhgorod National University, Narodna Sq., 3 88000, Uzhhorod, Ukraine*
[3] *Institute for Information Recording of the NAS of Ukraine, Zamkovi Skhody St., 88000, Uzhhorod, Ukraine*
[4] *Institute of Electron Physics NASU, 21, Universitetska St., 88017, Uzhhorod, Ukraine*
[5] *Zakarpattia Institute of Postgraduate Pedagogikal Edukation, Uzhhorod, Ukraine*

The possibility of practical application attracts the interest to the chalcoiodide glasses on the basis of ferroelectric-semiconductor SbSI (antimony sulphoiodide). In the structural network of such materials under certain heat treatment conditions, it is possible to form crystalline SbSI inclusions of different dimensions and, accordingly, to create nano- and microcomposites with ferroelectric properties.

It is known that the structure and properties of non-crystalline materials can be changed by varying the regimes of synthesis and subsequent heat treatment.

In the present report the results of investigation of technological conditions influence (different regimes of synthesis – homogenization temperature of the melt and melt cooling rates; different regimes of heat treatment – annealing (low and high) temperature and annealing time) on structure, thermal and dielectric properties of glasses and composites in As_2S_3-SbSI, As_2Se_3-SbSI and GeS_2-SbSI systems.

Chalcogenide glasses were prepared using the vacuum melting method. Cooling the melts was carried out in the air and into cold water.

By the DTA method at heating rates 3, 6, 9 and 10 K/min the temperatures of heat effects T_g, T_c (glassforming and crystallization (n=1-3) temperatures, respectively) of glasses were determined.

The structure and dielectric properties (ε and $\tan\delta$) of as-prepared and annealed glasses was studied by the methods of X-ray diffraction, Raman and dielectric spectroscopy.

It was established that the crystallization of stadied chalcoiodide glasses is accompanied by anomalies on the temperature dependences of dielectric characteristics. The structure of the phase that aries in the glassy network at low temperature annealing corresponds to the structure of the SbSI crystal. A mechanism of nanocrystalline inclusions formation in structural network of chalcoiodide glasses has been suggested. In the course of cooling the melts from lower homogenization temperatures and accordingly, at lower cooling rates, the presence of SbSI nanocrystals in the glassy matrix was detected.

It has been established that the sizes of SbSI crystalline inclusions increase with annealing temperature and time. The nature of crystalline inclusions, which are formed in the structural network in conditions of high-temperature annealing, is determined.

The influence of annealing conditions on the structure and dielectric properties of chalcoiodide ferroelectric composites are discussed.

NANOCOMPOSITIES WITH FERROELECTRIC PROPERTIES IN As(Ge)-Sb-S(Se)-I SYSTEM

Elouadi B.[1], Barj M.[2], Gasinets S.M.[3,4], Guranich P.P.[4], Makar L.I.[3], Mykaylo O.A.[3], Pop M.M.[4], Rizak I.M.[3], Rubish V.M.[3], Solomon A.M.[5]

[1] *University La Rochelle, La Rochelle, France*
[2] *Université Lille1 Sciences et Technologies Laboratoire de Spectrochimie Infrarouge et Raman LASIR, Lille, France*
[3] *Institute for Information Recording of the NAS of Ukraine, Uzhhorod, Ukraine*
[4] *Uzhgorod National University, Uzhhorod, Ukraine*
[5] *Institute of Electron Physics NASU, Uzhhorod, Ukraine*

Antimony sulphoiodide (SbSI) is the most well know member of group of $A^{V}B^{VI}C^{VII}$ compounds, have unique properties required for practical applications as ferroelectric memory elements, ferroelectric ceramics, nonlinear dielectrics, elements of various sensors and detectors. Much less studies have been carried out for chalcoiodide ferroelectric nanocrystals. In this respect, chalcoiodide glasses of As(Ge)-Sb-S(Se)-I system are wery attractive materials since in the structural network of such materials under certain conditions of annealing and laser irradiation exists the possibility of formation nano- and mycrocrystalline ferroelectric inclusions various morphology and obtaining of ferroelectric glassceramics with preset parameters, respectively.

In the present report obtaining peculiarities, structure, optical and dielectric properties of as-prepared and crystallized glasses and amorphous films of As(Ge)-Sb-S(Se)-I system are discussed. Glasses, amorphous films and composites on their basis of the following cuts are studied: As_2S_3-SbSI, Sb_2S_3-AsSI, As_2S_3-Sb_2S_3-SbI_3, As_2Se_3-SbSI, GeS_2-SbSI. The structure of as-prepared and crystallized glasses and amorphous films was studied by the methods of X-ray diffraction and Raman spectroscopy.

Nanoheterogenous structure of all studied antimony-contained glasses was established on the basis of Raman spectra investigations. It is shown that glassy matrix is formed by only binary structural groups with heteropolar bonds (for example, AsS_3, $AsSe_3$, AsI_3, SbI_3 and contains molecular fragments with homopolar (for example, As-As, S-S, Se-Se) bonds. Ternary structural units $SbS_{2/2}I$ in studied glasses and amorphous films not detected.

X-ray and Raman studies have shown that the structure of phase that arises in glass matrix at continuous heating in the “glass forming temperature (T_g) –crystallization temperature (T_c)” range and isothermal annealing (near T_c) corresponds to the structure of crystalline SbSI. Diffractograms and Raman spectra of annealed glasses and films have a number of reflexes and bands, which position satisfactory coinside with the positions of intensive lines and bands in the diffractograms and Raman spectra of polycrystalline SbSI. With annealing time increasing the intensity of reflexses and bands increases. This fact may by considered as the evidence about increasing the size of antimony sulphoiodide crystalline inclusions in glass matrix. Formation in the glass matrix at heating the nanosized crystals of SbSI and their growth are accompanied by anomalies on the temperature dependences of dielectric permittivity (ε) and tangent of dielectric loss angle ($\tan\delta$). Also, glass crystallization is attended to a sharp increase of dielectric parameters (ε and $\tan\delta$).

A mechanism of forming ferroelectric sulphoiodide antimony crystalline nanoinclusions in structural network of chalcoiodide glasses and films has been suggested.

The effects and annealing conditions on structure and properties of composites on chalcoiodide ferroelectrics basis is discussed.

ANALYSIS OF THE GROWTH AND CRYSTAL STRUCTURE FOR $Pb_{0.9}Cd_{0.1}Te$:Pb THIN FILMS

Kostyuk O.B.[1], Głowa Ł. [2], Naidych B.P.[3], Tsymbalyuk T.P.[3], Mezhylovska L.Y.[3], **Nykyruy L.I.**[3]

[1]*Ivano-Frankivsk national Medical University, Ivano-Frankivsk, Ukraine;*
[2]*Rszesow University, Rszesow, Poland;*
[3]*Vasyl Stefanyk Precarpathian National University, Ivano-Frankivsk, Ukraine*

The formation of ternary compounds based on binary PbTe leads to a disorder of the crystal structure, which causes an increase in thermal resistance and, consequently, an improvement in thermoelectric characteristics. One of the ternary compounds that has been actively studied in recent years is PbCdTe. Cadmium impurity has a weak effect on the electrical conductivity of lead telluride [1]. Accordingly, a solid solution of $Pb_{1-x}Cd_xTe$ can exhibit both n- and p-type conductivity. On the other hand, the introduction of Cd impurity into the base matrix of lead telluride increases the band gap compared to PbTe. Moreover, the bandgap increases with increasing Cd content [2]. Thus, several important effects are realized: improving the effective mass by changing the structure of energy zones; significant reduction of lattice thermal conductivity by ordering the crystal structure and the formation of micro- and nanodefects; reducing the effect of bipolar thermal conductivity by increasing the band gap.

Even more interesting is the study of $Pb_{1-x}Cd_xTe$ thin films. Inhomogeneities at the film-substrate interface improve the thermoelectric properties [3]. Due to the presence of a microstresses on the interface, numerous grains appeared, at the boundaries of which carriers or phonons are scattered.

This research investigates the thermoelectric characteristics (Seebeck coefficient, specific conductivity, Hall concentration of carriers, mobility of charge carriers) for a series of thin films of the ternary system $Pb_{0.9}Cd_{0.1}Te$: Pb (3 at.%.) in the region of room temperatures at which practical use as a thermoelectric material of a thin-film microthermogenerator. Analysis of the transport of charge carriers allows to determine the dominant types of scattering for them and, accordingly, to optimize the technological factors to obtain materials with improved thermoelectric properties. Establishing the relationship between the technology of film production and transport properties allows to obtain films with the most optimal thermoelectric parameters.

Studies of the composition and structure of the obtained thin films were used a scanning electron microscope (Tescan Vega3) equipped with energy dispersive X-ray spectroscopy Quantax (Bruker Nano GmbH, Germany). For each sample, SEM studies were performed at three different points, where the presence of defects or inclusions was visually observed. This was done in order to determine the presence of an excess of certain elements, to record and further recognize defects of various types. Using the EDS prefix, the quantitative content of elements in each investigated film was studied.

Thermoelectric characteristics (Seebeck coefficient S, specific conductivity σ, Hall carrier concentration p, charge carrier mobility μ) were measured in the temperature range (290-390) K by the 4-probe method in a constant magnetic field at the automated device DHM-1. The silver was deposited for forming Ohmic contact. The current through the samples was $\approx$ 1 mA. The magnetic field with induction B = 1.2 T directed perpendicular to the film plane [18]. Measurement error is no more than 5%.

SEM observations showed that the films have a granular structure with individual grain sizes of several tens of micrometers. Accordingly, in Fig. 2 shows SEM images of films of different thickness at a scale of 100 μm.

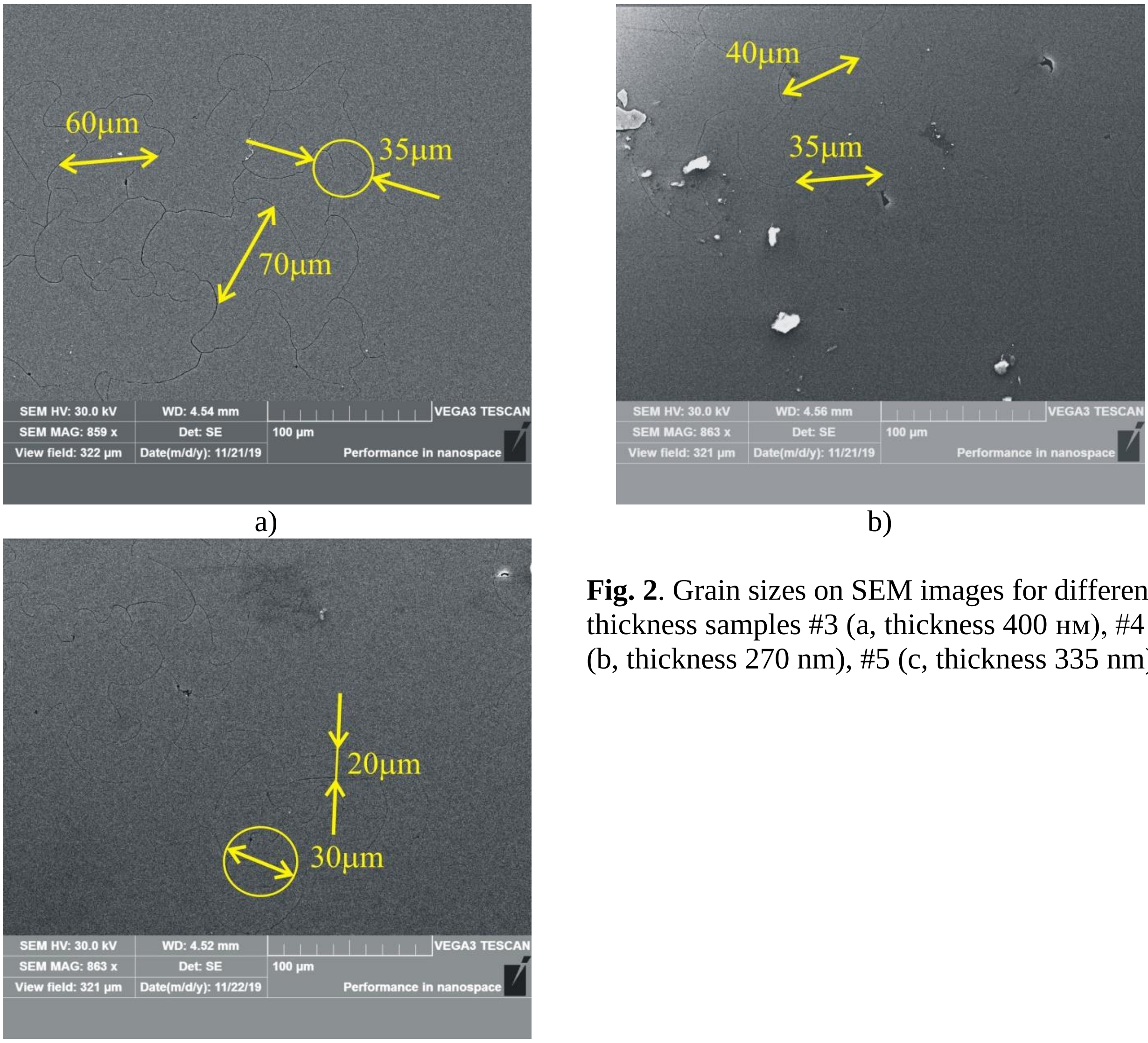

a)

b)

c)

Fig. 2. Grain sizes on SEM images for different thickness samples #3 (a, thickness 400 нм), #4 (b, thickness 270 nm), #5 (c, thickness 335 nm).

As it can be seen from Fig. 2, as the film thickness increases, the grain sizes decrease. The paper considered thin films with slightly different thicknesses (270 nm, 335 nm and 400 nm).

There is an important feature in the formation of grains from the growth of films. The thinnest films have the largest grain sizes. As the thickness increases, the grain size decreases (Fig. 2). The average grain size for the thinnest film is (60-70) microns. A slight increase in the film thickness (from 270 nm to 335 nm) causes a decrease in the average grain size to (35-40) nm. And for films with a thickness of 400 nm, the grain size is (20-25) nm. Another feature is that in thin films, along with large grains, there is a small number of small, within 15 µm (Fig. 2a). The increase in thickness leads to the fact that in the process of growth such small grains disappear (Fig. 2c), and grains of approximately the same size are formed.

The type of conductivity is different for the studied compositions: p-type for PbTe and n-type for PbCdTe. This is confirmed by measurements of the Seebeck coefficient S (fig. 7, c). Cadmium has a donor effect in PbTe [4]. And additional doping of Pb increases the concentration of electrons. In addition, the creation of the ternary compound $Pb_{1-x}Cd_xTe$ allows you to control the width of the band gap of the semiconductor. As the Cd content increases, the band gap increases. The authors of [5] give a theoretical value for the band gap at $x = 0.1$ $Eg = 0.4$ eV. Such changes significantly affect the electrical parameters (Fig. 7) of the investigated solid solution in comparison with binary PbTe.

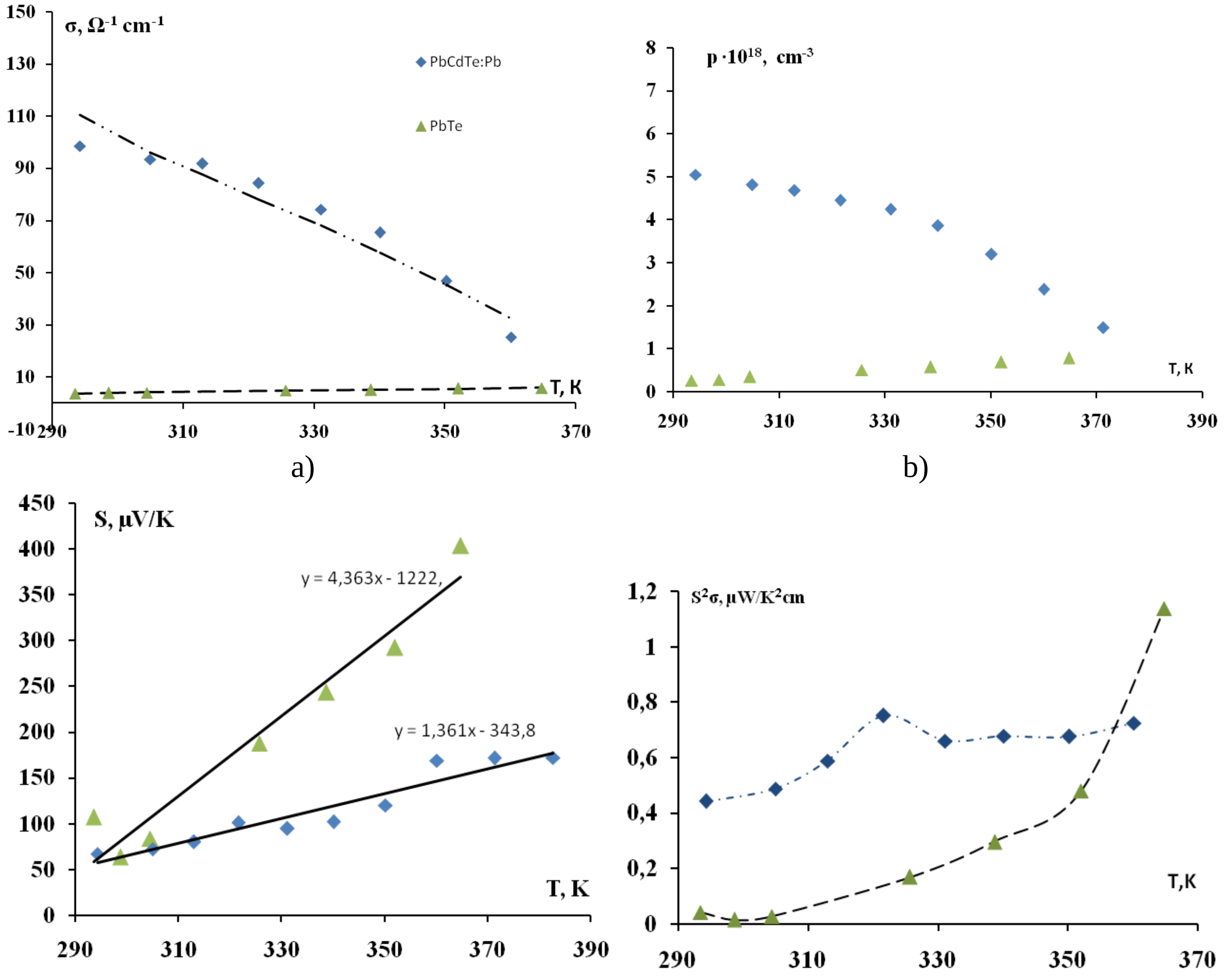

a) b)

c) d)

Fig. 7. Dependence of conductivity σ (a), Hall concentration p (b), Seebeck coefficient (c) and specific thermoelectric power S2σ (c) on temperature T for films of composition: ▲ - PbTe, ♦ - PbCdTe: Pb on fresh chips) mica-muscovite. Solid lines - calculation by formula (3), dashed lines - approximation by formula (2)

For the nondegenerate case, if the concentration, effective mass and scattering parameter r do not depend on temperature, then the Seebeck coefficient S is defined as

$$S = \frac{3}{2}\frac{k_B}{e}\ln \mathrm{T} + const, \quad \frac{3}{2}\frac{k_B}{e} = 129\,\text{мкВ}/К \qquad (1)$$

For degenerate statistics of charge carriers, thermo-EMF increases in proportion to temperature:

$$S = \frac{2\pi^{2/3}k_B^2 m^*(r+3/2)}{3^{5/3}e\hbar^2 p^{2/3}}\cdot \mathrm{T} + const. \qquad (2)$$

The carriers scattering in films has certain features. Typically, all scattering mechanisms that are important for bulk materials (scattering on acoustic and optical phonons, scattering on the short-range potential of vacancies and on their Coulomb potential) should be taken into account. However, the effects associated with surface contribution and scattering on the grains of boundaries, as well as the effects characteristic of multicomponent compounds, become important [6].

To calculate the effective mass of carriers (m*) was used a convenient value marked as weighted mobility, which approximates the exact model of the free Drude - Sommerfeld electron, which was proposed in [7]:

$$\mu_w = \frac{3h^3\sigma}{8\pi e(2m_e k_0 T)^{3/2}}\left[\frac{exp\left[\frac{|S|}{k_0/e}-2\right]}{1+exp\left[-5\left(\frac{|S|}{k_0/e}-1\right)\right]} + \frac{\frac{3}{\pi^2}\frac{|S|}{k_0/e}}{1+exp\left[5\left(\frac{|S|}{k_0/e}-1\right)\right]}\right]. \quad (3)$$

Acknowledgements. This research was supported by the MES of Ukraine in framework of Ukrainian-Belarus project (the state registration number 0119U103330).

1. Sealy B. J. and Crocker A. J, J. Mater. Sci. 8, 1731 (1973).
2. Szot, M., et el., 2020. Two-valence band electron and heat transport in monocrystalline PbTe-CdTe solid solutions with Cd content up to 10 atomic percent. Physical Review Materials, 4(4), p.044605.
3. Venkatasubramanian, R., Siivola, E., Colpitts, T., & O'quinn, B. (2001). Thin-film thermoelectric devices with high room-temperature figures of merit. Nature, 413(6856), 597-602.
4. Hellmut Fritzche, Devid Adler. Localization and Metal-Insulator Transitions, Plenum Press, New York and London, 2012 p. - 533 стор.
5. Bukała, M., Sankowski, P., Buczko, R., & Kacman, P. (2012). Structural and electronic properties of $Pb_{1-x}Cd_xTe$ and $Pb_{1-x}Mn_xTe$ ternary alloys. *Physical Review B, 86*(8), 085205.
6. Dzumedzey, R. (2019). Scattering of Charge Carriers in Thin Films PbTe:Bi. Physics and Chemistry of Solid State, 20(2), 171-174.
7. Jeffrey Snyder G., Snyder Alemayouh H., Wood Maxwell, Gurunathan Ramya, Snyder Berhanu H., and Niu Changning, Weighted Mobility, Adv. Mater. 2020, 2001537.

INVESTIGATION OF LASER INDUCED EFFECTS IN As-Se GLASSES AND FILMS BASED ON THEM BY NANO AND MICROINDENTATION METHODS

Lofaj F.[1], Shylenko O.[2], Bilanych V.S.[3], Bilanych B.V.[3], Komanicky V.[2], Feher A.[2], Rizak V.M.[3]

[1]Institute of Materials Research of SAS, Watsonova 47, 040 01 Košice, Slovakia
[2] Faculty of Science, Safarik University, Park Angelinum 9, 04001 Košice, Slovakia
[3]Uzhhorod National University, Pidhirna 46, 88000 Uzhgorod, Ukraine

Interesting unique photoinduced phenomena are observed in chalcogenide glassy materials, thanks to which the possibilities of their practical application are expanded. Studies of such phenomena are also of scientific interest, since they provide information on the fundamental properties that appear during laser irradiation of these materials in the region of their intrinsic absorption edge.

These properties are usually studied in chalcogenide films. However, studies of the photo- (laser) -induced properties of bulk chalcogenide glasses are of interest. Recently, due to the discovery of the photoplastic effect, polarization-dependent photoinduced properties, and mass transport in chalcogenide films the As-Se system have been intensively studied.

This paper presents the results of studies of photoinduced changes in the mechanical properties of As_xSe_{100-x} glasses and films based on them by micro - and nanoindentation methods. The study of microhardness in the “in situ” mode was carried out using a PMT 3 microhardness tester. Laser irradiation (650 nm, ~ 100 mW) of the glasses was carried out from above through the base of the Vickers indenter.

Thus, irradiation region completely covered the contact area when the indenter was lowered onto the glass surface. Figure 1 shows the images of the Vickers indenter imprints in some investigated As_xSe_{100-x} glasses in the dark and at 100 s of laser irradiation. Figure 1 shows that giant decreases in hardness (photoplastic effect) are observed in glasses with a high concentration of arsenic with a maximum changes in As_4Se_{96} glass. The photoinduced changes in hardness decrease with increasing As concentration.

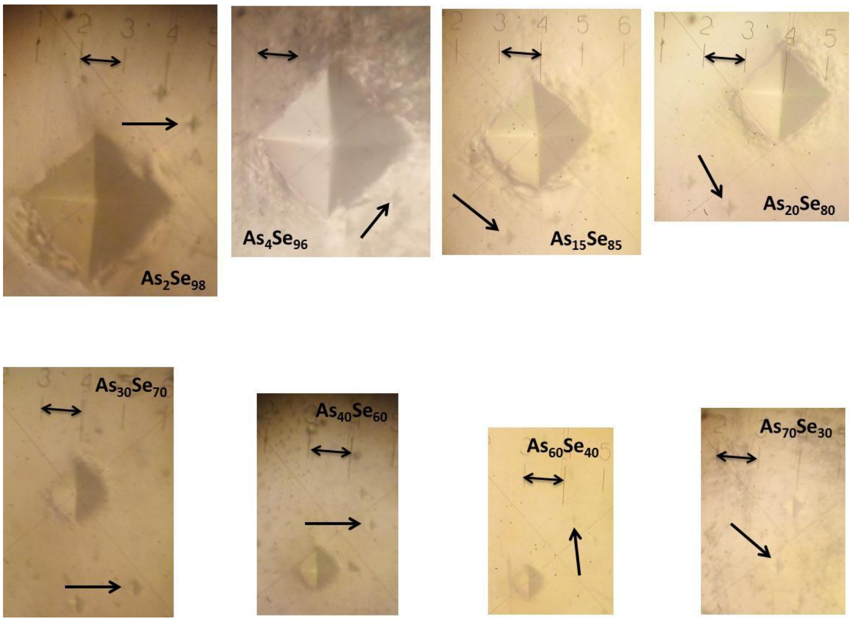

Picture 1. Images of Vickers indenter imprints (on the same scale) without laser irradiation (near the arrow-pointer) and during irradiation for 100 s.

Figure 2. shows the concentration dependence of the microhardness of As_xSe_{100-x} glasses in the dark and under laser irradiation for 10 s and 100 s, as well as the relative change in microhardness under laser irradiation. It is seen that glasses with a high selenium concentration have the minimum values of microhardness. Moreover, significant photoinduced changes in microhardness are observed with the addition of 2 at.% arsenic in selenium.

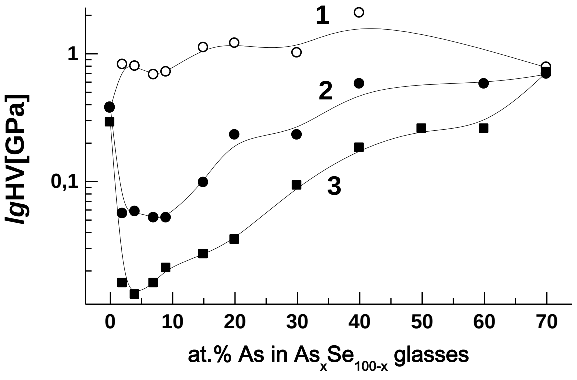

Figure 2*a*. Concentration dependence of the microhardness of As$_x$Se$_{100-x}$ glasses: 1 - indentation time 10 s without laser irradiation, 2 - indentation time 10 s with laser irradiation through the indenter, 3 - 100 s exposure with laser irradiation through the indenter.

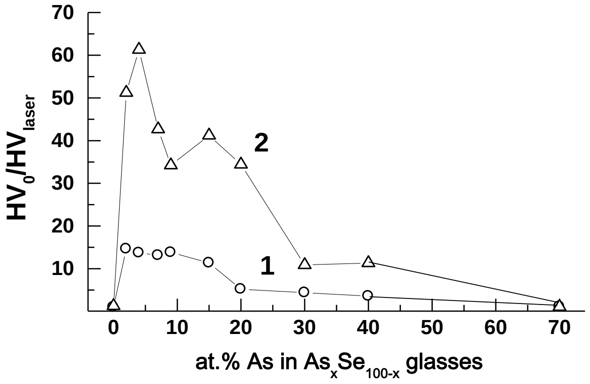

Figure 2*b*. Concentration dependence of the relative change in the microhardness of As$_x$Se$_{100-x}$ glasses under laser irradiation: 1 - indentation time 10 s with laser irradiation through an indenter, 2 - exposure 100 s with laser irradiation through an indenter.

The features of the photoinduced dynamics of microhardness correlate with the concentration regions of extreme changes in the physical properties of selenium-enriched As$_x$Se$_{100-x}$ glasses, including the assumptions about a topological structural transition at x = 4 at.% As. The revealed features of the laser-induced changes in the mechanical properties of As$_x$Se$_{100-x}$ glasses also correlate with the previously discovered electron-induced effects.

The effects of laser irradiation on hardness and Young's modulus of the current As$_x$Se$_{100-x}$ glasses were studied also by nanoindentation (depth sensing indentation) technique. The load – indentation depth curves exhibited size effects that may be attributed to different deformation mechanisms occurring under the indenter under different loads due to changes of their structure. This assumption was confirmed with the AFM-scans of indents on the surface of the studied glasses and films of the As-Se system.

Acknowledgments

This work has been supported the grant of the Slovak Research and Development Agency under the contract No. APVV-17-0059.

BACTERIORHODOPSIN AS A BIOLOGICAL MATERIAL FOR OPTICAL RECORDING, PROCESSING AND SECURITY INFORMATION

Korposh S. O.[1], Trikur I. I.[2], Tsoma I. Y.[2], Sichka M.Y.[2], Rizak V. M.[2]

[1]*The University of Nottingham, United Kingdom, University Park, Nottingham NG7 2RD;*
[2]*Uzhgorod National University, Ukraine, 88000, Uzhhorod, Voloshina Str., 54;*

Photochromic proteins are very rare in nature, however, these several proteins, due to their unique properties, play a key role in photosynthesis and visual perception. Even among these complex and highly specialized proteins, bacteriorhodopsin (BR) stands out for its unique properties, making it a promising material for a wide range of applications [1, 2]. The main advantages of bacteriorhodopsin include: high thermal and photochemical stabilities, robustness to degeneration by environmental perturbations, high quantum efficiency of converting light into a charge, wide range absorption of visible light, extremely large optical nonlinearities, low cost, environmental friendliness of production and the existence of genetic variants with enhanced spectral properties for specific device applications [3–5].

One of the main directions of the applied use of materials based on BR is information systems. The properties of bacteriorhodopsin make it possible to effectively use it for optical recording, processing and protection of information. For long-term data storage, the recording density is an important parameter. Theoretically every 5 nm a binary information could be recorded in a BR layer by switching a single BR molecule or a BR trimer, that would mean about 200 000 lines/mm resolution. In addition, various methods of 3-D information storage using materials based on BR are being actively investigated [4, 6, 7].

The astonishingly high reversibility of BR can be used in optical data processing system[1,2,4]. Here the number of write-read-erase cycles required is much higher. For example, in real-time image processing at video frame rate, about 10^6 write-read-erase cycles for a single day of operation are required [4].

The properties of BR can also be effectively used in the field of information security. The color change of BR-inks can be checked without any expensive equipment. Reversible color change under illumination can be used for visual identification and copy protection [8]. Due to the availability of genetically enhanced variants of BR, which show a significantly improved light sensitivity, color changes in areas printed with BR-based inks can be achieved even at low light exposures. The two-photon-absorption-dependent conversion of BR allows permanent photo-anisotropy to be induced in BR films, which may be used—independently from and in addition to the reversible photochromism — for data storage and encription [6]. BR film containing data recorded with a linearly polarized laser beam allows direct reading of polarization data with only one polarizer. The display of a conventional mobile phone can be used as a linearly polarized light source for reading secured data from a BR film. This feature of the BR is very important for information protection, since the polarization features can be visually checked without special optics.[7]

Bacteriorhodopsin is a test example of a new approach in nanotechnology, in which biotechnology and genetic engineering are used to create a material with unique properties. The BR molecule combines several properties at the molecular level, making it a unique material for optical data storage and information processing, as well as for security applications.

1. Bio-nano hybrid materials based on bacteriorhodopsin potential applications and future strategies B. Mahyad, S. Janfaza, E. S. Hosseini // Adv Colloid Interface Sci., - 2015, - Vol. 225. - P. 194–202.
2. A Review on bacteriorhodopsin-based bioelectronic devices Y. T. Li, Y. Tian, H. Tian, T. Tu, G.-Y. Gou, Q. Wang, Y. C. Qiao, Y. Yang, T. L. Ren // Sensors (Basel), - 2018, - Vol. 18(5). 1368

3. Stabilization of the membrane protein bacteriorhodopsin to 140 °C in two-dimensional films Y Shen, C. R. Safinya, K. S. Liang, A. F. Ruppert, K. J. Rothschild // Nature, - 1993, - Vol. 366. P. 48–50.
4. Bacteriorhodopsin as a photochromic retinal protein for optical memories N. Hampp // Chem. Rev., - 2000, - Vol. 100(5). -P. 1755–1776.
5. Study of nonlinear optical properties of multilayer Langmuir–Blodgett films containing bacteriorhodopsin Yu. O. Barmenkov, A. V. Kir'yanov, A. N. Starodumov, I. A. Maslyanitsyn, V. D. Shigorin, H. Lemmetyinen // Photochemistry and Photobiology, - 2000. - Vol. 72(2). - P. 151-154.
6. Biomolecular Optical Data Storage and Data Encryption T. Fischer, M. Neebe, T. Juchem, N. A. Hampp // IEEE Transactions on NanoBioscience, - 2003. - Vol. 2(1). - P. 1-5.
7. Two-photon polarization data storage in bacteriorhodopsin films and its potential use in security applications M Imhof, D Rhinow, N Hampp // Appl. Phys. Lett. - 2014. - Vol. 104.
8. Printing Inks Containing the Photochromic Protein Bacteriorhodopsin N. Hampp, M. Neebe, A. Seitz // Proceedings of SPIE, 2000. - Vol. 3973.

SCAPS SIMULATION OF ZnO/CdS/CdTe/CuO HETEROSTRUCTURE FOR PHOTOVOLTAIC APPLICATION

Zapukhlyak Z.R.[1], Rubish V.M.[2], Wisz G.[3], Yavorskyi R.S.[1], Nykyruy L.I.[1]

[1]Vasyl Stefanyk Precarpathian National University, Ivano-Frankivsk, Ukraine
[2]Uzhgorod Laboratory of Institute for Information Recording of NAS of Ukraine, Uzhgorod, Ukraine
[3]Rszesow University, Rszesow, Poland

By the beginning of the 21st century, the market share of silicon batteries was over 99.8%, and over the last 20 years it has decreased by 22.8%, and continues to decline rapidly. Instead, 2nd generation photovoltaic converters based on the thin film technologies appeared, which have already demonstrated competitiveness with silicon analogues. Thin-film solar panels have a lower weight of ~ 20-25%, increased efficiency and much better functionality.

The most promising materials on the basis of which it is possible to obtain effective thin-film photovoltaic cells are compounds II-VI (based on CdTe, CdS) [1]. To improve the efficiency of thin-film systems, heterostructures are created on the basis of these materials [2]. Unlike ideal but expensive CIGS models, cadmium telluride-based hybrid thin films are much cheaper, but no less reliable and durable.

CdTe is an active part of the solar cell, where the largest generation and accumulation of carriers occurs. The SCAPS-1D software package was used for J-V characteristics simulation of CdS/CdTe solar cells. The main screen that appears after SCAPS-1D is started is shown in Fig. 1. The measurements were simulated in light under the solar spectrum with an incident solar power of P=1000 W/m^2 at temperature of 300 K.

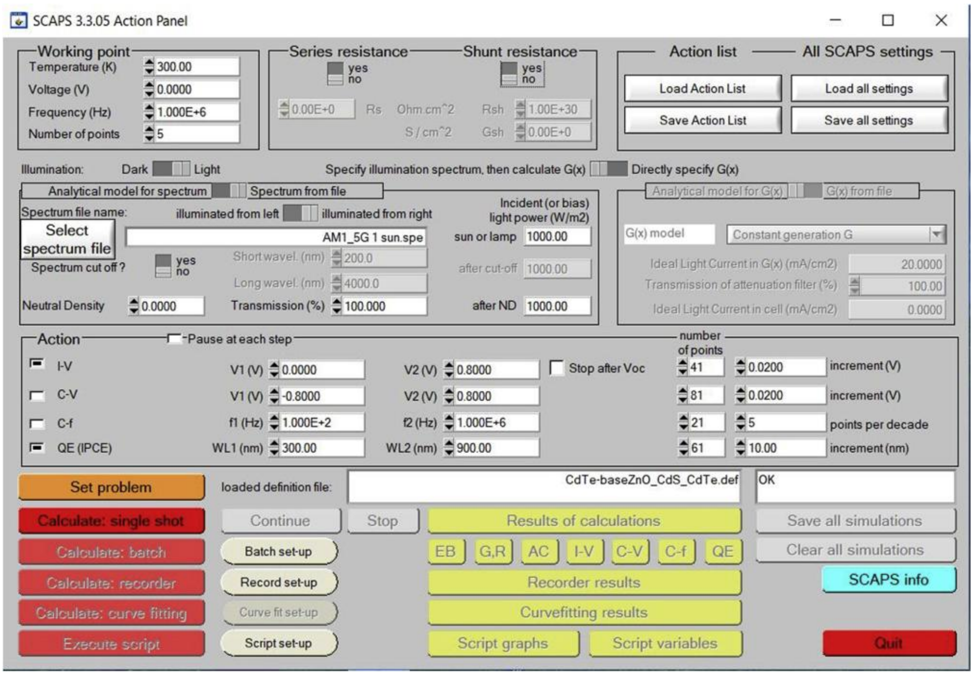

SCAPS 3.3.05 Action Panel

Working point
Temperature (K) 300.00
Voltage (V) 0.0000
Frequency (Hz) 1.000E+6
Number of points 5

Series resistance: Rs 0.00E+0 Ohm.cm^2
Shunt resistance: Rsh 1.00E+30, Gsh 0.00E+0 S/cm^2

Illumination: Dark / Light
Specify illumination spectrum, then calculate G(x) / Directly specify G(x)
Analytical model for spectrum / Spectrum from file
Spectrum file name: AM1_5G 1 sun.spe
illuminated from left / illuminated from right
Incident (or bias) light power (W/m2): sun or lamp 1000.00; after cut-off 1000.00; after ND 1000.00
Spectrum cut off? yes / no
Short wavel. (nm) 200.0
Long wavel. (nm) 4000.0
Neutral Density 0.0000
Transmission (%) 100.000

Analytical model for G(x) / G(x) from file
G(x) model: Constant generation G
Ideal Light Current in G(x) (mA/cm2) 20.0000
Transmission of attenuation filter (%) 100.00
Ideal Light Current in cell (mA/cm2) 0.0000

Action — ☐ Pause at each step

Action						number of points		
☑ I-V	V1 (V)	0.0000	V2 (V)	0.8000	☐ Stop after Voc	41	0.0200	increment (V)
☐ C-V	V1 (V)	-0.8000	V2 (V)	0.8000		81	0.0200	increment (V)
☐ C-f	f1 (Hz)	1.000E+2	f2 (Hz)	1.000E+6		21	5	points per decade
☑ QE (IPCE)	WL1 (nm)	300.00	WL2 (nm)	900.00		61	10.00	increment (nm)

loaded definition file: CdTe-baseZnO_CdS_CdTe.def
OK

Fig.1. SCAPS start-up panel.

The J-V dependence is the most common tool for solar cell characterizing. In addition to simulated J-V curves SCAPS shows simultaneously the table of values of Voc, Jsc, FF and efficiency at various thicknesses of the variable layer while the thicknesses of the other layers remain unchanged. In particular, the FF was obtained by the equation:

$$FF = \frac{I_{max} \cdot V_{max}}{I_{sc} \cdot V_{oc}} \quad (1)$$

where I_{max} and V_{max} – are the photocurrent and the photovoltage for maximum power output, respectively, and I_{SC} is the short-circuit photocurrent.

The η parameter has been determined by relation:

$$\eta = \frac{I_{sc} \cdot V_{oc} \cdot FF}{P_{in}} \tag{2}$$

The authors developed a simple, cheap and reproducible technology for obtaining thin-film heterostructures based on CdTe with a given surface morphology during open evaporation in vacuum, which allows to obtain homogeneity of the base layer for better absorption of solar radiation and contributes to their low cost [3, 4]. The critical dimensions (thicknesses) of individual layers of the heterostructure were substantiated, the simulations were performed and a wide range of optical properties were investigated [5]. It is shown that for the deposited CdS/CdTe heterostructure on glass substrate it is possible to obtain an efficiency of 15.8%.

In [6] the authors tried to improve the efficiency of the CdS/CdTe heterostructure on glass substrate by introducing a conductive ZnO layer, performed simulations for ZnO/CdS/CdTe heterostructure using SCAPS programm and determined the best efficiency value of 19.22% (Fig.2).

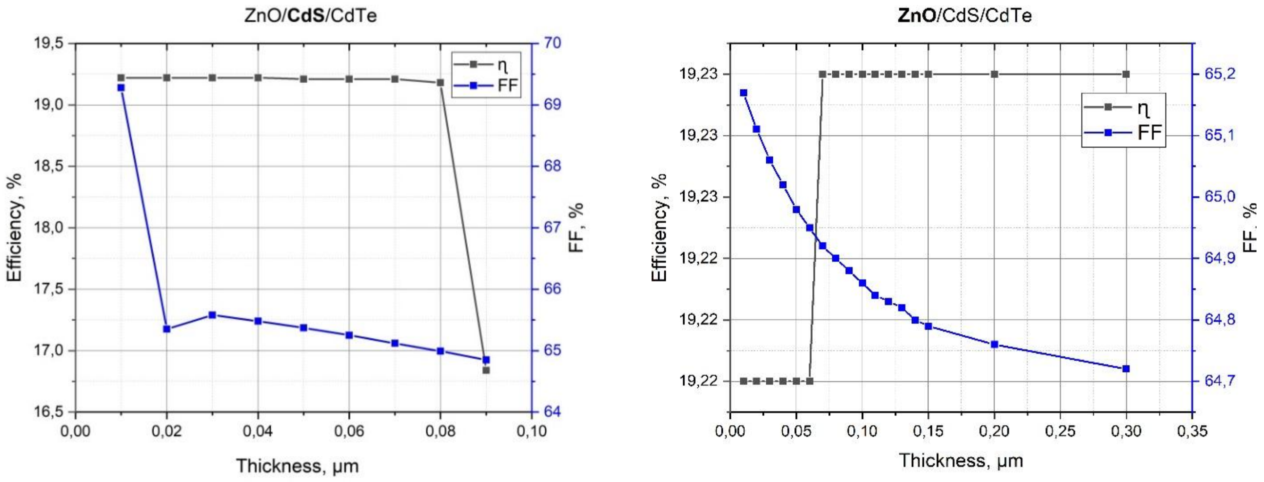

a) b)

Fig.2. Variation of the efficiency *η* and *FF* of ZnO/CdS/CdTe heterojunction as a function of "window layer" thickness:
(a) CdS (d_{CdTe} = 4 μm, d_{ZnO} = 10 nm); (b) ZnO (d_{CdTe} = 4 μm, d_{CdS} = 100 nm).

Considering thin films are relatively new systems, their study can offer much wider opportunities for technological improvement of photovoltaic energy converters. According to the analysis of current literature data, the authors checked whether the transparent conductive ZnO layer really significantly affects the efficiency of the final heterostructure using the same simulation program, and tried to increase the efficiency of ZnO/CdS/CdTe heterostructure by introducing a CuO layer and performing the appropriate modeling on glass substrates, in order to choose the optimal thickness of this layer.

As soon as modeling the ZnO / CdS / CdTe / CuO heterostructure using the program was performed, the authors made a number of significant conclusions and determined the best value of efficiency for this heterostructure, which is 21.27% and is shown in Fig. 3.

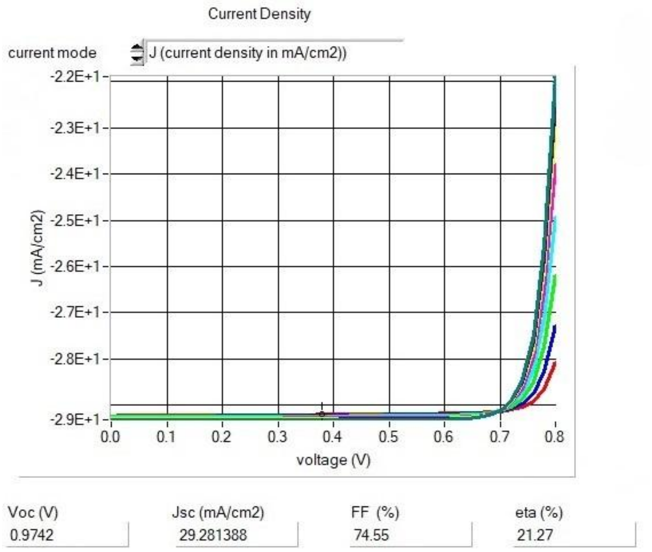

current mode: J (current density in mA/cm2))

Voc (V): 0.9742

Jsc (mA/cm2): 29.281388

FF (%): 74.55

eta (%): 21.27

Fig.3. The results of J-V dependence modeling in SCAPS program for ZnO/CdS/CdTe/CuO heterostructure

1. Ghosh, B.K., Saad, I., Teo, K.T.K. and Ghosh, S.K., 2020. mcSi and CdTe solar photovoltaic challenges: Pathways to progress. Optik, p.164278.
2. Kumar, S.G. and Rao, K.K., 2014. Physics and chemistry of CdTe/CdS thin film heterojunction photovoltaic devices: fundamental and critical aspects. Energy & Environmental Science, 7(1), pp.45-102.
3. Yavorskyi, R. Et el. 2019. Structural and optical properties of cadmium telluride obtained by physical vapor deposition technique. Applied Nanoscience, 9(5), pp.715-724.
4. R. Yavorskyi, Features of optical properties of high stable CdTe photovoltaic absorber layer. Physics and Chemistry of Solid State, 2020, 21(2), 243-253. (Scopus, Web of Science) https://doi.org/10.15330/pcss.21.2.243-253.
5. Nykyruy, L.I., Yavorskyi, R.S., Zapukhlyak, Z.R., Wisz, G. and Potera, P., 2019. Evaluation of CdS/CdTe thin film solar cells: SCAPS thickness simulation and analysis of optical properties. Optical Materials, 92, pp.319-329.
6. Nykyrui, L., Saliy, Y., Yavorskyi, R., Yavorskyi, Y., Schenderovsky, V., Wisz, G., & Górny, S. (2017, September). CdTe vapor phase condensates on (100) Si and glass for solar cells. In *2017 IEEE 7th International Conference Nanomaterials: Application & Properties (NAP)* (pp. 01PCSI26-1). IEEE.

STUDIES OF As-Se GLASSES AND FILMS BASED ON THEM BY DIFFERENTIAL SCANNING CALORIMETRY

Csach K.[1], Bilanych V.S.[2], Jurikova A.[1], Miskuf J.[1], Bilanych V.V.[2], Rizak V.M.[2]

[1]*Institute of Experimental Physics of SAS, Watsonova 47, 040 01 Košice, Slovak Republic*
[2]*Uzhhorod National University, Pidhirna 46, 88000 Uzhgorod, Ukraine*

Chalcogenide glasses have a wide range of properties which are important for their practical applications. With changing the chemical composition in the As-Se system, can be obtained glasses with different values of physical parameters, which change non-monotonically depending on the concentration. This paper presents the results of studies of thermal effects in glasses and films of the As-Se system in a wide temperature range by the method of differential scanning calorimetry (DSC).

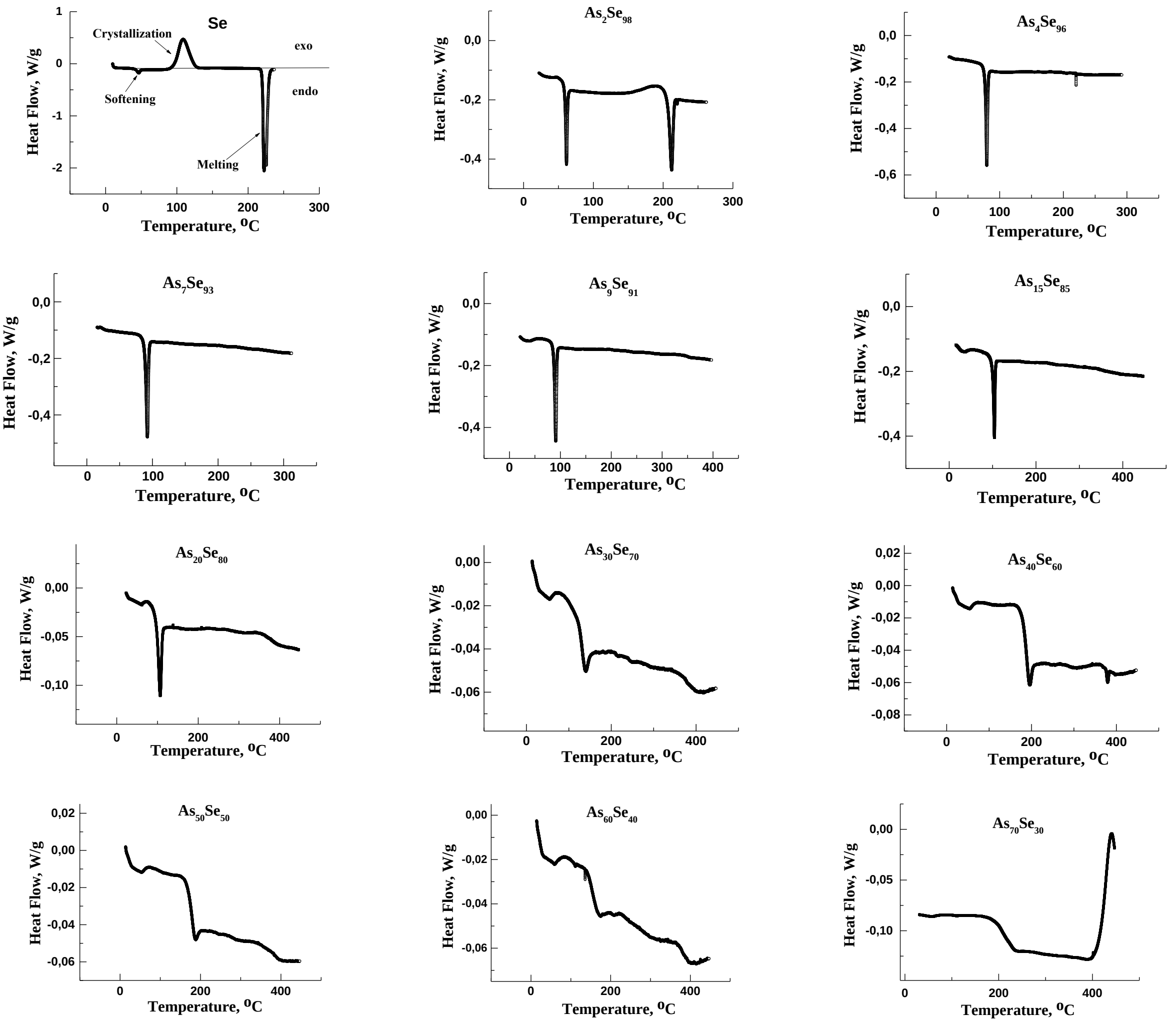

Figure 1. DSC curves for various As_xSe_{100-x} glasses at a heating rate of 10 K / min.

For each concentration *x*, 4 samples were prepared in one cycle of manufacturing As_xSe_{100-x} glass powders and films. In DSC measurements, separate samples from the same batch were used for each heating rate. The measurement mode consisted of three cycles: heating at a rate V_1 from 20° C to T_g + 70 °C and cooling at a rate of 30 K/min. in one cycle. (V_1 = 1 K/min, 2 K/min, 4 K/min, 8 K/min, 13 K/min). The thermodynamic properties of As_xSe_{100-x} samples were studied using a TA Instrument Q2000 differential scanning calorimeter. TA Instruments Universal Analysis

2000 software was used to process the results of DSC studies and determine the glass transition temperature, softening, temperature range and enthalpy of the thermal process. The temperature and energy calibrations of the Q2000 instrument were carried out with melts of pure metals In and Sn with known exact values of the temperature and enthalpy of melting. The determination of the activation energy during softening was carried out by the temperature shift of the maximum of the endothermic effect of softening at different heating rates.

The determination of the enthalpy of softening was carried out according to the area of the endothermic effect during glass softening. (Figure 2.)

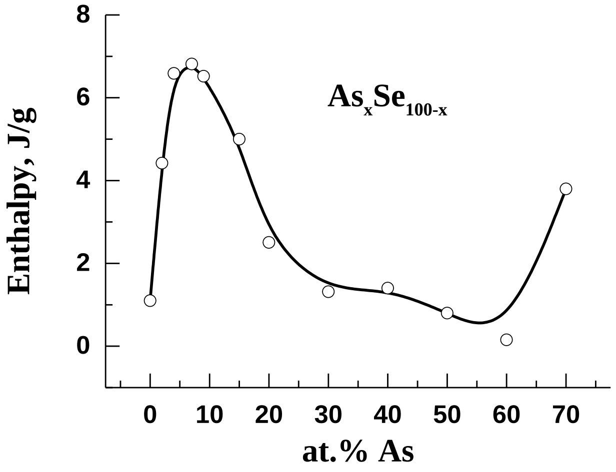

Figure 2. Enthalpy of glass softening As_xSe_{100-x}.

As can be seen from Figure 1. DSC curves show thermal effects associated with glass softening, crystallization, and melting. Among the studied glasses in the range of 20 °C - 400 °C, the exothermic effects of crystallization are seen in the DSC curves for Se and $As_{70}Se_{30}$. With the addition of 2 at.% As in Se, the crystallization exo-process is no longer present. The enthalpy of softening (first heating) has a maximum near the As_7Se_{93} composition. The minimum enthalpy value is observed for the $As_{60}Se_{40}$ composition. In the second and third cycles of DSC measurements at the same heating rates, the activation energies during softening for glasses with a high selenium content increase significantly. The maximum increase in the activation energy is observed for As_4Se_{96} glass. The thermal effects in As_xSe_{100-x} glasses and films of similar compositions are compared.

[1] *This work was supported by the Slovak Academy of Sciences - grant VEGA No. 02/0039/18.*

APPLICATION OF THE PHOTOELECTRON SPECTROSCOPY TO STUDY THE ORGANIC MATERIALS PROPERTIES: ADENINE MOLECULES AND AMYLOID FIBERS

Popovych N.[1], Gažova Z.[2], Rizak V.M.[1]

[1]Uzhhorod National University, Pidhirna St. 46, 88000 Uzhhorod, Ukraine
[2]Institute of Experimental Physics, Slovak Academy of Sciences, Watsonova 47, SK-04001 Košice, Slovakia

Important components of nucleic acids are of nitrogen bases molecules, derivatives of pyrimidine (cytosine, thymine and uracil) and purines (adenine and guanine). Elementary biomolecules (including adenine), a constituent blocks of nucleic acids, are also the building blocks of the genetic code. These molecules could be undergoing transformations in response to the environmental variations, like UV and thermal treatment. Because of complicated structure of biomolecules it is relevant to investigate interaction of DNA bases and amino acids with surfaces considering a model system in which the simplest biomolecule adsorbs on a nanostructured surfaces under ultrahigh vacuum (UHV) conditions. With such approach, we can explore the nature, geometry and electronic structure of the biointerface and provide fundamental knowledge that can use in further development of real applications.

The adenine biomolecules interaction with the polycrystalline TiO_x surface by photoelectron spectroscopy (XPS and SRPES) was investigate. Analysis of the measured XPS and SRPES spectra adenine film on TiO_x we can see that N 1s core level spectra of adenine film consist of the two components at 399.2 eV and 400.6 eV binding energies, which can be attributed to nitrogen with unsaturated chemical bonds (-N =) and (NH + NH2), respectively. C 1s core level spectra of this film contain two components at E_b=285.3 eV and 286.8 eV, which can be attributed to carbon in the CC/CH groups and a CN-carbon bonds of the adenine rings, respectively.

In addition, the adsorption of adenine was studied on the (110) termination of rutile titanium dioxide in order to understand the thermal stability and gross structural parameters of the interaction between a strongly polar adsorbate and a highly corrugated transition metal oxide surface. Near-edge X-ray absorption fine structure (NEXAFS), Synchrotron Radiation Photoelectron Spectroscopy (SRPES), temperature programmed XPS and temperature programmed desorption indicated the growth of a room temperature stable multilayer, which could only be removed by annealing to 100˚C. The remaining first layer was remarkably robust, surviving annealing up to 250˚C before undergoing N–H bond scission. This discovery, alongside the deprotonation of one of the first layer's purine or amino nitrogen atoms at room temperature, suggests that the adenine molecules in the first layer bind to the undercoordinated surface Ti atoms. The NEXAFS results indicate that the molecule binds to the TiO_2(110) surface at a sharper angle when there is less surface coverage.

The misfolding of amyloid peptides is associated with a number of human diseases such as type II diabetes mellitus (T2DM), Alzheimer's disease (AD), and Parkinson's disease (PD) [1–3].

Metal ions play a critical role in human islet amyloid polypeptide (hIAPP) aggregation, which is believed to be closely associated with β-cell death in type II diabetes. The effect of Al3+ on the aggregation of hIAPP (11-28) was studied by several different experimental approaches.

X-ray photoelectron spectroscopy measurement indicated that Al ions might form chemical bonds with neighboring atoms and destroy the secondary structures of the protein. This studies could deepen the understanding of the role of metal ions in the aggregation of amyloid peptides.

Last investigations showed that Al3+ had strong inhibiting effects on the peptide self-assembly behavior. It could modulate the final fibrillar structure as well as aggregation kinetics. XPS data suggested that Al ions could interact with hIAPP (11-28) and might destroy the secondary structures of hIAPP (11-28). In several neurodegenerative diseases, especially AD, spherical aggregates are often found in tissue deposits. Therefore, Al ions may play an important role in fibrillar deposition in vivo. In contrast, Zn2+ could accelerate hIAPP (11-28) fibrillation in some way, we speculate that it may be caused by the fact that Zn2+ has a strong affinity for the imidaziole group of the histidine residue [4]. XPS study may provide an insight into the role of metal ions in the aggregation of amyloid peptides.

1. Dobson C.M. Principles of protein folding, misfolding and aggregation. // Semin. Cell Dev. Biol., 2004, 15: 3–16.
2. Ashraf G. M., Greig N. H., Khan T. A., Hassan I., Tabrez S., Shakil S., Sheikh I.A., et al. Protein misfolding and aggregation in Alzheimer’s disease and type 2 diabetes mellitus. // CNS Neurol. Disord. Drug Targets, 2014, 13: 1280–1293.
3. Detoma A. S., Salamekh S., Ramamoorthy A., Lim M. H. Misfolded proteins in Alzheimer’s disease and type II diabetes. // Chem. Soc. Rev., 2012, 41: 608–621.
4. Brender J.R., Hartman K., Nanga R.P.R., Popovych N., Bea R.D., Vivekanandan S., Marsh E.N.G., et al. Role of zinc in human islet amyloid polypeptide aggregation. // J. Am. Chem. Soc., 2010, 132: 8973–8983.

CONTENT

PLENARY

ORAL

POSTERS

PHOTOLUMINESCENT AND STRUCTURAL PROPERTIES OF THIN ZnO FILMS DOPED WITH RARE EARTH METALS

MASS SPECTROMETRY STUDY OF CLUSTERS FORMATION BETWEEN DIMETHYL SULFOXID AND ANTIBIOTICS

OPTICAL PROPERTIES OF X-RAY IRRADIATED $(Ga_{0.4}In_{0.6})_2Se_3$ FILMS

X-RAY AND FESEM STUDY OF MERCURY MODIFIED CRYSTALLIZED SELENIUM FILMS

ELECTRICAL CONDUCTIVITY OF SUPERIONIC CERAMIC BASED ON Ag_7SiS_5I NANOPOWDER

USING MECHANICAL ALLOYING FOR MAX PHASES FORMATION AS PRECURSORS OF GRAPHENE-LIKE CARBIDES OF MXENES TYPE

MODEL CALCULATIONS OF THE LAWS OF DISPERSION OF THE PHONON SPECTRUM OF $BaTiO_3$ CRYSTALS WITH PARTIAL INHABITANCE OF DIFFERENT CRYSTALLOGRAPHIC POSITIONS

INFLUENCE OF MONOMER STRUCTURES ON THE MORPHOLOGIES AND OPTICAL PROPERTIES OF J-AGGREGATES

COOLING OF SUPERHEATED SURFACES BY NANOFLUIDS AND IT SIMULATION BY CFD.

MODIFICATION OF TEXTILE MATERIALS FOR MEDICAL PURPOSE BY NATURAL NANOTUBES

CRIOCHEMICAL SYNTHESIS OF $Ni_XZn_{1-X}Fe_2O_4$ NANOPARTICLES AND STUDY OF THEIR PROPERTIES

FORMATION OF SURFACE RELIEF GRATINGS IN AMORPHOUS As-Se FILMS BY POLARIZATION HOLOGRAPHY

Наукове видання

МАТЕРІАЛИ 6-ї МІЖНАРОДНОЇ КОНФЕРЕНЦІЇ «КЛАСТЕРНІ ТА НАНОСТРУКТУРНІ МАТЕРІАЛИ »

(м. Ужгород, 5-9 жовтня 2020 року)

МАТЕРІАЛИ 6-ї МІЖНАРОДНОЇ КОНФЕРЕНЦІЇ «КЛАСТЕРНІ ТА НАНОСТРУКТУРНІ МАТЕРІАЛИ» (м. Ужгород, 5-6 жовтня 2020 року) – Ужгород, 2020. – 374 с.
ISBN 978-966-02-9366-3

Наведено основний зміст доповідей за результатами фундаментальних та прикладних науково-дослідних робот з актуальних питань в області наноструктурних систем, наноматеріалів та нанотехнологій. Головну увагу приділено розгляду проблем нанофізики та наноелектроніки, електронній і атомній будові кластерних та наноструктурних матеріалів, аморфних сплавів, апатитоподібних біосистем, колоїдних нанорозмірних систем, наноструктурних плівок та покриттів, дослідженню їх фізико-хімічних властивостей. Представлено результати досліджень в області фізико-хімії поверхневих явищ, супрамолекулярної хімії, синтезу наночастинок, наноструктур і багатофункціональних наноструктурних матеріалів. Відображено особливості діагностики наносистем.

УДК 536:669
ББК 34